



Faculty
of Science

Palacký University
Olomouc

Department of Physical Chemistry
Habilitation Thesis

**Nanostructures and nanohybrids based on
TiO₂ and α -Fe₂O₃ for photocatalytic and
photoelectrochemical applications**

**(Nanostruktury a nanohybridy na bázi TiO₂ a α -Fe₂O₃ pro
fotokatalytické a fotoelektrochemické aplikace)**

Olomouc 2019

Ing. Štěpán Kment, Ph.D.

Acknowledgements

Above all, I would like to thank to my family, to my wife Hana and daughters Marie and Anna, for they love, endless support, and patience. This habilitation thesis is dedicated to them.

I would also like to sincerely thank my colleagues who have been valuable assets to various areas of my scientific life.

Table of Content

1. Introduction.....	1
2. Renewable energy based on photocatalytic and PEC processes [A1].....	4
3. Properties of TiO₂ and α-Fe₂O₃ photoanodes.....	8
4. Nanostructuring of the photocatalytic materials.....	11
5. Plasma assisted deposition methods for the preparation of thin films and nanostructures.....	13
6. Photoelectrochemically active nanostructures based on TiO₂.....	17
6.1. <i>1D nanostructuring of the TiO₂ photoanodes [A2]</i>	<i>17</i>
6.2. <i>Correlation between the properties of magnetron sputtered titanium films and TiO₂ nanotubes after their transformation by electrochemical anodization[A3]</i>	<i>21</i>
6.3. <i>Advanced impedance spectroscopy methods for the determination of the most active anatase/rutile heterojunction towards enhanced PEC performance [A4]</i>	<i>24</i>
6.4. <i>Heterojunctions based on TiO₂ nanorods and carbon based materials for enhanced PEC and photocatalytic performance [A5, A6]</i>	<i>27</i>
6.5. <i>Plasmonic Au nanostars/TiO₂ heterostructure nanorod arrays: Broadband UV-Vis-NIR enhancement in PEC water oxidation performance [A7]</i>	<i>29</i>
6.6. <i>Advanced plasma deposition of very-thin thermally stable TiO₂ blocking layers with enhanced electron transfer ability for solar cells [A8]</i>	<i>31</i>
7. Photoelectrochemically active nanostructures based on α-Fe₂O₃.....	34
7.1. <i>Preparation of very-thin hematite films by means of high-energy plasma deposition methods [A9]</i>	<i>35</i>
7.2. <i>Approach to addressing the sluggish surface oxidation reaction kinetics via deposition of ultra-thin isostructural alumina films via atomic layer deposition (ALD) method [A10]</i>	<i>36</i>
7.3. <i>Introduction to the defect engineering in photoactive semiconductors</i>	<i>39</i>
7.4. <i>Defect engineering of hematite very thin films by HiPIMS technique: Controlling over the hematite crystalline texture towards the high electrically conductive (110) orientation [A11]</i>	<i>40</i>
8. Hierarchical photoanode nanostructures based on the combination of TiO₂ and α-Fe₂O₃ [A12].....	43
9. Conclusions and outlooks.....	46
References.....	49
Appendix A1.....	52
Appendix A2.....	108
Appendix A3.....	116
Appendix A4.....	131
Appendix A5.....	148

Appendix A6.....	159
Appendix A7.....	167
Appendix A8.....	177
Appendix A9.....	186
Appendix A10.....	194
Appendix A11.....	202
Appendix A12.....	214

List of Attached Papers for This Habilitation Thesis

- [A1] **S. Kment***, F. Riboni, S. Pausova, L. Wang, H. han, Z. Hubicka, J. Krysa, P. Schmuki*, R. Zboril*, *Photoanodes based on TiO₂ and α -Fe₂O₃ for solar water splitting—superior role of 1D nanoarchitectures and of combined heterostructures*, Chem. Soc. Rev. 46, 3716-3769, 2017.
- [A2] H. Kmentova, **S. Kment***, L. Wang, S. Pausova, T. Vaclavu, R. Kuzel, H. Han, Z. Hubicka, M. Zlamal, J. Olejnicek, M. Cada, J. Krysa, R. Zboril, *Photoelectrochemical and structural properties of TiO₂ nanotubes and nanorods grown on FTO substrate: Comparative study between electrochemical anodization and hydrothermal method used for the nanostructures fabrication*, Catal. Today 287, 130-136, 2017.
- [A3] M. Zelny, **S. Kment***, R. Ctvrtlik, S. Pausova, H. Kmentova, J. Tomastik, Z. Hubicka, R. Yalavarthi, J. Krysa, A. Naldoni, P. Schmuki, R. Zboril*, *TiO₂ Nanotubes on Transparent Substrates: Control of Film Microstructure and Photoelectrochemical Water Splitting Performance*, Catalysts 8, 25, 2018.
- [A4] R. Yalavarthi, A. Naldoni*, **S. Kment***, L. Mascaretti, H. Kmentova, O. Tomanec, P. Schmuki, R. Zboril*, *Radiative and Non-Radiative Recombination Pathways in Mixed-Phase TiO₂ Nanotubes for PEC Water-Splitting*, Catalysts 9, 204, 2019.
- [A5] A. J. Rathi, H. Kmentova, A. Naldoni, A. Goswami, M. B. Gawande*, R. S. Varma, **S. Kment***, R. Zboril*, *Significant Enhancement of Photoactivity in Hybrid TiO₂/g-C₃N₄ Nanorod Catalysts Modified with Cu–Ni-Based Nanostructures*, ACS Appl. Nano Mater. 1, 2526-2535, 2018.
- [A6] H. Kmentova*, D. Nandan, **S. Kment***, A. Naldoni, M. B. Gawande, Z. Hubicka, R. Zboril*, *Significant enhancement of photoactivity in one-dimensional TiO₂ nanorods modified by S-, N-, O-doped carbon nanosheets*, Catal. Today 328, 111-117, 2019.
- [A7] L. Wang, Y. Wang, P. Schmuki, **S. Kment***, R. Zboril*, *Nanostar morphology of plasmonic particles strongly enhances photoelectrochemical water splitting of TiO₂ nanorods with superior incident photon-to-current conversion*, Electrochim. Acta 260, 212-220, 2018.
- [A8] **S. Kment***, H. Krysova, Z. Hubicka, H. Kmentova, L. Kavan*, R. Zboril*, *Very thin thermally stable TiO₂ blocking layers with enhanced electron transfer for solar cells*, Appl. Mater. Today 9, 122-129, 2017.
- [A9] **S. Kment***, Z. Hubicka, J. Krysa, J. Olejnicek, M. Cada, M. Zlamal, M. Brunclikova, Z. Remes, N. Liu, L. Wang, R. Kirchgeorg, Ch. Y. Lee, P. Schmuki, *High-power pulsed plasma deposition of hematite photoanode for PEC water splitting*, Catal. Today 230, 8-14, 2014.
- [A10] **S. Kment***, Z. Hubicka, J. Krysa, D. Sekora, M. Zlamal, J. Olejnicek, M. Cada, P. Ksirova, Z. Remes, P. Schmuki, E. Schubert, R. Zboril, *On the improvement of PEC activity of hematite thin films deposited by high-power pulsed magnetron sputtering method*, Appl. Catal. B Environ. 265, 344-350, 2015.

[A11] **S. Kment***, P. Schmuki, Z. Hubicka, L. Machala, R. Kirchgeorg, N. Liu, L. Wang, K. Lee, J. Olejnicek, M. Cada, I. Gregora, R. Zboril*, *Photoanodes with fully controllable texture: the enhanced water splitting efficiency of thin hematite films exhibiting solely (110) crystal orientation*, ACS Nano 9, 7113-7123, 2015.

[A12] H. Han, F. Riboni, F. Karlicky, **S. Kment**, A. Goswami, P. Sudharag, J. Yoo, L. Wang, O. Tomanec, M. Petr, O. Haderka, Ch. Terashima, A. Fujishima, P. Schmuki, R. Zboril, *α -Fe₂O₃/TiO₂ 3D hierarchical nanostructures for enhanced photoelectrochemical water splitting*, Nanoscale 9, 134-142, 2017.

1. Introduction

Modern civilization depends on energy. Without it, further development would be unthinkable. Energy transforms lives, businesses, and economies. However, it dramatically changes our planet—its climate, natural resources, and ecosystems. Therefore, a sustainable world is currently one of the biggest challenges to address by our society. “A *sustainable world is the one in which human needs are met equitably without harm to the environment, and without sacrificing the ability of future generations to meet their needs.*” [1] To this end, we must shift our electric power generation from fossil fuels to other renewable energy sources such as a mix of wind, water, and solar. This is reflected in the fact that during the last decades researchers have directed their focus towards environmentally clean technologies and renewable energy sources. As a result, photocatalytic, photoelectrochemical (PEC), and photovoltaic processes based on solar energy harvesting, transformation, and utilization have gained enormous attention. In these fields, particularly thin films, nanostructures, and nanohybrids of various photoactive semiconductors are currently the most investigated because of their unique and suitable properties such as high photoactivity, high chemical and (photo)stability, non-toxicity, and particularly low cost. Up to the present, a broad range of nanotechnologies utilizing different kinds of preparation sources and deposition techniques have been developed and commercialized in this regard.

Preparation, characterization, and functional properties of photoactive semiconducting nanomaterials have been the main topic of the author’s whole research carrier. At Palacký University Olomouc, Institute of Physics of the ASCR and at the Department of Electrical Engineering of the University Of Nebraska—Lincoln, USA, the author extensively studied materials and nanostructures based on various oxides including titanium dioxide (TiO₂), iron oxide (Fe₂O₃), tungsten trioxide (WO₃), zinc oxide (ZnO), etc. for their application in the area of photocatalysis and photoelectrochemistry. In order to address their main limitations for these processes, the author, together with his collaborators, combined these core semiconductors with other materials such as graphene derivatives, other photoactive carbon based materials, plasmonic materials, quantum dots, other semiconductors, etc. in various complex nanohybrids.

One of the most frequently used methods for the fabrication of these materials were plasma-assisted deposition techniques; however, other chemical methods including the sol-gel and hydrothermal techniques were also applied. The nanostructures were always thoroughly characterized by a broad range of advanced techniques involving x-ray diffraction (XRD),

Raman spectroscopy, x-ray photoelectron spectroscopy (XPS), UV-Vis spectrophotometry, scanning electron microscopy (SEM), high-resolution transmission electron spectroscopy (HRTEM), Mössbauer spectroscopy, glow discharge optical emission spectroscopy (GDOES), etc., and finally tested for their photoinduced behaviour and activity by various PEC and photocatalytic experimental set-ups.

All the different aspects of the author's research activities are summarized in this habilitation thesis on the basis of 12 published scientific papers, which have been selected for these purposes, and in which the author acted as a key researcher (mostly as the first author or corresponding author). These are peer-reviewed papers that were published in prestigious and respected scientific journals in the fields of materials research, nanotechnology, photocatalysis, and/or (photo)electrochemistry.

The presented habilitation thesis is divided into nine chapters containing commentaries on the aforementioned publications. In particular, after this Introductory chapter, a theoretical background and motivation for the photocatalytic and PEC energy related processes are described in Chapter 2. Chapter 3 continues to describe basic properties of titanium dioxide (TiO_2) and hematite ($\alpha\text{-Fe}_2\text{O}_3$), which are the two key photoactive oxides studied and discussed in this thesis. Chapter 4 deals with various approaches to the fabrication of nanostructures based on their dimensionality, such as one- and two-dimensional approaches (1D and 2D). This chapter further describes the key features of these nanostructures in terms of PEC processes. Chapter 5 provides description of the plasma deposition techniques that have been designed and developed by the author of this thesis and their applications for the deposition of TiO_2 and $\alpha\text{-Fe}_2\text{O}_3$ based nanostructures. While these four chapters are relatively general and primarily based on an extensive review paper published in the journal *Chemical Society Reviews*, [A1] the following Chapters 6 and 7 summarize the research findings related to the TiO_2 and $\alpha\text{-Fe}_2\text{O}_3$ based photoanodes, respectively. With respect to TiO_2 , Chapter 6 provides description of the main results regarding the preparation and properties of 1D TiO_2 nanostructures including nanotubes and nanorods, [A2-A4] hybrid nanostructures combining TiO_2 nanorods and carbon based materials serving as the co-catalysts; charge transfer mediators; and optical sensitizers, [A5, A6] optical sensitization of TiO_2 by advanced plasmonic nanostructures, [A7] and the advanced plasma deposition technique for the preparation of very-thin TiO_2 layers working as the blocking layers in PEC solar cells. [A8] In the case of $\alpha\text{-Fe}_2\text{O}_3$, the attention is focused on the high-energy plasma deposition of hematite very thin photoanodes, [A9] plasma induced structural defects enhancing the hematite's PEC

activity, [A10] and the strategy to address the drawback of surface states by the combination of plasma deposition of hematite photoanodes and atomic layer deposition (ALD) of isocrystalline alumina passivation overlayer. [A11] Chapter 9 consequently introduces the synthetic procedure for the preparation of hybrid nanocomposites based on TiO₂ nanotubes branched with α -Fe₂O₃ nanoflakes as an example of combined nanostructured photoanodes. [A12] Finally, summary remarks and a long-term outlook are provided in Chapter 9.

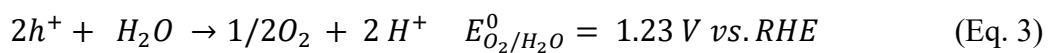
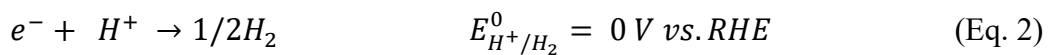
2. Renewable energy based on photocatalytic and PEC processes [A1]

Production of energy through solar light harvesting and conversion ranks among the most viable options for tackling the continuously threatening climate change and global warming caused by huge dependence of energy demand on fossil fuels, which leads to the persistent emissions of CO₂ into the atmosphere. In spite of the social relevance of these energy-related issues, a valuable alternative to the use of oil-based energy sources is still far from industrial and commercial applications. Given this scenario, the urgency to secure alternative, sustainable, clean, and renewable energy suppliers has been prioritized. In this context, the development of cost-competitive materials capable of producing fuels or electricity directly from the energy harvested from sunlight offers a desirable approach towards fulfilling the need of clean energy, with minimal environmental impact. Semiconductor metal oxides (e.g. TiO₂, α -Fe₂O₃, WO₃, ZnO) are the most widely adopted materials for the conversion of solar energy into transportable chemical energy that could be stored in the form of di-hydrogen (H₂) produced via photo-electrochemical (PEC) splitting of water. In addition, the production of electricity with perovskite solar cells (PSCs) or similar hybrid cells is also attracting a great deal of attention. Nowadays, the scientific research mainly focuses on the development of effective pathways that could couple (i) light absorption, (ii) steady-state production and transfer of photogenerated charge carriers, and (iii) a PEC water splitting reaction into one single device, and also focuses on the engineering of composite assemblies that could maximize the efficiency of the single processes. Unfortunately, none of the previously mentioned metal oxides simultaneously meet the thermodynamic and kinetic requirements that would ensure high performance in the mutually interconnected (i–iii) processes. This thesis summarizes the results that have been achieved by the author and explains how they have contributed to solving the aforementioned issues.

Hydrogen production via photoelectrochemical splitting of water—background and basic requirements. One of the approaches for PEC light-to-chemical energy conversion consists in the reduction of water into hydrogen (hydrogen evolution reaction—HER) accompanied by water oxidation to oxygen (oxygen evolution reaction—OER). [2-5] The photoelectrolysis of water by using TiO₂ as one of the electrodes was firstly reported by Fujishima and Honda in their famous paper published in the journal Nature already in 1972. [2] The basic configuration of a PEC cell consists of a semiconductor photoelectrode and a metal (e.g. Pt) both immersed in the electrolyte solution. This category of the PEC devices is termed as the

Schottky type. The type of the electronic conductivity of the semiconductor determines its functionality in the PEC system so that the n-type semiconductor always works as the photoanode and analogously the p-type semiconductor can only work as the photocathode. The configurations in which both photoelectrodes are applied as well as the systems utilizing a photovoltaic cell as the source of external solar-generated voltage are collectively referred to as the tandem cell approaches, and are currently extensively investigated. Nevertheless, this thesis exclusively deals with the application of TiO₂ and Fe₂O₃ as the photoelectrodes and since they are both the n-type semiconductors, only the PEC devices combining the semiconductor photoanode (TiO₂, Fe₂O₃ and various hybrids based on these semiconductors) and metallic cathode are hereafter described. The charge carriers that correspondingly promote H₂ and O₂ evolution (i.e. electrons and holes, respectively) are generated in the semiconductor(s) upon the absorption of photons. Figure 1 schematically illustrates the Schottky type PEC device with the photoanode and metallic cathode. It further shows the four consecutive steps representing the complete PEC water splitting process. Specifically these are: (i) light absorption in the photoanode, (ii) separation of the photogenerated electron and holes pairs (e^-/h^+), (iii) transport of the charges towards the electrodes' surfaces and (iv) corresponding surface redox reactions (photoanode oxidation and cathodic reduction). Once the n-type semiconductor comes into contact with a liquid electrolyte, a space-charge depletion layer is developed at the semiconductor/liquid junction (SCLJ) due to the established equilibrium between the energy of Fermi level in the semiconductor and the redox potential in the electrolyte. It consequently generates a band bending as well as a considerable space charge field at the SCLJ.

The PEC water splitting electrochemical redox reactions are described by Equations 1–4. First, the semiconductor absorbs light wavelengths with the energy equal or larger than its band gap. Upon the absorption, the electron-hole (e^-/h^+) pairs are generated (Eq. 1) and separated as a result of the space-charge field. While the holes in the valence band diffuse throughout the semiconductor towards its surface, where they promote the water oxidation half reaction (OER, Eq. 2), the electrons are withdrawn by an external circuit to the metallic cathode (e.g. Pt), where they undergo the water reduction half reaction (HER, Eq. 3).



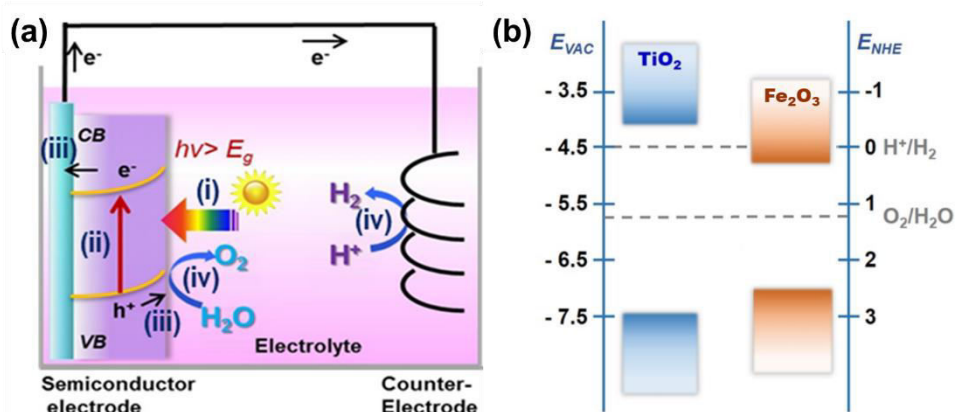
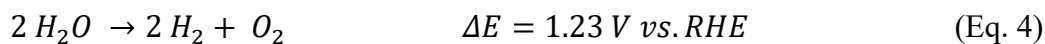


Figure 1. (a) Basic Schottky type PEC cell set-up with the four key steps of the photoelectrochemical water splitting, (b) position of conduction and valence band of TiO_2 and $\alpha\text{-Fe}_2\text{O}_3$ towards water splitting application half reactions (OER and HER). Reprinted and modified from Ref. [A1].

The overall water splitting (Eq. 4) is an energetically uphill reaction (e.g. endoenergetic), with a Gibbs free energy $\Delta_r G^0 = 273.2 \text{ kJ/mol}$ that, according to the Nernst equation, corresponds to the electrochemical potential of $\Delta E = 1.23 \text{ V}$ per each electron required. Therefore, the semiconductor used as the photo-electrode must absorb light with photons energy greater than 1.23 eV (that is, absorption edge at ca. 1100 nm). Furthermore, the adopted semiconductors should feature conduction band (E_{CB}) and valence band (E_{VB}) edges that straddle E°_{red} (Eq. 2) and E°_{ox} (Eq. 3), respectively. However, although the E_{CB} and E_{VB} edges of the semiconductor may have appropriate energies, unavoidable potential losses and kinetic overpotentials imply that 1.6–2.4 eV is the actual energy necessary to sustain the overall water splitting. Such a severe thermodynamic and kinetic restriction explains why a semiconductor that will be able to efficiently drive the overall reaction has yet to be identified. Moreover, the requirements for the commercialization of PEC devices (high efficiency, stability and scalability) further narrow the list of suitable material candidates. For instance, III-V semiconductors show large charge mobility and optimal band gap energy (E_g); however, they bear high manufacturing cost and reveal poor stability in PEC conditions. Therefore, long-term device durability cannot be afforded. Transition metal oxides rarely meet the criteria for an E_g suitable for sunlight activation, or for favourable band edges relative to E°_{red} and E°_{ox} . Hence, the well-renowned earth abundant materials potentially stable in the long-run, such as TiO_2 and $\alpha\text{-Fe}_2\text{O}_3$, still represent the most viable option for PEC applications. Both feature low processing cost and high stability even in harsh environments; however, TiO_2 absorbs only UV photons ($E_g = 3.2 \text{ eV}$), while $\alpha\text{-Fe}_2\text{O}_3$, with good stability and optimal band gap ($E_g = 2.3 \text{ eV}$), features a very short hole diffusion length compared with light penetration depth

(the description of TiO_2 and $\alpha\text{-Fe}_2\text{O}_3$ properties is provided in greater detail in the following chapter). These intrinsic limitations have been addressed in the presented thesis by: (i) careful material nanostructuring such as preparation of very-thin highly absorbing thin films (2D nanostructures) and/or preparation of the oxides in the form of 1D nanostructures (nanotubes, nanorods, nanoflakes) to overcome the short hole diffusion length and prevent the photogenerated charges' recombination; (ii) nanoengineering of internal properties of the oxides (defect nanoengineering, doping), (iii) the use of co-catalysts/sensitizers to enhance structural stability and extend the spectral range of light absorption and (iv) preparation of multi-component hybrid nanostructures.

Estimation of the PEC water splitting efficiency. The PEC experiments are usually carried out using a three-electrode system connecting a working electrode (WE), which is in our case the investigated photoanode, a metallic counter electrode (CE), and a reference electrode (RE, e.g. Ag/AgCl electrode). As the standardized light source, a broadband solar Air Mass 1.5 Global (AM 1.5 G) light simulator with the intensity of 100 mW cm^{-2} is commonly used.

The photoactivity of the photoanodes was determined on the basis of the PEC experiments including linear sweep voltammetry, chronoamperometry, open circuit potential, electrochemical impedance spectroscopy, etc. [6-8] These measurements quantify dynamics of the photogenerated carriers (electrons, holes). The prime characteristics derived from the PEC measurements are photocurrent curve (dependency of the current density— J on the applied potential to the WE— E). The most important parameters of the photocurrent curve are the onset potential and the photocurrent value at the 1.23 V vs. RHE. The value of the plateau current indicates how many photogenerated holes are reaching the SCLJ. The onset potential influences whether or not the photogenerated holes will suffer from surface recombination due to the slow electrochemical kinetics. It can be concluded that the highest photocurrent plateau is desired along with the onset potential shifted to a more cathodic direction.

Several approaches can be used to determine the performance of the PEC water splitting devices. Nevertheless, above all, the solar-to-hydrogen efficiency (STH, Eq. 5) is perhaps the most important. It is defined as the ratio between the amount of the produced chemical energy and the solar energy input. In this particular case, the PEC device uses only two electrodes that are separated into two compartments for the OER and HER. For both reactions, the electrolyte of the same pH and lacking in any sacrificial donors or acceptors must be used.

$$STH = \left[\frac{(mmolH_2) * (237000 Jmol^{-1})}{P_{total}(mW cm^{-2}) * area(cm^2)} \right] \quad (\text{Eq. 5})$$

When a BIAS applied to the working electrode is used, the efficiency can be estimated on the basis of the applied bias photon-to-current efficiency (ABPE).

$$ABPE = \left[\frac{J(mA cm^{-2}) * (1.299 - |V_{app}|)(V) * \eta_F}{P_{total}(mW cm^{-2})} \right] \quad (\text{Eq. 6})$$

Another possibility of evaluating the performance of the tested material is the incident photon-to-current efficiency (IPCE). It describes the percentage of the incident photon flux that is directly transformed into the photocurrent as a function of the incident light wavelengths.

$$IPCE(\lambda) = \frac{J_{ph}(\lambda)/e}{P_{mono}(\lambda)} = \frac{J_{ph}(\lambda) * 1239.8}{P_{mono}(\lambda) * \lambda} \quad (\text{Eq. 7})$$

The efficiency of a single photoelectrode in the three-electrode PEC system can be directly calculated from (J - V) polarization curves data according to equation 8.

$$\eta = \frac{J_m * V_m}{P_{in}} \quad (\text{Eq. 8})$$

The components in the above equations are: $J_{ph}(\lambda)$ in $mA cm^{-2}$ is the photocurrent density measured under monochromatic illumination at wavelength λ in nm, $P_{mono}(\lambda)$ in $mW cm^{-2}$ is the power intensity of incident monochromatic light at wavelength (λ), e is elementary charge, h is the Planck's constant, c is the speed of light, V_m is the photovoltage generated at the maximum power point, and P_n is the illumination power of light (standardly $100 mW cm^{-2}$).

Faradaic efficiency is the method that fairly reliably excludes the effect of photocorrosion, which can contribute to the overall photocurrent value. It is calculated as the ratio between the experimentally achieved amount of the oxygen gas and the theoretically calculated value based on the measured photocurrent.

$$Faradaic\ efficiency = \frac{Oxygen\ evolution\ measured}{Oxygen\ evolution\ based\ on\ the\ photocurrent} \quad (\text{Eq. 9})$$

Other approaches to calculating the efficiency of the PEC devices are described in the review paper published by the author. [A1]

3. Properties of TiO_2 and $\alpha-Fe_2O_3$ photoanodes

Titanium oxide (TiO_2). TiO_2 is the transition metal oxide that occurs in three main polymorphs, namely rutile, anatase, and brookite. While anatase and rutile are highly

abundant, brookite is rather rare in nature. Rutile and anatase both crystallize in a tetragonal structure, whereas brookite crystallize in an orthorhombic structure. [9]The crystalline structures are shown in Figure 2.

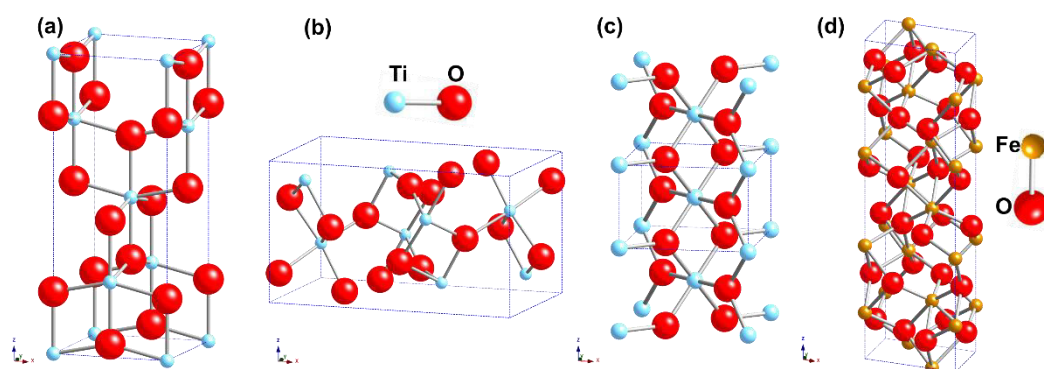


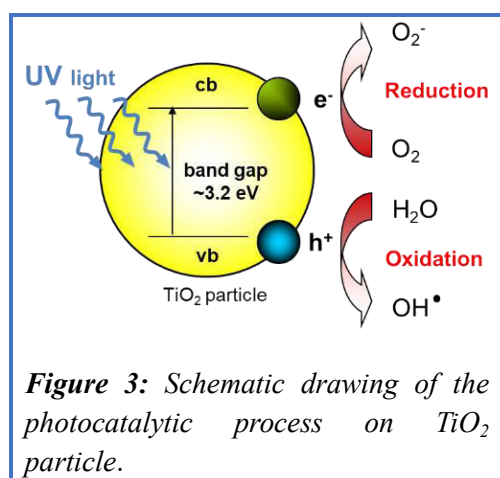
Figure 2. Crystalline structures of TiO_2 polymorphs. (a) anatase, (b) brookite, (c) rutile. Reprinted and modified from Ref. [10], (d) crystal structure of hematite Fe_2O_3 .

The thermodynamic stability of the polymorphs largely depends on their crystallite size. While rutile is thermodynamically the most stable phase in coarse materials (particle size above 35 nm), anatase is the common crystalline phase for nanoparticles (particle size below 11 nm). The brookite phase shows the highest stability in between these values (11–35 nm). The crystalline structure of TiO_2 polymorphs depends on chains of TiO_6 octahedra. The difference between anatase and rutile is found in the distortion of each octahedron (e.g. two Ti-O bonds are a little bit larger than the remaining four and some O-Ti-O bond angles deviate from 90°). The distortion is more pronounced for anatase. In contrast, brookite is formed by octahedra whose corners and edges are shared.

From the electronic point of view, TiO_2 is a typical n-type semiconductor with its valence band formed by oxygen $2p$ orbitals and the conduction band by the titanium $3d$ orbitals. The n-type conductivity originates particularly from the intrinsic defects such as oxygen vacancies. The band-gap energy width of ~ 3.0 eV corresponds to rutile and ~ 3.2 eV to anatase. Despite the higher band gap energy, the anatase phase features a higher photocatalytic activity, which is due to the better position of the conduction band minima that facilitate the reductive half-reactions.

TiO_2 is among the most studied transition metal oxides owing to its suitable properties, which are high chemical stability, non-toxicity, low cost and, particularly, high photocatalytic activity. Due to the semiconductor nature and its unique physical properties, TiO_2 is nowadays used in numerous applications including pigments, heterogeneous catalysis, dye-sensitized

and perovskite solar cells (DSSCs, PSCs), PEC devices, electric devices, corrosion-protective coatings, optical-interference coatings, and many others. Nevertheless, in the context of this habilitation thesis, the most important feature is its photocatalytic activity. [11]



The photocatalytic reactions belong to the family of advanced oxidation processes. It is a technology that is widely used for the degradation or mineralization of a broad range of organic and biological contaminants. The photocatalytic process on an anatase TiO_2 particle is illustrated in Figure 3, as it is the example of perhaps the most active photocatalyst. Upon the light irradiation from sunlight or other illuminating light source of the photocatalyst, electrons in the valence

band (VB) are excited to the conduction band (CB). This creates electron (e^-) - hole (h^+) pairs. After photoexcitation, the electrons and holes that do not recombine further diffuse/migrate to the surface of the photocatalyst, where they act as reducing and oxidizing agents, respectively. In other words the valence band holes oxidize water/hydroxide ions producing the OH^\bullet radicals, while the conduction band electrons reduce molecular oxygen to superoxide radical ions ($\text{O}_2^{\bullet-}$). Both of these radical species have very high oxidative potential that can mineralize almost all organic carbon into CO_2 . A further advantage is that the photocatalytic processes can be performed under mild ambient conditions without any mass transfer. On the other hand, the key and fundamental limitation is a high-energy band gap of TiO_2 , which allows only absorption of the UV light. This, in other words, means only $\sim 5\%$ of the solar spectrum.

Hematite iron oxide ($\alpha\text{-Fe}_2\text{O}_3$). Hematite crystallizes in a centred hexagonal structure within the R-3c space group symmetry, with the lattice parameters of $a = 5.034 \text{ \AA}$ and $c = 13.752 \text{ \AA}$ (Figure 2d). The structure is related to the corundum type of a close-packed oxygen lattice in which $2/3$ of the 12c octahedral sites are occupied by Fe^{3+} cations. The band gap of hematite is usually reported between 1.9 to 2.2 eV, which corresponds to the wavelengths of the incident light between 650 to 560 nm. Generally, three possible mechanisms of the electronic transitions upon the light absorption are known: (i) ligand field transition (d-d transition), (ii) ligand-to-metal charge transfer mechanism (LMCT), and (iii) pair excitations when two neighbouring Fe^{3+} ions undergo simultaneous excitation. Considering the hematite's bandgap, a photocurrent value of $\sim 12.5 \text{ mA cm}^{-2}$ at 1.23 V vs. RHE and under one sun illumination can

be potentially reached, which corresponds to a theoretical STH efficiency of $\sim 17\%$. However, hematite suffers from severe electronic and optical limitations, which are very low electrical conductivity and extremely short diffusion length of photogenerated holes. The poor electrical conductivity ($\sim 10^{-14} \text{ ohm}^{-1}$) and electron mobility ($10^{-2} \text{ cm}^2 \text{V}^{-1} \text{s}^{-1}$) is associated with a very specific electron transfer by hopping the electrons on $\text{Fe}^{2+}/\text{Fe}^{3+}$ iron atoms, which alternates on spatially localized iron ($3d$) orbitals. This phenomenon is known as small polaron conductivity, which can be described by a small polaron model considering both the effect of the relatively large size of the Fe^{2+} ion and associated lattice distortion (polaron). Despite the absorption of a substantial fraction of visible light, hematite provides a relatively poor absorptivity of photons ($\alpha^{-1} = 118 \text{ nm}$ at $\lambda = 550 \text{ nm}$) near its band-edge as a result of its indirect nature. Moreover, hematite exhibits an ultrafast recombination of the photogenerated carriers (time order within 10 ps) and low minority charge carrier mobility ($0.2 \text{ cm}^2 \text{V}^{-1} \text{s}^{-1}$). Consequently, the hole diffusion length (L_D) is only 2–4 nm. Furthermore, application of a large overpotential is required to observe the water splitting photocurrent due to the slow oxygen evolution reaction (OER) caused by surface traps and/or poor OER kinetics. [12-13] These non-ideal features still significantly hinder the performance of hematite that would be sufficient for industrial production of hydrogen. On the other hand, considerable effort has been put in to improve the photoresponse of hematite and some of the efficient approaches are described in this habilitation.

4. Nanostructuring of the photocatalytic materials

Nanoscale (more often, nanoscale) significantly influences many of the physical, chemical, and biological properties of materials and provides them with new unique functionalities. Indeed, nanoscale is the threshold beyond which surface area effects (i.e. quantum confinement) and the discrete changes of properties become more significant than bulk features. As miniaturization has profoundly changed the world of electronics, nanostructuring plays a major role in many fields including renewable energy. [14]

Nanostructured materials (NMs) are low dimensional materials composed of assemblies of building units with at least one dimension confined to the submicron or nanoscale regime. [15] According to this definition, zero- (0D), one- (1D), two- (2D) and three-dimensional (3D) NMs can be distinguished. Common characteristic is, compared with bulk materials, that NMs exhibit remarkably higher surface-to-area ratio and fundamental size effect. In particular, larger specific surface areas represent a great advantage when the materials are

intended for (photo)catalytic applications: a higher number of surface sites facilitate substrate adsorption, offer extended contact with solutions, etc. The size effect, instead, consists in the fact that nanomaterial dimensions (< 100 nm) are comparable to the critical length scale of physical phenomena such as the mean free path of electrons and phonons. This implies that charge carriers are more efficiently separated within the nanomaterials lattice and that NMs properties can be distinguished from those of bulk materials and those of quantum-sized materials. The first classification effort was introduced in 2000, [16] although only more recent reports also include other architectures. [15] In terms of this habilitation thesis, the 1D, 2D, and combined hierarchical nanoarchitectures are of particular importance.

1D–nanostructures. One-dimensional (1D) nanostructures such as nanotubes, nanorods, or nanofibers provide very high performance with respect to the overall charge collection and transfer efficiency. Usually highly-ordered 1D nanostructure arrays (particularly the nanotubes) not only maximizes the material specific surface area (a key factor for enhancing the performance of any heterogeneous catalytic reactions), but also features a number of characteristics (e.g. size confinement, atomically curved surface, extended surface-to-volume ratio, preferential percolation pathway for enhanced charge separation/transport/collection) beneficial for photo-electrocatalytic applications. Charge collection efficiency, which depends on both the recombination lifetime of photogenerated charge carriers and their collection lifetime, meaning that the time it takes the $e^-(h^+)$ to reach the semiconductor-electric contact (semiconductor/electrolyte interface) is, in comparison with other nanostructures' morphologies, thus significantly enhanced. The author of this thesis has focused particularly on 1D nanostructures with the morphology of highly-ordered self-organized nanotubes grown by electrochemical anodic oxidation, nanorod arrays synthesized by hydrothermal methods, and the ultrathin nanoflakes grown by thermal oxidation of metal substrates. In this regard, one of the outputs of the author's continuous research in this field was a review paper dealing with 1D nanostructures based on TiO_2 and $\alpha\text{-Fe}_2\text{O}_3$ published in the journal *Chemical Society Reviews*. [A1]

2D–nanostructures (thin films). Metal oxide films with a thickness that falls into the nanometer-sized regime are typical example of 2D-nanostructures. 2D thin films are frequently employed for photocatalytic and PEC applications. The comparison, in terms of properties and photocatalytic performance, between thicker films and the 2D-nanostructured counterparts reveals several advantages offered by the thinner layers. The superior

performance of nano-thick layers is ascribed to the enhanced photon absorption produced by: (i) multiple reflection and scattering of light at the semiconductor/electrolyte interface; (ii) the possibility of decoupling the directions of light absorption and of charge-carrier collection, which means that photogenerated charges will not diffuse through the bulky material and the charge recombination will be reduced; (iii) improved photogenerated charge-pairs separation driven by suitable internal electric field; (iv) the possibility of controlling crystal face exposure that influences the materials band-bending, flat band potential, surface states; (v) the possibility of manipulating the semiconductor band gap, taking advantage of nanoscale size effect; this translates into a CB edge shift towards more negative potential and/or into a VB edge shift in the opposite direction, etc. [17] The author of this thesis has particularly focused on the preparation of photoactive 2D thin and ultra-thin films by the low-temperature plasma assisted deposition techniques. These methods are in greater detail described in the following chapter.

5. Plasma assisted deposition methods for the preparation of thin films and nanostructures

Films of various semiconductors and metals are very often prepared with the aid of low-temperature plasma, allowing control of their thickness, compositions, and structure. Low temperature plasma is ionized gas far from thermodynamic equilibrium. Electron gas has usually a high effective electron temperature T_e in the range from $T_e \approx 10000\text{--}50000$ K, but the kinetic temperature of heavy particles is rather low, close to room temperature. Hot electron gas can excite electronic states in atoms and electronic, vibrational, and rotational states in molecules. These facts lead to molecular dissociation, creation of metastables, and chemically active particles, which can be produced at normal conditions close to thermodynamic equilibrium at very high temperatures. Consequently, the overall thermal load of substrates is relatively low. Exploiting this phenomenon, the low-temperature plasma-assisted deposition can be used for the coating of thermally sensitive samples. [18]

One of the most common ways of plasma-assisted depositions is introduced by the physical vapour deposition (PVD) process. Classical PVD processes are mostly realized by direct current (DC) or radio frequency (RF) ion sputtering of metallic or non-conductive targets made from a material that is further contained in the deposited layer using a suitable reactive gas mixture (Ar is regularly used as the working gas and O_2 , N_2 , etc. as the reactive gases). Particularly, various configurations based on magnetron sputtering are the most typical for

such PVD processes. Magnetron sputtering currently represents the most powerful physical method among the common industrial deposition technologies for producing thin films. Magnetrons are mainly operated at low pressures ($p \sim 0.1\text{--}10$ Pa). The magnetron systems have, compared with other sputtering methods, relatively high deposition rates due to the high plasma density at the target.

Very promising are systems employing low-temperature pulsed plasma. [19] These systems generally work with low average absorbed electrical power for plasma excitation and high pulse power during the active part of the period. By using plasma sources in the pulse-mode, a high flux of ions, radicals, or other particles on the substrate due to high power absorbed in the plasma during the active part of the period can be attained. Simultaneously, the plasma remains in the low-temperature domain. By changing the duty cycle, the substrate ion bombardment can be controlled, which can lead to the reduction of the compressive stress in the deposited film as well as controllably inducing many beneficial defects into the deposited material. We can further easily regulate the energy delivered into the discharge, and thus influence the other important features of the deposited films such as crystalline structure, grain size, texture of the films, density of the films, adhesion, etc. The pulsing mode of the magnetron sputtering also prevents the charging of dielectric material accumulated on the target, which crucially reduce problems associated with discharge arcing and consequent damage to the films [20]. Pulsed magnetrons can be operated as unipolar (the cathode of the magnetron is grounded during the idle part of the pulse, $V_c = 0$ V) or bipolar (the cathode of the magnetron is biased with some positive voltage during the idle part of the pulse, $V_c \sim 20\text{--}100$ V).

Recently, a modern direction in magnetron sputtering is the so-called high power pulsed ionized magnetron sputtering (HIPIMS) [21] and its various modifications such as the combination with medium frequency (MF) plasma excitation. The HIPIMS discharges are operated in a range of low repetition frequency of 50–500 Hz and short duty cycles $Ta/T \leq 1\%$. [22] Short duty cycles result in high-power pulse densities ($\sim \text{kW}/\text{cm}^2$) and high plasma density, about $10^{18}\text{--}10^{19} \text{ m}^{-3}$ in the pulse, [23] while the values averaged over the whole period are much smaller (comparable or even lower than in the DC mode). Because of the high energies and powers involved in a HiPIMS pulse, a large fraction of sputtered (metal) particles is ionized at the target region. The advantages of HIPIMS+MF systems is the possibility of utilizing the “off” time of the HiPIMS duty cycle, which crucially decreases the working pressure and improves the HIPIMS plasma generation due to MF plasma pre-

ionization, thus improving the properties of the generated films as well. [24] The voltage applied on the cathode during MF sputtering is usually pulsed in the mid-frequency range of 100–350 kHz with duty cycles of about 50% or more. Pure MF magnetron discharges are usually characterized by ion fluxes comparable to DC sputtering, high thermal energy flux [25], and a lower degree of ionization of the sputtered particles (plasma density $10^{15} - 10^{16} \text{ m}^{-3}$). [26]

The author of this thesis designed and built, in the laboratory at Palacký University Olomouc, a new sophisticated infrastructure based on a magnetron sputtering system for the deposition of thin films and various nanostructures. The plasmatic system at UPOL is equipped with five-magnetron deposition source (see Figure 4) including a main four-inch and additional four two-inch magnetron sources. The main large magnetron enables deposition of films featuring very high homogeneity over a large number of substrates as well as one large substrate (up to 10x10 cm) in one deposition cycle. The four additional magnetron sources allow deposition of various binary or ternary alloys (even thermodynamically difficult to obtain) and doped and/or co-doped (up to four dopants) versions of the 2D thin nanocrystalline films (metals, metal alloys, oxides, nitrides, carbides, etc.). Furthermore, the system involves a professional substrate holder (EpiCentre system, UHV Design Ltd.) capable of precise regulation and in situ control of the most important deposition conditions for substrates such as temperature, speed of rotation, and DC/RF biasing during the depositions.

Summary of the most important features that the system enables:

- 1) Deposited metal and metal-alloy (binary or ternary) films onto transparent FTO substrates can be used as starting materials for the preparation of nanotubes via the electrochemical anodization. This strategy represents a significant step forward in the PEC processes since the usage of transparent conductive substrate serving as a transparent electrode is of crucial importance.
- 2) Due to the HiPIMS mode, a majority of the sputtered particles are being ionized. This phenomena can be exploited for deposition of very thin films (metals, oxides, nitrides, etc.) inside the cavities of nanotubes and/or various scaffold-like functional nanostructures. The process can be considerably enhanced when the substrate (1D nanotubes or scaffolds deposited onto FTO substrate) are electrically BIASEd, which attracts the sputtered particles towards the substrates.

- 3) The HiPIMS mode provides very high ion flux towards the substrates, which can be regulated and controlled. This phenomenon is particularly important with respect to the defect engineering of 2D nanocrystalline thin films.
- 4) Due to the ionized nature of the sputtered particles, the HIPIMS mode is especially convenient for the doping and co-doping precise engineering and control.
- 5) An in situ diagnostic of the discharge usually runs along with the plasma deposition process. Besides the observation of basic plasma parameters, it also enables to control the deposition process, thus ensuring its reproducibility. The optical emission spectroscopy is regularly used as the diagnostic method. It provides information about the chemical composition of pulsed plasma and directly detects electronically excited atoms and molecules.

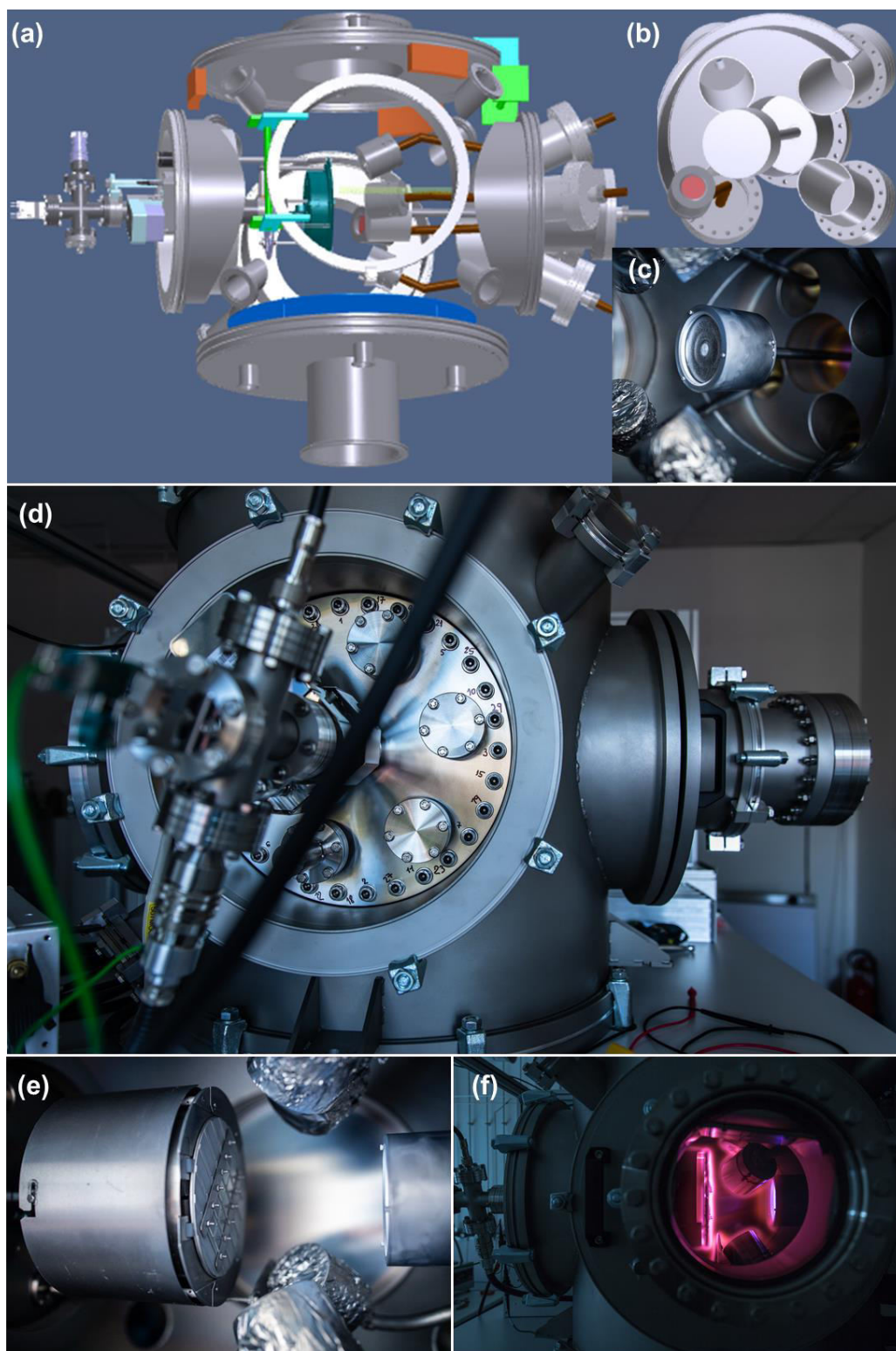


Figure 4. (a) Schematic drawing of the DC pulsed magnetron sputtering system for the deposition of thin films and nanostructures developed by the author at Palacký University Olomouc, (b) multiple magnetron sputtering sources including a central four-inch magnetron and four two-niche magnetrons, (c) photograph of the central 4-inch magnetron with titanium target installed, (d) photograph of the whole system from the side of the sophisticated substrate holder, (e) photograph of the substrate holder inside the reactor containing ten FTO substrates with the diameters of 25 x 35 mm, (f) photograph of the plasma discharge during the deposition and simultaneous substrate plasma

biasing.

6. Photoelectrochemically active nanostructures based on TiO₂

6.1. 1D nanostructuring of the TiO₂ photoanodes [A2]

As described in Chapter 4, the 1D nanostructuring of materials into the form of nanorods, nanotubes, nanofibers, or nanoflakes is one of the most straightforward strategies to crucially improve the photocatalytic and PEC activity of single semiconductors, compared with their bulk counterparts. 1D morphology provides several beneficial features that synergistically contribute to the overall enhanced photoactivity, namely: (i) considerable increase in the surface area, which enlarges the number of photocatalytically active sites (ii) increase in the amount of harvested/absorbed light, (iii) enhanced photocharge separation efficiency due to the directional electron transfer towards the charge collecting back contact (electrode). 1D morphology can further work as a suitable platform/scaffold for more complex hierarchical photoactive nanostructures. However, the final functionality of these complicated nanosystems strongly depends on the properties of the starting material. Several methods are generally applied for the production of 1D nanostructures including both the top-down and bottom-up nanotechnology approaches. The first category typically represents hydrothermal techniques carried out in autoclaves, which usually produces oriented nanorods or more rarely nanotubes. Electrochemical anodization of metal foils is the classical example of the top-down procedures. The electrochemical anodization of the metals creates various oxide nanostructures such as particularly nanotubes or porous nanostructures with the thickness of tents of nanometres to tents of micrometers (the morphology crucially depends on the metal and the anodization conditions and the thickness on the electrochemical parameters and duration) on the surface and the remaining metal then serves as the back contact. However, for the PEC applications, the metal substrate is not very convenient for several reasons. It is not transparent, which is a serious handicap to many PEC devices and, more importantly, the anodization process leads to the formation of different detrimental crystalline phases of the grown oxide at the interface of the desired oxide and the remaining metal. These unwanted crystalline phases act as the recombination centres for the charges and thus cause significant, overall (photo)efficiency losses. In this approach, these limitations were addressed by a two-step preparation procedure. First, a high quality metal film of a precise thickness on the required transparent conductive substrate was deposited by magnetron sputtering. In the case of PEC applications, the most commonly used substrate is a glass coated with a transparent conductive fluorine-doped tin oxide layer (hereafter termed as FTO substrate). In the

following step, the metal film was fully transformed into the desired oxide form by the electrochemical anodization. The full transformation ensures the transparency of the electrode along with avoiding the formation of other crystalline structures. The grown oxide nanostructures are usually amorphous and must be further thermally treated to provide the crystallization. The plasma deposition also allows preparations of various binary or ternary alloys, with highly controllable ratios between metals and multilayer metal assemblies than can be further used for the preparation of doped oxides and 1D oxide superstructures, respectively. The metal films (as well as metal foils) deposited on the FTO can also be used for the preparation of oxide nanofibers by a high temperature oxidation in air.

Nevertheless, this work reports on three different synthetic pathways for growing 1D nanostructured TiO_2 photoanodes including electrochemically anodized nanotubes and hydrothermally grown nanorods as well as hydrothermally prepared nanotubes. In the first case, the so-called self-organized TiO_2 nanotubes (TNT) were grown by electrochemical anodization of Ti layers deposited onto an FTO glass substrate by magnetron sputtering. The anodization was carried out at 50 V in a most typical electrolyte containing 0.5 wt% NH_4F + 2 wt% H_2O in ethylene glycol.

Further, the TiO_2 nanorod arrays (TNR) were fabricated on the FTO substrate by hydrothermal method. [27] In this case, the precursor solution mixture contained 14 mL of concentrated HCl mixed with 14 mL Milli-Q water (18.2 $\text{M}\Omega\text{-cm}$), followed by mixing 0.46 mL of titanium *n*-butoxide into the aqueous solution. The FTO glass (surface resistivity: 7 Ω/sq), pre-cleaned by DI water; acetone; and 2-propanol, and the clear mixture were transferred into a Teflon-lined stainless steel autoclave (50 mL volume) with the FTO conductive side facing down. The hydrothermal reaction was conducted in a laboratory oven at 150 °C for 8 h and then cooled down under flowing water for 15 min. The sample was rinsed with DI water and ethanol.

Finally, the TiO_2 nanotubes were deposited by sequential hydrothermal method (THNT). First, a thin ZnO seed layer was prepared onto the FTO glass by spin coating method with 0.02 M zinc acetate dihydrate solution at 4000 rpm for 35 s. Arrays of ZnO nanorods, which served as sacrificial templates for the nanotubes, were grown on the seed layer by hydrothermal method at 85 °C for 10 h using 0.025 M zinc nitrate hexahydrate and 0.025 M hexamethylenetetramine as precursor chemicals. The synthesized ZnO nanorod arrays were then immersed in aqueous solution consisting of 0.075 M ammonium hexafluorotitanate and 0.2 M boric acid at room temperature for 0.5 h. In this solution, ammonium hexafluorotitanate

hydrolyzed to TiO₂ on the individual ZnO nanorod, while ZnO dissolved simultaneously in the solution by acids produced by ammonium hexafluorotitanate hydrolysis. Subsequently, the resulting TiO₂ nanotube arrays immersed in a 0.5 M boric acid solution for 1 h to remove the residual ZnO inside the tubes. All these techniques enabled to grow the TiO₂ arrays vertically to the FTO substrates with sufficient adhesion and covering their large area. In the next step, the fabricated nanostructures were thoroughly characterized and particularly compared in terms of their PEC activity.

Figure 5 summarizes the main findings of this work. The SEM images show very different morphology and the degree of orderliness of the prepared TiO₂ film arrays (Figure 5a-c). The latter increases in the range THNT>TNR>TNT. While the diameter of single rods and anodized tubes is comparable (in average around 100 nm), the diameter of hydrothermal nanotubes is much smaller (around 50 nm). Due to the smaller diameter and relatively high thickness of the arrays, which is the same of 2.5 μm for all three types, the tubes in the THNT structure tend to cross each other. This morphology also shows the lowest density compared with the closely packed TNR and TNT nanostructures. The prepared nanostructures also differed in one of the most important parameter, which is the crystalline structure, although the as-grown film arrays were thermally treated under the same conditions of 500 °C for 1 hour in air. With the help of XRD, it was found out that the TNR arrays had the rutile crystalline structures with the preferred orientation of the (00 l) type. The rutile phase was apparently obtained owing to the isostructural SnO₂ (FTO) grains, which provided favourable nucleation sites for the formation of the rutile phase. The THNT films were fully transformed into the anatase structure. The anatase crystalline structures was also revealed for the TNT; however, these films contained residual traces of unreacted titanium.

The PEC properties were measured under standard conditions using a three-electrode configuration and AM 1.5G simulated solar light illumination (intensity 100 mW cm⁻²). Figure 5d shows linear sweep voltammetry scans of the tested nanostructures with the thickness of 2.5 μm. The hydrothermally grown TiO₂ nanorods (TNR type) exhibited the highest activity—630 μA cm⁻² at 0V vs. Ag/AgCl). This was more than three times higher than the photoactivity of the anodized nanotubes (TNT, 185 μA cm⁻² at 0V vs. Ag/AgCl) and more than six times higher than the activity of the hydrothermally grown nanotubes (THNT, 110 μA cm⁻² at 0V vs. Ag/AgCl). Generally, the rutile phase is referred to as a crystalline structure showing lower photocatalytic activity; in this case, the rutile TNR nanorods significantly overperformed both of the anatase nanotubular photoanodes. The relatively poor

performance of the TNT samples was attributed to the presence of the titanium residues coming from the starting sputtered titanium films. These titanium impurities may act as the recombination centres for the photogenerated charges. The lowest activity of the hydrothermally grown nanotubes probably resulted from the sequential synthetic procedure, which required a ZnO seed layer to be deposited prior to the hydrothermal growth. Subsequently, the seed layer had to be chemically etched away, which was a crucial step for keeping a good contact between the TiO₂ and the FTO layer. On the other hand, the TiO₂ nanorods (TNR) grew because of the isostructural FTO crystals, which ensured a very good electrical contact for the charge transfer. The charge transfer was even boosted owing to the preferential orientation of the individual rods along the (110) crystalline plane. Therefore, it can be concluded that the highest photoactivity of the titania nanorods hydrothermally grown on the FTO substrate resulted from the best dynamics/transfer ability of the photogenerated charges, which was proved by the calculation of the photogenerated electron life time (Figure 5e). For the following study, only the photoanodes based on hydrothermally deposited nanorods and anodized nanotubes were used.

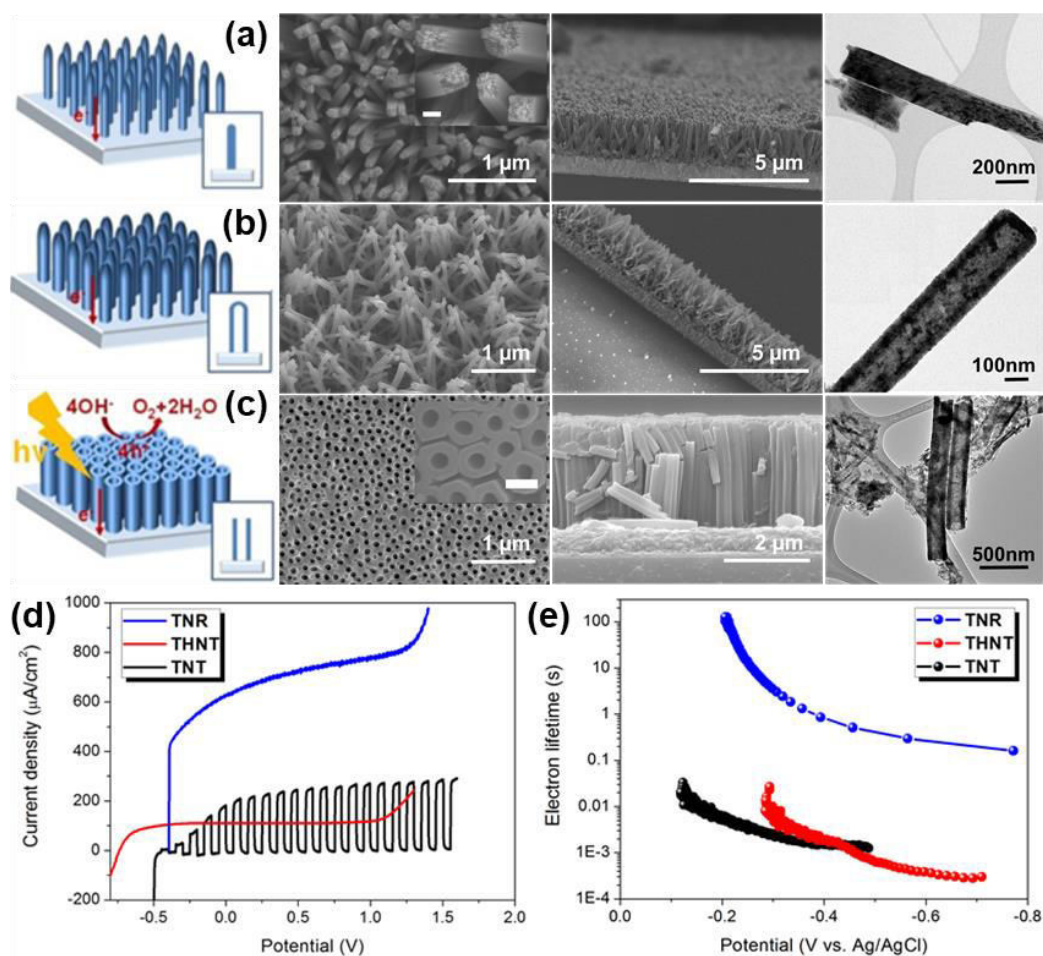


Figure 5. TiO_2 1D nanostructures deposited onto FTO substrate: schematic illustrations (left), SEM images (middle), TEM images (right). (a) Nanorods by hydrothermal method (TNR); (b) Nanotubes by hydrothermal method (THNT); (c) nanotubes by electrochemical anodization (TNT). (d) Linear sweep voltammetry scans. (e) Estimation of the electron lifetime from the open circuit potential measurements. The PEC measurements were performed under AM 1.5 G illumination with the intensity of 100 mW cm^{-2} and in the 1M NaOH electrolyte. Reprinted and modified from Ref. [A2].

6.2. Correlation between the properties of magnetron sputtered titanium films and TiO_2 nanotubes after their transformation by electrochemical anodization [A3]

Self-organizing electrochemical anodization of Ti metal substrate, often referred to as the most simple; low-cost; and straightforward approach leading to one-dimensional (1D) TiO_2 NTs, was adopted to fabricate highly ordered and vertically oriented TiO_2 nanotube arrays directly grown on a conductive FTO substrate (i.e. a back electrical contact), which is of clear usefulness when the layers are used for photo-electrochemical applications. [28] It is well known that under a specific set of electrochemical conditions (e.g. applied voltage, anodization time, electrolytic solution and its fluoride and water contents) nanotubular properties such as the degree of self-organization, tube length and diameter, electronic and ionic properties can be easily controlled. For instance, under otherwise optimized conditions, anodization voltage represents a key-factor in controlling the tube diameter, which typically shows a linear dependence on the applied potential. The duration of the anodization can be adjusted to determine the nanotube layer thickness as a longer anodization time leads to longer tubes. However, this is valid on the assumption that, after reaching a steady-state condition between the tube growth at the metal/oxide interface (tube bottom) and the chemical/electrochemical dissolution at the oxide/electrolyte interface tube top, no further increase in the nanotube length is observed. Furthermore, if all the other electrochemical parameters are kept constant, low amount of water in the electrolyte typically leads to smaller tube diameters, and higher concentration of F^- ions are desirable to grow a thicker layer (apart from the fact that above optimum fluoride concentration extensive etching of the newly formed oxide occurs and homogeneous structure can no longer be formed). Finally, since an anodization process yields an amorphous oxide, adequate annealing treatment is required before using titania nanotubular arrays for PEC applications; depending on the temperature and duration, annealing in air typically leads to anatase and rutile crystalline polymorphs (or a mixture of the two) formation. The author has extensively studied all these experimental conditions and parameters. Nevertheless, as stated above, one of the important steps forward in the field of anodized nanostructures is the preparation of the starting material by magnetron sputtering, i.e. instead of using a non-transparent metal foil, the metal is first deposited by

magnetron sputtering on a transparent substrate and then used for the electrochemical anodization. This strategy has generally two advantages: (i) the interface between the grown nanostructure and usually the charge-collecting layer can be controlled and (ii) the final device is fully transparent, which can remarkably improve the efficiency of many photonic applications including photoelectrochemical water splitting. The author of this thesis has dealt with this topic in several research papers.

The parameters of the magnetron-sputtered metal films that crucially influence the process of the electrochemical anodization itself as well as the properties and quality of the grown nanotubes are particularly adhesion to the glass/FTO substrate, grain size, and density. In this regard, the condition that is necessary for governing these parameters is the temperature of the substrate during the plasma deposition. Therefore, in this work the titanium films were deposited by pulsed DC magnetron sputtering onto the FTO substrate at four different temperatures: namely at room temperature (RT— the room temperature means that the substrate is not intentionally heated; however, during the deposition process the temperature rises up to ~ 80 °C as a consequence of the heavy ions bombardment), 150 °C, 300 °C, and 450 °C. All the other plasmatic conditions such as deposition pressure, flow rate of Argon working gas, applied voltage to the titanium target, pulsing frequency and duty cycle, plasma discharge current, and the distance between the magnetron gun and the substrate were kept fixed. The paper focused on the description of how the deposition temperature affects the mechanical, adhesion, and microstructural properties of the titanium films and how these parameters consequently correlate with the properties of the corresponding TiO₂ nanotubes and their PEC performance.

Figure 6 summarizes the main findings of this study. We observed a volcano trend dependence of the deposition rate on the temperature of the substrate with the maximum of ~ 47 nm/min for 150 °C and an opposite trend of the grain size with the minimum value of ~ 80 nm at the same temperature (see Figure 6). These phenomena can be described on the basis of a shadowing effect at low deposition temperature, and higher adatom mobility at higher temperatures, which are common features of the deposition of films via magnetron sputtering. The mechanical properties of the deposited titanium films were then investigated by nanointendation technique. It was found out that while the reduced modulus slightly increased with the temperature (109 GPa for RT to 130 GPa for 450 °C), the hardness values remained almost unchanged (~ 2.5 GPa), and, moreover, they were in relative proximity of the hardness values of pure titanium bulk, which reflected the high purity of the sputtered films. Figure 6b

shows the progressive load scratch tests revealing that the adhesion of titanium films to the FTO substrate increased with the increase in the deposition temperature. The SEM surface morphology image in Figure 6c showed that the titanium film deposited at 150 °C was formed by hexagonal platelets with sharp edges.

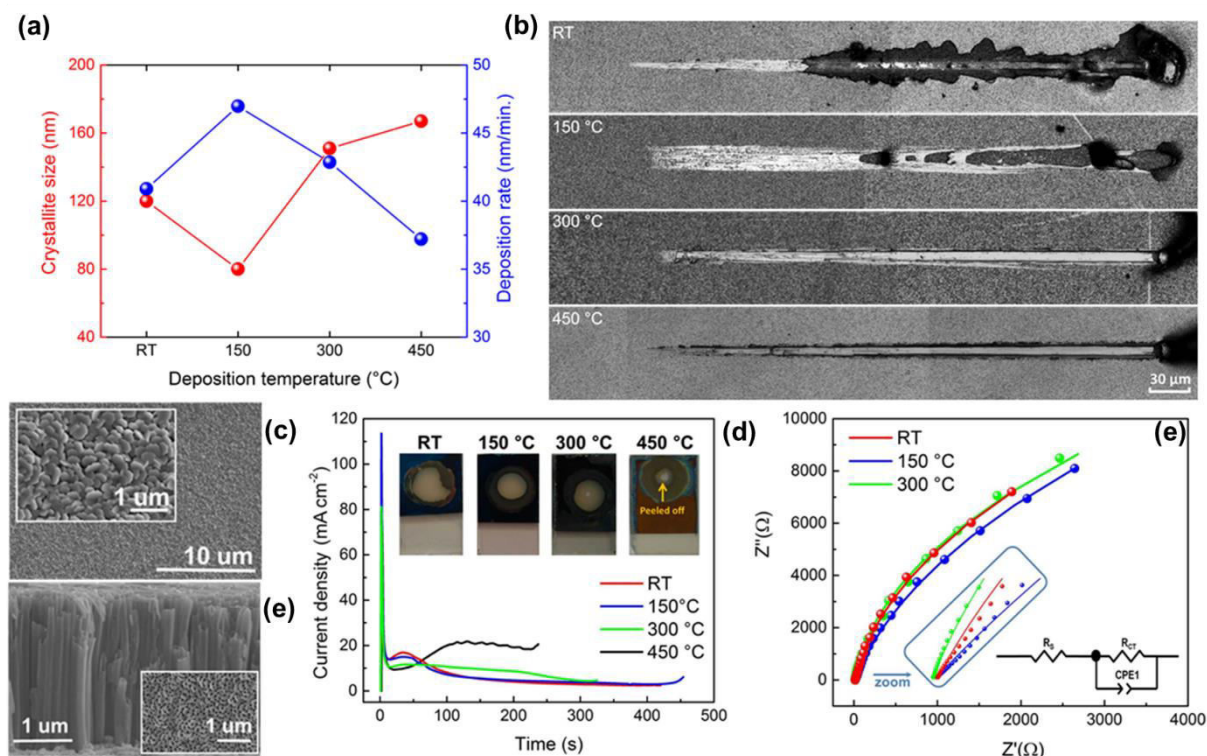


Figure 6. (a) Dependencies of crystallite size and deposition rate on the temperature of the FTO substrate during the DC pulsed magnetron sputtering of titanium films, (b) photographs of typical scratch tracks for the titanium samples deposited on the FTO substrate by DC pulsed magnetron sputtering with respect to the temperature of the substrate during the deposition, (c) SEM surface image of the titanium film deposited by DC pulsed magnetron sputtering at 150 °C of the FTO substrate, (d) typical photocurrent density curves recorded during the electrochemical anodization of the titanium films, the insert shows photographs of the samples after the anodization (the transparent circles are the anodized areas, the sample deposited at 450 °C delaminated during the anodization), (e) SEM cross-section image of the TiO₂ nanotubes grown from the titanium film deposited at 150 °C of the FTO substrate, (f) symbols are the experimentally measured impedance data; solid curves are fitted to the equivalent circuit shown (inset). R_s is solution resistance, R_{ct} is charge transfer resistance, Constant phase element (CPE1) is capacitance element. Photoelectrochemical (PEC) measurements were carried out in 1 M NaOH electrolyte under simulated solar light irradiation (air mass-AM-1.5G, 100 mW cm⁻²). Reprinted and modified from Ref. [A3].

The deposited films were then used as the working electrode to grow the nanotubes under the self-organized electrochemical anodization condition using a mixture of NH₄F, water and ethylene glycol as the anodization electrolyte. The current density vs. time plot characterizing the anodization procedure is displayed in Figure 6d. It contains also photographs of the

transparent nanotubes after the anodization in the insert. The three typical stages of the oxidation can clearly be distinguished in the current density plots. At the very beginning of the oxidation, a very sharp current density peak can be observed, which is characteristic for the formation of the formation of compact TiO₂ layer. Then relatively steady state region follows, which is associated with the development of the nanotubes under the self-organizing conditions. The end point of the reaction is accompanied by a sharp increase of the current density. From the graph, it can be concluded that the longest anodic oxidation time was observed for the films deposited at 150 °C, although all the tested films had the same starting thickness of 1.5 μm. This trend is in good correlation with the dependency of the crystalline size on the substrate temperature. In other words, the shorter the anodization time, the larger the crystallite sizes and simultaneously the denser the film is and thus the higher anodization current is needed. A balance between these parameters leading to a high quality nanotubes with a high adhesion to the FTO substrate must be found. In the case of this study, the temperature of 150 °C was identified as the most convenient for the deposition of titanium films with the lowest crystalline size. These films also provided TiO₂ nanotubes with the best degree of self-organization and the enhanced charge transfer at the semiconductor/electrolyte interface, which is confirmed by the cross-section SEM image of the nanotubes and impedance spectroscopy plots in Figure 6d and e, respectively. These properties were the reason for the best overall PEC performance among the tested layers showing the highest photocurrent density of 175 μA cm⁻² at 0.5 V vs. Ag/AgCl

6.3. Advanced impedance spectroscopy methods for the determination of the most active anatase/rutile heterojunction towards enhanced PEC performance [A4]

Among the reasons that proved TiO₂ nanotubes as a robust candidate for the use in PEC water splitting are the availability of high surface to volume ratio, facile synthesis process, and easy functionalization with other semiconducting materials. However, the PEC activity associated with TiO₂ nanotubes significantly decreased because of limited light absorption and poorer charge transport properties. Hence, facilitating better charge transport is an important aspect to improve the PEC activity. In order to address the charge transport issues and in turn to decrease the intrinsic recombination process associated with TiO₂ nanotubes, heterojunction formation with low bandgap semiconductors has been introduced. [29] Also, in recent past, the intrinsic heterojunction formed between the anatase and rutile phases during the annealing process proved to be effective in improving the PEC performance by suppressing the electron-

hole recombination. However, the charge transfer mechanism between the anatase and rutile phases has not been fully understood.

For this study, the conventional impedance spectroscopy (PEIS) and advanced techniques such as intensity modulated photoelectron spectroscopy (IMPS) and intensity modulated photovoltage spectroscopy (IMVS) were applied to probe the charge transfer/transport properties associated with TiO₂ anatase-rutile mixed phase nanotubes. However, due to the high temperature annealing of the grown TiO₂ nanotubes, we had to use the titanium foils (Ti foil, 0.125 nm thick) as the starting material substrate. The electrochemical conditions were similar to the ones described in the previous case. Briefly, the electrolyte contained 98 mL ethylene glycol, 2 mL DI water, and 0.25 wt% NH₄F.HF. A DC voltage of 60 V was applied between the electrodes, which were the titanium foil and Pt sheet. Subsequently, the as-prepared amorphous TiO₂ samples were cleaned in DI water and annealed in air at different temperatures for 30 min, keeping constant heating and cooling rates of 1°C/min. The photocurrent and impedance data were collected using Gamry G 300 potentiostat in 1 M NaOH solution under the illumination of 100 mW/cm² using three-electrode cell (Pt counter electrode, and Ag/AgCl reference electrode). The EIS measurements were performed in a frequency range of 0.1 Hz to 10⁵ Hz. IMPS and IMVS measurements were carried out using a Zahner PP 211 CIMPS setup with a LED of wavelength 369 nm in a frequency range 0.1 to 10⁵ Hz. The TiO₂ nanotubes were illuminated through the electrolyte side (1M NaOH) with the fixed intensity of 80 mW cm⁻². A sinusoidal perturbation of ~10% of the steady state illumination was superimposed on the constant base light intensity. The IMVS measurements were carried out at open circuit potential with a varying power intensity of LED (369 nm). All measurements were performed against an Ag/AgCl reference electrode (3M KCl), using Pt wire as a counter electrode.

Regarding the PEC activity associated with the prepared TiO₂ nanotubes, there are generally two factors, which can influence the overall performance—intrinsic charge transport/recombination and charge transfer across the semiconductor/electrolyte interface. The overall transport/transfer characteristics influenced the phase content as well as internal defects. To analyze the effect of these factors, the XRD measurements were carried out. XRD data are shown in Figure 7a. The change in the phase ratio of anatase to rutile with respect to annealing temperature can be suggested. The optimum ratio of anatase to rutile was obtained for the sample annealed at 600 °C (79:21), which exhibited improved photocurrent density

(Figure 7b), compared with the single anatase (500 °C) and the highest rutile content sample (700 °C).

To evaluate the charge transport phenomenon and the difference in the photocurrent density associated with TiO₂ mixed phase nanotubes, the IMPS (Figure 7c), IMVS (Figure 7d), and impedance (Figure 7e) measurements were performed. IMPS and IMVS are the perturbation techniques used to extract charge transfer kinetics across the semiconductor-electrolyte interface. In Figure 7c, the ratio of low-frequency intercept to high-frequency intercept (LFI to HFI) corresponds to the charge transfer efficiency (η_{ct}). The Nyquist plots obtained from the impedance data show smaller semicircular arch for the TiO₂ nanotubes annealed at 600 °C, compared with the single anatase (500 °C) and the highest rutile content sample (700 °C). This suggests lower charge transfer resistance thus facilitating better charge transfer to the electrolyte. To gain further insight into the associated impedance data, The Nyquist plots were fitted to an equivalent circuit shown in Figure 7f. The obtained double layer capacitance ($C_{SE, trap}$) plotted against V is presented in Figure 7h. The change in $C_{SE, trap}$ for the sample annealed at 600 °C shows significantly higher capacitance at all the applied potentials. This reveals increasing accumulation of holes at the interface of TiO₂ nanotubes and electrolyte, thus contributing to the higher photocurrent associated with optimum TiO₂ nanotubes (600 °C). Further, the results obtained from IMPS and IMVS also suggested the improved hole transfer efficiency (Figure 7g), which was consistent with the impedance measurements. Hence, it was concluded that the enhanced PEC activity of TiO₂ mixed phase nanotubes related to the improved hole transfer across the TiO₂/electrolyte interface as well as to the decrease in the intrinsic recombination.

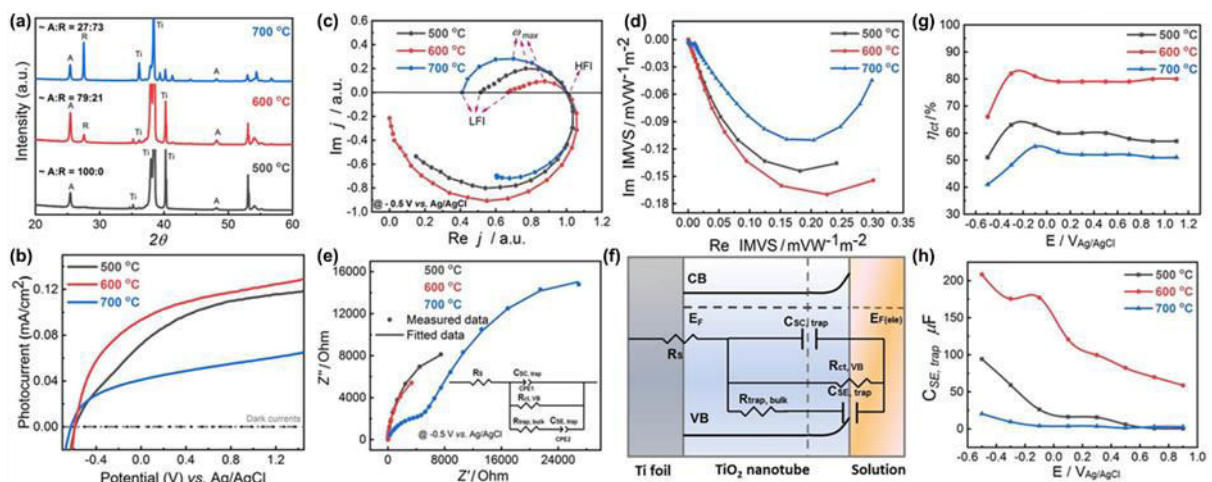


Figure 7. (a) XRD measurements (b) I-V curves obtained under illumination of 100 mW/cm^2 using 1M NaOH solution (c) IMPS data collected at -0.5 V vs. Ag/AgCl (d) IMVS data measured under open circuit conditions (e) Nyquist plots obtained under illumination at -0.5 V vs. Ag/AgCl (f) equivalent circuit used to fit Nyquist plots (g) charge transfer efficiency obtained from IMPS plots (h) double layer capacitance extracted from fitting parameters of EIS data. Reprinted and modified from Ref. [A4].

6.4. Heterojunctions based on TiO_2 nanorods and carbon based materials for enhanced PEC and photocatalytic performance [A5, A6]

It is known that the recombination of photogenerated charges occurs within the time scale of 10^{-9} s , while the time needed for the reaction of these charges with the absorbed particles is considerably longer ($10^{-8} - 10^{-3} \text{ s}$). To diminish the rapid charge recombination and thus the solar conversion efficiency losses, the formation of heterojunction between two semiconductors (S-S), semiconductor–metal (S-M), semiconductor–carbon based materials (S-C), and semiconductor–organic molecules has been proven as a highly efficient strategy. In general, the charges can be effectively separated when they migrate from one semiconductor to the other one (or analogously to metal, 2D nanomaterial, molecules, etc.), which acts as either an electron or a hole acceptor. The movement of the charges is achieved through various mechanisms depending on the partners of the heterostructure, specifically (i) via the formation of internal electric field at the heterojunction interface (S-S type), (ii) a Schottky barrier leading to the electron flow from the material with the higher Fermi level to the lower level until the equilibrium Fermi level alignment (S-M type), (iii) the electron injection from the light absorbing semiconductor to highly conductive carbon based materials such as graphene, carbon nanotubes, etc. (S-C type). The mostly adopted type of heterojunction is realized as the S-S configuration.

Two carbon-based materials such as Cu/Ni decorated graphitic carbon nitride ($\text{CuNi@gC}_3\text{N}_4$) and S, N, O-doped carbon nanosheets (SNOC) were chosen as suitable partners for constructing hybrid nanostructures with TiO_2 nanorods (TNR). Particularly, $\text{g-C}_3\text{N}_4$ has recently drawn great attention as a highly promising metal-free visible-light active photocatalyst. It is a conjugated polymer, which shows very high chemical and photochemical stability, nontoxicity, and bears low cost for potential large-scale production. In addition, $\text{g-C}_3\text{N}_4$ can be relatively easily decorated by other, usually metal, nanoparticles that can further boost its activity towards PEC and photocatalytic processes. In this work [A5], we

successfully incorporated $\text{Cu}(\text{OH})_2$ and $\text{Ni}(\text{OH})_2$ into the structure of $\text{g-C}_3\text{N}_4$ and then wrapped over the TNR. While ultra-small $\text{Cu}(\text{OH})_2$ nanoparticles work as the optical sensitizer, the ultra-thin $\text{Ni}(\text{OH})_2$ nanoflakes provides co-catalytic effect towards oxygen evolution reaction (OER) during the PEC-WS reaction. The synthetic pathway based on a one-pot hydrothermal reaction is depicted in Figure 8a. Figure 8b, c represent the high-angle annular dark-field (HAADF) image and the corresponding STEM-energy-dispersive X-ray spectroscopy (EDS) elemental mapping of the $\text{CuNi@gC}_3\text{N}_4$ sample. Since $\text{g-C}_3\text{N}_4$ as such is a photocatalytically active material and aiming to distinguish the contributions of individual components to the overall photocatalytic activity, we performed the photocatalytic degradation of an organic dye Rhodamine B (usually serves as a model contaminant) on pristine $\text{g-C}_3\text{N}_4$ based materials and bare TNR. Then these materials were combined with the spin-coating of the $\text{g-C}_3\text{N}_4$ based composites ($\text{Cu@g-C}_3\text{N}_4$, $\text{Ni@g-C}_3\text{N}_4$, $\text{CuNi@gC}_3\text{N}_4$) over the TNR and forming homogeneous nano-heterostructures (see SEM surface image of the $\text{CuNi@gC}_3\text{N}_4/\text{TNR}$ nanostructure) and further photocatalytic tests as well as PEC experiments were performed. Several important conclusions were reached on the basis of the obtained results. First, the pristine $\text{CuNi@gC}_3\text{N}_4$ nanostructure provided 3-fold and 5-fold higher photocatalytic activity than bare $\text{g-C}_3\text{N}_4$ and TiO_2 photocatalysts, respectively. Second, the combined $\text{CuNi@gC}_3\text{N}_4/\text{TNR}$ provided also the best activity in the PEC experiments, as it is shown in Figure 8e. The excellent photoactivity was attributed to several synergistically acting features. Specifically, these are: (i) establishing an efficient heterojunction that enhances charge separation at the interface between these two materials because of the energetically suitable positions of their conduction and valence band edges, (ii) improved light absorption mainly via the $\text{Cu}(\text{OH})_2$ component and (iii) accelerated surface OER reaction by $\text{Ni}(\text{OH})_2$ component serving as an effective co-catalyst.

In the following work, [A6] a S-, N- O-, tri-doped porous carbon sheets (SNOC) with graphitic crystalline nature were synthesized by using silica as a template non-reactive agent, which was mixed with other precursors (carrageenan, urea, tetraethyl orthosilicate–TEOS) and heated together. After its removal by immersing the product for 48 h in NH_4HF_2 , a highly porous carbon structure doped by the three elements and having remarkable high specific area of $\sim 380 \text{ m}^2\text{g}^{-1}$ was obtained. This nanostructure was, similarly to the previous case, deposited by spin coating over the TNR. The TEM image of this nanocomposite together with the corresponding HAADF image and EDS elemental mapping are shown in Figure 8f, g, h, respectively. The homogeneous distribution of the dopants is apparent in Figure 8h. Similarly

to the previous case, the multi-doped carbon nanocomposite in combination with TiO_2 showed the highest PEC and photocatalytic activity of the Rhodamine B degradation, compared with bare TiO_2 and nonporous SNOC (synthesized without silica agent). The results of the latter are summarized in Figure 8i. It was demonstrated in the paper that the superior photoefficiency was a result of the developed heterojunction between SNOC and TiO_2 , high electrical conductivity that improved the photocharges' dynamics, and also the co-catalytic effect of the SNOC composite.

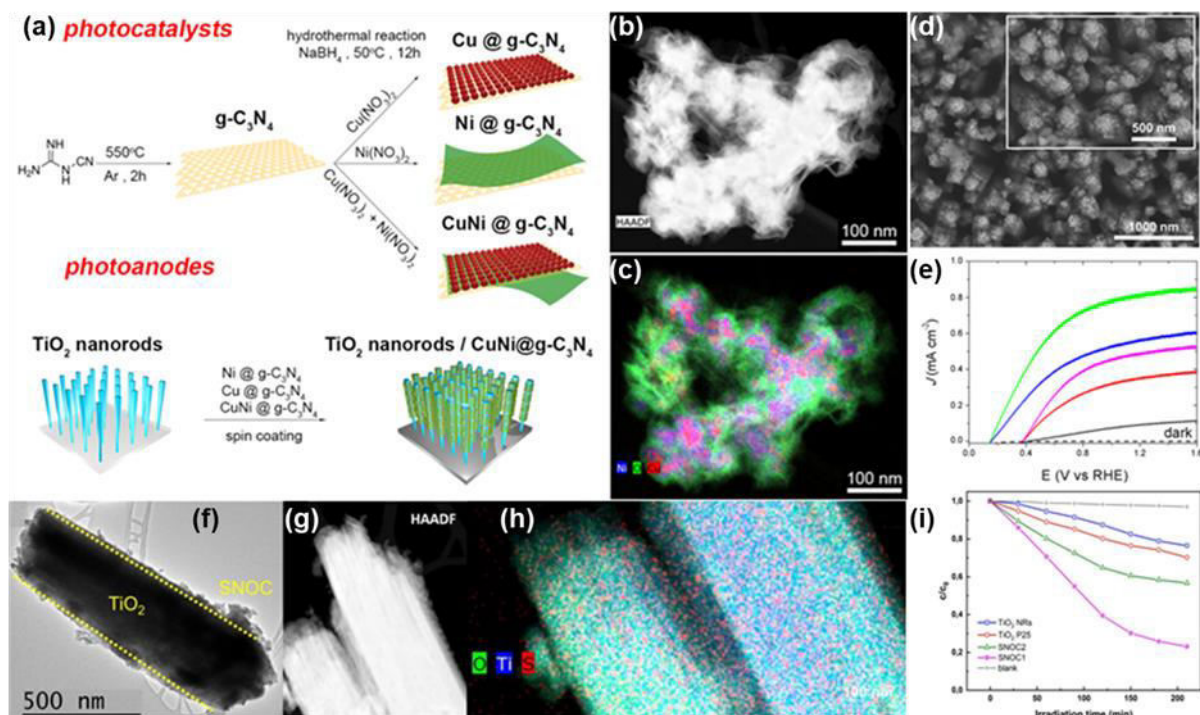


Figure 8. Schematic illustration of the preparation routes of the $g\text{-C}_3\text{N}_4$ pristine and Cu-, Ni-, CuNi-modified $g\text{-C}_3\text{N}_4$ photocatalysts (upper scheme) and TiO_2 nanorods functionalized $g\text{-C}_3\text{N}_4$ photoanodes (bottom scheme), (b) HAADF image and (c) corresponding Ni, O, Cu EDS elemental mapping, (d) SEM surface image of the $\text{CuNi}@g\text{-C}_3\text{N}_4$ deposited over the TiO_2 nanorods, (e) PEC linear sweep voltammetry curves for NRs (black), $\text{TiO}_2/g\text{-C}_3\text{N}_4$ (red), $\text{TiO}_2/\text{Cu}@g\text{-C}_3\text{N}_4$ (magenta), $\text{TiO}_2/\text{Ni}@g\text{-C}_3\text{N}_4$ (blue), and $\text{TiO}_2/\text{CuNi}@g\text{-C}_3\text{N}_4$ (green). recorded under AM 1.5G illumination (100 mW cm^{-2}) in 1M NaOH electrolyte, (f) TEM image of an individual TiO_2 nanorod conformally overcoated by S-, N-, O- doped porous carbon sheets, (g) HAADF image and corresponding (h) EDS O, Ti, S summary element map of the TiO_2/SNOC sample, (i) photocatalytic properties of TiO_2 NRs, TiO_2 P25, porous SNOC, and non-porous SNOC materials. Reprinted and modified from Ref. [A5, A6].

6.5. Plasmonic Au nanostars/ TiO_2 heterostructure nanorod arrays: Broadband UV-Vis-NIR enhancement in PEC water oxidation performance [A7]

Apparently, the most critical limitation for the broader application of TiO₂ in the aforementioned PEC applications is its band gap energy, which allows absorption only in the UV range of solar spectrum. The solar light induced PEC performance of TiO₂ systems can be greatly enhanced by anchoring the nanostructures of noble metals such as Au and Ag on TiO₂, which is enabled by the unique localized surface plasmon resonance properties of these nanosystems. [30] The increase in the solar energy conversion efficiency of TiO₂ systems upon incorporating the plasmonic nanostructures has been attributed to three factors involving effective light scattering, extension of light absorption to longer wavelengths, and direct charge injection from the metal to the semiconductor. In general, the enhancement of PEC performance with plasmonic nanoparticles is strongly dependent on their size and loading. [31, 32] However, the effect of the morphology of plasmonic particles on the enhancement of titania efficiency in PEC technologies has been addressed very rarely in literature. Indeed, almost all reports have focused on spherical or rod-like morphologies of plasmonic nanoparticles. In this work, it was shown for the first time that the use of plasmonic gold nanoparticles with a unique nanostar morphology resulted in the broadband enhancement of the photoactivity of TiO₂ nanorods over the whole UV-Vis-NIR region.

The unique Au nanostar morphology was achieved by a two-step synthetic procedure. First, Au nanoparticles (AuNPs) were prepared by mixing the precursor solution of HAuCl₄ with trisodium citrate dihydrate solution under refluxing conditions. Second, the solution of AuNPs was used as a seed solution, which was under rigorous stirring subsequently mixed with auric chloride, silver nitrate, and ascorbic acid solutions. Finally, the product was centrifuged at 6000 rpm to obtain precipitated AuNSs, which were then redispersed in Milli-Q water. Prior to the deposition of AuNSs, the TiO₂ nanorods were activated by their immersion in concentrated H₂SO₄ and 3-mercaptopropionic acid (MPA) to functionalize the nanorods' surface with thiol groups. Then the TiO₂ NRs substrate was immersed in the solution of AuNSs for 24 hours to conformally anchor the AuNSs. The final step was a thermal treatment of this hybrid nanostructure under mild conditions of 150 °C for 1 hour in order to remove residual MPA and to ensure an intimate contact between the AuNSa and TiO₂ NRs.

The TEM, HAADF images, and corresponding EDS elemental maps showing an individual TiO₂ nanorod decorated by AuNSs are displayed in Figure 9a, b, respectively. The PEC performance was assessed on the basis of the linear sweep voltammetry and transient chronoamperometry measurements under the visible light illumination using a cut-off filter for the light wavelengths below 420 nm as well as under standard solar light AM 1.5 G (100

mW cm⁻²) illumination. Specifically, when compared with bare TiO₂ nanorods, the gold nanostar decorated TiO₂ exhibited ca. 20% and even 350% increase in the photocurrent density under simulated sunlight (see Figure 9c) and visible light irradiation, respectively. Furthermore, to distinguish the contribution of plasmonic effect to the overall PEC performance, the nanostructures were carefully investigated in terms of IPCE characteristics (Figure 9d). Importantly, the achieved IPCE enhancement over the Vis-NIR region was an order of magnitude greater than the values reported in the other literature. [33] Therefore, it was proved that the synergistic interaction of the spherical Au core with the wire-like nanoarms resulted in an extraordinary enhancement of IPCE across the Vis-NIR region. This was the first time such an enhancement had been achieved with a single phase Au nanostructure in the Vis-NIR region. This was largely attributed to the long-wavelength plasmon resonances of gold nanostars and their ability to promote SPR-mediated hot electron transfer. The possible mechanism of the charge transfer is schematically depicted in Figure 9d. It is considered that upon the visible light irradiation the hot electrons are directly injected from AuNSs into the adjacent conduction band of TiO₂ NRs via the Schottky barrier, while the remaining holes in the AuNSs are assumed to promote water oxidation reaction.

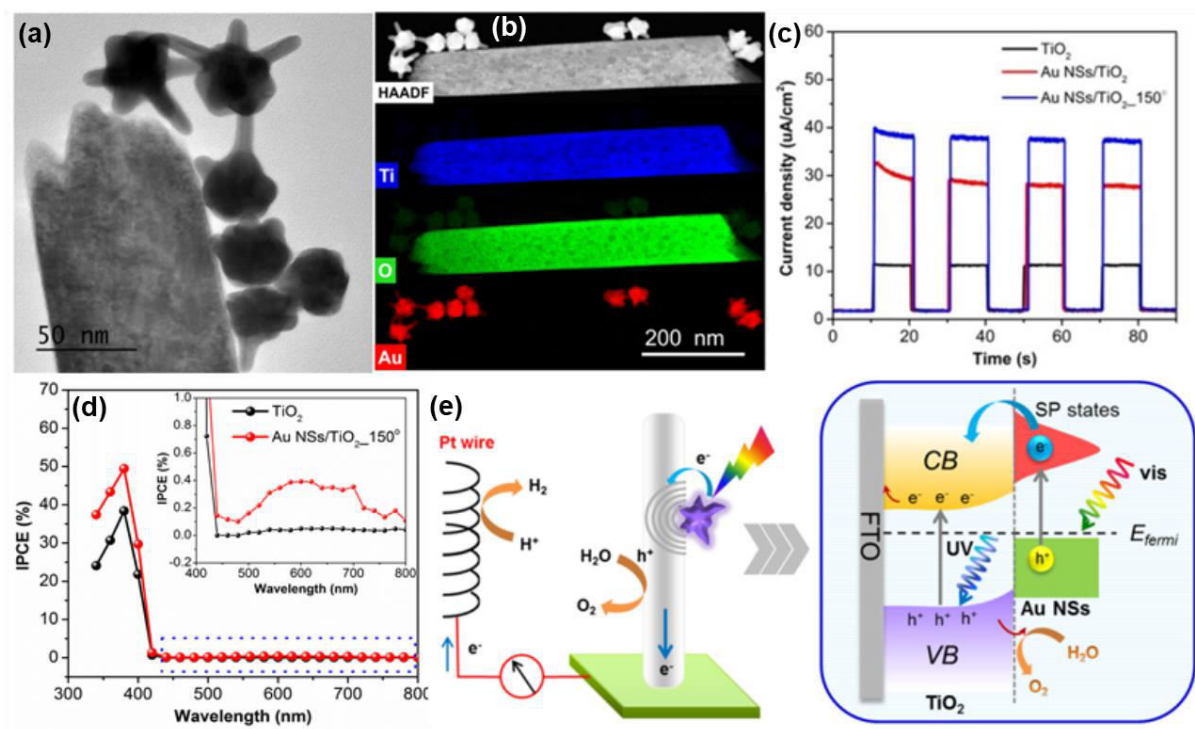


Figure 9. (a) HRTEM image of the AuNSs anchored on the surface of the individual TiO₂ NR, (b) HAADF-STEM image and corresponding EDS elemental mapping of the AuNSs on the TiO₂ nanorod, (c) Transient chronoamperometry scan recorded at 1V vs. NHE and under visible light illumination (λ

> 420 nm), (d) IPCE plots of AuNSs/TiO₂ NRs thermal treated under mild conditions at 150 °C. The PEC measurements were carried out in 1M NaOH electrolyte. Reprinted and modified from Ref. [A7].

6.6. Advanced plasma deposition of very-thin thermally stable TiO₂ blocking layers with enhanced electron transfer ability for solar cells [A8]

One of the crucial issues regarding PEC solar cells, which include well-known dye-sensitized solar cells (DSSCs) and more recent and also more important perovskite solar cells (PSCs), is the considerable efficiency loss due to the recombination of photogenerated charges. These charges have to diffuse through the materials of the solar cell as well having to pass several interfaces before they reach the charge collecting electrodes, which is typical for the FTO substrate. The photoexcited electrons tend to recombine easily also with the oxidized form of mediator (triiodide in the electrolyte) and/or with a hole transporter at both the TiO₂ surface and uncovered surface of the FTO layer, which can shunt the device. It has been clearly verified that such recombination lower the charge collection efficiency and results in lowering the short circuit current (J_{SC}) and the fill factor (FF) of the standardly recorded current–voltage PSCs curve. In order to address this limitation, usually a very thin homogeneous and dense semiconductor layer is deposited between the transparent conductive FTO substrate and the light absorbing layer. It prevents both the recombination of the carriers and also a direct contact of the charges with the conductive electrode and it is termed the blocking layer (BL).

The basic requirements for the BL involve homogeneously covering the full area of the relatively rough FTO substrate, absence of any pinholes and other microstructural defects, and sufficient crystallinity to provide efficient charge transfer (electrons passing through to the FTO contact). The BL's thickness is another key parameter; it should be thick enough to prevent charge tunneling from the FTO into the electrolyte but, at the same time, it should be as thin as possible to maintain the efficient charge transfer from the mesoporous TiO₂ into the FTO. The ultrathin coatings of TiO₂ are the most frequently used BLs. However, the thermal instability of TiO₂ has still remained an unsolved issue. In other words, during the thermal annealing of the ultrathin TiO₂ BLs, various cracks and other structural damages usually develop and then BLs loses their blocking functionality. On the other hand, the thermal calcination is usually one of the unavoidable steps during the construction of PSCs since they typically consist of mesoporous TiO₂ layer whose preparation commonly requires the thermal annealing.

In this work, the thermal instability issue was successfully addressed by using advanced plasma deposition conditions for the deposition of ultrathin TiO₂ films (~ 30 nm) over the FTO substrate, which enabled a careful control of very-high energy bombardment of the grown TiO₂ film during the deposition. The method effectively combined the HiPIMS technique and reactive medium frequency (MF) pulsed magnetron sputtering. The combination of these plasma generation modes increased the heating flux towards the substrate and simultaneously the high ion flux (ion bombardment) on the substrate benefited from the HiPIMS pulse. This double mode of action substantially reduced the internal stress of the deposited films, which is the essential property governing the compactness of the films after the thermal annealing. This phenomenon was verified by a direct comparison of blocking properties of TiO₂ BLs deposited by bare HiPIMS (BL1) and by HiMIS + MF (BL2) combined deposition plasma discharge. The deposited films were characterized and tested for the blocking ability before (as-deposited) and after their annealing at 450 °C for one hour in air. The crystalline structure of the TiO₂ BLs was analysed by Raman spectroscopy, which revealed that the rutile phase was already achieved for the as-deposited films; however, it was further improved after the thermal annealing. The main part of the study was devoted to electrochemical experiments in order to test the blocking ability of the TiO₂ films. Cyclic voltammetry (CV) is a suitable method to evaluate the blocking effect of the TiO₂ films studied. The CV measurements were carried out in aqueous electrolyte containing [Fe(CN)₆]³⁻/[Fe(CN)₆]⁴⁻ redox couple as the model pH independent redox probe with a simple one-electron transfer reaction. TiO₂ behaves as an electrochemically inactive dielectric material against the [Fe(CN)₆]³⁻/[Fe(CN)₆]⁴⁻ redox couple. Therefore, the defects in the BL such as cracks and/or pinholes are directly and sensitively observed as the presence of the anodic current, which is assigned to the ferrocyanide oxidation taking place solely at the uncovered (naked) parts of the FTO layer (see Figure 10a-d). On the basis of the complex characterization and (photo)electrochemical analysis of the deposited films, several major conclusions were reached. In summary: (i) It was demonstrated that although both types of the as-deposited TiO₂ films (BL1, BL2) provided the required blocking ability, they suffered from a very poor photoelectrochemical activity. (ii) After the thermal calcination, the blocking functionality was preserved only for the BL2 type of the films. This property was attributed to the reduced internal stress of the film due to the high-energy bombardment applied on the films during the plasma deposition, which avoided development of any micro-damages due to the annealing. This type of the BLs thus maintained their compactness and homogeneous coverage over the whole area of the FTO substrate. (iii) On the other hand, the

annealing of the BL2 films led to the better crystallinity, which then resulted in enhanced PEC activity, which was more than nine times higher than in the case of the BL1 type. Overall, the achieved results showed that very thin TiO_2 layers prepared by the combination of HiPIMS + MF plasma deposition discharges may function as not only the blocking layers but also highly efficient electron transfer layers.

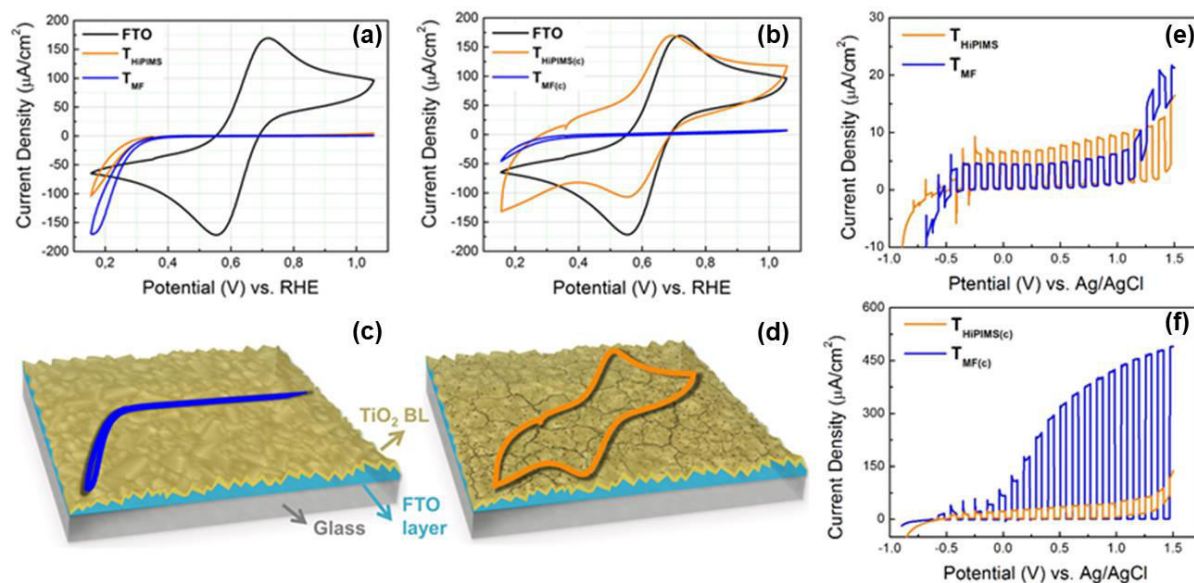


Figure 10. Cyclic voltammograms (CVs) of the bare FTO substrate and FTO deposited by TiO_2 BLs deposited under HiPIMS and HiPIMS+MF plasma discharges combination (a) as-deposited BLs without heat treatment and (b) after the annealing at $450\text{ }^\circ\text{C}$ for 1 hour in air. The scan rate was 100 mV s^{-1} and the electrolyte solution was $0.5\text{ mM K}_4[\text{Fe}(\text{CN})_6] + 0.5\text{ mM K}_3[\text{Fe}(\text{CN})_6]$ in aqueous 0.5 M KCl , $\text{pH } 2.5$ (c) schematic illustration of the ideal CV curve verifying full blocking ability of the coating and (d) CV of the BL containing damages such as cracks and/or pinholes (usually due to the thermal treatment at elevated temperatures). Linear sweep voltammograms of the HiPIMS and HiPIMS+MF TiO_2 BLs of (e) as-deposited films and (f) after the annealing at $450\text{ }^\circ\text{C}$ for 1 hour in air. The experiments were carried out under chopped light UV (360 nm) light irradiation. Reprinted and modified from Ref. [A8].

7. Photoelectrochemically active nanostructures based on $\alpha\text{-Fe}_2\text{O}_3$

Iron oxide ($\alpha\text{-Fe}_2\text{O}_3$) in hematite crystalline structure has been extensively examined for the application to solar water splitting using photoelectrochemical cells owing to its high chemical stability in aqueous environment, nontoxicity, abundance, ability to absorb within the significant part of the solar spectra, and the low cost of production. However, as described in greater detail in Chapter 3, hematite also suffers from several key limitations that still hinder its practical use. In particular, because the conduction band edge of hematite is below that of the H^+/H_2 redox potential (1.23 eV), spontaneous water splitting is not possible, and a

potential bias must be applied for effective carriers separation. This problem has been typically overcome by using another photoactive material working as the photocathode or the required voltage could be provided by a PV cell, e.g. PSC in so-called PEC tandem cell configuration. Further drawbacks are poor absorptivity especially for longer wavelengths, very short diffusion length of minority carriers, and poor majority carrier conductivity. This creates a disaccord between the depth where charge carriers are photogenerated (in the bulk) and the distance they diffuse before recombining. Usually complex strategies including, for example, nanostructure arrangements, very thin films, and high doping levels to increase the ionized donor concentration and thus the conductivity have to be applied simultaneously to suppress these limitations. A serious obstacle hindering the PEC-WS application is the sluggish kinetics of the oxidation reactions of holes at the hematite surface. One of the possible solutions is the surface decoration by nanoparticulates of catalytic materials such as cobalt phosphate (CoPi), IrO_2 , or FeOOH , etc. and/or by deposition of ultrathin films on the hematite surface to passivate its surface states that work as the recombination centers for holes. These serious handicaps were addressed by the author using several approaches that are described in the following chapters. Briefly, the main strategy was the deposition of very thin highly absorbing hematite layers with good crystallinity deploying the aforescribed plasma deposition techniques. Another approach was based on passivation of surface states by the deposition of ultrathin isostructure films of alumina using an atomic layer deposition (ALD) techniques. Finally, application of controlled defect engineering in order to modify intrinsic properties of hematite films was carried out.

7.1. Preparation of very-thin hematite films by means of high-energy plasma deposition methods [A9]

Two low-pressure, low-temperature plasma methods were used for the deposition of hematite thin films. The first one was HiPIMS technique and the second one was hollow cathode plasma jets system (HC). [6, 8, 34] Both of these methods are based on the principal of ion sputtering of the cathode made from pure iron (99.95 %) in the presence of oxygen as the reactive gas. The HiPIMS method was described in detail in Chapter 5. The hollow cathode plasma jet (Figure 11a) uses water-cooled insulated cylindrical nozzles also made from iron. The cathodes are connected with phase locked RF and DC power sources. Controlled flow of the working gas mixture is fed into the nozzles and subsequently pumped down from the reactor chamber. Owing to the generation of intensive DC or RF hollow cathode discharges

inside the nozzles, extremely dense plasma is excited as a result of the so called hollow cathode effects. Plasma jets carry the sputtered iron species to the reactor where they further react with oxygen producing the film on the substrate. Both methods yielded hematite phase directly during the coating. The Raman mapping was performed for the most intense peak at 225 cm^{-1} . The aim was to evaluate the extent of the crystallization over a larger area of the samples. It was revealed that better crystallinity was achieved via the hollow cathode plasma jet. By means of AFM and SEM, the morphology of the films were visualized. From the captured images it was shown that the HiPIMS films were formed by very small particles extremely densely packed. By contrast, the HC films embodied much bigger grains with a nanopyramids morphology (Figure 11b). This apparently influenced the overall photoefficiency evaluated via the photoelectrochemical measurements.

Since the films showed quite a high extent of crystallinity of the as-deposited samples, they were the subject of the initial PEC study. However, these films were almost inactive. A high extend of backward electron-hole pairs recombination of the as-deposited hematite films was probably the main reason for the poor photoactivity. This phenomenon was observed as the high and sharp photocurrent spikes under chopped light J-V characteristic (HC films), when the light was on, which immediately decreased to almost negligible photocurrent values. These positive photocurrent spikes represent the accumulation of holes at the hematite–electrolyte interface because of the surface recombination. Thus, in the second step, the films were thermally treated at 650°C for 30 minutes. At this temperature, the tin diffusion from the FTO films was promoted and the crystallinity was also enhanced. The significant increase in the photoresponse was observed. A better activity was identified for the HiPIMS films. This was apparently due to the nanoscale nature of these films and probably better uniformity. Moreover, as stated previously, in the HiPIMS mode the sputtered particles gain a very high energy, and, thus, they bombard also the substrate with very high energy. It has been demonstrated previously that this effect enhances the interface transfer of the carriers between the film and charge collecting layer. The HiPIMS method is particularly convenient for very low deposition temperature of crystalline thin films. In order to demonstrate this, we conducted the deposition of hematite film onto a polycarbonate substrate with a melting temperature around $150\text{ }^\circ\text{C}$; a photograph with the deposited hematite proving that the substrate did not sustain any damage during the deposition is shown in Figure 11c. The Raman spectrum shows that the hematite crystalline structure was achieved without any post-

deposition treatment (Figure 11d). This ability can be generally extended for preparation of the functional films onto lightweight and flexible supports.

7.2. Approach to addressing the sluggish surface oxidation reaction kinetics via deposition of ultra-thin isostructural alumina films via atomic layer deposition (ALD) method [A10]

Another serious problem the solution to which has attracted extensive attention is a large overpotential of about 0.4–0.6 V with respect to the flatband potential that is necessary to promote the water oxidation reaction at the surface of hematite. Certain portion of this required overpotential is due to the inappropriate energy position of the edge of the hematite conduction bands towards the water reduction reaction. The remaining overpotential requirement is generally attributed to two possible phenomena. The first one is the poor oxygen evolution reaction kinetics on hematite surfaces; the second one is believed to be caused by the presence of surface defects acting as traps. While the OER kinetics can be accelerated by decoration of hematite surface by various co-catalysts, the latter effect has been reduced by deposition of an Al_2O_3 or Ga_2O_3 ultra-thin films passivating the undesirable surface states [12, 13]. This work focused on the PEC process in terms of the reactions of the photogenerated holes. Particular attention was paid to addressing the problem of possible presence of surface states such as oxygen vacancies or crystalline disorders that decrease the overall PEC efficiency. Therefore, the effect of ultrathin (~ 2 nm) alumina coatings deposited by an atomic layer deposition method onto HiPIMS deposited very-thin (~ 25 nm) hematite films was thoroughly studied. This approach apparently suppresses the negative role of the short diffusion length of the photoholes owing to the very low thickness of hematite coating, decreasing the required overpotential for the photocurrent onset due to the effective passivation of the surface states, and increasing the overall current density value due to the elimination of the charge backward recombination.

The depositions of Al_2O_3 overlayers were performed using Cambridge Nanotech—Fiji commercial ALD system. As the precursors, the trimethylaluminum and water were used. The temperature during the ALD coatings was around 150 °C. Coatings with 4 (~ 4 Å), 6 (~ 6 Å), 10 (~ 10 Å), and 20 (~ 20 Å) ALD cycles were compared. The ALD process was monitored in situ by optical ellipsometry. The alumina films were deposited on the surface of HiPIMS thin films deposited under similar previously reported conditions. The as-deposited iron oxide films were annealed for this study at 650 °C or at 750 °C in air for 40 min. The annealing was applied in order to incite interdiffusion of Sn ions coming from the FTO substrate into the

hematite lattice leading to the Sn-doping. It increases the donor density in films and thus its electrical conductivity, which is another drawback to using hematite. Next, the 25 nm hematite films were homogeneously overlaid by Al₂O₃ ultra-thin films deposited by ALD. In Figure 11e, the comparison of PEC activity of the bare hematite (without Al₂O₃) and with the alumina overlayer films of various thicknesses is displayed. It is apparent from the graph that the bare hematite films encountered a typical problem, which is too anodic photocurrent onset potential at 1.09 V vs. RHE and thus relatively low water oxidation photocurrent density at 1.23 V (the thermodynamic potential for water splitting) vs. RHE of 0.08 mA cm⁻². The beneficial effect of the Al₂O₃ is then evident. The presence of alumina passivating layers contributed to the enhanced activity in two ways: (i) the overpotential needed to initiate the PEC reaction was reduced since the cathodic shift of 0.1 V vs. RHE was achieved, and (ii) a higher photocurrents were reached. These findings verified the theory that the surface defects (oxygen vacancies, crystallinity disorders, etc.) behave as traps for the photogenerated carriers (see the illustration in Figure 11e). These surface states are listed among the two main reasons causing the problematic overpotential [35]. Moreover, for the first time it was demonstrated that one annealing step of the as-deposited Fe₂O₃/as-deposited Al₂O₃ was more effective due to relaxation of the hematite film stress reducing the generation of the surface defects than the sequential annealing steps. In this work, the effect of the alumina coating thickness and the temperature of the annealing was further discussed together with the estimation of real hydrogen gas amount evolved.

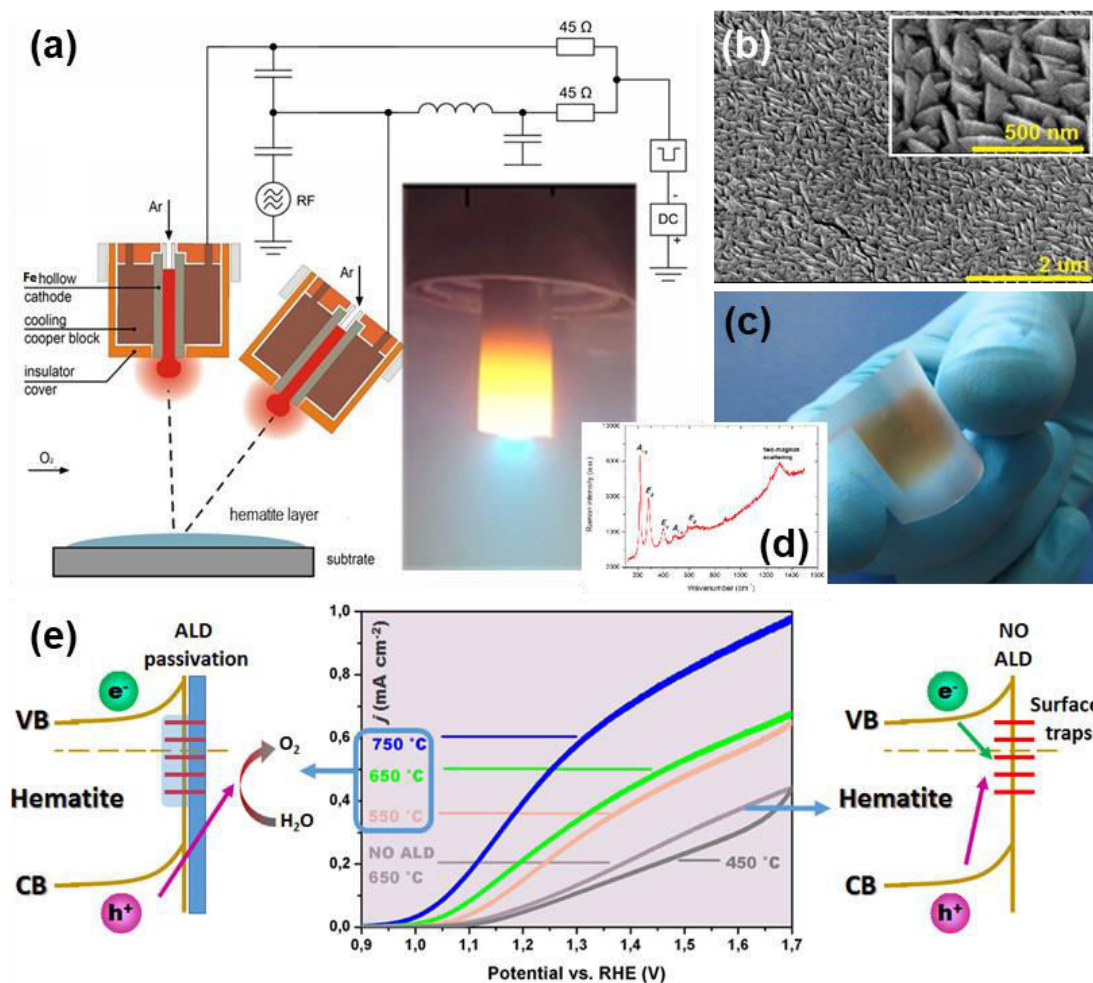


Figure 11. (a) Schematic drawing of a dual hollow cathode (HC) plasma jet systems applied for the deposition of hematite films along with the photograph of plasmatic discharge in one of the deposition nozzle made of pure iron. The whole system is placed in an ultra-high vacuum chamber (base pressure commonly of 10^{-7} mbar) and plasma deposition discharge is pulse modulated, (b) topography SEM image of the hematite film deposited by the HC method onto FTO substrate, (c) photograph picture of hematite thin film deposited onto a polycarbonate substrate with the melting point of $150\text{ }^{\circ}\text{C}$ by HiPIMS method, (d) corresponding Raman spectrum of the film on the polycarbonate substrate verifying well-developed pure hematite crystalline phase, (e) photoelectrochemical water-splitting activity of bare and ALD Al_2O_3 overlaid hematite films thermally treated at different temperatures. The bare (without ALD Al_2O_3 coating) hematite film annealed at $650\text{ }^{\circ}\text{C}$ was used as the reference. The HiPIMS $\text{Fe}_2\text{O}_3/\text{ALD } \text{Al}_2\text{O}_3$ films were then annealed at 450, 550, 650, and $750\text{ }^{\circ}\text{C}$ always for 40 min. The PEC characteristics were recorded under solar light AM 1.5 simulated conditions with the intensity of 100 mW cm^{-2} , using 1 M NaOH solution as the electrolyte, and with the scan rate 5 mV s^{-1} . The figure also schematically illustrates the negative behaviour of surface states and how to address this issue by deposition of passivating overcoatings. Reprinted and modified from Ref. [A9, A10].

7.3. Introduction to the defect engineering in photoactive semiconductors with examples of unpublished results

The defect engineering (DE) has become an attractive research direction for improving the optical and electronic properties of these semiconductors towards highly efficient PEC processes. For example, the discovery of black TiO₂ by Chen and Mao in 2011 [36] showing substantially enhanced solar absorption aroused worldwide interest in researching the reduced forms of TiO₂. In addition to the remarkable enhancement in visible light absorption, black TiO₂ has demonstrated unexpectedly high photocatalytic and PEC performance. The introduction of oxygen vacancies has also been shown as an effective approach to improving the activity of α -Fe₂O₃ PAs. [37, 38] On the other hand, the main limitation related to the current DE approaches is the fact that they are predominantly realized via a high-pressure, high-temperature gas reduction. However, this methodology severely reduces the possibility of influencing/controlling the DE process itself as well as modifying the final properties of the material in a very fine manner, which is undoubtedly the key to understanding precisely all the induced electronic changes and related phenomena. In the following chapter, it is demonstrated how this significant drawback can be effectively tackled by employing the novel deposition method based on modified high-impulse magnetron sputtering (HiPIMS) for the deposition of hematite films under the DE conditions. This specific plasma deposition mode offer the desired capability of high process controllability due to the unique deposition plasma properties. By adjusting the deposition conditions, the extent of the induced defects can be regulated, moreover, under a significantly lower operation temperature. Besides gaining understanding and description of the phenomena related to the DE, the aim was indeed to prepare materials with significantly enhanced PEC activity via proper DE of the α -Fe₂O₃ based photoanodes.

7.4. Defect engineering of hematite very thin films by HiPIMS technique: Controlling over the hematite crystalline texture towards the high electrically conductive (110) orientation [A11]

One of the examples of defect engineering is a possible variation of crystallite preferential orientation of hematite photoanodes induced by a different bombardment energy of the grown film during the plasma deposition.

The poor electrical conductivity is one of the crucial limitations reducing the hematite's efficiency in real experimental conditions. In spite of computing models suggesting that the electrical conductivity is extremely anisotropic, revealing up to four orders of magnitude higher electron transport with conduction along the (110) hematite crystal plane, synthetic approaches allowing the sole growth in that direction have not been reported yet. In this work,

a new strategy for controlling the crystal orientation of very thin hematite films during advanced pulsed reactive magnetron sputtering technique was presented.

Similarly to the previous cases, the highly textured hematite films were deposited by DC pulsed magnetron sputtering under different pulsing regimes of generated deposition plasma: (i) HiPIMS mode with the pulsing frequency of 0.1 kHz in this particular case, (ii) pulsing sputtering mode (PS, 1 kHz), and (iii) medium frequency sputtering mode (MFS, 50 kHz). Different pulsing frequencies influenced the cathode pulse current, and thus the degree of the plasma ionization, plasma density, and energy of the bombardment of FTO substrate as well as the grown hematite film itself. Nevertheless, the average current, I_{AV} , and, consequently, average current density, j_{AV} , were kept constant for all the deposition at 600 mA and 32 mA/cm², respectively. The deposition time was adjusted to yield hematite films with the same thickness ~ 30 nm.

Figure 12 shows results of chopped-light linear sweep voltammetry of the three types of tested hematite photoanodes. Although all the films had the same thickness of around 30 nm, the efficiency was very different, showing a certain trend. The HiPIMS films yielded the highest photocurrent density of 0.28 mA cm⁻² at 1.23 V and 0.65 mA cm⁻² at 1.55 V vs. RHE. Almost negligible photoactivity was measured for the PS hematite films (0.02 mA cm⁻² at 1.23 V vs. RHE). Finally, a moderate photoactivity of 0.14 mA cm⁻² at 1.23 V and 0.38 mA cm⁻² at 1.55 V vs. RHE was obtained for the polycrystalline hematite films deposited under MFS conditions. This phenomenon was unequivocally attributed to the texture effect and corresponding electrical conductivities. The surface topography images taken by AFM showed certain features indicating a different crystal growth with respect to the substrate. There was an indication of perpendicular arrangement of grains, which is characteristic for the desired (110) preferential orientation having the highest electrical conductivity unlike the parallel growth corresponding to the (104) plane, which is defined as having the worst conductivity. Therefore, these findings were in a perfect agreement with the theoretical predictions.

The texture effect was confirmed by X-ray diffraction and by measuring iron Fe⁵⁷ conversion electron Mössbauer spectroscopy (CEMS). X-ray diffractograms (Figure 12b) showed solely the peak corresponding to the plane (110) for the HiPIMS films, and, by contrast, the most intense peak belonging to (104) plane for the hematite film deposited under the pulsing frequency of 1 kHz. Rather polycrystalline structure was identified for the films deposited at 50 kHz. This particular type of hematite photoanode had also the moderate PEC activity. The

graph in Figure 12c shows the photocurrent maxima plotted against the angle theta derivate from the CEMS analysis. By estimating this angle, the texture effect can also be determined (details are provided in [A11]) and the obtained data very nicely matched the previous findings. In agreement with the XRD and Raman spectroscopy, the texture along the (110) plane was obtained for the HiPIMS type and the texture along the (104) plane for the 1 kHz deposited type.

The crystal growth is based on the surface diffusion of the sputtered particles, which strongly depends on the energy of ions bombarding the substrate during the plasma deposition. In situ measurement of the ion flux on the substrate during the depositions was based on the so-called Sobolewski method. [39] Figure 12e verifies our assumptions and the theory that we offered to explain such different crystalline structures growth. As expected, it was found out that the HiPIMS discharge provided almost one order of magnitude higher ion flux density on the substrate, which, in agreement with the literature, was the reason for the isolated texture of grains. Furthermore, the measurements with the calorimetric probe at position of the substrate to investigate the thermal power density on the substrate were performed and it was revealed that the overall thermal load on the substrate was much lower for the HiPIMS mode than in the case of higher pulsing frequency. It means that this technique generally enables to deposit crystalline films on thermally very sensitive materials such as plastics and it provides explanation to the results shown in Figure 11c. The HiPIMS mode generates extremely high energy during very short duty cycles in the range of μs of the plasma deposition cycles. At the same time, a majority of the sputtered particles is thus ionized. These heavy ions can be accelerated towards the substrate providing the desired bombardment that has a tremendous impact on the crucial parameters of the films such as crystalline structure, grain size, texture, morphology, adhesion, interface with the substrate, etc. The bombardment can be further controlled and manipulated by applying bias voltage on the substrate or additional plasma generation during the off-time of the HiPIMS discharge cycle. On the other hand, the off-time periods are sufficiently long to cool down the substrate, which prevents overheating during the deposition and allows using a thermally sensitive substrate as well.

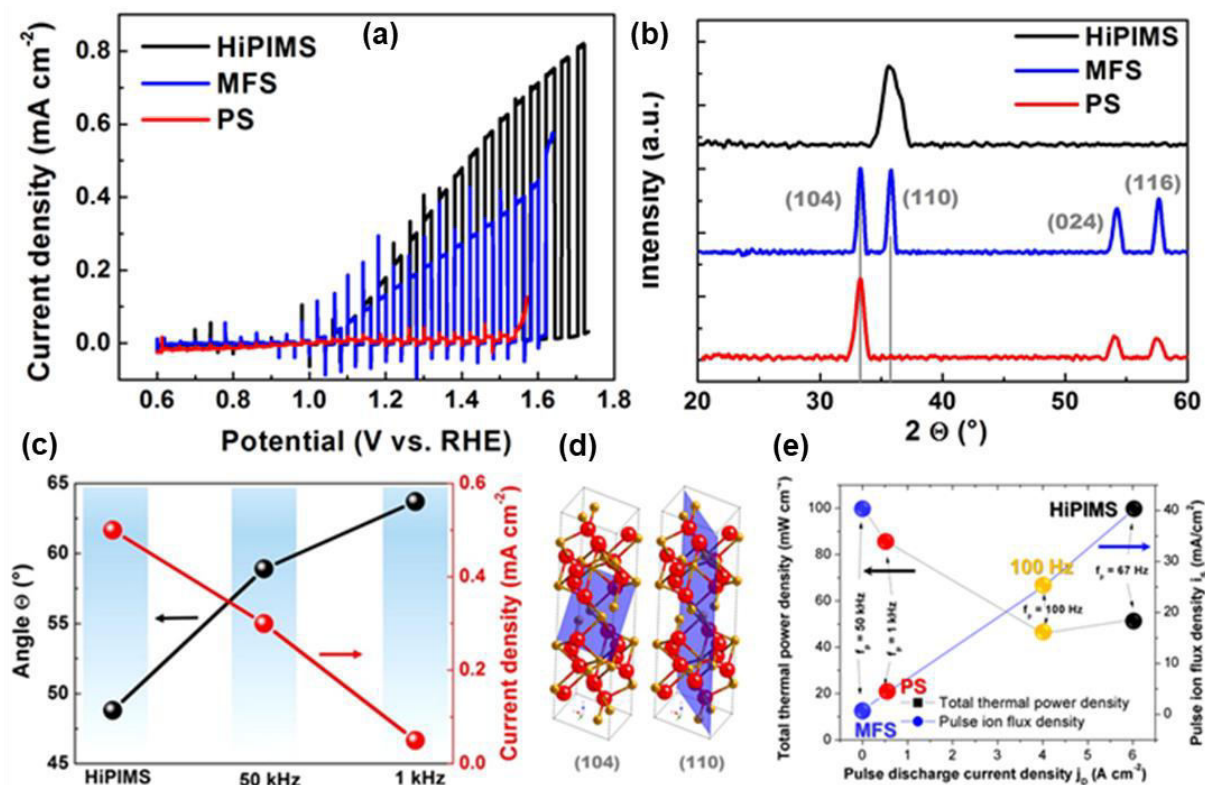


Figure 12. (a) Chopped-light linear sweep voltammetry of hematite photoanodes deposited under the different pulsing regimes and thus the heavy ion bombardment. The PEC measurements were performed under solar light AM 1.5 simulated conditions with an intensity of 100 mW cm^{-2} , using 1 M KOH solution as the electrolyte, and with a scan rate of 1 mV s^{-1} , (b) X-ray diffractograms of the hematite films deposited under identical conditions on the fused-silica substrate, (c) correlation between the texture effect expressed as the angle Θ and the PEC activity of the films expressed as the photocurrent value read at 1.5 V versus RHE, (d) models of the hematite crystal lattice with highlighted (104) and (110) preferentially oriented plane, (e) dependencies of the pulsed discharge current densities for various pulsing frequency modes on the total thermal flux (left y axis) and ion flux (right y axis) on the substrate during the deposition of hematite photoanodes. Reprinted and modified from Ref. [A11].

9. Hierarchical photoanode nanostructures based on the combination of TiO₂ and α -Fe₂O₃ [A12]

The intrinsic drawbacks of both particularly presented materials can be addressed by their own combinations. In this work, the 3D α -Fe₂O₃/TiO₂ hierarchical nanostructures with the carefully designed nanoarchitecture were prepared by sequential multi-hydrothermal steps synthetic procedure. First, the aligned TiO₂ nanotubes were prepared on the FTO substrate using the ZnO nanorods as the sacrificial template (more detailed description is provided in Chapter 6.1). The TiO₂ nanotubes were then modified with α -Fe₂O₃ nanostructures, whose morphologies was controlled as in the form of thin nanoflakes, up to surface agglomerates. The iron(iii) nitrate nonahydrate [Fe(NO₃)₃·9H₂O] with different concentrations ranging between (0.01–0.05 M) was used as the precursor solution. It formed a homogenous perpendicular nanobranches over the TiO₂ nanotubes. The nanobranches were initially formed by FeOOH, which had to be converted into the hematite crystalline structure by thermal annealing at 450 °C for two hours. The resulted nanostructure varied from thin nanoflakes, through nanorods, to surface agglomerates, depending on the concentration of Fe precursor. Schematically, the 3D hierarchical nanostructure is shown in Figure 13a. Figure 13b and 13c then show the SEM images of the bare TiO₂ nanotubes and with the overcoated hematite nanobranches, respectively. The 0.02 M Fe precursor concentration was identified as the most ideal from the PEC characteristics point of view. This concentration provided the hematite nanobranches with the diameter of ~ 10 nm and the lengths varied between 30–140 nm. The XRD analysis revealed the preferential orientation of hematite braches along the (110) crystalline plane, which, as it can be learnt from the previous chapter, is the structure having the highest electrical conductivity. This feature is beneficial for facilitating the charge transfer from the substrate (TiO₂) to the electrolyte, through α -Fe₂O₃, during the PEC reactions. The optical properties were evaluated on the basis of UV-Vis spectroscopy measurements. The optical absorption of the α -Fe₂O₃/TiO₂ composite extended into the visible light wavelengths compared with the bare TiO₂, which showed the usual absorption edge at around 400 nm. The shifted absorption was apparently due to the hematite branches, which typically shows the absorption edge around 600 nm. In this regard, the density functional theory (DFT) calculations were performed to gain further insight into these optical interactions, which were fully in line with the measured experimental data.

The PEC investigations were carried out under standard experimental conditions (AM 1.5 G light illumination with the intensity of 100 mW cm⁻², 1M KOH electrolyte). The PEC reaction

mechanism is schematically depicted as the inset in Figure 13d. The TiO_2 charge carriers were generated in TiO_2 constituent due to the absorption of UV photons. The photoelectrons in the conduction band were transported along the tubes to the back-contact (FTO) through a preferential orthogonal pathway, while the holes travelled from the TiO_2 valence band to that of $\alpha\text{-Fe}_2\text{O}_3$ and then they promoted the water oxidation half reaction. The highest photocurrent density was achieved for relatively low load of the $\alpha\text{-Fe}_2\text{O}_3$ on the TiO_2 NTs. It is very important that the coated hematite branches did not completely cover the TiO_2 NTs, as they did in the case of the 0.02 M hematite sample. Therefore, the partial coverage still left some parts of the TiO_2 surface exposed to both the electrolyte and incident light. In contrast, the full coverage blocked TiO_2 for the activation by the UV wavelengths along with leading to the recombination of photocharges and then, instead of the enhancement of the activity, a decrease was observed. This is reflected in the charge transfer characteristics recorded by the electrochemical impedance spectroscopy showing the best charge transfer for the low hematite loading and severe deterioration of the charge transfer ability for the high hematite loadings.

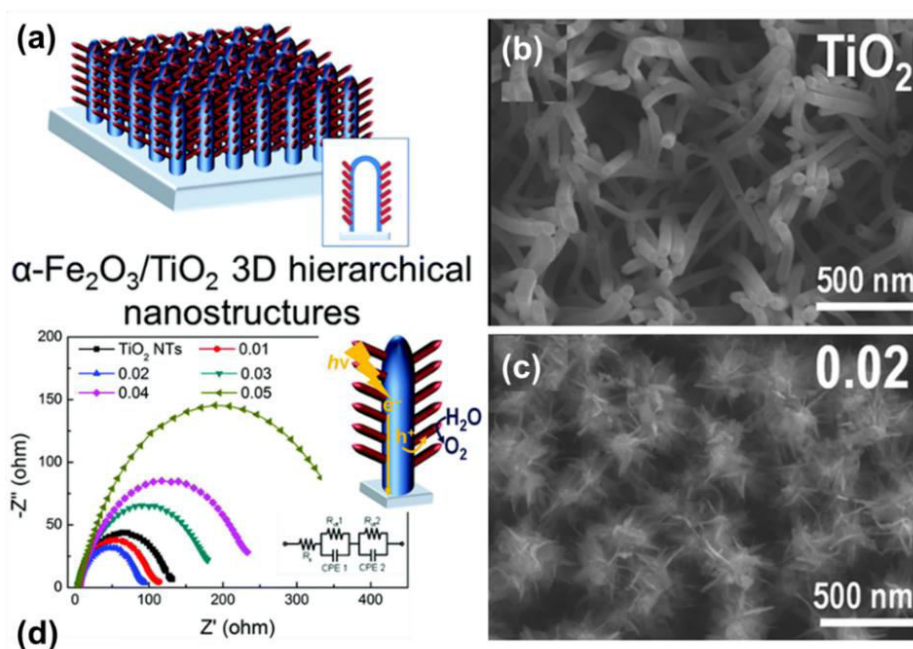


Figure 13. (a) Illustrative sketch of the hybrid nanostructure based on TiO_2 nanotubes combined with $\alpha\text{-Fe}_2\text{O}_3$ nanobranches, (b) bare TiO_2 nanotubes prepared by sequential hydrothermal procedure, (c) TiO_2 nanotubes coated by $\alpha\text{-Fe}_2\text{O}_3$ nanoflakes with the initial concentration of Fe precursor of 0.02 M, (d) Nyquist plots of electrochemical impedance measurements of TiO_2 and $\alpha\text{-Fe}_2\text{O}_3/\text{TiO}_2$ NT layers; inset 1: equivalent circuit for the nanotube structures; inset 2: the anticipated charge transfer mechanism. Reprinted and modified from Ref. [A12].

In summary, although an increase in the PEC performance was clearly observed, it still remained relatively low (the maximum 0.20 mA cm^{-2} at 0 V vs. Ag/AgCl). It is speculated that band bending between these two semiconductors is not perfectly convenient. The author and his co-workers have begun to study other semiconductor partners based on TiO_2 and Fe_2O_3 such as iron titanate (Fe_2TiO_5) showing much more suitable bands energy positions.

9. Conclusions and outlooks

Within the frame of this habilitation thesis, two metal oxide semiconductors such as TiO_2 and $\alpha\text{-Fe}_2\text{O}_3$ were described in terms of their application to photocatalytic and particularly photoelectrochemical processes. The latter was focused on PEC water splitting during which the semiconductors served as the light absorbing photoanodes. The main aim was to develop a new class of multicomponent hybrid systems composed of these central metal oxide semiconductors with controlled shape and dimensionality (e.g. 1D-nanotubes, 2D-ultrathin films). First, the materials were prepared and tested independently and then, in several cases, they were combined with various suitable partners in order to enhance their photocatalytic and/or PEC properties. Therefore, the nanostructured central semiconductors (TiO_2 and $\alpha\text{-Fe}_2\text{O}_3$) were coupled to counterparts with specific functionalities (extended visible light absorption, remarkable efficiency in charge transfer, and enhanced carrier mobility) such that the single components significantly benefited from these interactions with respect to the PEC efficiency of the composite system. The key-approach was presented as the simultaneous and synergistic combination of strategies such as nanostructuring, defect engineering, co-catalyst deposition, and/or surface sensitization. These were specifically: (i) Preparation of high quality TiO_2 and/or $\alpha\text{-Fe}_2\text{O}_3$ materials in the form of 2D nanocrystalline films, using plasmatic methods, as well as in the form of 1D nanotubes, nanorods, or nanoflakes. Self-organizing electrochemical anodization was the most straightforward approach to the fabrication of TiO_2 1D-nanotubes. When this approach was applied, magnetron-sputtered Ti films were used as the starting materials. (ii) Accelerating of surface OER reactions by anchoring the $\text{Ni}(\text{OH})_2$ co-catalysts on the surface of TiO_2 and passivating the surface states of $\alpha\text{-Fe}_2\text{O}_3$ by the deposition of alumina ultra-thin film. (iii) Extension of light absorption to the visible spectral range ($\lambda > 400$ nm) through the surface sensitization of TiO_2 with plasmonic Au nanostructures. (iv) The optimization of photogenerated e^-/h^+ separation and improvement of the hole reaction dynamics, by the formation of heterojunctions of TiO_2 and carbon based materials as well as by applying the approach of defect nano-engineering induced and controlled by HiPIMS plasma deposition technique in the case of $\alpha\text{-Fe}_2\text{O}_3$.

The defect engineering controlled by high-energy plasma deposition sources seem to be highly perspective in this field because it can address many drawbacks of the possibly suitable semiconductors and simultaneously keep the structure significantly simpler (thin films) than the morphologically very complicated multicomponent nanostructures, which are often used. The afore-described plasma deposition technique can also provide photocatalysts and

photoelectrodes with considerably higher mechanical stability than other chemical pathways. Last but not least, these techniques are also highly suitable for efficient scalability, thus offering a relatively easy large-scale industrial production. All these features will crucially reduce the production costs, which is an essential prerequisite for consequent building of real technological units. For these reasons, the current research activities of the author are dedicated to this topic.

Figure 14 summarizes some of the author's recent unpublished results related to the nonstoichiometric TiO_{2-x} (Figure 14 a1-a5) and $\alpha\text{-Fe}_2\text{O}_3$ (Figure 14 b1-b3) thin photoanodes deposited under highly defined reactive HiPIMS sputtering conditions with oxygen deficient atmosphere. Figure 14a3 shows photographs of HiPIMS sputtered TiO_{2-x} films with different degree of oxygen deficiency obtained at 450 °C of the substrate. Figure 14a1 shows a core-shell structure of nonstoichiometric TiO_{2-x} film deposited over hydrothermally grown stoichiometric titania nanorods. Figure 14a2 represents corresponding PEC-WS performance denoting that the nonstoichiometric shell (~ 5 nm) provides the co-catalytic effect, which increases the activity almost two times. The co-catalytic effect is attributed to the presence of Ti^{3+} species. These species were confirmed by XPS (Figure 14a4) and, more interestingly, by the EPR technique under the in-operando (under illumination) conditions (Figure 14a5). This evidently proves the ability to control induced defect concentrations and their chemical state(s). Interesting features were observed for the HiPIMS reactive sputtering of hematite. The combination of oxygen deficient plasma conditions and a platinized substrate led to incredible structural changes in the grown hematite films. Figure 14b1, 2 show Mössbauer spectra of hematite films deposited onto the platinized and common FTO substrates, respectively, under identical conditions. From the obtained results, it can be observed that the non-stoichiometry features were more pronounced on the Pt substrate, which finally led to almost a record-breaking PEC activity for very-thin hematite photoanode (see Figure b3). This phenomenon can be attributed to the formation of a few monolayer of the distorted hematite film at the interface of the Pt substrate and bulk hematite film (evident from the Mössbauer spectra) as well as the increased electrical conductivity of the deposited hematite.

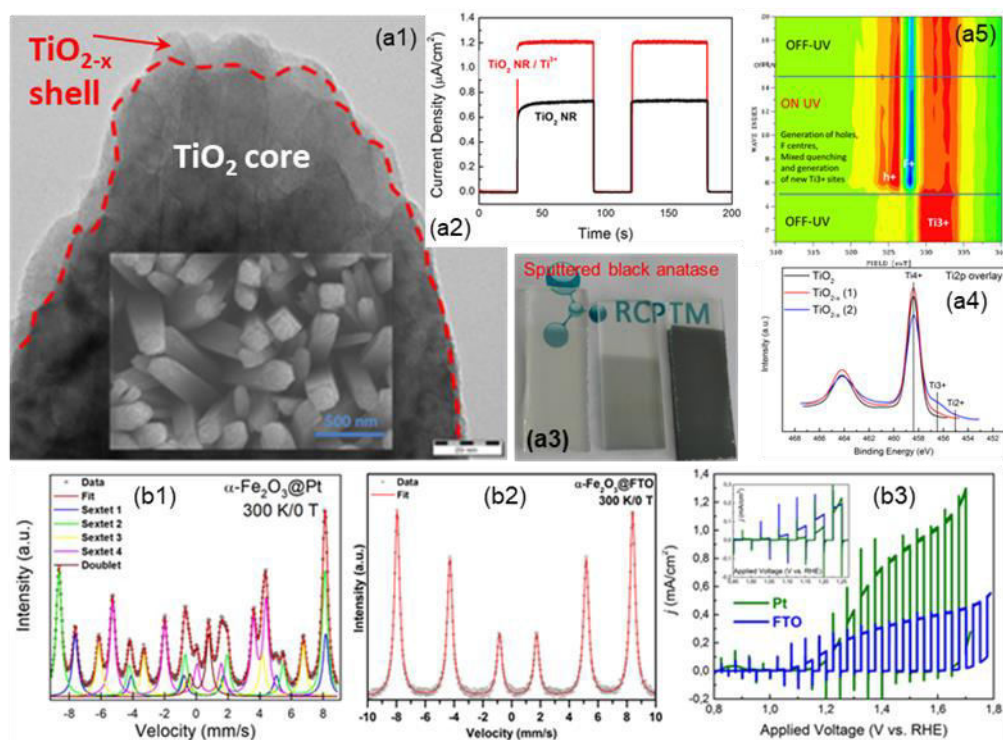


Figure 14. (a1) TEM and SEM (inset) images of the HiPIMS sputtered TiO_{2-x} shell deposited over the TiO_2 nanorods core (prepared by hydrothermal method), (b) PEC activity of bare TiO_2 NRs (black) and with the TiO_{2-x} shell, (a3) photographs of the TiO_{2-x} films deposited directly on FTO substrate, (a4) corresponding XPS spectra showing the Ti^{3+} species working as efficient co-catalysts, (a5) in-operando EPR map showing the evolution of the Ti^{3+} species under the illumination of UV light and in the water environment on reduced TiO_2 powder, Mössbauer spectra of the distorted (b1) and regular (b2) hematite films deposited on Pt and FTO substrates, respectively, (b3) corresponding photocurrent curves recorded under AM 1.5 light illumination and in 1 M KOH electrolyte.

References

- [1] www.nsf.gov.
- [2] Fujishima A, Honda K: Electrochemical photolysis of water at a semiconductor electrode. *Nature* 238, 37-38, 1972.
- [3] Walter MG, Warren EL, McKone JR, Boettcher SW, Mi QX, Santori EA, Lewis NS: Solar water splitting cells. *Chem. Rev.* 110, 6446-6473, 2010.
- [4] Osterloh FE: Inorganic nanostructures for photoelectrochemical and photocatalytic water splitting. *Chem. Soc. Rev.* 42, 2294-2320, 2013.
- [5] Kim JH, Hansora D, Sharma P, Jang JW, Lee JS: Toward practical solar hydrogen production-an artificial photosynthetic leaf-to-farm challenge. *Chem. Soc. Rev.* 48, 1908-1971, 2019.
- [6] Kment S, Kluson P, Stranak V, Virostko P, Krysa J, Cada M, Pracharova J, Kohout M, Morozova M, Adamek P, Hubicka Z: Photo-induced electrochemical functionality of the TiO₂ nanoscale films. *Elchem. Acta* 54, 3352-3359, 2009.
- [7] Kment S, Kmentova H, Kluson P, Krysa J, Hubicka Z, Cirkva V, Gregora I, Solcova O, Jastrabik L: Notes on the photo-induced characteristics of transition metal-doped and undoped titanium dioxide thin films. *J. Colloid Interface Sci.* 348, 198-205, 2010.
- [8] Kment S, Kluson P, Hubicka Z, Krysa J, Cada M, Gregora I, Deyneka A, Remes Z, Zabova H, Jastrabik L: Double hollow cathode plasma jet-low temperature method for the TiO_{2-x}N_x photoresponding films. *Elchem. Acta* 55, 1548-1556, 2010.
- [9] Diebold U: The surface science of titanium dioxide. *Surf. Sci. Rep.* 48, 53-229, 2003.
- [10] Kment S, Diploma thesis, Institute of Chemical Technology Prague, 2006.
- [11] Hoffmann MR, Martin ST, Choi WY, Bahnemann DW: Environmental applications of semiconductor photocatalysis. *Chem. Rev.* 95, 69-96, 1995.
- [12] Sivula K, Le Formal F, Graetzel M: Solar Water Splitting: Progress Using Hematite (alpha-Fe₂O₃) photoelectrodes. *ChemSusChem* 4, 432-449, 2011.
- [13] Tamirat AG, Rick J, Dubale AA, Su WN, Hwang BJ: Using hematite for photoelectrochemical water splitting: a review of current progress and challenges. *Nanoscale Horiz.* 1, 243-267, 2016.
- [14] Liu C, Li F, Ma LP, Cheng HM: Advanced materials for energy storage. *Adv. Mater.* 22, E28-62, 2010.
- [15] Tiwari JN, Tiwari RN, Kim KS: Zero-dimensional, one-dimensional, two-dimensional and three-dimensional nanostructured materials for advanced electrochemical energy devices. *Prog. Mater. Sci.* 57, 724-803, 2012.
- [16] Gleiter H: Nanostructured materials: Basic concepts and microstructure. *Acta Mater.* 48, 1-29, 2000.
- [17] He YM, Hamann T, Wang DW: Thin film photoelectrodes for solar water splitting. *Chem. Soc. Rev.* 48, 2182-2215, 2019.
- [18] Zheng J, Yang R, Xie L, Qu JL, Liu Y, Li XG: Plasma-assisted approaches in inorganic nanostructure fabrication. *Adv. Mater.* 22, 1451-1473, 2010.
- [19] Helmersson U, Lattemann M, Bohlmark J, Ehiasarian AP, Gudmundsson JT: Ionized physical vapor deposition (IPVD): A review of technology and applications. *Thin Solid Films* 513, 1-24, 2006.

- [20] Bradley JW, Welzel T: Physics and phenomena in pulsed magnetrons: an overview. *J. Phys. D-Appl. Phys.* 42, 093001, 2009.
- [21] Kouznetsov V, Macak K, Schneider JM, Helmersson U, Petrov I: A novel pulsed magnetron sputter technique utilizing very high target power densities. *Surf. Coat. Tech.* 122, 290-293, 1999.
- [22] Stranak V, Cada M, Quaas M, Block S, Bogdanowicz R, Kment S, Wulff H, Hubicka Z, Helm CA, Tichy M, Hippler R: Physical properties of homogeneous TiO₂ films prepared by high power impulse magnetron sputtering as a function of crystallographic phase and nanostructure. *J. Phys. D-Appl. Phys.* 42, 105204, 2009.
- [23] Stranak V, Hubicka Z, Adamek P, Blazek J, Tichy M, Spatenka P, Hippler R, Wrehde S: Time-resolved probe diagnostics of pulsed DC magnetron discharge during deposition of TiO_x layers. *Surf. Coat. Tech.* 201, 2512-2519, 2006.
- [24] Olejnicek J, Hubicka Z, Kment S, Cada M, Ksirova P, Adamek P, Gregora I: Investigation of reactive HiPIMS plus MF sputtering of TiO₂ crystalline thin films. *Surf. Coat. Tech.* 232, 376-383, 2013.
- [25] Bradley JW, Backer H, Kelly PJ, Arnell RD: Time-resolved Langmuir probe measurements at the substrate position in a pulsed mid-frequency DC magnetron plasma. *Surf. Coat. Tech.* 135, 221-228, 2001.
- [26] Kelly PJ, Beevers CF, Henderson PS, Arnell RD, Bradley JW, Backer H: A comparison of the properties of titanium-based films produced by pulsed and continuous DC magnetron sputtering. *Surf. Coat. Tech.* 174, 795-800, 2003.
- [27] Liu B, Aydil ES: Growth of oriented single-crystalline rutile TiO₂ nanorods on transparent conducting substrates for dye-sensitized solar cells. *J. Am. Chem. Soc.* 131, 3985-3990, 2009.
- [28] Lee K, Mazare A, Schmuki P: One-dimensional titanium dioxide nanomaterials: Nanotubes. *Chem. Rev.* 114, 9385-9454, 2014.
- [29] Moniz SJA, Shevlin SA, Martin DJ, Guo ZX, Tang J: Visible-light driven heterojunction photocatalysts for water splitting – a critical review. *Energy Env. Sci.* 8, 731-759, 2015.
- [30] Linic S, Christopher P, Ingram DB: Plasmonic-metal nanostructures for efficient conversion of solar to chemical energy. *Nat. Mater.* 10, 911-921, 2011.
- [31] Mascaretti L, Dutta A, Kment S, Shalaev VM, Boltasseva A, Zboril R, Naldoni A: Plasmon-enhanced photoelectrochemical water splitting for efficient renewable energy storage. *Adv. Mater.* 1805513, 2019.
- [32] Jiang R, Li B, Fang C, Wang J: Metal/semiconductor hybrid nanostructures for plasmon-enhanced applications. *Adv. Mater.* 26, 5274-5309, 2014.
- [33] Pu YC, Wang GM, Chang KD, Ling YC, Lin YK, Fitzmorris BC, Liu CM, Lu XH, Tong YX, Zhang JZ, Hsu YJ, Li Y: Au nanostructure-decorated TiO₂ nanowires exhibiting photoactivity across entire UV-visible region for photoelectrochemical water splitting. *Nano Lett.* 13, 3817-3823, 2013.
- [34] Hubicka Z, Kment S, Olejnicek J, Cada M, Kubart T, Brunclikova M, Ksirova P, Adamek P, Remes Z: Deposition of hematite Fe₂O₃ thin film by DC pulsed magnetron and DC pulsed hollow cathode sputtering system. *Thin Solid Films* 549, 184-191, 2013.

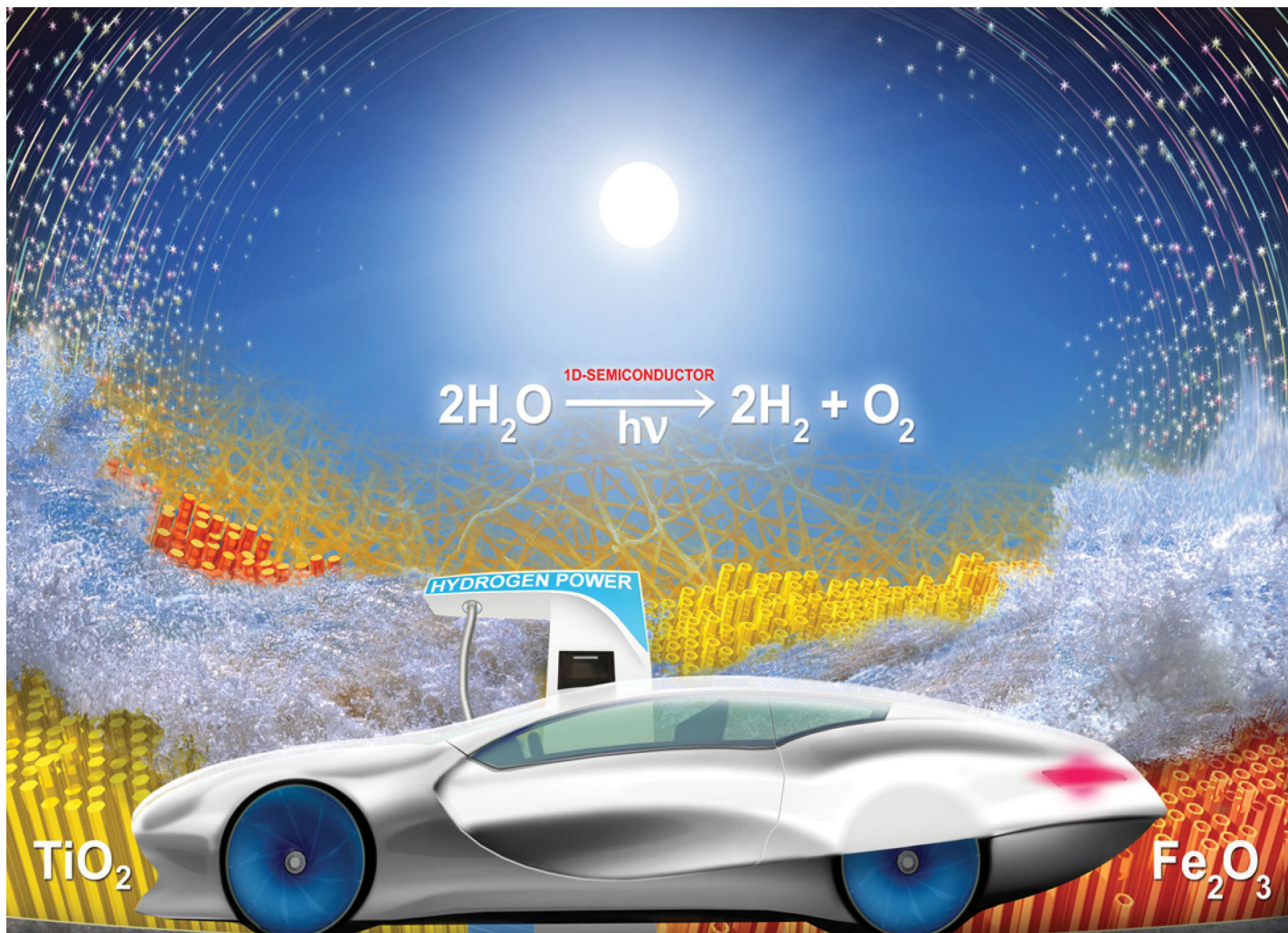
- [35] Sivula K: Metal oxide photoelectrodes for solar fuel production, surface traps, and catalysis. *J. Phys. Chem. Let.* 4, 1624-1633, 2013.
- [36] Chen X, Liu L, Yu PY, Mao SS: Increasing solar absorption for photocatalysis with black hydrogenated titanium dioxide nanocrystals. *Science* 331, 746-750, 2011.
- [37] Wang GM, Ling YC, Li Y: Oxygen-deficient metal oxide nanostructures for photoelectrochemical water oxidation and other applications. *Nanoscale* 4, 6682-6691, 2012.
- [38] Wang Z, Mao X, Chen P, Xiao M, Monny SA, Wang S, Konarova M, Du A, Wang L: Understanding the roles of oxygen vacancies in hematite-based photoelectrochemical processes. *Angew. Chem. Int. Ed.* 58, 1030-1034, 2019.
- [39] Kment S, Cada M, Hubicka Z, Krysa J, Kmentova H, Olejnicek J, Cilova Z, Zboril R: Role of ion bombardment, film thickness and temperature of annealing on PEC activity of very-thin hematite photoanodes deposited by advanced magnetron sputtering. *Int. J. Hydrogen Energy* 41, 11547

Appendix [A1]

Photoanodes based on TiO₂ and α -Fe₂O₃ for solar water splitting— superior role of 1D nanoarchitectures and of combined heterostructures

S. Kment*, F. Riboni, S. Pausova, L. Wang, H. han, Z. Hubicka, J.
Krysa, P. Schmuki*, R. Zboril*

Chemical Society Reviews 46, 3716-3769, 2017

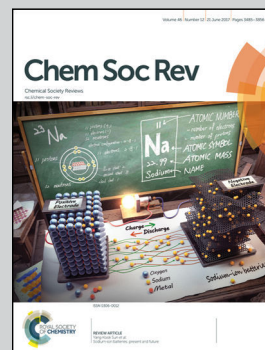


Featuring work from the research groups of Professor Patrik Schmuki, University of Erlangen-Nuremberg, Erlangen DE, and of Professor Radek Zboril, Palacky University, Olomouc, CZ.

Photoanodes based on TiO₂ and α -Fe₂O₃ for solar water splitting – superior role of 1D nanoarchitectures and of combined heterostructures

One-dimensional TiO₂ and α -Fe₂O₃ based nanostructures hold great promise as photoanodes for light-driven water splitting to renewable energy vectors and fuel sources, such as dihydrogen (H₂).

As featured in:





See Stepan Kment, Patrik Schmuki, Radek Zboril *et al.*, *Chem. Soc. Rev.*, 2017, 46, 3716.



Cite this: *Chem. Soc. Rev.*, 2017, 46, 3716

Photoanodes based on TiO₂ and α-Fe₂O₃ for solar water splitting – superior role of 1D nanoarchitectures and of combined heterostructures

Stepan Kment,^{†*a} Francesca Riboni,^{†ab} Sarka Pausova,^c Lei Wang,^{‡b} Lingyun Wang,^a Hyungkyu Han,^a Zdenek Hubicka,^a Josef Krysa,^c Patrik Schmuki ^{*abd} and Radek Zboril ^{*a}

Solar driven photoelectrochemical water splitting (PEC-WS) using semiconductor photoelectrodes represents a promising approach for a sustainable and environmentally friendly production of renewable energy vectors and fuel sources, such as dihydrogen (H₂). In this context, titanium dioxide (TiO₂) and iron oxide (hematite, α-Fe₂O₃) are among the most investigated candidates as photoanode materials, mainly owing to their resistance to photocorrosion, non-toxicity, natural abundance, and low production cost. Major drawbacks are, however, an inherently low electrical conductivity and a limited hole diffusion length that significantly affect the performance of TiO₂ and α-Fe₂O₃ in PEC devices. To this regard, one-dimensional (1D) nanostructuring is typically applied as it provides several superior features such as a significant enlargement of the material surface area, extended contact between the semiconductor and the electrolyte and, most remarkably, preferential electrical transport that overall suppress charge carrier recombination and improve TiO₂ and α-Fe₂O₃ photoelectrocatalytic properties. The present review describes various synthetic methods and modifying concepts of 1D-photoanodes (nanotubes, nanorods, nanofibers, nanowires) based on titania, hematite, and on α-Fe₂O₃/TiO₂ heterostructures, for PEC applications. Various routes towards modification and enhancement of PEC activity of 1D photoanodes are discussed including doping, decoration with co-catalysts and heterojunction engineering. Finally, the challenges related to the optimization of charge transfer kinetics in both oxides are highlighted.

Received 7th January 2016

DOI: 10.1039/c6cs00015k

rsc.li/chem-soc-rev

1. Introduction

The fulfilment of global energy demand still mainly relies on supply and use of fossil fuels such as coal, crude oil, natural gas, *etc.* The energy content of fossil fuels is typically released upon their combustion, which in turn generates significant

emissions of CO₂ into the atmosphere and ultimately promotes global warming and climate change. In 2013 the global primary energy consumption amounted to *ca.* 17 TW (90% of which was generated from fossil fuel).

Taking into account the pace at which the world economy grows, a consequent drastic increase of global energy consumption is predicted to take place in the near future.^{1,2}

Therefore, the urgency to find secure, sustainable, clean and renewable energy sources appears of primary importance and various alternatives to current sources have been introduced with the attempt of limiting CO₂ emissions.^{3,4}

Dihydrogen (H₂), in particular, is one of the most promising energy carriers and fuel sources due to its high energy-per-mass content, a wide range of available storage and transport approaches, and reduced harmful emissions. Indeed, the energy stored into its chemical bond can be used in fuel cells to produce clean electricity. In addition, H₂ represents the reactant for well-established industrial processes, such as petroleum refinement, ammonia synthesis, *etc.*

Although industrial mass scale production of dihydrogen is still based on fossil fuel combustion (*i.e.*, the most common

^a Regional Centre of Advanced Technologies and Materials, Faculty of Science, Palacky University, 17. listopadu 1192/12, 771 46 Olomouc, Czech Republic. E-mail: stepan.kment@upol.cz, schmuki@www.uni-erlangen.de, radek.zboril@upol.cz

^b Department of Materials Science and Engineering, University of Erlangen-Nuremberg, Martensstrasse 7, D-91058 Erlangen, Germany

^c Department of Inorganic Technology, University of Chemistry and Technology Prague, Technicka 5, 166 28 Prague 6, Czech Republic

^d Department of Chemistry, Faculty of Science, King Abdulaziz University, P.O. Box 80203, Jeddah 21569, Saudi Arabia

[†] These two authors contributed equally.

[‡] Current address: State Key Laboratory for Oxo Synthesis and Selective Oxidation, National Engineering Research Center for Fine Petrochemical Intermediates, Lanzhou Institute of Chemical Physics, Chinese Academy of Sciences, 730000 Lanzhou, China.

method for extracting H₂ is still the steam-reforming of methane),⁴ green alternatives that utilize only water (H₂O) as primary H₂ source are currently under development.

One of the most promising solutions is represented by the use of photoelectrochemical cells (PECs) for light-driven water splitting. In these devices, semiconductor materials are used as photoelectrodes that under illumination and an applied electric bias can split H₂O into H₂ and O₂. Ideally, the goal of this technology is to convert sunlight into clean energy available on demand.

1.1 Photoelectrolysis of water – background and basic requirements

After the pioneering work in 1972 by Fujishima and Honda,⁵ the photoelectrochemical water splitting (PEC-WS) reaction has been largely investigated as promising energy vector (H₂) supplying.

PEC-WS consists in the reduction of water into hydrogen (cathodic reaction) accompanied by the anodic reaction of oxygen generation.^{5–7} In a conventional PEC device, the reduction and oxidation reactions occur at the surface of photoelectrodes (*i.e.*, the photocathode and the photoanode, respectively) that are immersed in an aqueous electrolyte. The charge carriers that correspondingly promote H₂ and O₂ evolution (*i.e.*, electrons and holes, respectively) are generated in the semiconductor(s) upon absorption of photons of adequate energy ($h\nu \geq \text{band-gap}, E_g$).

Different configurations apply to PEC devices: in a so-called tandem cell configuration, both the electrodes are semiconductor materials, while in a Schottky type cell one of the two is a metal electrode. Regardless of the configuration, n-type semiconductors are used as photoanodes while p-type semiconductors as photocathode – this is related to the electronic properties of these materials and the type of majority carriers, *i.e.*, electrons (e⁻) or holes (h⁺) produced by photoexcitation.⁸



Stepan Kment

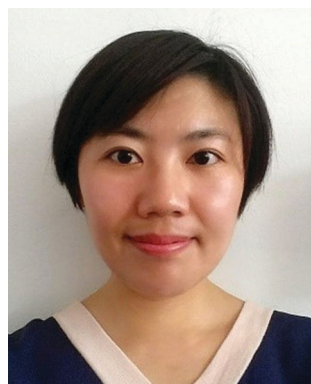
Researcher in the group of Photoelectrochemistry. His research is focused on development of new materials and nanostructures for PEC water splitting application mainly via advanced plasma deposition methods.

Stepan Kment received his PhD in solid state physics and photoelectrochemistry in 2010 from Czech Technical University in Prague, Czech Republic. He then spent one year as a postdoctoral research fellow at Department of Electrical Engineering, University of Nebraska – Lincoln, Lincoln, NE, USA. Since 2011 he has been working at the Regional Centre of Advanced Technologies and Materials of Palacky University, Olomouc, Czech Republic as a Senior



Francesca Riboni

Francesca Riboni studied Chemical Sciences at the University of Milan, Italy, and obtained her PhD in Chemistry from the University of Milan, Italy, in 2014. She joined the group of Prof. Schmuki at the University of Erlangen-Nuremberg, Germany, in 2015 as a post-doctoral fellow. Her research interests include the synthesis of functional nanomaterials by electrochemical processes and their application as energy conversion and storage devices.



Lei Wang

Her research interests include the fabrication of one-dimensional semiconductors for photoelectrochemical water splitting applications.

Lei Wang received her PhD degree from University of Science and Technology Beijing in 2010. From 2007–2010, she was an exchange student in National Institute for Materials Science, Japan. She worked as a postdoctoral fellow in Prof. Patrik Schmuki's research group in University of Erlangen-Nuremberg, Germany from 2011–2016. Since Aug. 2016, she is a professor in Lanzhou Institute of Chemical Physics, Chinese Academy of Science.



Josef Krýsa

materials, photoelectrochemistry, energy and environmental applications of photo(electro)catalysis.

Josef Krýsa graduated from University of Chemistry and Technology, Prague (UCT), where he obtained also PhD degree in 1995. In 2008 he obtained full professorship at UCT, Department of Inorganic Technology, where he is at the moment a leader of the group Photocatalysis (<http://www.josefkrýsagroup.com>). He published more than 106 papers, h-index is 24. His research interest is the preparation and characterization of nanostructured photocatalysts

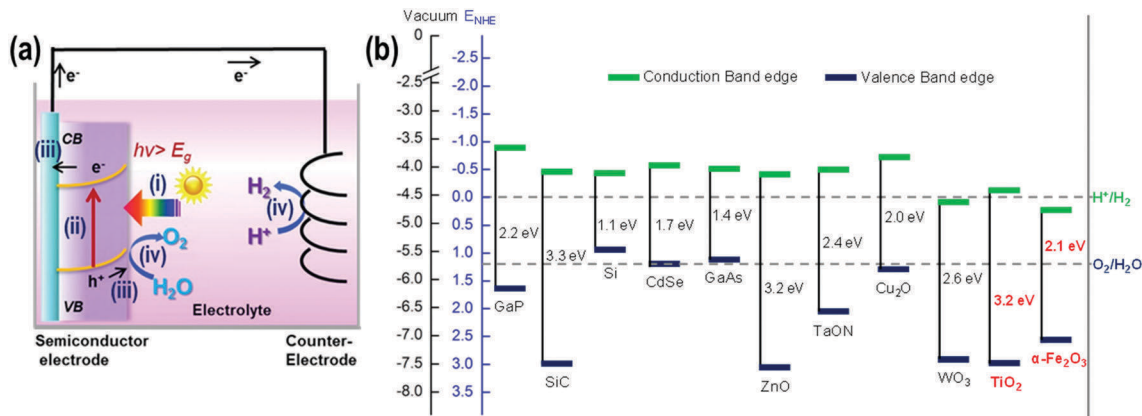
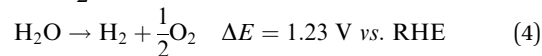
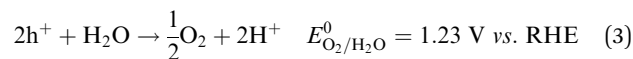
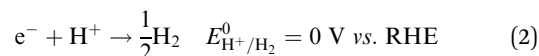
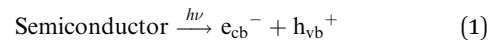


Fig. 1 (a) Principle of operation of a photoelectrochemical cell based on n-type semiconductor; the water splitting reaction steps (i–iv) are described in the text (Section 1.1). (b) Band edge positions of semiconductors in contact with an aqueous electrolyte at pH = 0, relative to NHE and to the vacuum level. For comparison HER and OER redox potentials are also reported.

The focus of the present review is on n-type photoanodes – as the most important class of materials discussed in this review, namely α -Fe₂O₃ and TiO₂, are in their most abundant forms intrinsically n-type materials.

Overall, the PEC-WS reaction consists of four main sequential steps (Fig. 1(a)): (i) light absorption, (ii) separation of photo-generated charge carriers, (iii) transport of charges (h⁺) towards the electrode surface (electrons to the back contact), and (iv) surface reactions (h⁺ transfer). In most cases of available n-type semiconductors in contact with a common electrolyte, a space-charge depletion layer is formed at the semiconductor/liquid junction (SCLJ). Upon light illumination, electron–hole (e[−]/h⁺) pairs are generated (1) and separated due to the space-charge field promoted by band-bending (band-bending depends on the intrinsic work-function (redox potential) differences between the semiconductor and the electrolyte).⁹

As a consequence, holes in the valence band (VB) diffuse and migrate towards the SCLJ where the oxygen evolution reaction (OER) occurs (3). By contrast, electrons promoted into the semiconductor conduction band (CB) are driven away from the SCLJ, transported through the anode towards the back-contact, and are conveyed through the external circuit to a metallic cathode (e.g., platinum), where the H₂O reduction to H₂ (hydrogen evolution reaction, HER – (2)) takes place. Hence, the photoelectrolysis of water can be summarized as follows:



Patrik Schmuki

Patrik Schmuki obtained his PhD from ETH Zurich, Switzerland, in 1992. From 1994–1997 he worked at Brookhaven National Laboratory, US, and at the Institute for Microstructural Sciences of the National Research Council of Canada. From 1997–2000, he has been Associate Professor for Microstructuring Materials at EPFL, Switzerland, and since 2000 he is Full Professor and Head of the Institute for Surface Science and Corrosion at the

Department of Materials Science and Engineering of the University of Erlangen-Nuremberg. His research interests target electrochemistry and materials science at the nanoscale, with a particular focus on functional materials and self-organization processes.



Radek Zboril

Prof. Radek Zboril, PhD after finishing the PhD study (2000) underwent several short-term stays e.g. at University of Delaware and University of Tokyo. From 2010, he is a professor at the Palacký University Olomouc and the general director of the Regional Centre of Advanced Technologies and Materials, RCPTM in Olomouc, Czech Republic. He is an author and co-author of more than 380 papers. He is focused on nanomaterials research including

iron, iron oxide, noble metal and carbon-based (graphene derivatives, carbon dots, etc.) nanostructures, magnetic nanoparticles, and hybrid systems. Their advanced nano-architecture and applications in water treatment, energy materials, catalysis, etc.

The overall reaction (4) is endoenergetic, with a Gibbs free energy $\Delta_r G^0 = 237.2 \text{ kJ mol}^{-1}$ per mole of H_2 produced (according to the Nernst equation, $\Delta E = 1.23 \text{ V}$). Therefore, the semiconductor used as photoelectrode must absorb light with photon energy greater than 1.23 eV (that is, the semiconductor should exhibit an absorption edge at $\lambda < ca. 1100 \text{ nm}$).

However, due to the intrinsic kinetic limitations of reactions (2) and (3) and the resulting overpotential needed for oxygen and hydrogen production, $\Delta G > \sim 2.0 \text{ eV}$ (corresponding to a limiting absorption edge λ of *ca.* 610 nm) is frequently reported as the threshold energy required to achieve a water splitting reaction at a reasonable rate.^{10,11}

Basic requirements for a photoanode material include low cost of production, high chemical stability, high carrier mobility, long carrier lifetime, and rapid interfacial charge transfer. Furthermore, it should feature a conduction band-edge (E_{cb}) more negative than the redox potential $E^\circ(\text{H}^+/\text{H}_2)$ and a valence band-edge (E_{vb}) more positive than the redox potential $E^\circ(\text{O}_2/\text{H}_2\text{O})$, with the electronic nature of the band edges that also provides photostability to the material itself. Additionally, it is also desired that the semiconductor absorbs a large fraction of visible light in order to enable sunlight-driven water splitting.

Band edges and band-gap energies of semiconductors typically explored for photoelectrochemical H_2O splitting are reported in Fig. 1(b).

Despite large efforts and hundreds of semiconductors explored, the thermodynamic and kinetic requirements for an efficient PEC-WS reaction have not yet been satisfied by a single semiconductor candidate. For instance, Si, Ge or III-V compounds suffer from severe photocorrosion and instability in water solutions, while transition metal oxides rarely meet the criteria of (i) a band-gap width suitable for sunlight activation, or of (ii) adequate band-edges to spontaneously promote OER and HER.

Nevertheless, metal oxides still represent one of the most viable options for PEC water splitting application, particularly owing to their low processing cost and high stability against photocorrosion even in harsh environments.

The engineering of metal oxide semiconductor photoelectrodes that exhibit long-term stability and a high photoefficiency could be realized using different strategies (applied individually or in combination).

A first approach can be based on theoretical prediction and synthesis of new materials that could intrinsically satisfy the aforementioned criteria.¹²

A second approach, based on experimental attempts, relies on bulk and/or surface modifications of already known/widely investigated semiconductors (*e.g.*, TiO_2 , $\alpha\text{-Fe}_2\text{O}_3$, WO_3 , BiVO_4 , *etc.*) in view of improving their properties and functionalities. This translates into strategies such as: (i) doping, that is by introducing other elements (metallic or non-metallic), into the semiconductor lattice, to modify electronic properties such as the donor density and thus the charge mobility, and/or to narrow the band-gap of the material and enable visible light photoresponse (this often applies to TiO_2); (ii) anchoring a co-catalyst onto the photoelectrode surface to promote charge carrier separation and to facilitate hydrogen and oxygen evolution

kinetics; (iii) surface modification by organic dyes, plasmonic materials or quantum dots to enhance visible light absorption; (iv) passivation of surface states or protection of the electrode by deposition of ultra-thin overlayers, to avoid surface charge recombination and enhance charge transfer to the environment (or to suppress photocorrosion).

Finally, another viable strategy is the nanostructuring of photoelectrode material into nanoparticles, nanotubes, nanoplatelets, *etc.* This is an efficient approach in the context of heterogeneous (*i.e.*, solid-liquid and solid-gas) reactions since it typically leads to large surface-to-volume ratio for the semiconductor (large surface area) that facilitates charge transfer at the SCLJ. Also, *e.g.*, for one-dimensional nanostructures (discussed below), their geometry is crucial for achieving high PEC-WS efficiency owing to the control over light absorption and orthogonal charge separation, as well as for establishing preferential percolation pathways.

1.2 Calculation of solar-to-hydrogen efficiency

To promote the advancement of PEC-WS technologies, the discovery and development of new materials are of primary importance. However, also the identification of protocols and standard parameters to cross-compare the materials (in terms of properties and efficiency) is highly necessary – reliable and reproducible protocols may accelerate knowledge transfer and process development.

Therefore, we discuss the most important parameters, that is, we provide a description of the most useful figures of merit (see below) typically reported to characterize the performance of a photoelectrochemical device in terms of light to energy conversion efficiency and indicate the limits within which each of these benchmarks may be applied.

Photoconversion efficiency (η) depends on many factors such as the spectrum of the incident radiation, the band-gap of the semiconductor, the reflection of light, and the transport of e^-/h^+ through the semiconductor.

The comparison of photoconversion efficiencies obtained for different semiconductor materials requires that these efficiencies are presented for a standard solar spectrum, usually the Air Mass AM 1.5 global solar spectrum at a given power density (100 mW cm^{-2}).

Most measurements of photoconversion efficiency are performed under illumination by artificial light sources. This is convenient mainly because artificial sources are stationary and their intensity is essentially constant with time (although the lamp spectrum varies in intensity with the lamp lifetime), while spectrum and intensity of solar radiation reaching the ground depend on the time of day and on the atmospheric conditions. A most suitable artificial light for this purpose is a Xe lamp which, adequately filtered and compared to other artificial lights, best replicates the solar spectrum.

Several measures are commonly used to determine the efficiency of materials for PEC-WS:

- solar-to-hydrogen conversion efficiency, STH
- applied bias photon-to-current efficiency, ABPE
- incident photon-to-current efficiency, IPCE
- absorbed photon-to-current efficiency, APCE.

STH describes the overall efficiency of a PEC-WS device exposed to a broadband solar AM 1.5G illumination, under zero bias conditions.¹¹ The working and the counter electrodes (WE and CE, respectively) should be short-circuited, that is, STH is measured in a 2-electrode system. In detail, STH represents the ratio of the chemical energy stored in the form of H₂ molecules to the solar energy input, and is expressed by (5):

$$\text{STH} = \left[\frac{r_{\text{H}_2} \times \Delta G}{P_{\text{in}} \times A} \right]_{\text{AM 1.5G}} \quad (5)$$

where r_{H_2} is the rate of hydrogen production (mmol_{H₂} s⁻¹) measured with a gas chromatograph or mass spectrometer, ΔG is the change in Gibbs free energy per mole of H₂ produced (237 kJ mol⁻¹), P_{in} is the incident illumination power density (mW cm⁻²) and A is the illuminated electrode area (cm²). STH can also be calculated as a function of the short-circuit photocurrent density, j_{SC} (6):¹³

$$\text{STH} = \left[\frac{j_{\text{SC}} \times 1.23 \text{ V} \times \eta_{\text{F}}}{P_{\text{in}}} \right]_{\text{AM 1.5G}} \quad (6)$$

where 1.23 V is the thermodynamic water splitting potential and η_{F} the Faradaic efficiency for H₂ generation. It should be emphasized that (5) and (6) can be considered valid only if experiments are performed under AM 1.5G illumination and in the absence of competing redox couples and sacrificial molecules in the electrolyte (that is, electron donors or acceptors).

A loss of faradaic efficiency for H₂ or O₂ evolution is observed not only when a sacrificial agent such as methanol, ethanol, *etc.*, is added to the electrolyte (this limits the O₂ evolution), but also when dissolved O₂ (from air) is present in the cathodic side of the PEC cell. That is, O₂ reduction to O₂^{-•} competes with the H₂ evolution reaction. O₂^{-•} radicals further react with water and form H₂O₂ which is a typical by-product detected in the cathodic compartment when the electrolyte is not purged with an inert gas prior to PEC-WS experiment, or if the anode material/electrolyte combination favors H₂O₂ production over O₂ production.

Therefore, a reliable evaluation of STH should imply (i) standard experimental conditions (such as purging the electrolyte to remove O₂, absence of sacrificial agents, checking for H₂O₂ in the cathodic compartment), and (ii) a comparison between the STH determined from measured j_{SC} (6) and that calculated from the actual amount of evolved gases (5) – this is crucial to avoid an overestimation of STH.

ABPE, IPCE and APCE are measured under applied bias in a 3-electrode PEC configuration.

Under electrical bias applied between working and counter electrodes, the current extracted from the device is higher compared to the bias-free condition of STH; therefore, it does not accurately reflect a solar-to-hydrogen conversion process but the so-called applied bias photon-to-current efficiency (ABPE) is determined (7):

$$\text{ABPE} = \left[\frac{j_{\text{ph}} \times (1.23 \text{ V} - |V_{\text{b}}|)}{P_{\text{in}}} \right]_{\text{AM 1.5G}} \quad (7)$$

where j_{ph} is the photocurrent density under bias V_{b} .

Noteworthy, V_{b} is applied across the working and counter electrodes, that is, the two electrodes across which the photocurrent

j_{ph} flows. The product ($j_{\text{ph}} \times V_{\text{b}}$) represents the electrical power loss that has to be subtracted in calculating the efficiency of the cell. By contrast, using the potential applied between working and reference electrodes ($V_{\text{W-R}}$) in place of V_{b} typically leads to an overestimation of the cell efficiency (because $V_{\text{W-R}} < V_{\text{b}}$).¹¹

One of the most adopted tools for the estimation of PEC properties of a semiconducting material is represented by IPCE. IPCE provides a measure of the efficiency of conversion of incident monochromatic photons to photocurrent flowing between WE and CE.

IPCE takes into account all the three fundamental steps of a light-driven process: (i) photon absorption (the absorption of one photon generates an e⁻/h⁺ pair); (ii) efficiency of h⁺ transport to the solid-liquid interface and collection of e⁻ at the back contact; (iii) efficiency of h⁺ transfer at the semiconductor-electrolyte interface. It is expressed as:

$$\text{IPCE} = \frac{j_{\text{ph}}(\lambda)}{eI(\lambda)} \quad (8)$$

where $j_{\text{ph}}(\lambda)$ is the photocurrent measured at the specific wavelength λ , $I(\lambda)$ is the incident photon flux, and e is the electronic charge. Due to photon losses associated with the reflection of light or imperfect absorption, and due to the recombination of photo-generated e⁻/h⁺ pairs, typical IPCE values are below 100%,¹¹ except for rare cases where *e.g.* current doubling occurs.¹⁴

Compared to STH, the main advantage of IPCE is that it is measured as a function of the irradiation wavelength and normalized vs. the irradiation intensity (8), and it can be measured under irradiation of a common Xe lamp combined with a monochromator. A most reliable estimation of the semiconductor PEC efficiency can then be obtained simply by integrating the IPCE spectrum (measured at the cell bias voltage of maximum efficiency) over the AM 1.5 global solar spectrum (9):

$$\eta = e(1.23 \text{ V} - V_{\text{b}}) \int_0^{\infty} \text{IPCE}(\lambda) I_{\lambda}(\lambda) d\lambda / E_{\text{s}} \quad (9)$$

where E_{s} is the incident irradiance that describes the spectrum of a light source.

Murphy *et al.* showed that his approach leads to efficiency results that are well in line with those measured under direct solar light irradiation, thus avoiding an under- or overestimation ascribed to spectral variations between different artificial sources.¹¹

Finally, to understand the intrinsic PEC performance of a material, APCE is particularly useful to describe the collected current per incident photon absorbed. APCE takes into account also losses caused by reflection and/or transmission of photons and can be obtained by combining (8) with the number of charge pairs generated per incident photon $\eta_{\text{e}^{-}/\text{h}^{+}}$ (10). Assuming that $\eta_{\text{e}^{-}/\text{h}^{+}}$ is equal to the number of photons absorbed (that is, no photon losses occur), then:

$$\eta_{\text{e}^{-}/\text{h}^{+}} = \frac{I_0 - I}{I_0} = 1 - \frac{I}{I_0} \quad (10)$$

Eqn (10) can be combined with the Lambert-Beer's law ($A = -\log(I/I_0)$):

$$\eta_{\text{e}^{-}/\text{h}^{+}} = 1 - 10^{-A} \quad (11)$$

Since APCE describes the collected current as a function of absorbed photons, that is:

$$\text{APCE} = \text{IPCE}/\eta_{e^-/\text{h}^+} \quad (12)$$

Then (12) combined with (8) and (11) leads to:

$$\text{APCE} = \frac{j_{\text{ph}}(\lambda)}{eI(\lambda) \times (1 - 10^{-A})} \quad (13)$$

However, regardless of the figure used to express the PEC efficiency of a certain device, an additional problem often encountered when cross-comparing the performances of different photoelectrodes is that PEC devices may also be operated under different electrochemical conditions such as applied potential, electrolyte composition, and reference electrode.

The lack of uniformity of electrochemical parameters can, in principle, be addressed by referring the applied bias to the Reversible Hydrogen Electrode (RHE) according to the Nernst equation:

$$E_{\text{RHE}} = E_{\text{ref}} + E_{\text{ref}}^0 + 0.059 \text{ pH} \quad (14)$$

where E_{ref} is the measured potential referred to the used reference electrode (e.g., Ag/AgCl, Saturated Calomel Electrode SCE, Hg/HgO, etc.), E_{ref}^0 is the potential of E_{ref} with respect to the Standard Hydrogen Electrode (SHE) at 25 °C, and the pH is that of the electrolyte solution.

This approach, when comparing different pHs, however implies that no significant changes in the water splitting mechanism occur with pH. Additionally, the Nernst equation assumes the linear dependence of E_{RHE} on the electrolyte pH. However, these assumptions are not always valid and, therefore, many material specific data are truly comparable only when different materials are tested in view of their PEC performance in the same electrolyte and at the same pH.

1.3 $\alpha\text{-Fe}_2\text{O}_3$ and TiO_2 based photoanodes

Among all the investigated metal oxide semiconductors, $\alpha\text{-Fe}_2\text{O}_3$ and TiO_2 have stimulated an immense research interest due to their natural abundance, chemical stability in liquid solutions, non-toxicity, high resistance to photocorrosion, and low production costs.^{5,8,15–17}

TiO_2 has suitable conduction and valence band energies to drive water reduction (to H_2) and oxidation (to O_2) – $E_{\text{CB}}(\text{TiO}_2) = ca. -0.2 \text{ V vs. RHE}$ and $E_{\text{VB}}(\text{TiO}_2) = ca. 3.0 \text{ V vs. RHE}$.⁸ However, a severe limitation of TiO_2 is represented by its optical band-gap (i.e., 3.2 and 3.0 for anatase and rutile polymorphs, respectively). This means that only UV light ($\lambda < ca. 380\text{--}410 \text{ nm}$) is absorbed and thus only ca. 4% of the solar spectrum can promote charge carrier generation in the material, and the consequent photoelectrochemical reactions.

By contrast, $\alpha\text{-Fe}_2\text{O}_3$ absorbs light in the visible range up to $\lambda \sim 600 \text{ nm}$ owing to its optical band-gap ($E_{\text{g}} = 2.0\text{--}2.2 \text{ eV}$). This corresponds to a light absorption of ca. 40% of the solar spectrum.¹⁸ Nevertheless, while the valence band of hematite matches the thermodynamic requirements for oxygen evolution from water ($E_{\text{CB}}(\alpha\text{-Fe}_2\text{O}_3) = ca. 2.4 \text{ vs. RHE}$, that is, the VB lies at more positive potential than $E^0(\text{O}_2/\text{H}_2\text{O})$),⁸ an external electrical

bias (and thus a PEC configuration) is needed to drive hydrogen generation due to the more positive conduction band position with respect to the HER potential ($E_{\text{CB}}(\alpha\text{-Fe}_2\text{O}_3) = ca. 0.4 \text{ vs. RHE}$) – in other words, H_2 evolution does not occur on $\alpha\text{-Fe}_2\text{O}_3$ under open circuit conditions.⁸

Furthermore, both TiO_2 and $\alpha\text{-Fe}_2\text{O}_3$ suffer from inherently low electrical conductivity, owing to bulk electron–hole recombination. In addition, TiO_2 and $\alpha\text{-Fe}_2\text{O}_3$ feature limited excited state lifetime (less than 10 ns and 10 ps, respectively) and a short hole diffusion distance (less than 20 nm and 5 nm, respectively), which significantly reduces the efficiency of hole transfer and collection at the SCLJ.^{9,17} All these aspects are typically reported to be primary reasons for a limited PEC performance in H_2O splitting.^{18,19}

While bulk materials have been extensively investigated (and reviewed) in classical photoelectrode configurations (deposited film layers, compacted particle layers or single crystals) – see e.g. ref. 5, 15, 17 and 19–23, a main focus of this review is to highlight the use of nanostructuring techniques to fabricate efficient photoanodes. Particularly, we will provide an overview of recent breakthroughs relative to synthesis and use of one-dimensional (1D) TiO_2 and $\alpha\text{-Fe}_2\text{O}_3$ photoanodes. The most explored strategies for doping, surface sensitization and the coupling of Ti and Fe oxides with narrow band-gap semiconductors will also be illustrated.

Moreover, we describe most recent results relative to $\alpha\text{-Fe}_2\text{O}_3\text{-TiO}_2$ heterojunction-based materials or combination compounds (e.g., Fe_2TiO_5) that were shown to outreach the PEC-WS performance of the single counterparts. For these materials, modification and exploitation of the (as such detrimental) conduction band offset between $\alpha\text{-Fe}_2\text{O}_3$ and TiO_2 has led to various new designs that combine (i) the efficient charge carrier separation, provided by TiO_2 that suppresses electron back injection in hematite, with (ii) the strong visible light absorption promoted by an $\alpha\text{-Fe}_2\text{O}_3$ thin layer. A comprehensive description of this approach will be presented in the final section, along with studies on charge carrier dynamic observed for these composites and useful tools for the rational design of potentially new platforms for efficient solar-driven water splitting.

2. Nanostructuring and nanostructures for PEC water splitting

Why micro- and nanostructuring? One of the reasons is that the properties of materials can be significantly different from the quantum-, to nano- and to bulk scale. Another reason is that defined structuring of electrode/electrolyte systems allows a much better control over light guiding, reactant diffusion, and electron pathways.

In regard to the first reason, nanostructured materials (NMs) can provide significantly modified physical, chemical, and biological properties and thus can exhibit unique functionalities.^{24–27}

NMs are low dimensional materials, i.e., in the nanoscopic size range, composed of assemblies of building units that have at least one dimension confined to the submicron- or nano-scale.²⁸

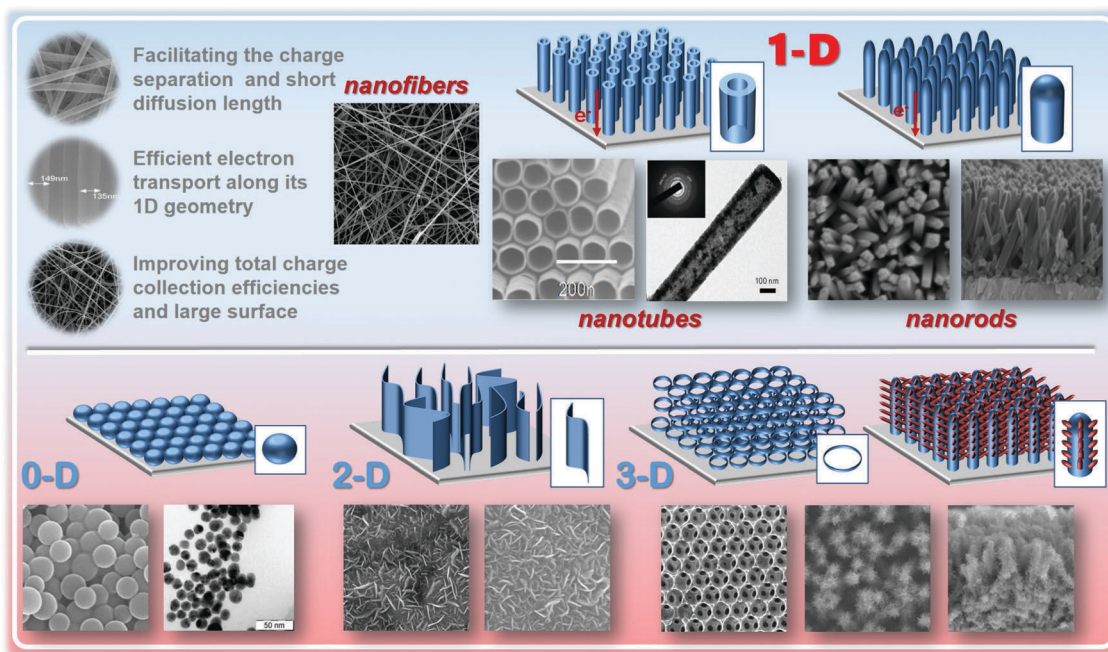


Fig. 2 Classification of nanostructures based on nanoscale dimensions – their structural and functional features are discussed in Section 3. 1D nanostructures (upper panel) include *e.g.* (i) carbon nanofibers fabricated by the spin-electrodeposition (reproduced from ref. 29 with permission from Elsevier), (ii) TiO₂ nanotubes by self-organizing electrochemical anodization (adapted with permission from *J. Phys. Chem. C*, 2014, **118**, 16562–16566. Copyright 2014 American Chemical Society) and (iii) TiO₂ nanorods grown on FTO substrate by a hydrothermal procedure (adapted with permission from *ACS Appl. Mater. Interfaces*, 2014, **6**, 4883–4890. Copyright 2014 American Chemical). The lower panel of the picture reports SEM and TEM images of (i) 0D nanoparticles (TiO₂ and Au nanoparticles, respectively – unpublished results); (ii) 2D sheaths of TiO₂ grown perpendicularly on FTO substrate, and of (iii) 3D nanostructures – left: inverse opal TiO₂ (reproduced from ref. 32 with permission from the National Academy of Science); right: TiO₂ nanorods branched with α -Fe₂O₃ nanosheets (reproduced from ref. 33 with permission from the Royal Society of Chemistry).

According to this definition, zero- (0D), one- (1D), two- (2D), and three-dimensional (3D) NMs can be distinguished (examples are sketched in Fig. 2).^{29–34}

Typical features of NMs that are beneficial for PEC applications are: (i) the possibility of decoupling the direction of light absorption and charge-carrier collection; that is, instead of a diffusion through the bulk material, orthogonal separation of photogenerated charges occurs and the probability of charge recombination is reduced; (ii) improved photogenerated charge pair separation, promoted by the internal electric field (*e.g.*, the upward band bending in the walls of TiO₂ nanotubes facilitate h⁺ transfer to the electrolyte and e⁻ collection in the center of the material); (iii) the possibility of controlling crystal faceting that, in turn, influences the material band-bending, flat band potential, surface states, *etc.*

Moreover, compared to bulk materials, NMs exhibit remarkable size effects owing to high surface-to-volume ratio. In particular, a larger specific surface area represents a great advantage when a material is intended for catalytic applications: a higher number of active surface sites facilitates the adsorption of reactants, offers extended contact with solutions, *etc.*, and typically leads to higher reaction rates.

Size effects imply that the nanomaterial dimensions (<100 nm) are comparable to the critical length scale of physical phenomena, *e.g.*, charge transport distances and light absorption depth, the mean free path of electrons and phonons, or (typically for particles <10 nm) the Bohr exciton radius.

On the one hand, this can be exploited for a more efficient charge carrier separation in the lattice of a nanomaterial in order to improve its PEC-WS performance. In other words, charge (*e.g.*, h⁺) diffusion towards the environment occurs over minimized distances since the size of the semiconductor is within the length scale of solid state charge diffusion.

On the other hand, quantum size electronic effects, such as ballistic electron transport or optical gap widening, can occur due to quantum confinement. This was experimentally demonstrated, *e.g.* in the case of TiO₂, for nanoparticle suspensions,^{35,36} and for ALD layers.³⁷ These works showed that a clear onset of quantum confinement for TiO₂ nanomaterials can be expected only if size-scales are <5 nm. This can be observed for hydrothermal TiO₂ nanotubes,^{38,39} which exhibit a measured band-gap of ~3.84 eV compared to $E_g \approx 3.2$ or 3.0 eV commonly reported for larger anatase or rutile TiO₂ crystals.⁴⁰ This difference is ascribed to the structure of hydrothermal tubes that is based on atomic sheets originating in quantum confinement effects.

Such size effects were already widely described in the 1960s,⁴¹ but the first classification attempts in materials science dates back to 2000,⁴² and only more recent reports consider also more complex architectures and mesoscale assemblies such as nanocones, nanohorns, nanoeegg-yolk, and nanoflowers (lilies, roses, tulips, *etc.*).²⁸

In the following sections we will provide a description of the different nanostructures (0D to 3D) and hierarchical

assemblies, in particular with respect to their application for the photoelectrochemical water splitting reaction.

2.1 From 0D to 3D

Zero-dimensional nanostructures feature all the three dimensions in the nanoscale regime (*i.e.*, no dimension is larger than 100 nm). Typical examples are nanoparticles (NPs), such as nanospheres, quantum dots (QDs), core-shell structures, hollow spheres, *etc.* An attractive feature is that 0D-NMs typically smaller than 5–10 nm (the Bohr exciton radius) show tunable band-gap. The smaller the size of a crystal the more affected its electronic structure: when a crystal is composed of a limited number of atoms, bulk electronic bands are discretized to distinct energy levels with a widening of the gap for smaller dot sizes. Subtraction or addition of just a few atoms alters the energy level distribution and thus leads to band-gap shift in the QDs.⁴³

Clearly, photoelectrochemical water splitting using a water dispersion of 0D nanoparticles is not possible, that is NPs should first be immobilized on an electrically conductive substrate (*e.g.*, ITO, FTO, *etc.*) to form various nanoparticulate assemblies or thin films that serve as electrodes in a photoelectrochemical cell arrangement.⁴⁴

Therefore, despite some fundamental early works on the electrochemical and photoelectrochemical investigation of TiO₂ colloidal solutions that led to a detailed mechanism of redox reactions occurring on hydroxylated titania surfaces,^{45,46} electrochemical studies of TiO₂ solutions remained scarce in

comparison to investigations of solid TiO₂ as electrode material.

However, films composed of stacked NPs often suffer from carrier recombination at grain boundaries (owing to the presence of trapping states) and long carrier diffusion paths (random walk) through the NP network (Fig. 3(a)). In this regard, replacing a nanoparticulate electrode with a one dimensional (1D) nanostructured electrode offers several advantages.

In terms of charge collection and transfer efficiencies, one-dimensional (1D) nanostructures exhibit superior performances in a wide range of applications (*e.g.*, nanoelectronics, nanodevices, energy-related fields) with respect to the other nanoarchitecture arrangements. In many cases, the size effects of a 0D material can be maintained but harvesting of charge carriers is facilitated.^{17,47–51}

Charge collection efficiency depends on both the recombination lifetime of photogenerated charge carriers and on their collection lifetime, that is, the time needed by the e⁻ (h⁺) to reach the semiconductor–electric contact (semiconductor/electrolyte interface).⁵² 1D nanostructures such as nanotubes (NTs), nanorods (NRs), and nanofibers (NFs) provide a preferential percolation pathway for charge carriers (Fig. 3(a)) that significantly enhances electron collection at the back-contact (typically, a metal foil or a conductive glass such as FTO and ITO). This leads to a remarkable improvement in the PEC efficiency.⁴⁸

Also, compared to 0D nanoparticles, the recombination time of e⁻/h⁺ pairs is longer in 1D-NMs (*e.g.*, in TiO₂ nanotubes recombination times are 10 times higher than in a TiO₂ nanoparticle layer) and this leads to larger charge collection efficiency.^{53–58}

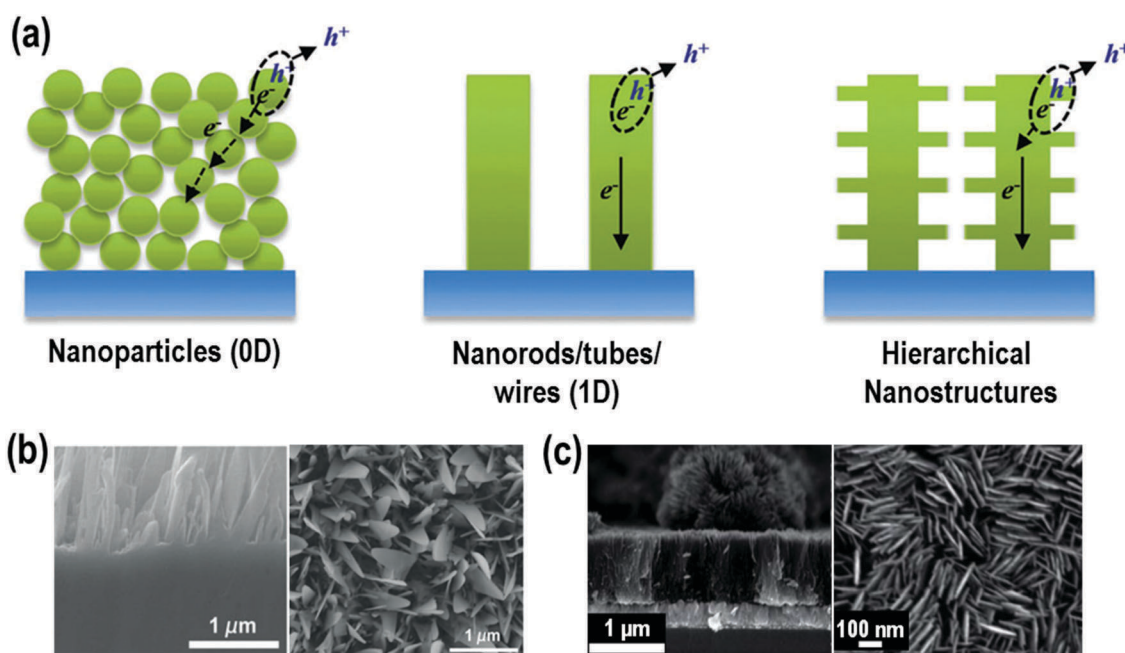


Fig. 3 (a) Schematic illustrating three typical photoelectrodes and their corresponding charge separation/transport behaviors. (b) Cross-sectional (left) and top (right) scanning electron microscopy (SEM) images of α -Fe₂O₃ nanoflake array, grown by thermal oxidation of Fe foil. (c) Cross-sectional (left) and top view (right) SEM images of single crystalline rutile TiO₂ nanoplatelet arrays, grown by chemical bath deposition on FTO glass. Fig. (a) is reproduced from ref. 69 with permission from the royal Society of Chemistry. Fig. (b) is reproduced from ref. 66 with permission from John Wiley & Sons. Fig. (c) is reproduced from ref. 62 with permission from the Royal Society of Chemistry.

We illustrate in detail one-dimensional nanoarchitectures and their application in PEC water splitting in Section 3.

Two-dimensional nanostructures have only one dimension in the nanoscale. Typical examples of 2D-NMs are nanoflakes, nanoplatelets, *etc.* (Fig. 3(b)), but also thin films (*i.e.*, with a thickness < 100 nm). 2D-NMs exhibit relatively large lateral size and a ultrathin thickness confined to the atomic scale regime that collectively lead to surface areas typically larger than those of 1D-NMs. Moreover, the ultrathin thickness of two-dimensional nanomaterials grants a high mechanical flexibility and optical transparency. These characteristics make 2D-NMs promising candidates particularly for high-performance flexible electronic and optoelectronic devices.^{59,60}

However, 2D-nanostructures are also advantageous when used in PEC devices particularly when perpendicularly oriented to the electrode (Fig. 3(b)).^{61–64} This arrangement simultaneously offers (i) enhanced charge transport properties, owing to a directional transport of charges to the back-contact, (ii) a facilitated access for electrolyte impregnation into the structure, owing to the high surface area, and (iii) a limited diffusion distance of photogenerated holes to the electrode/electrolyte interface that reduces the charge recombination rate.

Typical methods for the fabrication of 2D-NMs are *e.g.*, sputtering techniques,⁶⁵ hydrothermal and chemical bath deposition methods,^{61,62} thermal oxidation,⁶⁶ and spray pyrolysis techniques.⁶⁷

According to the definition of NMs, 3D-nanostructures should be more appropriately considered bulk materials as none of their dimensions is confined to the nanoscale. However, 3D-NMs feature properties that are locally confined to the nanoscale, when composed of nanosized crystals. These 3D-nanomaterials may include layers of *e.g.* nanoparticles, nanowires, and nanoplatelets where the 0D-, 1D- and 2D-nanostructured elements are in close contact.^{59,68,69}

A combination of their mesoporous matrix along with their nanoscopic structure (formed *e.g.* of nanoparticle aggregates) provides an ideal morphology for PEC-WS as the permeability of the scaffold is maximized and charge diffusion towards the environment has to occur over minimized distances (within each single nanoparticle). Moreover, 3D NMs have higher surface area and supply enough absorption sites for all involved molecules in a small space. In more details these structures are discussed in the following section and Section 4.

2.2 3D Hierarchical nanostructures

Hierarchical nanostructures (HNs) are 3D-NMs that, owing to their intrinsic properties and morphology, are attracting increasingly wider attention as scaffolds suitable for PEC-WS devices.

In general, a hierarchical nanostructure is composed of a distinct backbone (typically with a 1D-arrangement) onto which nanodimensional building blocks are grown – these usually include nanoparticles (0D), nanowires/rods/tubes (1D) and nanosheets (2D).

Therefore, HNs often resemble nanotrees that simultaneously combine the properties of the one-dimensional backbone

(*e.g.*, enhanced carrier separation and directional charge transport) with a significantly increased surface area and a much higher amount of active sites, owing to the highly porous arrangement provided by the branches.^{59,68,69}

In most cases, hierarchical structures can be produced by combining or modifying conventional processes for nanostructure synthesis: *e.g.*, hydrothermal growth, solution-phase chemical synthesis, chemical vapor deposition techniques or branch formation by *in situ* catalyst generation.^{70–72}

Regardless of the synthetic procedure, hierarchical nanostructures can either be composed of a single material (Fig. 4(a and b)) or be a combination of two or more (Fig. 4(c–e)).⁶⁰

In the first case, a hierarchical arrangement is mainly exploited in view of its significantly higher surface area and a major application is often as photoanode in a dye-sensitized solar cell (Fig. 4(a and b)). Higher dye loading, enhanced light harvesting, as well as a reduced charge recombination owing to preferential electron transport along the branches to the backbone, increase the power conversion efficiency of a TiO₂-HN photoanode compared to a more conventional 1D-TiO₂ arrangement.⁷² Such nanostructures can be for instance fabricated through a pulsed chemical vapor deposition (CVD) process, using an anodic aluminum oxide membrane as template. Upon template removal by etching under mild conditions, a nicely 3D spatially arranged TiO₂ nanorod network is observed.⁷³

Hierarchical nanostructures composed of two or more materials exhibit an additional advantage, that is, the possibility of combining materials with different (complementary) properties and band structures. This in turns can either be exploited to enhance electron collection from the branched-material to the back-bone nanostructure (*i.e.*, host-guest approach) and/or to extend the light absorption (and, hence, its conversion) over a broader wavelength range.

The so-called “host-guest approach” typically provides a support material (the “host”) for majority carrier conduction, into which a photoactive “guest” material can inject photo-generated electrons while, at the same time, providing proximity to the semiconductor/liquid junction (Fig. 4(c and d)). Therefore, the performance of such host-guest assemblies strictly depends on the availability of (i) a host material with good electronic transport properties, (ii) a guest material with optimized light absorption, and (iii) a suitable band alignment between the two counterparts that enable e[−] injection from the branches to the backbone, with holes accumulating at the (branched) semiconductor/electrolyte junction.⁷⁴ Examples of efficient host-guest HNs have been for instance reported for (n)-Si-TiO₂,^{75,76} WO₃- α -Fe₂O₃,⁷⁷ SnO₂-TiO₂,⁷⁸ and SnO₂- α -Fe₂O₃ combinations.^{74,79} In particular, the conducting properties of tin oxide as host-scaffold can be further improved by F- or Sb-doping as a consequence of growing (and annealing) SnO₂ 1D nanostructures on a FTO glass.^{74,80}

In the framework of this review, HNs composed of α -Fe₂O₃-TiO₂ assemblies are worth mentioning.^{33,81,82} Regardless of the architectural composition of the hierarchical assemblies (*i.e.*, titania branched on hematite⁸¹ or the opposite configuration^{33,82}) a photocurrent enhancement is typically achieved compared to the single oxide (α -Fe₂O₃ or TiO₂) cases.

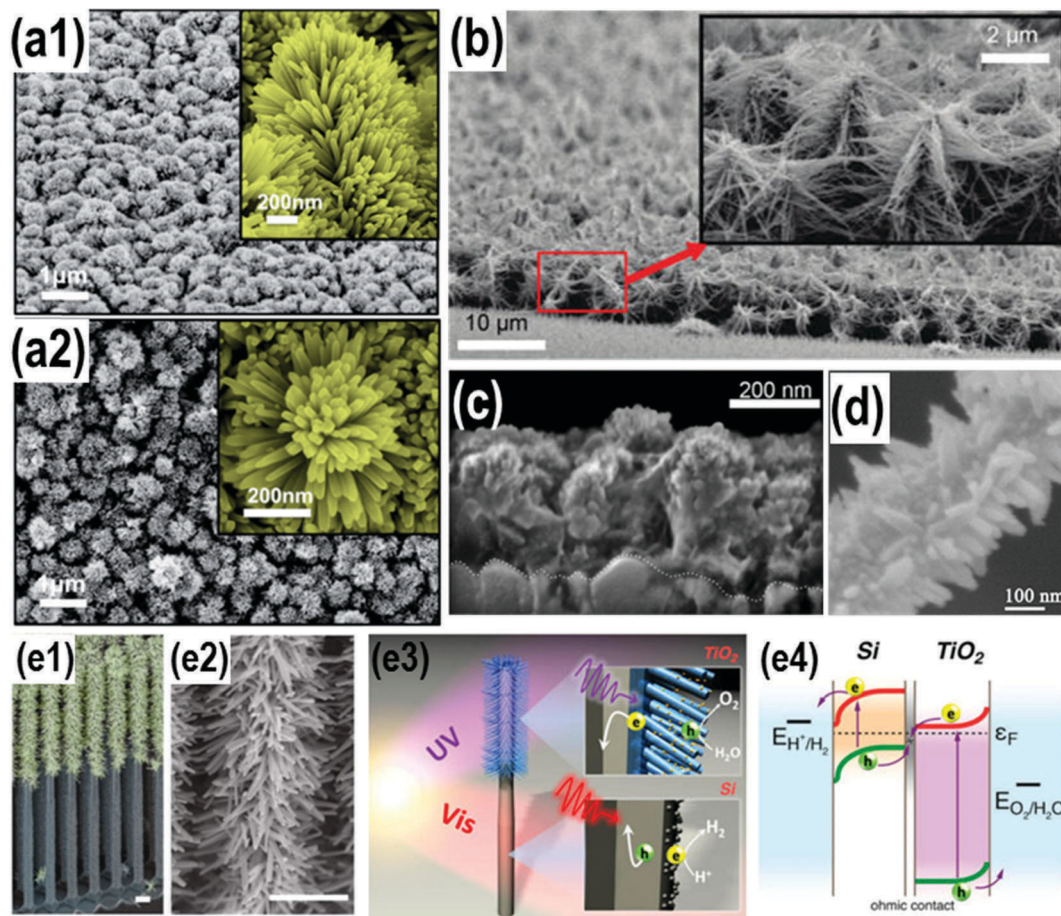


Fig. 4 (a) SEM images of 3D hierarchically branched TiO_2 NWs: (a1) tilted view, (a2) top view. The insets show high-magnification images of an individual hierarchically branched array. (b) Tilted view SEM picture of ZnO NW nanoforest. (c) Cross-sectional view SEM image of WO_3 - α - Fe_2O_3 host-guest film. The broken white line indicates the FTO/ WO_3 interface. (d) FESEM image of SnO_2 nanowire covered with TiO_2 nano needle leaf-like structures via TiCl_4 treatment. (e) SEM image of a nanotree heterostructure; (e2) magnified SEM image showing the large surface area of the TiO_2 segment used for water oxidation – scale bars are 1 μm . Structural schematics of the nanotree heterostructure: small diameter TiO_2 nanowires (blue) and Si nanowires (gray). The two insets report the separation of photoexcited electron-hole pairs. Energy band diagram of the nanotree heterostructure for solar-driven water splitting. Fig. (a1 and a2) are reproduced from ref. 72 with permission from the Royal Society of Chemistry. Fig. (b) is adapted with permission from *Nano Lett.*, 2011, **11**, 666–671. Copyright 2011 American Chemical. Fig. (c) is adapted with permission from *Chem. Mater.*, 2009, **21**, 2862–2867. Copyright 2009 American Chemical. Fig. (d) is reproduced from ref. 78 with permission from Elsevier. Fig. (e1–e4) are adapted with permission from *Nano Lett.*, 2013, **13**, 2989–2992. Copyright 2013 American Chemical.

In particular, a “Z-like scheme” resembling that of natural photosynthesis has been proposed to support the results observed with TiO_2 NRs branched on α - Fe_2O_3 NR arrays:⁸¹ both oxides are excited under AM 1.5G solar illumination and produce photoexcited e^-/h^+ pairs. Holes in the VB of TiO_2 migrate towards the electrolyte and electrons in the CB of α - Fe_2O_3 are collected at the layer back-contact (FTO glass). Simultaneously, photogenerated e^- (TiO_2) recombine with h^+ (α - Fe_2O_3) at the two oxide interface. This largely increases the separation between charge carriers and reduces the probability of their recombination, ultimately resulting in the enhanced PEC performance of TiO_2 -on- α - Fe_2O_3 HNAs.

An enhanced separation of photogenerated carriers has been reported also for the observed enhanced PEC-WS ability of α - Fe_2O_3 -on- TiO_2 HNAs:³³ in this case, e^- photogenerated in TiO_2 are collected at FTO, while h^+ are transferred to the

α - Fe_2O_3 nanobranches that serve as charge mediators to the electrolyte. In particular, for an improved PEC structure, a combination of critical factors that should be achieved has been identified, such as (i) TiO_2 light absorption and photo-activation vs. α - Fe_2O_3 -induced shadowing effect and (ii) the availability of free TiO_2 surface vs. α - Fe_2O_3 -coated surface.

Recently, also more advanced hierarchical systems composed of n- and p-type semiconductors have been shown to provide improved solar-driven PEC-WS ability. In this context, an assembly composed of Si nanowires branched with TiO_2 ⁸³ (or N-doped TiO_2)⁸⁴ nanowires has been reported. Here, the different intrinsic electronic properties of the two semiconductors allow for the production of O_2 and H_2 at the two separate sites (n-type (TiO_2) and p-type (Si) semiconductors, respectively): the photogenerated minority carriers (*i.e.*, h^+ in TiO_2 and e^- in Si) promote the corresponding oxidation/reduction half reactions, while the

majority carriers (*i.e.*, e^- in TiO_2 and h^+ in Si) recombine at the ohmic contact. PEC J - V curves showed that the system can promote solar water splitting under open circuit conditions, in contrast with the state-of-the-art materials typically used for photoelectrochemical applications.

p-Si NWs coated with a thin SnO_2 layer and a dense $\alpha\text{-Fe}_2\text{O}_3$ nanocrystal shell has been finally reported as photocathode for enhanced and stable (2.5 hours) solar water splitting.⁸⁵ This p-Si/ SnO_2 / $\alpha\text{-Fe}_2\text{O}_3$ hierarchical assembly exhibited considerably higher photocurrent and lower onset potential compared to both simple p-Si and p-Si/ SnO_2 NW arrays, revealing the potential of thin (SnO_2) and/or nanostructured ($\alpha\text{-Fe}_2\text{O}_3$) metal oxide layers in overcoming the poor stability and the HER kinetic limitation intrinsic of p-Si photocathodes.

3. $\alpha\text{-Fe}_2\text{O}_3$ and TiO_2 nanostructures for PEC water splitting

In the following sections we will deal with the different one-dimensional arrangements of TiO_2 and $\alpha\text{-Fe}_2\text{O}_3$ typically used for photoelectrochemical water splitting experiments.

We will mainly report on 1D-nanostructures such as nanorods (NRs), nanowires (NWs), and nanotubes (NTs).

In particular, we will show how the use of 1D-morphology is strategic to realize efficient electron transport and charge carrier separation and to overcome the short diffusion length of holes in both TiO_2 and $\alpha\text{-Fe}_2\text{O}_3$.

We will mainly focus on 1D-nanotubes, fabricated by various techniques such as hydrothermal methods and self-organizing electrochemical anodization.

Emphasis will be then on a number of modification strategies that (coupled to 1D-nanostructuring) have been adopted to address other critical aspects of hematite- and titania-based photoelectrodes, *e.g.*, the sluggish kinetic of hole injection into the electrolyte (that mainly affect $\alpha\text{-Fe}_2\text{O}_3$) and a limited use of solar light irradiation for promoting the PEC-WS reaction (for TiO_2).

3.1 Typical synthesis approaches

Solution-based growth techniques offer several major advantages including low-cost, simple processing, and good scalability. Many advanced nanomaterials that are currently commercially available are made *via* solution-based approaches, including colloidal NPs and QDs.⁸⁶

Despite the large number of morphologies that can be grown *via* solution-based methods (nanoparticles of different size and shapes, nanorods, nanowires, nanoflowers, nanotubes, *etc.*), in recent years other techniques, such as template-assisted synthesis and self-organizing anodization, have also been developed. These techniques allow a higher degree of control on morphology and physical properties, both crucial aspects when considering 1D nanostructured materials.

1D nanostructure arrays can be typically fabricated by either bottom-up or top-down approaches. Bottom-up methods are solution- and vapor-based methods but, despite the several advantages offered by these approaches (see above), optimization

and control over morphology and physical properties sometimes (still) represent a challenging aspect for practical applications.

On the other hand, top-down strategies (*e.g.*, (photo)lithography and focused-ion beam methods), in spite of a better control on the nanostructure morphology, are typically complex and expensive.

Here, we will give larger attention to the most versatile methods (in our view), *i.e.*, hydrothermal synthesis and self-organizing electrochemical anodization.

A remarkable aspect is the possibility of combining, *e.g.* hydrothermal and self-organizing anodization methods to other synthesis procedures (such as solution-based and/or sputtering techniques) to grow hierarchical composite nanomaterials.

3.1.1 Sol-methods for nanoparticles. Sol-gel methods certainly represent the most widely used approach for the synthesis of nanoparticles. It is based on the slow hydrolysis and polymerization reaction of a colloidal suspension of the metal oxide precursor (*i.e.*, alkoxide, halide, nitrate salt, *etc.*) that, at controlled rate and under specific conditions, evolves toward the formation of a solid gel phase.^{87–89}

Typical precursors for TiO_2 nanoparticles include titanium(IV) iso-propoxide (TTIP) or butoxide, and TiCl_4 .⁸⁶ Crucial for the nucleation of nanoparticles is the formation of Ti–O–Ti chains that is favored with a low content of water (that is, low Ti/ H_2O ratio), low hydrolysis rate (that is, relatively low temperature), and in the presence of excess titanium alkoxide in the reaction mixture. As-synthesized nanoparticles are amorphous and annealing (typically, ~ 400 – 700 °C in air) is required to attain a crystalline solid.

Inorganic precursors, such as iron nitrate, are commonly used for $\alpha\text{-Fe}_2\text{O}_3$ nanoparticles. In a typical synthesis procedure, $\text{Fe}(\text{NO}_3)_3$ is dispersed in an aqueous solution also containing EDTA as capping agent. Upon the formation of a solid gel, the evaporation of the liquid phase leads to iron oxide/oxy-hydroxide nanopowders. Annealing at 450 – 900 °C is typically reported to crystallize the amorphous powders into single phase hematite nanoparticles.^{87,89,90}

Despite simple processing and large versatility (*e.g.*, doping can be achieved by simply adding the dopant source into the colloidal solution), sol-gel methods lack of a precise control on nanoparticle size and shape distribution. Therefore, alternative approaches have been developed that include micelle and inverse micelle, hydrothermal, and solvothermal methods.⁸⁸

In particular, hydrothermal methods for TiO_2 lead to small particles (~ 5 – 25 nm), the size of which can be controlled by adjusting the concentration of Ti precursor and the solvent composition⁹¹ – *e.g.*, the presence of additives such as peptizers largely influenced the nanoparticle morphology.⁸⁶ Typical precursors are Ti alkoxide (*e.g.*, TTIP and Ti butoxide) colloidal solutions that, under acidic conditions, mainly form TiO_2 anatase NPs, with no secondary phase formation.^{86,91}

Colloidal synthesis of $\alpha\text{-Fe}_2\text{O}_3$ nanoparticles through hydrothermal route has been first introduced in the early 1980s.⁹² Nano-sphere, -disk, and -plate morphologies were reported depending on the precursor concentration,⁹² and follow-up works demonstrated that 60 – 100 nm $\alpha\text{-Fe}_2\text{O}_3$ NPs synthesized

through similar methods are ideal catalysts for the photocatalytic generation of hydrogen from water solutions, containing sacrificial agents (e.g., methanol) or electron donors (e.g., methyl viologen).^{93–95}

More recently, TiO₂ and α -Fe₂O₃ nanoparticles and hollow spheres have been reported by solvothermal method,^{96,97} that is, a procedure almost identical to the hydrothermal method except for the use of non-aqueous solvents – this enables the use of higher temperature, due to a large number of organic solvents with a high boiling point.⁸⁸

However, as mentioned before, the use of nanoparticle water dispersion is not possible in view of photoelectrochemical applications, and immobilization of NPs on a conductive substrate in the form of assemblies or thin films has several drawbacks (e.g., long (random) carrier diffusion pathways, enhanced carrier recombination at grain boundaries, lower surface area compared to NP suspensions, etc.).

Thus, a most elegant approach is one-dimensional nanostructuring of photoanode materials.

3.1.2 Hydrothermal methods. Hydrothermal synthesis certainly belongs to the most commonly used methods for the synthesis of nanorods/wires/tubes of various metal oxides.

As for sol-gel methods, titanium isopropoxide,⁹⁸ tetrabutyl titanate,⁹⁹ or titanium isobutoxide are typically used as TiO₂ precursors,^{100–102} while iron(III) chloride is mostly used as α -Fe₂O₃ precursor.^{103–107}

Hydrothermal synthesis is carried out in a pressure vessel under controlled temperature and/or pressure, in aqueous or organic based-solutions (as anticipated, in the latter case, the term solvothermal is more appropriate) and, in some cases, in the presence of surfactant agents.⁸⁸ Temperature, solution volume and nature of capping agent (e.g., F⁻ vs. SO₄²⁻) largely influence the internal pressure and, hence, the aspect ratio (i.e., the diameter/length ratio) of NRs, NWs and NTs.⁴⁹

α -Fe₂O₃ hydrothermal nanotubes are mostly prepared from a FeCl₃ solution in the presence of NH₄H₂PO₄ at 220 °C for several (2–3) days.^{108–110}

Under these conditions, the formation of α -Fe₂O₃ hydrothermal nanotubes has been reported to occur *via* a coordination-assisted dissolution process.¹⁰⁸ In particular, it was demonstrated that crucial factor to induce the formation of a tubular structure is the presence of phosphate ions (from NH₄H₂PO₄) that adsorb on the surface of hematite aggregates and coordinate with ferric ions.^{108–110} In detail, nanotube formation proceeds through controlled “dissolution” along the long axis of the spindle-like precursors formed at the early stage of the reaction; this generates rod-like nanocrystals and semi-nanotubes, and for sufficiently long times hollow tubes – remarkably, the inner part of tubes is only partially dissolved, and a non-uniform dissolution from spindle to spindle has also been reported.

More recently also alternative reactants have been proposed (e.g., [Fe(CN)₆]⁴⁻ precursor in H₂O₂ based solution) that significantly lowered both the temperature and the reaction time needed (160 °C for <2 h).¹¹¹

Regardless of the used precursors (and hence conditions), α -Fe₂O₃ tubes are single-crystalline (i.e., hematite is the only

crystalline phase) and are typically 200 nm–1 μ m long, with a diameter in the 100–150 nm range and a wall thickness of 25–30 nm.^{108–111}

Hydrothermal TiO₂ NTs were first reported by Kasuga *et al.*,³⁸ by alkaline treatment of anatase TiO₂ powders in a NaOH solution at 20–110 °C. Approximately 100 nm thick nanotubes with a \sim 8 nm diameter were obtained upon acidic washing of the reaction suspension. Several follow-up works demonstrated that amorphous and crystalline (that is, also rutile and commercial powders) TiO₂ as well as metallic Ti are suitable precursors,^{39,112} and that NaOH can be replaced by KOH – under these conditions, the reaction temperature can be increased and TiO₂ NWs can also be formed.¹¹³ In general, large NaOH concentrations and high operating temperatures facilitate the formation of tubes – and in particular the higher the *T*, the longer the tubes.

Most interesting feature of TiO₂ hydrothermal tubes is their multi-walled morphology, featuring inter-wall distance of \sim 0.7 nm¹¹⁴ and (in contrast to α -Fe₂O₃ tubes) a wall thickness in the range of atomic sheets.³⁸ That is, only TiO₂ hydrothermal tubes should be considered “real” nanotubes, with quantum confinement effects such as band-gap widening being practically observable (only) in the walls of tubes prepared through such a procedure.

Another remarkable aspect of hydrothermal methods is the possibility of growing 1D-nanostructures such as NRs and NWs anchored on a conductive substrate (usually a FTO layer immersed in the reaction vessel), for a direct use as photoelectrode – this, in contrast to nanotubes that grow in bundles/agglomerates, dispersed in a reaction media.⁴⁸

Normally, the F-SnO₂ side of FTO layers has to face the bottom of the reactor, so to enable the growth of NRs/NWs on the conductive substrate, while the metal oxo-species (e.g., TiO_x and FeOOH), which form on the glass side due to gravimetric precipitation from the precursor solution, can be easily washed away.¹¹⁵

Growing thin films directly from a substrate not only does considerably improve the adherence and mechanical stability of the film compared to standard deposition techniques (such as spin coating, dip coating, screen printing, or doctor blading), but also grants better charge transfer and collection to the back-contact with no extra binder layers to be tunneled.^{33,103}

Under these conditions, the formation mechanism relies on the constant supply of H₂O molecules at the hydrophilic surface of FTO (i.e., the F-SnO₂ side) through hydrolysis of the metal oxide precursor. Nuclei will appear on the entire substrate and if their formation rate is controlled and limited by the precipitation conditions, epitaxial crystal growth will take place (from the nuclei). If the concentration of precursors is high, a condensed phase of vertically aligned arrays perpendicular to the substrate will be generated.¹⁰³

Concerning TiO₂, it is known that acidic media set the conditions for rutile TiO₂ NR formation; key aspect to such a growth is the presence of Cl⁻ ions in solution, i.e., Cl⁻ ions preferentially adsorb on the rutile(110) plane and, by retarding the growth along this direction, promote NR formation.¹¹⁶

Accordingly, TiO₂ NRs were not formed when HCl was replaced by HNO₃ or H₂SO₄.

Nevertheless, a major limitation of Cl⁻ ions is their blocking effect towards the TiO₂ surface sites that are active for the water splitting reaction,¹¹⁶ and annealing at $T > 200\text{--}250\text{ }^{\circ}\text{C}$ represents a most common approach to remove the Cl⁻ termination.¹¹⁷

By contrast, alkaline media and an excess of OH⁻ ions favor the crystallization of anatase TiO₂¹¹⁸ – however, an alternative way to anatase is also the presence of an anatase-based seed layer on FTO.¹¹⁹ Moreover, it is reported that the reaction temperature (not time) has a critical effect on rod/wire morphology and crystal structure.¹²⁰

Inorganic iron salts such as FeCl₃^{103,104,121} and FeSO₄^{105,107} are most typical precursors for the hydrothermal synthesis of hematite rods/wires (~100 nm–1 μm long and with a ~5–10 nm diameter, reaction temperature varies within 100–120 °C and reaction time up to 24 h).

In particular, FeCl₃ is usually dissolved in a NaNO₃ based solution, also containing HCl to establish an acidic environment.^{103,104,121} On the other hand, FeSO₄ is used under milder conditions and in the presence of CH₃COONa.¹⁰⁵

Common aspect to all these procedures is that, contrary to the TiO₂ case, the formation of hematite rods/wires proceeds through the initial nucleation and aggregation of β-FeOOH 1D nanoarrays and hence annealing at $T > 400\text{ }^{\circ}\text{C}$ ¹⁰³ is required to convert the Fe oxide-hydroxide into hematite.

3.1.3 Template-assisted techniques. We mentioned that hydrothermal approaches for nanotube fabrication results in single tubes or loose agglomerates of tubes dispersed in a solution and that non-homogeneous tube lengths are typically obtained.

Most critical aspect to a use of these structures in electrically contacted devices (*e.g.*, photoelectrochemical cell) is that tubes need to be compacted to layers (similar to powders) on an electrode surface. This leads to an arbitrary orientation of the nanotubes on the electrode and, in turn, eliminates many advantages of their one-dimensional nature (*e.g.*, providing a 1D direct electron path to the electrode).⁴⁸

However, using aligned templates (or self-organizing electrochemical anodization, see below) not only leads to an array of oxide nanotubes oriented perpendicular to the substrate surface, but also tubes in the template can relatively easily be contacted by metal deposition (before removal of the template by selective dissolution).

Numerous different nanotube morphologies can be obtained by simply tuning the morphology of templates.^{40,122–124}

Most classic template for TiO₂ NTs is porous anodic aluminum oxide (AAO),^{125–127} which can be produced with a hexagonal pattern of nanopores in a virtually perfect (long-range) order, and with interpore distances between 10 and 500 nm.¹²⁸

Historically, the first attempt to produce TiO₂ NTs through a template-assisted method was seemingly that reported by Hoyer¹²⁵ who electrodeposited titanium oxide from a TiCl₃ solution. The oxide first is in the form of polymer-like hydrous titania, and after annealing crystallizes into anatase TiO₂ (Fig. 5(a)). More recently, also other filling approaches have been developed that include sol-gel techniques^{122,129,130} and atomic layer deposition (ALD).^{131–133}

As already discussed for the synthesis of NPs (Section 3.1.1), sol-gel methods are based on the hydrolysis reaction of Ti-alkoxide, TiCl₄, and TiF₄, followed by condensation into a solid gel phase.⁸⁷ After appropriate heat treatment, the alumina

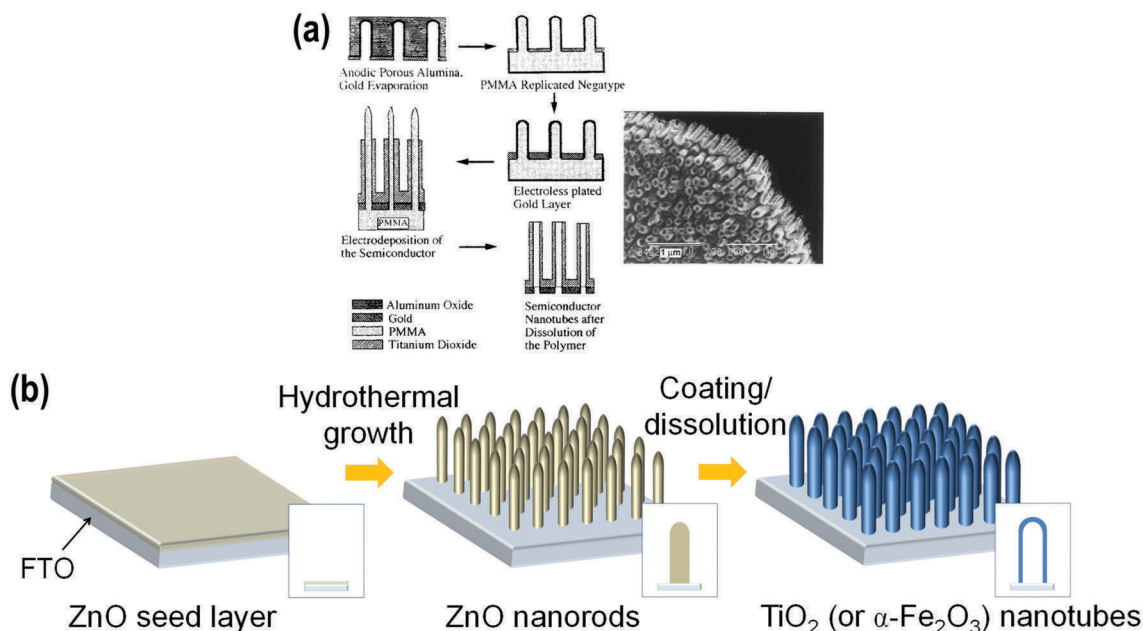


Fig. 5 (a) Schematic view of the replication process and SEM image of the corresponding TiO₂ NTs. (b) Schematic representation of TiO₂ (or α-Fe₂O₃) nanotube formation process: first a ZnO seed layer is deposited on FTO, and ZnO nanorods are grown through a hydrothermal method; afterwards, TiO₂ (or α-Fe₂O₃) nanotubes are grown and the ZnO sacrificial template is simultaneously dissolved. Fig. (a) adapted with permission from *Langmuir*, 1996, **12**, 1411–1413. Copyright 1996 American Chemical Society. Fig. (b) reproduced from ref. 33 with permission from the Royal Society of Chemistry.

template can be easily dissolved. ALD techniques offer an even larger control on tube morphology as conformal coating of the template with one atomic layer after the other can be achieved, also by alternating different titania precursors.^{131,132}

Another effective approach is the use of a ZnO nanorod array as sacrificial template (Fig. 5(b)).^{33,134,135} A thin ZnO seed layer is first deposited (*e.g.*, sputtered) on a FTO glass; hydrothermal growth of ZnO nanorods follows. As-synthesized ZnO NRs on FTO are then immersed into the Ti (or Fe) precursor solutions that also contain boric acid (H₃BO₃). Hydrolysis reaction of the metal oxide precursor to TiO_x (or FeOOH) on the individual ZnO nanorods results in the formation of TiO₂ (or α -Fe₂O₃) based nanotubes with the simultaneous dissolution of the ZnO template in the acidic environment.³³ Remarkably, in a one-step “NT growth/template dissolution” synthetic approach, no extra reactions are needed that may damage the NT array.

3.1.4 Self-ordering anodization. Electrochemical anodization is often considered a most straightforward synthesis path to fabricate one-dimensional vertically oriented layers for photoelectrochemical applications since it is scalable (it allows one to coat virtually any shape of various metal surfaces), offers an extended control over nanoscale geometry, produces directly back-contacted photoanodes, and is a versatile approach as it can be used to grow nanostructures of various metal oxides (Fig. 6(a)).^{47,48,136}

Classically, electrochemical anodization is carried out in a 2-electrode electrochemical arrangement where a metal substrate (M) is immersed in a suitable electrolyte (most commonly H₂SO₄) and subjected to a positive electrical bias (*U*).

In this configuration, with M as working electrode (anode) and platinum or carbon as counter electrode (cathode), oxidation of the metal substrate occurs and leads to the formation of a metal oxide (MO_{z/2}). Oxide growth is sustained by field-assisted ion-migration. Briefly, as long as high field conditions hold, metal cations are subjected to outward migration from the metal substrate towards the electrolyte, while at the same time O²⁻ ions migrate (from water) towards the anode (Fig. 6(b)).

This process is self-limited since the formed oxide is stable in the anodizing electrolyte: with increasing the oxide thickness (*d*), the electric field (*i.e.*, $\Delta E = \Delta U/d$) gradually drops and so does the inward/outward ion migration. This results in the formation of an oxide layer with a finite thickness. Such an oxide film is compact or, more generally, does not exhibit specific morphological features.

However, when using a suitable electrolyte and under specific electrochemical conditions (that largely depend on the metal of interest), a steady-state equilibrium can be established between the electrochemical oxide formation and its dissolution (Fig. 6(b)).

In particular, electrochemical parameters can be adjusted to establish controlled oxide growth and etching to form porous oxide layers or, even more, to enable the growth of one-dimensional self-organized metal oxide structures. Typically, the use of electrolytes containing ClO₄⁻, NO₃⁻ or F⁻ ions under self-organizing electrochemical conditions is key for the anodic growth of Ti and Fe oxide layers in the form of arrays of nanopores or nanotubes.^{47,48,137,138}

Key advantage of anodization is that the self-ordering degree of the formed one-dimensional nanostructures, their morphology and physicochemical properties can be adjusted by simple tuning of electrochemical parameters (electrolyte composition and temperature, applied voltage, anodization time, *etc.*).

As the effects of such parameters on the growth of α -Fe₂O₃ tubes are qualitatively comparable to what is observed for anodic TiO₂ NTs, general guidelines can be summarized as follows:

- electrolyte composition: tube growth in H₂O-based electrolytes is limited to a maximum length of ~ 2 – 3 μm . For TiO₂, significantly thicker NT layers (up to some hundreds nanometers) can be grown in organic-based electrolytes (ethylene glycol, glycerol, *etc.*). Also the fluoride concentration and the H₂O content play a crucial role, that is, the growth of thicker layers requires higher F⁻ concentration^{137,139} while limited H₂O contents lead to highly ordered tubes.^{140,141}

- electrolyte temperature: the higher the temperature, the faster the tube growth.^{142,143} Rapid tube growth can also be

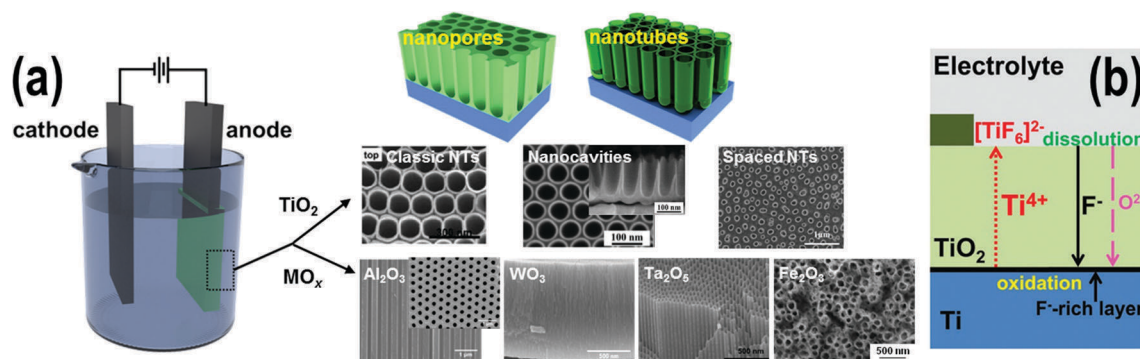


Fig. 6 (a) Typical 2-electrode electrochemical anodization set-up and possible anodic morphologies for different metal oxides: TiO₂ (upper row), and Al₂O₃, WO₃, Ta₂O₅, and α -Fe₂O₃ (lower row). (b) High field oxide (TiO₂) formation in the presence of fluoride ions: a steady-state is established between the oxide formation at the inner interface and its dissolution at the outer interface (due to dissolution/complexation of Ti⁴⁺ as TiF₆²⁻). Rapid fluoride migration leads to the formation of a fluoride-rich layer at the Ti/TiO₂ interface. Reproduced from ref. 136 with permission from the Royal Society of Chemistry.

achieved in the presence of complexing agents (lactic acid) in the electrolyte.¹⁴⁴

– anodization voltage: the larger the anodization voltage, the longer and wider the tubes. Long tubes are also grown by extended anodization time.¹⁴¹

A final aspect common to both α -Fe₂O₃ and TiO₂ is that as-formed tubes are amorphous and adequate thermal annealing (mostly in air at $T \sim 400$ – 700 °C) is required to convert the non-crystalline arrays into hematite and anatase (or rutile, or anatase/rutile mixed phases), respectively.^{48,138}

3.1.5 Other methods. A range of other approaches to form α -Fe₂O₃ and TiO₂ nanotubes/nanofibers have been reported.^{44,48} Among these, for instance, electrospinning represents a simple and versatile method for generating ultrathin fibers made of various materials (*i.e.*, functional polymeric materials such as hierarchical nanofibers, inorganic-doped hybrid nanofibers, core-shell nanofibers, *etc.*).

Moreover, if combined to other techniques, in particular sol-gel methods and annealing, electrospinning can be used to fabricate a large number of inorganic nanomaterials with controlled morphologies and properties.¹⁴⁵

In this process, a strong electric field is used to pull a thin jet out of a drop of polymer solution or melt through a nozzle.

The jet then is deposited in the form of a nanofiber. Ti and/or Fe precursors can be used to coat the fibers (most elegant is a simultaneous coating of the fibers while spinning, through a coaxial two-capillary spinneret nozzle system) and generate single hollow-nanofibers (nanotubes) that are well separated and can be uniformly distributed over a several centimeters range. Finally, annealing is carried out to induce thermal degradation of the organic fiber template and crystallize the amorphous metal oxide nanotubes (Fig. 7(a and b)).¹⁴⁶

Typically, NTs by electrospinning exhibit extremely high aspect ratios and a diameter that ranges from a few tens of nanometers to a few tens of micrometers.

TiO₂ nanotubes are fabricated, for example, by using titanate as well as Ti-alkoxide (Ti(IV) iso-propoxide) precursors,^{146–148} while iron inorganic salts (*e.g.*, iron nitrate) or organic precursors (*e.g.*, Fe(III) acetylacetonate) are used for α -Fe₂O₃^{149,150} – examples of such nanotubes are shown in Fig. 7(c).

Key to the fabrication of these hollow nanostructures is a use of two immiscible liquids, that is, the solvent to dissolve the Ti or Fe precursor (*e.g.*, an ethanol-based solution) and the polymer to fabricate the nanofibrous array (*e.g.*, a heavy mineral oil) – Fig. 7(c).¹⁴⁶

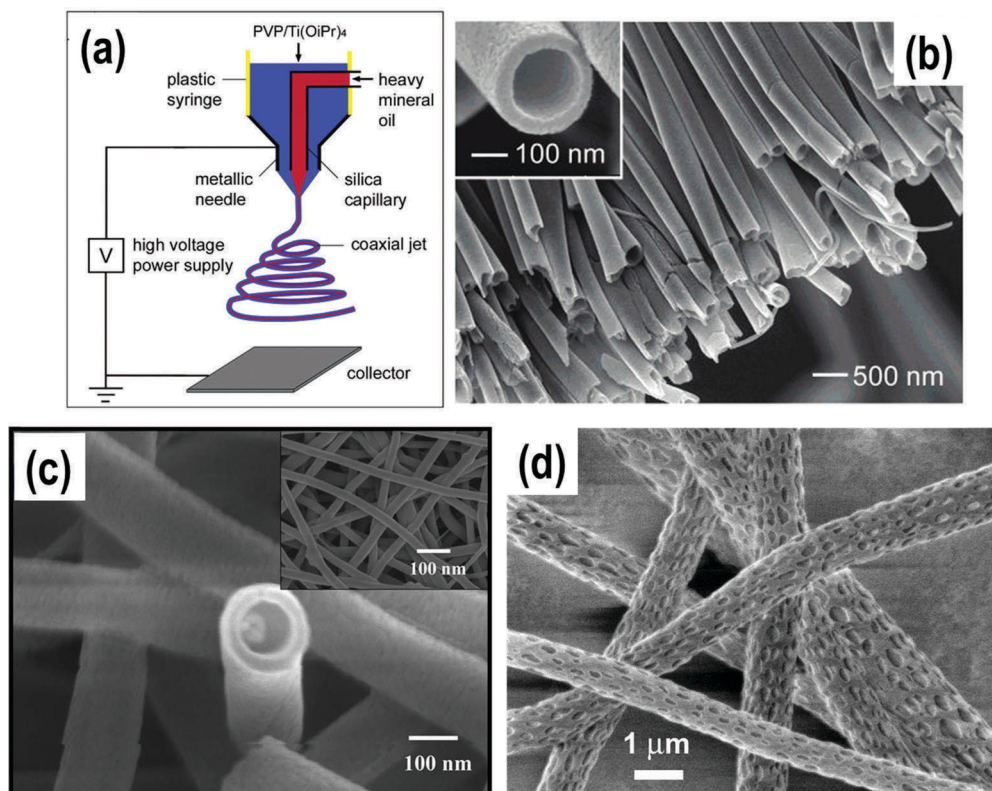


Fig. 7 (a) Schematic illustration of the setup for electrospinning nanofibers. Spinneret is fabricated by means of a two-capillary coaxial jet, through which heavy mineral oil and an ethanol solution of Ti precursor are simultaneously ejected. (b) SEM image of a uniaxially aligned array of anatase hollow-nanofibers. (c) FESEM images of α -Fe₂O₃ hollow fibers by electrospinning an iron acetylacetonate (Fe(acac)₃) and polyvinylpyrrolidone (PVP) solution. (d) SEM image of porous fibers obtained *via* electrospinning of a polymer solution in dichloromethane. Fig. (a and b) adapted with permission from *Nano Lett.*, 2004, **4**, 933–938. Copyright 2004 American Chemical Society. Fig. (c) reproduced from ref. 149 with permission from the Royal Society of Chemistry. Fig. (d) reproduced from ref. 151 with permission from John Wiley & Sons.

In addition, it is possible to use this method to obtain nanofibers/nanotubes, with specific surface topologies. Since electrospinning to a first approximation involves fast evaporation of the solvent, the use of a solvent that evaporates rapidly (*e.g.*, dichloromethane) induces rapid phase separation. The following rapid solidification generates fibers as those reported in Fig. 7(d), with pores of regular shape and narrow size distribution (diameter $\sim 100\text{--}200\text{ nm}$).¹⁵¹

3.2 Typical modification approaches

Experimental conditions and parameters for the modification of $\alpha\text{-Fe}_2\text{O}_3$ and TiO_2 may be significantly different. However, for both oxides two main strategies can be distinguished, namely methods that modify the intrinsic electronic properties of the oxide (charge mobility, donor density, band-gap, *etc.*), and methods that provide a co-catalytic effect for chemical reactions (*e.g.*, deposition of a co-catalyst to improve the kinetics of water oxidation). In addition, also other methods are reported that enable for instance visible light PEC-WS and/or generate suitable surface states for enhanced charge transport/transfer properties (*e.g.*, surface decoration with plasmonic metals and quantum dots, or the formation of a heterojunction).

3.2.1 Doping. Semiconductors for practical applications are often modified (doped) by introducing a secondary active species into the lattice. In particular, doping is carried out to (i) improve the material electronic properties, by adjusting a desired conductivity (typically, at low dopant concentrations), or to (ii) adjust (that is, in the case of TiO_2 , to narrow) its band-gap and extend the light absorption properties (usually at high dopant concentrations).

The incorporation of dopants into TiO_2 and $\alpha\text{-Fe}_2\text{O}_3$ can be achieved through a range of different methods, *e.g.*, hydrothermal procedures, thermal diffusion of ions from the substrate (FTO), drop casting, wet chemical treatments, thermal treatments under controlled atmospheres (containing the dopant), high-energy ion implantation.^{44,48,49,51}

For TiO_2 , band-gap narrowing is necessary in view of enhancing its visible-light absorption and promoting photoelectrochemical and photocatalytic reactions under solar irradiation.

Since the report by Asahi on N-doped TiO_2 and the photocatalytic degradation of methylene blue and acetaldehyde under visible light,¹⁵² there have been (and still there are) a large number of attempts to produce differently doped TiO_2 . This is typically achieved by introducing a non-metal element into its lattice, such as C, N, S, P, *etc.*^{153–159}

The presence of non-metallic dopants forms electronic intra-gap states and this influences the oxide light absorption characteristics by leading to a redshift in the light absorption threshold.

However, more recently, some studies underlined the difficulty in unequivocally ascribing a photoresponse under visible light to the influence of anion dopants. In some cases, the anion dopant may be confined to the surface and promote the formation of surface trap states that typically lead to detrimental charge recombination, which in turn limits the photoactivity of the material.¹⁶⁰

Also some metal dopants such as Cr, V and Fe were reported to be successful in activating a TiO_2 response under visible light.¹⁶¹ However, the photocurrents for, *e.g.*, Fe- or Cr-doped TiO_2 are typically low, and a use of cation doping to improve the visible light absorption of wide band-gap semiconductors is only partially considered in photoelectrochemistry.⁴⁴

Finally, an aspect that is often overlooked in the literature is that to an extended light absorption to visible light wavelengths (that is, determined by reflectivity measurements) does not always correspond the generation of mobile charge carriers. This was deeply investigated by Murphy, who pointed out that the effects on vis light induced PEC activity of *e.g.* TiO_2 should be anyway considered valid only if IPCE spectra that demonstrate this ability are also measured. Even more, a most reliable estimation of photoresponse is provided if photocurrent spectra are associated to photocurrent transients measured under monochromatic λ .^{11,162}

Another promising way to enhance the photoelectrochemical response of TiO_2 is to improve its charge transport abilities, therefore reducing charge carrier recombination. This can be achieved, *e.g.*, by introducing a metal dopant (electron donor) such as Ru, Nb or Ta into TiO_2 lattice.^{163–165} The amount of dopants is usually limited to 1–2 at% that corresponds to a carrier concentration of $\sim 10^{21}\text{ cm}^{-3}$. Higher concentrations are not likely to be effective, and may even lead to segregation of the dopant phase.

Finally, it is well established that, regardless of their non-metallic/metallic nature, some dopants such as F and Nb also inhibit the transition from anatase to rutile when annealing TiO_2 at relatively high temperature ($>400\text{ }^\circ\text{C}$) – rutile is detrimental in photoelectrochemical applications due to its poor electronic properties compared with anatase.^{166–168} The presence of such dopants retards the seeding of the rutile phase and, therefore, allows annealing at relatively high temperature. This in turn increases the crystallinity degree of TiO_2 and enhances the charge transport properties as electron transport becomes considerably faster.^{169,170}

On the other hand, $\alpha\text{-Fe}_2\text{O}_3$ exhibits absorption properties that already fit to a solar spectrum. That is, light absorption of hematite extends up to $\lambda \sim 600\text{ nm}$ and any doping attempt is clearly performed with the only aim of increasing its intrinsically limited conduction properties that are inadequate for PEC applications.¹⁷

This is commonly achieved by substitutional doping using elements with oxidation states +4 to +6, such as Ti^{4+} , Sn^{4+} , Zr^{4+} , Nb^{5+} .^{171,172} By substituting at sufficient levels, high carrier conductivities can be attained.

In general, titanium is less effective compared to other +4 ions as it may form Ti_{surf} sites that may also act as electron-hole recombination centers. However, it has also been recently reported that Ti^{4+} surface species might effectively capture and store photogenerated holes and facilitate their transfer to the electrolyte for O_2 evolution by water oxidation.¹⁷³

Zr^{4+} doped into $\alpha\text{-Fe}_2\text{O}_3$ single crystals led to one order of magnitude higher donor densities (in the order of 10^{19} cm^{-3}), and increased conductivity and electron mobility compared to undoped hematite.¹⁷⁴

Also for hematite, optimum impurity concentrations are *ca.* 1 at% or less and, while introducing inter-band gap energy states that are beneficial for α -Fe₂O₃ conductivity, doping does not significantly alter the oxide band-gap or its absorption properties.¹⁷

3.2.2 Heterojunction engineering. The recombination of photopromoted charge carriers in solid-state semiconductors typically takes place within μ s, while the time for electrons and holes to react with acceptor and donor species, respectively, is in the ns– μ s.

The time scale for charge transfer to a donor or acceptor molecule largely depends on its specific nature, in particular, on its red-ox potential and chemical adsorption to the surface. It is, therefore, apparent that charge recombination and charge transfer to the electrolyte are competing processes.^{50,175–178}

One of the most common strategies to tackle the rapid charge recombination and thus to increase solar conversion efficiencies is increasing the charge spatial separation by creation of a heterojunction.

Heterojunctions are typically designed to combine the functionality of the two (or more) constituent phases, with the aim of addressing (at least one of) the primary requirements for an efficient PEC-WS using solar energy: visible light activity, chemical stability, appropriate band-edge characteristics, and potential for low-cost fabrication.¹⁷⁹

Heterojunctions may be formed by combining, *e.g.* (i) two semiconductors (S–S), or (ii) a semiconductor and a metal (S–M).

Enhancement of charge separation can be achieved through various mechanisms that mainly depend on the electronic properties of the partner materials:

(i) *via* the formation of an internal electric field at the heterojunction interface, in S–S type heterostructure. Upon favorable band bending, e^- will tend to move from the higher to the lower lying CB, while h^+ will follow the opposite direction (*i.e.*, from the lower to the higher lying VB).

(ii) driven by the Schottky barrier that typically forms when interfacing a semiconductor with a metal (in S–M type heterojunction). This promotes electron flow from the material with the higher Fermi level to that with a lower Fermi level, until steady-state equilibrium is reached.

Different configurations may apply to the S–S type heterojunction: both semiconductors are photoactive, that is, they generate e^-/h^+ pairs (*e.g.*, α -Fe₂O₃–WO₃, TiO₂–WO₃, TiO₂–BiVO₄, α -Fe₂O₃–SrTiO₃, TiO₂–ZnO, TiO₂–SrTiO₃ *etc.*)^{77,180–188} or only one component absorbs light and generates energetic charge carriers (*e.g.*, metal oxide/QDs, metal oxide/OEC). It is also remarkable that narrow band-gap semiconductors can be combined to a larger band-gap semiconductor and complementary light absorption properties can be exploited (*e.g.*, NiO/TiO₂ systems). Therefore, an additional advantage is the photosensitization of the large band-gap material, as observed for instance in metal oxide/QDs configurations (see below).

A detailed description of heterojunction formation and working principles is out of the scope of this review and additional information can be found elsewhere.^{1,189,190} In the following sections we will provide examples and describe

strategies that apply to α -Fe₂O₃ and/or TiO₂ for photoelectrochemical applications.

3.2.3 Decoration with a co-catalyst. A widely investigated strategy towards higher PEC ability is the surface decoration of photoanodes with an oxygen evolution catalyst (OEC) and/or the decoration of cathodes with a hydrogen evolution catalyst (HER, such as MoS₂ and WS₂^{191,192}).

As discussed in Section 1.1, the oxygen evolution reaction (OER) kinetics is sluggish: this reaction requires a four-electron oxidation of two water molecules (that is, the concerted transfer of four holes from the photoanode surface to the electrolyte) coupled to the removal of four protons to form a relatively weak oxygen–oxygen bond.

If O₂ evolution from water splitting represents only a minor challenge for TiO₂-based photoelectrode (some examples of co-catalyst decoration for the EOR have been anyway reported in the literature and are shown in Section 3.4.3), the poor match between the orbitals of hematite valence band (that partially exhibits Fe 3d character) and those of H₂O (that is, O 2p states – see Section 3.3 for discussion) significantly limits the efficiency of hematite in water photooxidation.

To overcome the limitation of poor OER kinetics, various catalysts have been coupled to hematite photoanodes to assist hole transport from the hematite surface to the electrolyte.

Typical OECs are noble metals such as IrO₂ and RuO₂. Though efficient and stable under working conditions, Ir and Ru based catalysts are however preferentially replaced with cheap and earth-abundant elements for a significant reduction of the costs.

In this context, Co oxide-based catalysts¹⁹³ and the more recent amorphous cobalt-phosphate (Co-Pi)¹⁹⁴ catalyst represent valuable candidates. While the mechanism behind the improvement obtained with Co-Pi is still not completely understood, the electrocatalytic activity of cobalt oxides/hydroxides for water oxidation is well established and involves the Co^{II}/Co^{III} and Co^{III}/Co^{IV} couples and the formation of high-valent Co(IV)–O intermediates that can “store” up to four holes from the valence band of hematite. Holes injection into the electrolyte for the generation of O₂ then regenerates again Co^{II} centers.¹⁹³

Finally, recently also more complex structures (*e.g.*, NiFe double-layered hydroxide (LDH) and NiFe oxide)^{195,196} have been introduced. NiFe based co-catalysts have been shown to possess excellent electrocatalytic activity and durability for OER catalysis; even more, although the active site of NiFe still remains unclear, its transparency towards visible light irradiation (that can therefore be absorbed by hematite) represents an intrinsic advantage, particularly with respect to more common cobalt-based co-catalysts.^{195,196}

3.2.4 Other strategies. Aside from doping and surface-decoration with a co-catalyst, a number of various other approaches have been developed to improve the photoelectrochemical response of α -Fe₂O₃ and TiO₂. Some of these methods are here described, but a more complete overview can be found in Section 3.3.3 and in Section 3.4.3 for hematite and titania, respectively.

In view of the “too” large optical band-gap of TiO₂ for efficient sunlight absorption, the recent finding of “black”

TiO₂ by Chen and Mao¹⁹⁷ is often mentioned as a promising approach to (partially) address this issue.^{100,198–200}

Black TiO₂ is typically obtained by exposing TiO₂ to a reduction treatment (*e.g.*, high pressure/high temperature treatment in H₂, vacuum annealing, electrochemical reduction, Ar/H₂ annealing under atmospheric conditions) that produces the typical dark coloration ascribed to the formation of oxygen vacancies or Ti³⁺ defect states.²⁰¹ This in turn generates a strong light absorption in the visible range.

In particular, Chen and Mao reported that compared to conventional “white” TiO₂, black TiO₂ loaded with a Pt co-catalyst could reach a significantly higher open-circuit water-splitting activity, with the photoactivity enhancement ascribed to a thin amorphous TiO₂ hydrogenated layer encapsulating the TiO₂ anatase core.

However, the findings of Mao and many of the follow-up studies seem to limit the outstanding properties of black TiO₂ to its visible-light extended photoabsorption.

Only more recently, a unique co-catalytic effect towards efficient water splitting could be observed for “black” TiO₂ anatase nanoparticles and nanotubes treated with H₂ under high pressure^{202,203} or high-energy proton implantation.²⁰⁴ Such a co-catalyst effect enabled strongly enhanced photocatalytic activity for hydrogen production in the absence of any noble metal co-catalyst. A combination of different characterization techniques pointed out that hydrogenation generates voids in the anatase nanoparticles^{202,203} and nanotubes (an additional discretization of walls on the length scale of around 10–20 nm was observed for the implanted tubes)²⁰⁴ that are responsible for the observed outstanding photoactivity.

Therefore, “black” titania not only should be regarded as a tool to extend the absorption properties of TiO₂ into the visible light region, but hydrogenation should also be considered a powerful tool for the engineering of suitable structural defects that can activate TiO₂ for noble metal-free photocatalytic water splitting.

Thermal reducing treatments have also been explored for hematite. However, the reduction of α -Fe₂O₃ crystals is typically reported to generate a Fe₃O₄ surface layer which typically acts as a recombination center.²⁰⁵ For instance, the exposure of α -Fe₂O₃ pellets to an inert He-atmosphere produced conductive pellets that are also visibly darker than untreated hematite, but a photocurrent drop due to the enhanced surface recombination promoted by Fe₃O₄ is observed.

More recent studies suggested that a low amount of oxygen vacancies in α -Fe₂O₃ may be beneficial for solar water splitting, as long as no lattice distortions are formed and no incorporation of Fe₃O₄ inclusions occurs.²⁰⁶

Another popular approach for the adjustment of α -Fe₂O₃ and TiO₂ optical properties, namely for enhancing their light absorption, is the incorporation of a plasmonic metal nanostructure (*e.g.*, nanoparticles, nanorods, nanopillars, nanohole arrays) on the semiconductor surface.^{207–215}

Briefly, a plasmonic metal (such as Ag, Au and Cu) can harvest visible light due to localized surface plasmon resonance (LSPR), *i.e.*, the oscillation of free electrons with the incident

radiation that promotes either electron injection (hot e⁻) or energy transfer (PRET) into the adjacent semiconductor.

A most efficient method for capturing hot electrons is the formation a Schottky barrier (ϕ_{SB}) with an appropriate semiconductor (see Section 3.2.2), that is, proper alignment of the Fermi level of the plasmonic nanostructure with the bands of the semiconductor is crucial. Therefore, important factors to consider are (i) the band-gap of the semiconductor, which affects the height of the Schottky barrier and (ii) the density-of-states (DOS) available in the CB, which affects the efficiency of the hot electron injection process.^{214,216} PRET is based on the generation of an intense electric field at the surface of the plasmonic nanostructure that is able to increase the efficiency of electron-hole pair generation in the nearby semiconductor. The basic principle that regulates PRET is that the LSPR wavelength should be resonant with the band-gap energy of the semiconductor (or excite some intra-band gap transition).^{207,217}

In other words, regardless of the mechanism, a plasmonic metal can be thought as an antenna that absorbs light, and the semiconductor as the reaction center that promotes the photoreaction.

Since the resonance frequency of plasmonic metals depends (primarily) on the nature of the metal and can be tuned from visible to near infra-red wavelengths by adjusting the nanostructure shape and size, LSPR can be envisaged as a versatile strategy for the sensitization of semiconductors below their band-gap and/or to increase the range of solar light absorption.^{213–215,218}

For solar water splitting applications, studies have been mainly limited to Ag and Au (LSPR at $\lambda = 400$ –450 nm and 530–560 nm, respectively). This is due to the relatively large optical cross sections of the two metals and, in particular for Au, due to its stability under the harsh conditions (pH, potential) that are needed for water splitting.²¹¹

Early studies on water splitting with plasmonic-metal/semiconductor photoelectrodes report Au/TiO₂ and Ag/TiO₂ nanocomposites, synthesized by immersion of mesoporous TiO₂ films in solutions containing nanoparticles of either Au or Ag.^{219,220}

Photocurrent and photovoltage action spectra of Au/TiO₂ and Ag/TiO₂ showed an increased photoresponse compared to a pure TiO₂ photoelectrode, that also matched the LSPR of the metal nanoparticles (*i.e.*, $\lambda = 450$ and 550 nm for Ag and Au, respectively). Although the increase in the absolute value of IPCE was modest (~ 1 –2%), these works paved the way for follow-up studies.

In particular, more recently, plasmonic-metal/semiconductor arrangements other than the more conventional “plasmonic-nanostructure on metal oxide-array” have been developed, *e.g.*, by using a thin Ag mirror underneath a α -Fe₂O₃ film, the photocurrent of hematite could be significantly enhanced due to the metallic film promoting photon re-trapping schemes that increase resonant light trapping into the oxide layer.²²¹

Further improvements in terms of water splitting efficiency have also been reported for a plasmonic/semiconductor/mirror photoanode arrangement, with TiO₂ “sandwiched” between an Au/Cr-based metallic mirror and plasmonic gold nanodisks.²²²

The optimized architecture exhibited multiple resonance peaks due to hybridized LSPR in the nanodisks and multiple internal photoemission between the mirror and the plasmonic nanostructures that enabled an 8–10 time photocurrent enhancement under resonant conditions.

Besides sensitization by plasmonic resonance, also quantum dots of semiconductors such as CdS, CdSe, PbS, PbSe, InAs, MoS₂, *etc.* can be used as light harvesting functionalities and combined to a semiconductor photoelectrode for solar water splitting.

Quantum dots (QDs) are semiconductor nanoparticles (with $d \sim 5\text{--}10$ nm) subjected to quantum-confinement effect, *i.e.*, their dimension is smaller than the exciton Bohr radius. Above mentioned semiconductor QDs can absorb visible light ($E_g \sim 2.2\text{--}2.4$ eV) and generate photoexcited states (electron-hole pairs) that once separated can be used to enable redox processes with suitable acceptor and donor species.

In our context, the electron acceptor is the conduction band of a (large) band-gap semiconductor (*e.g.*, TiO₂) – clearly, for an efficient charge injection, a suitable alignment of the CB of the QD semiconductor with that of *e.g.* TiO₂ is a prerequisite.^{223–225}

Moreover, charge recombination in some QDs (*e.g.*, PbSe and CdS–CdSe dual QDs) leads to the emission of photons that are then absorbed by the semiconductor and generate reactive e^-/h^+ pairs.^{226,227}

Numerous studies of QDs show that their light absorption/emission features can be controlled adjusting their particle size.⁴³

However, in spite of the large number of reports on QD-sensitized semiconductor scaffolds for light conversion reactions and of the significant IPCE enhancement (*e.g.*, for CdS/TiO₂ an IPCE as high as 20% has been determined at $\lambda \sim 450$ nm),^{224,228} two main limitations still remain to be addressed: (i) the slower interfacial hole transfer rate (to a donor species, *e.g.* in the electrolyte) compared to electron injection into the semiconductor; that is, for the efficient II–VI materials, QDs typically suffer of photochemical instability due to hole-induced corrosion; (ii) a low internal quantum efficiency in the visible region, ascribed to a slow hole transfer kinetics compared to the rate of surface-mediated electron-hole recombination.

Recently, carbon quantum dots (CDs) have been introduced and regarded as promising materials due to their lower toxicity and eco-friendly properties compared with traditional metal sulphide and selenide QDs.²²⁹

Among the superior and unique features of carbon-based QDs are their broad and strong absorption across a major portion of the solar spectrum, and their efficiency in generating and separating photopromoted charges. In view of PEC-WS applications, electrons in the excited energetic level of CDs can be efficiently injected into the conduction band of *e.g.* TiO₂ and $\alpha\text{-Fe}_2\text{O}_3$, while the holes left in the ground state have a redox potential to oxidize a suitable donor species in the environment. Thus, a co-catalytic effect towards the oxygen evolution reaction can also be exploited.

In addition, two other characteristics of CDs are beneficial for enhancing solar energy conversion efficiency: first, a

so-called up-conversion photoluminescence (PL) effect, associated with the radiative recombination of electrons and holes, where the emitted λ is lower (more energetic) than absorbed λ .²³⁰ Charge recombination in the CDs leads to photon emission that can be absorbed by the adjacent semiconductor, provided that the emitted λ is in resonance with the band-gap energy of the semiconductor; this then generates reactive e^-/h^+ pairs in the semiconductor.

Also, the relatively weak intensity of fluorescence from “naked” carbon nanoparticles can be easily addressed by surface passivation with organic molecules or polymeric species – in this case, a main concern remains however the photostability of the surface ligands.^{231,232}

3.3 $\alpha\text{-Fe}_2\text{O}_3$ for photoelectrochemical applications

In its fully oxidized form, Fe₂O₃ exists as crystalline as well as amorphous material. In particular, crystalline Fe₂O₃ may assume one of the four α , β , γ , ϵ possible forms.

$\alpha\text{-Fe}_2\text{O}_3$ (hematite) is the most thermodynamically stable polymorph of iron oxide under ambient conditions. It crystallizes in a rhombohedral lattice system, with lattice parameters $a = 5.0356$ Å and $c = 13.7489$ Å, and exhibits the same crystal structure as corundum (Al₂O₃). That is, O²⁻ atoms arrange in a hexagonally close-packed lattice along the [001] direction and Fe³⁺ atoms occupy octahedral interstices in the (001) basal planes.²³³

A combination of hexagonally packed oxygen atoms with interstitially positioned iron atoms results in a highly dense structure ($d = 5.26$ g cm⁻³), with high polarizability and, hence, high refractive index. This in turn may lead to complex behavior while interacting with photons and electrons.

In particular, the electronic nature of the band-gap in hematite is of great interest to understand its performance as a material for solar energy conversion, and Tauc analysis of the band-gap absorption onset has shown an indirect (phonon-assisted) band-gap nature of the material.²³⁴ *Ab initio* calculations by the Hartree–Fock approach²³⁵ and density functional theory approximation,²³⁶ also supported by soft X-ray absorption and emission spectroscopies at the O K-edge,²³⁷ showed that the valence band of $\alpha\text{-Fe}_2\text{O}_3$ primarily exhibits a O 2p character, with a significant contribution from the Fe 3d orbitals (much higher compared to other metal oxide semiconductor such as TiO₂).²³⁸

Photon absorption of hematite starts in the visible-near infrared region at $\lambda > 650$ nm (with low absorption coefficient $\alpha \sim 10^3$ cm⁻¹), that is well below its optical band-gap (*i.e.*, $E_g \sim 2.1$ eV that corresponds to $\lambda \sim 550\text{--}580$ nm). This is most likely due to spin-forbidden d–d transitions associated to Fe³⁺ ions ($\text{Fe}^{3+} + \text{Fe}^{3+} \xrightarrow{h\nu} \text{Fe}^{4+}(\text{h}^+) + \text{Fe}^{2+}(\text{e}^-)$).²³⁹ However, although increasing its conductivity, photoexcitation of hematite at these wavelengths does not produce any significant photocurrent in PEC systems and confirms that, in view of a measurable photocurrent, efficient e^-/h^+ pairs are associated to a charge transfer process of the type $\text{O}^{2-} + \text{Fe}^{3+} \xrightarrow{h\nu} \text{O}^-(\text{h}^+) + \text{Fe}^{2+}(\text{e}^-)$, that is, an O(2p)–Fe(3d) indirect transition.^{17,44}

The first report on the use of α -Fe₂O₃ as a photoanode material for splitting water dates back to 40 years ago, when Hardee and Bard produced hematite thin films on Ti or Pt foils by chemical vapor deposition and observed a photocurrent from $\lambda = 550$ nm, under 0.8 V vs. SCE in a KCl-based electrolyte.¹⁵

Later works explored crystal faceting of α -Fe₂O₃,²⁴⁰ and n-type doping with elements from the IVa (*i.e.*, Si, Ge, Sn, and Pb)^{241–243} and IVb (*e.g.*, Ti and Zr)²⁴⁴ groups as a mean to ameliorate the performance of hematite by tackling its intrinsic low carrier mobility. In particular, the introduction of an extra e[−] in the conduction band of α -Fe₂O₃ by substitutional doping leads to higher photocurrent (under anodic bias).²⁴³

Particularly relevant is the work by Sanchez *et al.* who reported on Nb-doped (1.5 mol%) α -Fe₂O₃ single crystals with a quantum efficiency for water splitting as high as *ca.* 40% at 370 nm at +0.5 V vs. SCE.^{245,246}

This value was only recently outperformed by Pt-doping single-crystalline α -Fe₂O₃ nanostructures. In particular, IPCE as high as 60–80% in the 300–400 nm range was reported upon decoration of the Pt/ α -Fe₂O₃ surface with a Co-Pi layer.²⁴⁷

Common to all these early studies is the conclusion that hematite exhibits a flat-band potential that cannot spontaneously reduce water to H₂ and, therefore, an external bias is needed to complete the water splitting reaction. Not only this, but also a few other critical points have to be addressed when considering α -Fe₂O₃ as photoanode material for PEC-WS applications, namely low water oxidation (OER) kinetics, low light absorption coefficient, and short diffusion length of holes.

Poor OER kinetics, which translates into a relatively high overpotential for the anodic reaction, is related to two different factors:^{17,44} (i) the presence of oxygen vacancies and crystalline disorder on the surface of hematite that, by trapping and accumulating h⁺ at the interface, may lead to Fermi level pinning, and (ii) the partial Fe³⁺ character of the valence band that results in the energy mismatch between d orbitals (where the hole moves) and the p orbitals of *e.g.* the hydroxide donor species in solution (*i.e.*, the acceptor) resulting in a slow charge transfer.

One of the most commonly adopted strategies to overcome surface crystalline disorder is the decoration of α -Fe₂O₃ with thin surface passivation layers that reduce (h⁺ trapping) surface defects and limit hole back injection (see below).^{248–252}

In addition, the use of a co-catalyst (*e.g.*, Co-Pi and IrO₂, see below) is known to (i) increase the kinetics of hole transfer to the electrolyte, limiting their accumulation at the interface and therefore leading to an overall higher photocurrent, (ii) reduce the photocurrent-onset overpotential and enhance the overall energy conversion efficiency, and (iii) extend the long-term stability of the photoanode under operating conditions.

More recent efforts have been devoted to optimizing the hematite-based electrode morphology by nanostructuring to address the intrinsic low absorption coefficient and short hole diffusion length of α -Fe₂O₃. However, as described in the next paragraphs, a combination of all mentioned strategies (*i.e.*, doping, surface decoration and nanostructuring) is key to

an ideal hematite photoanode that features an optimal material composition/structural configuration and therefore a maximized PEC ability.

In the next sections we will primarily focus on one-dimensional hematite-based nanostructures for improved PEC performance, along with examples of the most promising and rationally designed architectures obtained by a tailored combination of above mentioned strategies. Table 1 provides some examples of different synthetic/modification approaches to 1D α -Fe₂O₃ nanostructures and their PEC performances.

3.3.1 Doping to enhance α -Fe₂O₃ conductivity. As briefly outlined in previous sections, α -Fe₂O₃ suffers from very low electrical conductivity ($\sim 10^{-14}$ ohm^{−1}), low carrier density (10¹⁸ cm^{−3}), and limited electron mobility (10^{−2} cm² V^{−1} s^{−1}).^{253,254} All these aspects result from a Fe³⁺/Fe²⁺ valence alternation on spatially localized 3d orbitals.

Concerning conductivity, empirical data well match the theoretical predictions of a conduction mechanism based on small polarons' hopping for both electron and hole transport.²⁵⁵ In particular, the extremely low mobility of electrons leads to severe energy loss due to electron–hole recombination.

Doping hematite with a metallic element, either n-type doping (*i.e.*, with ions with a net charge higher than 3+) or p-type doping (*i.e.*, with elements in their I or II oxidation state), is a practical solution to these limitations.^{255–258} DFT calculations showed that transition metals (TMs, *e.g.*, Ti, Cr, Mn, Ni, *etc.*) can provide a dual functionality, namely not only TMs enhance the electron conductivity, but they can also influence other parameters, such as morphology, stoichiometry, crystallinity, lattice symmetry, grain size, *etc.*²⁵⁹

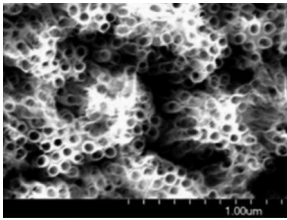
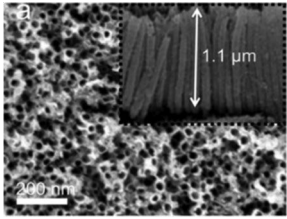
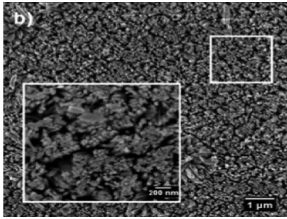
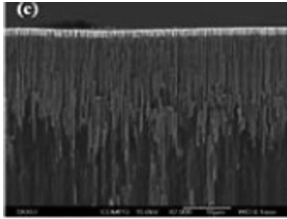
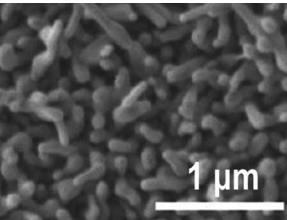
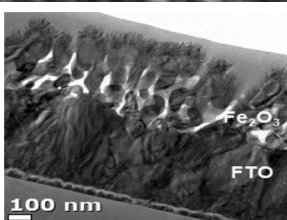
For instance, addition of titanium carbonitride (TiCN) as Ti precursor during the hydrothermal growth of α -Fe₂O₃ changes the morphology from porous α -Fe₂O₃ to Ti-doped 1D urchin-like nanostructures and leads to a photocurrent density of 1.9 mA cm^{−2} (measured at 1.23 V vs. RHE under AM 1.5G and in 1 M NaOH).²⁶⁰

Combining Ti-doping with the formation of oxygen vacancies introduced in hematite by controlling the oxygen pressure during α -Fe₂O₃ nanorod growth has been reported to lead to Ti-doped α -Fe₂O₃ with a coral-like morphology that exhibits a significantly larger surface area with respect to the undoped α -Fe₂O₃ case. The high PEC performance obtained (2.25 mA cm^{−2} and 4.56 mA cm^{−2} at 1.23 V and 1.6 V vs. RHE, respectively) was attributed to the synergistic effect of the high specific area of the nanorod/nanocoral morphology and the increased donor density, due to oxygen vacancies and Ti doping (Fig. 8(a and b)).²⁶¹

However, the effect induced on hematite by Ti-doping has been reported to largely depend on the synthesis procedure.^{262–264} This in turn makes very challenging to identify a model that could be generally valid to describe the impact of Ti doping on α -Fe₂O₃ photoelectrochemical activity.²⁶² Recent studies report that keys are the homogeneity²⁶³ and distribution of Ti centers (that is, shallow doping vs. bulk doping)²⁶⁴ in the hematite nanostructures.

In particular, Wang *et al.* showed that hematite layers with a larger concentration of Ti⁴⁺ accumulated in the bulk exhibited a 100% higher photocurrent than that of samples with Ti⁴⁺ segregated on the surface.²⁶⁴

Table 1 Selected examples of 1D α -Fe₂O₃ based photoanodes and their PEC performance

Structure	Preparation	SEM	Electrolyte	$j/\text{mA cm}^{-2}$	Ref.
α -Fe ₂ O ₃ NTs	Anodization (H ₂ annealing)		1 M KOH	1.4 at 1.5 V _{RHE}	450
Ni-doped α -Fe ₂ O ₃ NTs	Anodization and electrochemical deposition		1 M KOH	~3.3 at 1.45 V _{RHE}	451
α -Fe ₂ O ₃ NRs	Hydrothermal synthesis		1 M NaOH	3 at 1.6 V _{RHE}	452
α -Fe ₂ O ₃ NRs	Template synthesis		1 M NaOH	8 at 1.6 V _{RHE}	311
Sn-doped α -Fe ₂ O ₃ NWs	Hydrothermal synthesis		1 M NaOH	1.2 at 1.23 V _{RHE}	121
Pt-doped α -Fe ₂ O ₃ NRs, with Co-Pi co-catalysts	Solution-based methods and two-step annealing		1 M NaOH	4.3 at 1.23 V _{RHE}	247

In all cases solar light AM 1.5G (100 mW cm⁻²) was used for irradiation. SEM images (from top to bottom): adapted with permission from *Chem. Mater.*, 2009, 21, 3048–3055. Copyright 2009 American Chemical Society; adapted with permission from *J. Phys. Chem. C*, 2012, 116, 24060–24067. Copyright 2012 American Chemical Society; reproduced from ref. 452 with permission from Elsevier; reproduced from ref. 311 with permission from the Royal Society of Chemistry; adapted with permission from *Nano Lett.*, 2011, 11, 2119–2125. Copyright 2011 American Chemical Society; reproduced from ref. 247 with permission from Springer Nature.

Also the distribution of a nonmetallic dopant (*e.g.*, P) has been recently reported to be crucial for achieving an enhancement in α -Fe₂O₃ PEC activity.^{258,265} Although doping hematite is a means to promote charge conductivity, doped α -Fe₂O₃ still suffers of a high charge recombination rate in the bulk.

Gradient phosphorous doping, obtained by short-time annealing (10 min at 750 °C) of hematite nanobundle arrays after immersion in a Na₃PO₄ aqueous solution, widens the band bending region at the electrode/electrolyte interface and hence improves the separation of charge carriers. A photocurrent

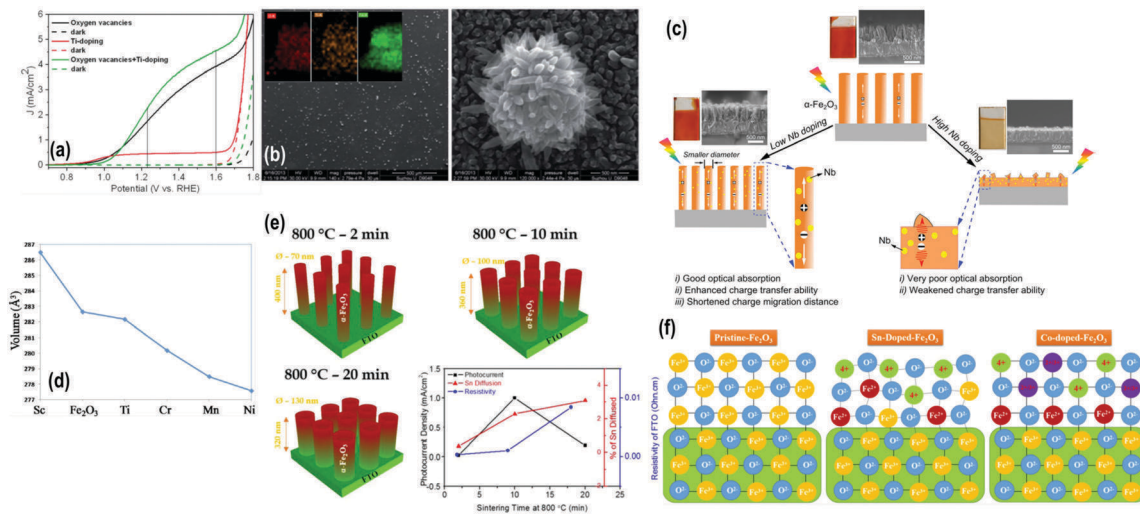


Fig. 8 (a) Linear sweep voltammograms of reduced and Ti-doped α -Fe₂O₃ nanoarrays, showing the synergistic effect induced by Ti and oxygen vacancies on the photoanode PEC performance (measurements were performed under simulated solar light AM 1.5G irradiation, 100 mW cm⁻²). (b) SEM images and TEM elemental mapping of Ti-doped α -Fe₂O₃ nanorods. (c) Effects on α -Fe₂O₃ morphology and properties induced by low (left) and high (right) Nb doping amounts. (d) Calculated volumes of defective α -Fe₂O₃ supercells containing 3d TM substitutions. (e) Schematic representation of thermally induced Sn-doping of α -Fe₂O₃ nanorod arrays and dependence of photoanode performance, extent of Sn diffusion and FTO resistivity on the annealing time. (f) Schematic representation of the destabilizing effect induced in the α -Fe₂O₃ lattice by Sn⁴⁺ dopants, and the recovery of a more ordered structure promoted by Be²⁺ dopants. Fig. (a and b) reproduced from ref. 261 with permission from the Royal Society of Chemistry. Fig. (c) reproduced from ref. 267 with permission from the Royal Society of Chemistry. Fig. (d) reproduced from ref. 259 with permission from the American Institute of Physics. Fig. (e) adapted with permission from *J. Phys. Chem. C*, 2015, **119**, 3810–3817. Copyright 2015 American Chemical Society. Fig. (f) reproduced from ref. 278 with permission from Nature Publishing Group.

density of 1.5 mA cm⁻² was measured at 1.23 V vs. RHE under AM 1.5G illumination, that is a 50% enhancement compared to uniformly P-doped α -Fe₂O₃ nanobundles.²⁶⁵

Clearly, one of the most critical aspects to take into account when introducing a dopant element into a “host” structure is the identification of the optimal dopant amount, in order to achieve the desired effects (*e.g.*, increased donor density and charge conductivity), with a minimum of side effects.

For α -Fe₂O₃, for instance, an excess amount of Ta has been reported to negatively affect nanorod growth along the [110] direction, with a consequent drop of the material overall PEC performance²⁶⁶ – remarkably, the (110) plane of hematite with its surface termination dominated by Fe(III) ions features high conductivity.¹⁹³

A similar effect was also observed for an excess amount of Nb dopant, as reported in Fig. 8(c).²⁶⁷

A significant lattice cell reduction, which in turn promotes larger probability for localized charge carrier (polaron) hopping and thus increases the conductivity, has been calculated for Mn-doped α -Fe₂O₃ (Fig. 8(d)).^{268,269} Mn-Doped hematite nanorods (with a dopant content in the 5–7 mol% range) has been fabricated through hydrothermal methods and photocurrent density as high as 1.6 mA cm⁻² at 1.23 V vs. RHE has been reported. Remarkably, 5% Mn-doped hematite NRs have been recently reported to enable unassisted (bias-free) light-induced water splitting, when combined to CH₃NH₃PbI₃ perovskite in a tandem solar cell, with a solar-to-hydrogen conversion efficiency of 2.4%.²⁷⁰

Also Pt and Ru have been considered as TM dopants for α -Fe₂O₃. Guo *et al.* recently developed a synthetic procedure to

dope ultrathin α -Fe₂O₃ nanorods with Ru cations.²⁷¹ α -FeOOH nanorods coated with a ruthenium(III) acetylacetonate-based layer were deposited on FTO substrate *via* doctor blading technique; annealing in air at 700 °C converted the amorphous nanorods into crystalline hematite NRs and produced Ru nanoparticles with different valence states (+4 and +3). Such photoanodes showed a photocurrent density as high as 5.7 mA cm⁻² that was attributed to (i) an enhanced carrier transport promoted by tetra- and lower-valent Ru cations, and to (ii) the absence of intra-gap trapping states in α -Fe₂O₃.

A most straightforward strategy for doping α -Fe₂O₃ nanostructures grown on FTO glass is the thermally-induced diffusion of Sn from the substrate, while annealing at temperatures above 750 °C.^{16,121,272,273}

Among the first reports on “unintentional” Sn-doping of hematite layer on FTO is the study of Sivula *et al.*¹⁶ The significant enhancement of photocurrent observed upon annealing at 800 °C was attributed to a two-fold enhancement of the optical absorption coefficient, due to the structural distortion of the hematite lattice induced by tin-doping.

A similar strategy was applied by Ling *et al.*¹²¹ who reported a photocurrent density of 1.24 mA cm⁻² at 1.23 V vs. RHE and attributed the enhanced PEC performance to an increased donor density (*i.e.*, from 1.89 × 10¹⁹ cm⁻³ and 5.38 × 10¹⁹ cm⁻³ for undoped and Sn-doped hematite, respectively) and hence higher carrier conductivity.

From these early studies it is apparent that to achieve a desired functionality associated to Sn-doping, high temperature annealing is required; however, annealing FTO at 800 °C

also leads to a significant change in the material stoichiometry, already after 20 min, and typically doubles tin oxide resistivity – a 10 min annealing was reported to be optimal to establish a trade-off between a desired increase in conductivity and the drawbacks related with treatment at high T (Fig. 8(e)).²⁷² Moreover, another side effect associated with high T treatment is the collapse of α -Fe₂O₃ nanostructure morphology. Clearly, both effects have a negative impact on the photoanode overall PEC performance.

Therefore, different techniques including *e.g.* solution-based approaches, microwave hybrid annealing or chemical encapsulation have also been reported that overcome the requirement of a high temperature annealing (see also Section 3.3.3).^{121,274,275} For instance, efficient Sn doping of hematite was achieved starting from hydrated tin(IV) chloride as metal precursor. As for Ti-doped α -Fe₂O₃,²⁶⁰ a morphology change from nanowires for undoped hematite to nanocoral-like structures for Sn-hematite was observed, together with a surface area increase and an improved electrical conductivity that were identified as dominant factors leading to a higher photoactivity.

In situ doping of α -Fe₂O₃ nanotube layers was investigated by Lee *et al.* and Chitrada *et al.*^{276,277} Self-organizing anodization on Fe–Si alloys with various Si content (1, 2, and 5 at%) led to the simultaneous formation of iron oxide-based NT arrays and to the incorporation of Si. The introduction of Si decreased the layer growth rate and led to a more pronounced nanotubular morphology.

In particular, hematite layer with 5 at% Si exhibited a 5-fold increase in the photocurrent, along with a negative shift of the onset potential compared to the undoped sample.²⁷⁶

Iron oxide based nanoporous layers were also synthesized by electrochemical anodization of Fe₁₄Nd₂B permanent magnet. Highly regular structure with a pore diameter ranging from 30 to 60 nm and a thickness of about 0.5 μ m were produced, while incorporation of Nd³⁺ and B³⁺ resulted in a direct band-gap of 2.05 eV for doped iron oxide, and shifted the flatband potentials to -0.8 V vs. Ag/AgCl.²⁷⁷

Despite the abovementioned beneficial effects observed upon doping α -Fe₂O₃, the introduction of a single dopant into the oxide lattice may induce also some undesired side effects, such as narrowing of the space charge layer and generation of impurity states within the oxide band-gap that act as recombination centers. A rational combination of two (or more) dopants can then be crucial for overcoming such drawbacks.

This has been *e.g.*, reported in the case of Sn⁴⁺ and Be²⁺ co-doped α -Fe₂O₃ nanorods (Fig. 8(f)).

Sn⁴⁺ alone, despite providing an enhanced charge conductivity, (i) introduces shallow n-type defect states beneath the conduction band minimum of hematite, thus leading to an undesired band edge shift, and (ii) increases micro-strain in the α -Fe₂O₃ lattice, decreasing the Fe–O bond ordering.

Nevertheless, the co-presence of Be²⁺ ions attenuates these negative effects, by recovering α -Fe₂O₃ CBM and reducing lattice distortion in hematite – remarkably, the sequence in which the co-doping is carried out was also found to be very crucial. For the optimized Sn(4%)–Be(6%) containing α -Fe₂O₃

NR array, a maximum photocurrent density of 1.7 mA cm⁻² at 1.23 V vs. RHE has been reported.²⁷⁸

Similar effects have been demonstrated also for other co-dopant couples, including *e.g.* Ti–Sn,²⁷⁹ In–Sn²⁸⁰ and Ti–Si,²⁸¹ while DFT calculations showed that metal/non-metal dopant combinations, such as Ti–N and Zr–N can effectively reduce the band-gap of hematite and increase its absorption properties in the visible region. Moreover, the charge distribution of the CBM and the VBM becomes spatially separated after co-doping, which is beneficial for extending the charge carrier lifetime.²⁸²

Worth mentioning are also Zn-doped (*i.e.*, p-type doping) α -Fe₂O₃ NTs fabricated by means of electrodeposition.²⁸³ A precursor ZnO nanorod array simultaneously served as sacrificial template and Zn source, while a FeCl₂ aqueous solution was used as the electrolyte for iron deposition. Under optimized conditions (1 V_{SCE} anodic potential and 5–15 min reaction time), Fe²⁺ to Fe³⁺ oxidation occurs in the electrolyte, and trivalent-Fe ions precipitate and form an amorphous γ -FeOOH layer on the surface of ZnO nanorods. During this oxidation/precipitation process, ZnO is gradually dissolved due to the acidic environment and the applied anodic potential, and some of the Zn²⁺ ions are eventually incorporated as p-type doping species into the γ -FeOOH layer. A positive flat band potential of 1.82 V vs. RHE and an acceptor density of 4.19×10^{18} cm⁻³ were determined for the optimally Zn doped α -Fe₂O₃ NTs array, together with a cathodic photocurrent of 40.4 μ A cm⁻² measured at 0.5 V vs. RHE.

3.3.2 Co-catalyst decoration. A most effective approach to accelerate the oxygen evolution reaction (OER) kinetics in α -Fe₂O₃ by increasing h⁺ transfer rate to the electrolyte is the modification of hematite with an oxygen evolution catalyst (OEC).

Tilley *et al.* demonstrated that IrO₂ nanoparticles (*ca.* 2 nm diameter) on hematite nanostructure photoanodes lead to a 200 mV cathodic shift in the onset potential and increase the photocurrent from 3.45 to 3.75 mA cm⁻²,²⁸⁴ while non-stoichiometric IrO_x nanoparticles (with $x = ca.$ 2.1) on α -Fe₂O₃ were reported to decrease the overpotential for the water oxidation reaction to an even larger extent.²⁸⁵ However, despite the fact that iridium oxide (IrO_x) co-catalysts typically exhibit the highest performance in terms of OER activity,²⁸⁴ only a few reports deal with IrO_x-decorated hematite for PEC applications, the main limitation being the high cost of Ir.

Other reported efficient co-catalyst materials for α -Fe₂O₃ photoelectrode include cobalt-phosphate (Co-Pi), Ni–Fe and Zn–Co based layered double hydroxides (LDH), FeOOH, NiOOH, *etc.*

In particular, Co-Pi on 1D α -Fe₂O₃ nanostructures improves the overall photoanode current density and shifts the current onset potential to more cathodic values, due to the bridging effect of phosphate ions that facilitate hole injection from α -Fe₂O₃ to Co ions.^{248,249,286}

Several methods are reported to deposit Co-Pi on hematite nanostructure surface, such as chemical immersion deposition, electrodeposition and photoassisted electrodeposition.^{248,250}

In particular, photoassisted electrodeposition of Co-Pi catalyst enables the formation of an optimized junction between hematite

and the catalyst for a maximized interfacial charge transfer, with the amount of co-catalyst that can be easily controlled by deposition time and current density. For these reasons, such technique provides Co-Pi/ α -Fe₂O₃ layers with superior photoelectrochemical water oxidation ability compared to both Co-Pi electrodeposition and Co²⁺ wet impregnation methods.^{287,288}

More recently, NiOOH, FeOOH, and Ni-Fe LDH, NiFeO_x and Zn-Co LDH layers have shown remarkable performance used in combination with α -Fe₂O₃ for photoelectrocatalytic water oxidation.^{251,252,289,290} Several methods are known for the deposition of oxy-hydroxide and LDH layers onto hematite nanostructures, the most common being *e.g.* solvothermal techniques, electrodeposition or photoelectrodeposition and pulsed laser deposition (PLD).^{291–294} For all these co-catalyst/ α -Fe₂O₃ combinations, a remarkable increase in photocurrent and decrease in water oxidation overpotential has been reported compared to naked hematite layers. In particular, a NiFeO_x-decorated hematite layer prepared by a photochemical deposition technique exhibited a significant cathodic shift of the water oxidation overpotential, primarily due to improvement in the interface energetics. Moreover, used as photoanode in combination with a TiO₂/Pt-modified Si photocathode, NiFeO_x-decorated α -Fe₂O₃ provided one of the first examples of a tandem solar cell made of earth-abundant elements that could enable unassisted light-induced water splitting.²⁹⁰

Although the co-catalysts studied for PEC water splitting reactions are typically inorganic materials, also organic based ones have been recently explored. Among these, Ru-based molecular water oxidation catalysts, also conveniently functionalized (*e.g.*, with a strong 2,6-pyridine-dicarboxylic acid anchoring group), are worth mentioning.^{295,296} In spite of improving the PEC performance of hematite-based photoanodes, a major challenge for the use of such materials still remains their poor photostability.

3.3.3 Other strategies. As previously mentioned (Section 3.2.4), strategies that can be used to improve the PEC performance of 1D hematite photoanodes include *e.g.* surface passivation, the formation of heterostructures, sensitization by quantum dots and plasmonic metal nanoparticles, the use of graphene derivatives for enhancing the photogenerated charge dynamics, *etc.*

Modification of α -Fe₂O₃ nanostructures by solution methods (*e.g.*, impregnation) has been explored to protect/modify the oxide surface and enable higher PEC efficiency and longer stability under operating conditions.

Kim *et al.* reported that upon impregnation in a phosphate-based solution, the isoelectric point (IEP) of hematite is shifted to a considerably lower value (*i.e.*, from pH 8.3 for the bare oxide, to pH 4.8 for the PO₄³⁻-modified oxide). For photocurrent measurements performed in a potassium phosphate buffered electrolyte (pH 7), the negatively charged PO₄³⁻ ions attached to the α -Fe₂O₃ surface promoted hole extraction and injection from the photoanode into the electrolyte, thus increasing the electron-hole pair separation in hematite and leading to a three-time higher photocurrent density than that measured with the bare oxide.²⁹⁷

Improved efficiency of charge separation and enhanced photocurrent have been also observed upon acetic acid treatment of

hematite nanowires doped with Sn from FTO glass (see Section 3.3.1). Transient absorption and transient photocurrent spectroscopies provided evidence that this effect may be ascribed to a minimization of surface electron-hole recombination due to the passivation of surface electron trap states by acetic acid.²⁹⁸

A popular approach to enhance the intrinsically low visible light absorption coefficient of hematite is to integrate a plasmonic nanostructure (*e.g.*, Au and Ag) with the semiconductor.²⁹⁹ In contrast with *e.g.* Au on TiO₂ (see Section 3.4.2), the intense local field enhancement of gold at the LSPR wavelength overlaps with the absorption band edge of hematite and can thus enhance solar energy collection at energies below the band edge of α -Fe₂O₃ through a plasmon-induced energy transfer effect.^{66,212,300}

In particular, plasmonic nanostructures can be designed to concentrate LSPR effects into small regions and, if the absorbed photon flux is simultaneously confined within a ultrathin film of *e.g.* α -Fe₂O₃, this clearly shortens the diffusion distance of photogenerated holes to the electrolyte, thus reducing the charge recombination rate and leading to an overall increase in PEC performance.^{301–303}

Gao *et al.* showed a \sim 30% enhancement in the photocurrent of a α -Fe₂O₃ thin-film photoanode coated on arrays of Au nanopillars (\sim 0.4 mA cm⁻² at 1.5 V_{RHE} under AM 1.5G illumination), compared to a α -Fe₂O₃/Au flat electrode (\sim 0.3 mA cm⁻²), and attributed the effect to an increased LSPR-induced optical absorption and to a photonic light trapping mode in the nanostructured film.³⁰¹

Similar light and plasmonic effect confinements were reported also for more complex semiconductor-plasmonic-metal-metal-oxide core-multishell (CMS) nanowire arrays, composed of a Si core (40 nm diameter) – Si is known to reduce the overpotential of hematite for OER, and of Al (50 nm) and a α -Fe₂O₃ ultrathin film (<50 nm) as inner and outer shells, respectively (Fig. 9(a)). Under ideal conditions, a maximum photocurrent density of \sim 12 mA cm⁻² was achieved that corresponds to a STH efficiency of 14.5%,³⁰² *i.e.*, about 93% of the theoretical maximum efficiency reported for bulk hematite.¹⁷ This outlined that nanostructuring (of both the metal oxide and the plasmonic metal) is key to manipulate and concentrate the incident light in small regions where photogenerated charges can reach the reaction site (*i.e.*, the semiconductor/electrolyte interface) with minimal recombination.

Moreover, Si-Al- α -Fe₂O₃ CMS NWs were also shown to outperform Si-Au- α -Fe₂O₃ arrays (Fig. 9(a)) and indicate that Al may be an excellent alternative plasmonic material compared to more precious and conventional metals, such as Ag and Au.³⁰²

Charge injection (*i.e.*, hot electron transfer) from a plasmonic metal to hematite has been demonstrated for Ag NPs on α -Fe₂O₃ nanosheets (NSSs) with exposed active (001) facets; for this assembly, the introduction of Ag NPs led to significantly improved light harvest in a broad wavelength region, from UV to the NIR.³⁰⁴ The possibility of charge injection from Ag to α -Fe₂O₃ is enabled by the higher energy position of the metal Fermi level with respect to that of hematite. This led to a photocurrent increase from 1.5 mA cm⁻² at 1.23 V_{RHE} for pristine hematite NS photoanode to 3.2 mA cm⁻² at 1.23 V_{RHE}

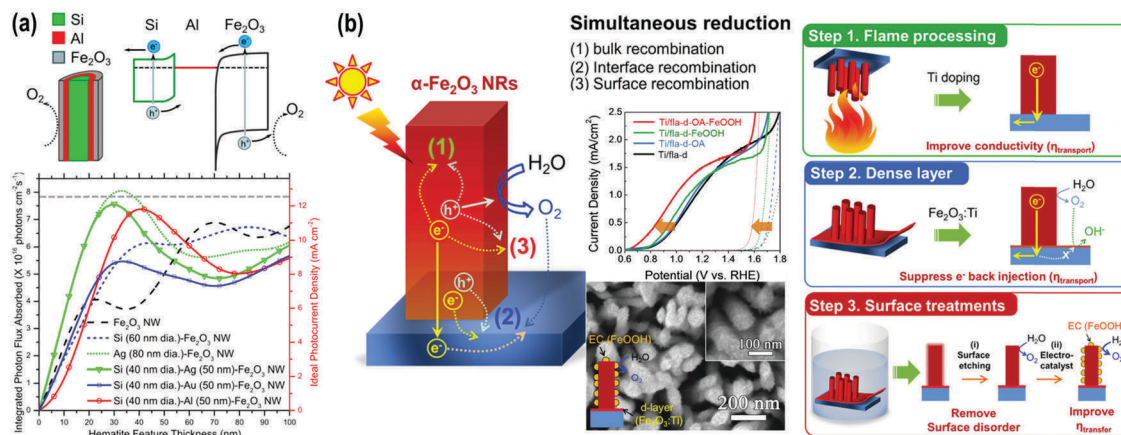


Fig. 9 (a) Schematic and band-structure of a Si–Al– α -Fe₂O₃ CMS NW photoelectrode (upper panel). Integrated absorbed photon flux and ideal photocurrent density of various CSM NW arrays – the gray dashed line indicates the theoretical maximum absorption in bulk hematite (lower panel). (b) Schematic representation of the main electron–hole recombination pathways in hematite NRs photoanodes for solar water splitting, and of the three-step approach to reduce bulk, interface, and surface recombination. SEM image of the Ti/flame hematite NRs after sequential oxalic acid etching and FeOOH decoration. *J*–*V* curves measured at 0.8 V_{RHE} of Ti/flame hematite NRs, also modified according to different surface treatments: (i) oxalic acid (OA) etching, (ii) FeOOH deposition, and (iii) combined OA etching and FeOOH deposition. (a) Adapted with permission from *Nano Lett.*, 2014, **14**, 4517–4522. Copyright 2014 American Chemical Society. (b) Reproduced from ref. 326 with permission from John Wiley & Sons.

for the Ag/ α -Fe₂O₃ layer. Moreover, by further decoration of the Ag/ α -Fe₂O₃ photoanode with Co-Pi, a remarkable photocurrent density of 4.68 mA cm⁻² at 1.23 V_{RHE} was achieved that could be attributed to the solely co-catalytic effect of Co-Pi for the OER, as no significant change in the light absorption properties of the layer was correspondingly observed.

In the context of C-based co-catalytic materials, a multi-heterojunction assembly consisting of α -Fe₂O₃ (core)/reduced graphene oxide (rGO, interlayer)/BiV_{1-x}Mo_xO₄ (shell) has been investigated by Hou *et al.* as photoanode material for PEC water splitting.³⁰⁵ According to the authors, the system provides multiple beneficial functionalities: the BiV_{1-x}Mo_xO₄ shell enhances light harvesting properties, while the rGO interlayer bridges the photoactive shell with the hematite core and enables shuttling of photogenerated electrons from BiV_{1-x}Mo_xO₄ to α -Fe₂O₃, significantly reducing charge recombination due to enhanced e⁻/h⁺ separation. For such a system, a negative shift of the onset potential has been observed, along with an increased photocurrent density of 1.97 mA cm⁻² measured at 1.6 V vs. RHE.

A synergistic co-catalytic effect has been also described for carbon nanodots (CDots) and a Co₃O₄ layer, both deposited on α -Fe₂O₃.³⁰⁶ In particular, the interaction between CDots and Co₃O₄ co-catalyst improves the PEC efficiency of pure α -Fe₂O₃ by accelerating the two-step-two-electron O₂ evolution from H₂O. That is, the kinetically slow process of water oxidation molecule to H₂O₂ that takes place at Co₃O₄ sites is significantly accelerated by the fast oxidation reaction of H₂O₂ to O₂, catalyzed by CDots.

Other efficient heterojunction partners for α -Fe₂O₃ include n-Si,^{303,307} ZnFe₂O₄,³⁰⁸ MgFe₂O₄,³⁰⁹ and Ag_xFe_{2-x}O₃.³¹⁰

A heterojunction based on Co-doped α -Fe₂O₃ nanorod array branched with a MgFe₂O₄ ultrathin layer has been reported by Hou *et al.*³⁰⁹ A Co-doped α -Fe₂O₃ nanorod photoanode

prepared by hydrothermal method is decorated with an MgFe₂O₄ film using a wet impregnation method, in combination with thermal annealing. Due to the suitable band alignment between the two components, electrons photo-promoted in the MgFe₂O₄ overlayer migrate to the conduction band of Co- α -Fe₂O₃ and, along the nanorods, to the back contact. At the same time, holes from the valence band of Co- α -Fe₂O₃ are transferred to that of MgFe₂O₄ where they react with water to form O₂.

A significant enhancement in PEC performance has also been reported for an inverse heterostructure consisting of ZnO nanowires (core)/ultrathin α -Fe₂O₃ (~5 nm, shell). This n/n heterojunction generates a negative shift in the flat-band potential and increases surface band bending, thus promoting charge carrier separation. Both these features resulted in a 2-fold enhancement of the PEC activity compared to that of a bare ZnO photoanode.¹⁸⁸

Mao *et al.* reported on a template-assisted method for use of noble metals (such as Pt and Au) as conducting support to enhance charge conductivity in α -Fe₂O₃.³¹¹ At first, Au nanorods are grown in an aluminum oxide template (AAO). Afterwards, Fe ions are electrodeposited onto the Au nanorods, followed by annealing in oxygen atmosphere. Upon removal of the AAO template, a photocurrent density of 8 mA cm⁻² was measured, with 10 μ m long NRs. Following a similar procedure, Pt-supported α -Fe₂O₃ nanorods were also prepared that exhibited a photocurrent density of 10 mA cm⁻² at 1.5 V vs. RHE.

Clearly, for both Au- and Pt-supported heterostructures, a crucial contribution to such a high PEC performance is given by the high conductivity of the noble metals, although also their contribution towards an increased light absorption cannot be excluded.

The use of 1D (or 3D) transparent conductive oxides (TCOs), namely ITO (In:SnO₂),³¹² FTO (F:SnO₂),³¹³ ATO (Sb:SnO₂),^{74,314–316}

NTO (Nb:SnO₂),⁷⁹ as electron collecting scaffolds has been investigated as a means to hinder the intrinsically low conductivity of hematite. Such host-guest architectures (*i.e.*, TCO- α -Fe₂O₃) have been shown to meet both the electronic and the optical requirements to achieve high PEC performance with a hematite-based photoelectrode.

Supported by first-principle full-field electromagnetic simulations, Wang *et al.* demonstrated that an ITO nanocone array decorated with a 20 nm α -Fe₂O₃ light absorbing layer can in principle exhibit a nearly total above band-gap solar absorption, which corresponds to a maximum theoretical photocurrent density of 12.5 mA cm⁻².³¹⁷

Zhang *et al.* showed that ITO (core)/ α -Fe₂O₃ (shell) nanostructures, also decorated with a reduced graphene oxide (rGO) layer, exhibit a photocurrent as high as 5.38 mA cm⁻² at 0.6 V *vs.* SCE – that is, a 3.5-fold enhancement compared to ITO/ α -Fe₂O₃ photoelectrodes.

In this configuration, not only the TCO/hematite assembly is crucial for optimizing electron transport/collection, but also the rGO layer forms an ohmic contact with hematite that facilitates the transfer of photogenerated holes to the electrolyte and, hence, accelerates the oxygen evolution reaction kinetics.³¹²

Similar to the more commonly reported black TiO₂, also reduced α -Fe₂O₃ has been prepared by hydrogen plasma treatment of an α -Fe₂O₃ layer.³¹⁸ “Black-like” hematite consists of mixed Fe₃O₄ and α -Fe₂O₃ phases, where the mixed Fe:O stoichiometry (due to the valence switching between Fe³⁺ and Fe²⁺) is crucial to increase hematite donor density and hence improve its conductivity.³¹⁹ This aspect, in combination with a reduced band-gap, led to a considerable increase of photocurrent density and a most significant cathodic shift in the photocurrent onset potential (from 1.68 to 1.28 V *vs.* RHE upon hydrogen plasma treatment), most likely due to the appearance of new surface-states.^{206,320,321}

Oxygen vacancies engineering in α -Fe₂O₃ can also be achieved upon annealing under various other (reducing) atmospheres. Highly conductive Fe₂O_{3-x} nanowire arrays were for instance reported for a thermal decomposition of β -FeOOH akaganeite at 550 °C in N₂-air mixture (with an oxygen content as low as 0.43%).

Remarkably, the relatively low temperature did not damage the film wire morphology. A significant increase of the donor density from $\sim 3.3 \times 10^{19}$ cm⁻³ (for a hematite NW layer annealed at 550 °C in air) to $\sim 3.7 \times 10^{20}$ cm⁻³ (for the N₂-air annealed sample) was attributed to Fe²⁺ shallow donors and a photocurrent of 3.37 mA cm⁻² at 1.5 V *vs.* RHE was reported.³²² A comparable effect has been more recently reported upon multi-step annealing of as-deposited β -FeOOH films at even lower temperatures (*i.e.*, 1 hour annealing at 350 °C in pure N₂, followed by 30 min annealing in air at the same *T*).³²³

As shown by Moir *et al.*, oxygen vacancies can also be generated by annealing crystalline α -Fe₂O₃ thin-films (produced from amorphous layer by thermal treatment at 450 °C in air for 2 h) in an Ar/H₂(5%) atmosphere at 450 °C for 2 h.³²¹

Aside from thermal treatments in oxygen-poor atmosphere at *T* \sim 450–550 °C, annealing hematite at higher temperatures

(*e.g.* in the 650–800 °C range) in air is also often explored as a means to increase its PEC performance; however, under such conditions, sintering and collapse of the ordered one-dimensional arrays often occur.

Brillet *et al.* and Morrish *et al.* observed that the energy barrier for hematite activation is higher than that for morphology evolution. Therefore, decoupling the two events can enable (i) the growth of highly ordered 1D nanostructures, upon annealing performed at lower *T* and (ii) hematite activation to higher PEC performance (*e.g.*, owing to Sn-doping from FTO glass), upon annealing at higher *T* (>600 °C).^{274,324}

In particular, if the nanostructured α -Fe₂O₃ layer (that is, the layer obtained after the first annealing step) is protected through conformal coating with a rigid SiO₂ layer, the desired film morphology can be preserved up to 800 °C – however, anodic shift of the onset potential is observed, and the desired hematite PEC features can be restored only upon removal of the SiO₂ coating.²⁷⁴

Remarkably, also decorating FTO glass with Sb-doped SnO₂ (ATO) NPs enables the growth of sintering-resistant α -Fe₂O₃ nanorods. Wang *et al.* reported that the high lattice energy of the ATO-FTO interface can control hematite morphology evolution during annealing at high temperature (800 °C), and a photocurrent density of 2.12 mA cm⁻² was measured at 1.23 V *vs.* RHE under AM 1.5G solar illumination – for such a heterostructure, a contribution similar to that mentioned for TCO-hematite host-guest composites (see above) should not be anyway excluded.³²⁵

Finally, an example of a sequential-multifold approach applied to α -Fe₂O₃ nanorods for (i) reducing electron-hole recombination in the bulk oxide, (ii) promoting electron transport to the back-contact, while simultaneously enabling fast hole injection into the electrolyte has been provided by Cho *et al.* (Fig. 9(b)).³²⁶

A flame-treatment in the presence of a Ti precursor can be used to produce Ti-doped α -Fe₂O₃ nanorods, with reduced bulk and surface charge recombination, without affecting the morphology of the hematite NRs. The addition of a dense-layer between the hematite array and the fluorine-doped SnO₂ substrate effectively reduced the interfacial recombination by suppressing electron back-injection. The deposition of a FeOOH on the surface of Ti-doped α -Fe₂O₃ nanorods passivated hematite surface states and provided a highly active interface for hole injection into the electrolyte. These sequential treatments led to an overall significant decrease of the photocurrent onset potential (*ca.* 400 mV).

3.4 TiO₂ for photoelectrochemical applications

Titanium dioxide crystallizes in three major different polymorphs, namely anatase (A), brookite (B), and rutile (R). In particular, anatase and rutile TiO₂ represent the crystalline forms more widely investigated for photoelectrochemical and photocatalytic applications.²⁰¹ It is commonly reported that, for bulk TiO₂, anatase into rutile transition occurs at annealing *T* > 600 °C, under ambient atmospheric conditions.³²⁷

While holding for TiO₂ nanopowders, this observation is however not always valid: as we will discuss in the following section, amorphous TiO₂ may even crystallize directly in the form of rutile, or the anatase-into-rutile transformation may occur at lower temperature. These are the cases of *e.g.* hydrothermal TiO₂ nanorods that, fabricated at high pressure (~15–20 atm) and at $T \sim 150\text{--}200\text{ }^\circ\text{C}$, typically nucleate with a rutile crystal structure, or of anodic TiO₂ nanotubes on Ti metal foil.^{328,329}

Both anatase and rutile TiO₂ exhibit a tetragonal structure with lattice cell parameters $a = b = 3.782\text{ \AA}$ and $c = 9.502\text{ \AA}$ for anatase, and $a = b = 4.594\text{ \AA}$ and $c = 2.953\text{ \AA}$, respectively.²⁰¹ In both structures, crystalline units consist of TiO₆ octahedra (*i.e.*, each Ti⁴⁺ atom is surrounded by six O²⁻ atoms), with a more or less pronounced distorted configuration: two long bonds between the (central) Ti atom and the O atoms at the apices and four shorter Ti–O equatorial bonds (*i.e.*, 1.966 Å vs. 1.937 Å in anatase, and 1.983 Å vs. 1.946 Å in rutile).³³⁰ Despite having the same chemical composition, differences in the coordination environments and chemical bonding of anatase and rutile TiO₂ strongly affect the electronic properties of the material.

Early studies by Earle in 1942 demonstrated that TiO₂ is an n-type semiconductor, with a valence band that exhibits a strong O 2p character and a conduction band mainly composed of Ti 3d orbitals.³³¹

In its amorphous form, TiO₂ has a mobility gap of 3.2–3.5 eV and a very low electron mobility. Upon crystallization to anatase or rutile an indirect optical band-gap of 3.2 eV and 3.0 eV is obtained, respectively, with both polymorphs showing a higher mobility than amorphous TiO₂.³³² In particular, a crystallization into anatase is often reported to be crucial to obtain a high electron mobility.³³³

Not only the crystal structure, but also oxygen vacancies and Ti³⁺ states in the lattice largely influence the electronic and optical properties of TiO₂. Electrons may be trapped in Ti³⁺ states (or holes in the oxygen vacancies) and injected in the nearby conduction (or valence) band by thermal excitation. Electron conductivity of TiO₂ is therefore dominated by Ti³⁺ trap states and, in the polycrystalline materials, also by the grain size.^{334,335}

Spectro-/photo-/electrochemical characterization^{336,337} performed on anatase and rutile crystals showed that both polymorphs exhibit positive holes with adequate oxidative power to promote H₂O oxidation to O₂ and mainly differ for the position of their conduction band edges; in particular, while the conduction band of rutile is slightly more positive than $E^\circ(\text{H}^+/\text{H}_2)$, the flat-band potential of anatase is 0.2 V more negative than rutile. Therefore, splitting of water into H₂ and O₂ is in principle thermodynamically possible (that is, spontaneous) without external bias on anatase only. However, due to the slow kinetics of the cathodic HER, also a TiO₂ anatase-based photoanode is often assisted by an applied voltage that by inducing favorable band bending increases charge separation.

The first study on the use of TiO₂ as electrode material in a photoelectrochemical arrangement dates back to 1968;³³⁸ rutile (single crystal) reduced in H₂ atmosphere was shown to evolve O₂

from a phosphate buffered aqueous solution, under chopped UV illumination from a mercury arc lamp and 0–50 V vs. SCE applied bias. Only the anodic reaction was considered and tunneling of electrons from occupied levels at the surface directly into the empty conduction band was suggested to produce upward band bending near the surface, at the TiO₂ electrode.

However, only after the ground-breaking work of Fujishima and Honda in 1972 on the “complete” photoelectrochemical water splitting reaction (*i.e.*, into H₂ and O₂), TiO₂ has been regarded as the key semiconductor material for photoelectrochemical and photocatalytic applications.

This not only because of its intrinsic electronic and optical properties, but also because it is abundant, cheap, non-toxic and stable against (photo)corrosion – all relevant aspects when targeting the production of *e.g.* large-scale devices for energy conversion.

A large number of studies have been promoted to address one of the (still) biggest limitations of TiO₂, that is, its relatively wide band-gap (as mentioned, 3.0–3.2 eV) that rules out any possible use of $\lambda > 400\text{ nm}$ for light-promoted reactions.

After various early findings^{339,340} and, in particular, since the report by Asahi on the visible light activity of nitrogen-doped titania,¹⁵² doping has been (one of) the leitmotifs for the fabrication of visible light active materials.

As discussed in the previous Section (3.2.1), doping of TiO₂ is achieved by replacing metal (titanium) or nonmetal (oxygen) atoms with a nonmetal or a transition metal cation (*i.e.*, substitutional doping), or by filling in interstitial lattice spaces (*i.e.*, interstitial doping). Typical nonmetal dopants for TiO₂ nanomaterials are B, C, N, F, P, S, Cl, and Br;^{88,152,159,160,341} on the other hand, Cr, V, W, Ta and Nb are commonly used as metal dopants.^{342–346}

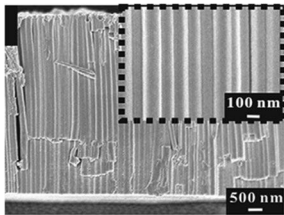
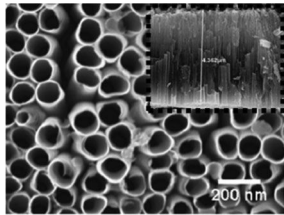
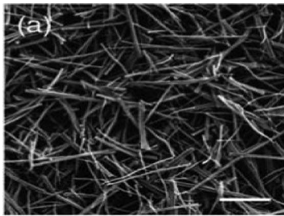
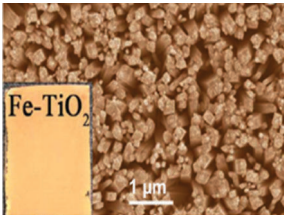
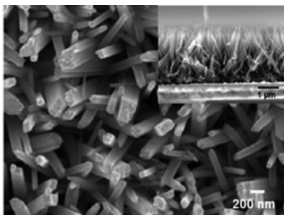
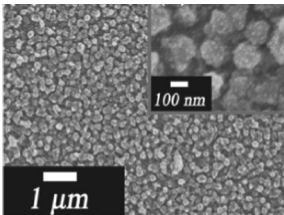
Along with the development of strategies for its sensitization, nanostructuring (in particular one-dimensional nanostructuring) of TiO₂ has also attracted tremendous interest in view of improving charge separation and collection in TiO₂-based (photo)electrodes.

In the following sections we will deal with one-dimensional TiO₂-based nanostructures, that exhibit improved PEC-WS ability and that were obtained by a rational design of complementary strategies (doping, co-catalytic effects, and other (more recent) strategies) to tackle the specific (mentioned) limitations of the material – Table 2 reports some examples of different synthetic/modification approaches to 1D TiO₂ nanostructures and their PEC performances.

3.4.1 TiO₂ one-dimensional arrays. The beneficial characteristics of one-dimensional nanoarrays (*e.g.*, enhanced charge carrier separation, improved e⁻ transport, large carrier collection efficiency, *etc.* – see Section 2.1) combined with the intrinsic electronic and optical properties of TiO₂ (see above) contributed to the development of 1D-TiO₂ based nanostructures for a large variety of (but not limited to) light-related applications: for photoelectrochemistry and photocatalysis, in Grätzel-type solar cells, for photovoltaic and electrochromic devices, *etc.*^{47–49,347,348}

In many of these applications, the efficiency depends to a large extent on the available surface area, that is, on the surface

Table 2 Selected examples of 1D TiO₂ based photoanodes and their PEC performance

Structure	Preparation	SEM	Electrolyte	$j/mA\text{ cm}^{-2}$	Ref.
TiO ₂ NTs	Anodization		1 M KOH	0.90 at 1.23 V _{RHE}	453
Ru-doped TiO ₂ NTs	Anodization		1 M KOH	1.8 at 1.23 V _{RHE}	364
TiO ₂ NWs	Hydrothermal		1 M NaOH	2.6 at 1.23 V _{RHE}	454
Fe-doped TiO ₂ NRs	Hydrothermal method		1 M KOH	3.0 at 1.23 V _{RHE}	344
CdS–Au–TiO ₂ NRs	Hydrothermal method and chemical bath deposition		0.25 M Na ₂ S and 0.35 M Na ₂ SO ₃	4.1 at 0.0 V _{Ag/AgCl}	455
TiO ₂ /In ₂ S ₃ /AgInS ₂ core-shell branched NRs	Two-step hydrothermal method and SILAR		1 M KOH	22.1 at 0.56 V _{Ag/AgCl}	428

In all cases solar light AM 1.5G (100 mW cm⁻²) was used for irradiation. SEM images (from top to bottom): reproduced from ref. 453 with permission from Elsevier; adapted with permission from *J. Am. Chem. Soc.*, 2011, **133**, 5629–5631. Copyright 2011 American Chemical Society; reproduced from ref. 454 with permission from the Royal Society of Chemistry; reproduced from ref. 344 with permission from the Royal Society of Chemistry; adapted with permission from *J. Am. Chem. Soc.*, 2014, **136**, 8438–8449. Copyright 2014 American Chemical Society; reproduced from ref. 428 with permission from John Wiley & Sons.

area of the electrode that is accessible to both the electrolyte and the incident irradiation.

However, it has been observed that for nanoparticle and nanotube layers with the same thickness, although the effective surface area of the particles is higher than that of the

nanotubes, the quantum efficiency for nanotubes is higher (Fig. 10(a)).³⁴⁹ Therefore, also other factors should be considered that play an important role in the photoelectrochemical characteristics of 1D-TiO₂ based nanostructures, *e.g.*, the lower number of surface states in nanotubes and the upward band bending.

Moreover, the photoelectrochemical performance of one-dimensional nanostructures is largely influenced by the geometrical aspect of the arrays, that is, it varies with the thickness and/or diameter of the nanostructures; overall, the different carrier mobility (in different structures and morphologies) seems to dominate the efficiency.

For TiO₂ nanotube arrays, the work of Lynch *et al.* outlined how the morphology of nanotubes affects their photoelectrochemical properties also in comparison to other TiO₂ nanostructures.³⁴⁹ In particular, the IPCE efficiency of tubes was shown to increase with increasing the layer thickness up to a critical maximum length (*i.e.*, $d = ca.$ 5–6 μm for ethylene glycol-based nanotubes – Fig. 10(b)). When an e^-/h^+ pair is generated in the tube walls, holes are promptly transferred to the electrolyte – this as long as depletion conditions are established in the tube walls,^{350,351} while electrons must be transported to the substrate (*e.g.*, metallic back-contact, FTO, ITO). The longer the tube, the larger is the contribution of charge recombination.

Other morphological features were also shown to be crucial to enhance the PEC-WS ability of TiO₂ NTs, such as the

smoothness of the tube walls,³⁴⁹ and the geometry of the tube top.³⁵² In particular, tubes grown in organic electrolyte exhibit superior performance compared to tubes grown in aqueous electrolyte (*i.e.*, ripple-walled NTs); a possible reason could be the increased wall smoothness and the greater order of the formers that also lead to a significant increase in the charge carrier diffusion length compared to ripple-walled tubes.³⁴⁹ On the other hand, the presence of “grass” on the tube tops was shown to be highly detrimental for photoelectrochemical solar light water splitting, more likely due to a trap filling mechanism predominant in the “grass” part of the tubes.³⁵²

Compared to classic TiO₂ thin films (with no specific 1D morphology), also TiO₂ NW arrays exhibit significantly higher PEC ability.³⁵³ In particular, also for nanowires on conductive ITO substrate photocurrent measurements showed that the layer thickness plays a significant role and a maximum photocurrent can be achieved for $\sim 5 \mu\text{m}$ thick layers,³⁵⁴ confirming that under specific conditions a critical thickness exists to enable efficient transport and collection of electrons in TiO₂-based one-dimensional arrays.^{98,349,354}

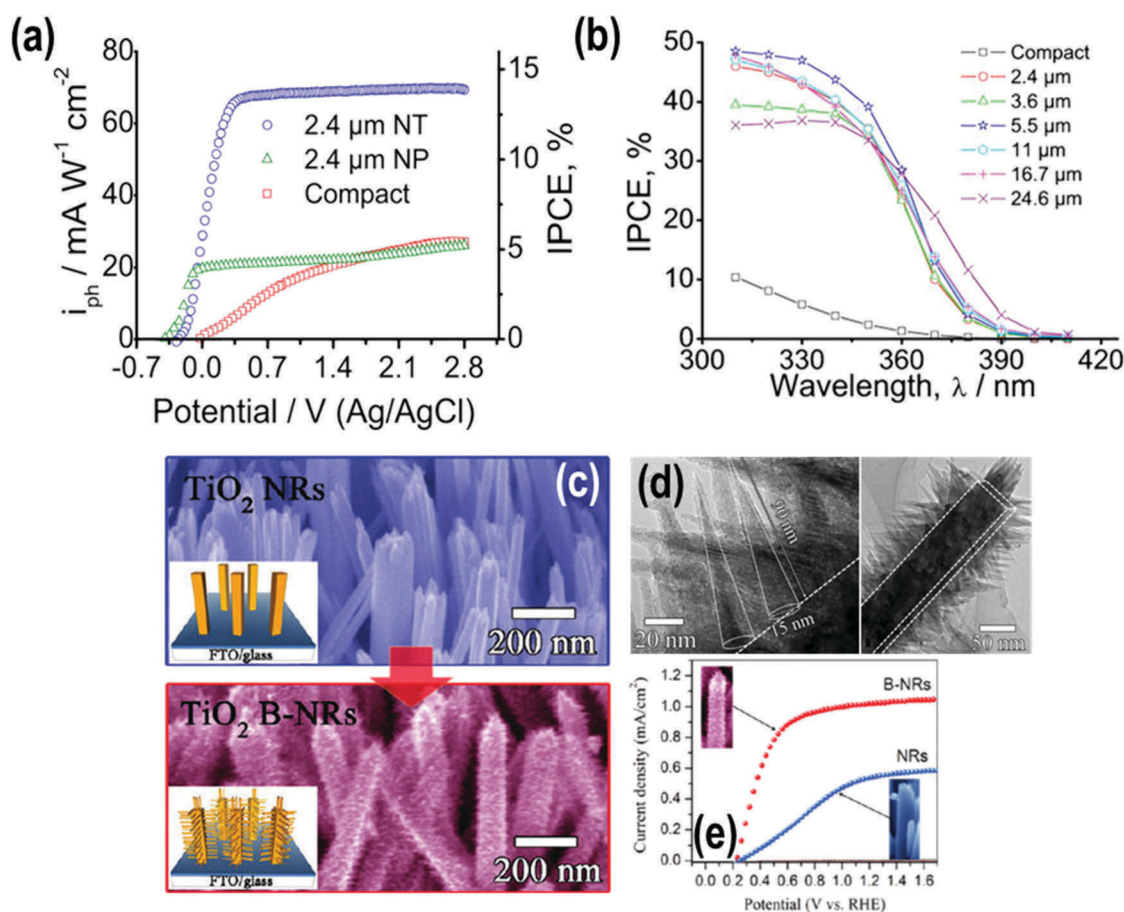


Fig. 10 (a) Photocurrent and IPCE vs. applied potential measured for flat compact oxide (60 nm thick), 2.4 μm thick nanoparticle, and 2.4 μm thick nanotube TiO₂ layers under incident $\lambda = 350 \text{ nm}$. (b) IPCE vs. wavelength spectra measured for different thicknesses of nanotube layers anodized in an ethylene glycol-based electrolyte. (c) SEM images of TiO₂ NRs and branched TiO₂ NRs (B-NRs). (d) TEM images of a branched nanorod. (e) Photocurrent vs. applied potential measured for TiO₂ NRs and B-NRs. Fig. (a and b) reprinted with permission from *J. Electrochem. Soc.*, 2010, **157**(3), G76. Copyright 2010, The Electrochemical Society. Fig. (c and d) adapted with permission from *Nano Lett.*, 2011, **11**, 4978–4984. Copyright 2011 American Chemical Society.

Moreover, for TiO₂ in particular a crystallization into anatase is crucial for photoelectrochemical applications.^{333,355}

However, for titania nanotubes, a common problem of annealing tubes on Ti metal substrate is that such a thermal treatment also induces the formation of undesired rutile phase at the metal/oxide interface, due to the thermal oxidation of metallic Ti, and typically catalyzes the anatase to rutile transition in the NT walls.³²⁸ Therefore, large efforts are dedicated to the identification of strategies for overcoming this detrimental crystal phase transition: *e.g.*, optimized annealing rate profile,³⁵⁶ doping the TiO₂ NTs with low amount of Nb,³⁵⁷ detachment of tubes from the metallic substrate,³²⁹ *etc.*

Nevertheless, also TiO₂-based nanomaterials with a rutile crystal structure are reported for efficient photoelectrochemical water splitting.

This is particularly relevant for single-crystalline TiO₂ NRs grown on FTO glass by hydrothermal methods. Such nanorods exhibit a rutile crystal structure due to the significantly low lattice mismatch ($\sim 2\%$)³⁵⁸ between tetragonal FTO ($a = b = 0.4687$ nm)³⁵⁹ and rutile TiO₂ ($a = b = 0.4594$ nm),²⁰¹ and typically grow vertically oriented from the FTO substrate, along the (110) crystal plane with a preferred (001) orientation.^{120,358,360,361} The single-crystalline nature of these NRs plays a critical role for the observed PEC efficiency. Clearly, the absence of grain boundaries, which contribute to poor electron mobility in conventional polycrystalline TiO₂ films, suppresses charge carrier losses due to recombination and leads to relatively high performance (~ 0.5 – 1.0 mA cm⁻² under AM 1.5G illumination).^{116,360,361}

More recently, also the synthesis of branched single crystal rutile TiO₂ nanorods has been reported for PEC hydrogen production.³⁶² Due to their branched structure (Fig. 10(c–e)), these NRs exhibit larger surface area and excellent light-trapping characteristics due to enhanced light scattering phenomena that collectively contribute to the *ca.* four-fold enhancement in photocurrent density compared to more conventional NRs.

Although, in view of single crystal materials, rutile crystals are much easier to synthesize, produce defined surfaces, and are much better characterized on an atomic level, also the fabrication of single crystal anatase TiO₂ 1D nanostructures has been recently developed for light-induced applications. In this case, the use of an alkaline reaction media and, particularly, the presence of a seed layer on the FTO substrate are essential prerequisites (see Section 3.1). Due to the higher electron mobility that characterizes anatase with respect to rutile TiO₂,^{333,355} single crystal anatase TiO₂ nanorods/wires mostly find applications as photoanode for dye-sensitized solar cells.^{118,119}

3.4.2 Doping and defect engineering. When considering TiO₂ for solar PEC water splitting, strategies for a rational design are needed that address its intrinsic limitations, namely (i) a band-gap too large for an efficient use of solar light and (ii) a conduction band minimum (more appropriately, a Fermi level E_F) only slightly negative on an electrochemical potential scale to the hydrogen evolution potential (see Section 3.2.1).^{160,363} Typically, (i) is overcome by nonmetal doping of TiO₂, while (ii) is addressed with the introduction of a metal dopant into the oxide lattice.

For instance, the highest PEC-WS current density reported for anodic TiO₂ tubes, under most optimized conditions, is 0.25–0.3 mA cm⁻² measured in 1 M KOH under AM 1.5G illumination.³⁶⁴ This is ascribed to the slow transport of electrons along the nanotube length, *i.e.*, in the order of seconds,³⁴⁹ which cannot be overcome by simply adjusting the tube morphology. Nevertheless, clearly better results are obtained when the tubular morphology is combined to the modification of the TiO₂ physicochemical properties (see below).

In general, since the valence band minimum of TiO₂ is much lower than the H₂O/O₂ redox potential, band-gap reduction should be approached by shifting the VBM upwards, *i.e.*, without affecting the more “critical” position of the conduction band. This is typically accomplished by introducing a high density of states (or a band) above the original valence band of TiO₂, that is, by incorporating into the TiO₂ lattice anions with p orbitals that are more energetic than those of O 2p. To this regard, most appropriate dopants are substitutional nitrogen and carbon that, beside introducing suitable acceptor levels, also exhibit ionic radii similar to that of oxygen; hence, their incorporation causes minimal distortion in the oxide lattice.¹⁶⁰

Clearly, depending on the synthetic approach to 1D-nanostructured TiO₂ materials and also on the dopant element, different doping strategies are available.

For instance, nitrogen-doping and visible light driven PEC water splitting have been reported upon annealing single-crystal rutile TiO₂ NWs in NH₃ atmosphere under optimized conditions (*i.e.*, annealing temperature, time, and NH₃ pressure).⁹⁸ The low-energy threshold of IPCE spectra for N-doped TiO₂ was red-shifted to $\lambda \sim 520$ nm (Fig. 11(a)). A more significant shift of photocurrent threshold to $\lambda \sim 570$ nm was also reported upon nitridation (in NH₃ atmosphere) and hydrogenation (in H₂/Ar atmosphere) of a TiO₂ NW array. The interaction between substitutional N- and the Ti³⁺-centers induced by hydrogenation (*i.e.*, between midgap levels close to the valence and conduction bands, respectively – Fig. 11(b and c)) has been proposed as key for spectrum extension and visible light photoactivity.¹⁹⁹

However, the effects induced by substitutional N and by midgap state formation on the N-TiO₂ PEC activity are strongly debated. Despite several reports showing an improved PEC performance for N-doped TiO₂ nanostructures,^{98,199,365} other studies demonstrated that to a promoted vis-light activity of N-TiO₂ also corresponds an increase of carrier recombination rate under UV irradiation, particularly when the N amount exceeds the optimum concentration.¹⁵³

It should be noted that, with respect to various methods used to achieve nitrogen doping, different states of nitrogen are observed, and the active species may be present in bulk TiO₂ or on the surface. To determine the nature of doping-induced states, typically non-destructive surface spectroscopic techniques such as XPS are used. Low-dose N ion-implantation into TiO₂ tube layers shows an XPS peak at ~ 396 eV,^{154,155} which is in accordance with the peak position of Ti–N bonds in titanium nitride.¹⁵⁶

On the other hand, wet treatments in amine-based solutions typically lead to peaks at ~ 400 eV (or higher) and also yield

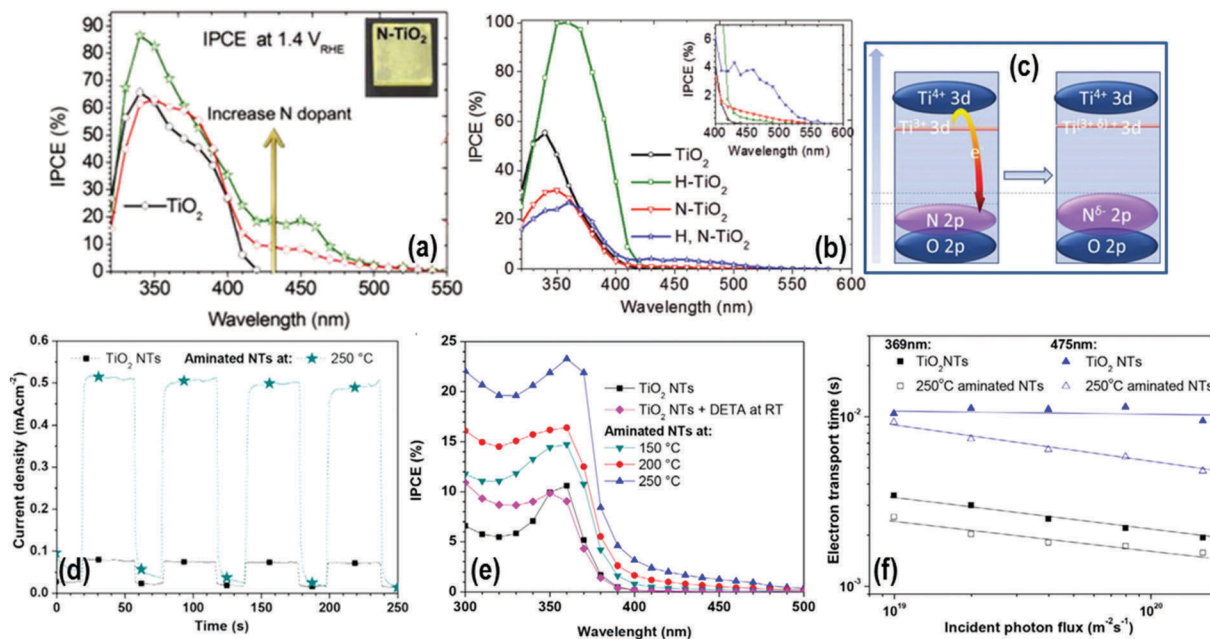


Fig. 11 (a) IPCE spectra of N-modified TiO₂ films at 1.4 V_{RHE} in 1 M KOH. (b) IPCE spectra measured at 1.23 V_{RHE}, 1 M KOH electrolyte and under AM 1.5G irradiation. (c) Proposed mechanism for the interaction between Ti³⁺ (formed upon hydrogenation) and substitutional N. (d) Photocurrent transient under monochromatic laser ($\lambda = 474$ nm) for aminated nanotubes; (e) IPCE spectra of the TiO₂ nanotube before and after hydrothermal treatment for amination; at different temperature in DETA; (f) comparison of transport time constants for bare and aminated TiO₂ nanotube as a function of the incident photon flux, for monochromatic 369 and 475 nm light illumination. Fig. (a) adapted with permission from *Nano Lett.*, 2012, **12**, 26–32. Copyright 2012 American Chemical Society. Fig. (b and c) adapted with permission from *J. Am. Chem. Soc.*, 2012, **134**, 3659–3662. Copyright 2012 American Chemical Society. Fig. (d–f) reproduced from ref. 371 with permission from Elsevier.

visible light response. This is the case, for instance, of nitrogen-doping from NH₄F contained in the electrolyte for the anodic growth of tubes,³⁶⁶ or of N-doping by hydrothermal treatment of TiO₂ nanotubes in the presence of trimethylamine.³⁶⁷ However, such a peak in many cases corresponds to adsorbed molecular nitrogen on TiO₂ and often leads to neither (or negligible) visible photocurrent nor photocatalytic activity.^{157,368} That is, although absorption spectra of such N-TiO₂ materials provide evidence of extended sub-band gap absorption, corresponding photocurrent spectra (if provided) may not show significant response.

Visible light photocurrent response and IPCE spectra of TiO₂ anodic layers modified with urea,^{369,370} and the photocurrent transients of aminated TiO₂ nanotubes under monochromatic laser ($\lambda = 474$ nm)³⁷¹ provided evidence of a significantly improved solar PEC activity compared to undoped TiO₂ (Fig. 11(d and e)). Remarkably, the decoration of the tubes with amino group (*i.e.*, formation of surface states), along with interstitial nitrogen doping, not only leads to an increase in the photocurrents for both UV and visible regions of the light spectrum, but also significantly improves the electrode conductivity due to a lower charge transfer resistance and hence a faster carrier transport in the nanotubes after amination (Fig. 11(f)).³⁷¹

In the case of carbon-doped TiO₂, reported findings are to a certain extent ambiguous and particularly limited amount of IPCE data on C-doped TiO₂ questions the actual role of C-doping on the visible light PEC-WS ability of these materials.¹⁶²

According to DFT calculations, carbon-doping TiO₂ leads to a modest variation of the oxide band-gap, while at the same time induces several midgap occupied states which may account for the observed red shift in the light absorption threshold and for the formation of oxygen vacancies, but may also promote charge carrier trapping.³⁷²

From the experimental point of view, little to no photocurrent in the visible range is usually reported for C-doped TiO₂ nanostructures.^{157–159} For instance, C-doping by annealing titania nanotube arrays under controlled CO gas flow showed a slight enhancement in the PEC-WS performance measured under visible light illumination with respect to undoped TiO₂ NTs.¹⁵⁹ Interestingly, C-containing tubes (that is, tubes with a double-walled morphology where carbon uptake is due to the decomposition of the anodizing organic electrolyte under applied voltage) also exhibit a change in the TiO₂ optical properties and sub-band gap response has been reported for carbon contaminations as low as ~ 3 at% (Fig. 12(a)).³⁴⁹

By contrast, in line with theory predicting that the incorporation of carbon and/or related defects strongly affects the electronic structure of TiO₂,³⁷² a drastic change to a semimetallic TiO_xC_y compound,³⁷³ also with improved mechanical stability,³⁷⁴ has been reported by thermal treatment of TiO₂ nanotubes in an acetylene atmosphere (Fig. 12(b and c)).

Finally, although theoretical calculations do not consider F as a suitable substitutional dopant for TiO₂ because it is in principle a donor at O sites,¹⁶⁰ Fang *et al.* reported on porous single-crystal F-doped TiO₂ NRs where fluorine-doping is

shown not only to improve the electron transport properties of single crystal rutile TiO_2 , but also to enhance the PEC activity under both UV and visible irradiation (Fig. 12(d-f)).^{375,376}

Doping TiO_2 with a metal (that is, a donor species) is reported to promote faster electron transport and, hence, to reduce charge recombination. As mentioned, it is of primary importance that any doping attempt in TiO_2 does not affect the conduction band minimum (or, even better, slightly upshifts the CBM) to satisfy the correct band-edge position relative to the H^+/H_2 redox potential and provides sufficient driving force for hydrogen production. For this, transition metals (TMs) are suitable dopant candidates, since they have d orbitals with energies higher than those of Ti and are similar in size. DFT calculations, in particular, showed that most suitable metal dopants are Ta, Nb, W, and Mo.¹⁶⁰ However, experimental evidence has been provided that also other transition metals are suitable for TiO_2 doping to achieve a better charge carrier transport.

In the case of self-organized NTs, a most unique approach to X-doped TiO_2 is offered by the possibility of anodizing Ti-X alloys (with *e.g.*, X = Ru, Ta, W, Nb, Cr). In this case, simple tailoring of the anodization parameters is sufficient to fabricate highly aligned and variously doped TiO_2 -based nanotube arrays.^{343,346,357,377–384}

For instance, RuO_2 -modified TiO_2 nanotubes grown from Ru-Ti alloys exhibit PEC characteristics that depend on the Ru content. In particular, strong and stable enhancement of the PEC activity has been obtained for a Ru concentration as low as 0.5 at% and for annealing at 450 °C (Fig. 13(a)). Under these

conditions, a 6-fold increase in photocurrent density was measured compared to pristine TiO_2 NTs, and the effect was also shown to be far superior compared to anodic TiO_2 NTs modified with RuO_2 nanoparticles.³⁶⁴ Here RuO_2 is considered to be dopant and co-catalyst for O_2 evolution.

In optimally doped and annealed TiO_2 tubes, both Nb and Ta act as electron donors and increase the electron conductivity of the NT layers. This was observed for nanotube arrays doped with small amounts (up to 0.1 at%) of Nb^{379,381,382} or Ta^{343,383} for which a significant enhancement of photoelectrochemical water splitting and dye-sensitized solar cell performances was observed (Fig. 13(b and c)). In particular for Nb-doped TiO_2 tubes, a more recent study shows that Nb doping is also beneficial in view of retarding rutile formation at the metal/oxide interface, while annealing the tube layers (Fig. 13(d-f)).³⁵⁷

Similar effects on the charge carrier transport properties of TM-doped TiO_2 arrays have also been observed for layers synthesized by wet chemical methods.

For instance, Xu *et al.* reported on the preparation and PEC activity of Sn-doped single-crystalline rutile TiO_2 nanowires.⁹⁹ Due to the low lattice mismatch between rutile and SnO_2 ,³⁵⁸ Sn dopants could be easily incorporated into TiO_2 NWs by hydrothermal synthesis. For low Sn doping levels (up to Sn/ $\text{TiO}_2 \sim 12\%$), a photocurrent increased under simulated sunlight illumination was observed compared to pure TiO_2 NWs. In particular, photocurrent spectra revealed that this effect is mainly ascribed to the enhancement of photoactivity in the UV region, while electrochemical impedance measurement confirmed the higher density of n-type charge carriers within the NWs produced by Sn doping.

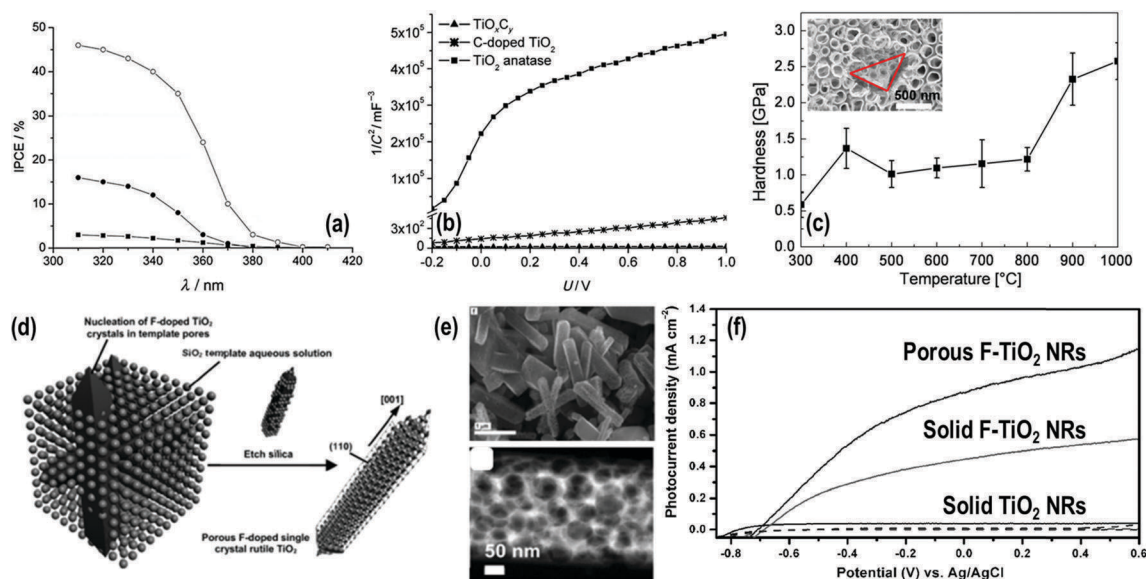


Fig. 12 (a) IPCE spectra of different C-contaminated TiO_2 nanotube layers that show sub-band gap response: (■) amorphous NTs, (●) NTs annealed in air, (○) NTs annealed in CH_3OH -containing atmosphere. (b) Potential-dependent capacity measurements of the different nanotube layers in 0.1 M Na_2SO_4 solution at 1 kHz and plotted in a Mott–Schottky graph. (c) Hardness vs. carbonization temperature plot for various treated TiO_2 nanotube layers, obtained from nanoindentation tests (the inset reports the SEM image of a nanoindentation test spot). (d) Schematic representation of the growth pathway of porous single-crystal rutile TiO_2 nanorods; (e) SEM image and dark-field TEM image of F-doped porous single-crystal rutile TiO_2 nanorods; (f) linear sweep voltammograms of undoped solid TiO_2 NRs, and F-doped solid and porous TiO_2 NRs. Fig. (a) reprinted with permission from *J. Electrochem. Soc.*, 2010, **157**(3), G76. Copyright 2010, The Electrochemical Society. Fig. (b) reproduced from ref. 373 with permission from John Wiley & Sons. Fig. (c) reproduced from ref. 374 with permission from Elsevier. Fig. (d–f) reproduced from ref. 376 with permission from John Wiley & Sons.

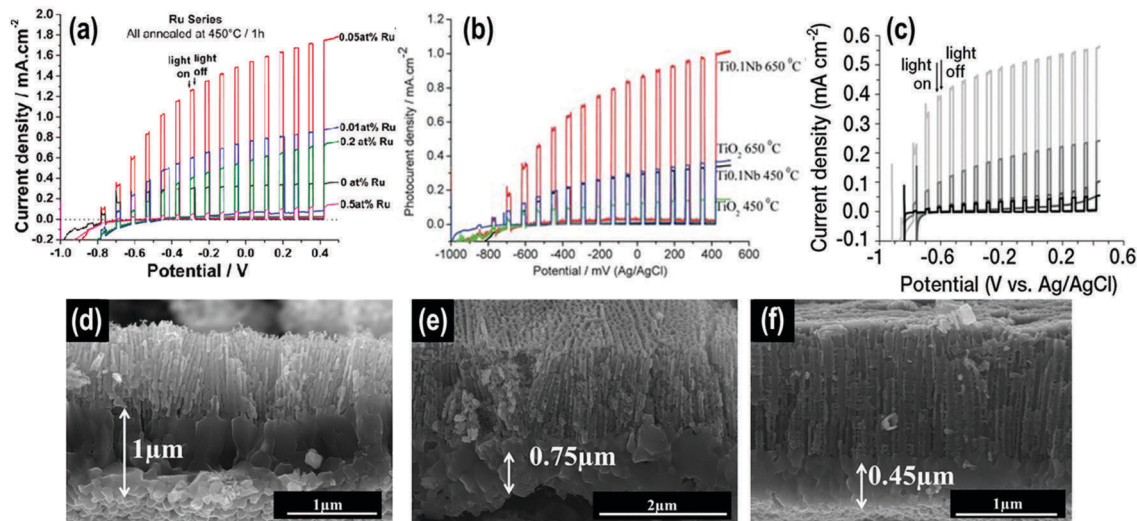


Fig. 13 (a) Photocurrent transient vs. potential curves of TiO_2 nanotube layers with different Ru contents (0–0.5 at%) after annealing at 450 °C for 1 h. Measurements were carried out in 1 M KOH electrolyte under AM 1.5G illumination. (b) Photocurrent transients vs. potential curves for TiO_2 and $\text{Ti}_{0.1}\text{Nb}$ nanotube layers after annealing at 450 or 650 °C. Measurements were carried out in 1 M KOH electrolyte under AM 1.5G illumination. (c) Photocurrent transient vs. potential curves of Ta-doped TiO_2 nanotube layers after annealing at 450 °C for 1 h, measured in 1 M KOH solution under AM 1.5G illumination – Ta contents (at%): light grey, 0.1% Ta; medium grey, 0.03% Ta; dark grey, 0.4% Ta; black, pure TiO_2 . (d–f) Cross-section SEM images of 2 μm TiO_2 nanotubes annealed at 650 °C in air: (d) pure TiO_2 NTs, (e) 0.1 at% Nb TiO_2 NTs, (f) 0.2 at% Nb TiO_2 NTs. A clear decrease of the rutile layer thickness underneath the nanotubular layer can be observed, from $\sim 1 \mu\text{m}$ for undoped TiO_2 , to $\sim 0.75 \mu\text{m}$ and $\sim 0.45 \mu\text{m}$ for 0.1 at% and 0.2 at% Nb doped TiO_2 , respectively. Fig. (a) adapted with permission from *J. Am. Chem. Soc.*, 2011, **133**, 5629–5631. Copyright 2011 American Chemical Society. Fig. (b) reproduced from ref. 382 with permission from the Royal Society of Chemistry. Fig. (c) reproduced from ref. 383 with permission from John Wiley & Sons. Fig. (d–f) reproduced from ref. 357 with permission from Elsevier.

Interestingly for some TM-doped TiO_2 combinations, beside the effect on charge carrier transport, also a shift in light absorption edge from UV to visible has been reported and, correspondingly, a visible-light activated photocurrent has been observed.

For instance, TiO_2 NRs doped with Fe, Mn or Co and synthesized through a hydrothermal method (Fig. 14(a)) produced higher photocurrent than undoped TiO_2 NRs, both under solar and visible light irradiation (Fig. 14(b and c)).³⁴⁴ In particular, Mott-Schottky analysis showed that a significant enhancement in the charge carrier density N_d can be obtained by Fe-doping; it was concluded that not only does iron significantly increase the concentration of electrons in the conduction band, with an overall beneficial effect on charge carrier separation and transport, but it also generates impurity states near the conduction band of TiO_2 , improving visible light absorption (by apparently reducing TiO_2 band-gap) and enabling visible light PEC activity.

For single crystal rutile TiO_2 nanowires doped with V, Cr, Mn, Fe, Co, Nb, Mo, and Rh by means of a molten-salt synthesis, a dual effect due to TM doping was reported.³⁴⁵ not only the doped layers exhibited optical absorption extended to the visible light (though not supported by the corresponding photocurrent spectra), but most interestingly a decrease in the overpotential for the OER was measured with respect to pure TiO_2 layers (Fig. 14(d)). Liu *et al.* attributed this result to the homogeneous distribution of dopants achieved by means of the molten-salt procedure. In particular, EXAFS spectra (Fig. 14(e)) showed that the introduction of TM atoms occurs uniformly at Ti subsurface sites with no significant alteration in the rutile

lattice (that is, neither crystal defects nor other phases could be observed). This affects the adsorption energy of water splitting reaction intermediates (O, OH, and OOH radicals) on the surface of the material, and accounts for the substantial decrease in the overpotential for OER.

Another method to achieve TiO_2 uniform doping has been reported by Resasco *et al.*³⁸⁵ TiO_2 NWS, prepared by hydrothermal method, are decorated with a thin MnO_x layer by ALD followed by a solid state reaction at high temperature (*i.e.*, 600–1000 °C) in Ar atmosphere.

For dopant concentration below 10%, that is, the solubility limit of manganese into titania, Mn could be homogeneously incorporated in the rutile TiO_2 lattice through an interstitial dissolution/diffusion mechanism,³⁸⁶ with no formation of new crystalline phases. Despite a decrease in the PEC performance with respect to pure TiO_2 NWS (in contrast with other studies³⁴⁵ and most likely due to the introduction of an impurity level in the band-gap of TiO_2), these nanowires show promising electrocatalytic activity for water oxidation, confirming the co-catalytic effect of Mn-doping on the OER. Noteworthy, this method could also be successfully extended to zirconium-doped TiO_2 with the maximum achievable dopant concentration being significantly lower than that of Mn, likely due to the lower solubility of Zr in TiO_2 .³⁸⁵

Crystal defect engineering can be achieved by reduction of TiO_2 to black titania, typically carried out by thermal treatment in a H_2 -containing atmosphere – more recently also alternative methods such as high-energy proton implantation have been investigated. As anticipated in Section 3.2.4, beside the extension

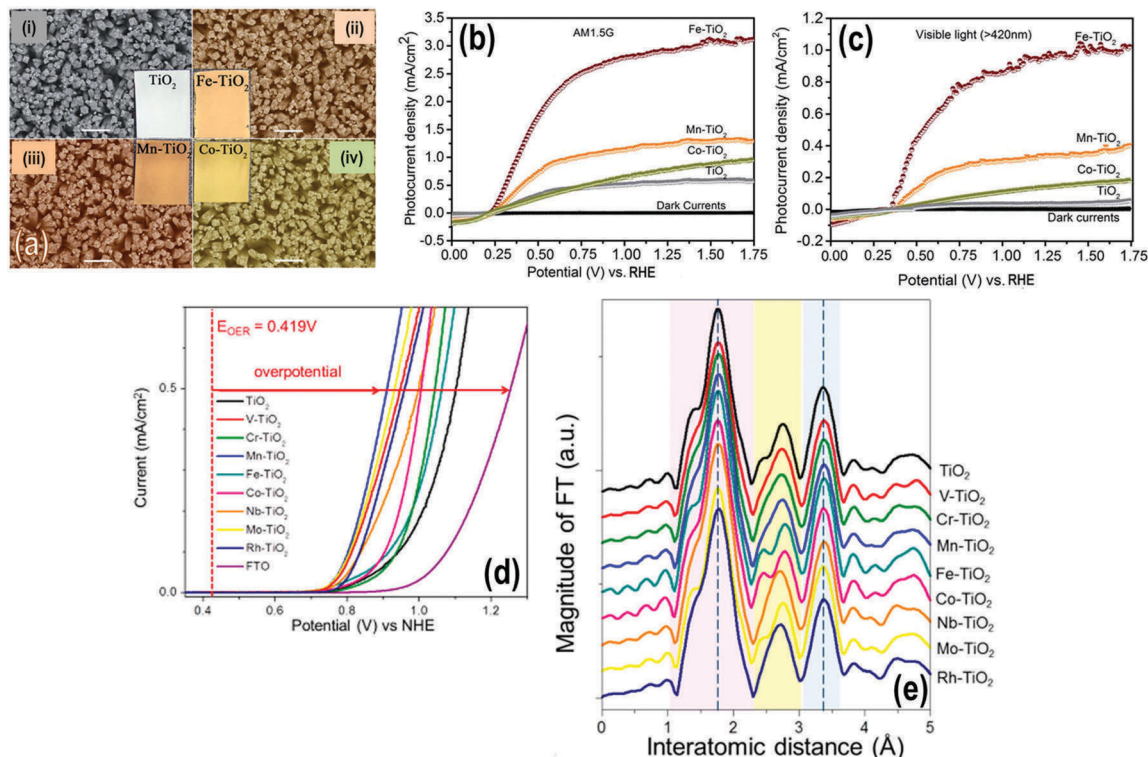


Fig. 14 (a) SEM images of (i) TiO₂, (ii) Fe-TiO₂, (iii) Mn-TiO₂, and (iv) Co-TiO₂ nanorod arrays on FTO substrates. Insets represent the corresponding digital pictures. All scale bars are 1 μm . (b) Photocurrent transient vs. potential curves of undoped and variously doped TiO₂ nanorod layers, under AM1.5G solar illumination. (c) Photocurrent transient vs. potential curves of undoped and variously doped TiO₂ nanorod layers, under visible light illumination ($\lambda > 420 \text{ nm}$). (d) Overpotential measurement for OER using FTO and TiO₂ nanowire with/without transition metal doping of electrodes in basic solutions. The dashed vertical line represents the thermodynamic redox potential for water oxidation at pH ~ 13.6 . (e) Fourier transforms of EXAFS spectra of various transition metal-doped samples. Fig. (a–c) reproduced from ref. 344 with permission from the Royal Society of Chemistry. Fig. (d and e) adapted with permission from *J. Am. Chem. Soc.*, 2013, **135**, 9995–9998. Copyright 2013 American Chemical Society.

of the absorption properties of TiO₂ to visible light wavelengths, hydrogenation introduces voids and defects in the material (mainly in the outer shell) that exhibit a co-catalytic effect towards a stable and noble metal-free photocatalytic H₂ generation.^{202–204}

Hydrogenation of TiO₂ has been reported also for photoelectrochemical water splitting. For instance, H₂-treated single crystal TiO₂ NWs have been shown to provide stable photocurrent and higher PEC efficiency compared to TiO₂ NWs annealed in air. Mott–Schottky plots demonstrated an enhanced donor density in H-TiO₂, due to the increased concentration of oxygen vacancies. This in turn positively affects the electron conductivity and enables a more efficient charge transport in the reduced array.¹⁰⁰

Similar results were also reported for TiO₂ NWs that underwent a rapid flame-reductive treatment in a CO/H₂ atmosphere (Fig. 15). Compared to other reduction methods, flame reduction can be operated at ambient conditions and provides an adjustable concentration of oxygen vacancy by controlling the reduction time. That is, reduction treatment as short as 5 s has been reported to double the photocurrent density of TiO₂ NWs, compared to untreated titania nanowires. Clearly, the significantly short exposure time of the nanoarray to high temperature is of great advantage also in view of preserving the electrode morphology and crystallinity.¹⁰¹

3.4.3 Surface decoration and heterojunction formation.

Decoration of TiO₂ with metals, semiconductors, and polymers is frequently used to influence the electronic and physicochemical properties of the oxide and achieve a desired increment in PEC activity.

In particular, metal nanoparticles can introduce local variations in the band bending of the adjacent semiconductor (*i.e.*, pinning of the Fermi level of an energy that depends on the work function of the metal), inducing an effect similar to that observed by applying an external bias³⁸⁷ – remarkably, a great advantage is that such a Fermi level pinning is obtained under “open circuit conditions”, and thus this approach is often preferred for open circuit photocatalytic applications.

As for hematite, also the surface properties of TiO₂ can significantly limit the overall PEC reaction due to a limited kinetics of water oxidation as well as the charge recombination loss at the electrode surface. Photogenerated holes can be trapped by surface states and recombine with electrons before they can diffuse to the TiO₂/electrolyte interface for interfacial charge transfer and water oxidation.³⁸⁷

Therefore, techniques for passivating surface trap states and decreasing trap state-mediated charge recombination often apply also to TiO₂ photoanodes. Typically, atomic layer deposition (ALD)^{361,388} or treatments based on the use of different

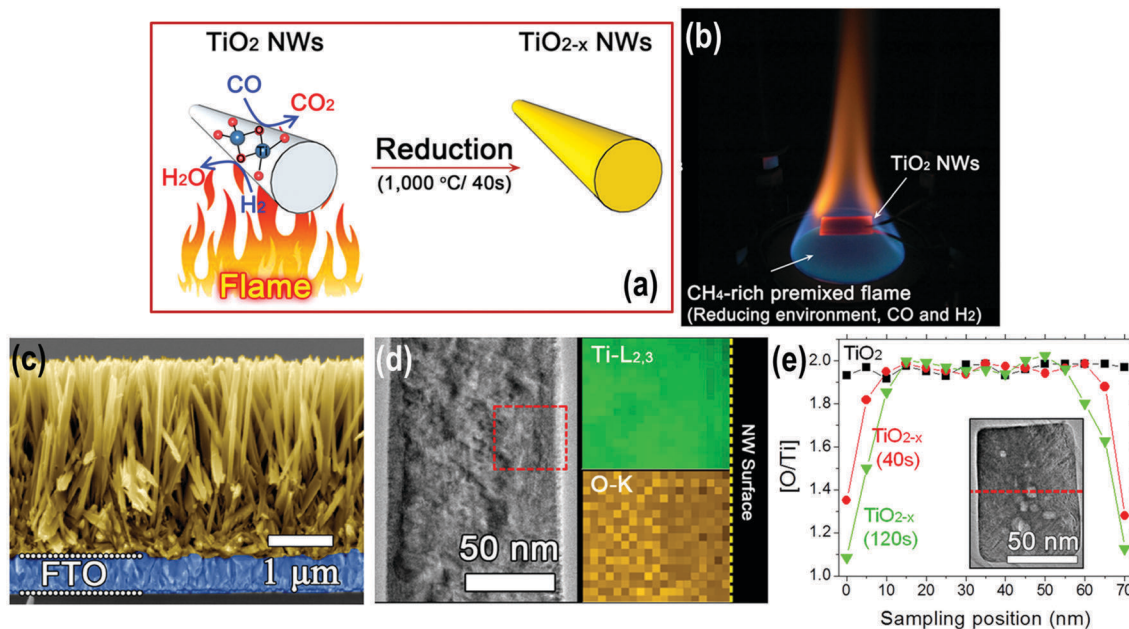


Fig. 15 Flame reduction process and characterization of oxygen vacancy distribution. (a) Schematic illustration of the flame reduction method. (b) A photograph of the flame reduction process. (c) Representative cross-sectional SEM image of the flame-reduced TiO_2 NWs. (d) Bright-field STEM image and the corresponding electron energy loss spectroscopy (EELS) elemental mapping of Ti-L_{2,3} and O-K edges inside the rectangular box, showing an oxygen deficiency near the NW surface. Darker color: lower concentration of oxygen. (e) O/Ti molar ratio distribution along the NW diameter (as-synthesized TiO_2 NW: black rectangles and flame-reduced TiO_2 NWs: red circles: 40 s, green triangles: 120 s), which is estimated using EELS spectra taken from a cross-line shown in the inset of a cross-sectional TEM image. Flame reduction conditions: $T = 1000^\circ\text{C}$, $\phi = 1.4$, and $t = 40$ or 120 s. Adapted with permission from *Chem. Mater.*, 2001, **13**, 233–235. Copyright 2001 American Chemical Society.

TiO_2 precursors (*e.g.*, TiCl_4 , $\text{Ti}(\text{O}i\text{P})_4$, $\text{Ti}(\text{O}i\text{Bu})_4$)¹⁰² are often applied to decorate the surface of TiO_2 nanoarrays (usually rods or wires) with a TiO_2 -based thin shell layer (Fig. 16(a)).

A combination of photoelectrochemical and photovoltage measurements with impedance spectroscopy demonstrated that the presence of a thin TiO_2 (anatase or rutile) shell passivates the surface trap states and, compared to naked TiO_2 arrays, significantly increases the PEC activity by promoting interfacial charge transfer at the TiO_2 /electrolyte interface as well as a better carrier utilization (Fig. 16(b–d)).^{102,361,388}

Also the more classical Co-based oxygen evolution catalyst is used to passivate TiO_2 surface states, and significantly higher photocurrent density has been reported with respect to unmodified TiO_2 .⁹⁸

In spite of a remarkable effect on the photoelectrochemical performance of TiO_2 electrodes, the long-term stability often represents an issue for oxygen evolution co-catalysts, as *e.g.* in the case of Ru-based molecular catalysts $[\text{Ru}(\text{bda})\text{L}_2]$ ($\text{bda}^{2-} = 2,2'$ -bipyridine-6,6'-dicarboxylate; L = *N*-cyclic aromatic ligands, such as pyridine and imidazole)^{296,389–392} and the more recently introduced Co³⁹³ complexes.

In details, major aspects to be considered are (i) the selection of an efficient anchoring group (*e.g.*, carboxylic *vs.* phosphonic acids, or silane groups) for the attachment of the Ru(bda) catalysts,²⁹⁶ and (ii) the possibility of tuning the length of the carbon link chain between the Ru catalyst and the anchoring group itself – long flexible alkane chains (such as, $-\text{CH}_2\text{CH}_2\text{CH}_2-$) have been shown to decrease the electron

recombination between TiO_2 and the Ru-catalyst mainly by hindering electron back transfer processes.³⁹²

Metal nanoparticles with plasmonic features (mainly Ag and Au) can be used to enable visible light photoelectrochemical water splitting on TiO_2 photoanodes (Fig. 17(a and b)).

Overall, this mechanism is particularly effective as the photogenerated holes remain on the surface of the photoanode, overcoming the relatively short exciton diffusion length of h^+ , while electrons percolate through the one-dimensional array to the back-contact.

A range of different methods is available for the decoration of TiO_2 surfaces with plasmonic metals: (i) photoreduction of the precursor (*e.g.*, HAuCl_4 to Au NPs),³⁹⁴ (ii) precipitation from a precursor-based solution,³⁹⁵ (iii) anodization of noble metal alloys of Ti such as Au–Ti (or Pt–Ti); in contrast to previous examples on Ti–X alloys (with X being a non-noble metal – Section 3.4.2), this approach leads to noble metal nanoparticle-decorated tubes as the noble metals are not oxidized during the anodization process (Fig. 17(c and d)),^{396–398} (iv) templated dewetting and dewetting/dealloying of sputtered metal thin films;^{208,399–401} when applied to a TiO_2 nanotube array, this approach is entirely based on self-ordering principles, that is, self-organized nanotubes offer an ideal topological substrate for a controlled split up of a metal thin film into nanoparticles whose size, density and placement are influenced by the nanotubes' geometry itself (Fig. 17(e–g)).⁴⁰²

Remarkably, for both (iii) and (iv), the decoration density of noble metal co-catalytic nanoparticles can be easily controlled

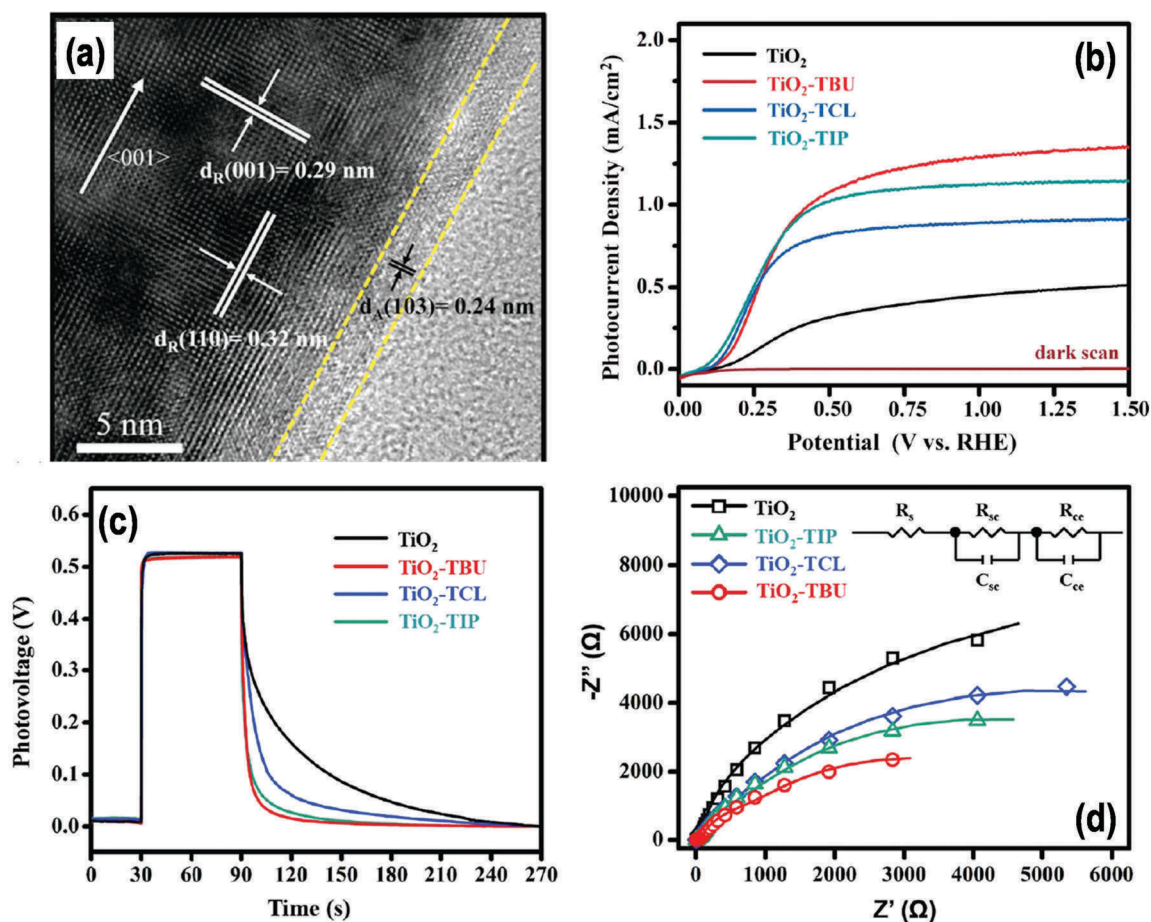


Fig. 16 (a) HR-TEM image of TiO_2 nanowire array decorated with a TiO_2 anatase thin layer prepared from a $\text{Ti}(\text{OBU})_4$ solution. (b) Linear sweep voltammograms of pristine TiO_2 and variously modified TiO_2 -based nanowire photoanodes recorded in 1 M KOH under AM 1.5G (100 mW cm^{-2}) illumination. (c) Photovoltage–time spectra collected for pristine TiO_2 and variously modified TiO_2 -based nanowire photoanodes. (d) EIS spectra of pristine TiO_2 and variously modified TiO_2 -based nanowire photoanodes. The inset shows the equivalent circuit used to fit the spectra. In (b–d) TCL, TiCl_4 ; TIP, $\text{Ti}(\text{OIP})_4$; TBU, $\text{Ti}(\text{OBU})_4$. Adapted with permission from *J. Phys. Chem. C*, 2014, **118**, 15086–15094. Copyright 2014 American Chemical Society.

by the amount of noble metal in the alloy or sputtered-deposited, respectively.

Pu *et al.* demonstrated that the performance of titania in PEC-WS can be enhanced in the entire UV-visible solar spectrum (from 300 to 800 nm) by tuning the shape of Au nanostructures (*i.e.*, nanoparticles *vs.* nanorods) decorating the surface of TiO_2 NW arrays.³⁹⁵ In particular, a combination of IPCE measurements, photovoltage experiments and Finite Difference Time Domain (FDTD) simulation pointed out that the observed enhancement in the UV region should be ascribed to Au NPs inducing a surface passivation effect and a two-fold electric field enhancement under irradiation – the amplified electric field in the UV region overlaps with the TiO_2 absorption spectrum and contribute to the generation of e^-/h^+ pairs in the metal oxide owing to Plasmon Resonance Energy Transfer (PRET). In the visible-light region both Au NPs and NRs contribute to the electric field amplification (*i.e.*, $\sim \times 5$ at 550 nm and $\sim \times 15$ at 750 nm for NPs and NRs, respectively) and to hot electron generation under LSPR irradiation, leading to an overall IPCE enhancement for $\lambda > 450 \text{ nm}$.

Visible light sensitization due to charge (electron) injection into TiO_2 is instead achieved by decoration with semiconductive quantum dots (CdS, CdSe, ZnS, *etc.* – see Fig. 18(a) and Section 3.2.3 for discussion on the mechanism).

Sun *et al.* reported that the synergy between the unique morphology of nanotubes and the visible light sensitization promoted by surface deposited QDs led to a 35-time higher photocurrent with respect to that of plain TiO_2 nanotubes.²²⁴ Due to their small band-gap of 2.4 and 1.7 eV, respectively, CdS and CdSe are the most common sensitizers or co-sensitizers for TiO_2 .^{224,403–405}

QDs are usually deposited on the nanotube/wire walls by different methods: (i) *in situ* growth of QDs by sequential chemical bath deposition (CBD), (ii) deposition of pre-synthesized colloidal QDs by direct adsorption, and (iii) linker-assisted adsorption.

The CBD method is based on repetitive cycles of immersion/rinsing of the oxide array into the quantum dot precursor solution. QDs form according to a deposition/aggregation process and uniformly cover the surface of the TiO_2 nanoarrays (Fig. 18(b)),^{224,403,404} clearly, the control on the number of cycles

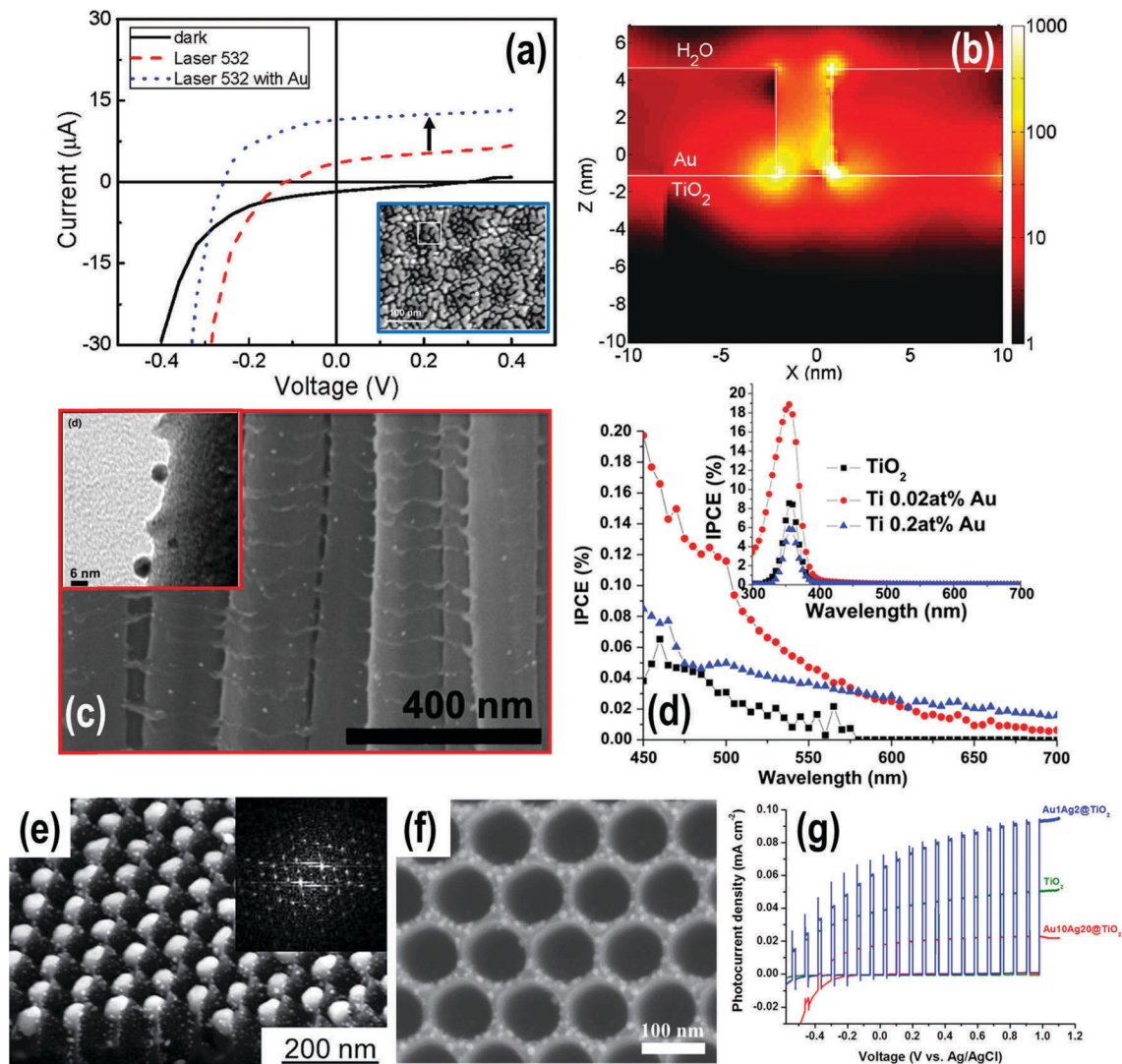


Fig. 17 (a) Photocurrent versus bias voltage of anodic TiO₂ with and without Au nanoparticles irradiated with visible light ($\lambda = 532$ nm) – inset: SEM image of a 5 nm thick Au island film deposited on anodic TiO₂ NTs. (b) Intensity of the plasmon-generated electric field at the interface of Au–TiO₂ calculated using FDTD. (c) Cross-sectional SEM image of Au decorated TiO₂ nanotubes on 0.2 at% of Au containing TiAu alloy (inset: TEM image of Au decorated TiO₂ nanotubes on Ti–(0.2 at%)Au alloy); (d) photoresponse spectra of 12 μm thick TiO₂ nanotubes with different contents of Au in TiAu alloy. Photoelectrochemical spectra were measured in 0.1 M Na₂SO₄ at 500 mV (Ag/AgCl). (e) Example of self-ordering templated dewetting of Au film (20 nm-thick) on a highly ordered TiO₂ nanocavity array leading to total filling with exactly one metal nanoparticle per TiO₂ cavity (inset: FFT conversion of a top-view SEM image of array of highly-ordered Au NPs embedded in TiO₂ nanocavities). (f) SEM image of TiO₂ NTs decorated with Au–Ag alloyed-dewetted NPs; (g) photocurrent density vs. potential curves under chopped solar light illumination under solar light illumination of TiO₂ NTs and TiO₂ NTs decorated with Au–Ag alloyed-dewetted NPs. Fig. (a and b) adapted with permission from *Nano Lett.*, 2011, **11**, 1111–1116. Copyright 2011 American Chemical Society. Fig. (c and d) reproduced from ref. 396 with permission from Elsevier. Fig. (e) reproduced from ref. 399 with permission from John Wiley & Sons. Fig. (f and g) reproduced from ref. 401 with permission from with permission from John Wiley & Sons.

is crucial to avoid excessive particle growth and aggregation that would in turn increase the chance of carrier recombination.

The adsorption of pre-synthesized QDs certainly offers a higher control on particle aggregation; in particular, the solvent used to disperse the QDs plays a critical role as the establishment of a favorable interaction of the QDs with both the solvent and the oxide surface leads to a high degree of coverage with a low degree of aggregation.⁴⁰⁶

However, the adsorption of pre-synthesized colloidal QDs often leads to a low surface coverage (*i.e.*, $\sim 14\%$)⁴⁰⁶ that limits

the efficiency of the QDs/TiO₂ assemblies compared to the CBD method.⁴⁰⁴ Also, a direct contact between the oxide matrix and the sensitizers is beneficial for a higher PEC efficiency – that is, QDs deposition by direct adsorption is preferred over the linker-assisted method.⁴⁰⁶

Regardless of the formation/deposition method, sensitization of TiO₂ with *e.g.* CdS QDs leads to a broadband light absorption that extends up to $\lambda \sim 600$ nm.^{403,406} Remarkably, light absorption up to $\lambda \sim 750$ nm has been reported for TiO₂ NT arrays decorated with CdS/CdSe/ZnS QDs,⁴⁰⁴ that is, as for plasmonic

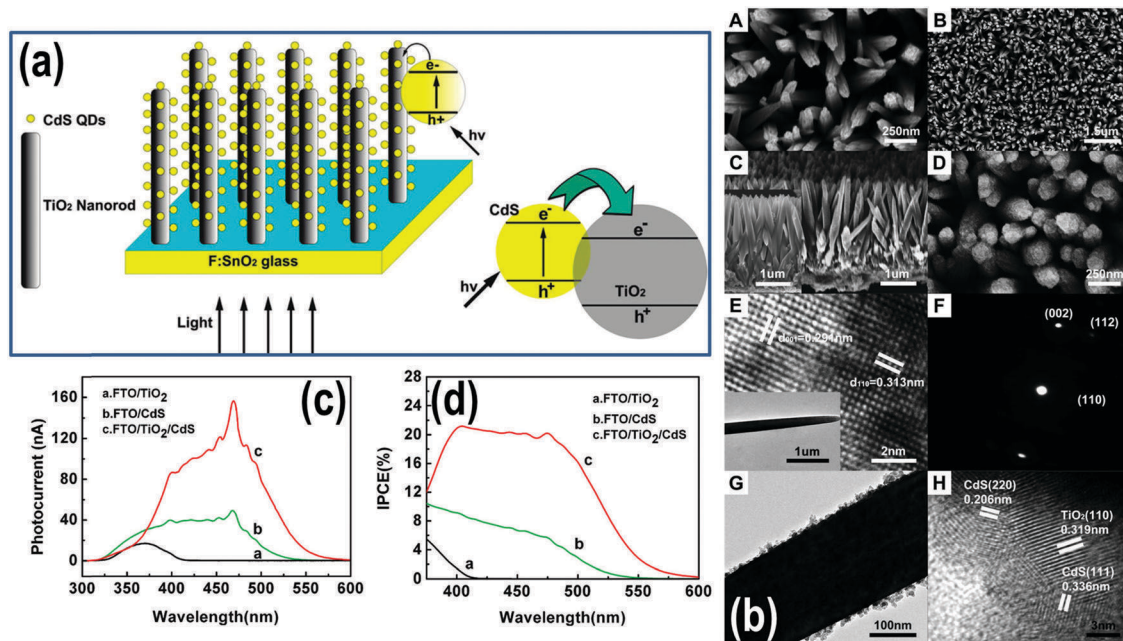


Fig. 18 (a) Schematic representation of CdS QDs deposited on TiO₂ nanorods, relative energy band alignment, and photoinduced charge separation and injection mechanisms. (b) Morphologies of FTO/TiO₂ and FTO/TiO₂/CdS electrodes: typical top view SEM images of FTO/TiO₂ electrode at (A) high and (B) low magnifications; (C) cross-sectional view of the well-aligned TiO₂ nanorod array; (D) FTO/TiO₂/CdS electrode; (E and F) HRTEM image and the corresponding selected area electron diffraction (SAED) pattern of bare TiO₂ nanorod array, respectively (inset in panel E: TEM image of a single bare TiO₂ nanorod); (G and H) TEM image and the corresponding HRTEM image of a single TiO₂ nanorod decorated with CdS QDs. (c) Photocurrent action spectra and (d) IPCE spectra of pristine TiO₂ and variously modified TiO₂ nanorod array. Photoelectrochemical spectra were measured under 475 nm (15 $\mu\text{W cm}^{-2}$) monochromatic irradiation. Adapted with permission from *J. Phys. Chem. C*, 2010, **114**, 16451–16455. Copyright 2010 American Chemical Society.

metals, also for semiconductive QDs the degree of extended light absorption depends on the material (but also on the size and shape of the nanoparticles). Typically, an enhancement in the IPCE and photocurrent is observed (Fig. 18(c and d)).⁴⁰³

In particular, comparative studies showed that CdSe/TiO₂ assemblies exhibit an initial higher photocurrent with respect to CdS/TiO₂, due to the smaller band-gap of the selenide-based QDs; however, CdSe/TiO₂ efficiency decreases quite rapidly as a consequence of the QDs low photostability. On the other hand, despite the lower PEC performance, CdS/TiO₂ exhibits higher e⁻ injection from the QDs and a lower charge recombination rate.

In line with this, a maximized photoelectrochemical performance was therefore observed for CdS/CdSe co-sensitized TiO₂ nanorod arrays that could exploit the advantages of both single cadmium-based materials.^{404,405}

Among the strategies more recently investigated for the visible-light sensitization of TiO₂ is the surface decoration of titania nanostructures with polydopamine (PDA).^{407–409}

PDA that forms from the oxidative self-polymerization of dopamine, a mussel-inspired building block, is a layer-structured polymer that can in principle stick on the surface of any substrate – *i.e.*, metal, metal oxide, metal alloy, polymer, glass, *etc.*, regardless of its chemical nature and morphology. Moreover, such a polymerization is a mild process and simple immersion of the substrate in an aqueous dopamine solution results in the spontaneous precipitation of the PDA film,

with the thickness of the film controlled by the immersion time.^{410–412}

In PDA-decorated TiO₂ layers under visible solar spectrum irradiation, polydopamine ($E_g \sim 2.2$ eV)⁴¹³ is the photo-active part while TiO₂ serves as semiconductive scaffold. In other words, after light absorption and charge carrier generation, electrons photopromoted in PDA are injected into the oxide CB (due to a favorable band alignment) and, owing to the one-dimensional porous structure of the TiO₂ film, percolate towards the back-contact. This configuration has been shown to provide up to $\sim 35\%$ photocurrent enhancement compared to uncoated TiO₂ NTs.⁴⁰⁷ Noteworthy, PDA exhibits low conductivity⁴¹⁴ and, therefore, a trade-off between a desired increase in visible light absorption and e⁻/h⁺ pair generation, and the drawbacks connected with its insulating properties should be established, that is, a 4 nm-thick PDA film has been shown to represent an optimum.⁴⁰⁷

PDA-coated titania tube arrays can also serve as a platform for the co-decoration of TiO₂ NTs with metal or metal oxide nanoparticles including *e.g.*, Ag, Pt and Co(OH)_x that further increase the material photoelectrochemical properties by co-catalytic and/or light absorption effects. In particular, Pt NPs-PDA co-decoration of TiO₂ NTs led to $\sim 70\%$ higher photocurrent, measured under AM 1.5G illumination with a 400 nm cut-off filter, compared to the efficiency of uncoated TiO₂ tubes. This effect has been attributed to metal-induced enhanced light absorption and low charge recombination rate.

Finally, it is worth mentioning that when annealed under reducing atmosphere (typically Ar or H₂/Ar mixtures) PDA can be graphitized and, therefore, represents a precursor to a graphite-like state.^{411,415,416} Remarkably, this can be further exploited towards an enhanced charge carrier transfer effect to increase the performance of TiO₂ nanostructures in photoelectrochemical applications.

Suitable electronic heterojunctions can be “built” also by surface decoration of TiO₂ with metal oxides including CuO₂,^{417,418} NiO,⁴¹⁹ ZnO^{420,421} and Bi₂O₃,⁴²² as well as with alkaline earth titanates (MTiO₃) with a cubic perovskite structure, such as SrTiO₃ and BaTiO₃.^{181,184,186,187} Slow hydrolysis of the precursors, electrochemical techniques, hydrothermal methods, microwave-assisted reactions, CVD or PVD deposition, and electrochemical polymerization are typically adopted as preparation procedures.

One of the most followed up schemes is the combination of TiO₂ with a p-type material (*e.g.*, Cu₂O or NiO) to establish useful p–n heterojunctions. This configuration enables solar light water splitting by combining a narrow band-gap semiconductor (p-type) to a larger band-gap semiconductor (n-type TiO₂) and utilizes both electron and hole majority charge carriers (from the n-type and p-type counterparts, respectively) for the PEC-WS reaction.^{418,419} Also, for TiO₂/NiO assemblies, a higher visible light photoresponse in comparison to other classical approaches (*e.g.*, N-doping) has been observed. For this assembly, a beneficial effect is attributed to charge injection from the NiO excited states to the conduction band of titanium oxide.⁴¹⁹

Nevertheless, it should be noted that for many of these compounds (namely, all II–VI and red-ox active materials) the long-time stability in photoelectrochemical applications still needs to be improved, not only in terms of resistance to corrosion or photocorrosion, but also due to the instability of some of the co-catalysts under applied voltage.

Hwang *et al.* showed that not only p–n, but also n–n heterojunctions may represent a promising alternative for increasing the performance of TiO₂ for PEC applications.⁴²³ In particular, n-type (B-doped) Si nanowire arrays coated with a TiO₂ conformal layer by ALD (*i.e.*, n-Si/n-TiO₂ core-shell array) have been fabricated that exhibited ~20–25% higher photocurrent and a more negative onset potential compared to a more conventional p-Si/n-TiO₂ core-shell arrangement. The result was attributed to the favorable band bending at both the n-Si/TiO₂ and the TiO₂/electrolyte interfaces that facilitates charge separation: under full lamp irradiation (450 W Xe lamp), e[−]/h⁺ pairs are photogenerated in both the shell and the core semiconductors (*i.e.*, TiO₂ and Si, respectively). Holes from TiO₂ move towards the interface with the electrolyte, while electrons tend to accumulate at the n-Si/TiO₂ interface and recombine with h⁺ photogenerated in the core material. Finally, photogenerated electrons in n-Si move to the counter electrode where the reduction reaction takes place.

By contrast, in p-Si/n-TiO₂, h⁺(TiO₂) can move either towards the electrolyte or to the interface with p-Si. This clearly reduces

the availability of positive charges for the OER and overall limits the anodic photocurrent.

MTiO₃ perovskites, with M = Ca, Sr or Ba, exhibit piezoelectric and ferroelectric properties, *i.e.*, feature an internal dipolar field that increases the separation of photogenerated electrons and holes. Owing to such a characteristic and to other superior properties, namely, high thermal stability, photocorrosion resistance, high stability as metal-ion dopant host, a CB more negative than that of TiO₂, *etc.*, SrTiO₃ and BaTiO₃ perovskite titanates.

For these features, SrTiO₃ and BaTiO₃ perovskite titanates have also been used in combination with 1D TiO₂ array, aiming at enhancing titania PEC performances.^{181,184,186}

A remarkable advantage of perovskite/TiO₂ assemblies is the possibility of fabricating such heterojunctions by *in situ* hydrothermal treatment of the TiO₂ one-dimensional scaffold in the presence of a Sr (or Ba) precursor. Such a direct and, hence, highly stable coupling of TiO₂ and SrTiO₃ (or BaTiO₃) causes the Fermi level of the two oxides to equilibrate and reduces the recombination of charge carriers at the two materials' interface. Nevertheless, MTiO₃ titanates exhibit a band-gap similar to that of TiO₂ (*i.e.*, $E_g \sim 3.1\text{--}3.2$ eV) and doping with *e.g.* Cr³⁺ cations that introduce intra band-gap levels is a typical approach to enable visible light induced photoelectrochemical activity.¹⁸⁷

More complex systems such as hierarchical ZnIn₂S₄/TiO₂,⁴²⁴ Cu_xZn_{1-x}In₂S₄/TiO₂,⁴²⁵ CuInS₂/TiO₂,^{426,427} TiO₂/In₂S₃/AgInS₂⁴²⁸ core-shell structures and “umbrella” hybrid (Bi₂S₃/rGO)₅/TiO₂ NR heterostructures⁴²⁹ have been recently shown (Fig. 19).

Common to all these hierarchical assemblies is a beneficial band misalignment that enables charge carrier separation, with the preferential collection of electrons in TiO₂ (and, thus, to the back-contact) through a cascade down-hill process, with holes accumulating in the shell material (*i.e.*, in the valence band with the least positive redox potential – see Fig. 19(a and b)).

This clearly suppresses charge carrier recombination and overall contributes to the enhancement of the multi-junction electrode PEC performance.

In particular, for 2D ZnIn₂S₄ nanosheets/TiO₂ 1D NR assemblies, aside from an enhancement in charge carrier separation, the improved PEC performance of the hybrid nanostructures with respect to a benchmark TiO₂ NR photoelectrode has been attributed to the unique features of two-dimensional materials including *e.g.* a larger surface area that not only provides a larger number of surface active sites, but also promotes an increased photon-matter interaction *via* multiple reflection and scattering at the semiconductor/electrolyte interface.

Noteworthy, the ZnIn₂S₄/TiO₂ assembly also exhibits a remarkable shift in the onset of photocurrent (*i.e.*, from 0.05 V vs. RHE to −0.53 V vs. RHE in Na₂SO₃/Na₂S electrolyte) with respect to 1D TiO₂ NRs.⁴²⁴

In addition to the previously mentioned strategies, theoretical studies showed that geometrical modulation of the TiO₂ nanostructure architecture can be used in view of enhancing the material light absorption properties.^{430,431} In particular,

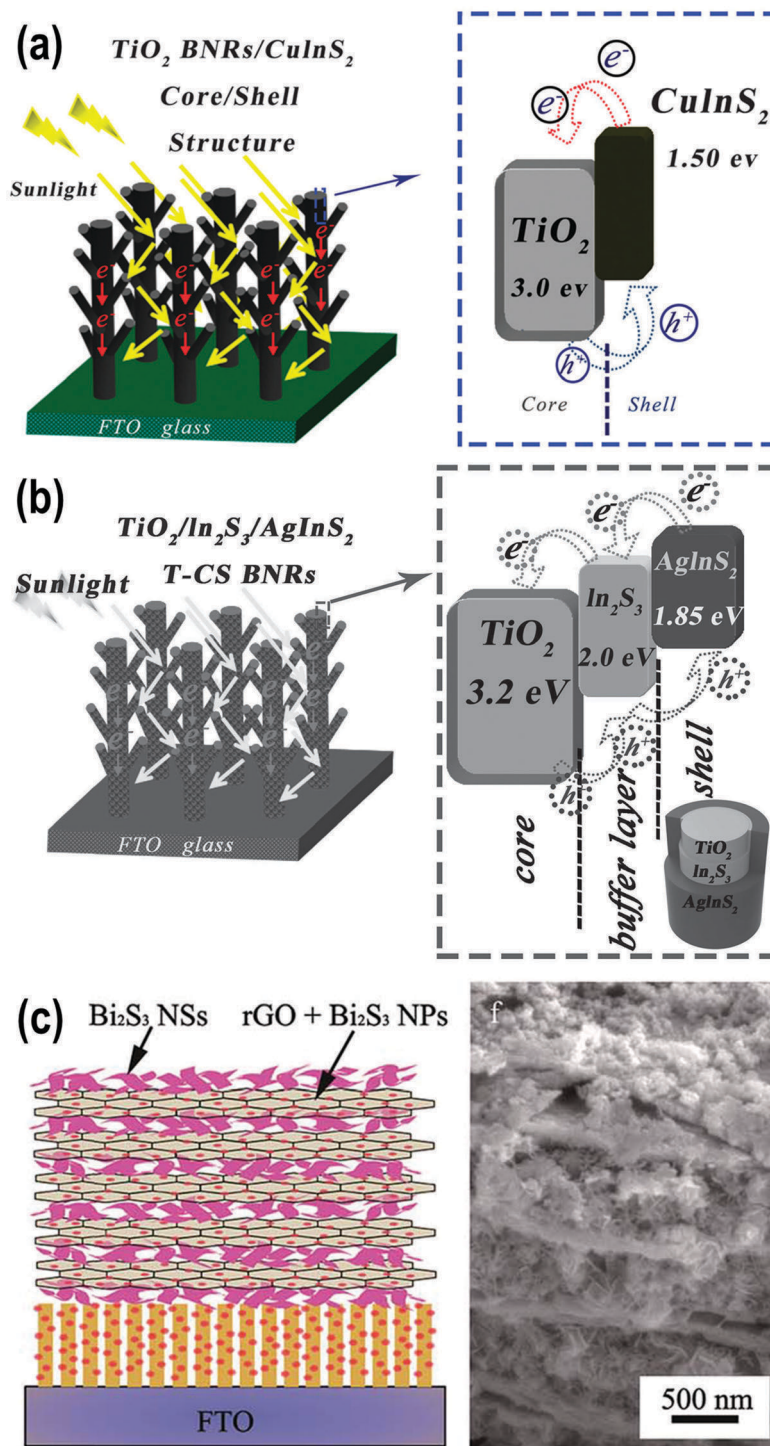


Fig. 19 Schematic representations of (a) the TiO_2 BNRs– CuInS_2 core–shell structure and (b) $\text{TiO}_2/\text{In}_2\text{S}_3/\text{AgInS}_2$ branched NRs electrode and relative band alignment. (c) Schematic diagram and SEM image of five layers of $\text{Bi}_2\text{S}_3/\text{rGO}$ (purple and light yellow) modified $\text{Bi}_2\text{S}_3/\text{TiO}_2$ NRs. Fig. (a) reproduced from ref. 427 with permission from the PCCP Owner Societies. Fig. (b) reproduced from ref. 428 with permission from John Wiley & Sons. Fig. (c) reproduced from ref. 429 with permission from the Royal Society of Chemistry.

integrating photonic crystals (PCs), such as 1D $\text{SiO}_2/\text{TiO}_2$ alternate layers or 3D TiO_2 (or Si) inverse opal layer,⁴³² with nanoporous structures (e.g., TiO_2 NTs) has been used to optimize photon management and, hence, to increase light harvesting of the absorbing (TiO_2 NT) layer.

Owing to their periodicity, photonic crystals allow to localize the incident radiation, that is, to trap and *slow* photons, in a specific wavelength range that depends on the PC periodicity. If the energy of the slow photons overlaps with the optical band-gap of the light absorbing layer, then an enhancement of

light absorption can be expected as a result of the increased optical length. Photonic crystals also find application in dye-sensitized solar cells. In this case the periodicity of the PCs is adjusted to match with the light absorption features of the dye (*i.e.*, in the visible range).^{433–435}

Recently, Al-Haddad *et al.* showed that the optical band-gap of TiO₂ NT arrays can be tuned by controlling geometrical parameters.⁴³⁶ The authors concluded that the optical absorption edge of TiO₂ nanotubes can be red-shifted with increasing the tube diameter while simultaneously decreasing their inter-distance – this assuming that the wall thickness remains constant and, therefore, excluding any contribution from quantum confinement effects.^{35,36} Supported by FDTD simulations, this effect was attributed to a strong confinement of the local electric field between the tubes, as their inter-distance becomes smaller.

4. α -Fe₂O₃–TiO₂ heterojunction-based materials – the Fe₂TiO₅ case

We have already pointed out that the relative misalignment of α -Fe₂O₃ and TiO₂ band edges can be exploited to design a suitable heterojunction for enhanced charge carrier separation, that is, holes generated in TiO₂ will be transferred to α -Fe₂O₃ with electrons preferentially accumulating in TiO₂ at the same time.^{33,437,438}

Under specific conditions, hybrid composites, *i.e.*, iron titanates (*e.g.*, Fe₂TiO₅, Fe₃TiO₄, and FeTiO₃) form at the interface between hematite and titania that, despite some controversial results, exhibit remarkable performances as photoanode materials in PEC devices.

Typically, iron titanates are formed *via* solid-state reaction between TiO₂ and α -Fe₂O₃. Due to the similar ion sizes of Ti and Fe, thermal annealing of the two oxides generates the composite – the various stoichiometric forms of titanates are given by the different valence configurations of the metal ions (such as Fe²⁺Ti⁴⁺, Fe³⁺Ti³⁺, *etc.*).

Among all the possible titanates, Fe₂TiO₅ has been recently the most widely explored Fe–Ti combination compound as photoanode material.^{439–443}

Fe₂TiO₅ has a pseudobrookite structure and, as TiO₂, has a valence and a conduction band that are (in principle) suitable to drive spontaneous water oxidation and reduction reactions, respectively. Moreover, it has a band-gap of *ca.* 2.0 eV and thus can generate e⁻/h⁺ pairs under visible light illumination (Fig. 20). Clearly, both aspects are highly desired for materials intended for PEC applications.

Keys to efficient Fe₂TiO₅ for PEC-WS are a layer thickness of only a few nm and a use of Fe₂TiO₅ in combination with TiO₂ or α -Fe₂O₃.

In fact, early studies on iron titanates based photoanodes for direct solar water oxidation,⁴⁴⁴ showed that for a “pure” Fe₂TiO₅ layer (not supported on TiO₂ or α -Fe₂O₃) an applied bias higher than that required for α -Fe₂O₃ is needed to promote efficient PEC water splitting, and that composites

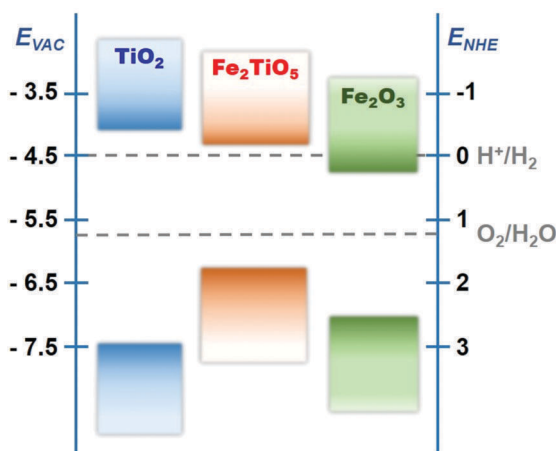


Fig. 20 Energy band structure of TiO₂, α -Fe₂O₃, and Fe₂TiO₅ relative to the vacuum level (E_{VAC}) and the normal hydrogen electrode (E_{NHE}).

such as FeTiO₃ and Fe₂TiO₄ suffer from significant photo-corrosion.

Typically, two different approaches are reported that instead lead to improved PEC efficiency in the presence of Fe₂TiO₅: (i) a use of nanostructured TiO₂ array as core material, where a thin α -Fe₂O₃ overlayer is deposited, or (ii) nanotubes/nanorods of α -Fe₂O₃ on FTO as supporting scaffold modified with a thin TiO₂ layer. In both cases, thermal annealing at 500–700 °C in air converts the thin overlayers into Fe₂TiO₅.^{439–443}

For the Fe₂TiO₅(overlayer)/TiO₂(core) configuration, two aspects contribute to the enhancement of the PEC activity: the titanate layer significantly extends the absorption spectrum of the material to visible wavelengths, and contributes to the generation of e⁻/h⁺ pairs up to $\lambda \sim 600$ nm. In addition, while h⁺ are preferentially transferred to the electrolyte, e⁻ are injected into the TiO₂ CB.

Although, in principle, the CBs of TiO₂ and Fe₂TiO₅ are not suitably located to promote e⁻ transfer from Fe₂TiO₅ into TiO₂ – see Fig. 20, enhanced charge separation has been reported and suggested as the origin for the higher photoelectrochemical activity compared to both TiO₂ and α -Fe₂O₃ photoelectrode counterparts.⁴³⁹

Different synthesis methods have been explored for the deposition of α -Fe₂O₃ thin layers on one-dimensional TiO₂ scaffolds: (i) electrodeposition (*e.g.*, from a Fe(NO₃)₃ solution – Fig. 21(a)), (ii) thermal pyrolysis of Fe-based organic solutions (*e.g.*, FeCl₃ ethanol solution – Fig. 21(c)), (iii) chemical bath deposition.^{440,441}

In general, the PEC performance is largely influenced by the thickness of the Fe₂TiO₅ layer, that is, there is a threshold thickness (~ 100 nm) that grants both significant light absorption and carrier separation. Above this limit, h⁺ and e⁻ tend to recombine due to a high charge transport resistivity, with a detrimental effect on the overall PEC performance of the composite (Fig. 21(d)).⁴⁴¹

To overcome this issue and further promote carrier utilization, Liu *et al.* reported on the use of a Co-based layer as a

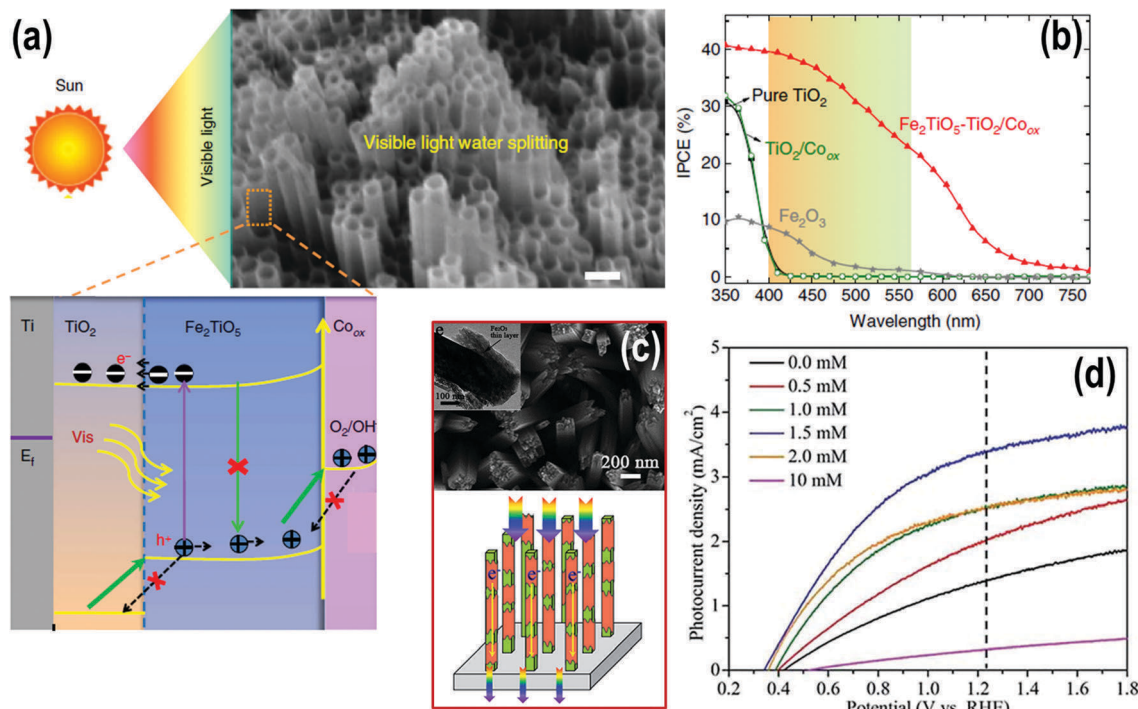


Fig. 21 (a) SEM image of Fe₂TiO₅-TiO₂/Co_{ox} nanoarchitecture and schematic drawing of the photoanode design with most likely water oxidation mechanism considering the idealized electronic structure alignment of the composite photoanode, E_F represents the Fermi level; (b) IPCE spectra of pure TiO₂, pure α-Fe₂O₃, Co_{ox} decorated TiO₂ and Co_{ox} decorated Fe₂TiO₅/TiO₂ layers. The spectra were measured in 1 M KOH at 1.23 V for α-Fe₂O₃, and at 0.4 V vs. RHE for the other layers. (c) SEM and TEM (inset) images, and schematic representation of TiO₂ nanorod array covered by a thin α-Fe₂O₃ layer; (d) linear sweep voltammetry plots of α-Fe₂O₃/TiO₂ nanorod photoanodes, containing different amounts of α-Fe₂O₃. The data were collected in 1.0 M NaOH, under Xe lamp irradiation (100 mW cm⁻²). Fig. (a and b) Reproduced from ref. 440 with permission from Nature Publishing Group. Fig. (c and d) reproduced from ref. 441 with permission from the Royal Society of Chemistry.

(more) efficient co-catalyst for the anodic reaction.⁴⁴⁰ A current density of 4.1 mA cm⁻² at 1.23 V *versus* RHE was measured along with a lower photocurrent onset potential (*i.e.*, 0.18 V *versus* RHE) with respect to pure TiO₂. The authors proposed that the natural band bending at the interface between the three oxides (Fe₂TiO₅, TiO₂, and CoO_x) enables holes produced in Fe₂TiO₅ to accumulate in CoO_x, while electrons from Fe₂TiO₅ are transferred to TiO₂ (Fig. 21(b)).

For the second core/shell configuration, that is, a Fe₂TiO₅(shell)/α-Fe₂O₃(core) composite, enhanced PEC efficiency is mainly attributed to the beneficial role of Fe₂TiO₅ in passivating hematite surface trapping states. This clearly reduces surface e⁻/h⁺ recombination. Moreover, due to the favorable band offset between the two oxides, e⁻ photogenerated in Fe₂TiO₅ are injected into the CB of α-Fe₂O₃ that supplies a direct transport path to the back-contact; similarly to the previous case, holes migrate to the Fe₂TiO₅/electrolyte interface and the increased charge separation results in an overall increase of the photoefficiency.⁴⁴²

Experimental evidence for this mechanism was provided by transient absorption spectra (TAS) measured with Fe₂TiO₅/α-Fe₂O₃ and pure α-Fe₂O₃ (Fig. 22).⁴⁴⁵

With respect to pure α-Fe₂O₃, Fe₂TiO₅ features an increased density of energy states near the CB and improved hole dynamics. This creates competitive trapping pathways for

photogenerated electrons, decreases e⁻/h⁺ recombination probabilities and, clearly, increases the lifetime of photogenerated holes.

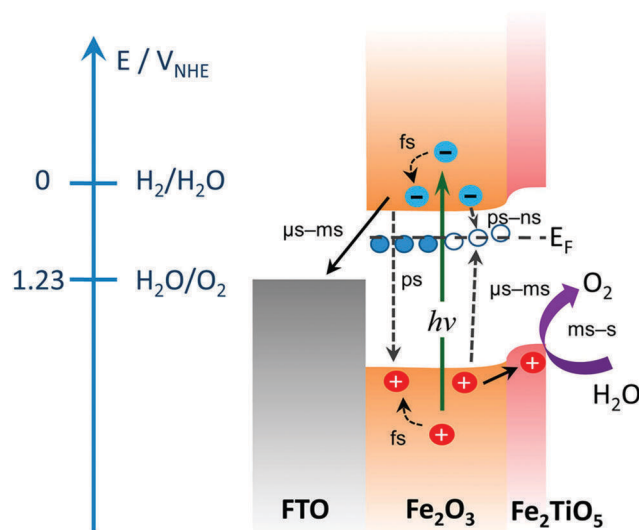


Fig. 22 Charge generation, recombination, and transfer in the nanocomposite photoelectrodes. Adapted with permission from *J. Phys. Chem. Lett.*, 2015, **6**, 2859–2864. Copyright 2015 American Chemical Society.

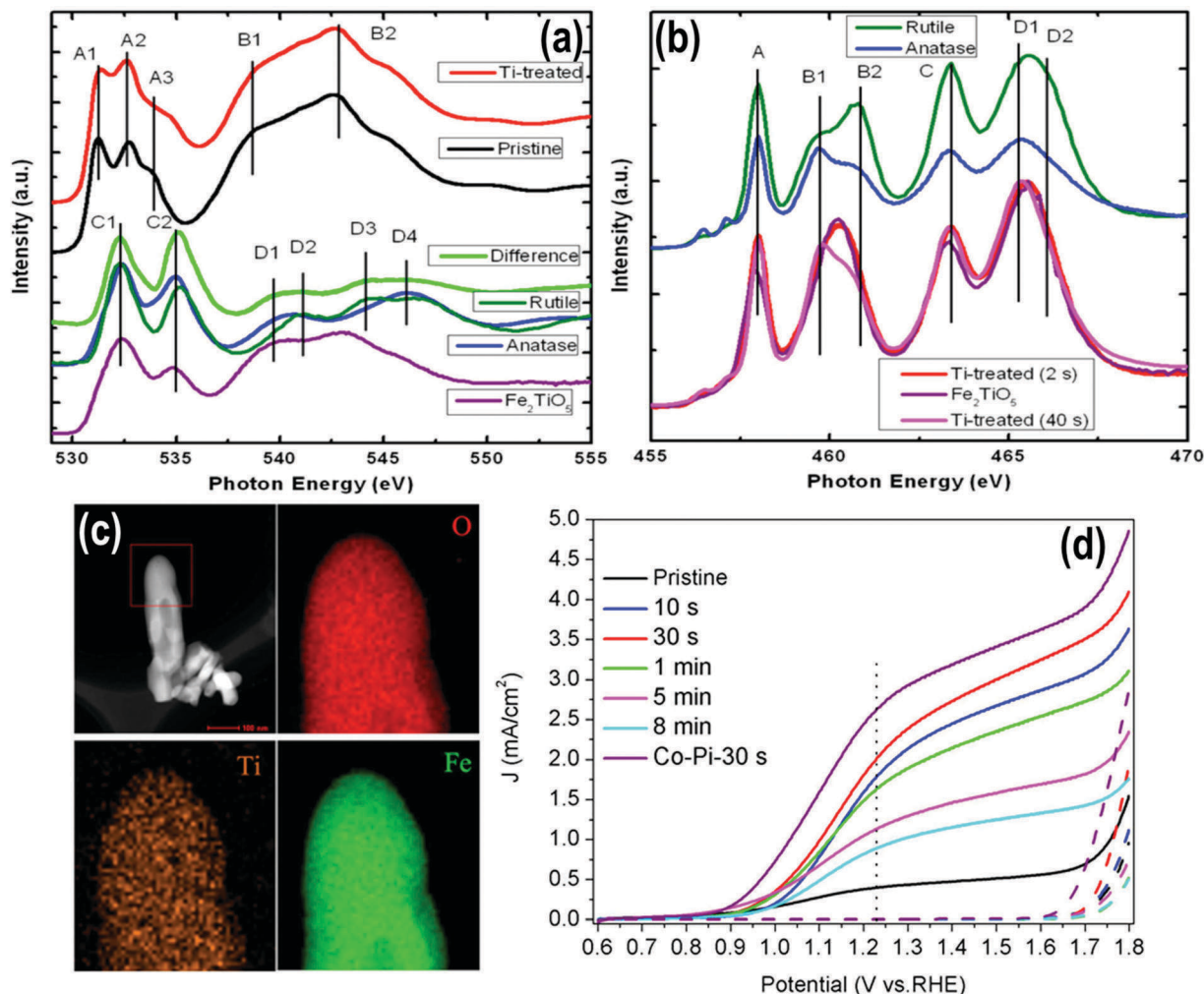


Fig. 23 (a) O K-edge XAS spectra of pristine and Ti-treated (2 s) hematite nanostructures compared with the spectra of rutile TiO_2 , anatase TiO_2 , and Fe_2TiO_5 . The difference spectrum between pristine and Ti-treated hematite is also shown; (b) Ti L-edge XAS spectra of Ti-treated (2 and 40 s) hematite nanostructures compared with the spectra of rutile TiO_2 , anatase TiO_2 , and Fe_2TiO_5 ; (c) dark field TEM image and corresponding TEM elemental mappings of HF-Ti treated (30 s) hematite 1D nanostructured photoanode; (d) J - V characteristics of pristine hematite photoanode, HF-Ti treated hematite photoanodes for different times (10 s, 30 s, 1 min, 5 min, and 8 min), and a Co-Pi deposited HF-Ti treated (30 s) hematite photoanode. Adapted with permission from *ACS Nano*, 2015, 9, 5348–5356. Copyright 2015 American Chemical Society.

Therefore, the pseudobrookite/hematite heterojunction generates a large amount of long-lived surface holes and, at the same time, acts as a block layer for the photogenerated electrons transferred to $\alpha\text{-Fe}_2\text{O}_3$. By preventing e^- back injection (and therefore e^-/h^+ recombination), Fe_2TiO_5 leads to an overall increase of the photoanode efficiency.

Two possible approaches have been proposed to grow a Fe_2TiO_5 ultra-thin film over vertically aligned hematite $\alpha\text{-Fe}_2\text{O}_3$ nanorods. In the first case, a FeOOH photoanode is immersed in a HF solution containing the Ti precursor; the second procedure is based on the evaporation of TiCl_4 on the surface of FeOOH . In both cases, adequate thermal treatment produced a Fe_2TiO_5 film.⁴⁴³

Fe_2TiO_5 was identified by synchrotron-based soft X-ray absorption spectroscopy (Fig. 23(a and b)) and TEM mapping (Fig. 23(c)), and a suitable lattice match between pseudobrookite Fe_2TiO_5 and $\alpha\text{-Fe}_2\text{O}_3$ was suggested to favor a specific

crystallographic growth direction, *i.e.*, the (110) plane for hematite and the (101) plane for pseudobrookite.

As for the $\text{Fe}_2\text{TiO}_5/\text{TiO}_2$ composite system, also $\text{Fe}_2\text{TiO}_5/\alpha\text{-Fe}_2\text{O}_3$ exhibits enhanced solar water oxidation activity, also supported by IPCE spectra; particularly, the HF-assisted synthesis of $\text{Fe}_2\text{TiO}_5/\alpha\text{-Fe}_2\text{O}_3$ resulted in a photocurrent density of 2.0 mA cm^{-2} at $1.23 \text{ V versus RHE}$ that was significantly higher than that measured with pure hematite nanorods, and that could be further improved by coupling with Co-Pi catalyst (Fig. 23(d)).

The beneficial effect of an oxygen evolution co-catalyst on the overall PEC activity of $\text{Fe}_2\text{TiO}_5/\text{TiO}_2$ assemblies has been also pointed out with the use of less “conventional” materials (other than Co-Pi⁴⁴³ and Co-based⁴⁴⁶ co-catalysts).

Passivation of surface states, reduction of electron-hole recombination, and, therefore, a photocurrent improvement have been reported by decorating $\text{Fe}_2\text{TiO}_5/\text{TiO}_2$ photoanodes with an SnO_x ^{447,448} (Fig. 24) or with a FeNiO_x ⁴⁴⁹ overlayer

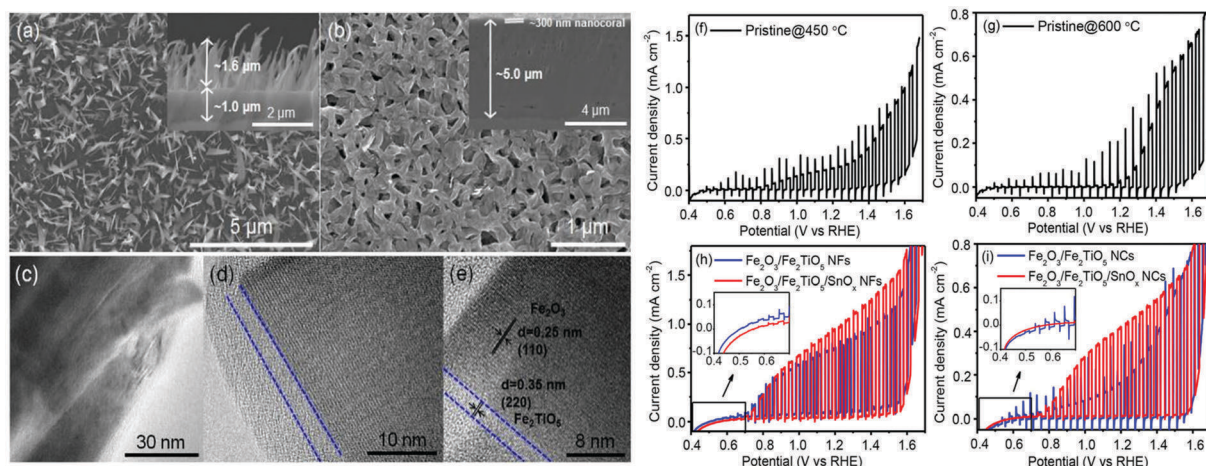


Fig. 24 SEM images of hematite α - Fe_2O_3 photoanodes prepared by thermal oxidation of Fe foils: (a) 1D nanoflakes (NFs) and (b) nanocorals (NCs); (c–e) TEM images of α - $\text{Fe}_2\text{O}_3/\text{Fe}_2\text{TiO}_5$ NFs; PEC polarization curves of hematite-based photoanodes: (f and h) NFs and (g and i) NCs. The PEC experiments were performed in 1 M KOH electrolyte AM 1.5G simulated solar light irradiation (intensity 100 mW cm^{-2}) at a scan rate of 10 mV s^{-1} . Reproduced from ref. 448 with permission from John Wiley & Sons.

(Fig. 25). This overall enabled enhanced photoanode stability for up to 5 h under operating conditions.⁴⁴⁹

5. Conclusion and perspective

Decades of experimental research on TiO_2 and α - Fe_2O_3 have pointed out that the two semiconductor metal oxides are promising candidates as anodes for photoelectrochemical water splitting. The reason for this is that, compared to other efficient materials such as CdS, CdSe, GaAs, *etc.*, TiO_2 and α - Fe_2O_3 are chemically stable against (photo)corrosion in a wide range of (electro)chemical conditions. Additionally, they are cheap, abundant and nontoxic.

In spite of these positive features, still some specific limitations hamper the development of highly efficient PEC devices based on the use of TiO_2 and α - Fe_2O_3 that could meet the requirements for high-scale applications. A main issue is certainly represented by the limited charge transfer kinetics intrinsic to both oxides. In this review, we have shown that key to overcoming such a limitation in a PEC arrangement is the use of one-dimensional oxide nanostructures (*i.e.*, nanotubes, nanorods, nanowires).

To this regard, we provided a range of available techniques and illustrate their possibilities and potentials. Particularly, we focused on the most promising routes that, in our view, are electrochemical anodization and hydrothermal methods: by adjusting simple experimental parameters, they offer a fine morphology control over the fabricated materials. In this context, we outlined how the resulting 1D geometry of the oxides is crucial towards a photoelectrochemical enhancement. This should be mainly ascribed to the possibility of decoupling the direction of light absorption and charge-carrier collection, as well as to establishing a preferential percolation pathway for charges (*i.e.*, h^+ transfer to the electrolyte and e^- vertical diffusion towards the back-contact).

We highlighted the main morphological parameters that affect the PEC activity of the bare oxides; in particular, for α - Fe_2O_3 -based photoanodes, key is a use of (1D) nanostructures the size of which is within the length scale of solid state charge diffusion (typical hole diffusion length in hematite, $\sim 5 \text{ nm}$). In the case of TiO_2 , 1D nanotubular arrays from self-organizing anodization were shown to be very convenient for PEC applications as, besides their morphology, they are fabricated in the form of directly back-contacted photoanodes; worth mentioning are also TiO_2 nanorods, owing to their single-crystalline nature: the absence of grain boundaries, which contribute to poor electron mobility in conventional polycrystalline TiO_2 films, suppresses charge carrier losses due to recombination and leads to relatively high performance.

Besides, these structures represent suitable platforms for further modifications, namely to induce doping effects or by the deposition of co-catalysts, light absorbers, charge transfer mediators, *etc.* We outlined how *e.g.* Ta- or Nb-doping TiO_2 is a most efficient approach to overcome its intrinsically low conductivity, while non-metal doping (mainly, N) and/or surface decoration with sensitizers are mostly carried out to extend the titania absorption features to the visible light. Two major approaches, often used in combination, were reported for α - Fe_2O_3 : (i) a use of earth abundant co-catalysts to improve the poor oxygen evolution kinetics, (ii) metal doping (mainly Zr^{4+} , Sn^{4+} and Nb^{5+}) to increase charge conductivity. In this context, thermally-induced Sn-doping, promoted by tin diffusion from FTO layers, represents one of the most straightforward strategies.

In addition to the (surface or bulk) modification of these two oxides, we illustrated achievements and outlooks regarding the use of TiO_2 - α - Fe_2O_3 systems that combine the complementary features and functionalities of the two counterparts in terms of light absorption, charge transport and, for open circuit photocatalysis, in terms of band energy positions. Although only limited attention has been given to such composites and the

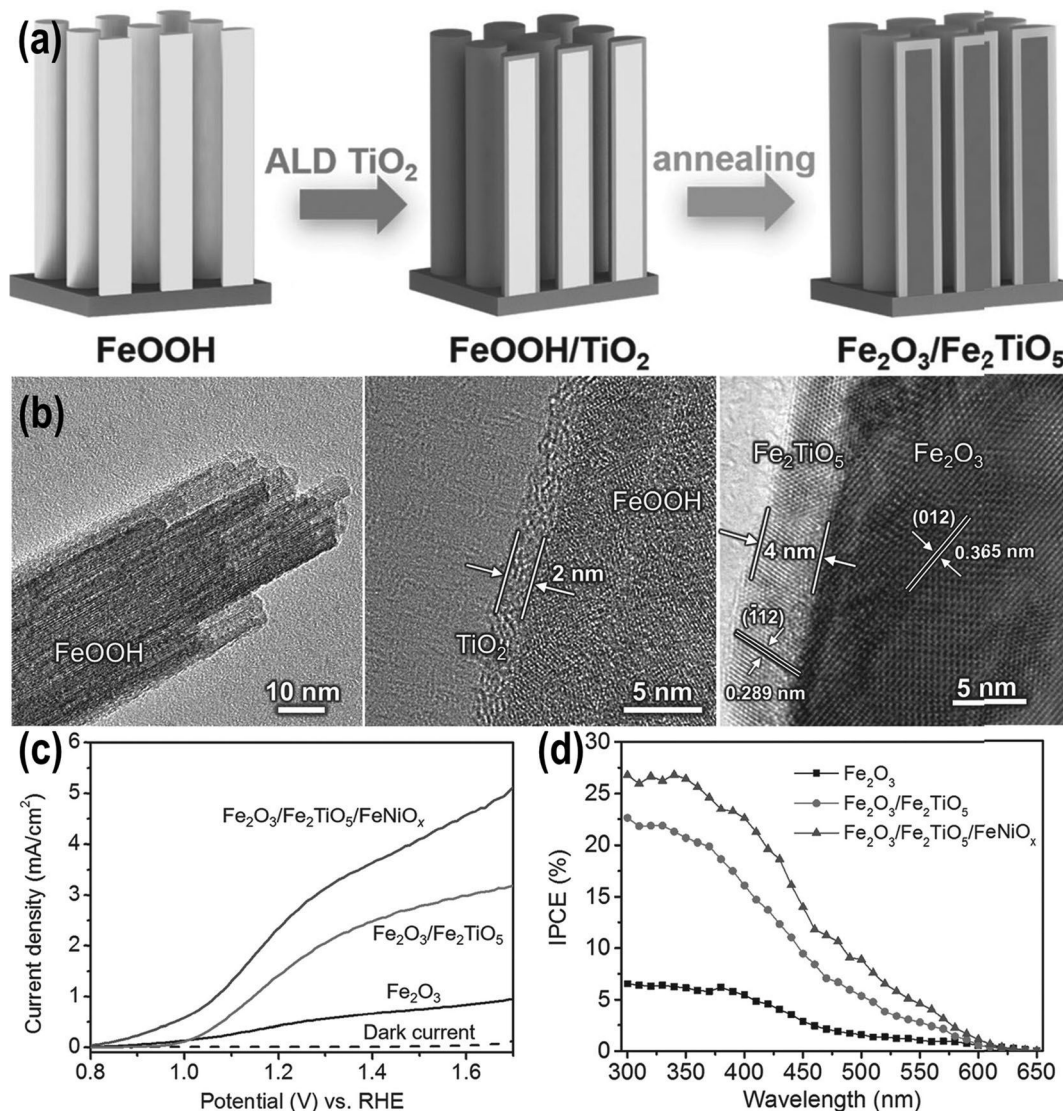


Fig. 25 (a) Representation of the process used to fabricate α -Fe₂O₃/Fe₂TiO₅ NR photoanodes; (b) HRTEM images of pristine FeOOH nanorod (left), after 90 cycles of TiO₂ ALD deposition (middle), and α -Fe₂O₃/Fe₂TiO₅ heterojunction NR after a two-step thermal treatment of FeOOH/TiO₂ (right); (c) linear sweep voltammetry (under AM 1.5G irradiation, in 1 M KOH), and (d) IPCE spectra (under 150 W Xe lamp irradiation, in 1 M KOH at 1.23 V vs. RHE) of pristine α -Fe₂O₃, α -Fe₂O₃/Fe₂TiO₅, and α -Fe₂O₃/Fe₂TiO₅/FeNiO_x based photoanodes. Reproduced from ref. 449 with permission from John Wiley & Sons.

mechanism underlying their working principle is still under debate, promising results have been reported in the recent literature. Further investigations on these TiO₂- α -Fe₂O₃ heterostructures may generate a new promising research trend in the frame of energy conversion processes.

Acknowledgements

This work was supported by the projects LO1305 and 8E15B009 of the Ministry of Education, Youth and Sports of the Czech Republic and by the project 15-19705S of the Grant Agency of the Czech Republic. ERC, DFG, and the DFG cluster of excellence "Engineering of Advanced Materials", as well as DFG "funCOS" are also

gratefully acknowledged for financial support. The authors gratefully acknowledge the support by the Operational Programme Research, Development and Education - European Regional Development Fund, project no. CZ.02.1.01/0.0/0.0/15_003/0000416 of the Ministry of Education, Youth and Sports of the Czech Republic.

References

- 1 S. J. A. Moniz, S. A. Shevlin, D. J. Martin, Z.-X. Guo and J. Tang, *Energy Environ. Sci.*, 2015, **8**, 731–759.
- 2 J. Michael and H. Jérôme, *Nature*, 2015, **517**, 150–152.
- 3 S. J. Davis, K. Caldeira and H. D. Matthews, *Science*, 2010, **329**, 1330–1333.

- 4 K. Mazloomi and C. Gomes, *Renewable Sustainable Energy Rev.*, 2012, **16**, 3024–3033.
- 5 A. Fujishima and K. Honda, *Nature*, 1972, **238**, 37–38.
- 6 F. E. Osterloh, *Chem. Soc. Rev.*, 2013, **42**, 2294–2320.
- 7 M. G. Walter, E. L. Warren, J. R. McKone, S. W. Boettcher, Q. X. Mi, E. A. Santori and N. S. Lewis, *Chem. Rev.*, 2010, **110**, 6446–6473.
- 8 M. Grätzel, *Nature*, 2001, **414**, 338–344.
- 9 A. J. Bard, A. B. Bocarsly, F. F. Fan, E. G. Walton and M. S. Wrighton, *J. Am. Chem. Soc.*, 1980, **102**, 3671–3677.
- 10 J. R. Bolton, S. J. Strickler and J. S. Connolly, *Nature*, 1985, **316**, 495–500.
- 11 A. B. Murphy, P. R. F. Barnes, L. K. Randeniya, I. C. Plumb, I. E. Grey, M. D. Horne and J. A. Glasscock, *Int. J. Hydrogen Energy*, 2006, **31**, 1999–2017.
- 12 I. E. Castelli, F. Hüser, M. Pandey, H. Li, K. S. Thygesen, B. Seger, A. Jain, K. A. Persson, G. Ceder and K. W. Jacobsen, *Adv. Energy Mater.*, 2015, **5**, 14009151.
- 13 Z. Chen, T. F. Jaramillo, T. G. Deutsch, A. Kleiman-Shwarscstein, A. J. Forman, N. Gaillard, R. Garland, K. Takanabe, C. Heske, M. Sunkara, E. W. McFarland, K. Domen, E. L. Miller, J. A. Turner and H. N. Dinh, *J. Mater. Res.*, 2010, **25**, 3–16.
- 14 N. Hykaway, W. M. Sears, H. Morisaki and S. R. Morrison, *J. Phys. Chem.*, 1986, **90**, 6663–6667.
- 15 K. L. Hardee and A. J. Bard, *J. Electrochem. Soc.*, 1976, **123**, 1024–1026.
- 16 K. Sivula, R. Zboril, F. Le Formal, R. Robert, A. Weidenkaff, J. Tucek, J. Frydrych and M. Grätzel, *J. Am. Chem. Soc.*, 2010, **132**, 7436–7444.
- 17 K. Sivula, F. Le Formal and M. Grätzel, *ChemSusChem*, 2011, **4**, 432–449.
- 18 Z. Li, W. Luo, M. Zhang, J. Feng and Z. Zou, *Energy Environ. Sci.*, 2013, **6**, 347–370.
- 19 D. a Tryk, A. Fujishima and K. Honda, *Electrochim. Acta*, 2000, **45**, 2363–2376.
- 20 T. Lindgren, L. Vayssieres, H. Wang and S. E. Lindquist, in *Chemical Physics of Nanostructured Semiconductors*, ed. A. I. Kokorin and D. W. Bahnemann, CRC Press, 2003, pp. 83–110.
- 21 A. Fujishima, K. Kohayakawa and K. Honda, *J. Electrochem. Soc.*, 1975, **122**, 1487–1489.
- 22 N. Getoff, *Int. J. HydrogenEnergy*, 1990, **15**, 407–417.
- 23 V. M. Aroutiounian, V. M. Arakelyan and G. E. Shahnazaryan, *Sol. Energy*, 2005, **78**, 581–590.
- 24 J. Kim, Y. Piao and T. Hyeon, *Chem. Soc. Rev.*, 2009, **38**, 372–390.
- 25 E. Boisselier and D. Astruc, *Chem. Soc. Rev.*, 2009, **38**, 1759–1782.
- 26 C. Liu, F. Li, L.-P. P. Ma and H.-M. M. Cheng, *Adv. Energy Mater.*, 2010, **22**, E28–E62.
- 27 L. Q. Jing, W. Zhou, G. H. Tian and H. G. Fu, *Chem. Soc. Rev.*, 2013, **42**, 9509–9549.
- 28 J. N. Tiwari, R. N. Tiwari and K. S. Kim, *Prog. Mater. Sci.*, 2012, **57**, 724–803.
- 29 S. Kment, Z. Hubicka, H. Kmentova, P. Kluson, J. Krysa, I. Gregora, M. Morozova, M. Cada, D. Petras, P. Dytrych, M. Slater and L. Jastrabik, *Catal. Today*, 2011, **161**, 8–14.
- 30 K. Lee, R. Kirchgeorg and P. Schmuki, *J. Phys. Chem. C*, 2014, **118**, 16562–16566.
- 31 J. Bian, C. Huang, L. Wang, T. Hung, W. A. Daoud and R. Zhang, *ACS Appl. Mater. Interfaces*, 2014, **6**, 4883–4890.
- 32 B. Hatton, L. Mishchenko, S. Davis, K. H. Sandhage and J. Aizenberg, *Proc. Natl. Acad. Sci. U. S. A.*, 2010, **107**, 10354–10359.
- 33 H. Han, F. Riboni, F. Karlický, S. Kment, A. Goswami, P. Sudhagar, J. Yoo, L. Wang, O. Tomanec, M. Petr, O. Haderka, C. Terashima, A. Fujishima, P. Schmuki and R. Zboril, *Nanoscale*, 2017, **9**, 134–142.
- 34 T. Guo, M.-S. Yao, Y.-H. Lin and C.-W. Nan, *CrystEngComm*, 2015, **17**, 3551–3585.
- 35 M. Anpo, T. Shima, S. Kodama and Y. Kubokawa, *J. Phys. Chem.*, 1987, **91**, 4305–4310.
- 36 C. Kormann, D. W. Bahnemann and M. R. Hoffmann, *J. Phys. Chem.*, 1988, **92**, 5196–5201.
- 37 D. M. King, X. Du, A. S. Cavanagh and A. W. Weimer, *Nanotechnology*, 2008, **19**, 445401.
- 38 T. Kasuga, M. Hiramatsu, A. Hoson, T. Sekino and K. Niihara, *Langmuir*, 1998, **14**, 3160–3163.
- 39 T. Kasuga, M. Hiramatsu, A. Hoson, T. Sekino and K. Niihara, *Adv. Mater.*, 1999, **11**, 1307–1311.
- 40 D. V. Bavykin, J. M. Friedrich and F. C. Walsh, *Adv. Mater.*, 2006, **18**, 2807–2824.
- 41 V. N. Lutskii, *Phys. Status Solidi*, 1970, **1**, 199–220.
- 42 H. Gleiter, *Acta Mater.*, 2000, **48**, 1–29.
- 43 P. V. Kamat, *J. Phys. Chem. C*, 2008, **112**, 18737–18753.
- 44 R. van de Krol and M. Grätzel, *Photoelectrochemical Hydrogen Production*, Springer Link, New York, 2012, vol. 102.
- 45 W. J. Albery, *J. Electrochem. Soc.*, 1984, **131**, 2896.
- 46 M. Heyrovsky and J. Jirkovsky, *Langmuir*, 1995, **11**, 4300–4308.
- 47 P. Roy, S. Berger and P. Schmuki, *Angew. Chem., Int. Ed.*, 2011, **50**, 2904–2939.
- 48 K. Lee, A. Mazare and P. Schmuki, *Chem. Rev.*, 2014, **114**, 9385–9454.
- 49 X. Wang, Z. Li, J. Shi and Y. Yu, *Chem. Rev.*, 2014, **114**, 9346–9384.
- 50 D. A. Wheeler, G. Wang, Y. Ling, Y. Li and J. Z. Zhang, *Energy Environ. Sci.*, 2012, **5**, 6682.
- 51 A. G. Tamirat, J. Rick, A. A. Dubale, W.-N. Su and B.-J. Hwang, *Nanoscale Horiz.*, 2016, **1**, 243–267.
- 52 L. Bertoluzzi and S. Ma, *Phys. Chem. Chem. Phys.*, 2013, **15**, 4283–4285.
- 53 J. M. Macak, M. Zlamal, J. Krysa and P. Schmuki, *Small*, 2007, **3**, 300–304.
- 54 K. Zhu, T. B. Vinzant, N. R. Neale and A. J. Frank, *Nano Lett.*, 2007, **7**, 3739–3746.
- 55 O. K. Varghese, M. Paulose and C. A. Grimes, *Nat. Nanotechnol.*, 2009, **4**, 592–597.
- 56 M. Wang, J. Iocozia, L. Sun, C. Lin and Z. Lin, *Energy Environ. Sci.*, 2014, **4**, 2182–2202.
- 57 Q. X. Zhou, Z. Fang, J. Li and M. Y. Wang, *Microporous Mesoporous Mater.*, 2015, **202**, 22–35.
- 58 S. So, I. Hwang and P. Schmuki, *Energy Environ. Sci.*, 2015, **8**, 849–854.

- 59 J. Lee and S. H. Ko, *Hierarchical Nanostructures for Energy Devices*, 2015, pp. 7–25.
- 60 D. Lee and C. P. Grigoropoulos, in *Hierarchical Nanostructures for Energy Devices*, ed. S. H. Ko and C. P. Grigoropoulos, Royal Society of Chemistry, 2015, pp. 174–203.
- 61 J. S. Chen and X. W. Lou, *Electrochem. Commun.*, 2009, **11**, 2332–2335.
- 62 S. Hoang, S. P. Berglund, R. R. Fullon, R. L. Minter and C. B. Mullins, *J. Mater. Chem. A*, 2013, **1**, 4307.
- 63 L. Wang, C.-Y. Y. Lee, A. Mazare, K. Lee, J. Mueller, E. Spiecker, P. Schmuki, J. Müller, E. Spiecker and P. Schmuki, *Chem. – Eur. J.*, 2014, **20**, 77–82.
- 64 M. Ji, J. Cai, Y. Ma and L. Qi, *ACS Appl. Mater. Interfaces*, 2016, **8**, 3651–3660.
- 65 S. Kment, P. Schmuki, Z. Hubicka, L. Machala, R. Kirchgeorg, N. Liu, L. Wang, K. K. Lee, J. Olejnicek, M. Cada, I. Gregora and R. Zboril, *ACS Nano*, 2015, **9**, 7113–7123.
- 66 L. Wang, X. Zhou, N. T. Nguyen and P. Schmuki, *ChemSusChem*, 2015, **8**, 618–622.
- 67 E. Thimsen, F. Le Formal, M. Grätzel and S. C. Warren, *Nano Lett.*, 2011, **11**, 35–43.
- 68 C. W. Cheng and H. J. Fan, *Nano Today*, 2012, **7**, 327–343.
- 69 H. N. Chen, S. H. Yang, W. Chen, Y. Qiu, S. H. Yang, M. A. Butler, D. S. Ginley, R. Memming, A. J. Bard, P. V. Kamat and M. Gratzel, *Nanoscale Horiz.*, 2016, **1**, 96–108.
- 70 P. X. Gao and Z. L. Wang, *Appl. Phys. Lett.*, 2004, **84**, 2883–2885.
- 71 S. H. Ko, D. Lee, H. W. Kang, K. H. Nam, J. Y. Yeo, S. J. Hong, C. P. Grigoropoulos and H. J. Sung, *Nano Lett.*, 2011, **11**, 666–671.
- 72 D. Lee, Y. Rho, F. I. Allen, A. M. Minor, S. H. Ko and C. P. Grigoropoulos, *Nanoscale*, 2013, **5**, 11147–11152.
- 73 J. Shi, C. Sun, M. B. Starr and X. Wang, *Nano Lett.*, 2011, **11**, 624–631.
- 74 L. Wang, A. Palacios-Padrós, R. Kirchgeorg, A. Tighineanu and P. Schmuki, *ChemSusChem*, 2014, **7**, 421–424.
- 75 S. Y. Noh, K. Sun, C. Choi, M. Niu, M. Yang, K. Xu, S. Jin and D. Wang, *Nano Energy*, 2013, **2**, 351–360.
- 76 J. Shi, Y. Hara, C. Sun, M. A. Anderson and X. Wang, *Nano Lett.*, 2011, **11**, 3413–3419.
- 77 K. Sivula, F. Le Formal, M. Grätzel, F. Le Formal and M. Gratzel, *Chem. Mater.*, 2009, **21**, 2862–2867.
- 78 S. Park, C. W. Lee, I. S. Cho, S. Kim, J. H. Park, H. J. Kim, D. W. Kim, S. Lee and K. S. Hong, *International Journal of Hydrogen Energy*, Elsevier Ltd, 2014, vol. 39, pp. 17508–17516.
- 79 M. Stefik, M. Cornuz, N. Mathews, T. Hisatomi, S. Mhaisalkar and M. Grätzel, *Nano Lett.*, 2012, **12**, 5431–5435.
- 80 H. K. Dunn, J. M. Feckl, A. Müller, D. Fattakhova-Rohlfing, S. G. Morehead, J. Roos, L. M. Peter, C. Scheu and T. Bein, *Phys. Chem. Chem. Phys.*, 2014, **16**, 24610–24620.
- 81 Y. Li, X. Wei, B. Zhu, H. Wang, Y. Tang, T. C. Sum and X. Chen, *Nanoscale*, 2016, **8**, 11284–11290.
- 82 D. Wang, G. Chang, Y. Zhang, J. Chao, J. Yang, S. Su, L. Wang, C. Fan and L. Wang, *Nanoscale*, 2016, **8**, 12697–12701.
- 83 C. Liu, J. Tang, H. M. Chen, B. Liu and P. Yang, *Nano Lett.*, 2013, **13**, 2989–2992.
- 84 Z. Li, F. Wang, A. Kvit and X. Wang, *J. Phys. Chem. C*, 2015, **119**, 4397–4405.
- 85 A. Kargar, S. J. Kim, P. Allameh, C. Choi, N. Park, H. Jeong, Y. Pak, G. Y. Jung, X. Pan, D. Wang and S. Jin, *Adv. Funct. Mater.*, 2015, **25**, 2609–2615.
- 86 X. Chen and S. S. Mao, *J. Nanosci. Nanotechnol.*, 2006, **6**, 906–925.
- 87 J. L. Dormann, N. Viart, J. L. Rehspringer, A. Ezzir and D. Niznansky, *Hyperfine Interact.*, 1998, **112**, 89–92.
- 88 X. Chen and S. S. Mao, *Chem. Rev.*, 2007, **107**, 2891–2959.
- 89 P. P. Sarangi, S. R. Vadera, M. K. Patra, C. Prakash and N. N. Ghosh, *J. Am. Ceram. Soc.*, 2009, **92**, 2425–2428.
- 90 P. P. Sarangi, B. Naik and N. N. Ghosh, *J. Am. Ceram. Soc.*, 2008, **91**, 4145–4147.
- 91 A. Gurav, T. Kodas, T. Pluym and Y. Xiong, *Aerosol Sci. Technol.*, 1993, **19**, 411–452.
- 92 R. S. Sapiesszko and E. Matijević, *J. Colloid Interface Sci.*, 1980, **74**, 405–422.
- 93 R. D. Stramel and J. K. Thomas, *J. Colloid Interface Sci.*, 1986, **110**, 121–129.
- 94 J. Kiwi and M. Grätzel, *J. Chem. Soc., Faraday Trans. 1*, 1987, 1101.
- 95 S. Chatterjee, S. Sarkar and S. N. Bhattacharyya, *J. Photochem. Photobiol., A*, 1993, **72**, 183–187.
- 96 S. Lian, E. Wang, L. Gao, D. Wu, Y. Song and L. Xu, *Mater. Res. Bull.*, 2006, **41**, 1192–1198.
- 97 B. Wang, X.-Y. Lu, L. K. Yu, J. Xuan, M. K. H. Leung and H. Guo, *CrystEngComm*, 2014, **16**, 10046–10055.
- 98 S. Hoang, S. Guo, N. T. Hahn, A. J. Bard and C. B. Mullins, *Nano Lett.*, 2012, **12**, 26–32.
- 99 M. Xu, P. Da, H. Wu, D. Zhao and G. Zheng, *Nano Lett.*, 2012, **12**, 1503–1508.
- 100 G. Wang, H. Wang, Y. Ling, Y. Tang, X. Yang, R. C. Fitzmorris, C. Wang, J. Z. Zhang and Y. Li, *Nano Lett.*, 2011, **11**, 3026–3033.
- 101 I. S. Cho, M. Logar, C. H. Lee, L. Cai, F. B. Prinz and X. Zheng, *Nano Lett.*, 2014, **14**, 24–31.
- 102 Y. C. Pu, Y. Ling, K. Der Chang, C. M. Liu, J. Z. Zhang, Y. J. Hsu and Y. Li, *J. Phys. Chem. C*, 2014, **118**, 15086–15094.
- 103 L. Vayssieres, N. Beermann, S. E. Lindquist and A. Hagfeldt, *Chem. Mater.*, 2001, **13**, 233–235.
- 104 H. F. Shao, X. F. Qian, J. Yin and Z. K. Zhu, *J. Solid State Chem.*, 2005, **178**, 3130–3136.
- 105 B. Tang, G. Wang, L. Zhuo, J. Ge and L. Cui, *Inorg. Chem.*, 2006, **45**, 5196–5200.
- 106 B. Baruwati, K. Madhusudan Reddy, S. V. Manorama and S. S. Madhavendra, *J. Am. Ceram. Soc.*, 2006, **89**, 2602–2605.
- 107 S. Zeng, K. Tang and T. Li, *J. Colloid Interface Sci.*, 2007, **312**, 513–521.
- 108 C.-J. Jia, L.-D. Sun, Z.-G. Yan, L.-P. You, F. Luo, X.-D. Han, Y.-C. Pang, Z. Zhang and C.-H. Yan, *Angew. Chem., Int. Ed.*, 2005, **44**, 4328–4333.
- 109 J. Lu, D. Qi, C. Deng, X. Zhang and P. Yang, *Nanoscale*, 2010, **2**, 1892.

- 110 Y. P. F. H. M. Fan, G. J. You, Y. Li, Z. Zheng, H. R. Tan, Z. X. Shen and S. H. Tang, *J. Phys. Chem. C*, 2009, 9928–9935.
- 111 L. Song, S. Zhang, B. Chen, J. Ge and X. Jia, *Colloids Surf., A*, 2010, 360, 1–5.
- 112 A. Nakahira, W. Kato, M. Tamai, T. Isshiki, K. Nishio and H. Aritani, *J. Mater. Sci.*, 2004, 39, 4239–4245.
- 113 X. Pan, Y. Zhao, S. Liu, C. L. Korzeniewski, S. Wang and Z. Fan, *ACS Appl. Mater. Interfaces*, 2012, 4, 3944–3950.
- 114 D. V. Bavykin, V. N. Parmon, A. A. Lapkin and F. C. Walsh, *J. Mater. Chem.*, 2004, 14, 3370.
- 115 A. Kumar, A. R. Madaria and C. Zhou, *J. Phys. Chem. C*, 2010, 114, 7787–7792.
- 116 C. Fàbrega, T. Andreu, A. Tarancón, C. Flox, A. Morata, L. Calvo-Barrio and J. R. Morante, *Int. J. Hydrogen Energy*, 2013, 38, 2979–2985.
- 117 E. L. D. Hebenstreit, W. Hebenstreit, H. Geisler, C. A. Ventrice, D. A. Hite, P. T. Sprunger and U. Diebold, *Surf. Sci.*, 2002, 505, 336–348.
- 118 X. Yu, H. Wang, Y. Liu, X. Zhou, B. J. Li, L. Xin, Y. Zhou and H. Shen, *J. Mater. Chem. A*, 2013, 1, 2110–2117.
- 119 J. Wang, C. Chen, Z. Ren and Z. Wang, *Semicond. Sci. Technol.*, 2014, 29, 055006.
- 120 X. Sun, Q. Sun, Q. Zhang, Q. Zhu, H. Dong and L. Dong, *J. Phys. D: Appl. Phys.*, 2013, 46, 095102.
- 121 Y. C. Ling, G. M. Wang, D. A. Wheeler, J. Z. Zhang and Y. Li, *Nano Lett.*, 2011, 11, 2119–2125.
- 122 M. S. Sander, M. J. Côté, W. Gu, B. M. Kile and C. P. Tripp, *Adv. Mater.*, 2004, 16, 2052–2057.
- 123 M. S. Sander and H. Gao, *J. Am. Chem. Soc.*, 2005, 127, 12158–12159.
- 124 G. Wu, T. Nishikawa, B. Ohtani and A. Chen, *Chem. Mater.*, 2007, 19, 4530–4537.
- 125 P. Hoyer, *Langmuir*, 1996, 12, 1411–1413.
- 126 E. Moyen, L. Santinacci, L. Masson, W. Wulffhekel and M. Hanbücken, *Adv. Mater.*, 2012, 24, 5094–5098.
- 127 O. Nishinaga, T. Kikuchi, S. Natsui and R. O. Suzuki, *Sci. Rep.*, 2013, 3, 2748.
- 128 H. Masuda and K. Fukuda, *Science*, 1995, 268, 1466–1468.
- 129 B. B. Lakshmi, C. J. Patrissi and C. R. Martin, *Chem. Mater.*, 1997, 9, 2544–2550.
- 130 H. Imai, Y. Takei, K. Shimizu, M. Matsuda and H. Hirashima, *J. Mater. Chem.*, 1999, 9, 2971–2972.
- 131 H. Shin, D. K. Jeong, J. Lee, M. M. Sung and J. Kim, *Adv. Mater.*, 2004, 16, 1197–1200.
- 132 M. Knez, K. Nielsch and L. Niinistö, *Adv. Mater.*, 2007, 19, 3425–3438.
- 133 S. J. Ku, G. C. Jo, C. H. Bak, S. M. Kim, Y. R. Shin, K. H. Kim, S. H. Kwon and J.-B. Kim, *Nanotechnology*, 2013, 24, 085301.
- 134 J. Qiu, W. Yu, X. Gao and X. Li, *Nanotechnology*, 2006, 17, 4695–4698.
- 135 H. Han, T. Song, E. K. Lee, A. Devadoss, Y. Jeon, J. Ha, Y. C. Chung, Y. M. Choi, Y. G. Jung and U. Paik, *ACS Nano*, 2012, 6, 8308–8315.
- 136 F. Riboni, N. T. Nguyen, S. So and P. Schmuki, *Nanoscale Horiz.*, 2016, 1, 445–466.
- 137 H. E. Prakasam, O. K. Varghese, M. Paulose, G. K. Mor and C. A. Grimes, *Nanotechnology*, 2006, 17, 4285–4291.
- 138 L. Wang, C.-Y. Lee, R. Kirchgeorg, N. Liu, K. Lee, Š. Kment, Z. Hubička, J. Krýsa, J. Olejníček, M. Čada, R. Zbořil and P. Schmuki, *Res. Chem. Intermed.*, 2015, 41, 9333–9341.
- 139 S. P. Albu, A. Ghicov, J. M. Macak and P. Schmuki, *Phys. Status Solidi RRL*, 2007, 1, R65–R67.
- 140 J. M. Macak, H. Tsuchiya, L. Taveira, S. Aldabergerova and P. Schmuki, *Angew. Chem., Int. Ed.*, 2005, 44, 7463–7465.
- 141 J. M. Macak, H. Tsuchiya, A. Ghicov, K. Yasuda, R. Hahn, S. Bauer and P. Schmuki, *Curr. Opin. Solid State Mater. Sci.*, 2007, 11, 3–18.
- 142 T. Ruff, R. Hahn and P. Schmuki, *Appl. Surf. Sci.*, 2011, 257, 8177–8181.
- 143 T. J. Latempa, X. Feng, M. Paulose, C. A. Grimes, V. Uni, U. V. Park and V. Pennsylv, *J. Phys. Chem. C*, 2009, 113, 16293–16298.
- 144 S. So, K. Lee and P. Schmuki, *J. Am. Chem. Soc.*, 2012, 134, 11316–11318.
- 145 D. H. Reneker and I. Chun, *Nanotechnology*, 1996, 7, 216–223.
- 146 M. Bognitzki, H. Q. Hou, M. Ishaque, T. Frese, M. Hellwig, C. Schwarte, A. Schaper, J. H. Wendorff and A. Greiner, *Adv. Mater.*, 2000, 12, 637–640.
- 147 D. Li and Y. Xia, *Nano Lett.*, 2004, 4, 933–938.
- 148 K. Nakane, N. Shimada, T. Ogihara, N. Ogata and S. Yamaguchi, *J. Mater. Sci.*, 2007, 42, 4031–4035.
- 149 S. Chaudhari and M. Srinivasan, *J. Mater. Chem.*, 2012, 22, 23049–23056.
- 150 N. Saveh-Shemshaki, M. Latifi, R. Bagherzadeh, M. Malekshahi Byranvand, N. Naseri and A. Dabirian, *Polym. Adv. Technol.*, 2016, 27, 358–365.
- 151 M. Bognitzki, W. Czado, T. Frese, A. Schaper, M. Hellwig, M. Steinhart, A. Greiner and J. H. Wendorff, *Adv. Mater.*, 2001, 13, 70–72.
- 152 R. Asahi, T. Morikawa, T. Ohwaki, K. Aoki and Y. Taga, *Science*, 2001, 293, 269–271.
- 153 J. Wang, D. N. Tafen, J. P. Lewis, Z. Hong, A. Manivannan, M. Zhi, M. Li and N. Wu, *J. Am. Chem. Soc.*, 2009, 131, 12290–12297.
- 154 A. Ghicov, J. M. Macak, H. Tsuchiya, J. Kunze, V. Haeublein, L. Frey and P. Schmuki, *Nano Lett.*, 2006, 6, 1080–1082.
- 155 X. Zhou, V. Häublein, N. Liu, N. T. Nguyen, E. M. Zolnhofer, H. Tsuchiya, M. S. Killian, K. Meyer, L. Frey and P. Schmuki, *Angew. Chem., Int. Ed.*, 2016, 55, 3763–3767.
- 156 D. Kim, S. Fujimoto, P. Schmuki and H. Tsuchiya, *Electrochem. Commun.*, 2008, 10, 910–913.
- 157 S. Liu, L. Yang, S. Xu, S. Luo and Q. Cai, *Electrochem. Commun.*, 2009, 11, 1748–1751.
- 158 C. S. Enache, J. Schoonman and R. Van De Krol, *J. Electroceram.*, 2004, 13, 177–182.
- 159 J. H. Park, S. Kim and A. J. Bard, *Nano Lett.*, 2006, 6, 24–28.
- 160 W. J. Yin, H. Tang, S. H. Wei, M. M. Al-Jassim, J. Turner and Y. Yan, *Phys. Rev. B: Condens. Matter Mater. Phys.*, 2010, 82, 045106.

- 161 M. Anpo and M. Takeuchi, *J. Catal.*, 2003, **216**, 505–516.
- 162 A. B. Murphy, *Sol. Energy Mater. Sol. Cells*, 2008, **92**, 363–367.
- 163 P. Triggs and F. Lévy, *Phys. Status Solidi*, 1985, **129**, 363–374.
- 164 D. Morris, Y. Dou, J. Rebane, C. E. J. Mitchell, R. G. Egddell, D. S. L. Law, A. Vittadini and M. Casarin, *Phys. Rev. B: Condens. Matter Mater. Phys.*, 2000, **61**, 13445–13457.
- 165 Y. Furubayashi, T. Hitosugi, Y. Yamamoto, K. Inaba, G. Kinoda, Y. Hirose, T. Shimada and T. Hasegawa, *Appl. Phys. Lett.*, 2005, **86**, 1–3.
- 166 A. Ghicov, S. P. Albu, R. Hahn, D. Kim, T. Stergiopoulos, J. Kunze, C. A. Schiller, P. Falaras and P. Schmuki, *Chem. – Asian J.*, 2009, **4**, 520–525.
- 167 P. Roy, D. Kim, K. Lee, E. Spiecker and P. Schmuki, *Nanoscale*, 2010, **2**, 45–59.
- 168 J. Yu and B. Wang, *Appl. Catal., B*, 2010, **94**, 295–302.
- 169 D. A. H. Hanaor and C. C. Sorrell, *J. Mater. Sci.*, 2011, **46**, 855–874.
- 170 S. Bauer, A. Pittrof, H. Tsuchiya and P. Schmuki, *Electrochem. Commun.*, 2011, **13**, 538–541.
- 171 J. B. Goodenough, *Prog. Solid State Chem.*, 1971, **5**, 145–399.
- 172 R. Shinar and J. H. Kennedy, *Sol. Energy Mater. Sol. Cells*, 1982, **6**, 323–335.
- 173 F. Amano, B. Ohtani and H. Yoshida, *J. Electroanal. Chem.*, 2016, **766**, 100–106.
- 174 J. C. Launay and G. Horowitz, *J. Cryst. Growth*, 1982, **57**, 118–124.
- 175 N. Lewis, *Annu. Rev. Phys. Chem.*, 1991, **42**, 543–580.
- 176 D. Philip Colombo, K. a. Roussel, J. Saeh, D. E. Skinner, J. J. Cavaleri and R. M. Bowman, *Chem. Phys. Lett.*, 1995, **232**, 207–214.
- 177 D. P. Colombo and R. M. Bowman, *J. Phys. Chem.*, 1995, **99**, 11752–11756.
- 178 I. Paramasivam, H. Jha, N. Liu and P. Schmuki, *Small*, 2012, **8**, 3073–3103.
- 179 C. X. Kronawitter, L. Vayssieres, S. Shen, L. Guo, D. A. Wheeler, J. Z. Zhang, B. R. Antoun and S. S. Mao, *Energy Environ. Sci.*, 2011, **4**, 3889.
- 180 Y. Wang, T. Yu, X. Chen, H. Zhang, S. Ouyang, Z. Li, J. Ye and Z. Zou, *J. Phys. D: Appl. Phys.*, 2007, **40**, 3925–3930.
- 181 J. Zhang, J. H. Bang, C. Tang and P. V. Kamat, *ACS Nano*, 2010, **4**, 387–395.
- 182 K. J. McDonald and K.-S. Choi, *Chem. Mater.*, 2011, **23**, 4863–4869.
- 183 W. Smith, A. Wolcott, R. C. Fitzmorris, J. Z. Zhang and Y. P. Zhao, *J. Mater. Chem.*, 2011, **21**, 10792–10800.
- 184 R. Li, Q. Li, L. Zong, X. Wang and J. Yang, *Electrochim. Acta*, 2013, **91**, 30–35.
- 185 S. Hernández, V. Cauda, A. Chiodoni, S. Dallorto, A. Sacco, D. Hidalgo, E. Celasco and C. F. Pirri, *ACS Appl. Mater. Interfaces*, 2014, **6**, 12153–12167.
- 186 J.-R. Huang, X. Tan, T. Yu, L. Zhao, S. Xue and W.-L. Hu, *J. Mater. Chem. A*, 2014, **2**, 9975.
- 187 Z. Jiao, Y. Zhang, T. Chen, Q. Dong, G. Lu and Y. Bi, *Chem. – Eur. J.*, 2014, **20**, 2654–2662.
- 188 Y.-K. Hsu, Y.-C. Chen and Y.-G. Lin, *ACS Appl. Mater. Interfaces*, 2015, **7**, 14157–14162.
- 189 Y.-P. P. Yuan, L.-W. W. Ruan, J. Barber, S. C. Joachim Loo, C. Xue, S. C. J. Loo and C. Xue, *Energy Environ. Sci.*, 2014, **7**, 3934–3951.
- 190 X. Li, J. G. Yu, J. X. Low, Y. P. Fang, J. Xiao and X. B. Chen, *J. Mater. Chem. A*, 2015, **3**, 2485–2534.
- 191 D. Merki and X. Hu, *Energy Environ. Sci.*, 2011, **4**, 3878.
- 192 J. D. Benck, T. R. Hellstern, J. Kibsgaard, P. Chakthranont and T. F. Jaramillo, *ACS Catal.*, 2014, **4**, 3957–3971.
- 193 A. Kay, I. Cesar and M. Grätzel, *J. Am. Chem. Soc.*, 2006, **128**, 15714–15721.
- 194 M. W. Kanan and D. G. Nocera, *Science*, 2008, **321**, 1072–1075.
- 195 M. Gong, Y. Li, H. Wang, Y. Liang, J. Z. Wu, J. Zhou, J. Wang, T. Regier, F. Wei and H. Dai, *J. Am. Chem. Soc.*, 2013, **135**, 8452–8455.
- 196 C. G. Morales-Guio, M. T. Mayer, A. Yella, S. D. Tilley, M. Grätzel and X. Hu, *J. Am. Chem. Soc.*, 2015, **137**, 9927–9936.
- 197 X. Chen, L. Liu, P. Y. Yu and S. S. Mao, *Science*, 2011, **331**, 746–750.
- 198 F. Zuo, L. Wang, T. Wu, Z. Zhang, D. Borchardt and P. Feng, *J. Am. Chem. Soc.*, 2010, **132**, 11856–11857.
- 199 S. Hoang, S. P. Berglund, N. T. Hahn, A. J. Bard and C. B. Mullins, *J. Am. Chem. Soc.*, 2012, **134**, 3659–3662.
- 200 A. Naldoni, M. Allieta, S. Santangelo, M. Marelli, F. Fabbri, S. Cappelli, C. L. Bianchi, R. Psaro and V. Dal Santo, *J. Am. Chem. Soc.*, 2012, **134**, 7600–7603.
- 201 U. Diebold, *Surf. Sci. Rep.*, 2003, **48**, 53–229.
- 202 N. Liu, C. Schneider, D. Freitag, U. Venkatesan, V. R. R. Marthala, M. Hartmann, B. Winter, E. Spiecker, A. Osvet, E. M. Zolnhofer, K. Meyer, T. Nakajima, X. Zhou and P. Schmuki, *Angew. Chem., Int. Ed.*, 2014, **53**, 14201–14205.
- 203 N. Liu, C. Schneider, D. Freitag, M. Hartmann, U. Venkatesan, J. Müller, E. Spiecker and P. Schmuki, *Nano Lett.*, 2014, **14**, 3309–3313.
- 204 N. Liu, V. Häublein, X. Zhou, U. Venkatesan, M. Hartmann, M. Mackovic, T. Nakajima, E. Spiecker, A. Osvet, L. Frey and P. Schmuki, *Nano Lett.*, 2015, **15**, 6815–6820.
- 205 R. F. G. Gardner, F. Sweett and D. W. Tanner, *J. Phys. Chem. Solids*, 1963, **24**, 1183–1196.
- 206 M. Rioult, D. Stanescu, E. Fonda, A. Barbier and H. Magnan, *J. Phys. Chem. C*, 2016, **120**, 7482–7490.
- 207 D. B. Ingram and S. Linic, *J. Am. Chem. Soc.*, 2011, **133**, 5202–5205.
- 208 Z. Liu, W. Hou, P. Pavaskar, M. Aykol and S. B. Cronin, *Nano Lett.*, 2011, **11**, 1111–1116.
- 209 D. B. Ingram, P. Christopher, J. L. Bauer and S. Linic, *ACS Catal.*, 2011, **1**, 1441–1447.
- 210 S. Linic, P. Christopher and D. B. Ingram, *Nat. Mater.*, 2011, **10**, 911–921.
- 211 S. C. Warren and E. Thimsen, *Energy Environ. Sci.*, 2012, **5**, 5133–5146.
- 212 J. Li, S. K. Cushing, P. Zheng, F. Meng, D. Chu and N. Wu, *Nat. Commun.*, 2013, **4**, 2651.
- 213 W. Hou and S. B. Cronin, *Adv. Funct. Mater.*, 2013, **23**, 1612–1619.

- 214 C. Clavero, *Nat. Photonics*, 2014, **8**, 95–103.
- 215 A. Naldoni, F. Riboni, U. Guler, A. Boltasseva, V. M. Shalae and A. V. Kildishev, *Nanophotonics*, 2016, **5**, 112–133.
- 216 R. Sundararaman, P. Narang, A. S. Jermyn, W. A. Goddard III and H. A. Atwater, *Nat. Commun.*, 2014, **5**, 5788.
- 217 J. Li, S. K. Cushing, F. Meng, T. R. Senty, A. D. Bristow and N. Wu, *Nat. Photonics*, 2015, **9**, 601–607.
- 218 S. Linic, P. Christopher, H. Xin and A. Marimuthu, *Acc. Chem. Res.*, 2013, **46**, 1890–1899.
- 219 G. Zhao, H. Kozuka and T. Yoko, *Thin Solid Films*, 1996, **277**, 147–154.
- 220 Y. Tian and T. Tatsuma, *Chem. Commun.*, 2004, 1810–1811.
- 221 H. Dotan, O. Kfir, E. Sharlin, O. Blank, M. Gross, I. Dumchin, G. Ankonina and A. Rothschild, *Nat. Mater.*, 2013, **12**, 158–164.
- 222 Y. Fang, Y. Jiao, K. Xiong, R. Ogier, Z. J. Yang, S. Gao, A. B. Dahlin and M. Käll, *Nano Lett.*, 2015, **15**, 4059–4065.
- 223 J. C. Lee, T. G. Kim, H. J. Choi and Y. M. Sung, *Cryst. Growth Des.*, 2007, **7**, 2588–2593.
- 224 W. T. Sun, A. Yu, H. Y. Pan, X. F. Gao, Q. Chen and L. M. Peng, *J. Am. Chem. Soc.*, 2008, **130**, 1124–1125.
- 225 A. Kongkanand, K. Tvrđy, K. Takechi, M. Kuno and P. V. Kamat, *J. Am. Chem. Soc.*, 2008, **130**, 4007–4015.
- 226 Z. Deutsch, L. Neeman and D. Oron, *Nat. Nanotechnol.*, 2013, **8**, 649–653.
- 227 A. Teitelboim and D. Oron, *ACS Nano*, 2016, **10**, 446–452.
- 228 M. Qorbani, N. Naseri, O. Moradlou, R. Azimirad and A. Z. Moshfegh, *Appl. Catal., B*, 2015, **162**, 210–216.
- 229 K. Hola, Y. Zhang, Y. Wang, E. P. Giannelis, R. Zboril and A. L. Rogach, *Nano Today*, 2014, **9**, 590–603.
- 230 H. Liu, T. Ye and C. Mao, *Angew. Chem., Int. Ed.*, 2007, **46**, 6473–6475.
- 231 S. N. Baker and G. A. Baker, *Angew. Chem., Int. Ed.*, 2010, **49**, 6726–6744.
- 232 K. A. S. Fernando, S. Sahu, Y. Liu, W. K. Lewis, E. A. Gulians, A. Jafariyan, P. Wang, C. E. Bunker and Y. P. Sun, *ACS Appl. Mater. Interfaces*, 2015, **7**, 8363–8376.
- 233 R. M. Cornell and U. Schwertmann, *The Iron Oxides. Structure, Properties, Reactions and Uses*, Wiley-VCH, Weinheim, Germany, Weinheim, Germany, 1st edn, 1996.
- 234 J. H. Kennedy and K. W. Frese, *J. Electrochem. Soc.*, 1978, **125**, 709–714.
- 235 M. Catti, G. Valerio and R. Dovesi, *Phys. Rev. B: Condens. Matter Mater. Phys.*, 1995, **51**, 7441–7450.
- 236 W. H. Butler, A. Bandyopadhyay and R. Srinivasan, *J. Appl. Phys.*, 2003, **93**, 7882–7884.
- 237 Y. Ma, P. D. Johnson, N. Wassdahl, J. Guo, P. Skytt, J. Nordgren, S. D. Kevan, J. E. Rubensson, T. Böske and W. Eberhardt, *Phys. Rev. B: Condens. Matter Mater. Phys.*, 1993, **48**, 2109–2111.
- 238 M. P. Dare-Edwards, J. B. Goodenough, A. Hamnett and P. R. Trevellick, *J. Chem. Soc., Faraday Trans. 1*, 1983, 2027.
- 239 M. Barroso, S. R. Pendlebury, A. J. Cowan and J. R. Durrant, *Chem. Sci.*, 2013, **4**, 2724–2734.
- 240 R. K. Quinn, R. D. Nasby and R. J. Baughman, *Mater. Res. Bull.*, 1976, **11**, 1011–1017.
- 241 M. Gori, H. R. Grüniger and G. Calzaferri, *J. Appl. Electrochem.*, 1980, **10**, 345–349.
- 242 J. H. Kennedy, R. Shinar and J. P. Ziegler, *J. Electrochem. Soc.*, 1980, **127**, 2307–2309.
- 243 J. H. Kennedy, *J. Electrochem. Soc.*, 1981, **128**, 2371.
- 244 G. Horowitz, *J. Electroanal. Chem.*, 1983, **159**, 421–436.
- 245 C. Sanchez, M. Hendewerk, K. D. Sieber and G. A. Somorjai, *J. Solid State Chem.*, 1986, **61**, 47–55.
- 246 C. Sanchez, K. D. Sieber and G. A. Somorjai, *J. Electroanal. Chem.*, 1988, **252**, 269–290.
- 247 J. Y. Kim, G. Magesh, D. H. Youn, J.-W. Jang, J. Kubota, K. Domen and J. S. Lee, *Sci. Rep.*, 2013, **3**, 2681.
- 248 L. Fu, H. M. Yu, C. K. Zhang, Z. G. Shao and B. L. Yi, *Electrochim. Acta*, 2014, **136**, 363–369.
- 249 G. J. Ai, R. Mo, H. X. Li and J. X. Zhong, *Nanoscale*, 2015, **7**, 6722–6728.
- 250 D. K. Zhong, M. Cornuz, K. Sivula, M. Grätzel and D. R. Gamelin, *Energy Environ. Sci.*, 2011, **4**, 1759.
- 251 X. Zou, A. Goswami and T. Asefa, *J. Am. Chem. Soc.*, 2013, **135**, 17242–17245.
- 252 M. W. Louie and A. T. Bell, *J. Am. Chem. Soc.*, 2013, **135**, 12329–12337.
- 253 F. J. Morin, *Phys. Rev.*, 1951, **83**, 1005–1010.
- 254 F. J. Morin, *Phys. Rev.*, 1954, **93**, 1195–1199.
- 255 P. L. Liao, M. C. Toroker and E. A. Carter, *Nano Lett.*, 2011, **11**, 1775–1781.
- 256 M. A. Lukowski and S. Jin, *J. Phys. Chem. C*, 2011, **115**, 12388–12395.
- 257 P. S. Bassi, Gurudayal, L. H. Wong and J. Barber, *Phys. Chem. Chem. Phys.*, 2014, **16**, 11834–11842.
- 258 Y. Zhang, S. Jiang, W. Song, P. Zhou, H. Ji, W. Ma, W. Hao, C. Chen and J. Zhao, *Energy Environ. Sci.*, 2015, **8**, 1231–1236.
- 259 M. N. Huda, A. Walsh, Y. F. Yan, S. H. Wei and M. M. Al-Jassim, *J. Appl. Phys.*, 2010, **107**, 123712.
- 260 J. Deng, J. Zhong, A. Pu, D. Zhang, M. Li, X. Sun and S. T. Lee, *J. Appl. Phys.*, 2012, **112**, 6.
- 261 A. Pu, J. Deng, M. Li, J. Gao, H. Zhang, Y. Hao, J. Zhong and X. Sun, *J. Mater. Chem. A*, 2014, **2**, 2491.
- 262 C. X. Kronawitter, I. Zegkinoglou, S.-H. Shen, P. Liao, I. S. Cho, O. Zandi, Y.-S. Liu, K. Lashgari, G. Westin, J.-H. Guo, F. J. Himpsel, E. A. Carter, X. L. Zheng, T. W. Hamann, B. E. Koel, S. S. Mao and L. Vayssieres, *Energy Environ. Sci.*, 2014, **7**, 3100–3121.
- 263 D. Wang, H. Chen, G. Chang, X. Lin, Y. Zhang, A. Aldalbahi, C. Peng, J. Wang and C. Fan, *ACS Appl. Mater. Interfaces*, 2015, **7**, 14072–14078.
- 264 T. Wang, W. Luo, X. Wen, Z. Zou and W. Huang, *ChemNanoMat*, 2016, **2**, 652–655.
- 265 Z. Luo, C. Li, S. Liu, T. Wang and J. Gong, *Chem. Sci.*, 2017, **8**, 91–100.
- 266 Y. Fu, C.-L. Dong, Z. Zhou, W.-Y. Lee, J. Chen, P. Guo, L. Zhao and S. Shen, *Phys. Chem. Chem. Phys.*, 2016, **18**, 3846–3853.
- 267 Y. Fu, C.-L. Dong, W.-Y. Lee, J. Chen, P. Guo, L. Zhao and S. Shen, *ChemNanoMat*, 2016, **2**, 704–711.

- 268 J. Huang, G. Hu, Y. Ding, M. Pang and B. Ma, *J. Catal.*, 2016, **340**, 261–269.
- 269 Gurudayal, S. Y. Chiam, M. H. Kumar, P. S. Bassi, H. L. Seng, J. Barber and L. H. Wong, *ACS Appl. Mater. Interfaces*, 2014, **6**, 5852–5859.
- 270 Gurudayal, D. Sabba, M. H. Kumar, L. H. Wong, J. Barber, M. Grätzel and N. Mathews, *Nano Lett.*, 2015, **15**, 3833–3839.
- 271 X. L. Guo, L. L. Wang and Y. W. Tan, *Nano Energy*, 2015, **16**, 320–328.
- 272 A. Annamalai, A. Subramanian, U. Kang, H. Park, S. H. Choi and J. S. Jang, *J. Phys. Chem. C*, 2015, **119**, 3810–3817.
- 273 J. Krýsa, M. Zlámal, Š. Paušová, T. Kotrla, Š. Kment and Z. Hubička, *Catal. Today*, 2016, DOI: 10.1016/j.cattod.2016.12.022.
- 274 J. Brilllet, M. Grätzel and K. Sivula, *Nano Lett.*, 2010, **10**, 4155–4160.
- 275 J. Y. Kim, D. H. Youn, J. H. Kim, H. G. Kim and J. S. Lee, *ACS Appl. Mater. Interfaces*, 2015, **7**, 14123–14129.
- 276 C. Y. Lee, L. Wang, Y. Kado, R. Kirchgeorg and P. Schmuki, *Electrochem. Commun.*, 2013, **34**, 308–311.
- 277 K. Chitrada, K. S. Raja, D. Rodriguez and D. Chidambaram, *J. Electrochem. Soc.*, 2015, **162**, H220–H228.
- 278 A. Annamalai, H. H. Lee, S. H. Choi, S. Y. Lee, E. Gracia-Espino, A. Subramanian, J. Park, K. Kong and J. S. Jang, *Sci. Rep.*, 2016, **6**, 23183.
- 279 L. Wang, C. Y. Lee and P. Schmuki, *Electrochem. Commun.*, 2013, **30**, 21–25.
- 280 A. Kaouk, T.-P. Ruoko, M. Pyeon, Y. Gönüllü, K. Kaunisto, H. Lemmetyinen and S. Mathur, *J. Phys. Chem. C*, 2016, **120**, 28345–28353.
- 281 M. Zhang, W. Luo, Z. Li, T. Yu and Z. Zou, *Appl. Phys. Lett.*, 2010, **97**, 42105.
- 282 H. Pan, X. Meng, D. Liu, S. Li and G. Qin, *Phys. Chem. Chem. Phys.*, 2015, **17**, 22179–22186.
- 283 X. Qi, G. She, M. Wang, L. Mu and W. Shi, *Chem. Commun.*, 2013, **49**, 5742–5744.
- 284 S. D. Tilley, M. Cornuz, K. Sivula and M. Graetzel, *Angew. Chem., Int. Ed.*, 2010, **49**, 6405–6408.
- 285 L. Badia-Bou, E. Mas-Marza, P. Rodenas, E. M. Barea, F. Fabregat-Santiago, S. Gimenez, E. Peris and J. Bisquert, *J. Phys. Chem. C*, 2013, **117**, 3826–3833.
- 286 B. Klahr, S. Gimenez, F. Fabregat-Santiago, J. Bisquert and T. W. Hamann, *J. Am. Chem. Soc.*, 2012, **134**, 16693–16700.
- 287 M. Barroso, A. J. Cowan, S. R. Pendlebury, M. Gratzel, D. R. Klug and J. R. Durrant, *J. Am. Chem. Soc.*, 2011, **133**, 14868–14871.
- 288 M. W. Kanan, Y. Surendranath and D. G. Nocera, *Chem. Soc. Rev.*, 2009, **38**, 109–114.
- 289 D. Friebel, M. W. Louie, M. Bajdich, K. E. Sanwald, Y. Cai, A. M. Wise, M.-J. Cheng, D. Sokaras, T.-C. Weng, R. Alonso-Mori, R. C. Davis, J. R. Bargar, J. K. Norskov, A. Nilsson and A. T. Bell, *J. Am. Chem. Soc.*, 2015, **137**, 1305–1313.
- 290 J.-W. Jang, C. Du, Y. Ye, Y. Lin, X. Yao, J. Thorne, E. Liu, G. McMahon, J. Zhu, A. Javey, J. Guo and D. Wang, *Nat. Commun.*, 2015, **6**, 7447.
- 291 D. H. Youn, Y. Bin Park, J. Y. Kim, G. Magesh, Y. J. Jang and J. S. Lee, *J. Power Sources*, 2015, **294**, 437–443.
- 292 D. Xu, Y. Rui, Y. Li, Q. Zhang and H. Wang, *Appl. Surf. Sci.*, 2015, **358**, 436–442.
- 293 F. Malara, A. Minguzzi, M. Marelli, S. Morandi, R. Psaro, V. Dal Santo and A. Naldoni, *ACS Catal.*, 2015, **5**, 5292–53000.
- 294 W. D. Chemelewski, H.-C. Lee, J.-F. Lin, A. J. Bard and C. B. Mullins, *J. Am. Chem. Soc.*, 2014, **136**, 2843–2850.
- 295 K. Fan, F. Li, L. Wang, Q. Daniel, H. Chen, E. Gabrielsson, J. Sun and L. Sun, *ChemSusChem*, 2015, **8**, 3242–3247.
- 296 F. Li, K. Fan, L. Wang, Q. Daniel, L. Duan and L. Sun, *ACS Catal.*, 2015, **5**, 3786–3790.
- 297 J. Y. Kim, J. W. Jang, D. H. Youn, G. Magesh and J. S. Lee, *Adv. Energy Mater.*, 2014, **4**, 14004761.
- 298 Y. Yang, M. Forster, Y. Ling, G. Wang, T. Zhai, Y. Tong, A. J. Cowan and Y. Li, *Angew. Chem., Int. Ed.*, 2016, **55**, 3403–3407.
- 299 I. Thomann, B. A. Pinaud, Z. B. Chen, B. M. Clemens, T. F. Jaramillo and M. L. Brongersma, *Nano Lett.*, 2011, **11**, 3440–3446.
- 300 B. Kong, J. Tang, C. Selomulya, W. Li, J. Wei, Y. Fang, Y. Wang, G. Zheng and D. Zhao, *J. Am. Chem. Soc.*, 2014, **136**, 6822–6825.
- 301 H. Gao, C. Liu, H. E. Jeong and P. Yang, *ACS Nano*, 2012, **6**, 234–240.
- 302 S. Ramadurgam, T. G. Lin and C. Yang, *Nano Lett.*, 2014, **14**, 4517–4522.
- 303 X. Wang, K. Q. Peng, Y. Hu, F. Q. Zhang, B. Hu, L. Li, M. Wang, X. M. Meng and S. T. Lee, *Nano Lett.*, 2014, **14**, 18–23.
- 304 P. Peerakiathajohn, J. H. Yun, H. Chen, M. Lyu, T. Butburee and L. Wang, *Adv. Mater.*, 2016, 6405–6410.
- 305 Y. Hou, F. Zuo, A. Dagg and P. Y. Feng, *Nano Lett.*, 2012, **12**, 6464–6473.
- 306 P. Zhang, T. Wang, X. X. Chang, L. Zhang and J. L. Gong, *Angew. Chem., Int. Ed.*, 2016, **55**, 5851–5855.
- 307 M. T. Mayer, C. Du and D. Wang, *J. Am. Chem. Soc.*, 2012, **134**, 12406–12409.
- 308 Z. Luo, C. Li, D. Zhang, T. Wang and J. Gong, *Chem. Commun.*, 2016, **52**, 9013–9015.
- 309 Y. Hou, F. Zuo, A. Dagg and P. Y. Feng, *Angew. Chem., Int. Ed.*, 2013, **52**, 1248–1252.
- 310 S. Shen, J. Zhou, C.-L. Dong, Y. Hu, E. N. Tseng, P. Guo, L. Guo and S. S. Mao, *Sci. Rep.*, 2014, **4**, 6627.
- 311 A. Mao, G. Y. Han and J. H. Park, *J. Mater. Chem.*, 2010, **20**, 2247.
- 312 Z. Zhang, C. Gao, Y. Li, W. Han, W. Fu, Y. He and E. Xie, *Nano Energy*, 2016, **30**, 892–899.
- 313 J. Li, Y. Qiu, Z. Wei, Q. Lin, Q. Zhang, K. Yan, H. Chen, S. Xiao, Z. Fan and S. Yang, *Energy Environ. Sci.*, 2014, **7**, 3651–3658.
- 314 Y. Sun, W. D. Chemelewski, S. P. Berglund, C. Li, H. He, G. Shi and C. B. Mullins, *ACS Appl. Mater. Interfaces*, 2014, **6**, 5494–5499.
- 315 I. Kondofersky, H. K. Dunn, A. Müller, B. Mandlmeier, J. M. Feckl, D. Fattakhova-Rohlfing, C. Scheu, L. M. Peter

- and T. Bein, *ACS Appl. Mater. Interfaces*, 2015, **7**, 4623–4630.
- 316 Y.-F. Xu, H.-S. Rao, B.-X. Chen, Y. Lin, H.-Y. Chen, D.-B. Kuang and C.-Y. Su, *Adv. Sci.*, 2015, **2**, 1500049.
- 317 K. X. Wang, Z. Yu, V. Liu, M. L. Brongersma, T. F. Jaramillo and S. Fan, *ACS Photonics*, 2014, **1**, 235–240.
- 318 A. Mettenboerger, T. Singh, A. P. Singh, T. T. Jaervi, M. Moseler, M. Valldor and S. Mathur, *Int. J. Hydrogen Energy*, 2014, **39**, 4828–4835.
- 319 M. Forster, R. J. Potter, Y. Ling, Y. Yang, D. R. Klug, Y. Li and A. J. Cowan, *Chem. Sci.*, 2015, **6**, 4009–4016.
- 320 M. T. Nguyen, S. Piccinin, N. Seriani and R. Gebauer, *ACS Catal.*, 2015, **5**, 715–721.
- 321 J. Moir, N. Soheilnia, K. Liao, P. O'Brien, Y. Tian, K. S. Burch and G. A. Ozin, *ChemSusChem*, 2015, **8**, 1557–1567.
- 322 Y. Ling, G. Wang, J. Reddy, C. Wang, J. Z. Zhang and Y. Li, *Angew. Chem., Int. Ed.*, 2012, **51**, 4074–4079.
- 323 Y. Ling, G. Wang, H. Wang, Y. Yang and Y. Li, *ChemSusChem*, 2014, **7**, 848–853.
- 324 R. Morrish, M. Rahman, J. M. D. MacElroy and C. A. Wolden, *ChemSusChem*, 2011, **4**, 474–479.
- 325 D. Wang, Y. Zhang, C. Peng, J. Wang, Q. Huang, S. Su, L. Wang, W. Huang and C. Fan, *Adv. Sci.*, 2015, **2**, 15000051.
- 326 I. S. Cho, H. S. Han, M. Logar, J. Park and X. Zheng, *Adv. Energy Mater.*, 2016, **6**, 1501840.
- 327 A. Fujishima, X. Zhang and D. A. Tryk, *Surf. Sci. Rep.*, 2008, **63**, 515–582.
- 328 K. Zhu, N. R. Neale, A. F. Halverson, J. Y. Kim and A. J. Frank, *J. Phys. Chem. C*, 2010, **114**, 13433–13441.
- 329 S. So, I. Hwang, F. Riboni, J. E. Yoo and P. Schmuki, *Electrochem. Commun.*, 2016, **71**, 73–78.
- 330 J. K. Burdett, T. Hughbanks, G. J. Miller, J. W. Richardson and J. V. Smith, *J. Am. Chem. Soc.*, 1987, **109**, 3639–3646.
- 331 M. D. Earle, *Phys. Rev.*, 1942, **61**, 56–62.
- 332 H. Tang, K. Prasad, R. Sanjinès, P. E. Schmid, F. Lévy, R. Sanjines, P. E. Schmid and F. Levy, *J. Appl. Phys.*, 1994, **75**, 2042–2047.
- 333 L. Forro, O. Chauvet, D. Emin, L. Zuppiroli, H. Berger and F. Lévy, *J. Appl. Phys.*, 1994, **75**, 633–635.
- 334 J. Yu, G. Dai and B. Cheng, *J. Phys. Chem. C*, 2010, **114**, 19378–19385.
- 335 S. So and P. Schmuki, *Angew. Chem., Int. Ed.*, 2013, **52**, 7933–7935.
- 336 L. Kavan, M. Grätzel, S. E. Gilbert, C. Klemenž and H. J. Scheel, *J. Am. Chem. Soc.*, 1996, **118**, 6716–6723.
- 337 T. Kawahara, Y. Konishi, H. Tada, N. Tohge, J. Nishii and S. Ito, *Angew. Chem., Int. Ed.*, 2002, **41**, 2811–2813.
- 338 P. J. Boddy, *J. Electrochem. Soc.*, 1968, **115**, 199–203.
- 339 S. Sato, *Chem. Phys. Lett.*, 1986, **123**, 126–128.
- 340 M. Anpo, *Catal. Surv. Jpn.*, 1997, **1**, 169–179.
- 341 A. Ghicov, J. M. Macak, H. Tsuchiya, J. Kunze, V. Haeublein, S. Kleber and P. Schmuki, *Chem. Phys. Lett.*, 2006, **419**, 426–429.
- 342 A. Ghicov, B. Schmidt, J. Kunze and P. Schmuki, *Chem. Phys. Lett.*, 2007, **433**, 323–326.
- 343 K. Lee and P. Schmuki, *Electrochem. Commun.*, 2012, **25**, 11–14.
- 344 C. Wang, Z. Chen, H. Jin, C. Cao, J. Li and Z. Mi, *J. Mater. Chem. A*, 2014, **2**, 17820–17827.
- 345 B. Liu, H. M. Chen, C. Liu, S. C. Andrews, C. Hahn and P. Yang, *J. Am. Chem. Soc.*, 2013, **135**, 9995–9998.
- 346 Y. C. Nah, N. K. Shrestha, D. Kim and P. Schmuki, *J. Appl. Electrochem.*, 2013, **43**, 9–13.
- 347 J. Tian, Z. Zhao, A. Kumar, R. I. Boughton and H. Liu, *Chem. Soc. Rev.*, 2014, **43**, 6920–6937.
- 348 M. Ge, C. Cao, J. Huang, S. Li, Z. Chen, K.-Q. Zhang, S. S. Al-deyab and Y. Lai, *J. Mater. Chem. A*, 2016, **4**, 6772–6801.
- 349 R. P. Lynch, A. Ghicov and P. Schmuki, *J. Electrochem. Soc.*, 2010, **157**, G76.
- 350 J. J. Kelly and D. Vanmaekelbergh, *Electrochim. Acta*, 1998, **43**, 2773–2780.
- 351 R. Beranek, H. Tsuchiya, T. Sugishima, J. M. Macak, L. Taveira, S. Fujimoto, H. Kisch and P. Schmuki, *Appl. Phys. Lett.*, 2005, **87**, 1–3.
- 352 A. Mazzarolo, K. Lee, A. Vicenzo and P. Schmuki, *Electrochem. Commun.*, 2012, **22**, 162–165.
- 353 S. U. M. Khan and T. Sultana, *Sol. Energy Mater. Sol. Cells*, 2003, **76**, 211–221.
- 354 M. G. Mali, S. An, M. Liou, S. S. Al-Deyab and S. S. Yoon, *Appl. Surf. Sci.*, 2015, **328**, 109–114.
- 355 H. Tang, K. Prasad, R. Sanjinès, P. E. Schmid and F. Lévy, *J. Appl. Phys.*, 1994, **75**, 2042–2047.
- 356 F. Mohammadpour, M. Moradi, K. Lee, G. Cha, S. So, A. Kahnt, D. M. Guldi, M. Altomare and P. Schmuki, *Chem. Commun.*, 2015, **51**, 1631–1634.
- 357 S. Ozkan, A. Mazare and P. Schmuki, *Electrochim. Acta*, 2015, **176**, 819–826.
- 358 B. Liu and E. S. Aydil, *J. Am. Chem. Soc.*, 2009, **131**, 3985–3990.
- 359 M. Abd-Lefdil, R. Diaz, H. Bihri, M. Ait Aouaj and F. Rueda, *Eur. Phys. J.: Appl. Phys.*, 2007, **38**, 217–219.
- 360 X. J. Feng, K. Shankar, O. K. Varghese, M. Paulose, T. J. Latempa and C. A. Grimes, *Nano Lett.*, 2008, **8**, 3781–3786.
- 361 Y. J. Hwang, C. Hahn, B. Bin Liu and P. Yang, *ACS Nano*, 2012, **6**, 5060–5069.
- 362 I. S. Cho, Z. Chen, A. J. Forman, D. R. Kim, P. M. Rao, T. F. Jaramillo and X. Zheng, *Nano Lett.*, 2011, **11**, 4978–4984.
- 363 P. Deák, J. Kullgren, B. Aradi, T. Frauenheim and L. Kavan, *Electrochim. Acta*, 2016, **199**, 27–34.
- 364 P. Roy, C. Das, K. Lee, R. Hahn, T. Ruff, M. Moll and P. Schmuki, *J. Am. Chem. Soc.*, 2011, **133**, 5629–5631.
- 365 X. Zhang, B. Zhang, Z. Zuo, M. Wang and Y. Shen, *J. Mater. Chem. A*, 2015, **3**, 10020–10025.
- 366 H. Wu and Z. Zhang, *Int. J. Hydrogen Energy*, 2011, **36**, 13481–13487.
- 367 L. Sun, J. Cai, Q. Wu, P. Huang, Y. Su and C. Lin, *Electrochim. Acta*, 2013, **108**, 525–531.
- 368 S. M. Prokes, J. L. Gole, X. Chen, C. Burda and W. E. Carlos, *Adv. Funct. Mater.*, 2005, **15**, 161–167.

- 369 R. Beranek and H. Kisch, *Electrochem. Commun.*, 2007, **9**, 761–766.
- 370 R. Beranek and H. Kisch, *Photochem. Photobiol. Sci.*, 2008, **7**, 40–48.
- 371 S. Hejazi, N. T. Nguyen, A. Mazare and P. Schmuki, *Catal. Today*, 2017, **281**, 189–197.
- 372 C. Di Valentin, G. Pacchioni and A. Selloni, *Chem. Mater.*, 2005, **17**, 6656–6665.
- 373 R. Hahn, F. Schmidt-Stein, J. Sahnén, S. Thiemann, Y. Song, J. Kunze, V. P. Lehto and P. Schmuki, *Angew. Chem., Int. Ed.*, 2009, **48**, 7236–7239.
- 374 F. Schmidt-Stein, S. Thiemann, S. Berger, R. Hahn and P. Schmuki, *Acta Mater.*, 2010, **58**, 6317–6323.
- 375 W. Q. Fang, X. L. Wang, H. Zhang, Y. Jia, Z. Huo, Z. Li, H. Zhao, H. G. Yang and X. Yao, *J. Mater. Chem. A*, 2014, **2**, 3513–3520.
- 376 W. Q. I. Fang, Z. Huo, P. Liu, X. L. U. Wang, M. Zhang, Y. Jia, H. Zhang, H. Zhao, H. G. U. Yang and X. Yao, *Chem. – Eur. J.*, 2014, **20**, 11439–11444.
- 377 S. B. Aldabergenova, A. Ghicov, S. Albu, J. M. Macak and P. Schmuki, *J. Non-Cryst. Solids*, 2008, **354**, 2190–2194.
- 378 W. Wei, S. Berger, N. Shrestha and P. Schmuki, *J. Electrochem. Soc.*, 2010, **157**, C409.
- 379 M. Yang, D. Kim, H. Jha, K. Lee, J. Paul and P. Schmuki, *Chem. Commun.*, 2011, **47**, 2032–2034.
- 380 Y. Yang, D. Kim, M. Yang and P. Schmuki, *Chem. Commun.*, 2011, **47**, 7746–7748.
- 381 M. Yang, H. Jha, N. Liu and P. Schmuki, *J. Mater. Chem.*, 2011, **21**, 15205–15208.
- 382 C. Das, P. Roy, M. Yang, H. Jha and P. Schmuki, *Nanoscale*, 2011, **3**, 3094–3096.
- 383 M. Altomare, K. Lee, M. S. Killian, E. Selli and P. Schmuki, *Chem. – Eur. J.*, 2013, **19**, 5841–5844.
- 384 T. Mishra, L. Wang, R. Hahn and P. Schmuki, *Electrochim. Acta*, 2014, **132**, 410–415.
- 385 J. Resasco, N. P. Dasgupta, J. R. Rosell, J. Guo and P. Yang, *J. Am. Chem. Soc.*, 2014, **136**, 10521–10526.
- 386 J. Sasaki, N. L. Peterson and K. Hoshino, *J. Phys. Chem. Solids*, 1985, **46**, 1267–1283.
- 387 W. H. Leng, Z. Zhang, J. Q. Zhang and C. N. Cao, *J. Phys. Chem. B*, 2005, **109**, 15008–15023.
- 388 G. Yun, G. Y. Song, B. E. Ahn, S. K. Lee, J. Heo, K. S. Ahn and S. H. Kang, *Appl. Surf. Sci.*, 2016, **366**, 561–566.
- 389 L. Li, L. Duan, Y. Xu, M. Gorlov, A. Hagfeldt and L. Sun, *Chem. Commun.*, 2010, **46**, 7307–7309.
- 390 L. Wang, L. Duan, Y. Wang, M. S. G. Ahlquist and L. Sun, *Chem. Commun.*, 2014, **50**, 12947–12950.
- 391 Y. Gao, X. Ding, J. Liu, L. Wang, Z. Lu, L. Li and L. Sun, *J. Am. Chem. Soc.*, 2013, **135**, 4219–4222.
- 392 Y. Gao, L. Zhang, X. Ding and L. Sun, *Phys. Chem. Chem. Phys.*, 2014, **16**, 12008–12013.
- 393 J. Li, Y. Jiang, Q. Zhang, X. Zhao, N. Li, H. Tong, X. Yang and L. Xia, *RSC Adv.*, 2017, **7**, 4102–4107.
- 394 F. Su, T. Wang, R. Lv, J. Zhang, P. Zhang, J. Lu and J. Gong, *Nanoscale*, 2013, **5**, 9001–9009.
- 395 Y. C. Pu, G. Wang, K. Der Chang, Y. Ling, Y. K. Lin, B. C. Fitzmorris, C. M. Liu, X. Lu, Y. Tong, J. Z. Zhang, Y. J. Hsu and Y. Li, *Nano Lett.*, 2013, **13**, 3817–3823.
- 396 K. Lee, R. Hahn and P. Schmuki, *Electrochem. Commun.*, 2014, **43**, 105–108.
- 397 K. Lee, R. Hahn, M. Altomare, E. Selli and P. Schmuki, *Adv. Mater.*, 2013, **25**, 6133–6137.
- 398 S. N. Basahel, K. Lee, R. Hahn, P. Schmuki, S. M. Bawaked and S. A. Al-Thabaiti, *Chem. Commun.*, 2014, **50**, 6123–6125.
- 399 J. E. Yoo, K. Lee, M. Altomare, E. Selli and P. Schmuki, *Angew. Chem., Int. Ed.*, 2013, **52**, 7514–7517.
- 400 N. T. Nguyen, J. Yoo, M. Altomare and P. Schmuki, *Chem. Commun.*, 2014, **50**, 9653–9656.
- 401 N. T. Nguyen, M. Altomare, J. Yoo and P. Schmuki, *Adv. Mater.*, 2015, **27**, 3208–3215.
- 402 M. Altomare, N. T. Nguyen and P. Schmuki, *Chem. Sci.*, 2016, 1–22.
- 403 H. Wang, Y. Bai, H. Zhang, Z. Zhang, J. Li and L. Guo, *J. Phys. Chem. C*, 2010, **114**, 16451–16455.
- 404 S. Cheng, W. Fu, H. Yang, L. Zhang, J. Ma, H. Zhao, M. Sun and L. Yang, *J. Phys. Chem. C*, 2012, **116**, 2615–2621.
- 405 J. Luo, L. Ma, T. He, C. F. Ng, S. Wang, H. Sun and H. J. Fan, *J. Phys. Chem. C*, 2012, **116**, 11956–11963.
- 406 N. Guijarro, T. Lana-Villarreal, I. Mora-Seró, J. Bisquert and R. Gómez, *J. Phys. Chem. C*, 2009, **113**, 4208–4214.
- 407 G. Loget, J. E. Yoo, A. Mazare, L. Wang and P. Schmuki, *Electrochem. Commun.*, 2015, **52**, 41–44.
- 408 J. Tripathy, G. Loget, M. Altomare and P. Schmuki, *J. Nanosci. Nanotechnol.*, 2016, **16**, 5353–5358.
- 409 S. Kim, G. Moon, G. Kim, U. Kang, H. Park and W. Choi, *J. Catal.*, 2017, **346**, 92–100.
- 410 H. Lee, S. M. Dellatore, W. M. Miller and P. B. Messersmith, *Science*, 2007, **318**, 426–430.
- 411 R. Li, K. Parvez, F. Hinkel, X. Feng and K. Müllen, *Angew. Chem., Int. Ed.*, 2013, **52**, 5535–5538.
- 412 C. Lim, J. Huang, S. Kim, H. Lee, H. Zeng and D. S. Hwang, *Angew. Chem., Int. Ed.*, 2016, **55**, 3342–3346.
- 413 H. J. Nam, B. Kim, M. J. Ko, M. Jin, J. M. Kim and D. Y. Jung, *Chem. – Eur. J.*, 2012, **18**, 14000–14007.
- 414 R. a. Zangmeister, T. a. Morris and M. J. Tarlov, *Langmuir*, 2013, **29**, 8619–8628.
- 415 X. Yu, H. Fan, Y. Liu, Z. Shi and Z. Jin, *Langmuir*, 2014, **30**, 5497–5505.
- 416 L. Yang, J. Kong, D. Zhou, J. M. ing Ang, S. L. ei Phua, W. A. ik Yee, H. Liu, Y. Huang and X. Lu, *Chemistry*, 2014, **20**, 7776–7783.
- 417 Y. Hou, X. Li, X. Zou, X. Quan and G. Chen, *Environ. Sci. Technol.*, 2009, **43**, 858–863.
- 418 A. Mazare, N. Liu, K. Lee, M. S. Killian and P. Schmuki, *ChemistryOpen*, 2013, **2**, 21–24.
- 419 N. K. Shrestha, M. Yang, Y. C. Nah, I. Paramasivam and P. Schmuki, *Electrochem. Commun.*, 2010, **12**, 254–257.
- 420 Z. Zhang, Y. Yuan, L. Liang, Y. Cheng, G. Shi and L. Jin, *J. Hazard. Mater.*, 2008, **158**, 517–522.
- 421 Y. Lei, G. Zhao, M. Liu, Z. Zhang, X. Tong and T. Cao, *J. Phys. Chem. C*, 2009, **113**, 19067–19076.

- 422 X. Zhao, H. Liu and J. Qu, *Appl. Surf. Sci.*, 2011, **257**, 4621–4624.
- 423 Y. J. Hwang, A. Boukai and P. Yang, *Nano Lett.*, 2009, **9**, 410–415.
- 424 Q. Liu, H. Lu, Z. Shi, F. Wu, J. Guo, K. Deng and L. Li, *ACS Appl. Mater. Interfaces*, 2014, **6**, 17200–17207.
- 425 Z. Wu, C. Gong, J. Yu, L. Sun, W. Xiao and C. Lin, *J. Mater. Chem. A*, 2017, **5**, 1292–1299.
- 426 H. Y. Chang, W. J. Tzeng and S. Y. Cheng, *Solid State Ionics*, 2009, **180**, 817–821.
- 427 K. Guo, Z. Liu, J. Han, Z. Liu, Y. Li, B. Wang, T. Cui and C. Zhou, *Phys. Chem. Chem. Phys.*, 2014, **16**, 16204–16213.
- 428 Z. Liu, K. Guo, J. Han, Y. Li, T. Cui, B. Wang, J. Ya and C. Zhou, *Small*, 2014, **10**, 3153–3161.
- 429 X. Wang, J. Xie and C. M. Li, *J. Mater. Chem. A*, 2015, **3**, 1235–1242.
- 430 E. Yablonovitch, *Phys. Rev. Lett.*, 1987, **58**, 2059–2062.
- 431 A. Arie and N. Voloch, *Laser Photonics Rev.*, 2010, **4**, 355–373.
- 432 S. Colodrero, A. Mihi, L. Häggman, M. Ocaña, G. Boschloo, A. Hagfeldt and H. Míguez, *Adv. Mater.*, 2009, **21**, 764–770.
- 433 S. Nishimura, N. Abrams, B. A. Lewis, L. I. Halaoui, T. E. Mallouk, K. D. Benkstein, J. Van de Lagemaat and A. J. Frank, *J. Am. Chem. Soc.*, 2003, **125**, 6306–6310.
- 434 C. T. Yip, H. Huang, L. Zhou, K. Xie, Y. Wang, T. Feng, J. Li and W. Y. Tam, *Adv. Mater.*, 2011, **23**, 5624–5628.
- 435 M. Guo, K. Xie, J. Lin, Z. Yong, C. T. Yip, L. Zhou, Y. Wang and H. Huang, *Energy Environ. Sci.*, 2012, **5**, 9881.
- 436 A. Al-Haddad, Z. Wang, R. Xu, H. Qi, R. Vellacheri, U. Kaiser and Y. Lei, *J. Phys. Chem. C*, 2015, **119**, 16331–16337.
- 437 H. Zhao, W. Fu, H. Yang, Y. Xu, W. Zhao, Y. Zhang, H. Chen, Q. Jing, X. Qi, J. Cao, X. Zhou and Y. Li, *Appl. Surf. Sci.*, 2011, **257**, 8778–8783.
- 438 T. H. Jeon, W. Choi and H. Park, *J. Phys. Chem. C*, 2011, **115**, 7134–7142.
- 439 J.-S. Yang, W.-H. Lin, C.-Y. Lin, B.-S. Wang and J.-J. Wu, *ACS Appl. Mater. Interfaces*, 2015, **7**, 13314–13321.
- 440 Q. H. Liu, J. F. He, T. Yao, Z. H. Sun, W. R. Cheng, S. He, Y. Xie, Y. H. Peng, H. Cheng, Y. F. Sun, Y. Jiang, F. C. Hu, Z. Xie, W. S. Yan, Z. Y. Pan, Z. Y. Wu and S. Q. Wei, *Nat. Commun.*, 2014, **5**, 5122.
- 441 L. Jia, J. Xie, C. Guo and C. M. Li, *RSC Adv.*, 2015, **5**, 62611–62618.
- 442 D. Monllor-Satoca, M. Bärtisch, C. Fàbrega, A. Genç, S. Hilaire, T. Andreu, J. Arbiol, M. Niederberger and J. R. Morante, *Energy Environ. Sci.*, 2015, 3242–3254.
- 443 J. J. Deng, X. X. Lv, J. Y. Liu, H. Zhang, K. Q. Nie, C. H. Hong, J. O. Wang, X. H. Sun, J. Zhong and S. T. Lee, *ACS Nano*, 2015, **9**, 5348–5356.
- 444 D. S. Ginley and M. A. Butler, *J. Appl. Phys.*, 1977, **48**, 2019–2021.
- 445 T.-P. Ruoko, K. Kaunisto, M. Bärtisch, J. Pohjola, A. Hiltunen, M. Niederberger, N. V. Tkachenko and H. J. Lemmetyinen, *J. Phys. Chem. Lett.*, 2015, **6**, 2859–2864.
- 446 P. S. Bassi, R. P. Antony, P. P. Boix, Y. Fang, J. Barber and L. H. Wong, *Nano Energy*, 2016, **22**, 310–318.
- 447 P. S. Bassi, S. Y. Chiam, Gurudayal, J. Barber and L. H. Wong, *ACS Appl. Mater. Interfaces*, 2014, **6**, 22490–22495.
- 448 L. Wang, N. T. Nguyen and P. Schmuki, *ChemSusChem*, 2016, 1–7.
- 449 C. Li, T. Wang, Z. Luo, S. Liu and J. Gong, *Small*, 2016, 3415–3422.
- 450 S. K. Mohapatra, S. E. John, S. Banerjee and M. Misra, *Chem. Mater.*, 2009, **21**, 3048–3055.
- 451 W. Cheng, J. He, Z. Sun, Y. Peng, T. Yao, Q. Liu, Y. Jiang, F. Hu, Z. Xie, B. He and S. Wei, *J. Phys. Chem. C*, 2012, **116**, 24060–24067.
- 452 V. A. N. De Carvalho, R. A. D. S. Luz, B. H. Lima, F. N. Crespilho, E. R. Leite and F. L. Souza, *J. Power Sources*, 2012, **205**, 525–529.
- 453 Z. Zhang, M. F. Hossain and T. Takahashi, *Int. J. Hydrogen Energy*, 2010, **35**, 8528–8535.
- 454 M. Liu, N. de Leon Snapp and H. Park, *Chem. Sci.*, 2011, **2**, 80–87.
- 455 J. Li, S. K. Cushing, P. Zheng, T. Senty, F. Meng, A. D. Bristow, A. Manivannan and N. Wu, *J. Am. Chem. Soc.*, 2014, **136**, 8438–8449.

Appendix [A2]

Photoelectrochemical and structural properties of TiO₂ nanotubes and nanorods grown on FTO substrate: Comparative study between electrochemical anodization and hydrothermal method used for the nanostructures fabrication

H. Kmentova, **S. Kment***, L. Wang, S. Pausova, T. Vaclavu, R. Kuzel, H. Han, Z. Hubicka, M. Zlamal, J. Olejnicek, M. Cada, J. Krysa, R. Zboril*

Catalysis Today 287, 130-136, 2017



Photoelectrochemical and structural properties of TiO₂ nanotubes and nanorods grown on FTO substrate: Comparative study between electrochemical anodization and hydrothermal method used for the nanostructures fabrication



Hana Kmentova^a, Stepan Kment^{a,*}, Lingyun Wang^a, Sarka Pausova^b, Tereza Vaclavu^{c,d}, Radomir Kuzel^d, Hyungkyu Han^a, Zdenek Hubicka^a, Martin Zlamal^b, Jiri Olejnicek^a, Martin Cada^a, Josef Krysa^b, Radek Zboril^a

^a Regional Centre of Advanced Technologies and Materials, Joint Laboratory of Optics and Department of Physical Chemistry, Faculty of Science, Palacky University, Slechtitelu 27, 783 71 Olomouc, Czechia

^b University of Chemistry and Technology, Department of Inorganic Technology, Technicka 5, 166 28 Prague, Czechia

^c Faculty of Mathematics and Physics, Charles University in Prague, Ke Karlovu 5, 121 16, Praha 2, Czechia

^d Institute of Physics ASCR, v.v.i., Na Slovance 2, 182 21, Praha 8, Czechia

ARTICLE INFO

Article history:

Received 30 June 2016

Received in revised form

30 September 2016

Accepted 23 October 2016

Available online 31 October 2016

Keywords:

1D nanostructures

Nanorods

Nanotubes

Hydrothermal method

Self-organized anodization

Photoelectrochemical water splitting

Photocurrents

Electron lifetime

ABSTRACT

Titanium dioxide in the form of one-dimensional (1D) nanostructure arrays represent widely studied morphological arrangement for light harvesting and charge transfer applications such as photocatalysis and photoelectrochemistry (PEC). Here we report a comparative structural and PEC study of variously grown 1D TiO₂ nanostructures including i) nanorod arrays prepared by a hydrothermal method (TNR), ii) nanotube arrays fabricated by a two-step hydrothermal method using a ZnO nanorod array film as a template (THNT) and finally iii) nanotubes grown by self-organized electrochemical anodization of Ti films deposited on the FTO substrate (TNT). These nanostructures are assumed to be utilized as photoanodes in PEC water splitting devices. Field-emission scanning electron microscopy (FESEM), X-ray diffraction (XRD), TEM images and UV–vis absorption spectra were used to characterize TiO₂ nanostructures. The SEM and TEM morphology images revealed that the main difference among the nanostructures grown on the FTO are the shape and diameter of the individual nanotubes/nanorods and also the array's density in the range of TNR > THNT > TNT and the degree of organization in the range of TNT > TNR > THNT. The obtained photocurrents at 0 V vs. Ag/AgCl increased in the order of THNT (110 μA cm⁻²) < TNT (185 μA cm⁻²) < TNR (630 μA cm⁻²). Extended electron lifetime and light absorption shifted to the longer wavelengths were attributed to the enhanced PEC performance of TNR.

© 2016 Elsevier B.V. All rights reserved.

1. Introduction

Titanium dioxide (TiO₂) has been dominantly used as a core material in several modern solar energy conversion approaches involving predominantly dye sensitized solar cells (DSSC) [1,2], more recently perovskite solar cells [3,4], and photoelectrochemical water splitting (PEC-WS) [5,6]. The latest represents one of the most widely investigated approach for a sustainable and environmentally friendly production of hydrogen, considered the most significant renewable energy source of the future [7]. TiO₂ has been

widely studied as the photoanode material for PEC-WS since the pioneering work by Fujishima and Honda [8] due to its highly beneficial properties such as nontoxicity, high chemical stability, resistance to photocorrosion, abundance, and low production cost [9]. However, conventional TiO₂ film photoanodes provide an insufficient surface area and electron collection efficiency, which are crucial parameters for an optimized PEC performance. Nanostructuring of photocatalysts and photoelectrodes has been recognized as a powerful strategy to dramatically improve overall solar-to-fuel conversion efficiencies [10]. In view of geometry recently 1D TiO₂ nanostructures, such as nanotubes (NTs) [11–14], nanorods (NRs) [15–17], nanowires (NWs) [18–21], etc. attracted wide interest because they provide a significant enlargement of the material surface area (simultaneously increase the number of catalytically

* Corresponding author.

E-mail address: stepan.kment@upol.cz (S. Kment).

active sites and improves the light harvesting), facilitate the electrical transport, and suppress the negative effect of short diffusion length of holes and the recombination losses. Furthermore 1D nanostructures features a number of other characteristics (e.g., size confinement, atomically curved surface, extended surface-to-volume ratio, preferential percolation pathway for enhanced charge separation/transport/collection) that are highly beneficial for aforementioned photo-electrocatalytic applications. As a direct consequence, the nanoscale effects give rise to 50%-90% PEC efficiency gain [6]. The efficiency of TiO₂ photoanodes has been even more enhanced by adding impurities to improve their electronic properties [22–24] as well as by a combination with heterogeneous partners [25,26], quantum dots [27–29], and plasmonic materials [19,30] to optically sensitize the large-band gap TiO₂. However, a research study directly comparing the performance of various unmodified 1D TiO₂ nanostructure for PECs water splitting is still missing although the high activity of pristine TiO₂ photoelectrode is the essential prerequisite for a high-performance of whole PEC-WS device. Here, we present a systematic comparing study of directly grown 1D TiO₂ nanostructures based on nanotube and nanorod arrays using two principally different fabrication methods; namely electrochemical anodization and hydrothermal procedure. Self-organizing electrochemical anodization of a metal substrate (here Ti film deposited onto FTO substrate), is often referred to as the simplest, low-cost and straightforward approach leading 1D highly-ordered NTs [31]. Under a specific set of experimental conditions (e.g., applied voltage, anodization time, electrolytic solution), nanotubular properties, such as the degree of self-organization, tube length and diameter, electronic and ionic properties can be easily controlled [32]. Similarly in case of more commonly applied hydrothermal approach the properties of 1D nanostructures (e.g. crystalline structure, morphology, length, density, and array ordering) grown can be influenced and controlled by the synthetic conditions such as concentration of the precursor solution, hydrothermal growth temperature, and reaction times [33–35]. This work refers on three different approaches to grow 1D nanostructured TiO₂ photoanodes including electrochemically anodized nanotubes and hydrothermally grown nanorods as well as nanotubes. The three nanostructured TiO₂ photoanodes were judged on the basis of physical properties such as crystalline structure, optical absorption, and surface topography. The functional properties were investigated under simulated photoelectrochemical (PEC) water splitting conditions.

2. Experimental

2.1. Preparation of 1D nanostructured TiO₂ photoanode

Chemicals: Titanium *n*-butoxide (Sigma-Aldrich, 97%) and hydrochloric acid (HCl, 37%) were used for photocatalyst preparation. Sodium hydroxide (NaOH) was used as an electrolyte. All solutions were prepared using distilled water. All the three types of TiO₂ 1D nanostructures were grown on fluorine doped tin oxide glass substrate (FTO, TCO22-7, surface resistivity: 7 Ω/sq Solaronix). Prior to the depositions the FTO substrates were ultrasonically cleaned using a mixture of acetone, isopropyl alcohol and distilled water in volume ratio of 1:1:1, respectively. After the sonication the FTO substrates were washed by DI water and dried by nitrogen flow.

2.1.1. Preparation of TiO₂ nanorod arrays by hydrothermal method (TNR)

TiO₂ nanorod arrays were prepared by hydrothermal method described by Liu et al. [36] In typical experiment, 15 mL of hydrochloric acid and 15 mL of distilled water was mixed for five

minutes. Then, 0.5 mL of titanium *n*-butoxide was added dropwise under vigorous stirring for another five minutes. Then, the as prepared clear solution and FTO substrate were placed into Teflon-liner stainless steel autoclave (50 mL) while the conductive side of FTO substrate was facing down. The hydrothermal reaction was conducted at 150 °C for 20 h. Then, the autoclave was cooled down under flowing water. The FTO substrate was rinsed with distilled water and air dried. Afterwards, the as prepared TiO₂ nanorods were annealed in air at 500 °C for 1 h with heating rate of 5 °C/min.

2.1.2. Preparation of TiO₂ nanotube arrays by hydrothermal method (THNT)

A thin ZnO seed layer was prepared on FTO glass by spin coating method with 0.02 M zinc acetate dihydrate solution at 4000 rpm for 35 s. Arrays of ZnO nanorods, which serve as sacrificial templates for the nanotubes, were grown on the seed layer by hydrothermal method at 85 °C for 10 h. 0.025 M zinc nitrate hexahydrate and 0.025 M hexamethylenetetramine were used as precursor chemicals. The synthesized ZnO nanorod arrays on the FTO were immersed in aqueous solution containing 0.075 M ammonium hexafluorotitanate and 0.2 M boric acid at room temperature for 0.5 h. In this solution, ammonium hexafluorotitanate hydrolyzed to TiO₂ on the individual ZnO nanorod while ZnO dissolved simultaneously in the solution with acids produced by ammonium hexafluorotitanate hydrolysis. Subsequently, the resulting TiO₂ nanotube arrays were immersed in a 0.5 M boric acid solution for 1 h to remove the residual ZnO inside the tubes. The arrays were finally rinsed with DI water and calcined at 500 °C for 1 h to increase crystallinity.

2.1.3. Preparation of anodized TiO₂ nanotube arrays (TNT)

Self-organized highly ordered TiO₂ nanotubes were grown by electrochemical anodization of titanium films deposited directly on FTO substrate by pulsed magnetron sputtering of pure titanium target (99.995%, Lesker). The depositions were carried out under a constant operating pressure of 0.2 Pa. The duty cycle of the pulse was 90%, the frequency was 50 kHz, and the deposition rate was 30.0 nm/min. Prior to the deposition an advanced plasma cleaning and activation of FTO substrate was performed in order to attain sufficient adhesion of the titanium film to the substrate. For this purpose the substrate holder the FTO glass substrate were treated by radio-frequency (RF) plasma using O₂/Ar working gas mixture with the pressure 10 Pa in the reactor chamber. The substrate holder worked as a RF electrode connected to the RF power supply working at frequency 13.6 MHz. The deposition process followed immediately after RF plasma treatment without interruption of vacuum in the reactor chamber. In the following procedure the magnetron sputtered titanium films on FTO glass were washed with ethanol before electrochemical anodization. TiO₂ nanotubes were grown at 50 V using a power source STATRON 3253.3 under self-organization conditions using a two-electrode configuration with the Ti films acting as the working electrode and a counter electrode made of platinum. As the electrolyte the solution of 0.2 M NH₄F + 4 M H₂O in ethylene glycol was used. The as deposited TiO₂ nanotube photoanodes were heat treated at 500 °C for 1 h in air (cylindrical furnace-Clasic CLARE 4.0) to ensure proper crystallization.

2.2. Physical characterization

X-ray diffraction was performed at two instruments-Rigaku SmartLab diffractometer and Siefert XRD7 diffractometer. The Rigaku SmartLab diffractometer is equipped with 9 kW rotation X-ray tube. The Johansson monochromator was used in primary beam in order to obtain only CuKα1 radiation. Soller slit 2.5°, 5 mm incident slit and 5 mm beam mask were placed in primary beam. Soller slits of 2.5°, 20 mm receiving slits and lin-

ear detector were in the diffracted beam. Samples were also measured with Seifert XRD7 powder diffractometer (CuK α 12 radiation primary beam slit of width 0.92 mm and height of 4 mm, receiving slit 0.15 mm, graphite monochromator and scintillation point detector). The surface and cross-section morphology images were captured by Hitachi SU6600 field-emission scanning electron microscopy (FESEM). Transmission electron microscopy (TEM) images were obtained with help of a JEOL 2010 microscopy operated at 200 kV. UV–vis absorption spectra were measured using a UV–vis spectrophotometer (Lambda 35, PerkinElmer) with BaSO₄ as a reference standard.

2.3. Evaluation of electrochemical properties

The photoelectrochemistry experiments were carried out in an electrochemical cell with three electrodes in the system. The titania-containing films served as the working electrode, the Ag/AgCl in 3 M KCl as the reference electrode and the Pt wire is used as the counter one. The size of the photoanode was limited to 0.785 cm² by an O-ring. All three electrodes were immersed in the 1 M NaOH electrolyte solution (pH = 13.5). The TiO₂ layers were illuminated by 150 W Xenon lamp coupled with AM 1.5 G filter. The power intensity was kept at 1 sun (100 mW/cm²) which was calibrated by Silicon reference cell (Newport). The Gamry Series G 300 Potentiostat was used for photoelectrochemical measurements. The PEC performance was investigated by means of three methods: linear sweep voltammetry, chronoamperometry and open circuit potential measurement. In linear sweep voltammetry tests the as prepared photoanodes were irradiated and the polarization curves were measured as the dependence of current density on the applied potential (from –400 mV to 1000 mV). The chronoamperometry tests are based on expressing of current density on time with constant potential of 600 mV. The electron/hole pair recombination can be estimated from the value of open circuit potential. These experiments started in the dark for 30 s and followed by 60 s irradiation. The photoelectrochemical experiments are described in more details in our previous reports [37–39]. The basic theory related to the photoelectrochemistry of semiconductors and PEC water splitting experiments have been summarized in this book [40] and several excellent reviews such as e.g. [2,41,42]

3. Results and discussions

Fig. 1 illustrates morphology of the three different types of TiO₂ 1D nanostructures studied including hydrothermally grown nanorods, hydrothermally grown nanotubes, and nanotubes fabricated by self-organized electrochemical anodization, which are in the text coded as TNR, THNT, and TNT, respectively.

Fig. 2 shows electron microscope (SEM and TEM) morphology images of the grown TiO₂ 1D nanostructures on FTO substrate. The 1D nanostructures formed a uniform film-like array coatings over whole area of the deposited substrates with efficiently high adhesion enabling easy manipulation. All the three types of TiO₂ 1D arrays were grown vertically from their bases on the FTO substrate

with the comparable thickness of 2.5 μ m. Moreover, the cross-sectional SEM images evidently confirmed the existence of a direct contact between the 1D nanostructures (see Fig. 2a, c and e) and charge-collecting FTO layer. The main differences among the tested nanostructures observed from the SEM scans were apparently the shape and diameter of individual nanotubes/nanorods as well as the density and degree of organization of the formed arrays. The degree of organization decreases in the order of TNT > TNR > THNT while in the case of arrays' density the order was TNR > THNT > TNT. Furthermore except the nanorods both nanotubular types of arrays exhibited highly homogenous diameter size distributions of the single nanotubes over the coatings. As it is clearly seen in Fig. 2a and b the TiO₂ nanorods are tetragonal in shape with square top facets, the expected growth habit for the tetragonal crystal structure [36]. The diameter size distribution of TNR is in the region between 80 and 150 nm. The cross-sectional image show that individual nanorods are well-aligned nearly perpendicularly to the FTO support. Much less degree of orderliness was identified for the TiO₂ nanotubes (THNT) grown on FTO substrates by the hydrothermal method using the ZnO nanorods as the sacrificial templates. One can easily observe that the individual nanotubes often crossed each other and some of them even lied on FTO substrate. These feature might be a consequence of the array less density. The low magnification TEM image shown in Fig. 2d revealed that the TiO₂ THNT had the internal diameter of 80 nm and the thickness of the walls of 20 nm. It is also obviously seen that these parameters were almost the same for all the THNT individual nanotubes. The highest degree of organization was achieved by the electrochemical anodic oxidation carried out under so-called self-organization conditions. This method yielded nanotubes with very regular channels having the orientation perpendicular to the FTO substrate. However, the surface SEM image in Fig. 2c shows rather irregular porous motive. It is due to a non-organized top thin porous layer covering the highly organized nanotube layer. This undesired porous top layer can be removed by e.g. sonication in diluted HCl, immersion in diluted HF, or by Ar ion sputtering [43]. The surface structure after the sonication of as-deposited TNT in HCl is depicted as the inset in Fig. 2e. The diameter of the nanotube channel of 100 nm and the wall thickness of 20 nm were measured by analyzing the low magnification TEM image (see Fig. 2f). One of the common features of the anodic oxidation is that it provides nanotubes with very narrow size distribution. Rather surprising result was obtained from the measurements of UV–vis absorption spectra (Fig. 3). The absorption edges are very similar for the THNT and TNT photoanodes. In both cases they are positioned at around 360 nm, which well corresponds to the tabulated anatase TiO₂ band gap of 3.2 eV. In contrast the absorption edge of the TNR was remarkably shifted towards longer wavelengths at around 420 nm. This effect was probably caused by multiple light scattering inside the nanorod array [44].

Fig. 4 shows crystalline structure of the 1D TiO₂ nanostructures deposited on FTO substrate after their thermal treatment at 500 °C for 1 h. The measured X-ray patterns were fitted by the program MSTRUCT. The X-ray diffractogram of well aligned TiO₂ nanorods (TNR, Fig. 4a) clearly indicate rutile phase in addition to SnO₂ (FTO).

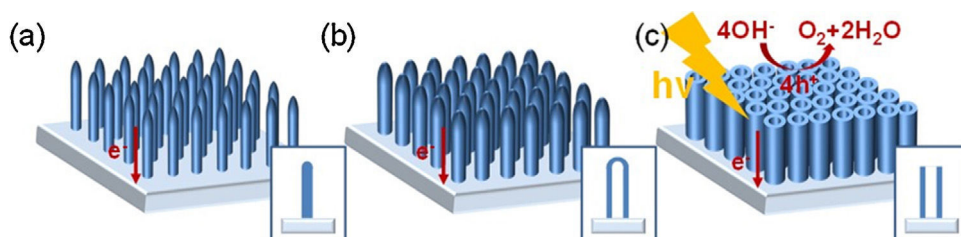


Fig. 1. Schematic illustrations of (a) TiO₂ nanorod-TNR, (b) hydrothermally grown TiO₂ nanotubes-THNT, and (c) anodized TiO₂ nanotubes-TNT.

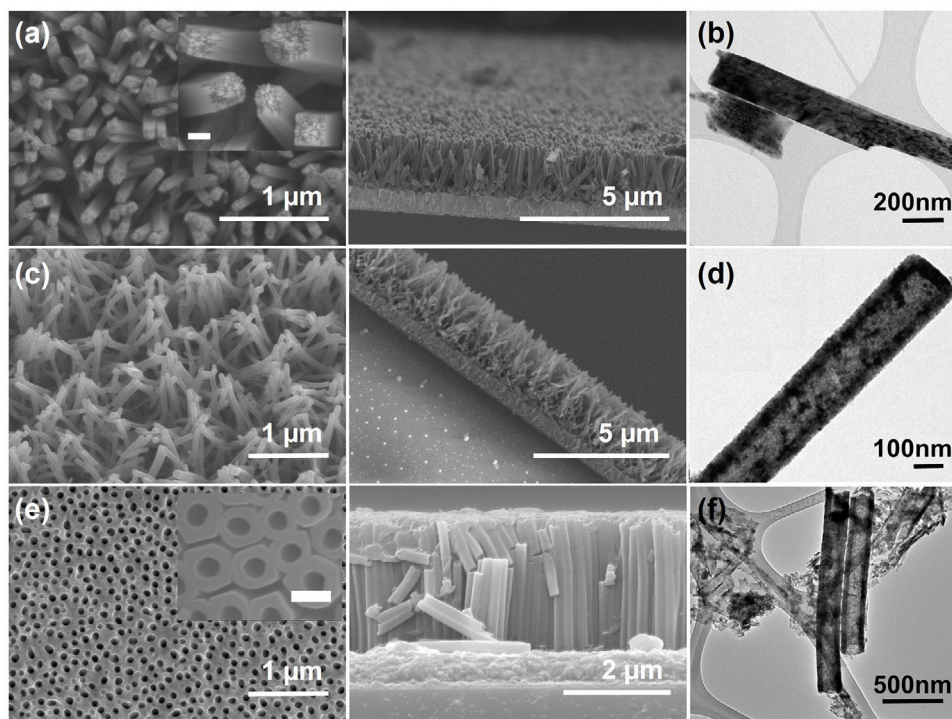


Fig. 2. SEM surface (left column) and cross-sectional (middle column) morphology images of (a) TNR, (c) THNT, and (e) TNT; TEM images of (b) TNR, (d) THNT, and (f) TNT. The scale bars in the insets represent 100 nm.

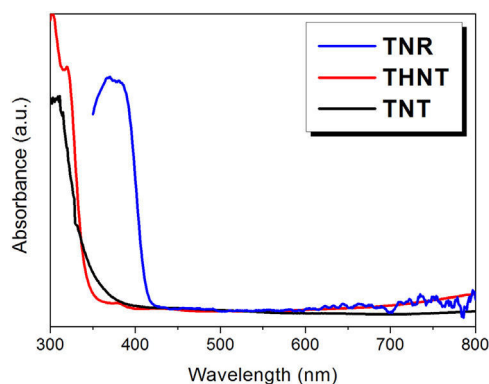


Fig. 3. UV-vis absorption spectra of the fabricated TiO₂ nanostructures on FTO substrate.

Preferred orientation of (001) type can be detected from the fit. In comparison with the SEM images this would prove that the nanorods have these basal planes (001), as it can be expected. The randomly distributed nanotubes grown by hydrothermal method (THNT, Fig. 4b) also show two phases—SnO₂ from the substrate and the anatase TiO₂ peaks. Finally the highly-ordered nanotubes show anatase and narrow peaks of well-crystalline pure titanium (Fig. 4c). The anatase nanotubes have relatively strong texture with planes (001) parallel to the substrate. More detailed XRD analysis of the microstructure including the measurement on different sample inclinations is out of the scope of this contribution and will be the subject of our next communication.

Photoelectrochemical behaviors of the TiO₂ 1D photoanodes are summarized in Fig. 5. The experiments were carried in conventional three-electrode configuration and under standard AM 1.5 G (intensity 100 mW/cm²) illumination. All the tested 1D layer photoanodes had similar thickness of 2.5 μm. Fig. 5a presents linear sweep voltammetry (LSV) curves, i.e. the dependency of current density on applied potential. The plateau-like photocurrent

responses were obtained for all the three photoanodes measured. Rather surprisingly, the PEC performance increased in the order of THNT < TNT < TNR. It is generally accepted that anatase possess a higher photocatalytic activity compared to rutile TiO₂ due to larger surface area, lower extent of backward recombination of photogenerated species, and better mobility of the charges [45]. However, in our case the hydrothermally grown nanorods (TNR) exhibited more than three times higher activity than the anodically made nanotubes and almost six times higher than the hydrothermally synthesized nanotubes. In particular from the *j*-*V* polarization curves (see Fig. 5a) the following values of photocurrent density can be read at 0 V vs. Ag/AgCl: 630 μA cm⁻², 185 μA cm⁻², and 110 μA cm⁻² for the TNR, TNT, and THNT photoanodes respectively. Both TNR and TNT photoanodes showed highly oriented growth with respect to the plane of the substrate, along the [001] direction of their unit cells and almost perpendicular alignment of the TiO₂ 1D arrays towards the FTO substrate. Therefore the preferential orientation should not significantly contribute to the very different performances observed. The suppressed activity of TNT photoanodes is more likely a consequence of a high extent of photocharges recombination due to the impurities such as titanium and carbon [32,46,47]. Although the TNT array films showed the highest transparency among the nanostructures examined traces of residual titanium possibly due to the unanodized sputtered titanium were identified in the films by X-ray diffraction. This XRD Ti signal might, on the other hand, be extended from the borders between the anodized and unionized parts of the samples. Similarly carbon coming from the electrolyte can also be expected in the nanotube walls [48]. The presence of titanium and/or carbon may induce impurity states acting as recombination centers significantly reducing the overall photoactivity [48,49]. In addition the boosted activity of TNR can also be attributed to two recently referred phenomena. Firstly Zhang and co-workers reported that the modified chloride on the surfaces of rutile TiO₂ nanorods may perhaps effectively trap photogenerated holes so as to induce the charge separation, leading to the enhanced photoactivities for PEC water oxidation [16]. Since

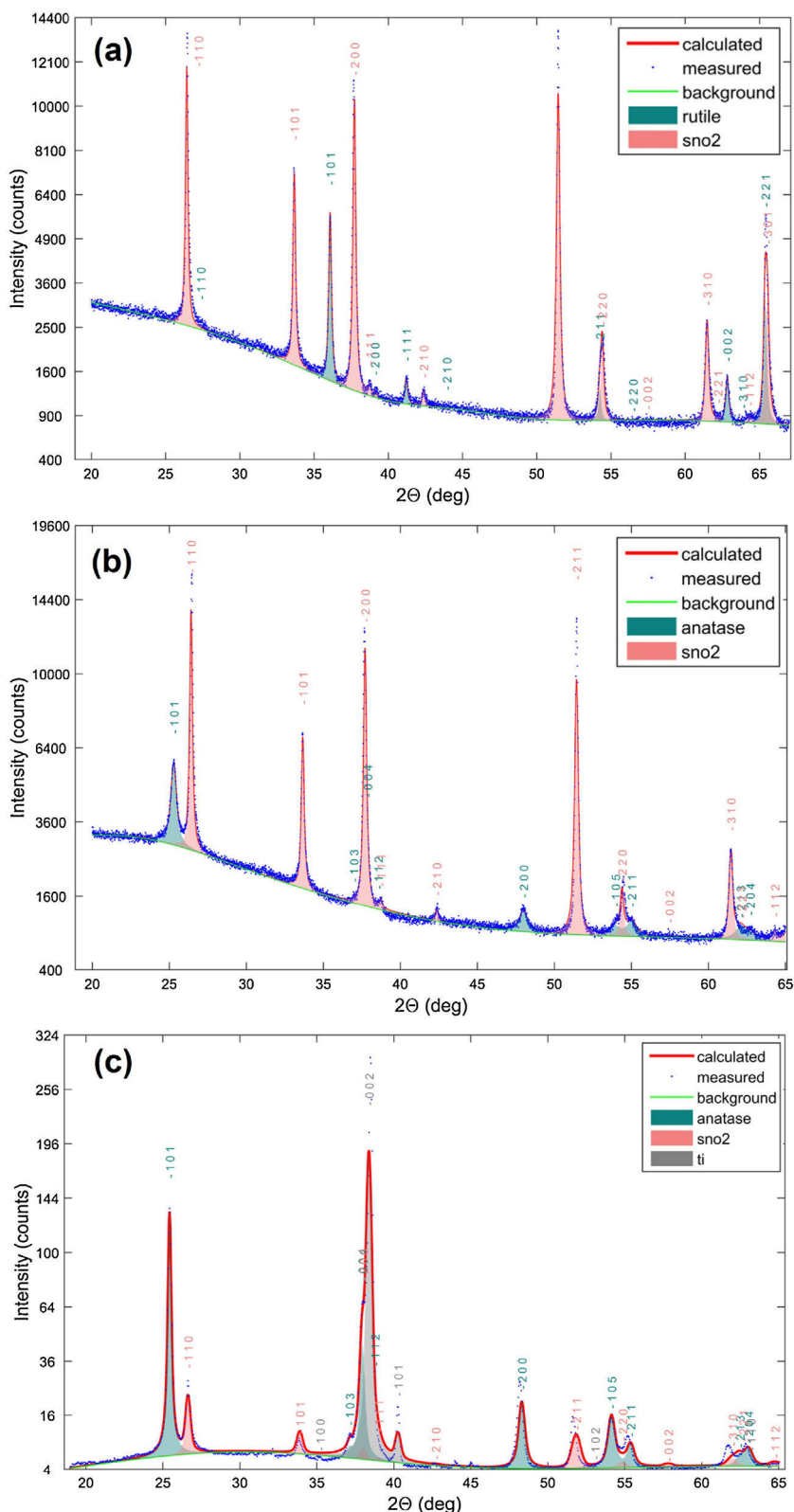


Fig. 4. X-ray diffractograms and corresponding fits of TiO_2 photoanodes: (a) TNR, (b) THNT, and (c) TNT.

the chloride is introduced via the presence of hydrochloric acid as one of the reactants of the hydrothermal procedure, which is principally corresponding to the one here presented the similar effect can also be expected. Secondly Chen et al. [50] attributed better photoinduced performance of TiO_2 nanorods comparing to nanotubes

to the superior photoelectron transfer property of the nanorods. The lowest PEC activity was revealed for the hydrothermally grown nanotubes. In this approach the nanotubes were deposited over the ZnO nanorods serving as template, which were subsequently removed by etching. This procedure apparently did not create a

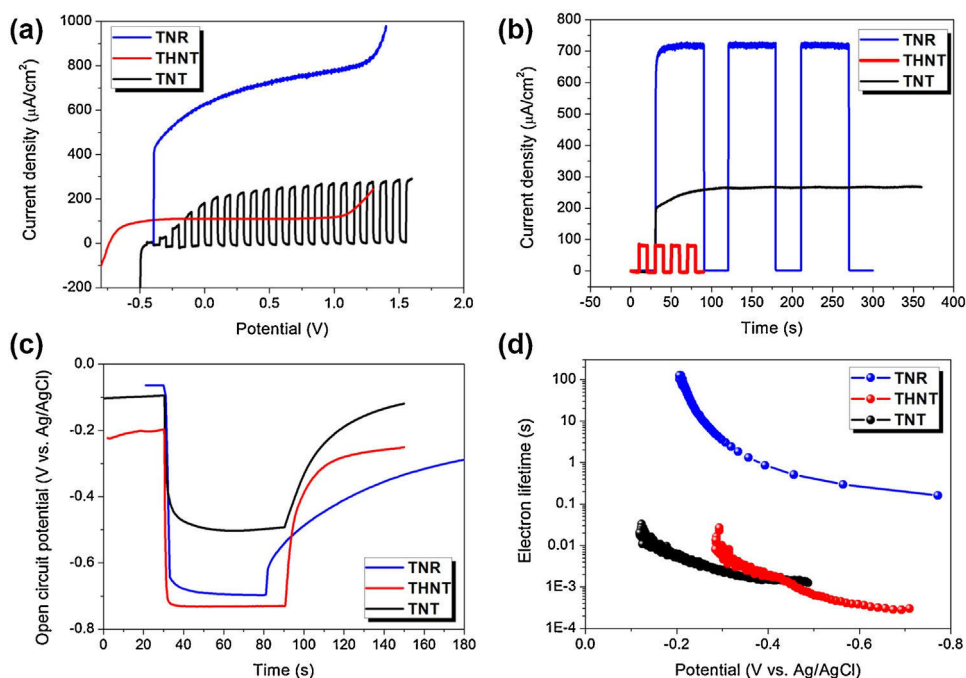


Fig. 5. Photoelectrochemical characteristics of the 1D TiO₂ photoanodes: (a) linear sweep voltammetry polarization curves; (b) chronoamperometry data recorded at 0 V vs. Ag/AgCl; (c) open circuit potentials curves. All PEC data were collected under solar light (AM 1.5G, intensity 100 mW/cm²) simulating illumination in 1 M NaOH electrolyte.

well-developed interface and connection between the nanotubes and charge collecting FTO substrate for efficient charge transfer. Fig. 5b shows chronoamperometry characteristics recorded at 0.5 V vs Ag/AgCl denoting the photostability of the 1D nanostructures. The chopped light measurements of the TNR and THNT photoanodes complete the similar LSV scan of the TNT photoanode (Fig. 5a). The sufficient photostability and very fast response on quick light/dark periods changes can be seen for every type of the photoanodes. The photocurrent densities correspond to the results of the LSV shown in Fig. 5a. Finally in order to quantify the charge transport properties the electron lifetime (τ_n) of the photoanodes was calculated using an open-circuit voltage decay (OCVD) technique [51,52]. Under the light irradiation a steady open-circuit voltages V_{oc} were generated and remarkably varied depending on the type of photoanode as it is seen in Fig. 5c. Upon the turn off the light the V_{oc} decayed due to the recombination of the electrons from conduction band with the holes with different pace. The average electron lifetime were determined according to the OCVD method as present in Eq. (1):

$$\tau_n = -\frac{k_B T}{q} \left(\frac{dV_{oc}}{dt} \right)^{-1} \quad (1)$$

where k_B is the Boltzmann's constant, T is temperature and q is the elementary charge. The method provides an effective in-situ method to explore the recombination kinetics of interfacial charge transfer process on the semiconductor-liquid junction [53]. As shown in Fig. 5d highest electron lifetime was revealed for the TNR type of photoanodes, which is in good agreement to Chen et al. [50], and to the all aforementioned PEC results. Accordingly slightly higher electron lifetime was observed for TNT photoanode comparing to the THNT. The shorter electron lifetime is another indication of a fast recombination of photocarriers due to the contaminants (TNT) and a poorly developed interface between the FTO and nanotubes (THNT).

4. Conclusion

This study provides a direct comparison of TiO₂ nanostructured photoanodes grown on transparent FTO substrate in terms of structural and functional (PEC) properties. A one- and two-step hydrothermal methods were used to fabricate TiO₂ nanorod and nanotube arrays, respectively. In addition a self-organized electrochemical anodization yielded highly organized nanotube arrays. Despite the same thermal annealing conditions (500 °C/1 h) of the as-prepared TiO₂ nanostructures the hydrothermally grown nanorods had rutile crystalline structure while the two nanotubular photoanodes showed more expected anatase phase. These two photoanodes, however, revealed much lower PEC performance than the rutile nanorod-based photoanode. This result was attributed to several features: i) remarkably prolonged electron lifetime verified by method, ii) extended light absorption towards visible part of spectrum, and iii) higher purity. The lowest PEC activity was observed for the hydrothermally fabricated nanotubes using ZnO nanorods as sacrificial template, which, likely suppressed the interface between the nanotubes and FTO substrate to be well-developed.

Acknowledgements

This work was supported by the Grant Agency of the Czech Republic project 15-19705S. The crystallographic part was supported by the project 14-03276S of the Czech Science Foundation using instruments of the ASTRA lab established within the Operation program Prague competitiveness – project CZ.2.16/3.1.00/24510.

References

- [1] B. Oregan, M. Gratzel, A low-cost, high-efficiency solar-cell based on dye-sensitized colloidal TiO₂ films, *Nature* 353 (1991) 737–740.
- [2] M. Gratzel, Photoelectrochemical cells, *Nature* 414 (2001) 338–344.
- [3] J. Burschka, N. Pellet, S.J. Moon, R. Humphry-Baker, P. Gao, M.K. Nazeeeruddin, M. Gratzel, Sequential deposition as a route to high-performance perovskite-sensitized solar cells, *Nature* 499 (2013) 316 (–).

- [4] S. Kazim, M.K. Nazeeruddin, M. Gratzel, S. Ahmad, Perovskite as light harvester: a game changer in photovoltaics, *Angew. Chem. Int. Ed.* 53 (2014) 2812–2824.
- [5] M.G. Walter, E.L. Warren, J.R. McKone, S.W. Boettcher, Q.X. Mi, E.A. Santori, N.S. Lewis, Solar water splitting cells, *Chem. Rev.* 110 (2010) 6446–6473.
- [6] F.E. Osterloh, Inorganic nanostructures for photoelectrochemical and photocatalytic water splitting, *Chem. Soc. Rev.* 42 (2013) 2294–2320.
- [7] X.G. Yang, R. Liu, Y.M. He, J. Thorne, Z. Zheng, D.W. Wang, Enabling practical electrocatalyst-assisted photoelectron-chemical water splitting with earth abundant materials, *Nano Res.* 8 (2015) 56–81.
- [8] A. Fujishima, K. Honda, Electrochemical photolysis of water at a semiconductor electrode, *Nature* 238 (1972) 37 (–+).
- [9] T. Berger, D. Monllor-Satoca, M. Jankulovska, T. Lana-Villarreal, R. Gomez, The electrochemistry of nanostructured titanium dioxide electrodes, *Chemphyschem* 13 (2012) 2824–2875.
- [10] Z.S. Li, J.Y. Feng, S.C. Yan, Z.G. Zou, Solar fuel production: strategies and new opportunities with nanostructures, *Nano Today* 10 (2015) 468–486.
- [11] G.K. Mor, K. Shankar, M. Paulose, O.K. Varghese, C.A. Grimes, Enhanced photocleavage of water using titania nanotube arrays, *Nano Lett.* 5 (2005) 191–195.
- [12] I.S. Cho, J. Choi, K. Zhang, S.J. Kim, M.J. Jeong, L.L. Cai, T. Park, X.L. Zheng, J.H. Park, Highly efficient solar water splitting from transferred TiO₂ nanotube arrays, *Nano Lett.* 15 (2015) 5709–5715.
- [13] Q.H. Liu, J.F. He, T. Yao, Z.H. Sun, W.R. Cheng, S. He, Y. Xie, Y.H. Peng, H. Cheng, Y.F. Sun, Y. Jiang, F.C. Hu, Z. Xie, W.S. Yan, Z.Y. Pan, Z.Y. Wu, S.Q. Wei, Aligned Fe₂TiO₅-containing nanotube arrays with low onset potential for visible-light water oxidation, *Nat. Commun.* 5 (2014).
- [14] Z.X. Pei, M.S. Zhu, Y. Huang, Y. Huang, Q. Xue, H.Y. Geng, C.Y. Zhi, Dramatically improved energy conversion and storage efficiencies by simultaneously enhancing charge transfer and creating active sites in MnOx/TiO₂ nanotube composite electrodes, *Nano Energy* 20 (2016) 254–263.
- [15] A. Wolcott, W.A. Smith, T.R. Kuykendall, Y. Zhao, J.Z. Zhang, Photoelectrochemical water splitting using dense and aligned TiO₂ nanorod arrays, *Small* 5 (2009) 104–111.
- [16] X.L. Zhang, H.Q. Cui, M. Humayun, Y. Qu, N.Y. Fan, X.J. Sun, L.Q. Jing, Exceptional performance of photoelectrochemical water oxidation of single-crystal rutile TiO₂ nanorods dependent on the hole trapping of modified chloride, *Sci. Rep.* 6 (2016) 8.
- [17] S. Jiang, Y. Li, X. Zhang, Y. Li, Enhancing the photoelectrochemical water splitting activity of rutile nanorods by removal of surface hydroxyl groups, *Catal. Today* 259 (2016) 360–367.
- [18] Y.J. Hwang, C. Hahn, B. Liu, P. Yang, Photoelectrochemical properties of TiO₂ nanowire arrays: a study of the dependence on length and atomic layer deposition coating, *ACS Nano* 6 (2012) 5060–5069.
- [19] Y.C. Pu, G.M. Wang, K.D. Chang, Y.C. Ling, Y.K. Lin, B.C. Fitzmorris, C.M. Liu, X.H. Lu, Y.X. Tong, J.Z. Zhang, Y.J. Hsu, Y. Li, Au nanostructure-decorated TiO₂ nanowires exhibiting photoactivity across entire UV-visible region for photoelectrochemical water splitting, *Nano Lett.* 13 (2013) 3817–3823.
- [20] M. Xu, P. Da, H. Wu, D. Zhao, G. Zheng, Controlled Sn-doping in TiO₂ nanowire photoanodes with enhanced photoelectrochemical conversion, *Nano Lett.* 12 (2012) 1503–1508.
- [21] I.S. Cho, C.H. Lee, Y. Feng, M. Logar, P.M. Rao, L. Cai, D.R. Kim, R. Sinclair, X. Zheng, Codoping titanium dioxide nanowires with tungsten and carbon for enhanced photoelectrochemical performance, *Nat. Commun.* 4 (2013).
- [22] J.H. Park, S. Kim, A.J. Bard, Novel carbon-doped TiO₂ nanotube arrays with high aspect ratios for efficient solar water splitting, *Nano Lett.* 6 (2006) 24–28.
- [23] P. Roy, C. Das, K. Lee, R. Hahn, T. Ruff, M. Moll, P. Schmuki, Oxide nanotubes on Ti–Ru alloys: strongly enhanced and stable photoelectrochemical activity for water splitting, *J. Am. Chem. Soc.* 133 (2011) 5629–5631.
- [24] H. Zhu, J. Tao, X. Dong, Preparation and photoelectrochemical activity of Cr-doped TiO₂ nanorods with nanocavities, *J. Phys. Chem. C* 114 (2010) 2873–2879.
- [25] W. Smith, A. Wolcott, R.C. Fitzmorris, J.Z. Zhang, Y.P. Zhao, Quasi-core-shell TiO₂/WO₃ and WO₃/TiO₂ nanorod arrays fabricated by glancing angle deposition for solar water splitting, *J. Mater. Chem.* 21 (2011) 10792–10800.
- [26] M.R. Gholipour, C.T. Dinh, F. Beland, T.O. Do, Nanocomposite heterojunctions as sunlight-driven photocatalysts for hydrogen production from water splitting, *Nanoscale* 7 (2015) 8187–8208.
- [27] F.L. Su, J.W. Lu, Y. Tian, X.B. Ma, J.L. Gong, Branched TiO₂ nanoarrays sensitized with CdS quantum dots for highly efficient photoelectrochemical water splitting, *Phys. Chem. Chem. Phys.* 15 (2013) 12026–12032.
- [28] Z. Li, L. Yu, Y. Liu, S. Sun, CdS/CdSe quantum dots Co-sensitized TiO₂ nanowire/nanotube solar cells with enhanced efficiency, *Electrochim. Acta* 129 (2014) 379–388.
- [29] J. Bian, C. Huang, L. Wang, T. Hung, W.A. Daoud, R. Zhang, Carbon dot loading and TiO₂ nanorod length dependence of photoelectrochemical properties in carbon Dot/TiO₂ nanorod array nanocomposites, *ACS Appl. Mater. Interfaces* 6 (2014) 4883–4890.
- [30] M.-Z. Ge, C.-Y. Cao, S.-H. Li, Y.-X. Tang, L.-N. Wang, N. Qi, J.-Y. Huang, K.-Q. Zhang, S.S. Al-Deyab, Y.-K. Lai, In situ plasmonic Ag nanoparticle anchored TiO₂ nanotube arrays as visible-light-driven photocatalysts for enhanced water splitting, *Nanoscale* 8 (2016) 5226–5234.
- [31] P. Roy, S. Berger, P. Schmuki, TiO₂ nanotubes: synthesis and applications, *Angew. Chem. Int. Ed.* 50 (2011) 2904–2939.
- [32] K. Lee, A. Mazare, P. Schmuki, One-dimensional titanium dioxide nanomaterials: nanotubes, *Chem. Rev.* 114 (2014) 9385–9454.
- [33] X.J. Feng, K. Shankar, O.K. Varghese, M. Paulose, T.J. Latempa, C.A. Grimes, Vertically aligned single crystal TiO₂ nanowire arrays grown directly on transparent conducting oxide coated glass: synthesis details and applications, *Nano Lett.* 8 (2008) 3781–3786.
- [34] D.V. Bavykin, J.M. Friedrich, F.C. Walsh, Protonated titanates and TiO₂ nanostructured materials: synthesis, properties, and applications, *Adv. Mater.* 18 (2006) 2807–2824.
- [35] N. Liu, X. Chen, J. Zhang, J.W. Schwank, A review on TiO₂-based nanotubes synthesized via hydrothermal method: formation mechanism, structure modification, and photocatalytic applications, *Catal. Today* 225 (2014) 34–51.
- [36] B. Liu, E.S. Aydil, Growth of oriented single-crystalline rutile TiO₂ nanorods on transparent conducting substrates for dye-sensitized solar cells, *J. Am. Chem. Soc.* 131 (2009) 3985–3990.
- [37] S. Kment, P. Kluson, H. Bartkova, J. Krysa, O. Churpita, M. Cada, P. Virostko, M. Kohout, Z. Hubicka, Advanced methods for titanium (IV) oxide thin functional coatings, *Surf. Coat. Technol.* 202 (2008) 2379–2383.
- [38] S. Kment, Z. Hubicka, J. Krysa, D. Sekora, M. Zlamal, J. Olejnicek, M. Cada, P. Ksirova, Z. Remes, P. Schmuki, E. Schubert, R. Zboril, On the improvement of PEC activity of hematite thin films deposited by high-power pulsed magnetron sputtering method, *Appl. Catal. B Environ.* 165 (2015) 344–350.
- [39] S. Kment, P. Schmuki, Z. Hubicka, L. Machala, R. Kirchgeorg, N. Liu, L. Wang, K. Lee, J. Olejnicek, M. Cada, I. Gregora, R. Zboril, Photoanodes with fully controllable texture: the enhanced water splitting efficiency of thin hematite films exhibiting solely (110) crystal orientation, *ACS Nano* 9 (7) (2015) 7113–7123.
- [40] R. Krishnan, Fundamentals of semiconductor electrochemistry and photoelectrochemistry, in: *Encyclopedia of Electrochemistry*, Wiley-VCH Verlag GmbH & Co. KGaA, 2007.
- [41] T. Hisatomi, J. Kubota, K. Domen, Recent advances in semiconductors for photocatalytic and photoelectrochemical water splitting, *Chem. Soc. Rev.* 43 (2014) 7520–7535.
- [42] Z.S. Li, W.J. Luo, M.L. Zhang, J.Y. Feng, Z.G. Zou, Photoelectrochemical cells for solar hydrogen production: current state of promising photoelectrodes, methods to improve their properties, and outlook, *Energy Environ. Sci.* 6 (2013) 347–370.
- [43] O. Kuzmich, K. Nonomura, E.M.J. Johansson, T. Nyberg, A. Hagfeldt, M. Skompska, Defect minimization and morphology optimization in TiO₂ nanotube thin films grown on transparent conducting substrate, for dye sensitized solar cell application, *Thin Solid Films* 522 (2012) 71–78.
- [44] M. Gao, L. Zhu, W.L. Ong, J. Wang, G.W. Ho, Structural design of TiO₂-based photocatalyst for H₂ production and degradation applications, *Catal. Sci. Technol.* 5 (2015) 4703–4726.
- [45] T. Luttrell, S. Halpegamage, J. Tao, A. Kramer, E. Sutter, M. Batzill, Why is anatase a better photocatalyst than rutile?—Model studies on epitaxial TiO₂ films, *Sci. Rep.* 4 (2014).
- [46] S. Kment, Z. Hubicka, H. Kmentova, P. Kluson, J. Krysa, I. Gregora, M. Morozova, M. Cada, D. Petras, P. Dytrych, M. Slater, L. Jastrabik, Photoelectrochemical properties of hierarchical nanocomposite structure: carbon nanofibers/TiO₂/ZnO thin films, *Catal. Today* 161 (2011) 8–14.
- [47] J. Schneider, M. Matsuoka, M. Takeuchi, J.L. Zhang, Y. Horiuchi, M. Anpo, D.W. Bahnemann, understanding TiO₂ photocatalysis: mechanisms and materials, *Chem. Rev.* 114 (2014) 9919–9986.
- [48] H. Mirabolghasemi, N. Liu, K. Lee, P. Schmuki, Formation of ‘single walled’ TiO₂ nanotubes with significantly enhanced electronic properties for higher efficiency dye-sensitized solar cells, *Chem. Commun.* 49 (2013) 2067–2069.
- [49] J. Lin, X. Liu, S. Zhu, Y. Liu, X. Chen, Anatase TiO₂ nanotube powder film with high crystallinity for enhanced photocatalytic performance, *Nanoscale Res. Lett.* 10 (2015).
- [50] J. Chen, H. Zhang, P. Liu, Y. Wang, X. Liu, G. Li, T. An, H. Zhao, Vapor-phase hydrothermal synthesis of rutile TiO₂ nanostructured film with exposed pyramid-shaped (111) surface and superiorly photoelectrocatalytic performance, *J. Colloid Interface Sci.* 429 (2014) 53–61.
- [51] A. Zaban, M. Greenshtein, J. Bisquert, Determination of the electron lifetime in nanocrystalline dye solar cells by open-circuit voltage decay measurements, *Chemphyschem* 4 (2003) 859–864.
- [52] J. Bisquert, A. Zaban, M. Greenshtein, I. Mora-Sero, Determination of rate constants for charge transfer and the distribution of semiconductor and electrolyte electronic energy levels in dye-sensitized solar cells by open-circuit photovoltage decay method, *J. Am. Chem. Soc.* 126 (2004) 13550–13559.
- [53] J.S. DuChene, B.C. Sweeny, A.C. Johnston-Peck, D. Su, E.A. Stach, W.D. Wei, Prolonged hot electron dynamics in plasmonic-metal/semiconductor heterostructures with implications for solar photocatalysis, *Angew. Chem. Int. Ed.* 53 (2014) 7887–7891.

Appendix [A3]

TiO₂ Nanotubes on Transparent Substrates: Control of Film Microstructure and Photoelectrochemical Water Splitting Performance

M. Zelny, **S. Kment***, R. Ctvrtlik, S. Pausova, H. Kmentova, J. Tomastik, Z. Hubicka, R. Yalavarthi, J. Krysa, A. Naldoni, P. Schmuki, R. Zboril*

Catalysts, 8, 25, 2018

Article

TiO₂ Nanotubes on Transparent Substrates: Control of Film Microstructure and Photoelectrochemical Water Splitting Performance

Matus Zelny¹, Stepan Kment^{1,*}, Radim Ctvrtlik¹ , Sarka Pausova², Hana Kmentova¹, Jan Tomastik¹, Zdenek Hubicka³, Yalavarthi Rambabu¹, Josef Krysa², Alberto Naldoni¹ , Patrik Schmuki^{1,4} and Radek Zboril^{1,*}

- ¹ Regional Centre of Advanced Technologies and Materials, Faculty of Science, Palacky University, 17. Listopadu 1192/12, 771 46 Olomouc, Czech Republic; matus.zelny01@upol.cz (M.Z.); radim.ctvrtlik@upol.cz (R.C.); hana.kmentova@upol.cz (H.K.); jan.tomastik@upol.cz (J.T.); rambabu.yalavarthi@upol.cz (Y.R.); alberto.naldoni@upol.cz (A.N.); schmuki@ww.uni-erlangen.de (P.S.)
- ² Department of Inorganic Technology, University of Chemical Technology Prague, Technicka 5, 166 28 Prague, Czech Republic; Sarka.Pausova@vscht.cz (S.P.); josef.krysa@vscht.cz (J.K.)
- ³ Institute of Physics, Academy of Sciences of the Czech Republic, Na Slovance 2, 14800 Prague, Czech Republic; hubicka@fzu.cz
- ⁴ Department of Materials Science and Engineering, University of Erlangen-Nuremberg, Martensstrasse 7, D-91058 Erlangen, Germany
- * Correspondence: stepan.kment@upol.cz (S.K.); radek.zboril@upol.cz (R.Z.); Tel.: +42-058-563-4365 (S.K.)

Received: 13 December 2017; Accepted: 11 January 2018; Published: 15 January 2018

Abstract: Transfer of semiconductor thin films on transparent and or flexible substrates is a highly desirable process to enable photonic, catalytic, and sensing technologies. A promising approach to fabricate nanostructured TiO₂ films on transparent substrates is self-ordering by anodizing of thin metal films on fluorine-doped tin oxide (FTO). Here, we report pulsed direct current (DC) magnetron sputtering for the deposition of titanium thin films on conductive glass substrates at temperatures ranging from room temperature to 450 °C. We describe in detail the influence that deposition temperature has on mechanical, adhesion and microstructural properties of titanium film, as well as on the corresponding TiO₂ nanotube array obtained after anodization and annealing. Finally, we measure the photoelectrochemical water splitting activity of different TiO₂ nanotube samples showing that the film deposited at 150 °C has much higher activity correlating well with the lower crystallite size and the higher degree of self-organization observed in comparison with the nanotubes obtained at different temperatures. Importantly, the film showing higher water splitting activity does not have the best adhesion on glass substrate, highlighting an important trade-off for future optimization.

Keywords: titanium; anodization; TiO₂ nanotubes; hardness; adhesion; photoelectrochemistry

1. Introduction

Titanium dioxide (TiO₂) is one of the most widely studied semiconductor photocatalysts owing to its ability to catalyze numerous redox reactions [1], high stability, nontoxicity and low cost [2,3]. Nanocrystalline TiO₂ has highly promising optical, photocatalytic and photoelectrochemical (PEC) performance [4], which have been extensively used for a broad range of applications including environmental purification, organic oxidations [5], solar cells, PEC water splitting, and hydrogen peroxide production [1,2,4,6–12].

The photocatalytic performance of TiO₂ is strongly affected by its morphology and structure. With the decrease of the material's dimensions to nanoscale, surface-to-volume ratio and specific surface

area increase as well as electronic properties that may also deviate from ideal behavior [13]. Crystal phase and orientation in nanocrystals and thin films have shown a dramatic role in enhancing charge separation, band gap, and surface catalytic properties of TiO₂ nanomaterials [6,11–13].

Furthermore, TiO₂ nanomaterials have shown shape-dependent photocatalytic performance [14]. For thin films, various TiO₂ one-dimensional (1D) nanostructures involving self-organized nanotubes, highly-ordered nanorod arrays, and nanowires, have attracted much attention due to the combination of highly functional features and controllable nanoscale geometry with the possibility of adjusting length, diameter, and spacing [13,15–17]. In particular, 1D TiO₂ nanotubes (TNT) show better PEC performance than thin compact layers due to higher surface area, favorable charge transfer along the nanotube *y*-axis perpendicular to charge collecting bottom layer, and enhanced light harvesting efficiency [18].

Self-organized oxide tube arrays can be fabricated by electrochemical anodization of a suitable metal foil under specific anodic conditions and proper electrolytes [18–23]. For instance, highly ordered TiO₂ nanotube arrays are typically grown by electrochemical anodization of titanium foils [23]. However, fully transparent photoelectrodes or photonic devices are highly desirable in many applications including photovoltaics and PEC cells [18,24]. For instance, TNT reaching transparency higher than 65% and producing stable photocurrent can be employed in PEC tandem cells, in which the illumination from the support—semiconductor interface is a required condition, enabling the efficient excitation of both photoanode and photocathode materials [24].

Recently, the anodization of titanium thin films deposited on glass substrates via different Physical Vapor Deposition methods [18,25], especially magnetron sputtering, have proven to be a promising route to achieve devices with high stability and performance [16,24–29].

In particular, the properties of TNT are highly influenced by the properties of the starting magnetron sputtered metal films, which in turn have shown strong tenability depending on energy of impinging ions, degree of ionization of the sputtered-particles [30], deposition temperature [31], and concentration of oxygen or nitrogen [32]. Nevertheless, a study exclusively focused on the influence of temperature of a glass substrate during the pulsed DC magnetron sputtering on the properties of the deposited titanium films and consequently on the properties and functionality of final TiO₂ nanotubes is still missing. In this work, we report a detailed investigation of mechanical and adhesion properties of Ti films sputtered at different temperatures, as well as how these different sputtering conditions influence crystallographic and photoelectrochemical water splitting activity of the self-organized TiO₂ nanotubes grown from these Ti films.

2. Results and Discussion

2.1. Structure and Morphology of Sputtered Ti Films

Titanium films were sputtered onto fluorine-doped tin oxide (FTO) substrate at different temperatures such as room temperature (RT), 150 °C, 300 °C, and 450 °C. For the sake of clarity, despite the fact that the RT condition did not include intentional heating, the substrate's temperature slightly rose up to 80 °C due to the bombardment of the FTO surface by plasma discharge ions. The deposition rate follows a volcano-shaped trend with increasing the deposition temperature and reaches the maximum of 47 nm/min for 150 °C (Figure 1). The grain size follows an opposite trend and the minimum value of ~80 nm is reached for the Ti sample deposited at 150 °C. This dependence can be ascribed to the processes occurring during the sputtering deposition such as extent of shadowing effect at low deposition temperatures, and surface and volume diffusion of condensing atoms at higher temperatures in accordance with the structure zone models [33].

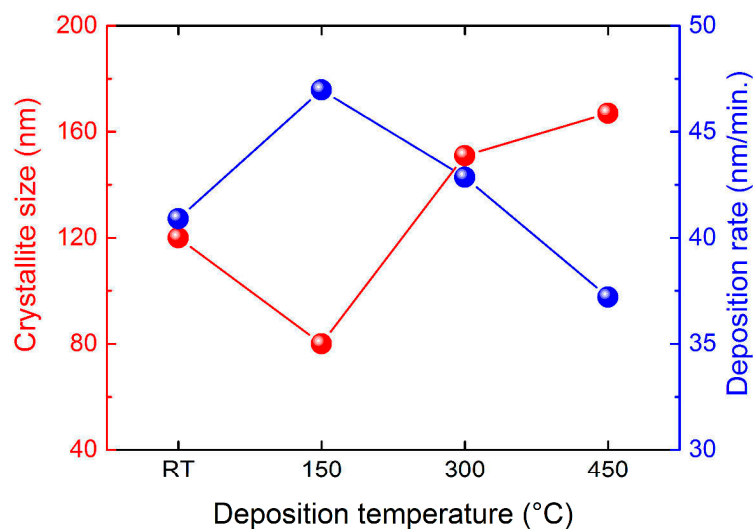


Figure 1. Crystallite size and deposition rate as a function of deposition temperature for the direct current magnetron sputtered Ti films. Deposition rate shows a volcano shape dependence on temperature, while crystallite size has an opposite trend. RT: room temperature.

The as-deposited titanium samples were well adherent to the FTO substrate regardless of the temperature used without any visually observable defects. The morphological images of all deposited films are displayed in the scanning electron microscopy (SEM) micrographs reported in Figure 2a–d. With increasing temperature, the shape of grains and their size distribution varied considerably: Ti films deposited at RT showed globular morphology, while fully developed hexagonal platelets with sharp edges were clearly seen for the film deposited at 150 °C. The platelets were randomly distributed and placed on top of each other. The change of morphology is associated with a decrease of the crystallite size from 120 nm (RT) to 80 nm (150 °C) as summarized in Table 1 and Figure 1. Further increase of the deposition temperature led to a higher surface and bulk diffusivity of sputtered atoms promoting formation of angular grains, especially for film deposited at 450 °C, thus leading to a substantial increase of crystallite size (see Table 1).

Table 1. Thickness and roughness from profilometry of Ti films; crystallite size of the deposited Ti films and anodized TiO₂ nanotubes. RT: room temperature.

Temperature, °C	Thickness, μm	Roughness, μm	Crystallite Size Ti, nm	Crystallite Size TiO ₂ , nm
RT	1.35	0.080	120	39
150	1.61	0.125	80	14
300	1.50	0.118	151	25
450	1.48	0.028	167	87

X-ray diffraction was used to determine the crystalline structures of deposited Ti films. Irrespective of the deposition temperature, the as-prepared films exhibited a variation of peak intensities corresponding to hexagonal polycrystalline structure of titanium with preferential orientation along the (002) crystalline plane that is generally the densest plane for hexagonal close packed structures. It is worth noting the evolution of (100) and (110) peaks with the increase of the deposition temperature in agreement with previous work [34]. The development of these crystalline planes may be attributed to the presence of a compressive stress induced in the films' microstructure [34,35]. Crystallite size was estimated by using the Scherrer's equation and retrieved values are shown in Table 1. Figure 2f shows the energy dispersive X-ray spectroscopy (EDS) spectrum of the titanium film deposited at 150 °C on FTO glass. The SEM-EDS analysis revealed traces of Sn in all samples (not shown here) due to the presence of Sn ions into the FTO (i.e., F-doped SnO₂) underneath substrate. The surface

roughness (R_a) of deposited Ti layers was tested by contact profilometry and the obtained values of standard R_a parameters are provided in Table 1. Surprisingly, the smoothest surface was identified for the films composed of the biggest crystalline size. It was also visually observable as a very flat mirror-like surface. Film thickness obtained from profilometry measurements ranges from 1.35 to 1.60 μm , thus being comparable for all Ti films.

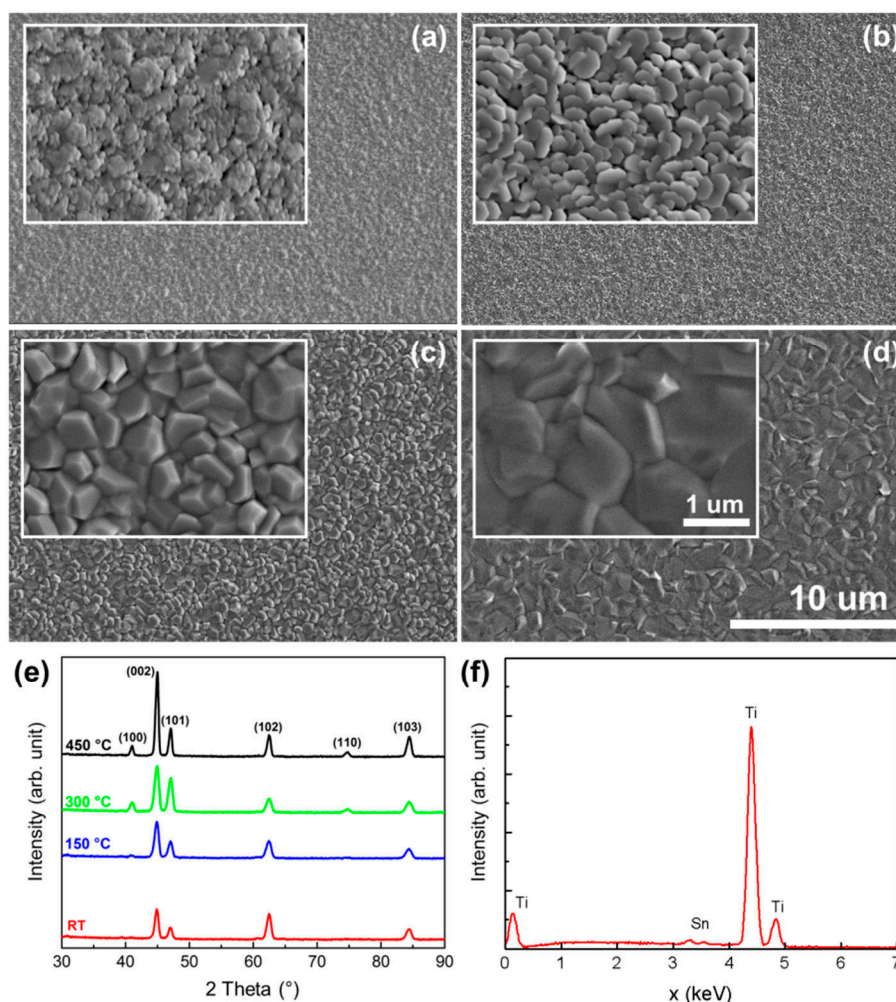


Figure 2. Scanning electron microscope (SEM) images of titanium samples deposited without substrate heating at (a) RT, (b) 150 $^\circ\text{C}$, (c) 300 $^\circ\text{C}$ and (d) 450 $^\circ\text{C}$. (e) X-ray diffraction (XRD) spectra of all deposited Ti films; (f) energy dispersive X-ray spectroscopy spectrum of titanium film deposited at 150 $^\circ\text{C}$ on fluorine-doped tin oxide (FTO) substrate.

2.2. Mechanical Properties of Sputtered Titanium Films

Analysis of nanoindentation data (Figure 3) evidenced significant differences in mechanical properties between the deposited Ti films. Substrate heating led to an increase in reduced modulus from 109 GPa for RT sample (and similar values observed for 150 and 300 $^\circ\text{C}$) to 130 GPa for the film deposited at 450 $^\circ\text{C}$. Similarly, hardness values are almost the same regardless of the deposition temperature up to 300 $^\circ\text{C}$ (~ 3.75 GPa), while a small increase can be observed for the film deposited at 450 $^\circ\text{C}$. Nanoindentation hardness of the films is only slightly higher in comparison to the coarse grained Ti bulk sheet (~ 2 GPa) measured at the same experimental setup, especially for the films deposited up to 300 $^\circ\text{C}$. This fact correlates well with the fine-grained structure, where dislocation activity for crystallite with size around 100 nm is suppressed as explained by the well known Hall–Petch effect [36]. Nevertheless, the relative proximity of hardness values of the Ti films and pure Ti metal bulk

reflects the high purity of the films, since oxygen or nitrogen impurities strongly affect the mechanical properties and increase both the hardness and elastic modulus values [32]. No traces of oxygen were detected using EDS. Hardness increase up to 4 GPa was reported for Ti sputtered films under similar conditions but under Ar/O₂ gas mixture [18]. It should be noted that either oxides (TiO₂) or nitrides (TiN_x) can reach much higher hardness. In case of magnetron sputtered TiO₂ films hardness values of pure anatase is in the range of 6–11 GPa, whereas rutile can reach around 20 GPa [37].

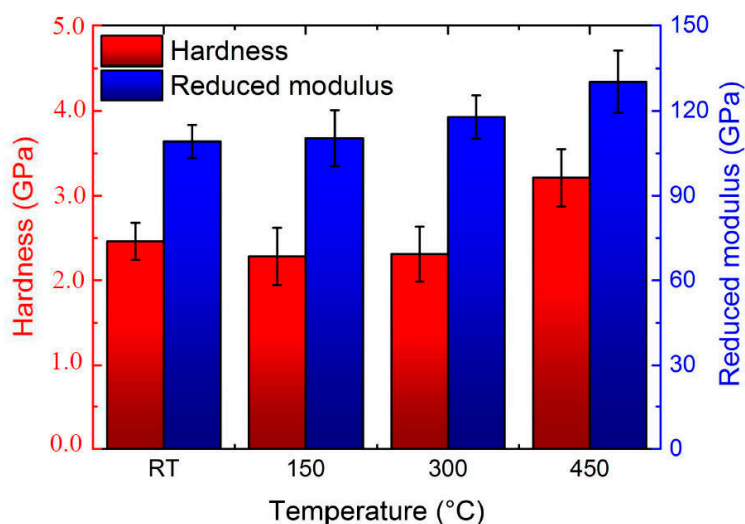


Figure 3. Hardness and reduced modulus of the Ti films deposited at different temperatures.

Progressive load scratch tests revealed increasing endurance of Ti films with the increase of deposition temperature, as demonstrated from the residual grooves tracks shown in Figure 4. Sample deposited without applying external heating (RT) exhibits full coating delamination starting from 1/3 of the scratch track. Large spalled areas uncovering the bare substrate, far beyond the residual groove, show that coating-to-substrate adhesion as well as cohesion strength are weak and become a main reason for the system failure. Substrate heating up to 150 °C led to better adhesion, as no delamination is observed and coating is scratched through after approximately half of the scratch track. Deposition temperature of 300 °C and especially 450 °C has a significant impact on scratch resistance as coatings were not scratched through. The residual scratch tracks' surface morphologies are almost smooth and dominated by plastic deformation (see beginnings of the scratches). This is in accordance with the high level of plasticity index of approx. 83%, defined as the ratio of the plastic work to total indentation work. With increasing load, formation of faint pile up around the wear track occurs. Only slightly worn particle packing is observed at the sides of the wear track. It should be noted that findings of scratch test performed at lower maximum force of 100 mN coincide with those reported in [18].

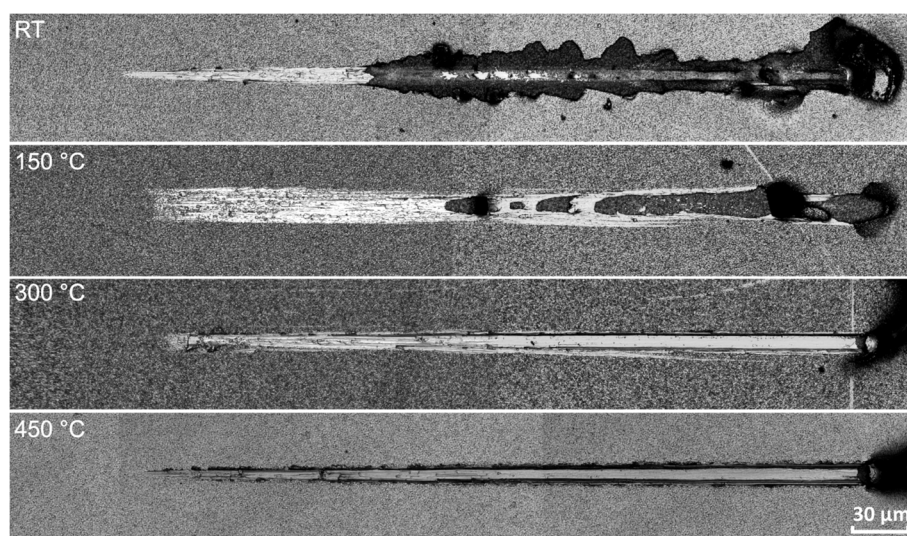


Figure 4. Typical scratch tracks for Ti films deposited at temperatures ranging from room temperature (RT) to 450 °C.

2.3. Electrochemical Anodization to Grow TiO₂ Nanotubes

Figure 5a shows the current density plot in time during the anodic oxidation of the sputtered Ti layers sputtered on FTO glass at different temperatures (RT, 150, 300 and 450 °C). All the current transient curves can be divided into three typical stages, already described in detail elsewhere [16,38]. Briefly, the very sharp current density peak observed during the first seconds of the anodization process is associated with the formation of an initial compact TiO₂ layer. A relatively steady state region followed, denoting the self-organizing electrochemical reaction underlying the formation of TiO₂ nanotubes. Finally, a sudden increase of current density marks the end point of the reaction, which may be accompanied with the creation of random cracks within the TNT and/or their partial delamination [39].

Notably, two trends can be observed when the current density curves are compared. The titanium films deposited at higher temperature required higher current density to be anodically oxidized, while electrochemical reaction lasted for a much shorter time than the titanium films prepared under lower temperature. Due to the elevated temperatures, the crystallite size and density of layers are significantly increased, along with a change in crystallite preferential orientation towards the (002) planes. The shorter the anodization duration the larger the crystallite sizes; at the same time the denser the films the higher current density is required for TNT formation. Interestingly, the TNT peeled off in the center of the anodized area only for the 450 °C sample (Figure 5a). The photographs were captured after the thermal annealing of the as-grown amorphous TiO₂ nanotubes in air at 500 °C for 1 h to obtain the crystalline structure. The delamination already occurred during the anodization process despite thermal annealing. It should be noted that the dominant (002) plane is the one with the highest thermally induced strain energy per unit volume [40]. Taking into account the crystallographic planes observed in Figure 2e, the strain energy decreases in the following order (002), (103), (102), (101), (100) and (110), where the last two are equal [40]. Hence, the problematic anodization of the film deposited at 450 °C stems from the combination of high current density (high thermal load) during anodization and the highest thermally induced strains of the film's dominant (002) plane.

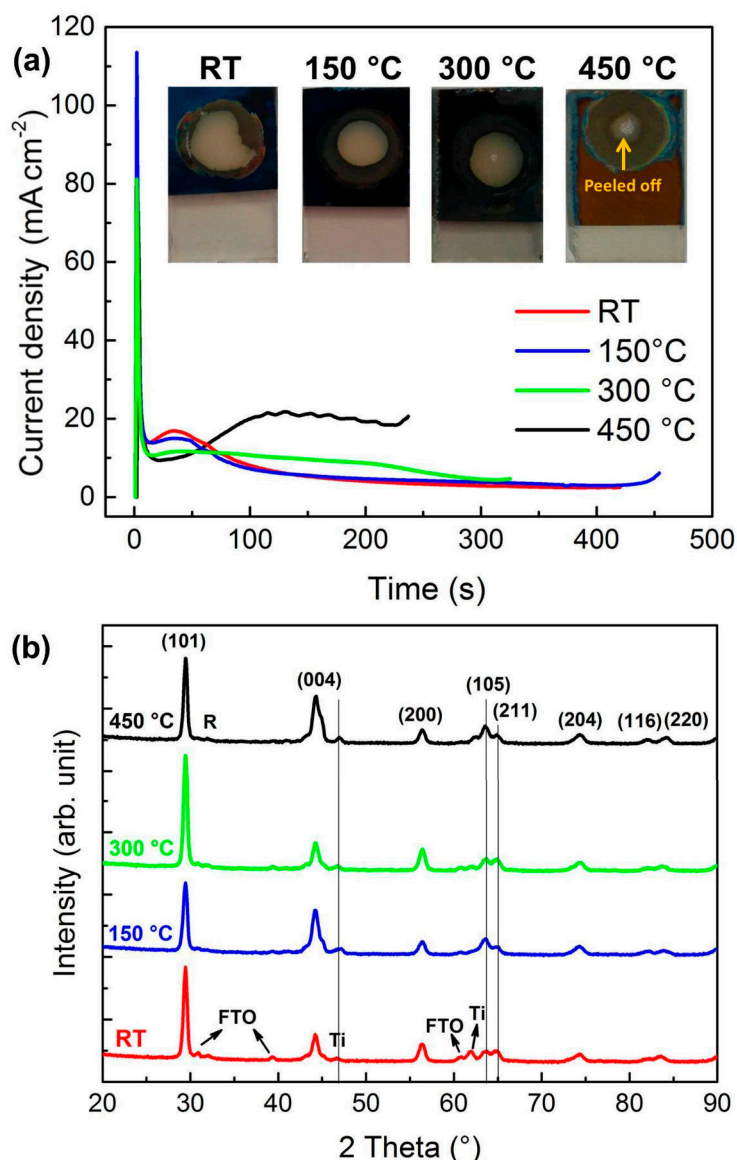


Figure 5. (a) Current density versus time plot recorder during the electrochemical anodization of titanium films with the pictures of grown and annealed TiO₂ nanotubes; (b) XRD spectra of TiO₂ nanotubes after thermal annealing at 450 °C for 3 h in air.

XRD spectra of the thermally annealed TiO₂ nanotubes show only characteristic peaks related to the polycrystalline anatase phase (Figure 5b). The crystallite size, obtained through the Sherrer equation, followed the same trend as observed for titanium films, i.e., the smallest grain size of 14 nm was revealed for the TNT grown from the titanium films deposited at 150 °C, while with the increase of the deposition temperature the grain sizes increased up to 87 nm for 450 °C. In the diffractograms, the signals related to metallic titanium as well as the cassiterite (SnO₂) of the FTO substrate were detected. The source of Ti signal is probably due to the side unanodized parts of the samples rather than residual Ti impurities in the TNTs.

The cross-sectional and surface SEM morphology images of the prepared nanotubes are shown in Figure 6. The anodization formed self-organized arrays of highly transparent nanotubes grown vertically on the FTO substrate. All the prepared nanotubes had a similar thickness of 3 μm, which corresponds to a volume expansion factor of ~2 due to the anodization procedure. This value is in agreement with findings from Albu and Schmuki, describing how key parameters such as content of water in the electrolyte and overall anodization potential influence the expansion factor of TNTs [41].

The surface SEM images (see inserts in Figure 6) are very similar for RT, 150 °C, and 300 °C deposited Ti films. The similarity is due to a nanoporous thin initiation layer which is always present at the top of nanotubes due to the TiO₂ layer formed at the first stage of the anodization process (see description above). By comparing these three types of nanotube arrays a widening of the tube diameters can be indicated. The surface morphology is slightly different for the film deposited at 450 °C. In this case, pores with higher diameters are formed at edges of the very large titanium grains (see Figures 2d and 6d) [39]. The highest quality of nanotubes in terms of homogeneity, degree of organization, smoothness, and compactness was observed for the TNT grown from Ti films deposited at 150 °C. A much higher number of defects was observed for the TNT grown from RT and 300 °C titanium films. For comparison, the parts of TNT made from Ti films deposited at 450 °C, which were not delaminated from the FTO substrate are also shown. The very low quality of these nanotubes is mainly due to numerous cracks and is evident (Figure 6d).

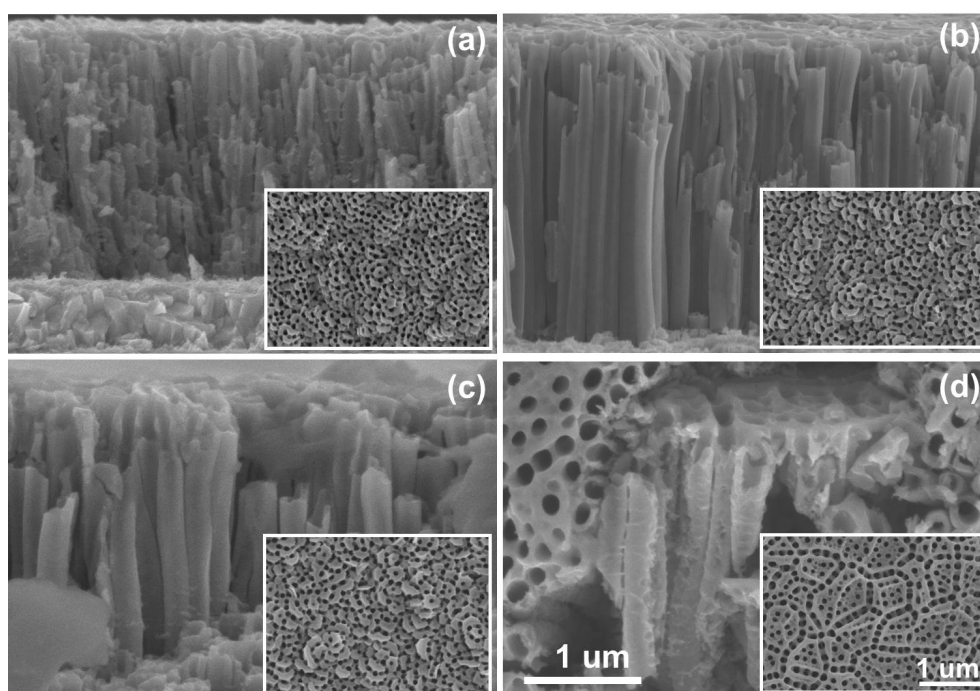


Figure 6. Cross-sectional and corresponding surface (inserts) SEM images of the TiO₂ nanotubes (TNT) arrays grown from titanium films deposited at RT (a), 150 °C (b), 300 °C (c), and 450 °C (d).

2.4. Photoelectrochemical Measurements

Photoelectrochemical properties were investigated based on linear sweep voltammetry and electrochemical impedance spectroscopy (EIS) measurements. The polarization curves showing the dependence of current density on applied potential are presented in Figure 7a. The performance of TNT obtained from Ti film sputtered at 450 °C was not measured due to the collapse of the structure upon air annealing. The experiments were carried out in a conventional three-electrode configuration in 1 M NaOH and under standard AM1.5G (intensity 100 mW/cm²) illumination. All three measured photoanodes showed a similar voltammetry profile characterized by an onset potential at ~0.74 V vs. Ag/AgCl and reaching a photocurrent plateau. From the polarization curves (see Figure 7a), the photocurrent density at 0.5 V (at the end point of the steady-state plateau-like photocurrents and before the electrochemical oxygen evolution onset potential) are as follows: 175 μA cm⁻², 125 μA cm⁻², and 116 μA cm⁻² for 150 °C, RT, and 300 °C TNT photoanodes, respectively. The highest photocurrent value obtained for the sample TNT-150 can be ascribed to the smallest crystallite size, the defect-free morphology of high quality nanotubes for the 150 °C sample.

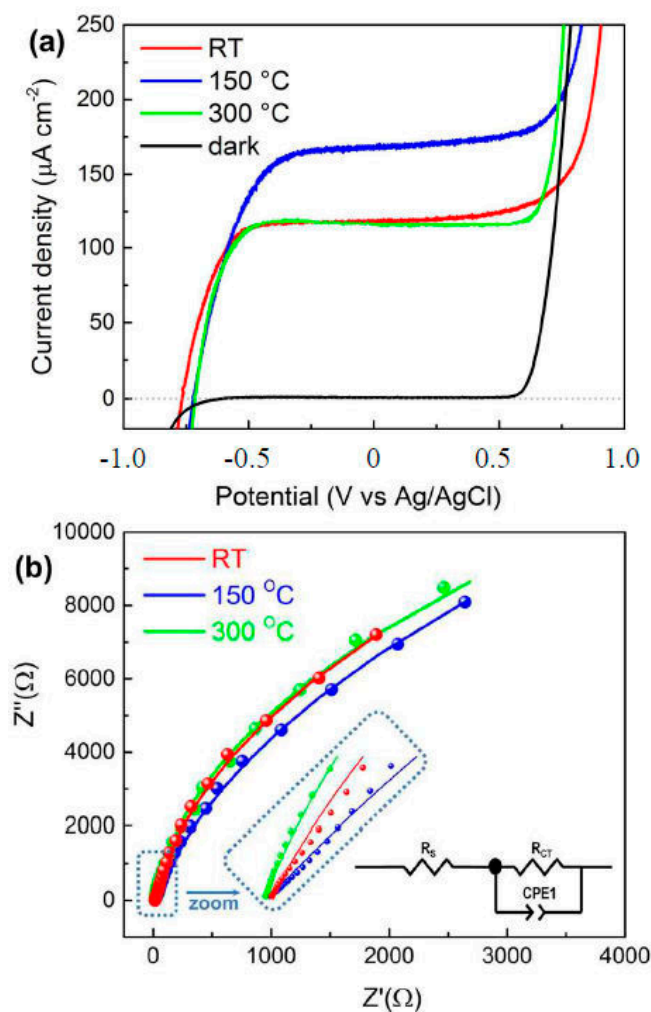


Figure 7. Linear sweep voltammetry curves of the TiO₂ nanotubes (a). Nyquist plots for TNT-RT, TNT-150, and TNT-300 measured at an applied bias potential of 0 V vs. Ag/AgCl under illumination of AM1.5G with the intensity of 100 mW cm⁻² (b). Symbols are experimentally measured impedance data; solid curves are fitted to the equivalent circuit shown (inset). R_s is solution resistance, R_{CT} is charge transfer resistance, Constant phase element (CPE1) is capacitance element. Photoelectrochemical (PEC) measurements were carried out in 1 M NaOH electrolyte under simulated solar light irradiation (air mass-AM1.5G, 100 mW/cm²).

To investigate the reasons underlying the photocurrent trend, we carried out EIS measurements under AM1.5G illumination at 0 V vs. Ag/AgCl (Figure 7b). The semicircular arch diameter indicates the charge transfer ability of the examined photoelectrode. To extract the charge transfer parameters associated with EIS curves, we fitted the curves with an equivalent Randle's circuit (see inset of Figure 7b), where R_s is the series/solution resistance, R_{CT} is the charge transfer resistance, and CPE1 is the constant phase element (capacitance) of semiconductor/electrolyte interface. The fitted parameters for each sample are shown in Table 2. R_s slightly decreases with increasing temperature of Ti sputtered films and shows comparable values. The double layer capacitance CPE1 is higher for TNT-RT due to higher accumulation of charge at the electrode/electrolyte interface; it may be because of grain size differences or accumulation of more charges at the grain boundaries of the sample. The charge transfer resistance R_{CT} for TNT-150 sample is 33.7 kΩ, lower compared to TNT-RT (39.7 kΩ) and TNT-300 (36.4 kΩ) suggesting a higher charge transfer rate at the semiconductor/electrolyte interface that, thus, underlies the observed enhancement in the photocurrent.

Table 2. Electrochemical Impedance spectroscopy data from measurement taken at 0 V vs. Ag/AgCl under 1 sun illumination.

Sample	R_S, Ω	R_{CT}, Ω	CPE1, μF
RT	16.71	$39,799 \pm 1149$	201 ± 0.57
150	15.70	$33,698 \pm 279$	172 ± 0.33
300	13.37	$36,430 \pm 841$	165 ± 0.44

3. Experimental

3.1. Deposition of Titanium Films by Magnetron Sputtering

Titanium thin films, with thickness of $\sim 1.5 \mu\text{m}$, were deposited by pulsed DC magnetron sputtering of the titanium target (size of 4" and purity of 99.995%) on a commercially available FTO coated glasses substrates (Solaronix, Aubonne, Switzerland) with dimensions of $25 \times 15 \times 2 \text{ mm}$. A standardized three-step cleaning protocol was used before film deposition. rinsing the substrates in an ultrasound bath in acetone, ethanol and distilled water, each step lasting 5 min. Subsequent drying at RT was applied to remove residual water from the glass samples. The chamber was evacuated to the base pressure of $1 \times 10^{-4} \text{ Pa}$. The depositions were performed at a pressure of 0.2 Pa for 240 min on unheated as well as heated substrates at various temperatures of 150, 300 and 450 °C. Although no intentional heating was applied the substrate temperature increased up to 90 °C during deposition as a result of its interaction with plasma. The DC power of 700 W (power density of 8.6 W/cm^2) was applied in a pulsed mode at pulse frequency of 50 kHz and duty cycle of 50%. Prior the deposition a substrate pre-treatment was employed. First the substrate surfaces were cleaned using radio frequency (RF) (13.56 MHz) plasma etching in argon and then activated in the RF discharge in the mixture 50:50 of Ar and forming gas (10% of H_2 and 90% of N_2). The RF power of 130 W was typically used.

3.2. Mechanical and Tribological Properties

Mechanical and tribological characteristics were explored using a fully calibrated NanoTest instrument (MicroMaterials, Wrexham, UK) in a load-controlled mode. Nanoindentation at a peak force of 3 mN with a diamond pyramidal Berkovich indenter was employed for hardness and elastic modulus measurement [42,43]. The indentation curves were analyzed using the standard method [44].

Sphero-conical Rockwell indenter with a nominal radius of $10 \mu\text{m}$ was used for scratch test to assess the adhesion-cohesion properties of the films. During the standard scratch procedure, the initially constant topographic load of 0.02 mN was applied over the first $50 \mu\text{m}$ and then ramped to 500 mN at constant loading rate of 13 mN/s to initiate films failure and reveal their cohesive and/or adhesive limits. Evaluation of the scratch test was performed on the basis of the indenter on-load depth record and analysis of the residual scratch tracks. Laser scanning confocal microscope LEXT OLS 3100 (Olympus, Tokyo, Japan) was used for high-resolution imaging.

3.3. Electrochemical Anodization to Grow Self-Organized TiO_2 Nanotubes

The titanium films on FTO glass were washed with ethanol. TiO_2 nanotubes were then grown at 60 V using a power source (STATRON 3253.3, Statron AG, Mägenwil, Switzerland) in a two-electrode configuration with a counter electrode made of platinum (cathode) and the working electrode was the titanium film (anode). The electrolyte contained $0.2 \text{ mol dm}^{-3} \text{ NH}_4\text{F}$ and $4 \text{ mol dm}^{-3} \text{ H}_2\text{O}$ in ethylene glycol. After the anodization process, the samples were washed in ethanol and then dried in a nitrogen stream. The as-prepared amorphous TNT were annealed at 500 °C for 1h in air using cylindrical furnace (Clasic CLARE 4.0, CLASIC, Revnice, Czech Republic) with temperature increase $5 \text{ }^\circ\text{C min}^{-1}$ to obtain the crystalline phase. The nanotubes grown from titanium films deposited at different temperatures such as RT, 150 °C, 300 °C, and 450 °C, are in the text coded as TNT-RT, TNT-150, TNT-300, and TNT-450, respectively.

3.4. Characterization of the Titanium Films and TiO₂ Nanotubes

Structure of the Ti films was determined using the Empyrean (PANalytical, Almelo, The Netherlands) diffractometer equipped with Co. radiation source, focusing mirror, and Pixcell detector via grazing angle regime with incident angle 2°. Mean crystallite size was determined using the Scherrer equation. Surface of the films and its cross-sections were observed using Scanning Electron Microscope Hitachi SU6600 (Hitachi, Tokyo, Japan).

3.5. Photoelectrochemistry

The photoelectrochemical data were collected using a standard three-electrode electrochemical cell with a Gamry Series G 300 Potentiostat (Warminster, PA, USA). The TiO₂ nanotubes served as working electrode (photoanode), the Ag/AgCl (3 M KCl) as the reference electrode and the Pt wire was used as the counter electrode. A 150 W Xenon lamp coupled with an AM1.5G filter was used as a light source. The power intensity was kept at 1 sun (100 mW/cm²) which was calibrated through a silicon reference solar cell (Newport Corporation, Irvine, CA, USA). The photoelectrochemical behavior of prepared electrodes was investigated by means of linear sweep voltammetry measurements in 1 M NaOH electrolyte (pH 13.5). The electrochemical impedance spectroscopy (EIS) data were recorded using a Gamry instrument (ESA 410, Gamry, Warminster, PA, USA) in the frequency range from 0.1 Hz to 100 kHz under 1 sun illumination at a bias of 0 V vs. Ag/AgCl. At least three electrodes of each type were fabricated and tested. All electrodes showed similar J-V curves, and representative data are reported.

4. Conclusions

In this study, we have reported a detailed investigation of mechanical and adhesion properties of Ti films sputtered at different temperatures, showing that temperatures as high as 450 °C produce Ti films with well-defined platelet texture and with best mechanical and adhesion properties. However, we have found that these different sputtering conditions strongly influence crystallographic and photoelectrochemical water splitting activity of self-organized TiO₂ nanotubes grown from Ti films. The more active TiO₂ nanotube sample towards photoelectrochemical water splitting was obtained from Ti substrate sputtered at 150 °C showing the lowest crystallite size, best degree of self-organization, and enhanced charge transfer at the semiconductor/liquid interface. This work remarks the challenge behind achieving highly active and durable materials for photonics applications and shows that advanced magnetron sputtering may enable good control over microstructural properties and, thus, performance of semiconductor thin films.

Acknowledgments: The authors gratefully acknowledge the support by the Operational Programme Research, Development and Education—European Regional Development Fund, project no. CZ.02.1.01/0.0/0.0/15_003/0000416 and the project 8E15B009 of the Ministry of Education, Youth and Sports of the Czech Republic. The authors also acknowledge the financial support from Grant Agency of Czech Republic (project number 15-19705S and 17-20008S) and the Internal Grant of Palacky University (IGA_PrF_2017_005).

Author Contributions: S.K. and Z.H. conceived and designed the experiments; M.Z., R.C., H.K., S.P., J.T., Y.R., A.N., J.K. performed the experiments, analyzed the data and contributed reagents/materials/analysis tools; M.Z., R.C., S.K., A.N. wrote the paper, P.S. and R.Z. supervised the project.

Conflicts of Interest: The authors declare no conflicts of interest.

References

1. Papoutsis, D.; Lianos, P.; Yianoulis, P.; Koutsoukos, P. Sol-gel derived TiO₂ microemulsion gels and coatings. *Langmuir* **1994**, *10*, 1684–1689. [[CrossRef](#)]
2. Kment, S.; Kmentova, H.; Kluson, P.; Krysa, J.; Hubicka, Z.; Cirkva, V.; Gregora, I.; Solcova, O.; Jastrabik, L. Notes on the photo-induced characteristics of transition metal-doped and undoped titanium dioxide thin films. *J. Colloid Interface Sci.* **2010**, *348*, 198–205. [[CrossRef](#)] [[PubMed](#)]

3. Krysa, J.; Zlamal, M.; Kment, S.; Brunclikova, M.; Hubicka, Z. TiO₂ and Fe₂O₃ films for photoelectrochemical water splitting. *Molecules* **2015**, *20*, 1046. [[CrossRef](#)] [[PubMed](#)]
4. Kment, S.; Kluson, P.; Stranak, V.; Virostko, P.; Krysa, J.; Cada, M.; Pracharova, J.; Kohout, M.; Morozova, M.; Adamek, P.; et al. Photo-induced electrochemical functionality of the TiO₂ nanoscale films. *Electrochim. Acta* **2009**, *54*, 3352–3359. [[CrossRef](#)]
5. Naldoni, A.; Riboni, F.; Marelli, M.; Bossola, F.; Ulisse, G.; Di Carlo, A.; Pis, I.; Nappini, S.; Malvestuto, M.; Dozzi, M.V.; et al. Influence of TiO₂ electronic structure and strong metal-support interaction on plasmonic photocatalytic oxidations. *Catal. Sci. Technol.* **2016**, *6*, 3220–3229. [[CrossRef](#)]
6. Chen, X.; Mao, S.S. Titanium dioxide nanomaterials: Synthesis, properties, modifications, and applications. *Chem. Rev.* **2007**, *107*, 2891–2959. [[CrossRef](#)] [[PubMed](#)]
7. Kavan, L.; Grätzel, M.; Rathouský, J.; Zukalb, A. Nanocrystalline TiO₂ (anatase) electrodes: Surface morphology, adsorption, and electrochemical properties. *J. Electrochem. Soc.* **1996**, *143*, 394–400. [[CrossRef](#)]
8. Naldoni, A.; Montini, T.; Malara, F.; Mróz, M.M.; Beltram, A.; Virgili, T.; Boldrini, C.L.; Marelli, M.; Romero-Ocaña, I.; Delgado, J.J.; et al. Hot electron collection on brookite nanorods lateral facets for plasmon-enhanced water oxidation. *ACS Catal.* **2017**, *7*, 1270–1278. [[CrossRef](#)]
9. Ren, L.; Li, Y.; Hou, J.; Zhao, X.; Pan, C. Preparation and enhanced photocatalytic activity of TiO₂ nanocrystals with internal pores. *ACS Appl. Mater. Interfaces* **2014**, *6*, 1608–1615. [[CrossRef](#)] [[PubMed](#)]
10. Chen, X.; Shen, S.; Guo, L.; Mao, S.S. Semiconductor-based photocatalytic hydrogen generation. *Chem. Rev.* **2010**, *110*, 6503–6570. [[CrossRef](#)] [[PubMed](#)]
11. Ma, Y.; Wang, X.; Jia, Y.; Chen, X.; Han, H.; Li, C. Titanium dioxide-based nanomaterials for photocatalytic fuel generations. *Chem. Rev.* **2014**, *114*, 9987–10043. [[CrossRef](#)] [[PubMed](#)]
12. Straňák, V.; Čada, M.; Quaas, M.; Block, S.; Bogdanowicz, R.; Kment, S.; Wulff, H.; Hubička, Z.; Helm, C.A.; Tichý, M.; et al. Physical properties of homogeneous TiO₂ films prepared by high power impulse magnetron sputtering as a function of crystallographic phase and nanostructure. *J. Phys. D: Appl. Phys.* **2009**, *42*, 105204. [[CrossRef](#)]
13. Roy, P.; Berger, S.; Schmuki, P. TiO₂ nanotubes: Synthesis and applications. *Angew. Chem. Int. Ed.* **2011**, *50*, 2904–2939. [[CrossRef](#)] [[PubMed](#)]
14. Gordon, T.R.; Cargnello, M.; Paik, T.; Mangolini, F.; Weber, R.T.; Fornasiero, P.; Murray, C.B. Nonaqueous synthesis of TiO₂ nanocrystals using TiF₄ to engineer morphology, oxygen vacancy concentration, and photocatalytic activity. *J. Am. Chem. Soc.* **2012**, *134*, 6751–6761. [[CrossRef](#)] [[PubMed](#)]
15. Dong, F.; Zhao, W.; Wu, Z. Characterization and photocatalytic activities of C, N and S co-doped TiO₂ with 1D nanostructure prepared by the nano-confinement effect. *Nanotechnology* **2008**, *19*, 365607. [[CrossRef](#)] [[PubMed](#)]
16. Kment, S.; Riboni, F.; Pausova, S.; Wang, L.; Wang, L.; Han, H.; Hubicka, Z.; Krysa, J.; Schmuki, P.; Zboril, R. Photoanodes based on TiO₂ and α-Fe₂O₃ for solar water splitting—Superior role of 1D nanoarchitectures and of combined heterostructures. *Chem. Soc. Rev.* **2017**, *46*, 3716–3769. [[CrossRef](#)] [[PubMed](#)]
17. Paramasivam, I.; Jha, H.; Liu, N.; Schmuki, P. A review of photocatalysis using self-organized TiO₂ nanotubes and other ordered oxide nanostructures. *Small* **2012**, *8*, 3073–3103. [[CrossRef](#)] [[PubMed](#)]
18. Krysa, J.; Lee, K.; Pausova, S.; Kment, S.; Hubicka, Z.; Ctvrtlik, R.; Schmuki, P. Self-organized transparent 1D TiO₂ nanotubular photoelectrodes grown by anodization of sputtered and evaporated Ti layers: A comparative photoelectrochemical study. *Chem. Eng. J.* **2017**, *308*, 745–753. [[CrossRef](#)]
19. Fahim, N.F.; Sekino, T.; Morks, M.F.; Kusunose, T. Electrochemical growth of vertically-oriented high aspect ratio titania nanotubes by rapid anodization in fluoride-free media. *J. Nanosci. Nanotechnol.* **2009**, *9*, 1803–1818. [[CrossRef](#)] [[PubMed](#)]
20. Kmentova, H.; Kment, S.; Wang, L.; Pausova, S.; Vaclavu, T.; Kuzel, R.; Han, H.; Hubicka, Z.; Zlamal, M.; Olejnicek, J.; et al. Photoelectrochemical and structural properties of TiO₂ nanotubes and nanorods grown on FTO substrate: Comparative study between electrochemical anodization and hydrothermal method used for the nanostructures fabrication. *Catal. Today* **2017**, *287*, 130–136. [[CrossRef](#)]
21. Lee, K.; Kim, D.; Berger, S.; Kirchgeorg, R.; Schmuki, P. Anodically formed transparent mesoporous TiO₂ electrodes for high electrochromic contrast. *J. Mater. Chem.* **2012**, *22*, 9821–9825. [[CrossRef](#)]

22. Macak, J.M.; Schmuki, P. Anodic growth of self-organized anodic TiO₂ nanotubes in viscous electrolytes. *Electrochim. Acta* **2006**, *52*, 1258–1264. [[CrossRef](#)]
23. Zwillig, V.; Aucouturier, M.; Darque-Ceretti, E. Anodic oxidation of titanium and TA6V alloy in chromic media. An electrochemical approach. *Electrochim. Acta* **1999**, *45*, 921–929. [[CrossRef](#)]
24. Paušová, Š.; Kment, Š.; Zlámál, M.; Baudys, M.; Hubička, Z.; Krýsa, J. Transparent nanotubular TiO₂ photoanodes grown directly on fto substrates. *Molecules* **2017**, *22*, 775. [[CrossRef](#)] [[PubMed](#)]
25. Berger, S.; Ghicov, A.; Nah, Y.C.; Schmuki, P. Transparent TiO₂ nanotube electrodes via thin layer anodization: Fabrication and use in electrochromic devices. *Langmuir* **2009**, *25*, 4841–4844. [[CrossRef](#)] [[PubMed](#)]
26. Krýsa, J.; Zlámál, M.; Paušová, Š.; Kotrla, T.; Kment, Š.; Hubička, Z. Hematite photoanodes for solar water splitting: Directly sputtered vs. Anodically oxidized sputtered Fe. *Catal. Today* **2017**, *287*, 99–105. [[CrossRef](#)]
27. Sadek, A.Z.; Zheng, H.; Latham, K.; Wlodarski, W.; Kalantar-zadeh, K. Anodization of Ti thin film deposited on ito. *Langmuir* **2009**, *25*, 509–514. [[CrossRef](#)] [[PubMed](#)]
28. Tang, Y.; Tao, J.; Zhang, Y.; Wu, T.; Tao, H.; Bao, Z. Preparation and characterization of TiO₂ nanotube arrays via anodization of titanium films deposited on fto conducting glass at room temperature. *Acta Physico-Chim. Sin.* **2008**, *24*, 2191–2197. [[CrossRef](#)]
29. Wang, J.; Wang, H.; Li, H.; Wu, J. Synthesis and characterization of TiO₂ nanotube film on fluorine-doped tin oxide glass. *Thin Solid Films* **2013**, *544*, 276–280. [[CrossRef](#)]
30. Olejníček, J.; Hubička, Z.; Kment, Š.; Čada, M.; Kšířová, P.; Adámek, P.; Gregora, I. Investigation of reactive HiPIMS + MF sputtering of TiO₂ crystalline thin films. *Surf. Coat. Technol.* **2013**, *232*, 376–383. [[CrossRef](#)]
31. Bukauskas, V.; Kaciulis, S.; Mezzi, A.; Mironas, A.; Niaura, G.; Rudzikas, M.; Šimkienė, I.; Šetkus, A. Effect of substrate temperature on the arrangement of ultra-thin TiO₂ films grown by a dc-magnetron sputtering deposition. *Thin Solid Films* **2015**, *585*, 5–12. [[CrossRef](#)]
32. Firstov, S.; Kulikovskiy, V.; Rogul, T.; Ctvrtlik, R. Effect of small concentrations of oxygen and nitrogen on the structure and mechanical properties of sputtered titanium films. *Surf. Coat. Technol.* **2012**, *206*, 3580–3585. [[CrossRef](#)]
33. Petrov, I.; Barna, P.B.; Hultman, L.; Greene, J.E. Microstructural evolution during film growth. *J. Vacuum Sci. Technol. A* **2003**, *21*, S117–S128. [[CrossRef](#)]
34. Chawla, V.; Jayaganthan, R.; Chawla, A.K.; Chandra, R. Microstructural characterizations of magnetron sputtered Ti films on glass substrate. *J. Mater. Process. Technol.* **2009**, *209*, 3444–3451. [[CrossRef](#)]
35. Savaloni, H.; Taherizadeh, A.; Zendeenam, A. Residual stress and structural characteristics in Ti and Cu sputtered films on glass substrates at different substrate temperatures and film thickness. *Phys. B Condens. Matter* **2004**, *349*, 44–55. [[CrossRef](#)]
36. Arzt, E. Size effects in materials due to microstructural and dimensional constraints: A comparative review. *Acta Mater.* **1998**, *46*, 5611–5626. [[CrossRef](#)]
37. Kulikovskiy, V.; Ctvrtlik, R.; Vorlicek, V.; Filip, J.; Bohac, P.; Jastrabik, L. Mechanical properties and structure of TiO₂ films deposited on quartz and silicon substrates. *Thin Solid Films* **2013**, *542*, 91–99. [[CrossRef](#)]
38. Lee, K.; Mazare, A.; Schmuki, P. One-dimensional titanium dioxide nanomaterials: Nanotubes. *Chem. Rev.* **2014**, *114*, 9385–9454. [[CrossRef](#)] [[PubMed](#)]
39. Kuzmych, O. Defect Minimization and Morphology Optimization in TiO₂ Nanotube Thin Films, Grown on Transparent Conducting Substrate, for Dye Synthesized Solar Cell Application. *Thin Solid Films* **2012**, *522*, 71–78. [[CrossRef](#)]
40. Witt, F.; Vook, R.W. Thermally induced strains in diamond cubic, tetragonal, orthorhombic, and hexagonal films. *J. Appl. Phys.* **1969**, *40*, 709–719. [[CrossRef](#)]
41. Albu, S.P.; Schmuki, P. Influence of anodization parameters on the expansion factor of TiO₂ nanotubes. *Electrochim. Acta* **2013**, *91*, 90–95. [[CrossRef](#)]
42. Ctvrtlik, R.; Al-Haik, M.; Kulikovskiy, V. Mechanical properties of amorphous silicon carbonitride thin films at elevated temperatures. *J. Mater. Sci.* **2015**, *50*, 1553–1564. [[CrossRef](#)]

43. Ctvrtlik, R.; Kulikovskiy, V.; Vorlicek, V.; Tomastik, J.; Drahokoupil, J.; Jastrabik, L. Mechanical properties and microstructural characterization of amorphous SiC_xN_y thin films after annealing beyond 1100 °C. *J. Am. Ceram. Soc.* **2016**, *99*, 996–1005. [[CrossRef](#)]
44. Oliver, W.C.; Pharr, G.M. An improved technique for determining hardness and elastic modulus using load and displacement sensing indentation experiments. *J. Mater. Res.* **1992**, *7*, 1564–1583. [[CrossRef](#)]



© 2018 by the authors. Licensee MDPI, Basel, Switzerland. This article is an open access article distributed under the terms and conditions of the Creative Commons Attribution (CC BY) license (<http://creativecommons.org/licenses/by/4.0/>).

Appendix [A4]

Radiative and Non-Radiative Recombination Pathways in Mixed-Phase TiO₂ Nanotubes for PEC Water-Splitting,

R. Yalavarthi, A. Naldoni*, **S. Kment***, L. Mascaretti, H. Kmentova, O. Tomanec, P. Schmuki, R. Zboril*

Catalysts 9, 204, 2019

Article

Radiative and Non-Radiative Recombination Pathways in Mixed-Phase TiO₂ Nanotubes for PEC Water-Splitting

Rambabu Yalavarthi ¹, Alberto Naldoni ^{1,*} , Štěpán Kment ^{1,*}, Luca Mascaretti ¹ ,
Hana Kmentová ¹, Ondřej Tomanec ¹, Patrik Schmuki ^{1,2} and Radek Zbořil ^{1,*}

¹ Regional Centre of Advanced Technologies and Materials, Faculty of Science, Palacký University Olomouc, 17. listopadu 1192/12, 771 46 Olomouc, Czech Republic; rambabu.yalavarthi@upol.cz (R.Y.); luca.mascaretti@upol.cz (L.M.); hana.kmentova@upol.cz (H.K.); ondrej.tomanec@upol.cz (O.T.); schmuki@ww.uni-erlangen.de (P.S.)

² Department of Materials Science and Engineering, University of Erlangen-Nuremberg, Martensstrasse 7, D-91058 Erlangen, Germany

* Correspondence: alberto.naldoni@upol.cz (A.N.); stepan.kment@upol.cz (Š.K.); radek.zboril@upol.cz (R.Z.)

Received: 22 January 2019; Accepted: 19 February 2019; Published: 23 February 2019



Abstract: Anatase and rutile mixed-phase TiO₂ with an ideal ratio has been proven to significantly enhance photoelectrochemical (PEC) activity in water-splitting applications due to suppressing the electron–hole recombination. However, the mechanism of this improvement has not been satisfactorily described yet. The PEC water oxidation (oxygen evolution) at the interface of TiO₂ photoanode and electrolyte solution is determined by the fraction of the photogenerated holes that reach the solution and it is defined as the hole transfer efficiency. The surface and bulk recombination processes in semiconductor photoanodes majorly influence the hole transfer efficiency. In this work, we study the hole transfer process involved in mixed-phase TiO₂ nanotube arrays/solution junction using intensity-modulated photocurrent and photovoltage spectroscopy (IMPS and IMVS); then, we correlate the obtained hole transfer rate constants to (photo)electrochemical impedance spectroscopy (PEIS) measurements. The results suggest that the enhanced performance of the TiO₂ mixed-phase is due to the improved hole transfer rate across the TiO₂/liquid interface as well as to the decrease in the surface trap recombination of the holes.

Keywords: charge transfer; intensity-modulated photocurrent spectroscopy; phase transitions; photoelectrochemical impedance spectroscopy; water-splitting

1. Introduction

Since the discovery of water photo-oxidation at semiconducting photoanodes, tremendous research has been undertaken to improve the practical efficiency of photoelectrochemical (PEC) water-splitting devices [1,2]. Upon proper light illumination, a semiconductor generates electron–hole pairs that must be adequately separated to simultaneously complete water oxidation and reduction processes [3–5]. However, in practice, the recombination of the photoinduced electron–hole pairs in the bulk of the materials, as well as at the electrode/electrolyte interface, limits the overall efficiency associated with photoelectrodes for PEC water-splitting [4–8]. Several strategies have been reported to minimize the recombination processes in semiconductor photoelectrodes, such as: increasing conductivity with doping [9–12], heterojunction formation [7,13,14], modification of photoanode surface with co-catalysts [15–17], and coatings of thin conformal layers using atomic layer deposition (ALD) [18–20]. Among these, the heterojunction formation has been widely reported for different combinations of materials and is proved to be particularly effective for the charge separation

in photoelectrodes [7,13,14]. This strategy has already been successfully employed for titanium dioxide (TiO₂), which is one of the most investigated materials in PEC water-splitting [12,21–23] thanks to its abundance, low toxicity, and chemical stability in harsh environments under light illumination [7,8]. The heterojunctions have been mostly realized by coupling TiO₂ with other semiconductor materials [13,14,24,25] but also using only TiO₂ and exploiting the slight bandgap offset (0.2 eV) of the anatase and rutile phases: this has been widely reported for photocatalytic water-splitting, in which the commercially available P25 TiO₂ powder is often employed [26,27]. The charge separation effect between the two phases, leading to increased photocatalytic efficiency, has been initially explained by an electron transfer from anatase to rutile due to the 0.2 eV higher conduction band minimum (CBM) of anatase with respect to rutile [21,28,29]. However, in 2003 Hurum et al. examined this phenomenon by means of EPR (Electron Paramagnetic Resonance Spectroscopy) experiments, suggesting that electrons could move from rutile to anatase trap states, allowing holes to reach the surface for photocatalytic reactions [30]. More recent calculations and experiments, furthermore, have suggested that the CBM of rutile is higher in energy than that of anatase, enabling the electron transfer from the former to the latter and a hole transfer in the opposite direction [31–34]. From the above discussion, it can be understood that the charge transfer/separation effect in mixed-phase TiO₂ nanomaterials has not been fully clarified, especially considering PEC photoelectrodes, which have been investigated in much fewer studies compared to the nanoparticulate forms. For example, it has been shown that TiO₂ photoelectrodes with a controlled anatase/rutile configuration could be obtained by rapid thermal treatments [34–36] thus, avoiding complex or costly synthetic processes to make a composite of different polymorphs. To probe the charge transport and charge transfer properties of such photoelectrodes, occurring respectively in the bulk and at the semiconductor/electrolyte junction, perturbation PEC techniques may be employed, such as light intensity-modulated photocurrent spectroscopy (IMPS), light intensity-modulated photovoltage spectroscopy (IMVS) and electrochemical impedance spectroscopy (EIS) [37–40]. Here, we report on the study of the bulk and surface state recombination processes in single and mixed-phase TiO₂ nanotube photoanodes by employing IMPS and IMVS to gain information on non-radiative recombination (i.e., electron/hole recombination mediated by emission of phonons). Nanotubes are chosen as a suitable morphology for TiO₂ photoanodes due to their high surface to volume ratio, preferential electron transport towards the Ti back-contact, and a scalable synthetic process by electrochemical anodization [7,24,41–44]. Further, we correlate the obtained results to electrical characteristics of our photoelectrodes retrieved from EIS and to the information on radiative recombination (i.e., electron/hole recombination mediated by emission of photons) gained by photoluminescence spectroscopy. In this way, we provide a complete picture regarding the charge transfer/transport properties associated with TiO₂ nanotubes samples. The obtained results provide more insights on the working principles of mixed-phase TiO₂ photoelectrodes: the photocurrent enhancement is underlied by lower radiative recombination and, at the same time, by a more efficient hole transfer and the decrease in the surface state recombination across the TiO₂/electrolyte interface.

2. Results and Discussion

2.1. Structural and Optical Properties

The TiO₂ nanotubes obtained from the electrochemical anodization were annealed at different temperatures; the corresponding FESEM images are shown in Figure 1. The average length of the nanotubes is ~2 μm, the internal diameter is about 90 nm, and the wall thickness is ~20 nm. The as-prepared nanotubes are amorphous in nature and are transformed to the crystalline state upon annealing in air.

To analyze the variation of the phase composition upon annealing, XRD patterns were recorded (Figure 2a). The TiO₂ nanotubes annealed at 500 °C (TNT500) show reflections belonging to the sole presence of the anatase phase. However, upon increasing the annealing temperature, a rise of rutile

phase fraction was observed. It is known that Ti metal beneath the TiO₂ nanotubes readily oxidizes and forms the rutile layer at the Ti/TiO₂ interface during the annealing [45–47]. This rutile layer acts as an initiation layer for further conversion of anatase to rutile in the TiO₂ nanotubes [48–50] (See Figure S1). In contrast, in the absence of the Ti metal, the formation of rutile layer and subsequent transition from anatase to rutile was not observed [46,49]. Further, the rutile layer formed due to thermal oxidation observed to be thicker with the shorter nanotubes because of the increase in the proximity of the metal to the top surface of the nanotubes [47,49]. Moreover, recent studies suggest that during the phase transition from anatase to rutile, the as-formed rutile layer plays a crucial role in further distortion of the TiO₆ octahedral across the interface of the Ti metal/nanotube and the reformation of the Ti-O bonds into the rutile phase. This process gradually continues along the tube length upon the temperature increase [48,50]. In our samples, the rutile phase appeared at 600 °C (TNT600) and it was confirmed in XRD patterns by the peak at 27.72° corresponding to (110) plane (JCPDS file no. 87-0920). Conversely, for the sample annealed at 700 °C (TNT700), the dominant phase is rutile; this indicates the transformation of a maximum number of anatase grains to rutile starting from the interface of the Ti metal and the nanotubes [48,50]. This transformation creates a layered structure of the TiO₂ nanotubes with rutile content at the bottom, anatase layer at the top, and an intermediate gradual transformation layer between the two phases of the nanotubes [50], resulting in the heterojunction between the two phases of TiO₂. The phase fraction of TiO₂ nanotubes annealed at different temperatures retrieved through Rietveld refinement of XRD measurements.

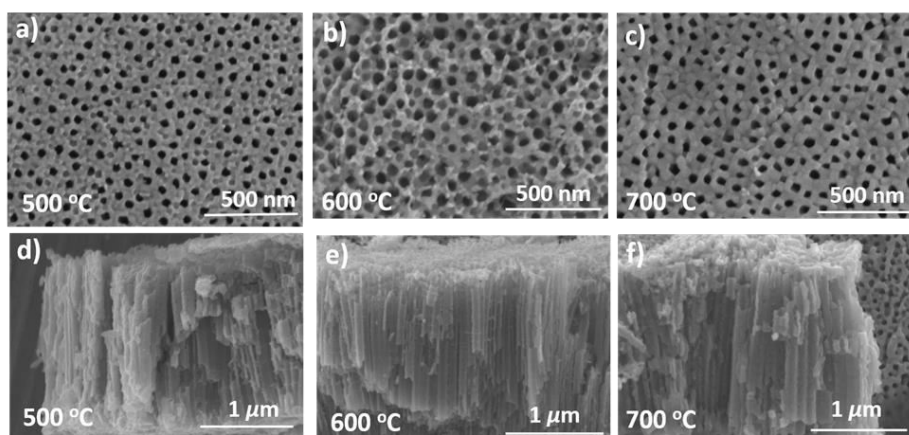


Figure 1. Field emission scanning electron microscope (FESEM) images of TiO₂ nanotubes (a–c) top view and (d–f) corresponding cross-sectional images.

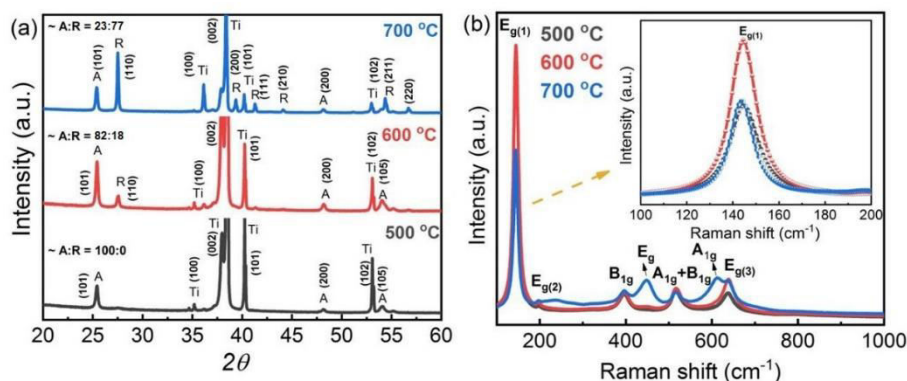


Figure 2. (a) X-ray diffraction patterns and (b) Raman spectra of TiO₂ nanotubes annealed at different temperatures. (inset) An enlarged view of the Raman E_{g(1)} peak.

The phase composition of TNT500 was 100% in anatase, while the weight ratio of rutile to anatase was determined 18:82 and 77:23 for TNT600 and TNT700, respectively. It indicates an increase in the rutile layer thickness upon the increase in the calcination temperature [49–51].

The crystallite size (grain growth) was calculated using the Debye–Sherrer formula shown below

$$d = 0.9\lambda / (\beta \cos\theta), \quad (1)$$

where d is crystallite size, λ is wavelength (0.154 nm) of X-rays, β is full-width half maximum in radians, and θ is the angle of diffraction.

As the annealing temperature changes, the decrease in anatase crystallite size and the transformation of anatase to rutile were observed. The crystallite size for TNT500 was 58 ± 2 nm corresponding to (101) planes, whereas it was decreased to 42 ± 3 for sample TNT600. At the same time, the rutile crystallization was observed and the size corresponding to (110) for TNT600 is 34 ± 1 nm. A further change in annealing temperature showed an increase of rutile crystallite size up to 74 ± 2 nm for the sample TNT700. During the process of annealing the distortion of TiO_6 octahedra takes places, which leads to the shrinking in size of anatase crystallite and transformation to rutile. [52–54].

The Raman spectra of the TiO_2 nanotube samples are shown in Figure 2b. The intense peak at 144 cm^{-1} and the other peaks at 391 cm^{-1} , 513 cm^{-1} , 638 cm^{-1} correspond to $E_{g(1)}$, B_{1g} , $A_{1g+B_{1g}}$, and $E_{g(3)}$ modes, which belong to anatase TiO_2 [34,55]. Further, the appearance of the peaks at 451 cm^{-1} , 610 cm^{-1} , and the second order peak at 240 cm^{-1} , besides the peak at 144 cm^{-1} , indicates the presence of rutile in TNT700 [55]. The observation of a small peak at 199 cm^{-1} suggests that the annealed samples are highly crystalline. Asymmetric broadening and shift in $E_{g(1)}$ the Raman peak position (inset of Figure 2b) indicates the existence of intrinsic defects and a crystallite size variation in the TiO_2 nanotubes annealed at different temperatures [54,56].

Phase content and microcrystalline structure were further analyzed using HR-TEM (Figure 3). The tube morphology is smooth for TNT500 in comparison to TNT600 (Figure 3a,c). Further, the lattice fringe spacing was 0.35 nm, corresponding to the (101) plane of anatase for the sample TNT500. The phase junction of anatase and rutile is observed for the sample TNT600, and the lattice fringe spacing 0.32 nm was assigned to the (110) rutile plane. The boundary line shown in Figure 3d represents phase junction and corresponding FFT images is also presented. The observation of anatase and rutile phases is well in agreement with the XRD and Raman measurements.

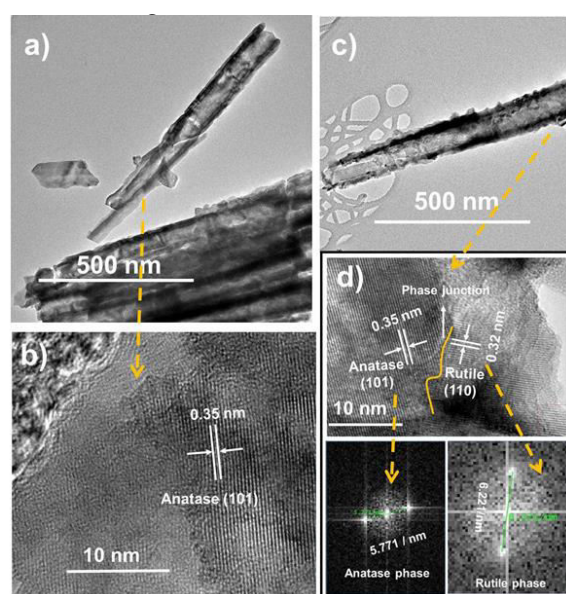


Figure 3. Transmission electron microscopy (TEM) (a) and high resolution (HR)-TEM images of TNT500 (b). (c) TEM image of TNT600. (d) HR-TEM image of TNT600 and corresponding FFT representations.

Further, in order to investigate the intrinsic recombination processes and the presence of defects, we carried out photoluminescence (PL) measurements on the TiO₂ nanotube samples annealed at different temperatures (with 350 nm or 3.54 eV excitation), as illustrated in Figure 4. It can be noted that: first, the higher the annealing temperature, the higher the PL signal; second, the low signal/noise ratio for all the samples, due to the weak emission of TiO₂ in air [57]; and third, the broad shape of all the PL curves, which suggests the presence of several recombination pathways. The spectra presented in Figure 4 were fitted with four Gaussian components (see Figure S5) with the following peak energies: 2.21–2.29 eV, 2.58–2.68 eV, 2.84–2.85 eV, and 3.00–3.02 eV. The same peaks were found independently on the phase composition of the nanotubes. The PL of rutile is characterized by an intense and narrow peak in the NIR region (1.48 eV or 835 nm) [57–60]; thus, the spectra in Figure 4, which show emissions occurring in the visible region, may be related only to the anatase PL. For this phase, emissions with sub-bandgap energies have been widely attributed to radiative recombination mediated by defect states. However, the PL of TiO₂ nanomaterials is strongly dependent on the material morphology, crystallinity, and defectivity, which leads to conflicting results in the literature [61]. The curves in Figure 4, in particular, are similar to the PL spectra reported by Lei et al. [62], who investigated highly ordered anatase nanowires. Based on their report and on other studies, the following spectral assignments may be proposed. The highest energy peak (3.00 eV) may be attributed to self-trapped exciton recombination in TiO₆ octahedra [57]. The peaks at 2.85 eV and at 2.58–2.68 eV may be related to oxygen vacancies [59,60,63], which exhibit a different energy level in the bandgap according to their charge state [64–66]. Finally, the lowest energy peak (2.21–2.29 eV) may be attributed to surface states, i.e., radiative recombination involving unsaturated Ti atoms on the surface (e.g., Ti³⁺) [57,63,67]. It should be noted that precise and univocal identification of the defect states in TiO₂ nanotubes was not the main scope of this work; rather, the PL measurements overall suggest that with the increasing fraction of rutile, radiative recombination in the remaining anatase crystals increase, thus, affecting the charge transport properties of the films. This effect may be explained by the fact that the rutile crystallites nucleate with a lower amount of defects. Alternatively, the increase of rutile fraction may induce the formation of trapping sites in anatase crystals at their interfaces with rutile ones [33]. In any case, the TNT600 sample could represent a good compromise between better charge separation (enabled by the presence of both anatase and rutile phases) and radiative recombination (mainly occurring via the defect states in anatase crystals).

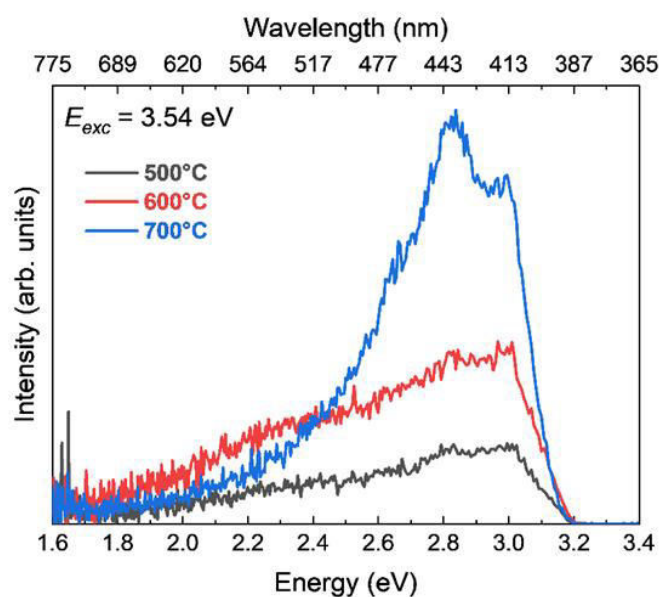


Figure 4. Photoluminescence spectra of TiO₂ nanotubes with UV excitation energy (3.54 eV).

The UV-Vis absorbance spectra for all the TiO₂ nanotube samples are shown in Figure 5. The onset of the optical absorption for TNT500 is observed at 390 nm corresponding to a band gap of ~3.18 eV, while for TNT600 and TNT700 red-shifted at 410 nm (~3 eV) due to the presence of rutile content in the samples. The UV-Vis absorbance spectra for all the TiO₂ nanotube samples are shown in Figure 5. The onset of the optical absorption for TNT500 is observed at 390 nm corresponding to a band gap of ~3.18 eV, while for TNT600 and TNT700 red-shifted at 410 nm (~3 eV) due to the presence of rutile content in the samples.

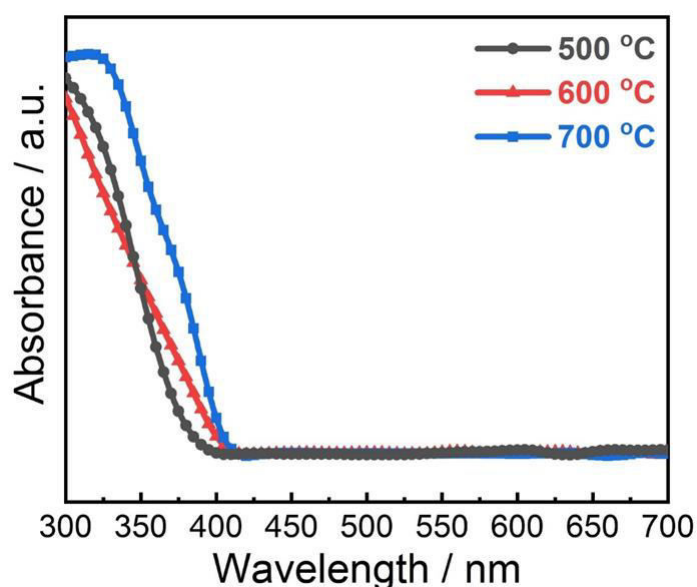


Figure 5. Normalized absorbance spectra of TiO₂ nanotubes annealed at different temperatures.

2.2. Photoelectrochemical Measurements

Linear sweep voltammetry (LSV) scans were recorded for the prepared samples under dark and illumination conditions using a three-electrode setup in 1 M NaOH solution against Ag/AgCl reference electrode. Figure 6a shows photocurrent measurements for TNT500, 600, and 700 under AM1.5G illumination. All samples show approximately the same photocurrent onset potential of -0.59 V vs. Ag/AgCl while showing a different steady-state photocurrent. Sample TNT600 showed the highest photocurrent density (0.11 mA cm⁻² at 0.5 V vs. Ag/AgCl) followed by TNT500 (0.10 mA cm⁻² at 0.5 V vs. Ag/AgCl) and TNT700 (0.05 mA cm⁻² at 0.5 V vs. Ag/AgCl). In addition, the photocurrent plots reveal that TNT600 had also a higher fill factor if compared to TNT500. To gain further information on the effect of the anatase/rutile heterojunction on the PEC performance of our samples, we carried out IPCE measurements at 0.5 V vs. Ag/AgCl (Figure 6b). The IPCE is defined as the ratio between the measured photocurrent and the power of the incident photons from the following relationship [23]

$$IPCE (\%) = (1240/\lambda) \times (J_{ph}/I_{light}) \times 100, \quad (2)$$

where λ is the incident wavelength in nm, J_{ph} is the photocurrent density in mA cm⁻² and I_{light} is the intensity of the incident light in mW cm⁻². The spectra showed high IPCE % below 400 nm because of significant absorption of UV light for above bandgap excitation. The measured IPCE for TNT600 is 52% at 370 nm, whereas for TNT500 it was 42% and decreased to 21% in the case of TNT700 sample. The same trend was reflected in the photocurrent measurements. However, for samples TNT600 and TNT700, there was a little higher (0.05) IPCE % observed in the wavelength region 400–420 nm, well in agreement with the absorption spectra and the increased light absorption related to rutile phase content.

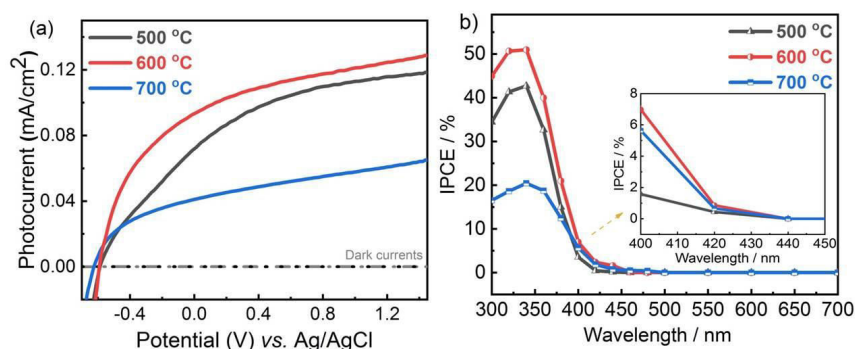


Figure 6. (a) Linear sweep voltammetry scans (LSV) of nanotubes measured in 1 M NaOH solution, under 1 sun illumination (100 mW cm^{-2} , AM1.5G) and (b) IPCE (%) spectra of TiO_2 nanotubes measured at 0.5 V vs. Ag/AgCl.

From these measurements, it is clear that the sample which contains a proper ratio of the anatase and rutile phases (TNT600) shows the highest photocurrent density compared to the single anatase phase (TNT500) and the highest rutile content phase sample (TNT700). This effect is in agreement with previous studies [40], but cannot simply be explained by the results of PL (Figure 4) or absorption (Figure 5) spectroscopy. Indeed, the effect of non-radiative recombination must also be taken into account, which is significant in TiO_2 [57]. Thus, to analyze the photocurrent enhancement and the recombination pathways in these samples in more detail, we employed intensity-modulated photocurrent and photovoltage (IMPS, IMVS) and electrochemical impedance spectroscopy (EIS) techniques. Figure 7 shows representative plots of IMPS, IMVS and EIS spectra (Figure 7a–c, respectively), measured at $-0.5 \text{ V vs. Ag/AgCl}$, and a schematic of an equivalent circuit used for the EIS data fitting (Figure 7d).

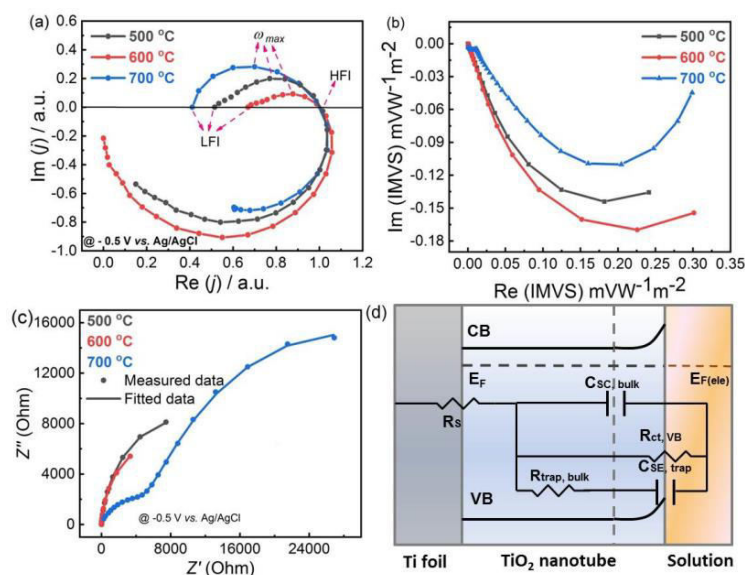


Figure 7. Representative perturbative PEC spectroscopy plots of TiO_2 nanotubes annealed at different temperatures. (a) Intensity-modulated photocurrent spectroscopy (IMPS, normalized), spectra measured at $-0.5 \text{ V vs. Ag/AgCl}$. (b) Intensity-modulated photovoltage spectroscopy (IMVS) measured under open circuit conditions. (c) Photoelectrochemical impedance spectroscopy (PEIS) measured at $-0.5 \text{ V vs. Ag/AgCl}$. (d) Schematic of an equivalent circuit used for fitting. R_s is the contact/solution resistance, $R_{trap,bulk}$ is the bulk charge transport resistance, $R_{ct,VB}$ is the charge transfer resistance across the semiconductor/electrolyte interface. $C_{sc,bulk}$ is the space charge layer capacitance, $C_{SE,trap}$ represents the capacitance of the semiconductor/electrolyte interface. All measurements were performed in 1 M NaOH electrolyte.

2.3. Intensity-Modulated Photocurrent Spectroscopy (IMPS)

IMPS is a perturbation method used to extract charge transfer kinetics across the semiconductor/electrolyte interface by a sinusoidal variation of the illumination light intensity (see Figure S3). The rate constants corresponding to both charge transfer and surface recombination were derived from the normalized IMPS spectra [68–70]. The complex Nyquist photocurrent response plots were recorded using a small sinusoidal perturbation light signal. The representative normalized IMPS plots obtained for TiO₂ nanotubes at −0.5 V vs. Ag/AgCl are shown in Figure 7a. Further, the rate constants were extracted using Equation (3) below. The ratio of low-frequency intercept to high-frequency intercept (LFI to HFI) in Figure 7a corresponds to the charge transfer efficiency as shown in the equation below [69,70].

$$\eta_{ct} = J_{ss}/J_{inst} = k_{trans}/(k_{trans} + k_{rec}) = \text{LFI}/\text{HFI}, \quad (3)$$

In Equation (4), the HFI in recombination semicircle (Figure 7a) represents instantaneous photocurrent and LFI corresponds to steady state photocurrent.

The time constant of the process is $\omega_{max} = k_{trans} + k_{rec}$ and it can be determined from the maximum of recombination semicircle perturbation frequency in a complex plane. Since the real part of semicircle at $\omega = 0$ tends towards $I_0(k_{trans}/(k_{trans} + k_{rec}))$, the radial maximum is assumed to occur at $k_{trans} + k_{rec}$ [68]. The diameter of the positive semicircle corresponding to normalized IMPS spectra in Figure 7a is smaller for TNT600 followed by samples TNT500 and TNT700, thus, suggesting the higher hole transfer ability of TNT600 compared to TNT500 and TNT700 samples. The calculated rate constants for both the hole transfer (K_{tr}) and the surface recombination of the holes (K_{sr}) are shown in Figure 8a,b. The maximum hole transfer rate is observed at the onset potential for all the samples and it decreased with increasing potentials, to finally become constant at higher potentials. TNT600 showed the highest hole transfer rate indicating the highest concentration of hole flux towards the solution. Further, the surface recombination rate constant is lower at potentials greater than 0 V leading to a decrease in surface state recombination. Further, it is to be noted that the overall photocurrent enhancement depends on the charge transfer efficiency (η_{ct}) as shown in Figure 8c, and it is higher for TNT600 followed by samples TNT500 and TNT700. These results shed more light on the increased performance of the TNT600: compared to the pure anatase photoanode (TNT500), the sample with low rutile content exhibits a higher charge transfer efficiency across the electrode/electrolyte interface, which greatly affects the magnitude of the photocurrent. This may be related to the presence of several anatase/rutile interfaces close to the electrolyte, leading to an efficient charge separation between the two phases.

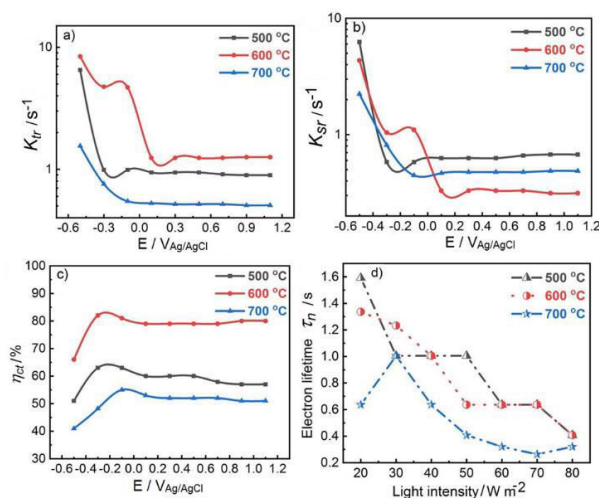


Figure 8. Kinetic parameters retrieved from IMPS and IMVS measurements. (a) Hole transfer rate (K_{tr}), (b) surface recombination rate of holes (K_{sr}), and (c) hole transfer efficiency (η_{ct}) at different applied potentials. (d) Bulk recombination rate of electron obtained from IMVS measurements performed under open circuit conditions.

2.4. Intensity-Modulated Photovoltage Spectroscopy (IMVS)

To examine the bulk electron transport properties of the TiO₂ nanotubes, we carried out the IMVS measurements with varying light intensity at open circuit conditions. The representative plots are shown in Figure 7b. The electron lifetime was calculated using the formula below:

$$\tau_n = 1/(2\pi f_{\min}(\text{IMVS})), \quad (4)$$

where f_{\min} is the minimum frequency of IMVS plot, τ_n is electron lifetime.

The electron lifetime is higher for TNT500 and TNT600 compared to TNT700 indicating that higher rutile content significantly increases the electron–hole recombination, in agreement with PL results. In order to confirm these results, we carried out additional PEC-EIS measurements as discussed below.

2.5. Electrochemical Impedance Spectroscopy (EIS)

To correlate the charge transport, charge transfer, and recombination rate constants achieved from IMPS and IMVS measurements, we additionally carried out EIS measurements under 1 sun illumination in a frequency range of 0.1–10⁵ Hz (see Figure S4). The representative spectra are shown in Figure 7c. The measured impedance data at each potential were fitted using the equivalent circuit reported in Figure 7d. The selection of the right equivalent circuit is crucial to extract the proper parameters [68]. This circuit has been previously employed for hematite (α -Fe₂O₃) as well as for TiO₂ nanotubes, neglecting charge transfer via surface states [38,71–73]. In wide bandgap semiconductors like TiO₂, the surface trap states act as spectators and then the hole transfer mainly occurs via the valence band as shown in the schematic reported in Figure 7d. (typical water oxidation process across photoanode/electrolyte illustrated in Figure S2). In the equivalent circuit, R_s is the solution resistance, $C_{SC,bulk}$ is the bulk capacitance or space charge layer capacitance corresponding to hole diffusion into the space charge layer, $R_{trap,bulk}$ is the bulk transport resistance related to electron–hole recombination from the valence band to the conduction band of TiO₂; $R_{ct,vb}$ is the hole transfer resistance from the valence band of TiO₂ to the solution; $C_{SE,trap}$ represents the Helmholtz capacitance or capacitance of double layer (CPE2 in equivalent circuit), which is also called the TiO₂/solution interfacial capacitance and it suggests the hole transfer ability of the TiO₂ nanotubes to the electrolyte [68,70].

The constant phase element (CPE) can be expressed as

$$Z_{CPE} = (1/C) j\omega n^{-1}, \quad (5)$$

where C is ideal capacitance, j is an imaginary number, ω is angular frequency, and n indicates microscopic roughness or slow adsorption of chemical species on TiO₂ electrode (for ideal capacitance behavior $n = 1$).

A smaller semicircular arch of the Nyquist plot is observed for the TNT600 sample compared to TNT500 and TNT700 (Figure 7c), indicating a lower charge transfer resistance and in turn an increased charge transfer rate to the electrolyte. Figure 9 shows the bulk charge transport resistance ($R_{trap,bulk}$) at different potentials for TNT500, 600, and 700. The charge transport resistance is lower for TNT500, followed by TNT600 (very similar) and TNT700. These results generally agree with PL results, where TNT700 showed the highest radiative recombination. In PL case though, TNT600 shows a slightly higher recombination than TNT500. This small discrepancy reflects the different conditions utilized in PL and EIS experiments: the former, indeed, were carried out in air (i.e., dried sample exposed to molecular O₂) and in open circuit, while the latter in basic pH under an applied bias, which can change the occupation of trap levels in the bandgap [74]. The increase in rutile content produces an increased $R_{trap,bulk}$ (sample annealed at 700 °C); this is consistent with the recombination time constant or electron lifetime (τ_n) extracted from IMVS measurements (Figure 8d) and with solid state conductivity measurements [75]. The charge transfer resistance ($R_{ct,trap}$) across TiO₂ nanotube/electrolyte interface is shown in Figure 9b. A monotonic increase in $R_{ct,trap}$ was observed for all the samples with an

increase in potential. This results from the increase in the hole flux upon increasing the bias potential as well as the recombination of the excess holes across the TNT/electrolyte interface [38]. The trend correlates to the photocurrent saturation observed at higher potentials. As obtained $R_{ct,trap}$ is lower for TNT600 compared to the single phase (TNT500) and the excess rutile phase content (TNT700), behaving accordingly with the charge transfer rate and collection efficiency shown in Figure 8a,c. This result emphasizes the increase in hole transfer rate towards the solution interface in the case of TNT600, i.e., when a proper anatase/rutile content is present in the material. Figure 9c shows the space charge layer capacitance ($C_{SC,bulk}$) obtained from impedance data fitting. These values are one order of magnitude smaller compared to the double layer capacitance ($C_{SE,trap}$), analogues to the negligible separation of charges in the space charge layer formed in TNT600 and TNT700, which results from the increase in bulk recombination, and it is consistent with $R_{trap,bulk}$. However, a different trend in $C_{SC,bulk}$ of TNT500 was observed compared to TNT600 and TNT700. The increase in $C_{SC,bulk}$ until 0 V vs. Ag/AgCl and later its monotonic decay indicates the slow diffusion and the separation of charges into the space charge layer because of the absence of the heterojunction, whereas in case of TNT600 and TNT700, the junction between the two phases avoids charge accumulation. Figure 9d shows the variation of double layer capacitance ($C_{SE,trap}$) for TNT600, TNT500, and TNT700. The most efficient sample (i.e., TNT600) shows significantly higher values of $C_{SE,trap}$ at all potentials, proving the accumulation of a higher concentration of the holes at the interface of TNT600/electrolyte compared to the other samples [71,73]. The monotonic decay in $C_{SE,trap}$ indicates that at a higher potential, the holes accumulate less in the photoanode/solution thus, contributing to generate higher current.

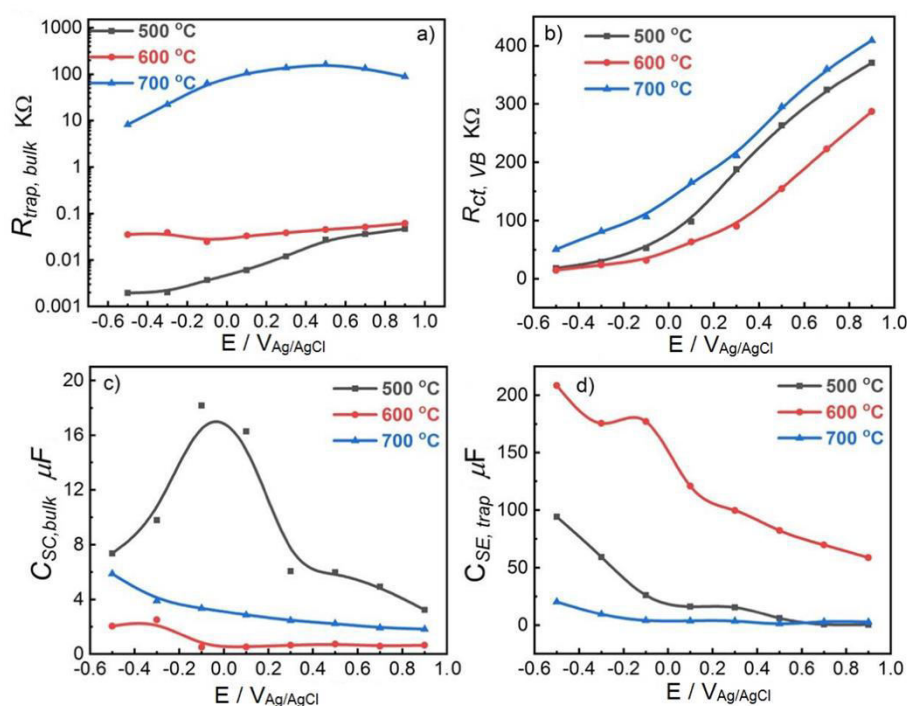


Figure 9. Electrical circuit parameters retrieved from the EIS measurements performed in 1 M NaOH and equivalent circuit fitting. (a) Bulk transport resistance ($R_{trap,bulk}$) represents the bulk recombination resistance and the trend suggests the increase in the electron–hole recombination with a change in the phase ratio of anatase to rutile, which is in agreement with the IMVS measurements. (b) Charge transfer resistance ($R_{ct,VB}$) indicates the resistance of the hole transfer from the valence band of the semiconductor to the electrolyte, which is in agreement with the charge transfer efficiency and the photocurrent trend observed for the TiO₂ nanotubes. (c) $C_{SC,bulk}$ is the space charge layer capacitance. The trend suggests an improved charge separation in TNT500 and a decrease in charge separation in mixed-phase TiO₂. It is in agreement with $R_{trap,bulk}$. (d) $C_{SE,trap}$ suggests the hole transfer ability to the electrolyte. It is in agreement with the trend observed in the photocurrent.

The charge transfer *via* the surface states in the TiO₂ nanotubes has been reported to be negligible [38] thus, the overall performance of the photoanodes can be assessed by the sum of the recombination resistance ($R_{\text{bulk,trap}}$) and the charge transfer resistance ($R_{\text{ct,trap}}$) across the TiO₂ nanotube/solution interface (considering solution resistance R_s to be the same for all photoanodes) [73]. The sum $R_{\text{bulk,trap}} + R_{\text{ct,trap}}$ is smaller for TNT600 followed by TNT500 and TNT700, which corresponds to hole transfer rate constant K_{tr} (k_1 in Figure S2a) and confirms once again the higher hole transfer ability of the mixed-phase TiO₂ nanotubes annealed at 600 °C (TNT600), which results in higher performance associated with TNT600 than that of TNT500 and 700. Figure S6, shows the Mott–Schottky plots of the photoanodes.

3. Materials and Methods

TiO₂ nanotubes were grown by electrochemical anodization from titanium foil. Prior to anodization, Ti foil (Goodfellow, 0.125 mm thick) was cleaned in a solution composed of isopropyl alcohol, acetone, and deionized with equal volume ratio followed by rinsing in DI water.

Eventually, the substrates were dried with nitrogen stream before mounting onto the anodization setup. A typical anodization setup consists of a PTFE (Teflon) beaker and two electrodes, in which Ti foil was the working electrode and Pt foil the counter electrode. The electrolyte comprises 98 mL ethylene glycol (Sigma Aldrich, St.Louis, MO, USA), 2 mL DI water, and 0.25 wt% NH₄F.HF. A DC voltage of 60 V was applied between the two electrodes keeping the distance 2 cm. After anodization the samples were cleaned in DI water and annealed in air at different temperatures for 30 min, keeping constant heating and cooling rates of 1 °C min⁻¹.

3.1. Characterization

The morphology of the TiO₂ nanotubes was characterized using a field emission scanning electron microscope (FESEM) Hitachi SU 6600 (Hitachi, Tokyo, Japan). The X-ray diffraction patterns were measured with an Empyrean (PANalytical, Almelo, The Netherlands) diffractometer equipped with Co radiation source. The absorbance and PL was measured using an FLS980 fluorescence spectrometer (Edinburg Instruments, Livingston, UK). The Raman spectra were collected using a DXR Raman spectroscope (Thermo Scientific, Waltham, MA, USA) and using a laser operating at a wavelength of 633 nm with laser power of 5 mW. The Raman spectra were evaluated using instrument control software (OMNIC, version 8, Thermo Scientific, Waltham, MA, USA). For TEM measurements, a High-Resolution Transmission Electron Microscope (HRTEM) Titan G2 (FEI, Waltham, MA, USA); accelerating voltage 80 kV was used. Images were taken with BM UltraScan CCD camera (Gatan, CA, USA).

3.2. Photoelectrochemical Measurements

The photocurrent measurements were carried out with a standard three-electrode electrochemical cell using Gamry series G 300 potentiostat (Gamry Instruments, Warminster, PA, USA) in 1 M NaOH solution (pH 13.5). The TiO₂ nanotubes on Ti foil were used as working electrode with an active area of 0.28 cm², Pt wire was the counter electrode, and Ag/AgCl (3 M KCl) was the reference electrode. A xenon lamp (150 W) equipped with AM1.5G filter was used as a light source. The illumination light intensity was 100 mW cm⁻² (1 sun), calibrated using a silicon reference solar cell (Newport Corporation, Irvine, CA, USA). The electrochemical impedance measurements (EIS) were carried out using Gamry series G 300 potentiostat (Gamry Instruments, Warminster, PA, USA) in a frequency range 0.1 Hz to 10⁵ Hz under 1 sun illumination. The incident photon-to-current conversion (IPCE) efficiency measurement was carried out using a xenon arc light source coupled to a Newport Oriel 1/8 Cornerstone monochromator. Electrolyte solutions were purged with nitrogen.

Intensity-modulated photocurrent spectroscopy (IMPS) and intensity-modulated photovoltage spectroscopy (IMVS) measurements were carried out using a Zahner PP 211 CIMPS (Zahner-Elektrik GmbH & Co.KG, Kronach, Germany) setup with a LED of wavelength 369 nm in a frequency range 0.1

to 10^5 Hz. The TiO₂ nanotube electrode was illuminated through the electrolyte side (1 M NaOH) with the fixed intensity of 80 mW cm^{-2} . A sinusoidal perturbation of ~10% of the steady state illumination was superimposed on the constant base light intensity. The IMVS measurements were carried out at open circuit potential with varying power intensity of LED (369 nm). All measurements were performed against an Ag/AgCl reference electrode (3 M KCl), using Pt wire as a counter electrode.

4. Conclusions

In conclusion, mixed-phase TiO₂ nanotubes have been fabricated using anodization of Ti foils and annealed at different temperatures to tune the phase composition of the nanotubes. The nanotubes annealed at 600 °C (TNT600) have the optimum anatase-to-rutile ratio (82:18) showing improved photocurrent compared to the single anatase phase (TNT500) and to the mixed-phase having a higher rutile content (77%, TNT700). To gain a better understanding of the mechanisms underlying the increase of performance, an analysis of both radiative (with PL spectroscopy) and non-radiative (with perturbative PEC techniques) recombination processes have been carried out. An increase of PL related to the increase of rutile fraction was found, revealing higher radiative recombination of electron–hole pairs mediated by the defects in anatase crystals or at their interface with rutile ones. On the other hand, the role of charge transport and of non-radiative recombination has been investigated with IMPS, IMVS, and EIS techniques. The rate constants related to the hole transfer and the recombination across the semiconductor/electrolyte interface have been retrieved and correlated to the electrical analogs obtained from fitting the EIS data to an equivalent circuit. The obtained results suggest that the increased hole transfer rate across the TiO₂ nanotube/solution interface in mixed-phase samples is crucial in regulating the improved photocurrent observed in the mixed-phase nanotubes. Follow-up studies on nanostructured mixed-phase TiO₂ electrodes are expected, aiming at further elucidating the enhancement mechanisms, studying the effect of different junctions (i.e., anatase/brookite), or optimizing the nanostructure to control the location of the different phases, which could allow a more efficient charge transport and, thus, higher performance.

Supplementary Materials: The following are available online at <http://www.mdpi.com/2073-4344/9/2/204/s1>.

Author Contributions: The authors thank Sergii Kalytchuk for his aid in photoluminescence spectroscopy measurements. R.Y. designed and performed the experiments; O.T. performed HR-TEM measurements; L.M. contributed to PL analysis; H.K. helped in IPCE measurements; R.Y., Š.K., A.N. analyzed the data and wrote the paper; P.S. and R.Z. supervised the project.

Funding: This research received no external funding.

Acknowledgments: The authors gratefully acknowledge the support by the Operational Programme Research, Development, and Education—European Regional Development Fund, project no. CZ.02.1.01/0.0/0.0/15_003/0000416. The authors thank Sergii Kalytchuk for his aid in photoluminescence spectroscopy measurements.

Conflicts of Interest: The authors declare no conflict of interest.

References

1. Boddy, P.J. Oxygen evolution on semiconducting TiO₂. *J. Electrochem. Soc.* **1968**, *115*, 199–203. [[CrossRef](#)]
2. Fujishima, A.; Honda, K. Electrochemical photolysis of water at a semiconductor electrode. *Nature* **1972**, *238*, 37–38. [[CrossRef](#)] [[PubMed](#)]
3. Krol, R.V.; Liang, Y.; Schoonman, J. Solar hydrogen production with nanostructured metal oxides. *J. Mater. Chem.* **2008**, *18*, 2311–2320. [[CrossRef](#)]
4. Chen, Z.; Jaramillo, T.F.; Deutsch, T.G.; Shwarsctein, A.K.; Forman, A.J.; Gaillard, N.; Garland, R.; Takanabe, K.; Heske, C.; Sunkara, M.; et al. Accelerating materials development for photo-electrochemical hydrogen production: Standards for methods, definitions, and reporting protocols. *J. Mater. Res.* **2010**, *25*, 3–16. [[CrossRef](#)]
5. Sivula, K.; Krol, R.V. Semiconducting materials for photo-electrochemical energy conversion. *Nat. Rev. Mater.* **2016**, *1*, 15010. [[CrossRef](#)]

6. Kment, S.; Schmuki, P.; Hubicka, Z.; Machala, L.; Kirchgeorg, R.; Liu, N.; Wang, L.; Lee, K.; Olejnicek, J.; Cada, M.; et al. Photoanodes with fully controllable texture: The enhanced water-splitting efficiency of thin hematite films exhibiting solely (110) crystal orientation. *ACS Nano* **2015**, *9*, 7113–7123. [[CrossRef](#)] [[PubMed](#)]
7. Lee, K.; Mazare, A.; Schmuki, P. One-Dimensional titanium dioxide nanomaterials: Nanotubes. *Chem. Rev.* **2014**, *114*, 9385–9454. [[CrossRef](#)] [[PubMed](#)]
8. Chen, X.; Mao, S.S. Titanium dioxide nanomaterials: Synthesis, properties, modifications and applications. *Chem. Rev.* **2007**, *107*, 2891–2959. [[CrossRef](#)] [[PubMed](#)]
9. Park, H.S.; Kweon, K.E.; Ye, H.; Paek, E.; Hwang, G.S.; Bard, A.J. Factors in the metal doping of BiVO₄ for improved photoelectrocatalytic activity as studied by scanning electrochemical microscopy and first-principles density-functional calculation. *J. Phys. Chem. C* **2011**, *115*, 17870–17879. [[CrossRef](#)]
10. Wang, J.; Tafen, D.N.; Lewis, J.P.; Hong, Z.; Manivannan, A.; Zhi, M.; Li, M.; Wu, N. Origin of photocatalytic activity of nitrogen-doped TiO₂ nanobelts. *J. Am. Chem. Soc.* **2009**, *131*, 12290–12297. [[CrossRef](#)] [[PubMed](#)]
11. Braun, A.; Akurati, K.K.; Fortunato, G.; Reifler, F.A.; Ritter, A.; Harvey, A.S.; Vital, A.; Graule, T. Nitrogen doping of TiO₂ photocatalyst forms a second e_g state in the oxygen 1s NEXAFS pre-edge. *J. Phys. Chem. C* **2010**, *114*, 516–519. [[CrossRef](#)]
12. Khan, S.U.M.; Al-Shahry, M.; Ingler, W.B., Jr. Efficient photochemical water-splitting by a chemically modified *n*-TiO₂. *Science* **2002**, *297*, 2243–2245. [[CrossRef](#)] [[PubMed](#)]
13. Liu, C.; Tang, J.; Chen, H.M.; Liu, B.; Yang, P. A Fully integrated nanosystem of semiconductor nanowires for direct solar water-splitting. *Nano Lett.* **2013**, *13*, 2989–2992. [[CrossRef](#)] [[PubMed](#)]
14. Liu, Z.; Guo, K.; Han, J.; Li, Y.; Cui, T.; Wang, B.; Ya, J.; Zhou, C. Dendritic TiO₂/In₂S₃/AgInS₂ trilaminar core-shell branched nanoarrays and the enhanced activity for photo-electrochemical water-splitting. *Small* **2014**, *10*, 3153–3161. [[CrossRef](#)] [[PubMed](#)]
15. Nakajima, H.; Mori, T.; Watanabe, M. Influence of platinum loading on photoluminescence of TiO₂ powder. *J. Appl. Phys.* **2004**, *96*, 925. [[CrossRef](#)]
16. Wu, G.P.; Chen, T.; Su, W.G.; Zhou, G.H.; Zong, X.; Lei, Z.B.; Li, C. H₂ production with ultra-low CO selectivity via photocatalytic reforming of methanol on Au/TiO₂ catalyst. *Int. J. Hydrogen Energy* **2008**, *33*, 1243–1251. [[CrossRef](#)]
17. Malara, F.; Minguzzi, A.; Marelli, M.; Morandi, S.; Psaro, R.; Dal Santo, V.; Naldoni, A. α -Fe₂O₃/NiOOH: An Effective heterostructure for photoelectrochemical water oxidation. *ACS Catal.* **2015**, *5*, 5292–5300. [[CrossRef](#)]
18. Cai, H.; Yang, Q.; Hu, Z.; Zhihua, D.; You, Q.; Sun, J.; Xu, N.; Wu, J. Enhanced photoelectrochemical activity of vertically aligned ZnO-coated TiO₂ nanotubes. *Appl. Phys. Lett.* **2014**, *104*, 053114. [[CrossRef](#)]
19. Gui, Q.; Xu, Z.; Zhang, H.; Cheng, C.; Zhu, X.; Yin, M.; Song, Y.; Lu, L.; Chen, X.; Li, D. Enhanced photoelectrochemical water-splitting performance of anodic TiO₂ nanotube arrays by surface passivation. *ACS Appl. Mater. Interfaces* **2014**, *6*, 17053–17058. [[CrossRef](#)] [[PubMed](#)]
20. Sopha, H.; Krbal, M.; Ng, S.; Prikryl, J.; Zazpe, R.; Yam, F.K.; Macak, J.M. One-dimensional anodic TiO₂ nanotubes coated by atomic layer deposition: Towards advanced applications. *Appl. Mater. Today* **2017**, *9*, 104–110. [[CrossRef](#)]
21. Kavan, L.; Gratzel, M.; Gilbert, S.E.; Klemen, C.; Scheel, H.J. Electrochemical and photoelectrochemical investigation of single-crystal anatase. *J. Am. Chem. Soc.* **1996**, *118*, 6716–6723. [[CrossRef](#)]
22. Naldoni, A.; Montini, T.; Malara, F.; Mroz, M.M.; Beltram, A.; Virgili, T.; Boldrini, C.L.; Marelli, M.; Romero-Ocaña, I.; Delgado, J.J.; et al. Hot electron collection on brookite nanorods lateral facets for plasmon-enhanced water oxidation. *ACS Catal.* **2017**, *7*, 1270–1278. [[CrossRef](#)]
23. Cho, I.S.; Chen, Z.; Forman, A.J.; Kim, D.R.; Rao, P.M.; Jaramillo, T.F.; Zheng, X. Branched TiO₂ nanorods for photoelectrochemical hydrogen production. *Nano Lett.* **2011**, *11*, 4978–4984. [[CrossRef](#)] [[PubMed](#)]
24. Kment, S.; Riboni, F.; Pausova, S.; Wang, L.; Wang, L.; Han, H.; Hubicka, Z.; Krysa, J.; Schmuki, P.; Zboril, R. Photoanodes based on TiO₂ and α -Fe₂O₃ for solar water-splitting—Superior role of 1D nanoarchitectures and of combined heterostructures. *Chem. Soc. Rev.* **2017**, *46*, 3716–3769. [[CrossRef](#)] [[PubMed](#)]
25. Altomare, M.; Nguyen, N.T.; Hejazi, S.; Schmuki, P. A Cocatalytic electron-transfer cascade site-selectively placed on TiO₂ nanotubes yields enhanced photocatalytic H₂ Evolution. *Adv. Funct. Mater.* **2018**, *8*, 1704259. [[CrossRef](#)]
26. Bickley, R.I.; Gonzalez-Carreno, T.; Lees, J.S.; Palmisano, L.; Tilley, R.J. A structural investigation of titanium dioxide photocatalysts. *J. Solid State Chem.* **1991**, *92*, 178–190. [[CrossRef](#)]

27. Ohtani, B.; Prieto-Mahaney, O.O.; Li, D.; Abe, R. What is Degussa (Evonik) P25? Crystalline composition analysis, reconstruction from isolated pure particles and photocatalytic activity test. *J. Photochem. Photobiol. A Chem.* **2010**, *216*, 179–182. [[CrossRef](#)]
28. Komaguchi, K.; Nakano, H.; Araki, A.; Harima, Y. Photoinduced electron transfer from anatase to rutile in partially reduced TiO₂ (P-25) nanoparticles: An ESR study. *Chem. Phys. Lett.* **2016**, *428*, 338–342. [[CrossRef](#)]
29. Kang, J.; Wu, F.; Li, S.-S.; Xia, J.B.; Li, J. Calculating band alignment between materials with different structures: The case of anatase and rutile titanium dioxide. *J. Phys. Chem. C* **2012**, *116*, 20765–20768. [[CrossRef](#)]
30. Hurum, D.C.; Agrios, A.G.; Gray, K.A.; Rajh, T.; Thurnauer, M.C. Explaining the enhanced photocatalytic activity of degussa P25 mixed-phase TiO₂ using EPR. *J. Phys. Chem. B* **2013**, *107*, 4545–4549. [[CrossRef](#)]
31. Scanlon, D.O.; Dunnill, C.W.; Buckeridge, J.; Shevlin, S.A.; Logsdail, A.J.; Woodley, S.M.; Catlow, C.R.A.; Powell, M.J.; Palgrave, R.G.; Parkin, I.P.; et al. Band alignment of rutile and anatase TiO₂. *Nat. Mater.* **2013**, *12*, 798–801. [[CrossRef](#)] [[PubMed](#)]
32. Nosaka, Y.; Nosaka, A.Y. Reconsideration of intrinsic band alignments within anatase and rutile TiO₂. *J. Phys. Chem. Lett.* **2016**, *7*, 431–434. [[CrossRef](#)] [[PubMed](#)]
33. Kullgren, J.; Aradi, B.; Frauenheim, T.; Kavan, L.; Deak, P. Resolving the controversy about the band alignment between Rutile and Anatase: The role of OH⁻/H⁺ adsorption. *J. Phys. Chem. C* **2015**, *119*, 21952–21958. [[CrossRef](#)]
34. Li, A.; Wang, Z.; Yin, H.; Wang, S.; Yan, P.; Huang, B.; Wang, X.; Li, R.; Zong, X.; Han, H.; et al. Understanding the anatase-rutile phase junction in charge separation and transfer in a TiO₂ electrode for photoelectrochemical water-splitting. *Chem. Sci.* **2016**, *7*, 6076–6082. [[CrossRef](#)] [[PubMed](#)]
35. Pena, P.A.; Carrera Crespo, J.E.; Gonzalez, F.; Gonzalez, I. Effect of heat treatment on the crystal phase composition, semiconducting properties and photoelectrocatalytic color removal efficiency of TiO₂ nanotubes arrays. *Electrochimica. Acta* **2014**, *140*, 564–571. [[CrossRef](#)]
36. Regonini, D.; Jaroenworarluck, A.; Stevens, R.; Bowen, C.R. Effect of heat treatment on the properties and structure of TiO₂ nanotubes: Phase composition and chemical composition. *Surf. Interface Anal.* **2010**, *42*, 139–144. [[CrossRef](#)]
37. Ponomarev, E.A.; Peter, L.M. A generalized theory of intensity modulated photocurrent spectroscopy (IMPS). *J. Electroanal. Chem.* **1995**, *396*, 219–226. [[CrossRef](#)]
38. Cachet, H.; Sutter, E.M.M. Kinetics of water oxidation at TiO₂ nanotube arrays at different pH domains investigated by electrochemical and light-modulated impedance Spectroscopy. *J. Phys. Chem. C* **2015**, *119*, 25548–25558. [[CrossRef](#)]
39. Klotz, D.; Ellis, D.S.; Dotan, H.; Rothschild, A. Empirical in operando analysis of the charge carrier dynamics in hematite photoanodes by PEIS, IMPS and IMVS. *Phys. Chem. Chem. Phys.* **2016**, *18*, 23438–23457. [[CrossRef](#)] [[PubMed](#)]
40. Cottineau, T.; Cachet, H.; Keller, V.; Sutter, E.M.M. Influence of the anatase/rutile ratio on the charge transport properties of TiO₂-NTs arrays studied by dual wavelength opto-electrochemical impedance spectroscopy. *Phys. Chem. Chem. Phys.* **2017**, *19*, 31469–31478. [[CrossRef](#)] [[PubMed](#)]
41. Riboni, F.; Nguyen, N.T.; So, S.; Schmuki, P. Aligned metal oxide nanotube arrays: Key-aspects of anodic TiO₂ nanotube formation and properties. *Nanoscale Horiz.* **2016**, *1*, 445–466. [[CrossRef](#)]
42. Ampelli, C.; Tavella, F.; Perathoner, S.; Centi, G. Engineering of photoanodes based on ordered TiO₂-nanotube arrays in solar photo-electrocatalytic (PECa) cells. *Chem. Eng. J.* **2017**, *320*, 352–362. [[CrossRef](#)]
43. Ampelli, C.; Tavella, F.; Genovese, C.; Perathoner, S.; Favaro, M.; Centi, G. Analysis of the factors controlling performances of Au-modified TiO₂ nanotube array based photoanode in photo-electrocatalytic (PECa) cells. *J. Energy Chem.* **2017**, *26*, 284–294. [[CrossRef](#)]
44. Saboo, T.; Tavella, F.; Ampelli, C.; Perathoner, S.; Genovese, C.; Marepally, B.C.; Veyre, L.; Elsje, A.Q.; Centi, G. Water-splitting on 3D-type meso/macro porous structured photoanodes based on Ti mesh. *Sol. Energy Mater. Sol. Cells* **2018**, *98*, 178. [[CrossRef](#)]
45. Abu, S.P.; Tsuchiya, H.; Fujimoto, S.; Schmuki, P. TiO₂ Nanotubes-annealing effects on detailed morphology and structure. *Eur. J. Inorg. Chem.* **2010**, *2010*, 4351–4356. [[CrossRef](#)]
46. Mohammadpour, F.; Altomare, M.; So, S.; Lee, K.; Mokhtar, M.; Alshehri, A.; Al-Thabaiti, S.A.; Schmuki, P. High-temperature annealing of TiO₂ nanotube membranes for efficient dye-sensitized solar cells. *Semicond. Sci. Technol.* **2016**, *31*, 014010. [[CrossRef](#)]

47. Yoo, J.E.; Altomare, M.; Mokhtar, M.; Alshehri, A.; Al-Thabaiti, S.A.; Mazare, A.; Schmuki, P. Photocatalytic H₂ generation using dewetted Pt-decorated TiO₂ nanotubes: Optimized dewetting and oxide crystallization by a multiple annealing process. *J. Phys. Chem. C* **2016**, *120*, 15884–15892. [[CrossRef](#)]
48. Jarosz, M.; Syrek, K.; Kapusta-Kołodziej, J.; Mech, J.; Malek, K.; Hnida, K.; Lojewski, T.; Jaskula, M.; Sulka, G.D. Heat treatment effect on crystalline structure and photo-electrochemical properties of anodic TiO₂ nanotube arrays formed in ethylene glycol and glycerol based electrolytes. *J. Phys. Chem. C* **2015**, *119*, 24182–24191. [[CrossRef](#)]
49. Li, J.; Wang, Z.; Wang, J.; Sham, T.K. Unfolding the Anatase-to-Rutile phase transition in TiO₂ nanotubes using X-ray spectroscopy and spectromicroscopy. *J. Phys. Chem. C* **2016**, *120*, 22079–22087. [[CrossRef](#)]
50. Scaramuzzo, F.A.; Dell’Era, A.; Tarquini, G.; Caminiti, R.; Ballirano, P.; Pasquali, M. Phase transition of TiO₂ nanotubes: An X-ray study as a function of temperature. *J. Phys. Chem. C* **2017**, *121*, 24871–24876. [[CrossRef](#)]
51. Li, W.; Ni, C.; Lin, H.; Huang, C.P.; Shah, S.I. Size dependence of thermal stability of TiO₂ nanoparticles. *J. Appl. Phys.* **2004**, *96*, 6663–6668. [[CrossRef](#)]
52. Naldoni, A.; Allieta, M.; Santangelo, S.; Marelli, M.; Fabbri, F.; Cappelli, S.; Bianchi, C.L.; Psaro, R.; Santo, V.D. Effect of nature and location of defects on bandgap narrowing in black TiO₂ nanoparticles. *J. Am. Chem. Soc.* **2012**, *134*, 7600–7603. [[CrossRef](#)] [[PubMed](#)]
53. Likodimos, V.; Stergiopoulos, T.; Falaras, P.; Kunze, J.; Schmuki, P. Phase composition, size, orientation, and antenna effects of self-assembled anodized titania nanotube arrays: A polarized micro-raman investigation. *J. Phys. Chem. C* **2008**, *112*, 12687–12696. [[CrossRef](#)]
54. Rambabu, Y.; Jaiswal, M.; Roy, S.C. Effect of annealing temperature on the phase transition, structural stability and photo-electrochemical performance of TiO₂ multi-leg nanotubes. *Catal. Today* **2016**, *278*, 255–261. [[CrossRef](#)]
55. Ohsaka, T.; Izumi, F.; Fujiki, Y. Raman spectrum of anatase TiO₂. *J. Raman Spectrosc.* **1978**, *7*, 321–324. [[CrossRef](#)]
56. Li Bassi, A.; Cattaneo, D.; Russo, V.; Bottani, C.E. Raman spectroscopy characterization of titania nanoparticles produced by flame pyrolysis: The influence of size and stoichiometry. *J. Appl. Phys.* **2005**, *98*, 074305. [[CrossRef](#)]
57. Knorr, F.J.; Mercado, C.C.; McHale, J.L. Trap-state distributions and carrier transport in pure and mixed-phase TiO₂: Influence of contacting solvent and interphasial electron transfer. *J. Phys. Chem. C* **2008**, *112*, 12786–12794. [[CrossRef](#)]
58. Shi, J.; Chen, J.; Feng, Z.; Chen, T.; Lian, Y.; Wang, X.; Li, C. Photoluminescence Characteristics of TiO₂ and Their Relationship to the photoassisted reaction of Water/Methanol Mixture. *J. Phys. Chem. C* **2017**, *111*, 693–699. [[CrossRef](#)]
59. Wang, X.; Feng, Z.; Shi, J.; Jia, G.; Shen, S.; Zhou, J.; Li, C. Trap states and carrier dynamics of TiO₂ studied by photoluminescence spectroscopy under weak excitation condition. *Phys. Chem. Chem. Phys.* **2010**, *12*, 7083–7090. [[CrossRef](#)] [[PubMed](#)]
60. Pallotti, D.K.; Passoni, L.; Maddalena, P.; Di Fonzo, F.; Lettieri, S. Photoluminescence mechanisms in anatase and rutile TiO₂. *J. Phys. Chem. C* **2017**, *121*, 9011–9021. [[CrossRef](#)]
61. Bergman, L.; McHale, J.L. *Handbook of Luminescent Semiconductor Materials*; CRC Press: Boca Raton, FL, USA, 2011; Volume 7.
62. Lei, Y.; Zhang, L.D.; Meng, G.W.; Li, G.H.; Zhang, X.Y.; Liang, C.H.; Chen, W.; Wang, S.X. Preparation and photoluminescence of highly ordered TiO₂ nanowire arrays. *Appl. Phys. Lett.* **2011**, *78*, 8. [[CrossRef](#)]
63. Iatsunskyi, I.; Pavlenko, M.; Viter, R.; Jancelewicz, M.; Nowaczyk, G.; Baleviciute, I.; Załęski, K.; Jurga, S.; Ramanavicius, A.; Smyntyna, V. Tailoring the structural, optical, and photoluminescence properties of porous silicon/TiO₂ nanostructures. *J. Phys. Chem. C* **2015**, *119*, 7164–7171. [[CrossRef](#)]
64. Di Valentin, C.; Pacchioni, G. Reduced and n-Type Doped TiO₂: Nature of Ti³⁺ Species. *J. Phys. Chem. C* **2009**, *113*, 20543–20552. [[CrossRef](#)]
65. Gerosa, M.; Bottani, C.E.; Caramella, L.; Onida, G.; Di Valentin, C.; Pacchioni, G. Defect calculations in semiconductors through a dielectric-dependent hybrid DFT functional: The case of oxygen vacancies in metal oxides. *J. Chem. Phys.* **2015**, *143*, 134702. [[CrossRef](#)] [[PubMed](#)]
66. Deak, P.; Aradi, B.; Frauenheim, T. Quantitative theory of the oxygen vacancy and carrier self-trapping in bulk TiO₂. *Phys. Rev. B* **2012**, *86*, 195206. [[CrossRef](#)]
67. Zhang, W.F.; Zhang, M.S.; Yin, Z.; Chen, Q. Photoluminescence in anatase titanium dioxide nanocrystals. *Appl. Phys. B* **2000**, *70*, 261–265. [[CrossRef](#)]

68. Klotz, D.; Grave, D.A.; Rothschild, A. Accurate determination of the charge transfer efficiency of photoanodes for solar water-splitting. *Phys. Chem. Chem. Phys.* **2017**, *19*, 20383–20392. [[CrossRef](#)] [[PubMed](#)]
69. Thorne, J.E.; Jang, J.W.; Liu, E.Y.; Wang, D. Understanding the origin of photoelectrode performance enhancement by probing surface kinetics. *Chem. Sci.* **2016**, *7*, 3347–3354. [[CrossRef](#)] [[PubMed](#)]
70. Zachaus, C.; Abdi, F.F.; Peter, L.M.; Krol, R.V. Photocurrent of BiVO₄ is limited by surface recombination, not surface catalysis. *Chem. Sci.* **2017**, *8*, 3712–3719. [[CrossRef](#)] [[PubMed](#)]
71. Klahr, B.; Gimenez, S.; Fabregat-Santiago, F.; Hamann, T.; Bisquert, J. Water Oxidation at Hematite Photoelectrodes: The role of surface states. *J. Am. Chem. Soc.* **2012**, *134*, 4294–4302. [[CrossRef](#)] [[PubMed](#)]
72. Lynch, R.P.; Ghicov, A.; Schmuki, P. A photo-electrochemical investigation of self-organized TiO₂ nanotubes. *J. Electrochem. Soc.* **2010**, *157*, 76–84. [[CrossRef](#)]
73. Gurudayal; Chee, P.M.; Boix, P.P.; Ge, H.; Yanan, F.; Barber, J.; Wong, L.H. Core-shell hematite nanorods: A Simple method to improve the charge transfer in the photoanode for photoelectrochemical water-splitting. *ACS Appl. Mater. Interfaces* **2015**, *7*, 6852–6859. [[CrossRef](#)] [[PubMed](#)]
74. Rex, R.E.; Knorr, F.J.; McHale, J.L. Surface Traps of TiO₂ nanosheets and nanoparticles as illuminated by spectroelectrochemical photoluminescence. *J. Phys. Chem. C* **2014**, *118*, 16831–16841. [[CrossRef](#)]
75. Tighineanu, A.; Ruff, T.; Albu, S.; Hahn, R.; Schmuki, P. Conductivity of TiO₂ nanotubes: Influence of annealing time and temperature. *Chem. Phys. Lett.* **2010**, *494*, 260–263. [[CrossRef](#)]



© 2019 by the authors. Licensee MDPI, Basel, Switzerland. This article is an open access article distributed under the terms and conditions of the Creative Commons Attribution (CC BY) license (<http://creativecommons.org/licenses/by/4.0/>).

Appendix [A5]

Significant Enhancement of Photoactivity in Hybrid TiO₂/g-C₃N₄ Nanorod Catalysts Modified with Cu–Ni-Based Nanostructures

A.J. Rathi, H. Kmentova, A. Naldoni, A. Goswami,
M. B. Gawande*, R. S. Varma, **S. Kment***, R. Zboril*

ACS Applied Nano Materials 1, 2526-2535, 2018

Significant Enhancement of Photoactivity in Hybrid $\text{TiO}_2/\text{g-C}_3\text{N}_4$ Nanorod Catalysts Modified with Cu–Ni-Based Nanostructures

Anuj K. Rathi,^{†,§} Hana Kmentová,^{†,§} Alberto Naldoni,^{†,§} Anandarup Goswami,^{†,‡} Manoj B. Gawande,^{*,†,§} Rajender S. Varma,^{†,§} Štěpán Kment,^{*,†} and Radek Zbořil^{*,†,§}

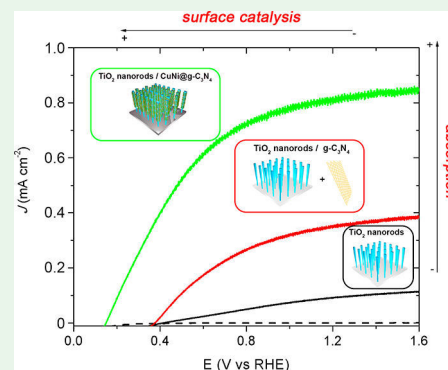
[†]Regional Centre of Advanced Technologies and Materials, Faculty of Science, Palacký University Olomouc, Šlechtitelů 27, 783 71 Olomouc, Czech Republic

[‡]Centre of Excellence in Advanced Materials, Manufacturing, Processing and Characterization (CoExAMMPC) and Division of Chemistry, Department of Sciences and Humanities, Vignan's Foundation for Science, Technology and Research University (VFSTRU; Vignan's University), Vadlamudi, Guntur 522 213, Andhra Pradesh, India

Supporting Information

ABSTRACT: Light-driven processes such as photocatalytic environmental remediation and photoelectrochemical (PEC) water splitting to produce hydrogen under sunlight are key technologies toward energy sustainability. Despite enormous efforts, a suitable photocatalyst fulfilling all the main requirements such as high photoactivity under visible light, chemical stability, environmental friendliness, and low cost has not been found yet. A promising approach to overcome these limitations is to use hybrid nanostructures showing improved activity and physicochemical properties when compared with single components. Herein, we present a novel photocatalytic nanocomposite system based on titania (TiO_2): titania nanorod wrapped with $\text{Ni}(\text{OH})_2$ and $\text{Cu}(\text{OH})_2$ composite carbon nitride ($\text{CuNi@g-C}_3\text{N}_4/\text{TiO}_2$). This carefully tuned photoanode nanostructure shows almost one order of magnitude higher photocurrent density compared to unsensitized TiO_2 nanorods for PEC water splitting upon solar-light illumination. The heterostructured $\text{g-C}_3\text{N}_4$ strongly improves visible absorption of light, separation of electrons and holes, and surface catalysis due to the effect of $\text{Cu}(\text{OH})_2$ nanoparticles and $\text{Ni}(\text{OH})_2$ nanosheets, respectively. The improved photoperformance ascribed to the integrative cooperation effect of all the counterparts resulting in a one-dimensional hybrid nanostructured photoanode with improved light absorption, facile charge separation, and efficient surface catalysis toward PEC oxygen evolution.

KEYWORDS: TiO_2 nanorods, doped $\text{g-C}_3\text{N}_4$, nickel hydroxide, copper hydroxide, photoelectrochemical water splitting



INTRODUCTION

Energy consumption is expected to double by 2050. There are significant ongoing efforts to find alternative, sustainable, and renewable sources of energy with a low impact on the environment. The transformation of solar light into energy is among the most feasible options for tackling the ecofriendly concerns triggered by the huge dependence of energy demand on fossil fuels. In this context semiconductor-based photocatalytic systems and photoelectrochemical (PEC) cells represent central solar-powered technologies for various promising applications such as manufacture of hydrogen through PEC water splitting, synthesis of liquid fuels through CO_2 reduction, and effective degradation and transformation of organic pollutants to high-value chemicals.

Titanium dioxide is the benchmark oxide semiconductor in photoelectrochemistry and photocatalysis.¹ In addition to its high photocatalytic activity, very high chemical stability, and high resistance against photocorrosion, nontoxicity, and low cost render this the most promising candidate. However, the high band gap energy (~ 3.0 eV), limiting absorption to a very narrow

part of the solar spectrum, and the fast recombination of photogenerated charges still represent the main limitations for its broader utilization, although tremendous efforts have been devoted to overcome these drawbacks.² For example, while the elemental doping,^{3,4} quantum dots,⁵ and plasmonic sensitization^{6–9} are the common strategies pursued to shift the absorption of TiO_2 from the ultraviolet to the visible part of the solar spectrum, the preparation of various TiO_2 nanostructures represents the methodology to conceal the fast recombination of charges.^{10–12}

Graphitic carbon nitride ($\text{g-C}_3\text{N}_4$) has developed into an important candidate and has been employed as a metal-free photocatalyst and for elimination of organic pollutants.^{13–15} Within two decades, $\text{g-C}_3\text{N}_4$ has started to emerge as important material for photocatalysis with visible light due to its exceptional electronic and surface characteristics.¹⁶ This conjugated polymer

Received: January 16, 2018

Accepted: May 14, 2018

Published: May 14, 2018



has high physicochemical stability, nontoxicity, low cost, easy availability, and photoresponse in the visible-light region.^{17,18} Recently, g-C₃N₄ has been designed via soft¹⁹ and hard²⁰ templating approaches, template-free preparation,²¹ functionalization of g-C₃N₄ by elemental doping²² and co-polymerization,²³ and its modification with another semiconductor²⁴ or a metal^{25–27} to form heterojunction nanostructures. Suitable semiconductor partners for g-C₃N₄ have been, for example, identified: BiVO₄ and Bi₂WO₆. The Z-scheme composites based on these constituents have been used for enhanced photocatalytic degradation of various contaminants including antibiotics.^{28–31} Additionally, the decoration of a g-C₃N₄ surface with metal and/or metal oxides nanoparticles allows remarkable flexibility in design strategy to decrease charge recombination and finally increase the overall photocatalytic and PEC performance.³²

Nanostructures composed of different combinations of TiO₂ and variously hybridized g-C₃N₄ have been shown to facilitate the charge carrier separation at their heterojunctions, thus improving the charge carriers' dynamics.^{33,34} This effect emerges from the proper positioning of the conduction and valence band edges of the materials that form a possible gradient at the interface, promote the charge separation, and hence inhibit the recombination.³⁵ Therefore, the TiO₂/g-C₃N₄ heterostructures have become widely studied as visible-light active photocatalysts with high activity toward numerous reactions for environmental remediation involving CO₂ reduction,^{36,37} degradation of organic compounds,³⁸ and NO_x removal.³⁹ Another key application is production of hydrogen by photoelectrochemical water splitting as the central renewable energy source.^{40,41}

Herein we report the strategy for how to significantly enhance the photoactivity of the TiO₂/g-C₃N₄ heterostructures by incorporation of Cu(OH)₂ and Ni(OH)₂ nanostructures acting as the optical sensitizer and a co-catalyst, respectively. In the presented approach, the g-C₃N₄ sheets are well-decorated with ultrasmall Cu(OH)₂ nanoparticles and/or ultrathin Ni(OH)₂ flakes grown around the g-C₃N₄ matrix. The developed hybrid photoanodes based on TiO₂ nanorods (NRs) and different g-C₃N₄ composites were synthesized through a one-pot hydrothermal synthesis. To retrieve the relative catalytic contributions from each individual component of the nanostructured composite photoanodes, we present first the photocatalytic activity of TiO₂ NRs, g-C₃N₄, Cu@g-C₃N₄, Ni@g-C₃N₄, and CuNi@g-C₃N₄ toward the decomposition of rhodamine B (RhB). Thereafter, the PEC water splitting performances of all these g-C₃N₄-based TiO₂ NRs systems were also investigated. The use of hybrid nanostructures here produces an increase in visible-light absorption and surface catalysis, while decreasing charge carrier recombination, which induced improved performance both in photocatalysis and photoelectrocatalysis. These performances are discussed in terms of nanostructured morphology and physicochemical properties probed through different characterization methods.

EXPERIMENTAL SECTION

Chemicals. All chemical reagents were purchased from the indicated suppliers and were used as received for the experiments: dicyandiamide (Sigma-Aldrich), Cu(NO₃)₂·3H₂O (Sigma-Aldrich), Ni(NO₃)₂·6H₂O (Sigma-Aldrich), titanium *n*-butoxide (Sigma-Aldrich), hydrochloric acid (Penta), sodium hydroxide (Lach-Ner), 2-isopropanol (Sigma-Aldrich), acetone (Sigma-Aldrich), Triton X-100 (Sigma-Aldrich), and rhodamine B (RhB, Sigma-Aldrich). For solutions preparation distilled water was used.

Materials Preparation. *Synthesis of g-C₃N₄.* g-C₃N₄ was prepared via pyrolysis of dicyandiamide (10 g) under inert atmosphere at 500 °C (2 h; heating rate, 10 °C/min), maintaining the inert atmosphere by flowing the nitrogen through the tube. Once it reaches 500 °C, the system was kept there for 2 h under N₂ atmosphere. Finally, the tube cooled to room temperature, and the final compound was obtained as a yellow solid.

Synthesis of Cu@g-C₃N₄. An aqueous solution of 1 g of g-C₃N₄ was prepared in 300 mL of water; further it was sonicated for 15 min and an aqueous solution of Cu(NO₃)₂·3H₂O (380 mg in 30 mL of water) was added to it. After stirring the reaction mixture for 12 h at room temperature, 1.5 g of sodium borohydride was added in portions with constant stirring, the reaction temperature was raised to 50 °C, and the mixture was stirred for another 12 h at 50 °C and then cooled to room temperature. The reaction mixture became black after NaBH₄ addition indicating the formation of nanoparticles. The Cu@g-C₃N₄ material was obtained by centrifugation followed by a methanol wash (40 mL × 4) and dried under vacuum at 60 °C.

Synthesis of Ni@g-C₃N₄. An aqueous solution of 1 g of g-C₃N₄ was prepared in 300 mL of water; further it was sonicated for 15 min and an aqueous solution of Ni(NO₃)₂·6H₂O (495 mg in 30 mL of water) was then added to it and the reaction mass was kept at room temperature for 12 h. After 12 h, 1.5 g of sodium borohydride was added in portions with constant stirring and the temperature was elevated to 50 °C. The ensuing black colored mixture was kept under stirring for an additional 12 h at 50 °C and then allowed to cool at low temperature. The photocatalyst was obtained by centrifugation followed by methanol wash (40 mL × 4) and dried under vacuum at 60 °C.

Synthesis of CuNi@g-C₃N₄. An aqueous solution of 1 g of g-C₃N₄ was prepared in 300 mL of water; further it was sonicated for 15 min and Cu(NO₃)₂·3H₂O (380 mg in 30 mL of water) was added to it and reaction mass was kept under stirring for 10 min at room temperature. After 10 min, the aqueous solution of Ni(NO₃)₂·6H₂O (495 mg in 30 mL of water) was added and kept under stirring for 12 h at room temperature. After 12 h, 1.5 g of sodium borohydride was added in portions with constant stirring, the reaction temperature was elevated to 50 °C, and the ensuing black mixture was stirred for another 12 h at 50 °C. After cooling, the catalyst was obtained by centrifugation followed by methanol wash (40 mL × 4) and dried under vacuum at 60 °C. The CuNi@g-C₃N₄ photocatalyst was isolated as a black powder.

Preparation of TiO₂ Nanorod Arrays (TiO₂ NRs). TiO₂ nanorods were prepared on commercially available conductive fluorine-doped tin oxide (FTO; TCO-22 Solaronix, Switzerland) by hydrothermal method.⁴² In a typical procedure, hydrochloric acid and distilled water were mixed in a volume ratio of 1:1 for 5 min. Then, 0.46 mL of titanium *n*-butoxide was added dropwise. Then, the FTO substrate was put into a Teflon-lined stainless steel autoclave together with the as-prepared solution. The FTO glass was partially dipped in the solution and placed against the wall with a down oriented conductive side.

Prior to the hydrothermal reaction, FTO substrate was ultrasonically cleaned using a mixture of acetone, 2-isopropanol, and distilled water in a volume ratio of 1:1:1, respectively. The synthesis was performed at 150 °C for 8 h under hydrothermal conditions. After cooling, the FTO glass was rinsed and dried by air stream. The thermal annealing of the as-prepared TiO₂ nanorods was carried out in air at 450 °C for 1 h (5 °C/min).

Preparation of Graphitic Carbon Nitrides Modified TiO₂ NRs (TiO₂/g-C₃N₄, TiO₂/Cu@g-C₃N₄, TiO₂/Ni@g-C₃N₄, and TiO₂/CuNi@g-C₃N₄). All produced powder samples of g-C₃N₄ and modified g-C₃N₄ were hand-ground with a mortar and pestle, dispersed in 2-isopropanol with the concentration of 0.1 mg/mL, and exfoliated by ultrasonic treatment for 2 h. The produced mixture was spun at 3000 rpm, and the liquid lying above a solid residue was mixed with Triton X-100 in the volume ratio of 1:1. The g-C₃N₄ samples were then deposited onto TiO₂ NRs by spin-coating method (1500 rpm, 20 s) and heated at 150 °C for 20 h.

Characterization Techniques. X-ray powder diffraction (XRD) patterns were recorded at room temperature (X'Pert PRO MPD diffractometer, PANalytical) with Co K α radiation (40 kV, 30 mA, λ = 0.1789 nm) furnished with an X'Celerator detector and diffracted beam anticatter slits. The identification of the crystalline phases in the

experimental XRD pattern was obtained. SRM660 (LaB6) standard was employed to assess the instrumental broadening. Microscopic images were obtained by HRTEM TITAN 60-300 with an X-FEG type emission gun, operating at 80 kV. This microscope is equipped with Cs image corrector and a STEM high-angle annular dark-field detector (HAADF). The point resolution is 0.06 nm in TEM mode. The elemental mappings were obtained by STEM–energy-dispersive X-ray spectroscopy (EDS) with acquisition time of 20 min. For HRTEM analysis, the powder samples were dispersed in ethanol and ultrasonicated for 5 min. One drop of this solution was placed on a copper grid with holey carbon film. The sample was dried at room temperature. XPS measurement has been accomplished on the PHI 5000 VersaProbe II XPS system with monochromatic Al K α source (15 kV, 50 W); photon energy of 1486.7 eV was employed. All the spectra were accomplished in a vacuum (1.3×10^{-7} Pa) and at 21 °C. The examined area on each material was a spot of 200 μ m in diameter. The spectra were evaluated with the MultiPak (Ulvac-PHI, Inc.) software. All binding energy (BE) values were documented to the carbon peak C 1s at 284.80 eV. Raman spectra were measured by a DXR Raman spectroscope (Thermo Scientific, USA) furnished with a laser functioning at a wavelength of 633 nm. The sample was deposited on a metal chip. The laser spot was focused on the sample surface, and the scattered light was collected. Measurements were performed with a laser power of 5 mW, and exposition time was set to 10 s. Acquired Raman data were the median of 16 experimental microscans. Raman spectra were assessed with instrument control software (Omnic, version 8, Thermo Scientific) and plotted by QtiPlot (ProIndep SERV SRL, Romania). For ICP-MS analysis, samples were dissolved in a mixture of concentrated HNO₃ and HCl (both Analpure, Analytika, spol. s r.o., Czech Republic) and filled to a defined volume with ultrapure water. All elements were quantified by ICP-MS (Agilent 7700x, Agilent, Japan) using external calibration and appropriate isotopes.

Evaluation of Photocatalytic Activity. Photocatalytic performance of the synthesized samples was assessed by the decoloration rate of rhodamine B (RhB) as a model organic pollutant under visible-light irradiation ($\lambda > 420$ nm; FSQ-GG420 filter, Newport). In each experiment the photocatalytic reactor comprised 10 mg of sample and 20 mL of RhB solution (10 mg/L). In order to ensure the adsorption–desorption equilibrium, the reaction mixture was kept in the dark for 30 min before starting measurement. A xenon lamp (150 W) was located approximately 5 cm from the reactor. At 30 min time interval, the solid catalyst was isolated using a centrifuge and the light absorbance spectrum of pure solution was detected by UV–vis spectrophotometer (Specord, S600).

Photoelectrochemical Properties. The PEC experiments were measured on a Gamry Series G 300 potentiostat using a conventional three electrode system. The components of the cell are titania-containing photoanode as the working electrode, Ag/AgCl (3 M KCl) as the reference electrode, and Pt wire as the counter electrode. The size of the photoanode was limited to 0.785 cm² by an O-ring. A 1 M amount of sodium hydroxide solution acted as the electrolyte (pH = 13.5). The potential (E) was related to the reversible hydrogen electrode (RHE) calculated through the Nernst equation:

$$E_{\text{RHE}} = E(\text{Ag}/\text{AgCl}) + (0.197 \text{ V}) + 0.059\text{pH} \quad (1)$$

where $E(\text{Ag}/\text{AgCl})$ is the measured potential vs the reference electrode and 0.197 V is the standard potential of the Ag/AgCl electrode.

The TiO₂ layers were illuminated using simulated AM 1.5 G solar light (100 mW/cm², 1 sun). Each type of electrode was measured at least five times in order to ensure reproducibility. We obtained similar results within 10% of standard deviation, and representative data are reported.

RESULTS AND DISCUSSION

Figure 1a summarizes the preparation procedures to synthesize g-C₃N₄ photocatalysts and TiO₂ nanorod array (NRs) photoanodes. After the initial synthesis of pristine g-C₃N₄ through the pyrolysis of dicyandiamide under controlled atmosphere, careful sonication and metal ions (Cu, Ni, or CuNi) adsorption steps followed by hydrothermal reaction enabled the efficient

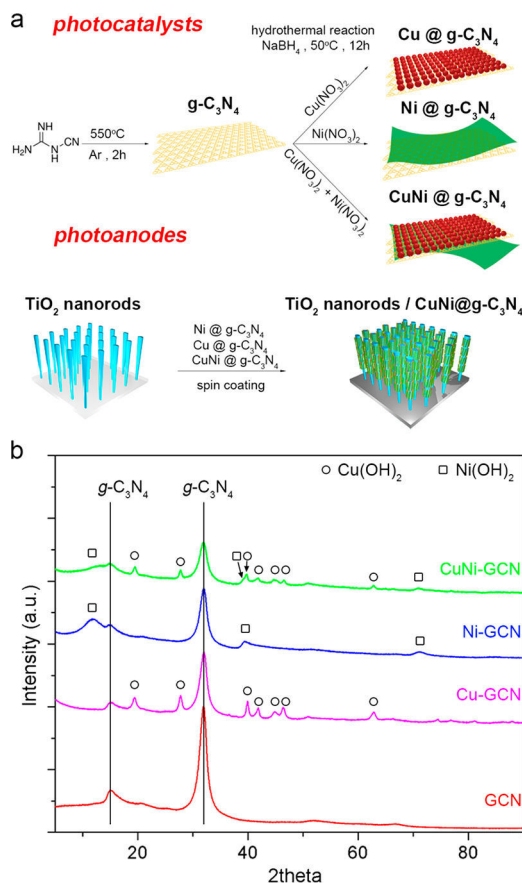


Figure 1. (a) Graphic illustration of strategies used to prepare pristine and Cu-, Ni-, CuNi-modified g-C₃N₄ photocatalysts (upper scheme) and TiO₂ nanorods functionalized g-C₃N₄ photoanodes (lower scheme). (b) XRD patterns of g-C₃N₄, Cu@g-C₃N₄, Ni@g-C₃N₄, and CuNi@g-C₃N₄.

exfoliation of g-C₃N₄ sheets and the deposition of ultrasmall Cu-based nanoparticles and Ni-based nanosheets. To prepare the photoanodes, photocatalysts were dispersed in solution and homogeneously deposited onto the surface of TiO₂ NRs grown on FTO-coated glass slide through spin-coating.

Before studying the TiO₂ NRs/g-C₃N₄ photoanode performance, the g-C₃N₄ materials were thoroughly characterized. Figure 1b shows XRD patterns of g-C₃N₄ (red), Cu@g-C₃N₄ (magenta), Ni@g-C₃N₄ (blue), and CuNi@g-C₃N₄ (green). All samples showed two main diffraction peaks at 2θ of 15° and 31.9°, which are related to the g-C₃N₄ (100) and (002) planes, respectively.¹⁶ The XRD pattern of Cu@g-C₃N₄ clearly exhibited the presence of crystalline Cu(OH)₂, while for Ni-GCN three main peaks related to Ni(OH)₂ were observed (Figure 1b). For the sample containing both Cu and Ni (CuNi@g-C₃N₄), the diffraction pattern highlighted the presence of Cu(OH)₂ and also Ni(OH)₂, confirming the successful functionalization of g-C₃N₄. The different peak intensities related to the C₃N₄ constituent among the diffraction patterns of Ni-, Cu-, or NiCu-modified samples are due to the different compositions in the samples. The functionalization of C₃N₄ with Cu or Ni(OH)₂ lower the concentration of C₃N₄ (which is equal to 1 in the pure sample), consequently leading to a decrease in diffraction peak intensity related to C₃N₄.

The structural morphology of the g-C₃N₄ photocatalysts was investigated using SEM (Supporting Information Figure S1) and TEM (Figure S2). Pristine g-C₃N₄ and Cu@g-C₃N₄ presented

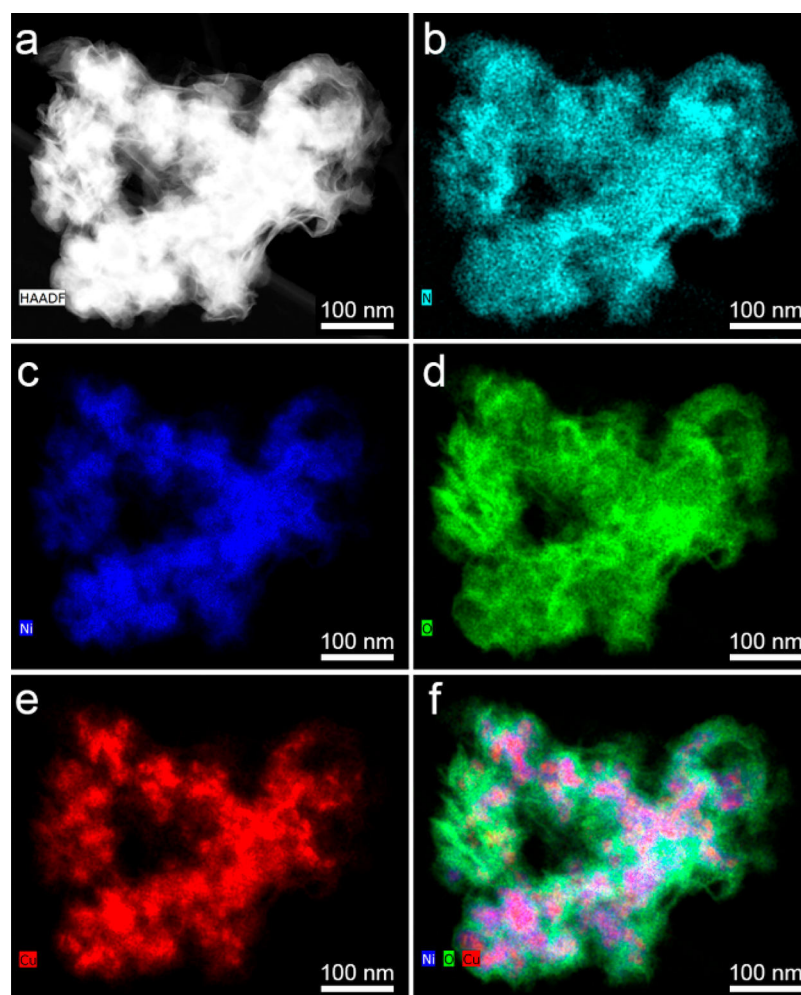


Figure 2. (a) High-angle annular dark-field (HAADF) image and (b–f) EDS elemental mapping of N, Ni, O, Cu, and joined CuNi/O for CuNi@g-C₃N₄.

the typical sheet-like morphology of carbon nitride having multilayer structure. Interestingly, a considerable difference was noticed in the morphology of Ni@g-C₃N₄ and CuNi@g-C₃N₄ where single layer or few layers g-C₃N₄ are attached to ultrathin sheets of Ni hydroxide (Figure S2). To further investigate the change in morphology due to Cu and Ni introduction, we used additional dark-field TEM analysis and elemental mapping of the CuNi@g-C₃N₄ sample. Figure 2a (see also Figure S3) shows that the introduction of Cu and Ni nanostructures (Cu(OH)₂ and Ni(OH)₂) produced the formation of intimate contact among the g-C₃N₄ matrix. Elemental mapping of nitrogen distribution (Figure 2b) confirmed the construction of the g-C₃N₄ matrix, while Ni and O maps evidenced that Ni(OH)₂ grew conformally around the g-C₃N₄ core (Figure 2c,d). Further, the Cu map and the joined Cu–Ni–O distributions (Figure 2e,f) demonstrated that Cu(OH)₂ nanocomposites were grown on the g-C₃N₄ sheet, while Ni(OH)₂ flakes protrude even further from the g-C₃N₄ surface.

The g-C₃N₄ composites materials were further investigated through XPS analysis. Table S1 summarizes the atomic composition of all g-C₃N₄ samples. The atomic percentages of metal ions in Cu and Ni@g-C₃N₄ were 10.4 and 19.7%, respectively. Although the metal content in the sample was found to be 6 wt % for each metal separately using ICP-MS analysis, the surfaces of Cu/Ni and CuNi@g-C₃N₄ (4.2% Cu, 9.2% Ni) were

2-fold richer in Ni. This richness in Ni probably reflects the stronger interaction between Cu and the g-C₃N₄ matrix, which results in multilayer sheets morphology in Cu@g-C₃N₄ and in a gradient composition structure in CuNi@g-C₃N₄ where Cu(OH)₂ nanoparticles are strongly associated with the graphitic sheets, whereas the Ni(OH)₂ flakes also protrude far from the g-C₃N₄ sheet.

All samples showed high-resolution C 1s and N 1s spectra containing three peaks at similar binding energies (Figure 3a and Figures S4–S6). The deconvolution of the C 1s region of CuNi@g-C₃N₄ (Figure 3a) revealed three signals positioned at 284.76, 286.10, and 287.90 eV. The highest intensity peak at 287.90 eV (~62%) corresponds to the –C–N linkages prevalent in the g-C₃N₄ framework, whereas peaks at 286.10 and 284.76 eV refer to the –C–O and –C–C– of adventitious carbon, respectively.⁴³

The presence of C–N bonds is further supported by the N 1s spectrum (Figure 3b and Figures S4–S6), where the peaks at 398.38, 399.44, and 400.68 eV resemble sp² hybridized nitrogen connected with carbon skeleton (–C=N_{sp²}, ~70%), tertiary/pyrrolic (~18%) nitrogen, and uncoordinated nitrogen probably present on the sheet edges, respectively. We also examined the possible oxidation states of Cu and Ni in CuNi@g-C₃N₄ using high-resolution convoluted spectra. In the case of the Cu 2p spectrum (Figure 3c), both Cu^{0/I} (copper in low valence state)

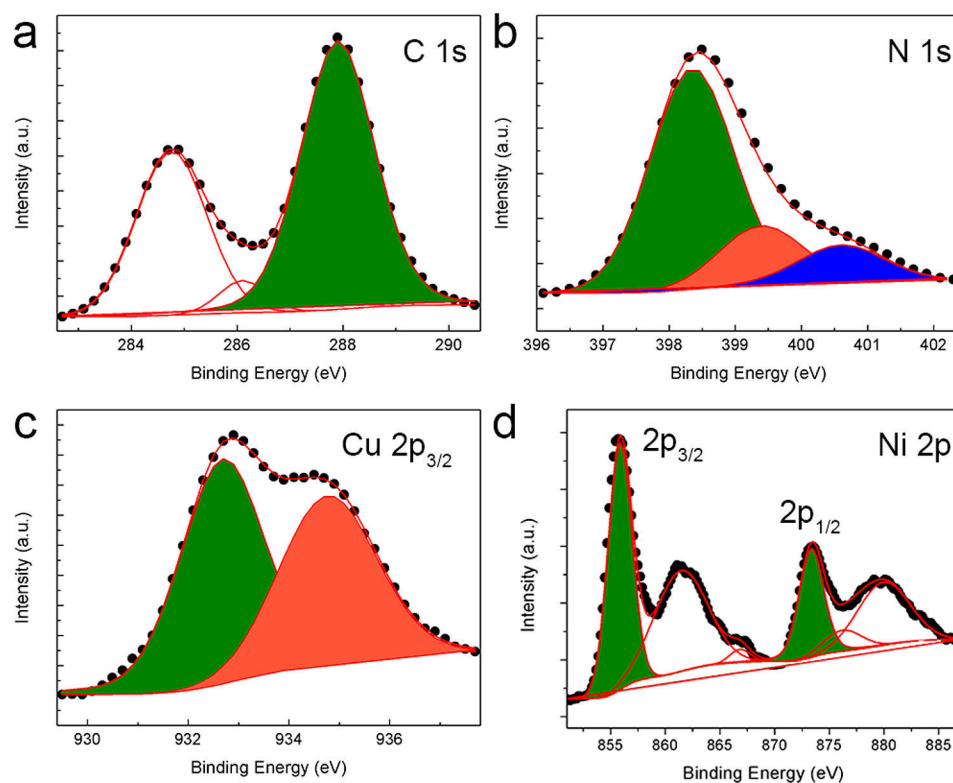


Figure 3. High-resolution XPS spectra of CuNi@g-C₃N₄ in the spectral region of (a) C 1s, (b) N 1s, (c) Cu 2p_{3/2}, and (d) Ni 2p.

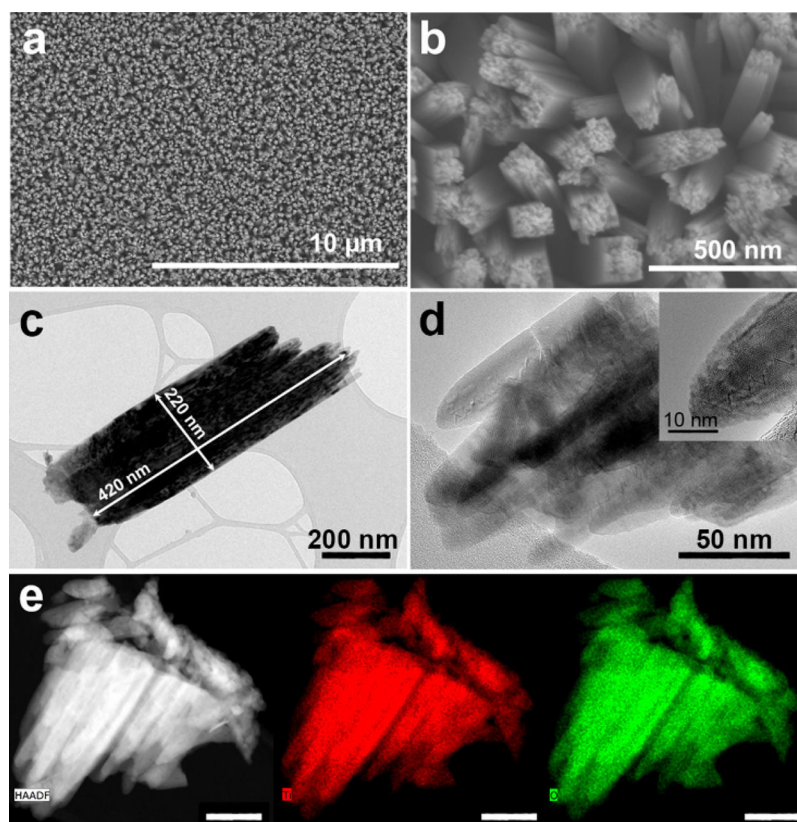


Figure 4. (a, b) SEM images, (c, d) TEM micrographs, and (e) HAADF image and EDS elemental mapping of Ti and O of rutile TiO₂ nanorods grown on FTO glass. Scale bar is 60 nm.

and Cu^{II} as Cu(OH)₂ are associated with components peaking at 932.68 and 934.75 eV, respectively.^{44,45} The atomic concen-

trations of Cu^{0/I} (55%) and Cu^{II} (45%) were the same in both Cu@g-C₃N₄ (see Figure S5) and CuNi@g-C₃N₄. Interestingly,

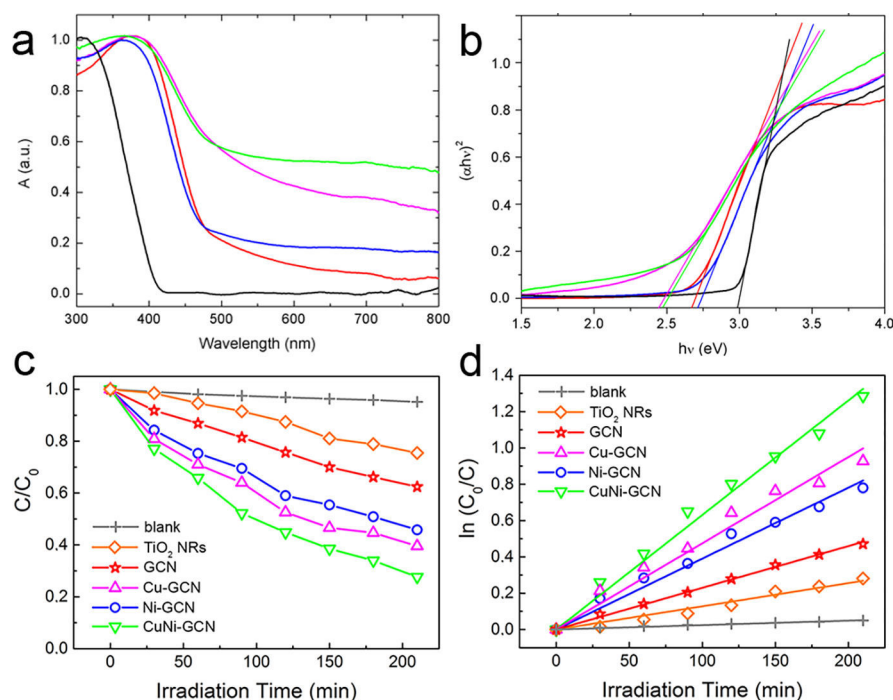


Figure 5. (a) UV–vis absorption spectra and (b) Tauc plots for all photocatalysts: TiO₂ NRs (black), g-C₃N₄ (red), Cu@g-C₃N₄ (magenta), Ni@g-C₃N₄ (blue), and CuNi@g-C₃N₄ (green). (c) Temporal evolution and (d) pseudo-first-order kinetics fitted data of the photocatalytic decomposition of rhodamine B under the wavelength $\lambda > 420$ nm for all photocatalysts: TiO₂ NRs (orange), g-C₃N₄ (red), Cu@g-C₃N₄ (magenta), Ni@g-C₃N₄ (blue), CuNi@g-C₃N₄ (green), and photolysis (gray).

XRD analysis evidenced only the Cu(OH)₂ phase for Cu-containing g-C₃N₄, while XPS highlighted that copper is present not only as Cu^{II} but also as Cu^{0/I}, suggesting a strong interaction with electron donor nitrogen species of the g-C₃N₄ matrix. On the contrary, the Ni 2p spectral region of CuNi@g-C₃N₄ evidenced only one intense peak at 855.94 eV associated with Ni(OH)₂ (Figure 3d), similarly to the sample Ni@g-C₃N₄ (Figure S6).^{46–49}

Figure 4 shows the electron microscopy (SEM and TEM) images of hydrothermally grown TiO₂ nanorods (NRs) on FTO substrate. The images revealed that TiO₂ NRs grew vertically from the substrate and are uniformly distributed over the FTO glass surface. The length of NRs determined from electron microscopy was 500 ± 20 nm and the diameter was 90 ± 5 nm on average, although some fragments of TiO₂ nanorods show diameters of ~20–40 nm (Figure 4c–e). The nanorods had well-developed tetragonal shape showing many surface step edges and smooth sides. The X-ray diffraction pattern of TiO₂ NRs identified that only the rutile crystalline structure in addition to SnO₂ came from the FTO glass (see Figure S7). The ensuing rutile phase is due to the preferential growth on the highly crystalline tetragonal FTO substrate. The small lattice disharmony of the tetragonal FTO and rutile titania is probably the reason for the epitaxial growth of TiO₂ rutile NRs on FTO.

The optical band gaps of g-C₃N₄ samples and TiO₂ NRs were retrieved by UV–vis absorption spectroscopy, and TiO₂ NRs powder was used as reference (Figure 5a). The g-C₃N₄ samples showed an increased absorption in the visible range compare to TiO₂ NRs and further red shift observed for the g-C₃N₄ containing Cu (e.g., Cu@ and CuNi@g-C₃N₄). Accordingly, the optical band gaps derived from the Tauc plots are reported in Figure 5b (where $(\alpha h\nu)^2$ is plotted vs the photon energy, α is the absorption coefficient, h is the Planck constant, and ν is the light frequency) and are 2.67 eV for pristine g-C₃N₄³⁴ and 2.72 eV for

Ni@g-C₃N₄. Differently, once we consider the heterostructure g-C₃N₄/Cu(OH)₂ we observed a 0.2 eV red shift of the band gap for both Cu@g-C₃N₄ (2.45 eV) and CuNi@g-C₃N₄ (2.47 eV) probably due to increased light scattering resulting from the heterostructures formation and not from Cu doping.⁵⁰

To validate this observation, a set of experiments including photocatalytic decoloration of RhB under visible-light illumination was carried out (Figure 5c,d). A blank test performed in the presence of any catalyst proved that the RhB is stable against the visible-light photolysis. As expected, CuNi@g-C₃N₄ showed the highest photocatalytic activity among all the tested catalysts. After 210 min of irradiation, more than 70% of RhB was degraded, while only 38% of RhB was decomposed by g-C₃N₄, 54% by Ni@g-C₃N₄, and 60% by Cu@g-C₃N₄ under the same conditions (see Table S2). For comparison purposes, a rutile TiO₂ NRs sample (in the same mass concentration of g-C₃N₄ materials) was tested showing the lowest photocatalytic activity with the 25% degradation. The observed activity of pristine titania under visible-light activation is due to a slight absorption in this spectral region as well as a light scattering due to the dense 1D morphology, which has also been observed in other works.^{51,52}

The photocatalytic decomposition of RhB followed the Langmuir–Hinshelwood mechanism for all photocatalysts (eq 2).

$$r = \frac{kKc}{1 + Kc} \quad (2)$$

where r is the photocatalytic reaction rate (mol/(L·min)), k is the photocatalysis rate constant (mol/(L·min)), K is the equilibrium adsorption coefficient (L/mol), and c is the reactant concentration (mol/L) at time t . At low substrate concentrations, the term Kc in the denominator can be neglected; then the reaction is

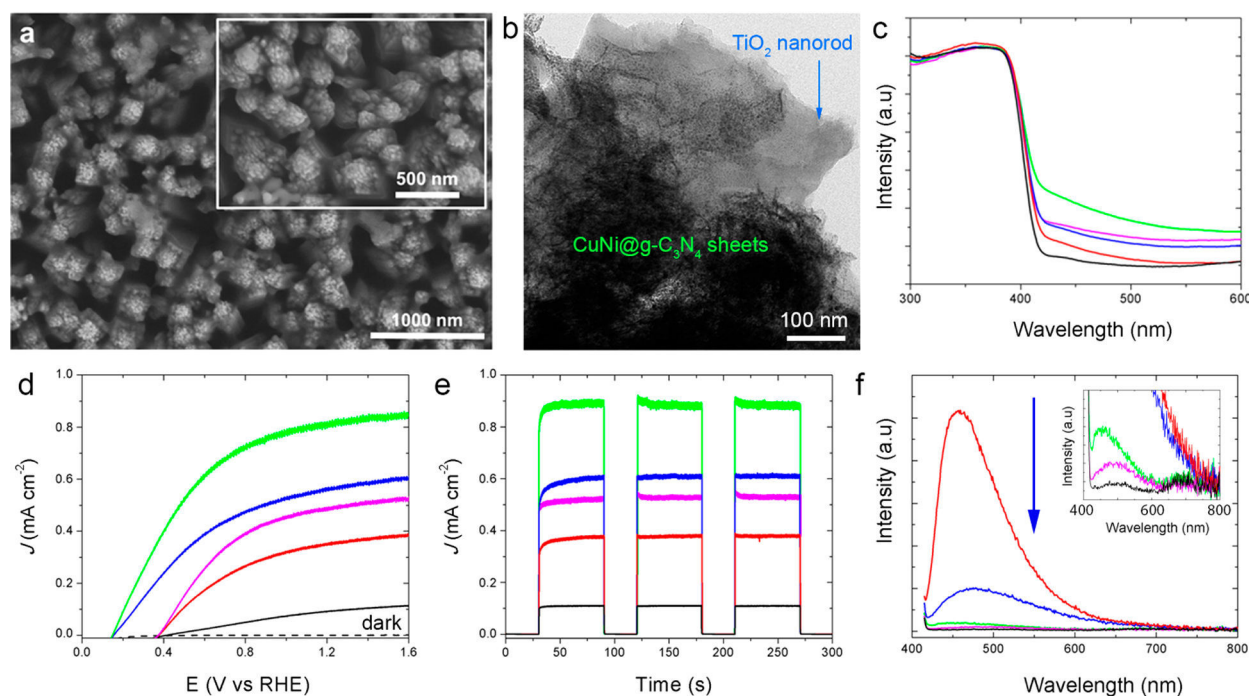


Figure 6. Representative SEM image (a) and TEM micrographs (b) of CuNi@g-C₃N₄ flakes deposited on TiO₂ nanorod array. (c) UV–vis diffuse reflectance spectra, (d) linear sweep voltammetry curves, and (e) chronoamperometry plots measured at 1.5 V vs RHE in 1 M NaOH under AM 1.5G illumination and (f) photoluminescence spectra for TiO₂ NRs (black), TiO₂/g-C₃N₄ (red), TiO₂/Cu@g-C₃N₄ (magenta), TiO₂/Ni@g-C₃N₄ (blue), and TiO₂/CuNi@g-C₃N₄ (green). Inset shows the region at low intensity to the highlight difference in PL among the samples.

of pseudo-first-order and we can write the equation in integral form (eq 3).

$$\ln\left(\frac{c_0}{c}\right) = kKt = k_{app}t \quad (3)$$

where c_0 is the starting concentration of reactant (mol/L) and k_{app} is the apparent rate constant (min^{-1}). The apparent rate constants determined from the slopes and conversions (x) of RhB (Figure 5d) are summarized in Table S2.

Graphitic carbon nitride showed a 1.6-fold increase in k_{app} in comparison to TiO₂ NRs owing to the enhanced absorption of visible light enabled by the band gap of 2.7 eV. Interestingly, the heterojunction formation in Cu@g-C₃N₄ caused a 2.2-fold increase in k_{app} with respect to the pure g-C₃N₄. The heterojunction formation between Cu(OH)₂ and the C₃N₄ sheets and the strong influencing between Cu and C₃N₄, as evidenced by XPS spectra, are important aspects in enhancing the performance of Cu@g-C₃N₄, while probably minor influence is played by the poor catalytic activity of Cu(OH)₂.⁵³ Differently, Ni(OH)₂ is widely used as a catalyst in photocatalysis and Ni(OH)₂/C₃N₄ composites have already shown improved performance toward photocatalytic hydrogen evolution.⁵⁴ In our samples, the functionalization of g-C₃N₄ with Ni(OH)₂ (i.e., Ni@g-C₃N₄) produced a 1.8-fold enhancement in k_{app} , thus showing a lower performance compared to Cu@g-C₃N₄. The modification of TiO₂ with CuNi nanostructures produced instead a 3-fold increase in k_{app} and demonstrated that the simultaneous heterojunction with Cu species and the functionalization with an efficient Ni catalyst is a powerful strategy to enhance at once light absorption, charge separation, and catalysis, achieving a very efficient nanocatalyst that works under visible light.

To prepare efficient photoanodes, we spin-coated solutions of different g-C₃N₄ photocatalysts on top of a titania NRs array

prepared on FTO glass. Figure 6a and its inset show representative SEM images of the TiO₂ NRs coated by CuNi@g-C₃N₄. The carbon nitride partner uniformly covered TiO₂ NRs, as a result of which bare TiO₂ NRs lost their sharp edges. TEM micrographs (Figures 6b and S8) evidenced the occurrence of Cu(OH)₂ nanoparticles and Ni(OH)₂ flakes distributed over the g-C₃N₄ sheets and wrapped around the TiO₂ nanorods. All the remaining types of the TiO₂ NRs/co-catalyst systems revealed the same core–shell-like morphology. The successful functionalization of TiO₂ NRs photoanodes with g-C₃N₄-based materials was confirmed also by UV–vis reflectance spectra (Figure 6c), which presented an improved absorption in the visible region in agreement with the trend observed for the single-g-C₃N₄ photocatalysts (see Figure 5a).

To investigate the PEC activity of all the prepared photoanodes, linear sweep voltammetry (LSV) and chronoamperometry measurements were performed. The polarization (J – E) curves under solar irradiation (1 sun, AM 1.5G) are depicted in Figure 6d. All the photocatalysts showed the typical n-type semiconductor behavior and almost plateau-like photocurrent with just a small increase in photocurrent density in the interval of applied potential from 0.6 to 1.6 V vs RHE. The obtained photocurrents increased following the order of bare TiO₂ NRs < TiO₂/g-C₃N₄ < TiO₂/Cu@g-C₃N₄ < TiO₂/Ni@g-C₃N₄ < TiO₂/CuNi@g-C₃N₄. Interestingly, the functionalization of TiO₂ with g-C₃N₄ or Cu@g-C₃N₄ produced only a modest cathodic (40 mV) shift in onset potential. The potential decreased from 0.41 V for pure TiO₂ to 0.37 V. Differently, a significant advance in onset potential of about 260 mV (onset at 0.15 V) was produced for TiO₂/Ni@g-C₃N₄ and TiO₂/CuNi@g-C₃N₄, demonstrating that the presence of Ni(OH)₂ sheets grown on g-C₃N₄ highly improve the oxygen evolution kinetics, as already shown for NiO_x on α -Fe₂O₃ and BiVO₄ photan-

odes^{48,49,55} finally also reducing the recombination losses at the g-C₃N₄ surface.

A more quantitative comparison picture can be drawn from the chronoamperometry plots (Figure 6e) showing the steady-state photocurrent recorded at fixed potential of 1.5 V vs RHE. The maximum photocurrent densities of 0.108, 0.377, 0.530, 0.612, and 0.890 mA/cm² were obtained for the bare TiO₂, TiO₂/g-C₃N₄, TiO₂/Cu@g-C₃N₄, TiO₂/Ni@g-C₃N₄, and TiO₂/CuNi@g-C₃N₄, respectively. The drastically enhanced PEC activity can be assigned to different reasons depending on the compositions of g-C₃N₄-based photocatalysts deposited on TiO₂ NRs. In the case of TiO₂/g-C₃N₄ and TiO₂/Cu@g-C₃N₄, the creation of an efficient heterojunction system consists of TiO₂ and g-C₃N₄ induced an increased absorption of light in the visible region and reduced charge carrier recombination (see photoluminescence spectra in Figure 6f), which is more pronounced for TiO₂/Cu@g-C₃N₄ because of the intimate interactions between Cu species and the C₃N₄, as evidenced by XPS results. This in turn translated into a 5-fold better photocurrent density in comparison with the reference TiO₂ NRs photoanode. Once Ni(OH)₂ is instead present in the photoanode (TiO₂/Ni@g-C₃N₄), the photocurrent enhancement is even higher (5.7 times), highlighting the important role played by the co-catalyst in suppressing charge recombination at the g-C₃N₄-electrolyte interface. If both Cu and Ni were present in TiO₂/CuNi@g-C₃N₄, a synergistic effect due to enhanced charge separation (Cu) and surface catalysis (Ni) finally led to a remarkable 8.2-fold improvement in the behavior in comparison with the pristine TiO₂ nanorod array. The combination of these two phenomena effectively reduces the recombination of generated electron and hole pairs. It has been presented that the valence (VB) and conductive bands (CB) of GCN are higher than those corresponding to TiO₂.^{33,56} Therefore, a well-matched heterojunction is formed when these two materials are in contact. Upon the simulated sunlight irradiation, the electrons are photoexcited from the valence band of the g-C₃N₄ into its conduction band and further transferred into the CB of TiO₂ and then through suitable 1D nanorod morphology directly to the FTO contact. Finally, the electrons arrived to the platinum electrode via the external circuit where they promote the H⁺ reduction generating molecular H₂. On the other side, minority carriers (i.e., holes) left in the VB of g-C₃N₄ can be efficiently collected in the Ni(OH)₂ that decrease the energetic requirement for the oxygen evolution. Simultaneously, the generated holes in TiO₂ can participate directly in water splitting or be transferred through vectorial charge transfer to the VB of g-C₃N₄ and then to Ni(OH)₂. The stability of all photoanodes fabricated was estimated by repeating the photoelectrochemical measurements after 2 months during which the photoanodes were left under standard laboratory environment (in air and under daylight exposure). All the samples showed only a very little decrease of the activity. Figure S9 displays a chronoamperometry scan of the 2 month old TiO₂/CuNi@g-C₃N₄ sample. The overall activity decrease was 7% and hence the prepared photoelectrodes were rather stable in time.

CONCLUSIONS

We have outlined a facile preparation of copper–nickel co-doped g-C₃N₄ hybrid nanocomposites by using inexpensive precursors. The as-prepared graphitic carbon nitrides samples were deposited onto TiO₂ nanorod array by spin-coating. The g-C₃N₄-based hybrid nanostructures were tested for photocatalytic decomposition of rhodamine B and for PEC water splitting. Notably, CuNi@g-C₃N₄ nanocatalyst appears to be the best

catalyst for rhodamine B photocatalytic degradation under visible-light irradiation as compared to other components showing the photocatalytic activity almost 3-fold and 5-fold higher than the bare g-C₃N₄ and TiO₂ NR photocatalysts, respectively. In photoelectrochemical studies, TiO₂ NRs, g-C₃N₄, Cu@g-C₃N₄, and Ni@g-C₃N₄ photoanodes displayed the photocurrent densities of 0.108, 0.377, 0.530, 0.612, and 0.890 mA/cm², respectively. The excellent PEC activity of the CuNi@g-C₃N₄ system can be ascribed to several cooperation effects resulting from the constituents including the creation of a heterojunction between TiO₂ and g-C₃N₄ photocatalysts, which improved optical absorption and enhanced charge separation due to Cu species and the co-catalytic effect of Ni(OH)₂ toward oxygen evolution reaction. The approach to use low-dimensional hybrid nanostructures to increase light absorption and reaction kinetics can be extended to other semiconductor photoelectrodes that suffer from poor light harvesting and slow surface kinetics such as hematite, ZnO, and so on.

ASSOCIATED CONTENT

Supporting Information

The Supporting Information is available free of charge on the ACS Publications website at DOI: 10.1021/acsnm.8b00078.

TEM micrographs, EDS elemental mapping, XPS spectra and table, XRD and photocatalytic data (PDF)

AUTHOR INFORMATION

Corresponding Authors

*E-mail: stepan.kment@upol.cz (Š.K.).

*E-mail: radek.zboril@upol.cz (R.Z.).

*E-mail: manoj.gawande@upol.cz (M.B.G.).

ORCID

Alberto Naldoni: 0000-0001-5932-2125

Manoj B. Gawande: 0000-0003-1575-094X

Rajender S. Varma: 0000-0001-9731-6228

Radek Zbořil: 0000-0002-3147-2196

Author Contributions

§A.K.R. and H.K. contributed equally to this work.

Notes

The authors declare no competing financial interest.

ACKNOWLEDGMENTS

We acknowledge the Operational Programme Research, Development and Education—European Regional Development Fund, Project No. CZ.02.1.01/0.0/0.0/15_003/0000416 and Project 8E15B00. The work is also funded by the Palacký University Institutional support and IGA grant (Project No. IGA-PrF-2015-017) and by the Grant Agency of the Czech Republic Project 15-19775S. We thank J. Stráská and O. Tomanec for TEM, M. Petr for XPS, C. Aparicio for XRD assistance.

REFERENCES

- (1) Fujishima, A.; Zhang, X. T.; Tryk, D. A. TiO₂ photocatalysis and related surface phenomena. *Surf. Sci. Rep.* **2008**, *63* (12), 515–582.
- (2) Schneider, J.; Matsuoka, M.; Takeuchi, M.; Zhang, J. L.; Horiuchi, Y.; Anpo, M.; Bahnemann, D. W. Understanding TiO₂ Photocatalysis: Mechanisms and Materials. *Chem. Rev.* **2014**, *114* (19), 9919–9986.
- (3) Choi, J.; Park, H.; Hoffmann, M. R. Effects of Single Metal-Ion Doping on the Visible-Light Photoreactivity of TiO₂. *J. Phys. Chem. C* **2010**, *114* (2), 783–792.

- (4) Naldoni, A.; D'Arienzo, M.; Altomare, M.; Marelli, M.; Scotti, R.; Morazzoni, F.; Selli, E.; Dal Santo, V. Pt and Au/TiO₂ photocatalysts for methanol reforming: Role of metal nanoparticles in tuning charge trapping properties and photoefficiency. *Appl. Catal., B* **2013**, *130–131*, 239–248.
- (5) Tada, H.; Fujishima, M.; Kobayashi, H. Photodeposition of metal sulfide quantum dots on titanium(IV) dioxide and the applications to solar energy conversion. *Chem. Soc. Rev.* **2011**, *40* (7), 4232–4243.
- (6) Liu, Z. W.; Hou, W. B.; Pavaskar, P.; Aykol, M.; Cronin, S. B. Plasmon Resonant Enhancement of Photocatalytic Water Splitting Under Visible Illumination. *Nano Lett.* **2011**, *11* (3), 1111–1116.
- (7) Naldoni, A.; Riboni, F.; Guler, U.; Boltasseva, A.; Shalae, V. M.; Kildishev, A. V. Solar-Powered Plasmon-Enhanced Heterogeneous Catalysis. *Nanophotonics* **2016**, *5* (1), 112–133.
- (8) Naldoni, A.; Montini, T.; Malara, F.; Mroz, M. M.; Beltram, A.; Virgili, T.; Boldrini, C. L.; Marelli, M.; Romero-Ocana, I.; Delgado, J. J.; Dal Santo, V.; Fornasiero, P. Hot Electron Collection on Brookite Nanorods Lateral Facets for Plasmon-Enhanced Water Oxidation. *ACS Catal.* **2017**, *7* (2), 1270–1278.
- (9) Naldoni, A.; Guler, U.; Wang, Z.; Marelli, M.; Malara, F.; Meng, X.; Besteiro, L. V.; Govorov, A. O.; Kildishev, A. V.; Boltasseva, A.; Shalae, V. M. Broadband Hot-Electron Collection for Solar Water Splitting with Plasmonic Titanium Nitride. *Adv. Opt. Mater.* **2017**, *5* (15), 1601031.
- (10) Asahi, R.; Morikawa, T.; Ohwaki, T.; Aoki, K.; Taga, Y. Visible-light photocatalysis in nitrogen-doped titanium oxides. *Science* **2001**, *293* (5528), 269–271.
- (11) Kment, S.; Riboni, F.; Pausova, S.; Wang, L.; Wang, L.; Han, H.; Hubicka, Z.; Krysa, J.; Schmuki, P.; Zboril, R. Photoanodes based on TiO₂ and α -Fe₂O₃ for solar water splitting - superior role of 1D nanoarchitectures and of combined heterostructures. *Chem. Soc. Rev.* **2017**, *46*, 3716–3769.
- (12) Krysa, J.; Lee, K.; Pausova, S.; Kment, S.; Hubicka, Z.; Ctvrtlik, R.; Schmuki, P. Self-organized transparent 1D TiO₂ nanotubular photoelectrodes grown by anodization of sputtered and evaporated Ti layers: A comparative photoelectrochemical study. *Chem. Eng. J.* **2017**, *308*, 745–753.
- (13) Tong, H.; Ouyang, S. X.; Bi, Y. P.; Umezawa, N.; Oshikiri, M.; Ye, J. H. Nano-photocatalytic Materials: Possibilities and Challenges. *Adv. Mater.* **2012**, *24* (2), 229–251.
- (14) Yang, Y. X.; Guo, Y. N.; Liu, F. Y.; Yuan, X.; Guo, Y. H.; Zhang, S. Q.; Guo, W.; Huo, M. X. Preparation and enhanced visible-light photocatalytic activity of silver deposited graphitic carbon nitride plasmonic photocatalyst. *Appl. Catal., B* **2013**, *142–143*, 828–837.
- (15) Ong, W.-J.; Tan, L.-L.; Ng, Y. H.; Yong, S.-T.; Chai, S.-P. Graphitic Carbon Nitride (g-C₃N₄)-Based Photocatalysts for Artificial Photosynthesis and Environmental Remediation: Are We a Step Closer To Achieving Sustainability? *Chem. Rev.* **2016**, *116* (12), 7159–7329.
- (16) Liu, J.; Liu, Y.; Liu, N. Y.; Han, Y. Z.; Zhang, X.; Huang, H.; Lifshitz, Y.; Lee, S. T.; Zhong, J.; Kang, Z. H. Metal-free efficient photocatalyst for stable visible water splitting via a two-electron pathway. *Science* **2015**, *347* (6225), 970–974.
- (17) Cao, S. W.; Low, J. X.; Yu, J. G.; Jaroniec, M. Polymeric Photocatalysts Based on Graphitic Carbon Nitride. *Adv. Mater.* **2015**, *27* (13), 2150–2176.
- (18) Wang, Y.; Wang, X. C.; Antonietti, M. Polymeric Graphitic Carbon Nitride as a Heterogeneous Organocatalyst: From Photochemistry to Multipurpose Catalysis to Sustainable Chemistry. *Angew. Chem., Int. Ed.* **2012**, *51* (1), 68–89.
- (19) Wang, Y.; Wang, X.; Antonietti, M.; Zhang, Y. Facile One-Pot Synthesis of Nanoporous Carbon Nitride Solids by Using Soft Templates. *ChemSusChem* **2010**, *3* (4), 435–439.
- (20) Goettmann, F.; Fischer, A.; Antonietti, M.; Thomas, A. Chemical synthesis of mesoporous carbon nitrides using hard templates and their use as a metal-free catalyst for friedel-crafts reaction of benzene. *Angew. Chem., Int. Ed.* **2006**, *45* (27), 4467–4471.
- (21) Han, K. K.; Wang, C. C.; Li, Y. Y.; Wan, M. M.; Wang, Y.; Zhu, J. H. Facile template-free synthesis of porous g-C₃N₄ with high photocatalytic performance under visible light. *RSC Adv.* **2013**, *3* (24), 9465–9469.
- (22) Ma, X.; Lv, Y.; Xu, J.; Liu, Y.; Zhang, R.; Zhu, Y. A Strategy of Enhancing the Photoactivity of g-C₃N₄ via Doping of Nonmetal Elements: A First-Principles Study. *J. Phys. Chem. C* **2012**, *116* (44), 23485–23493.
- (23) Chen, Y.; Lin, B.; Yu, W.; Yang, Y.; Bashir, S. M.; Wang, H.; Takanebe, K.; Idriss, H.; Basset, J.-M. Surface Functionalization of g-C₃N₄: Molecular-Level Design of Noble-Metal-Free Hydrogen Evolution Photocatalysts. *Chem. - Eur. J.* **2015**, *21* (29), 10290–10295.
- (24) Huang, Z. a.; Sun, Q.; Lv, K.; Zhang, Z.; Li, M.; Li, B. Effect of contact interface between TiO₂ and g-C₃N₄ on the photoreactivity of g-C₃N₄/TiO₂ photocatalyst: (0 0 1) vs (1 0 1) facets of TiO₂. *Appl. Catal., B* **2015**, *164*, 420–427.
- (25) Xu, J.; Long, K.-Z.; Wang, Y.; Xue, B.; Li, Y.-X. Fast and facile preparation of metal-doped g-C₃N₄ composites for catalytic synthesis of dimethyl carbonate. *Appl. Catal., A* **2015**, *496*, 1–8.
- (26) Li, Z.; Kong, C.; Lu, G. Visible Photocatalytic Water Splitting and Photocatalytic Two-Electron Oxygen Formation over Cu- and Fe-Doped g-C₃N₄. *J. Phys. Chem. C* **2016**, *120* (1), 56–63.
- (27) Kment, S.; Hubicka, Z.; Krysa, J.; Sekora, D.; Zlamal, M.; Olejniczek, J.; Cada, M.; Ksirova, P.; Remes, Z.; Schmuki, P.; Schubert, E.; Zboril, R. On the improvement of PEC activity of hematite thin films deposited by high-power pulsed magnetron sputtering method. *Appl. Catal., B* **2015**, *165*, 344–350.
- (28) Che, H.; Liu, C.; Hu, W.; Hu, H.; Li, J.; Dou, J.; Shi, W.; Li, C.; Dong, H. NGQD active sites as effective collectors of charge carriers for improving the photocatalytic performance of Z-scheme g-C₃N₄/Bi₂WO₆ heterojunctions. *Catal. Sci. Technol.* **2018**, *8* (2), 622–631.
- (29) Wang, J.; Tang, L.; Zeng, G.; Deng, Y.; Liu, Y.; Wang, L.; Zhou, Y.; Guo, Z.; Wang, J.; Zhang, C. Atomic scale g-C₃N₄/Bi₂WO₆ 2D/2D heterojunction with enhanced photocatalytic degradation of ibuprofen under visible light irradiation. *Appl. Catal., B* **2017**, *209*, 285–294.
- (30) Kong, H. J.; Won, D. H.; Kim, J.; Woo, S. I. Sulfur-Doped g-C₃N₄/BiVO₄ Composite Photocatalyst for Water Oxidation under Visible Light. *Chem. Mater.* **2016**, *28* (5), 1318–1324.
- (31) Jia, C.-J.; Sun, L.-D.; Yan, Z.-G.; You, L.-P.; Luo, F.; Han, X.-D.; Pang, Y.-C.; Zhang, Z.; Yan, C.-H. Single-crystalline iron oxide nanotubes. *Angew. Chem., Int. Ed.* **2005**, *44* (28), 4328–4333.
- (32) Gawande, M. B.; Goswami, A.; Asefa, T.; Guo, H.; Biradar, A. V.; Peng, D.-L.; Zboril, R.; Varma, R. S. Core-shell nanoparticles: synthesis and applications in catalysis and electrocatalysis. *Chem. Soc. Rev.* **2015**, *44* (21), 7540–7590.
- (33) Wang, Y. J.; Wang, Q. S.; Zhan, X. Y.; Wang, F. M.; Safdar, M.; He, J. Visible light driven type II heterostructures and their enhanced photocatalysis properties: a review. *Nanoscale* **2013**, *5* (18), 8326–8339.
- (34) Fan, X.; Wang, T.; Gao, B.; Gong, H.; Xue, H.; Guo, H.; Song, L.; Xia, W.; Huang, X.; He, J. Preparation of the TiO₂/Graphitic Carbon Nitride Core-Shell Array as a Photoanode for Efficient Photoelectrochemical Water Splitting. *Langmuir* **2016**, *32* (50), 13322–13332.
- (35) Marschall, R. Semiconductor Composites: Strategies for Enhancing Charge Carrier Separation to Improve Photocatalytic Activity. *Adv. Funct. Mater.* **2014**, *24* (17), 2421–2440.
- (36) Zhou, S.; Liu, Y.; Li, J. M.; Wang, Y. J.; Jiang, G. Y.; Zhao, Z.; Wang, D. X.; Duan, A. J.; Liu, J.; Wei, Y. C. Facile in situ synthesis of graphitic carbon nitride (g-C₃N₄)-N-TiO₂ heterojunction as an efficient photocatalyst for the selective photoreduction of CO₂ to CO. *Appl. Catal., B* **2014**, *158–159*, 20–29.
- (37) Reli, M.; Huo, P.; Šihor, M.; Ambrožová, N.; Troppová, I.; Matějová, L.; Lang, J.; Svoboda, L.; Kuštrowski, P.; Ritz, M.; Praus, P.; Kočí, K. Novel TiO₂/C₃N₄ Photocatalysts for Photocatalytic Reduction of CO₂ and for Photocatalytic Decomposition of N₂O. *J. Phys. Chem. A* **2016**, *120* (43), 8564–8573.
- (38) Munoz-Batista, M. J.; Fernandez-Garcia, M.; Kubacka, A. Promotion of CeO₂-TiO₂ photoactivity by g-C₃N₄: Ultraviolet and visible light elimination of toluene. *Appl. Catal., B* **2015**, *164*, 261–270.
- (39) Ma, J. Z.; Wang, C. X.; He, H. Enhanced photocatalytic oxidation of NO over g-C₃N₄-TiO₂ under UV and visible light. *Appl. Catal., B* **2016**, *184*, 28–34.

(40) Yan, J. Q.; Wu, H.; Chen, H.; Zhang, Y. X.; Zhang, F. X.; Liu, S. F. Fabrication of TiO₂/C₃N₄ heterostructure for enhanced photocatalytic Z-scheme overall water splitting. *Appl. Catal., B* **2016**, *191*, 130–137.

(41) Han, C.; Wang, Y. D.; Lei, Y. P.; Wang, B.; Wu, N.; Shi, Q.; Li, Q. In situ synthesis of graphitic-C₃N₄ nanosheet hybridized N-doped TiO₂ nanofibers for efficient photocatalytic H₂ production and degradation. *Nano Res.* **2015**, *8* (4), 1199–1209.

(42) Liu, B.; Aydil, E. S. Growth of Oriented Single-Crystalline Rutile TiO₂ Nanorods on Transparent Conducting Substrates for Dye-Sensitized Solar Cells. *J. Am. Chem. Soc.* **2009**, *131* (11), 3985–3990.

(43) Wu, Y.; Chen, S.; Zhao, J.; Yue, X.; Deng, W.; Li, Y.; Wang, C. Mesoporous graphitic carbon nitride and carbon–TiO₂ hybrid composite photocatalysts with enhanced photocatalytic activity under visible light irradiation. *J. Environ. Chem. Eng.* **2016**, *4* (1), 797–807.

(44) Zhu, S.; Wang, Z.; Huang, F.; Zhang, H.; Li, S. Hierarchical Cu(OH)₂@Ni₂(OH)₂CO₃ core/shell nanowire arrays in situ grown on three-dimensional copper foam for high-performance solid-state supercapacitors. *J. Mater. Chem. A* **2017**, *5* (20), 9960–9969.

(45) Chusuei, C. C.; Brookshier, M. A.; Goodman, D. W. Correlation of Relative X-ray Photoelectron Spectroscopy Shake-up Intensity with CuO Particle Size. *Langmuir* **1999**, *15* (8), 2806–2808.

(46) Sanchez-Ballester, N. M.; Ramesh, G. V.; Tanabe, T.; Koudelkova, E.; Liu, J.; Shrestha, L. K.; Lvov, Y.; Hill, J. P.; Ariga, K.; Abe, H. Activated interiors of clay nanotubes for agglomeration-tolerant automotive exhaust remediation. *J. Mater. Chem. A* **2015**, *3* (12), 6614–6619.

(47) Nesbitt, H. W.; Legrand, D.; Bancroft, G. M. Interpretation of Ni_{2p} XPS spectra of Ni conductors and Ni insulators. *Phys. Chem. Miner.* **2000**, *27* (5), 357–366.

(48) Malara, F.; Minguzzi, A.; Marelli, M.; Morandi, S.; Psaro, R.; Dal Santo, V.; Naldoni, A. α -Fe₂O₃/NiOOH: An Effective Heterostructure for Photoelectrochemical Water Oxidation. *ACS Catal.* **2015**, *5* (9), 5292–5300.

(49) Malara, F.; Fabbri, F.; Marelli, M.; Naldoni, A. Controlling the Surface Energetics and Kinetics of Hematite Photoanodes Through Few Atomic Layers of NiO_x. *ACS Catal.* **2016**, *6* (6), 3619–3628.

(50) Mitra, A.; Howli, P.; Sen, D.; Das, B.; Chattopadhyay, K. K. Cu₂O/g-C₃N₄ nanocomposites: an insight into the band structure tuning and catalytic efficiencies. *Nanoscale* **2016**, *8* (45), 19099–19109.

(51) Jiang, Z.; Liu, Y.; Jing, T.; Huang, B.; Wang, Z.; Zhang, X.; Qin, X.; Dai, Y. Enhancing visible light photocatalytic activity of TiO₂ using a colorless molecule (2-methoxyethanol) due to hydrogen bond effect. *Appl. Catal., B* **2017**, *200*, 230–236.

(52) Lu, D.; Zhang, G.; Wan, Z. Visible-light-driven g-C₃N₄/Ti³⁺-TiO₂ photocatalyst co-exposed {001} and {101} facets and its enhanced photocatalytic activities for organic pollutant degradation and Cr(VI) reduction. *Appl. Surf. Sci.* **2015**, *358*, 223–230.

(53) McCrory, C. C. L.; Jung, S. H.; Peters, J. C.; Jaramillo, T. F. Benchmarking Heterogeneous Electrocatalysts for the Oxygen Evolution Reaction. *J. Am. Chem. Soc.* **2013**, *135* (45), 16977–16987.

(54) Yu, J.; Wang, S.; Cheng, B.; Lin, Z.; Huang, F. Noble metal-free Ni(OH)₂-g-C₃N₄ composite photocatalyst with enhanced visible-light photocatalytic H₂-production activity. *Catal. Sci. Technol.* **2013**, *3* (7), 1782–1789.

(55) Kim, T. W.; Choi, K.-S. Nanoporous BiVO₄ Photoanodes with Dual-Layer Oxygen Evolution Catalysts for Solar Water Splitting. *Science* **2014**, *343* (6174), 990–994.

(56) Mamba, G.; Mishra, A. K. Graphitic carbon nitride (g-C₃N₄) nanocomposites: A new and exciting generation of visible light driven photocatalysts for environmental pollution remediation. *Appl. Catal., B* **2016**, *198*, 347–377.

Appendix [A6]

Significant enhancement of photoactivity in one-dimensional TiO₂ nanorods modified by S-, N-, O-doped carbon nanosheets

H. Kmentova*, D. Nandan, **S. Kment***, A. Naldoni, M. B. Gawande,
Z. Hubicka, R. Zboril*

Catalysis Today 328, 111-117, 2019



Significant enhancement of photoactivity in one-dimensional TiO₂ nanorods modified by S-, N-, O-doped carbon nanosheets

Hana Kmentová^{a,*}, Devaki Nandan^a, Štěpán Kment^{a,*}, Alberto Naldoni^a, Manoj B. Gawande^a, Zdeněk Hubička^b, Radek Zbořil^{a,*}

^a Regional Centre of Advanced Technologies and Materials, Faculty of Science, Palacký University, Šteptitelů 27, 783 71, Olomouc, Czech Republic

^b Institute of Physics CAS, v.v.i., Na Slovance 2, 182 21, Praha 8, Czech Republic

ARTICLE INFO

Keywords:

TiO₂ nanorods
S, N, O-doped mesoporous carbon
Photocatalysis
Photoelectrochemistry
Water splitting
Heterojunction

ABSTRACT

Titanium dioxide (TiO₂) represents one of the most active photocatalysts among metal oxides for the degradation of pollutants and for solar water splitting to produce hydrogen. The most critical drawbacks hindering its broad practical use are the absorption majorly in the UV part of solar spectrum and slow charge dynamics. Combination of TiO₂ with a suitable partner in a hybrid nanostructure can effectively address these drawbacks. Here we report a novel nanocomposite system based on one-dimensional TiO₂ nanorods wrapped with a sulfur-, nitrogen-, and oxygen-doped carbon (SNOC) nanosheets. The SNOC nanosheets are synthesized by a cost-effective and facile route using eco-friendly carrageenan as a sulfur, oxygen, and carbon source and urea as a nitrogen source. Silica was used as the templating agent that leads to large surface area materials after its removal at the end of the synthesis. Therefore, the synthesized material exhibits superior photocatalytic performance for decoloring representative Rhodamine B (RhB) under visible light irradiation. SNOC shows the apparent rate constant of $7.6 \times 10^{-3} \text{ min}^{-1}$, which is almost 3 times higher than that of a SNOC material without using silica ($2.8 \times 10^{-3} \text{ min}^{-1}$). This performance of doped carbon material can be assigned to the effect of large surface area and effective visible light adsorption. The TiO₂ NRs / SNOC nanocomposite was investigated for photoelectrochemical water splitting showing much higher photocurrent densities (0.85 mA cm^{-2}) than pure TiO₂ nanorod arrays (0.35 mA cm^{-2}), which was due to significant improvement in the charge transfer dynamics and co-catalytic effect of SNOC. All the materials prepared were evaluated on the basis of physical properties such as crystalline structure, optical absorption, surface topography, and electronic properties.

1. Introduction

Nowadays, there is a great interest in studying energy conversion systems due to environmental issues and due to the ever-increasing energy demand. Continuous effort is devoted to finding alternative sources of energy to fossil fuels with a low impact on the environment. Furthermore, suitable photocatalytic materials having ability to convert industrial harmful emissions such as CO₂ to other high value chemicals or fuels including hydrogen peroxide, and hydrocarbons are intensively being sought [1]. In this context, semiconductor-based photocatalytic systems and photoelectrochemical (PEC) cells represent central solar-powered technologies [2]. The photocatalytic splitting of water using solar light is a potentially renewable source for hydrogen fuel. A series of metal oxides such as WO₃, α-Fe₂O₃, BiVO₄, etc., have extensively been investigated to serve as photoanodes in the PEC cells [3–9]. Among them TiO₂ still remains as one of the most promising owing to

its low cost, photostability, and chemical inertness [10–12]. Especially one-dimensional (1D) titanium dioxide nanostructure arrays represent widely studied morphological arrangement for applications such as photocatalysis and photoelectrochemistry [13,14]. To improve the photocatalytic and water splitting efficiency of TiO₂ it is necessary to extend its absorption into visible part of solar spectrum and to increase the separation efficiency of photogenerated electron-hole pairs on its surface [15–17]. A promising approach to overcome these limitations is to use hybrid nanostructures showing improved activity and physicochemical properties when compared with single components [18–20].

Functionalized carbon-based materials have proven to be fascinating candidates for preparation of these hybrid nanostructures with many applications such as photocatalysis [21], photoelectrochemical water splitting [22], electrocatalysis [23], or Li-ion batteries [24]. The porosity, surface area, and stability are the most important characteristics of the carbon materials for the aforementioned applications [25].

* Corresponding authors.

E-mail addresses: hana.kmentova@upol.cz (H. Kmentová), stepan.kment@upol.cz (Š. Kment), radek.zboril@upol.cz (R. Zbořil).

<https://doi.org/10.1016/j.cattod.2019.01.024>

Received 14 July 2018; Received in revised form 26 November 2018; Accepted 7 January 2019

Available online 09 January 2019

0920-5861/ © 2019 Elsevier B.V. All rights reserved.

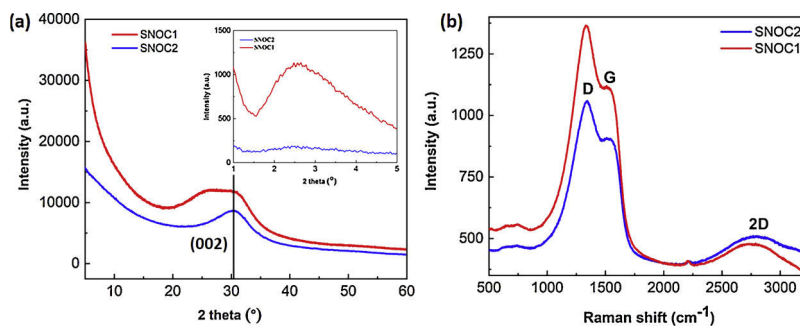


Fig. 1. (a) XRD and (b) Raman spectra of SNOC materials.

Table 1

Textural properties of SNOC materials.

Sample	$S_{\text{BET}}/[\text{m}^2 \text{g}^{-1}]$	$V_{\text{Total}}/[\text{cm}^3 \text{g}^{-1}]$
SNOC1	383	1.2
SNOC2	46	0.5

Recently, the use of biomass-based precursors for the preparation of porous materials attracted great interest, especially in the synthesis of heteroatom-doped carbon by using eggshell membranes [26], crabshell [27], fermented rice [28], or sodium alginate [29].

In our approach the tri-doped carbon was prepared by heating the precursors with silica (assigned as SNOC1) in order to obtain high porous material and also without using silica (SNOC2) for comparative reasons. Herein we further introduce a photocatalytic nanocomposite system based on one-dimensional TiO_2 nanorod arrays wrapped with S-, N-, O-doped carbon ($\text{TiO}_2/\text{SNOC1}$). To obtain the relative catalytic performance of each individual component of the developed hybrid photoanodes, we first present the photocatalytic activity of TiO_2 NRs, TiO_2 (P25), SNOC1, SNOC2 and $\text{g-C}_3\text{N}_4$ used as the reference to undoped carbon material, with respect to the decomposition rate of Rhodamine B as a model dye contaminant. Thereafter, the photoelectrochemical (PEC) measurements of SNOC1-based TiO_2 NRs systems are also presented. The use of hybrid nanostructures leads to a decrease in charge carrier recombination, which induces improved performance both in photocatalysis and photoelectrocatalysis. These performances are discussed in terms of nanostructured morphology and physico-chemical properties probed through different characterization methods.

2. Experimental

2.1. Preparation of tri-doped mesoporous carbon

The homogeneous precursor solution was prepared by dissolving carrageenan (3 g) in 80 ml of water at 80 °C. Then 40 ml of water containing 16 g of urea was slowly added into the solution under vigorous stirring followed by addition of 10 ml of TEOS (Scheme S1 in Supplementary Information). The mixture was left under stirring at 80 °C until the volume reduced to 50 ml and then immediately cooled down by deep-freezing, which resulted in strong gel formation. The gel was vacuum-dried at 70 °C and then transferred to a covered crucible and heated at 550 °C for 2 h (2°C min^{-1}) under nitrogen atmosphere. The as-prepared composite was washed using NH_4HF_2 for 48 h to remove silica and this material was named SNOC1. For comparison reasons the material was synthesized by the same method (with the same proportion) without using silica in the initial gel formation and named SNOC2.

2.2. Preparation of TiO_2 nanorod arrays and TiO_2/SNOC nanocomposites

TiO_2 nanorods were directly grown on commercially available

conductive fluorine-doped tin oxide (FTO) by hydrothermal method described elsewhere [30]. Briefly, hydrochloric acid and distilled water were mixed in volume ratio of 1:1 and titanium *n*-butoxide was added dropwise under vigorous stirring. This solution was placed into Teflon-lined stainless steel autoclave together with cleaned FTO glass and heated at 150 °C for 20 h. Finally, titania nanorods were annealed at 500 °C for 1 h (5°C min^{-1}) in air atmosphere. The TiO_2 NRs were prior the coatings of the SNOC plasma activated using radio frequency plasma with Ar/O_2 gas mixture for better loading of SNOC material.

All produced SNOC samples were hand-ground with a mortar, dispersed in isopropanol with the concentration of 0.1 mg mL^{-1} , and exfoliated by ultrasonic treatment for 2 h. The produced mixture was centrifuged at 3000 rpm for 10 min. The supernatant was collected by pipette and mixed with Triton X-100 in the volume ratio of 1:1. The samples were then deposited onto TiO_2 NRs by spin-coating method followed by thermal treatment at 150 °C and were named TiO_2/SNOC .

2.3. Physical characterization

X-ray powder diffraction (XRD) patterns were recorded at room temperature using an X'Pert PRO MPD diffractometer (PANalytical) in the Bragg–Brentano geometry, with iron-filtered, $\text{Co-K}\alpha$ radiation (40 kV, 30 mA, $\lambda = 0.1789 \text{ nm}$). The angular range of measurement was set as $2\theta = 0.5\text{--}105^\circ$, with a step size of 0.017° . The identification of the crystalline phases in the experimental XRD pattern was obtained using the X'Pert High Score Plus software that includes a PDF-4+ and ICSD databases. Raman spectra were measured by a DXR Raman spectroscope (Thermo Scientific, USA) furnished with a laser functioning at a wavelength of 633 nm. Nitrogen adsorption isotherms at 77.4 K were measured up to the saturation pressure of nitrogen and obtained by the static volumetric technique on the Autosorb iQ analyser (Quantachrome Instruments). Prior to the measurement, samples were degassed at room temperature for at least 10 h. Specific surface area (BET) was calculated using the multipoint BET (Brunauer–Emmet–Teller) model. The best linear fit was obtained using adsorption data in the relative pressures of 0.1–0.3 P/P_0 . The analyses were performed with the ASiQwin software package (Quantachrome Instruments). High-resolution TEM (HRTEM) images were captured by TITAN 60–300 with X-FEG type emission gun, operating at 80 kV. This microscope is equipped with Cs image corrector and a STEM high-angle annular dark-field detector (HAADF). The elemental mappings were obtained by STEM-energy dispersive X-ray spectroscopy (EDS). X-ray photoelectron spectroscopy (XPS) was performed on the PHI 5000 VersaProbe II XPS system (Physical Electronics) with monochromatic $\text{Al-K}\alpha$ source (15 kV, 50 W) and photon energy of 1486.7 eV. UV–vis diffuse reflectance absorption spectra were collected on a FLS980 fluorescence spectrometer (Edinburgh Instruments) equipped with an integrating sphere with its inner face coated with BENFLEC. The standard BENFLEC plate was used as reflectance standard.

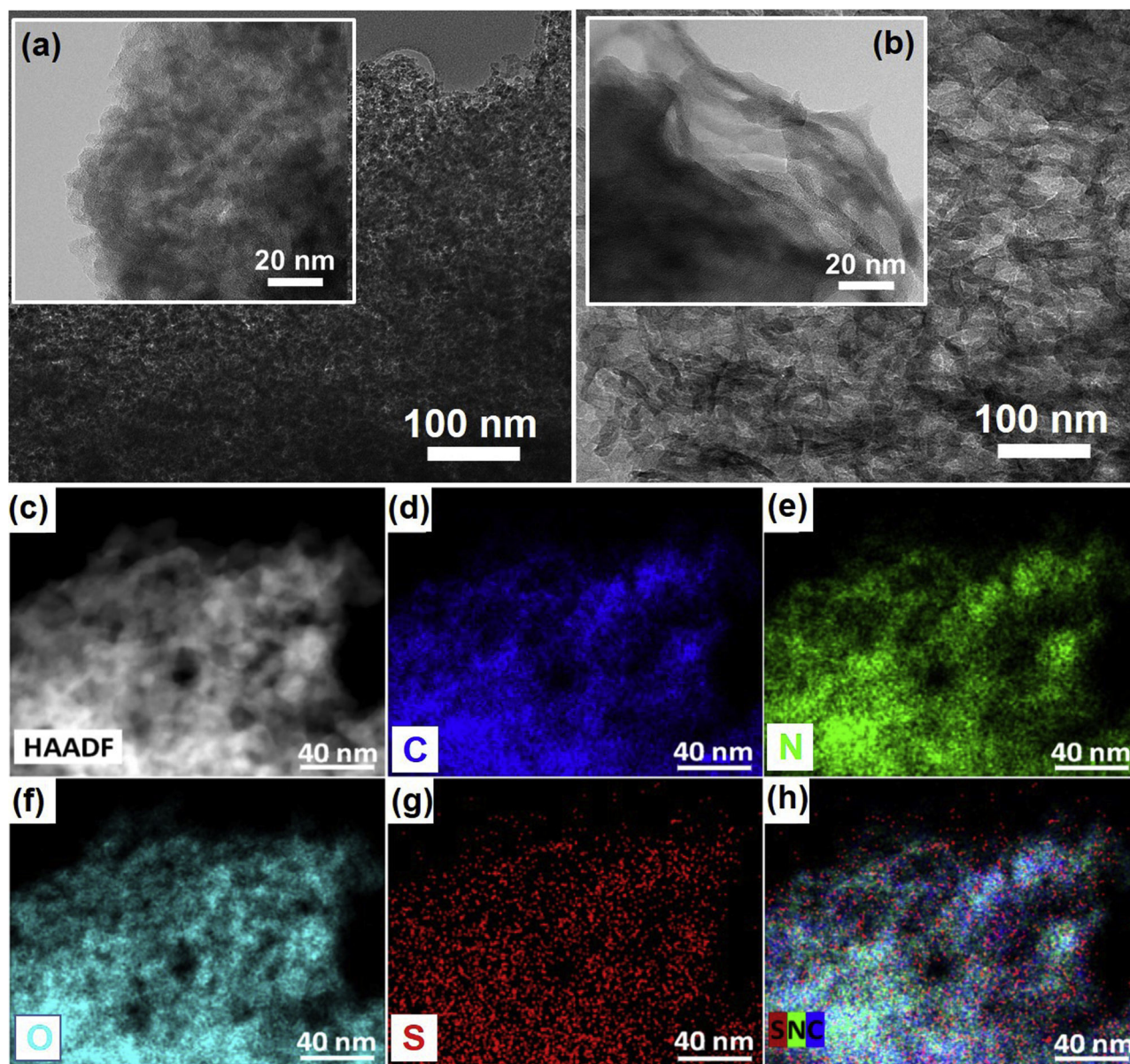


Fig. 2. (a) TEM images of SNOC1 and (b) SNOC2 materials at different magnification (see insets); (c) High-angle annular dark field (HAADF) image and (d–h) EDS elemental mapping of C, N, O, S and joined SNCO taken from the SNOC1 sample.

2.4. Evaluation of photocatalytic activity and PEC properties

Photocatalytic activity of the prepared samples was evaluated by decoloration rate of Rhodamine B as a model organic pollutant. In each experiment the photocatalytic reactor comprised 10 mg of sample and 20 ml of 10 mg L^{-1} RhB solution. Before light irradiation, the suspensions were kept in the dark for 30 min to ensure the adsorption–desorption equilibrium. A 150 W xenon lamp was located approximately 5 cm from the reactor. At 30 min time interval, the photocatalyst was separated from the sample solution by centrifugation and the light absorbance spectrum of clear solution was detected using a UV–Vis spectrophotometer.

The PEC experiments were carried out using a conventional three-electrode cell system with Gamry Series G 300 Potentiostat. The as-prepared photoanodes containing TiO_2 nanorods and TiO_2 nanorods wrapped with SNOC served as working electrode. An Ag/AgCl in 3 M KCl and a Pt wire were used as the reference and counter electrode, respectively. 1 M sodium hydroxide (pH 13.5) solution acted as the electrolyte. The measurements were performed under simulated solar

light illumination of 1.5 A.M. with the intensity of 100 mW/cm^2 light intensity.

3. Results and discussion

In the first part of this work the synthesized SNOC1 and SNOC2 materials were characterized and compared. The crystal structure of the as-prepared samples was investigated by XRD analysis and the results are shown in Fig. 1a. The XRD patterns of the two products show a strong and broad characteristic peak located at $2\theta = 30.5^\circ$, which is assigned to (002) plane (Fig. 1a), representing the hexagonal structure of carbon material (JCPDS X-ray Powder Diffraction Database no. 75-1621) [31]. The broad peak, which can be seen in the case of SNOC1 material (Fig. 1a inset), confirms its mesoporous structure [32]. From the Raman spectrum in Fig. 1b we can find the characteristic D and G bands of carbon located at around 1350 cm^{-1} and 1580 cm^{-1} , respectively. The D band is a common feature of amorphous carbon and arising from imperfection as the A_{1g} mode. Whereas the G band is relevant to a graphitic carbon phase and corresponds to the first-order

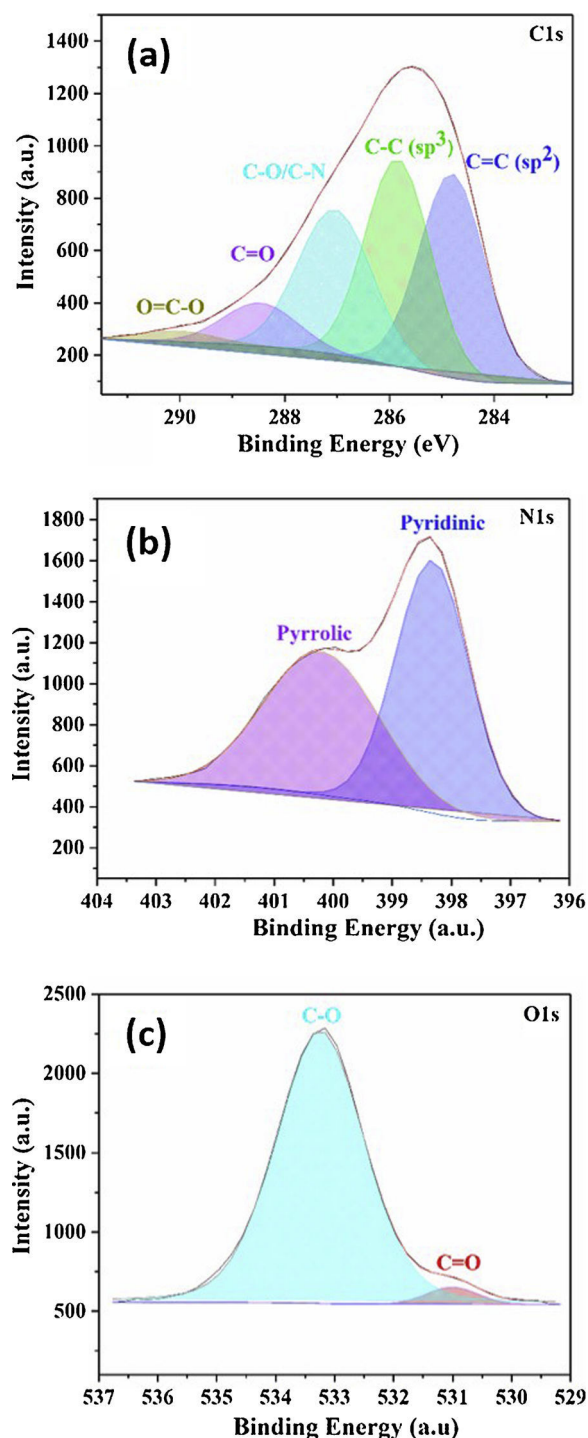


Fig. 3. XPS spectra of SNOC1: (a) C1s, (b) N1s, (c) O1s.

scattering of the E_{2g} mode. Besides the D and G bands, the 2D band located around 2750 cm^{-1} is associated with disorder feature of carbon-based materials [33].

The specific surface area and pore structure characterizations are summarized in Table 1. The surface area calculated by BET method is detected to be $383\text{ m}^2\text{ g}^{-1}$ and $46\text{ m}^2\text{ g}^{-1}$ for SNOC1 and SNOC2, respectively.

The microstructures and morphologies of the SNOC samples were characterized by transmission electron microscopy (TEM). The TEM images captured further verified the porous and non-porous nature of the SNOC1 and SNOC2 materials (Figs. 2a,b and S1). The TEM images of SNOC2 sample show more transparent and interconnected carbon

sheets forming a network. While in the case of SNOC1 we see a mesoporous sponge-like morphology. To investigate the structure and morphology due to the S, N, O introduction, we used additional dark-field TEM analysis (Fig. 2c) and elemental mapping of the SNOC1 sample. Elemental mapping shows the presence and homogeneous distributions of all the elements (C, N, O, and S) throughout the SNOC1 materials (Fig. 2d–h).

X-ray photoelectron spectroscopy (XPS) of the SNOC1 sample revealed the presence of oxygen and nitrogen along with carbon in the materials (Fig. 3a–c). The elemental compositions of nitrogen, oxygen, and carbon in the material was found to be 28.6, 17.4, and 47.9 at%, respectively, indicating different heteroatoms have been effectively incorporated into the carbon. The high resolution XPS spectra of material in C1s region can be deconvoluted into four peaks components with binding energy 284.75, 285.84, 286.81, 288.58, and 289.90 eV corresponding to $-\text{C}=\text{C}-\text{sp}^2$, $-\text{C}-\text{C}-\text{sp}^3$, C–O/C–N, C=O, and O=C–O type of carbons, thus showing the graphitic nature of carbon material (Fig. 3a). The presence of specific N1s peaks at 398.43 eV (54.48 at%) and 400.34 eV (45.52 at%) confirm the presence of pyridinic and pyrrolic type of nitrogen (Fig. 3b). The two peak components at 531.08 eV and 533.28 eV in O1s spectrum originated due to the presence of C=O and CO, which reveal that graphitic carbon is doped with oxygen. (Fig. 3c).

Fig. 4 summarizes the main physical properties of the TiO_2 NRs /SNOC1 composite photoanode. More detailed description was given in our previous contributions [30,34,35]. The crystalline structure of the composite was evaluated based on Raman spectroscopy and the results are depicted in Fig. 4a. The two strong Raman bands at 448 cm^{-1} and 611 cm^{-1} are assigned to E_g and A_{1g} vibration modes of well-developed rutile crystalline phase of TiO_2 , respectively. The rutile phase is preferentially grown due to the highly crystalline FTO substrate with isocrystalline tetragonal structure. The inset of Fig. 4a shows the cross-section image of bare TiO_2 NRs vertically grown on the FTO substrate. The length of the nanorods was around $1\text{ }\mu\text{m}$ and the width around 100 nm as it was determined by SEM analysis. The UV–vis absorption spectrum of bare TiO_2 NRs shows typical trend with the main absorption in the UV region; the slight shift into the Vis part is due to the scattering by the nanorods. Very different situation was observed for the TiO_2 NRs /SNOC1 composite exhibiting a broad absorption in the visible part apparently due to the SNOC1 component. It also confirms a successful loading of SNOC1 over the titania nanorods. This was further evidenced by a thorough analysis done using high-resolution transition electron microscopy (HRTEM). The homogenous coating of SNOC over the nanorod was observed either from the HRTEM image in Fig. 4c as well as it is evident from the elemental (Ti, O, N, S) EDS mapping provided in Fig. 4e–i.

SNOC-based and TiO_2 -based samples were applied to the degradation of RhB under visible light irradiation in order to evaluate the photocatalytic activity of prepared materials. The changes in degradation efficiency of RhB are displayed in Fig. 5a. A blank test was performed without photocatalyst for comparison and to exclude the role of photolysis. No degradation of RhB is observed in the absence of photocatalyst so that the photolysis of RhB is negligible. As we expected, SNOC1 exhibits highest photocatalytic activity among all measured samples. About 70% of RhB is degraded in the presence of SNOC1 after 210 min of irradiation, while 40% of RhB is decomposed by SNOC2, 32% by $g\text{-C}_3\text{N}_4$ (reference representing undoped carbon based material, see Fig. S2), 25% by TiO_2 P25, and 20% by TiO_2 NRs. The better photocatalytic activity is due to the higher specific area of mesoporous SNOC1 sample, which brings much more photocatalytically active centers. Another reason for the boosted photoactivity is the much higher absorption of visible light for the SNOC1 and SNOC2 samples comparing to TiO_2 samples, which as pristine absorbed only the UV light. To further understand the reaction kinetics, the experimental data are fitted according to the pseudo-first-order mechanism and the results are shown in Fig. 5b. The apparent reaction rate constants were

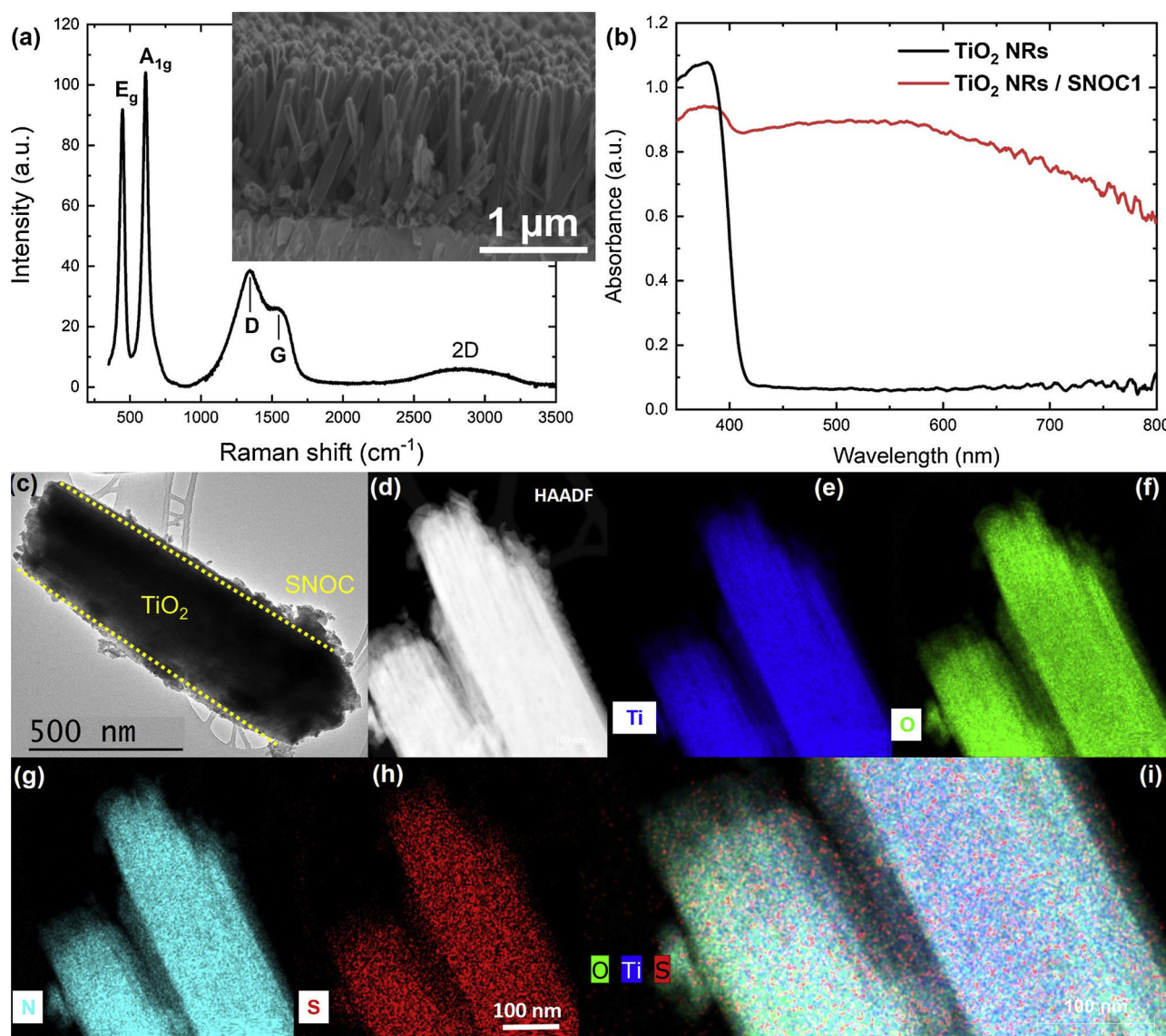


Fig. 4. (a) Raman spectrum with TiO₂ NRs with deposited SNOC1 with the insert showing the cross-section SEM image of TiO₂ nanorods grown on FTO substrate; (b) UV-vis absorption spectra of bare TiO₂ and TiO₂/SNOC1 composite photoanode; (c,d) HR-TEM and HAADF images of TiO₂/SNOC1 composite photoanode, respectively; (e–h) EDS mapping of Ti, O, N, S elements in the TiO₂/SNOC1 composite photoanode; (i) EDS O, Ti, S summary element map of the TiO₂/SNOC1 sample.

calculated and increase in the range of TiO₂ NRs (0.0822 s^{-1}) < TiO₂ P25 (0.1002 s^{-1}) < g-C₃N₄ (0.134 s^{-1}) < SNOC2 (0.168 s^{-1}) < SNOC1 (0.4554 s^{-1}). The lowest photocatalytic activity for TiO₂ is attributed to the visible light activation used for the reaction.

In the following experiments the PEC activity of the materials was tested under simulated solar light (AM 1.5 G, 100 mW cm^{-2}) illumination. In these experiments the bare TiO₂ NRs and TiO₂ NRs hybridized with SNOC materials were used as the photoanodes. From the linear voltammetry scans in Fig. 5c it is seen that the bare TiO₂, TiO₂/SNOC2 and TiO₂/gC₃N₄ (see Fig. S2, $379 \mu\text{A cm}^{-2}$) photoanodes showed relatively similar photoactivity with an increase of the photocurrent density from $372 \mu\text{A cm}^{-2}$ to $435 \mu\text{A cm}^{-2}$ at 0.5 V vs. Ag/AgCl, which denoted an improvement of about 17%. Much higher photocurrent density of $795 \mu\text{A cm}^{-2}$ at the same applied voltage was observed for the TiO₂/SNOC1 composite photoanode. In both cases the SNOC serve as the oxygen evolution reaction (OER) co-catalyst [36] as well as it improves the separation of photogenerated charges due to the band-bending developed at the interface between TiO₂ and SNOC [37]. The possible mechanism of the heterojunction and therefore better photoactivity is schematically illustrated in Fig. S3. The transfer of photogenerated

charges is then boosted via the high conductive carbon material and especially due to its doping by sulfur and nitrogen increasing the charge density. However, the higher activity of SNOC1 can be attributed to its mesoporous nature, which is beneficial for the co-catalytic performance as well as it allows more light to reach the TiO₂ surface. In contrast non-porous SNOC2 sample apparently blocked the TiO₂ surface towards the light irradiation and the contact with the electrolyte, which resulted in the lower photoactivity. The blocking effect was verified by the PEC amperometry measurements, i.e. the photocurrents recorded at fixed potential of 0.5 V vs. Ag/AgCl, performed with back and front sides' illumination geometry. As it is seen in Fig. S4 the back side illumination of SNOC2 sample led to the increase of the photoactivity by 18%, while for SNOC1 it was only around 5%. The amperometry scans of all sample are further shown in Fig. 5d. The bare TiO₂ photoanode generated a current spike, i.e., a transient when the light was switched on, which then gradually decreased to a steady state photocurrent value. The current spike generally denotes a certain level of surface recombination of photoexcited electron-hole pairs. Any transients were not detected for the TiO₂/SNOC composite photoanodes, which confirms the above-described effect of SNOC constituent in reducing the recombination of

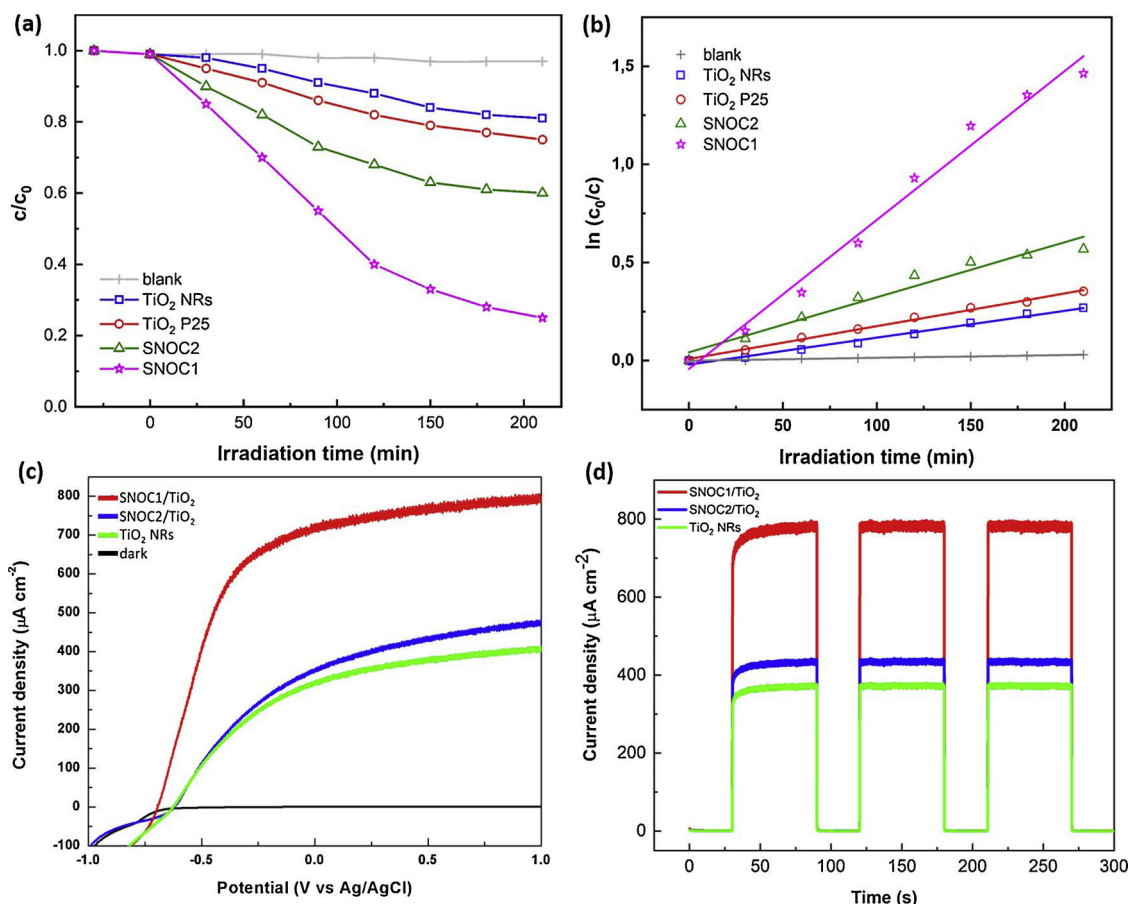


Fig. 5. (a, b) Photocatalytic properties of TiO_2 NRs, TiO_2 P25, SNOC1, and SNOC2 materials. The PEC analysis of TiO_2 NRs and modified composites of SNOC/ TiO_2 : (c) Linear sweep voltammetry measurements and (d) chronoamperometry measurements conducted at 0.5 V.

charges. Finally, the amperometry method was used to examine the stability of the TiO_2 /SNOC1 composite photoanode. The sample was measured for 210 min during which a negligible decrease of the photoactivity by $25 \mu\text{A cm}^{-2}$ was observed (see Fig. S5).

4. Conclusions

In this work we have introduced a novel synthesis of non-porous and mesoporous N-, S-, O-doped carbon material. They both showed graphitic crystalline nature, which was verified by XRD and Raman spectroscopy. The porosity of the structures was evaluated based on BET measurements and a remarkable surface area of $383 \text{ m}^2 \text{ g}^{-1}$ was identified for the porous doped carbon sample. Consequently this material also showed the highest photocatalytic activity towards decomposition of Rhodamine B. Accordingly the highest photoelectrochemical activity was obtained for a composite photoanode constituted of TiO_2 nanorods and conformally coated porous doped carbon. The enhanced activity was attributed to several beneficial features of porous doped carbon; namely its co-catalytic activity for oxygen evolution reaction and improvement of photogenerated charge dynamics due to a heterojunction developed between the TiO_2 and carbon as well as its high electrical conductivity originated from the S and N doping. We believe that this carbon material can be generally used as a platform for combinations with other semiconductors such as, e.g., WO_3 and/or ZnO , etc., to boost their PEC performance.

Acknowledgements

The authors gratefully acknowledge the support from the Ministry of Education, Youth and Sports of the Czech Republic under Project No.

LO1305, by the Operational Programme Research, Development and Education – European Regional Development Fund, Project No. CZ.02.1.01/0.0/0.0/15_003/0000416, and by the Grant Agency of the Czech Republic 17-20008S.

Appendix A. Supplementary data

Supplementary data associated with this article can be found, in the online version, at <https://doi.org/10.1016/j.cattod.2019.01.024>.

References

- [1] J.K. Stolarczyk, S. Bhattacharyya, L. Polavarapu, J. Feldmann, *ACS Catal.* 8 (2018) 3602–3635.
- [2] Z. Zou, K. Sayama, H. Arakawa, *Nature* 414 (2001) 625–627.
- [3] C. Burda, Y. Lou, X. Chen, A.C.S. Samia, J. Stout, J.L. Gole, *Nano Lett.* 3 (2003) 1049–1051.
- [4] S. Khan, J. Akikusa, *J. Phys. Chem. B* 103 (1999) 7184–7189.
- [5] C. Santato, M. Ulmann, J. Augustynski, *J. Phys. Chem. B* 105 (2001) 936–940.
- [6] S. Kment, Z. Hubicka, J. Krysa, D. Sekora, M. Zlamal, J. Olejnicek, M. Cada, P. Ksirova, Z. Remes, P. Schmuki, E. Schubert, R. Zboril, *Appl. Catal. B: Environ.* 165 (2015) 344–350.
- [7] S. Wang, P. Chen, Y. Bai, J.H. Yun, G. Liu, L. Wang, *Adv. Mater.* 30 (2018) 1800486.
- [8] B. Weng, C.R. Grice, J. Ge, T. Poudel, X. Deng, Y. Yan, *Adv. Energy Mater.* 8 (2018) 1701655.
- [9] S. Kment, P. Schmuki, Z. Hubicka, L. Machala, R. Kirchgeorg, N. Liu, L. Wang, K. Lee, J. Olejnicek, M. Cada, I. Gregora, R. Zboril, *ACS Nano* 9 (2015) 7113–7123.
- [10] M. Ni, M.K.H. Leung, D.Y.C. Leung, K. Sumathy, *Renew. Sustain. Energy Rev.* 11 (2007) 401–425.
- [11] S. Gunti, A. Kumar, M.K. Ram, *Int. Mater. Rev.* 63 (2018) 257–282.
- [12] T. Butburee, Y. Bai, H. Wang, H. Chen, Z. Wang, G. Liu, J. Zou, P. Khemthong, G.Q.M. Lu, L. Wang, *Adv. Mater.* 30 (2018) 1705666.
- [13] M. Ge, Ch. Cao, J. Huang, S. Li, Z. Chen, K.-Q. Zhang, S.S. Al-Deyab, Y. Lai, *J. Mater. Chem. A Mater. Energy Sustain.* 4 (2016) 6772–6801.
- [14] S. Kment, F. Riboni, S. Pausova, L. Wang, L. Wang, H. Han, Z. Hubicka, J. Krysa,

- P. Schmuki, R. Zboril, *Chem. Soc. Rev.* 46 (2017) 3716–3769.
- [15] R.M. Navarro Yerga, M.C. Alvarez Galvan, F. del Valle, J.A. Villoria de la Mano, J.L.G. Fierro, *ChemSusChem* 2 (2009) 471–485.
- [16] A.J. Corwan, J. Tang, W. Leng, J.R. Durrant, D.R. Klug, *J. Phys. Chem. C* 114 (2010) 4208–4214.
- [17] B. Song, N. Zhang, Ch. Gao, Y. Xiong, *Nano Energy* 53 (2018) 296–336.
- [18] K.R. Reddy, M. Hassan, V.G. Gomes, *Appl. Catal. A: Gen.* 489 (2015) 1–16.
- [19] F.X. Xiao, J. Miao, H.B. Tao, S.F. Hung, H.Y. Wang, H.B. Yang, J. Chen, R. Chen, B. Liu, *Small* 11 (2015) 2115–2131.
- [20] Y. Tan, Z. Shu, J. Zhou, T. Li, W. Wang, Z. Zhao, *Appl. Catal. B: Environ.* 230 (2018) 260–268.
- [21] H. Kwon, F.M. Mota, K. Chung, Y.J. Jang, J.K. Hyun, J. Lee, D.H. Kim, *ACS Sustain. Chem. Eng.* 6 (2018) 1310–1317.
- [22] J. Liu, Y. Liu, N. Liu, Y. Han, X. Zhang, H. Huang, Y. Lifshitz, S.T. Lee, J. Zhong, Z. Kang, *Science* 347 (2015) 970–974.
- [23] P. Ganesan, A. Sivanantham, S. Shanmugan, *J. Mater. Chem. A* 6 (2018) 1075–1085.
- [24] D. Wang, D. Choi, J. Li, Z. Yang, Z. Nie, R. Kou, D. Hu, Ch. Wang, L.V. Saraf, J. Zhang, I.A. Aksay, J. Liu, *ACS Nano* 3 (2009) 907–914.
- [25] M.R. Benzigar, S.N. Talapaneni, S. Joseph, K. Ramadass, G. Singh, J. Scaranto, U. Ravon, K. Al-Bahily, A. Vinu, *Chem. Soc. Rev.* 47 (2018) 2680–2721.
- [26] Z. Li, L. Zhang, B.S. Amirkhiz, X. Tan, Z. Xu, H. Wang, B.C. Olsen, C. Holt, D. Mitlin, *Adv. Energy Mater.* 2 (2012) 431–437.
- [27] H.J. Liu, X.M. Wang, W.J. Cui, Y.Q. Dou, D.Y. Zhao, Y.Y. Xia, *J. Mater. Chem.* 20 (2010) 4223–4230.
- [28] S. Gao, Y. Chen, H. Fan, X. Wei, C. Hu, H. Luo, L. Qu, *J. Mater. Chem. A* 2 (2014) 3317–3324.
- [29] C. Xuan, Z. Wu, W. Lei, J. Wang, J. Guo, D. Wang, *ChemCatChem* 9 (2017) 809–815.
- [30] H. Kmentova, S. Kment, L. Wang, S. Pausova, T. Vaclavu, R. Kuzel, H. Han, Z. Hubicka, M. Zlamal, J. Olejnicek, M. Cada, J. Krysa, R. Zboril, *Catal. Today* 287 (2017) 130–136.
- [31] Y. Xia, R. Mokaya, *Chem. Mater.* 17 (2005) 1553–1560.
- [32] L. Qie, W.M. Chen, Z.H. Wang, Q.G. Shao, X. Li, L.X. Yuan, X.L. Hu, W.X. Zhang, Y.H. Huang, *Adv. Mater.* 24 (2012) 2047–2050.
- [33] A.C. Ferrari, J. Robertson, *Phys. Rev. B* 61 (2000) 14095–14107.
- [34] A.K. Rathi, H. Kmentova, A. Naldoni, A. Goswamii, M.G. Gawande, R.S. Varma, S. Kment, R. Zboril, *ACS Appl. Nano Mater.* 1 (2018) 2526–2535.
- [35] L.Y. Wang, Y. Wang, P. Schmuki, S. Kment, R. Zboril, *Electrochim. Acta* 260 (2018) 212–220.
- [36] Y. Zhao, R. Nakamura, K. Kamiya, S. Nakanishi, K. Hashimoto, *Nat. Commun.* 4 (2013) 2390.
- [37] D.K.L. Chan, J.C. Yu, *Catal. Today* 310 (2018) 26–31.

Appendix [A7]

Nanostar morphology of plasmonic particles strongly enhances photoelectrochemical water splitting of TiO₂ nanorods with superior incident photon-to-current conversion

L. Wang, Y. Wang, P. Schmuki, **S. Kment***, R. Zboril*

Electrochimica Acta 260, 212-220, 2018



Nanostar morphology of plasmonic particles strongly enhances photoelectrochemical water splitting of TiO₂ nanorods with superior incident photon-to-current conversion efficiency in visible/near-infrared region



Lingyun Wang^a, Yu Wang^a, Patrik Schmuki^{a, b}, Stepan Kment^{a, **}, Radek Zboril^{a, *}

^a Regional Centre of Advanced Technologies and Materials, Joint Laboratory of Optics and Department of Physical Chemistry, Faculty of Science, Palacky University, Šlechtitelů 27, Olomouc, 783 71, Czech Republic

^b Department of Materials Science and Engineering, University of Erlangen-Nuremberg, Martensstrasse 7, D-91058, Erlangen, Germany

ARTICLE INFO

Article history:

Received 30 March 2017

Received in revised form

11 June 2017

Accepted 15 November 2017

Available online 16 November 2017

Keywords:

Photoelectrochemical water splitting
IPCE

Gold nanostars
Titanium dioxide
Schottky contact

ABSTRACT

Photoelectrochemical (PEC) water splitting with TiO₂ photoanodes is a promising technique for converting solar energy into a clean chemical energy. The key drawbacks of titania involve still a low PEC performance and its large band gap energy allowing absorption only in the UV region. Plasmonic nanostructures such as Au and Ag represent a powerful tool towards the light harvesting enhancement with the efficiency dependent on their size and loading. Here, the unique nanostar morphology of plasmonic particles is presented as a new principal factor allowing the significant improvement of the incident photon-to-current conversion efficiency (IPCE) and the extension of light absorption over the broadband UV–Vis–NIR region. A plasmonic metal/semiconductor heterostructure synthesis is based on *ex situ* deposition of multispired gold nanostars (Au-NSs) onto hydrothermally grown TiO₂ nanorods. Compared to bare TiO₂ nanorods, the Au-NSs-decorated TiO₂ exhibits 350% and *ca.* 20% increase in the photocurrent density under visible light and simulated sunlight irradiation, respectively. Importantly, a significant enhancement of IPCE over the Vis-NIR region is observed with single-phase Au-NSs, the value two times higher compared to the spherical morphology. This is largely attributed to the long-wavelength plasmon resonances of Au-NSs and their ability to promote surface plasmon resonance (SPR)-mediated hot electron transfer.

© 2017 Elsevier Ltd. All rights reserved.

1. Introduction

Hydrogen production by solar water splitting has been identified as a promising way of meeting the increasing demand for clean and sustainable energy. Photoelectrochemical (PEC) water splitting on the semiconductor TiO₂ was first reported by Fujishima and Honda in 1972, and has been studied extensively because TiO₂ is non-toxic, abundant, and photostable [1–6]. However, because of its intrinsic band gap of 3.0–3.2 eV, it can only absorb light in the UV range of the solar spectrum. Attempts to remove this limitation and extend its optical absorbance into the visible (or even near-

infrared) range have been made by using element doping [7–11], quantum dots [12–14], dye sensitization [15,16], and/or by combining it with other narrow-band gap semiconductors [17,18]. Recently, nanostructures of noble metals such as Au and Ag, have received considerable attention due to their unique localized surface plasmon resonance (SPR) properties, which could potentially be exploited in solar water splitting [19–22]. Importantly, Au nanostructures exhibit better photostability than quantum dots or dyes, which frequently suffer from photocorrosion issues [23]. The increase in the solar energy conversion efficiency of TiO₂ systems upon incorporating plasmonic nanostructures has been attributed to three factors: (1) effective light scattering, (2) extension of light absorption to longer wavelengths, and (3) direct charge injection from the metal to the semiconductor [24,25]. The performance of plasmonic nanoparticles with respect to all three factors depends strongly on their size and shape. For example, the photocatalytic

* Corresponding author.

** Corresponding author.

E-mail addresses: stepan.kment@upol.cz (S. Kment), radek.zboril@upol.cz (R. Zboril).

activity of Au–TiO₂ nanocomposites is governed by the size of the Au nanoparticles because this parameter determines the efficiency of electron transfer to the conduction band of TiO₂ and thus controls the system's reduction potentials [26]. Similarly, the light harvesting ability of TiO₂ nanocomposites incorporating Au nanorods can be extended deep into the visible range by manipulating the rods' length-to-width ratios [27,28]. Thus, previous studies on surface plasmon-mediated photoelectrochemical water splitting have predominantly focused on the effects of varying the size and loading of Au nanoparticles [26,29–32] or the aspect ratios of Au nanorods [27,28,30,33]. However, to our knowledge, there are no published studies on the effects of using branched gold nanostars as photosensitizers for adjacent semiconductors in PEC water splitting.

Here, we demonstrate that Au nanostars (AuNSs) are superior to other Au nanostructures in PEC applications, strongly increasing the overall photoelectrochemical performance of TiO₂ nanorod arrays (NRs) under both visible light irradiation and simulated solar light. A Mott-Schottky analysis showed that decoration with AuNSs improved the system's carrier density and thus increased the photocurrent. Interestingly, the Schottky junction at the Au-NSs/TiO₂-NR interface could be modified to facilitate charge transfer by annealing the assembled heterostructures (Au-NSs/TiO₂-NRs) at a low temperature. The improved performance induced by such treatment was demonstrated by electrochemical impedance spectroscopy (EIS) measurements and the fact that it increased the lifetime of excited electrons in the heterostructure. The long-wavelength plasmonic effect of Au-NSs resulting in enhanced incident photon-to-current conversion efficiency (IPCE) demonstrates that Au-NSs are good photosensitizers for increasing the PEC performance of semiconductors. The increase in the IPCE value observed for the Au-NSs/TiO₂ composite in the UV region was mainly attributed to the photon scattering effect of the Au-NSs, while the long-wavelength plasmon resonances of Au-NSs and their ability to promote SPR-mediated hot electron transfer may be primarily responsible for the increase in IPCE over the entire visible and NIR spectrum upon visible light illumination.

2. Experimental

2.1. Materials

The following materials were obtained from Sigma-Aldrich and used without further purification: titanium *n*-butoxide (97%), hydrochloric acid (HCl, 37 wt%), auric acid (HAuCl₄·3H₂O), trisodium citrate dihydrate (Na₃C₆H₅O₇·2H₂O), 3-Mercaptopropionic acid (MPA, ≥99%), L-ascorbic acid (AA), silver nitrate (AgNO₃).

2.2. Synthesis of TiO₂ nanorod arrays

TiO₂ nanorod arrays were fabricated on a fluorine-doped tin oxide (FTO) glass substrate by a hydrothermal method [34]. Typically, 14 mL of concentrated HCl was mixed with 14 mL Milli-Q water (18.2 MΩ cm), and 0.46 mL of titanium *n*-butoxide was mixed into the aqueous solution. The resulting clear solution was then placed in a Teflon-lined stainless steel autoclave (50 mL internal volume), and an FTO glass substrate (surface resistivity: 7 Ω sq⁻¹, Solaronix) that had been pre-cleaned with DI water, acetone, and 2-propanol was placed in the solution with the conductive FTO side facing downwards. The resulting system was heated in an electronic oven at 150 °C for 8 h and then cooled under flowing water for 15 min, after which the sample was rinsed with DI water and ethanol before being air-dried. The as-prepared TiO₂ nanorod film was then annealed in air at 450 °C for 1 h to improve the nanorods' crystallinity.

2.3. Synthesis of Au nanostars

We first synthesized a solution of Au NPs to serve as the seed material for the preparation of Au NSs. To this end, 20 mL of 1.0 mM aqueous HAuCl₄ was placed in a 50 mL flask and the solution was heated to 100 °C under refluxing conditions. 2 mL of 1% aqueous trisodium citrate dihydrate was then quickly added to the rapidly-stirred boiling solution, which gradually became deep red. After 10 min stirring at high temperature, the hot plate was removed and the mixture was stirred for further 15 min. The resulting suspension of Au NPs was stored in the fridge until needed. Au nanostar synthesis was performed using a surfactant-free wet chemistry method as previously reported [35]. Briefly, 100 μL of the Au NPs seed suspension was added to 10 mL of a 0.25 mM auric chloride solution at room temperature under vigorous stirring. Then, 100 μL of 1 mM silver nitrate and 50 μL of 0.1 M ascorbic acid were quickly added together. The solution rapidly changed color from light red to blue. As soon as this occurred, it was centrifuged at 6000 rpm for 15 min, after which the precipitated purple Au NSs were redispersed in Milli-Q water and stored in fridge for future use.

2.4. Preparation of Au NSs-decorated TiO₂ nanorod arrays

The film of TiO₂ NRs on FTO was pre-treated with a solution of concentrated H₂SO₄ for 5 h to modify the nanorods. The substrate bearing the nanorods was then immersed in a 1 M aqueous solution of MPA overnight to functionalize the nanorods' surfaces with thiol groups, after which the rods were washed with ethanol and dried under a flow of N₂. Finally, the sample was immersed in a suspension of Au NSs for 24 h to obtain the Au NSs-decorated TiO₂ NRs. The resulting samples were washed with DI water to remove loosely bound Au NSs and dried under a flow of N₂ before being characterized and subjected to PEC measurements.

2.5. Material characterization

The samples were dispersed in ethanol and sonicated for 5 min, after which one drop of the resulting suspension was placed on a copper grid with a holey carbon film. After drying in air at room temperature, the samples were imaged using a Titan G2 high resolution transmission electron microscope (HRTEM) (FEI) with an image corrector at an accelerating voltage of 80 keV. Images were acquired using a BM UltraScan CCD camera (Gatan). Energy dispersive spectrometry (EDS) was performed in scanning TEM (STEM) mode using a Super-X system with four silicon drift detectors (Bruker). X-ray diffraction (XRD) patterns were collected on an X'Pert diffractometer (PANalytical, Netherlands) using iron-filtered Co-Kα (λ = 1.78901 Å) radiation. The samples' morphologies were determined using a Hitachi SU6600 field-emission scanning electron microscope (FESEM). UV–Vis absorption spectra were acquired using a UV–Vis spectrophotometer (Lambda 35, PerkinElmer) using BaSO₄ as a reference standard.

2.6. Photoelectrochemical measurements

Photoelectrochemical performance measurements were performed in a standard three-electrode PEC cell, with either TiO₂ nanorods (bare or functionalized with Au nanomaterials), Ag/AgCl in a 3 M KCl solution, and Pt wire as the working electrode, reference electrode, and counter electrode, respectively. A 1 M NaOH solution (pH = 13.6) was used as the electrolyte, and was deaerated with N₂ for 20 min prior to each measurement. An O-ring was used to ensure that the area of the photoanode that was exposed to illumination did not vary during these measurements, and was held constant at around 0.785 cm². A 150 W Xenon lamp fitted with

an AM 1.5 G filter was used as the light source, and the power intensity was held at 1 sun (100 mW cm^{-2}) using a silicon reference cell (Newport). PEC performance was recorded on a Gamry Series G 300 Potentiostat. The incident photon-to-current conversion efficiency (IPCE) was measured with a 300 W Xenon lamp coupling with an aligned monochromator (Newport, Oriel TLS-300 X). The IPCE was calculated following the equation given by

$$IPCE\% = \frac{J_{sc}}{P_{in}} \times \frac{1240}{\lambda} \times 100\% \quad (1)$$

where J_{sc} refers to the photocurrent density (mA cm^{-2}) measured at 1 V vs. normal hydrogen electrode (NHE) at a given wavelength (λ), and P_{in} is the irradiance intensity (mW cm^{-2}) of monochromatic light incident on the electrode. Mott-Schottky (M-S) analysis was conducted at an AC frequency of 1 kHz with an amplitude of 5 mV. Electrochemical impedance spectroscopy (EIS) was performed in the dark or under AM 1.5 G solar illumination at open circuit voltage over a frequency range of $0.1\text{--}10^5$ Hz with an AC voltage of 10 mV. The potentials measured vs. Ag/AgCl reference electrode were converted to the reversible hydrogen electrode (RHE) scale according to the Nernst equation: $E_{RHE} = E_{Ag/AgCl} + 0.059 \text{ pH} + E_{Ag/AgCl}^{\circ}$, where E_{RHE} is the converted potential vs. RHE, $E_{Ag/AgCl}^{\circ} = 0.207 \text{ V}$ at 25°C , and $E_{Ag/AgCl}$ is the measured potential vs. Ag/AgCl.

3. Results and discussion

The process developed in our laboratory for fabricating rutile TiO_2 -NRs on fluorine-doped tin oxide (FTO) glass and then coating them with Au-NSs to create photoanodes is illustrated in Fig. 1 (for a detailed description of the methods used, see the Experimental section). In brief, vertically aligned TiO_2 -NRs were initially grown on an FTO substrate using a hydrothermal method that is described elsewhere [34]. The as-prepared TiO_2 -NRs were then annealed in air to improve their crystallinity and the contact between the film and the FTO substrate (step 2 in Fig. 1). Conventionally, deposition-precipitation [30,34] or photodeposition [31,36] methods are used to deposit Au nanostructures onto or over semiconductors to form metal/semiconductor Schottky contacts. However, although the size and morphology of the Au nanostructures strongly influences photocatalytic and PEC performance, neither of these two methods permit effective control of these parameters; both typically yield simple spherical nanoparticles. We therefore developed a different approach in which the synthesis of the Au-NSs is separated from their deposition. Because Au-NSs can be prepared quickly (see below), we combined freshly synthesized Au-NSs (Fig. S1 in Supplementary material) with TiO_2 NRs in the presence of the organic

ligand 3-mercaptopropionic acid (MPA). Thus, after air annealing, the TiO_2 rods were pre-treated with concentrated H_2SO_4 to increase the number of hydroxyl groups on their surfaces and their surface roughness (step 3). The activated TiO_2 NRs were then immersed in an MPA solution, causing the formation of bonding interactions between their surface hydroxyls and the ligand's carboxylic acid groups, and covering the rods' surfaces with free thiol groups that enabled efficient Au-NSs decoration (step 4).

Fig. 2 presents scanning electron microscopy (SEM) and high-resolution transmission electron microscopy (HRTEM) images of bare TiO_2 nanorods and rods decorated with Au-NSs, respectively. The TiO_2 -NRs were grown vertically on an FTO substrate, and had average lengths and diameters of $1.6 \mu\text{m}$ and of $80\text{--}140 \text{ nm}$, respectively (Fig. 2a and b). The uppermost SEM image (Fig. 2a) shows their well-developed tetrahedral morphology. The core and total sizes of the Au-NSs (Fig. 2c,d and Fig. S1) were $34.5 \pm 3.5 \text{ nm}$ and $58.0 \pm 5.5 \text{ nm}$, respectively. SEM images (Figs. S2a and S2b) and HRTEM images of the material obtained after combining the Au NSs with the TiO_2 NRs (Fig. 2c and d) show that the Au-NSs retained their star-like shapes and formed good contacts with the TiO_2 -NRs. A well-defined sharp interface between the TiO_2 -NRs and Au-NSs favors hot electron injection from the gold nanoparticles to TiO_2 via SPR excitation [30]. The formation of such an interface is demonstrated by the HRTEM images shown in Fig. S2 in Supplementary material. Fig. 2e shows a high-angle annular dark-field imaging scanning TEM (HAADF-STEM) image of Au NSs on a single TiO_2 nanorod along with an energy dispersive X-ray spectroscopy (EDS) elemental mapping that clearly shows the presence of Ti and O (corresponding to the TiO_2 NR) and Au (*i.e.*, Au NSs) in the nano-heterostructure. The latter image confirms that the nanostars consist entirely of gold. Further evidence supporting this conclusion is provided in Fig. S3 in Supplementary material, which presents the same elemental mapping as in Fig. 2e but with the distributions of the individual elements overlaid upon one another (Fig. S3 in Supplementary material), as well as an EDS cross-sectional compositional line scan profile of a different Au-NSs/ TiO_2 -NRs assembly, together with the full corresponding EDS spectrum. All of these results confirm that the photoanodes prepared as described above consist exclusively of Au-NSs and TiO_2 -NRs with no contaminants, that they exhibit the desired morphology, and that the Au-NSs are bound to the TiO_2 -NRs. Lattice spacings of 0.12 nm and 0.32 nm corresponding to the (222) plane of the Au fcc structure and the (110) crystalline plane of rutile TiO_2 , respectively, were determined by analyzing the HRTEM images shown in Fig. 2f and the corresponding selective area electron diffraction (SAED) patterns (the insets in Fig. 2f). Additionally, the XRD pattern for the composite nanostructures (Fig. S4 in Supplementary material)

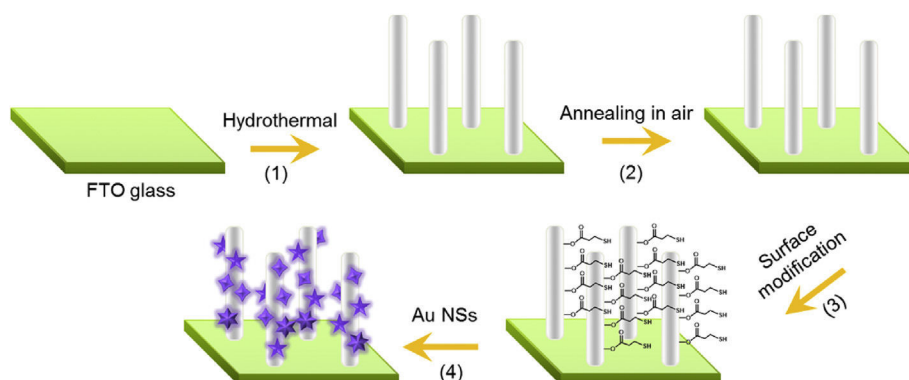


Fig. 1. Depiction of the process used to fabricate Au NSs/ TiO_2 photoanodes.

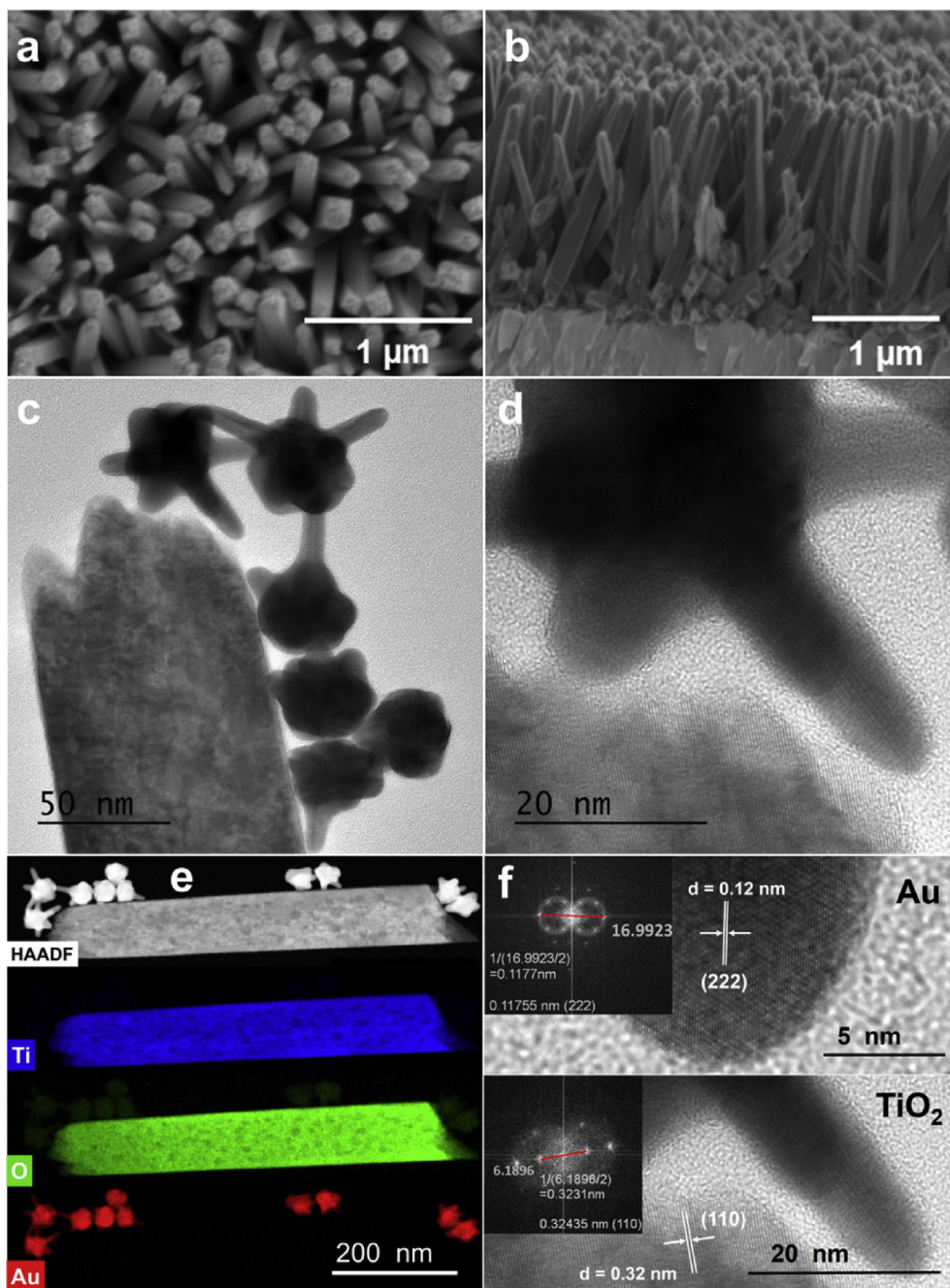


Fig. 2. SEM and HRTEM analysis of the nanostructure. (a, b) SEM images of bare TiO₂ NRs, (c, d) HRTEM images of TiO₂ NRs decorated with Au NSs, (e) HAADF-STEM image and EDS elemental mapping of a single Au NSs/TiO₂ rod, showing the distributions of Ti (blue), O (green), and Au (red), and (f) HRTEM images of Au NSs/TiO₂, with SAED patterns shown in the insets. (For interpretation of the references to color in this figure legend, the reader is referred to the web version of this article.)

confirms that TiO₂ NRs retained their rutile structure. However, the signal from the Au-NSs was too weak (or the corresponding peaks overlapped too extensively with those of the nanorods) to be detected by the X-ray diffraction system that was used.

Aqueous dispersions of the Au-NSs clearly exhibited a broad-band UV–Vis–NIR absorbance in the region between the wavelengths of 400–800 nm as shown in Fig. S5 in Supplementary material. This figure also contains the absorption spectrum corresponding to the spherical Au NPs for comparison. It is seen that the Au NPs exhibited only an absorption peak at around 500 nm, which for higher wavelengths sharply decreased. Fig. 3 shows the light

absorption and scattering spectra of TiO₂ with and without Au-NSs decoration. Notably, the amount of light absorbed or scattered by the Au-NSs/TiO₂ heterostructure is between 20 and 40% greater than that for bare TiO₂ over the entire visible to NIR range, presumably because of the long wavelength plasmon resonances of the Au NSs, which strongly enhance the local electric field [37,38].

The photoelectrochemical properties of AuNSs/TiO₂ were studied using a conventional three-electrode configuration, with the Au-NSs/TiO₂ heterojunction, Ag/AgCl (in 3 M KCl), and a Pt wire as the working, reference, and counter electrodes, respectively (see below). The bare TiO₂-NRs and Au-NSs/TiO₂ were first illuminated

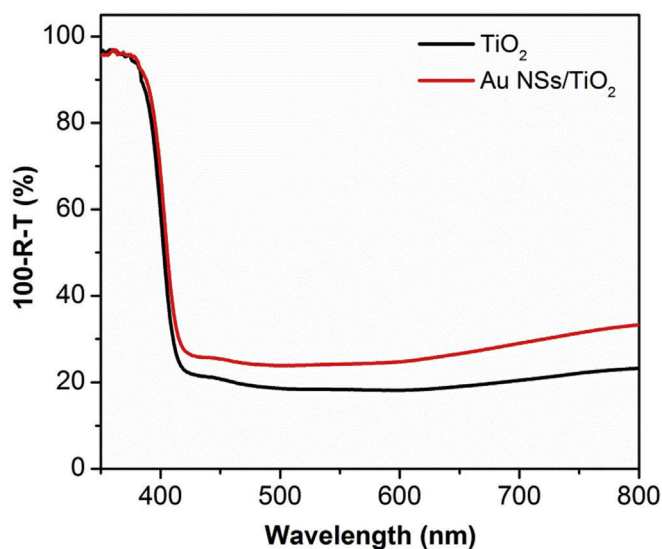


Fig. 3. Absorption plus scattering (%) spectra of TiO_2 and Au NSs/ TiO_2 .

by visible light using an AM 1.5 G solar simulator fitted with a cut-off filter (>420 nm). As shown in Fig. 4a the photocurrent density for the Au-NSs-decorated TiO_2 -NRs under visible light irradiation was $28 \mu\text{A cm}^{-2}$, which was substantially higher than that of bare TiO_2 -NRs yielding the photocurrent density of $11 \mu\text{A cm}^{-2}$ (both

read at 1 V vs. NHE). The photocurrent density further considerably increased to $38 \mu\text{A cm}^{-2}$ due to the thermal treatment of the Au-NSs/ TiO_2 at 150°C . The Schottky junction between the metal and the semiconductor strongly influences the ease of electron transport between them, and it has been demonstrated that a close interface is important for enhancing the visible activity of plasmonic nanostructures. Consequently, the ligand (MPA) that was used to facilitate the binding of the nanostars to the TiO_2 rods could, to some extent, retard direct charge transfer or reduce the intensity of localized SPR-induced electromagnetic fields [27]. Therefore, we subjected the Au-NSs-decorated nanorods to mild thermal annealing at 150°C to remove MPA in order to establish closer Schottky contacts between the Au-NSs and the TiO_2 -NRs. The relevance of this strategy and thus the successful formation of a closer interface following this procedure is demonstrated by the aforementioned increase of the photocurrents and the TEM results presented in Fig. S2 in Supplementary material.

To better characterize the charge transport properties of these systems, their electron lifetimes (τ_n) were determined using the open-circuit voltage decay (OCVD) technique [39,40]. Upon continuous visible light irradiation, a steady open-circuit voltage (V_{oc}) (Fig. S6) of around 1.7 V vs. NHE was detected; when the light source was deactivated, the V_{oc} decreased rapidly as the electrons in the conduction band (CB) recombined with holes trapped on the Au-NSs. The average electron lifetime was computed from the rate of change in the V_{oc} upon deactivation of the light source using equation given by

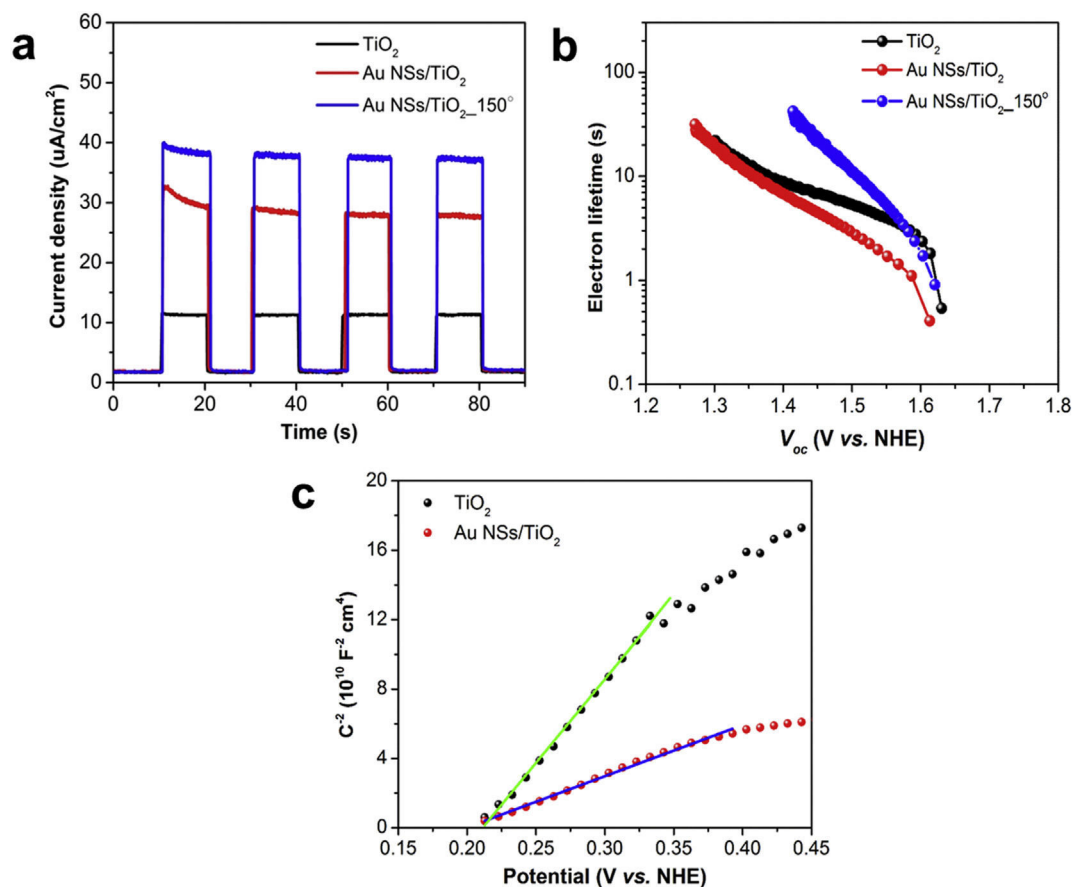


Fig. 4. Photoelectrochemical characteristics under visible light irradiation. (a) Transient photoresponse at 1 V vs. NHE under visible light ($\lambda > 420$ nm) with repeated light on-off cycles; (b) Electron lifetimes for bare TiO_2 , Au NSs/ TiO_2 , and Au NSs/ TiO_2 after annealing at 150°C , determined by the open circuit voltage decay technique; (c) Mott-Schottky plots for TiO_2 and Au NSs/ TiO_2 measured at a frequency of 1 kHz.

$$\tau_n = -\frac{k_B T}{q} \left(\frac{dV_{oc}}{dt} \right)^{-1} \quad (2)$$

where k_B is Boltzmann constant, T is the temperature, and q is the elementary charge. This method represents an effective *in situ* technique for studying the recombination kinetics of interfacial charge transfer processes at the semiconductor-liquid junction [36]. As shown in Fig. 4b, in the absence of annealing, the average electron lifetime of Au-NSs/TiO₂ was lower than that for the bare nanorods at higher V_{oc} values, which can be attributed to the separation of the Au-NSs and the TiO₂-NRs by surface ligands, which would tend to restrict electron transfer. In contrast, the annealed heterostructures have substantially higher electron lifetimes (for both free and trapped electrons) than bare nanorods: at 1.4 V vs. NHE, the τ_n of TiO₂ was ~8 s whereas that for Au-NSs/TiO₂_150° was 42 s. This indicates that closer Schottky contacts favor hot electron transfer and efficiently reduce the rate of charge recombination.

The Mott-Schottky analysis was performed to determine the flat-band potential and carrier density of TiO₂ and Au-NSs/TiO₂. The resulting plots are shown in Fig. 4c; positive slopes are observed for both materials, indicating that they are both n-type semiconductors. Their flat-band potential and carrier density were estimated using equation given by

$$\frac{1}{C_{SC}^2} = \frac{2}{\epsilon_r \epsilon_0 A^2 e N_d} \left(E - E_{fb} - \frac{kT}{e} \right) \quad (3)$$

where C_{SC} is the capacitance of the space charge, ϵ_r is the relative permittivity of rutile TiO₂ ($\epsilon_r = 170$), ϵ_0 is the permittivity of vacuum ($\epsilon_0 = 8.86 \times 10^{-12}$ F m⁻¹), e is the electron charge (1.6×10^{-19}), N_d is the carrier density, E is the applied potential, E_{fb} is the flat-band potential, k is the Boltzmann constant, and T is the temperature. The calculated flat-band potentials of TiO₂ and Au-NSs/TiO₂ were 0.18 and 0.17 V vs. NHE (*i.e.*, -0.83 and -0.84 V vs. Ag/AgCl), while the carrier densities were 9.5×10^{17} and 3.2×10^{18} cm⁻³, respectively. Decorating the TiO₂ NRs with Au nanostars thus caused a slight negative shift of 10 mV in the flat-band potential and a negative shift of the onset potential in the linear sweep voltammetry plot (see Fig. 5a and discussion below). This was attributed to a negative shift of the Fermi level resulting from charge equilibration that occurred when the metal-semiconductor systems were submerged in the electrolyte solution, which is consistent with the findings of earlier studies on Au nanoparticles [34]. The smallness of the negative shift can be explained by the size of Au nanostars. According to Subramanian et al. [41] and the results presented herein, larger metal nanoparticles give rise to smaller shifts because (compared to smaller nanoparticles) they require a greater number of electrons to induce a shift of a given amplitude. In the same study, it was also noted that the negative shift in the Fermi level improved the charge separation in the nano-heterostructure system [41]. In addition, the carrier density for TiO₂ NRs decorated with Au-NSs (3.2×10^{18} cm⁻³) is substantially higher than that for the bare nanorods (9.5×10^{17} cm⁻³), which increases the electron concentration in the conduction band and thus also increases the photocurrent density. Finally, the presence of the nanostars shifts the Fermi level closer to the edge of the conduction band, facilitating charge separation at the semiconductor/electrolyte interface [10]. All these outcomes are fully consistent with our observation of improved PEC activity in the AuNSs/TiO₂NRs.

Fig. 5a shows the linear sweep voltammetry (LSV) behavior of bare TiO₂-NRs and Au-NSs/TiO₂-NRs in the dark and under simulated solar light illumination (AM 1.5 G, 100 mW cm⁻²). The photocurrent density generated by the Au-NSs/TiO₂

heterostructure under white light irradiation (0.95 mA cm⁻²) was substantially greater than that for bare TiO₂ (0.80 mA cm⁻²) at 1 V vs. NHE. The transient photoresponse curves (*i.e.*, chronoamperometry scans) for the two samples recorded at 1 V vs. NHE under repeated light on-off cycles (Fig. 5b) further confirmed that the Au-NSs increased the photoactivity of the TiO₂ NRs by around 18%.

The properties of the interface between the electrolyte and photoanodes were characterized by electrochemical impedance spectroscopy (EIS), yielding the results shown in Fig. 5c. It is noted that the arc diameter for Au-NSs/TiO₂ was smaller than that of bare TiO₂, indicating that the introduction of Au-NSs reduced the interfacial resistance and charge transfer resistance. Impedance spectra were also acquired under illumination with simulated sunlight to confirm that the formation of a closer Schottky junction between the Au-NSs and TiO₂ after mild annealing favors charge transfer. Interestingly, the Nyquist plots shown in Fig. 5d feature two distinct semicircles. The smaller semicircles in the high frequency range (shown more clearly in the inset of Fig. 5d) were attributed to charge transfer processes in the depletion layer, while the arc in the low frequency range was ascribed to electron transfer in the Helmholtz layer [42,43]. The heterostructure annealed at 150 °C yielded the smallest semicircle in the high frequency region and thus had the lowest impedance, confirming that close Schottky contacts reduced the charge resistance in the bulk of the Au-NSs/TiO₂_150° heterostructure. This result is also consistent with the observation that the annealed material had the longest electron lifetime within the nanostructure, and with the results of HRTEM analyses (see Fig. S2 in Supplementary material). The semicircle due to the annealed material in the low frequency region was somewhat larger than that for the non-annealed heterostructure, which may indicate that the annealing process slightly increased the charge transfer resistance at the heterostructure/electrolyte interface. However, electronic processes in the semiconductor bulk are generally more important than charge transfer processes in the electrolyte [42], which explains why the PEC properties of the annealed material (Au-NSs/TiO₂_150°) were superior to those of the non-annealed heterostructure. The Au-NSs/TiO₂_150° photoanodes were also tested on their long-term PEC stability. It is seen in Fig. S7 that the heterostructure did not undergo any significant degradation and kept more than 95% of its PEC activity after 4 h of uninterrupted illumination.

The incident photon-to-current conversion efficiency (IPCE) was calculated for bare TiO₂ and Au-NSs/TiO₂_150° at specific wavelengths (see the Experimental section, Supplementary material); the corresponding spectra are shown in Fig. 6. The IPCE value for Au-NSs/TiO₂_150° in the UV region is substantially higher than that for TiO₂, increasing from 38.4% to 49.4% at 380 nm. This is mainly due to the high efficiency of photoconversion of UV light by TiO₂ NRs. Importantly, decoration with Au-NSs extends the photoactivity of TiO₂ into the visible and even NIR regions; as a result, the IPCE values for the heterostructure are 0.1–0.4% higher than those for the bare nanorods between 400 and 800 nm (see the inset in Fig. 6). This phenomenon is consistent with the presence of absorption peaks across the entire Vis and NIR regions for Au-NSs/TiO₂ (Fig. 3), which are due to the long wavelength plasmon resonances of AuNSs.

Pu et al. [30] have previously shown that decorating TiO₂ with Au nanostructures can lead to plasmon-enhanced photoactivity over specific wavelength ranges. However, in the systems studied by these authors, the extension of photoactivity depended heavily on the shape of the Au nanostructures [30]. Thus, decoration with Au nanoparticles yielded enhancement in the Vis range, while decoration with Au nanorods enhanced activity in the NIR range; to achieve enhancement over both ranges, it was necessary to

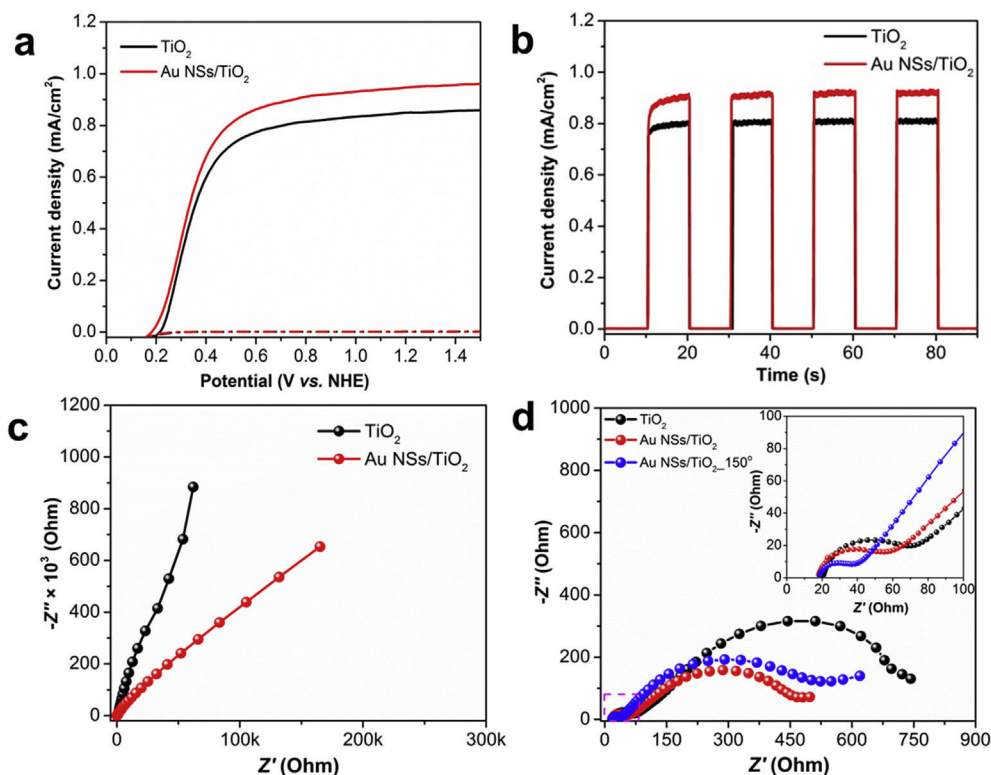


Fig. 5. Photoelectrochemical characteristics under simulated solar light irradiation. (a) Linear sweep voltammetry behavior; (b) Chopped light chronoamperometry curves recorded at 1 V vs. NHE under AM 1.5 G solar illumination; (c) Nyquist plots of TiO_2 and Au NSs/ TiO_2 measured at the open circuit potential over frequencies of 0.1–100 kHz with an amplitude of 10 mV in the dark and (d) under AM 1.5 G solar light illumination. The inset in panel (d) shows a magnification of the high frequency region enclosed in the dashed pink frame. (For interpretation of the references to color in this figure legend, the reader is referred to the web version of this article.)

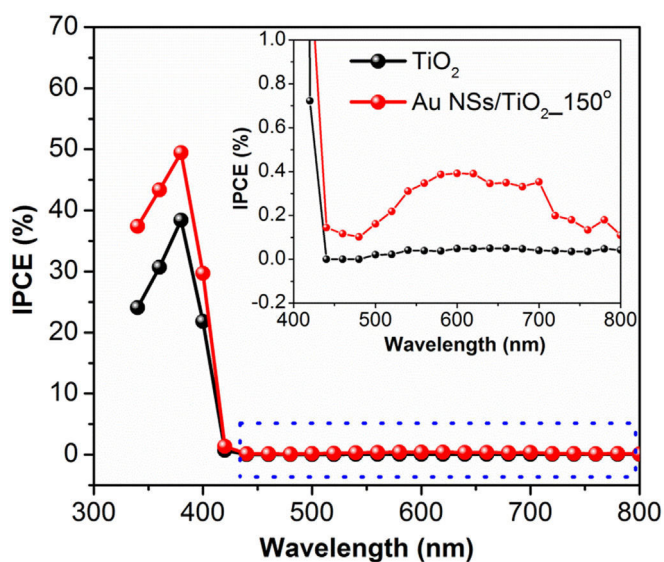


Fig. 6. IPCE plots for TiO_2 and Au NSs/ $\text{TiO}_2_{150^\circ}$ (The IPCE plot in the inset is a magnification of the main plot over the wavelength range of 400–800 nm).

separately decorate the TiO_2 with Au nanostructures of both kinds. An important advantage of the method we present herein is that the Au nanostars confer strong IPCE enhancement in both the Vis and NIR spectral regions. Moreover, if the ratios of the highest IPCE values in the Vis-NIR and UV regions are considered (0.4/50 in this work, compared to 0.015/25 in the work of Pu et al. [30]), it becomes clear that the overall IPCE efficiency in the Vis-NIR range

achieved with the Au-NSs is over 10 times greater than that achieved with the mixture of Au nanoparticles and nanorods reported by Pu et al. [30] The absorbed photon-to-current conversion efficiency (APCE), or internal quantum efficiency, was computed for the Au-NSs/ TiO_2 -NR system by dividing its IPCE value at a given wavelength by its absorption at the same wavelength (Fig. S8 in Supplementary material). The Au-NSs/ $\text{TiO}_2_{150^\circ}$ system exhibited APCE values between 0.3 and 1.5% over the entire Vis and NIR region, with a maximum of 1.5% at 600 nm, which is consistent with the SPR absorbance peak of Au-NSs.

On the basis of the analysis and discussion presented above, a mechanism was proposed to explain the improvement in PEC properties resulting from the incorporation of Au-NSs (see Fig. 7). The cores and elongated arms of the Au-NSs each play different and important roles in this mechanism. Because the Au-NSs are large plasmonic nanostructures, having diameters of more than ~ 50 nm, they are very effective at trapping light and increasing the system's optical path length [44]. The photon scattering induced by these particles increases the rate of electron-hole pair formation in the semiconductor and is responsible for the enhancement of the heterostructure's IPCE values across the UV region. Moreover, the Au nanostars' long wavelength plasmon resonances, together with the enlarged cross section for plasmon excitation due to the plasmons from their cores and arms, cause significant increases in the local electric field strength [38,45], which helps to increase the rate of carrier creation. We therefore suggest that the long-wavelength plasmon resonances promote SPR-mediated hot electron transfer and are also primarily responsible for the observed IPCE enhancement over the visible and NIR region upon visible light illumination. As shown in Fig. 7, visible light irradiation caused hot electrons to be directly injected from the Au-NSs into the adjacent

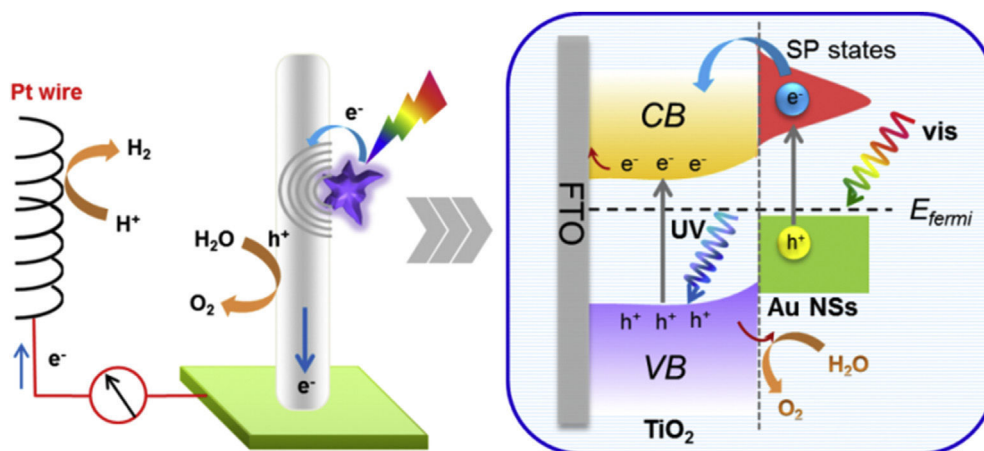


Fig. 7. Schematic depiction of the mechanism proposed to explain the improvement in the PEC properties of TiO₂ NRs resulting from binding to plasmonic Au NSs.

conduction band of TiO₂-NRs through the Schottky barrier. It should also be noted that direct contact between the metal and semiconductor facilitates the rapid transfer of charge carriers [44], which explains the improvement in the heterostructure's performance after thermal annealing. Finally, the energetic holes left behind in the Au-NSs are suggested to promote water oxidation [44].

4. Conclusions

In summary, we fabricated heterostructured plasmonic metal/semiconductor photoanodes by *ex situ* deposition of Au-NSs onto TiO₂-NRs. The resulting Au-NSs/TiO₂-NRs exhibited improved PEC properties under both visible light illumination and simulated sunlight. Mild thermal treatment at 150 °C improved the Schottky contacts within the heterostructures; this improvement was verified by an OCVD analysis, which showed that the thermal annealing increased the system's electron lifetime, and EIS measurements showing that annealing reduced a resistance to the charge transfer. The IPCE values for the heterostructure in the UV region and across the visible and NIR regions were both higher than those for bare TiO₂. The improvement in the UV region was attributed to the photon scattering effects of the Au-NSs. The drastic enhancement in the visible and NIR regions was attributed to long wavelength plasmon resonances and promotion of SPR-mediated hot electron transfer upon visible light illumination, which is facilitated by the developed Schottky junction. Importantly, the overall IPCE efficiency of the Au-NSs/TiO₂ system in the Vis-NIR range is over ten times higher than that previously reported for a related system based on mixtures of gold nanoparticles and gold nanorods [30]. We believe that this work paves the way for new applications of plasmonic nanoparticles with unique nanostar morphologies as tools for enhancing the photoelectrochemical performance of photoanodes allowing to exploit the entire solar spectrum in the direct photochemical water splitting.

Acknowledgements

This work was supported by the projects Operational Programme Research, Development and Education - European Regional Development Fund, project no. CZ.02.1.01/0.0/0.0/15_003/0000416 and LO1305 of the Ministry of Education, Youth and Sports of the Czech Republic and by the project 15-19705S of the Grant Agency of the Czech Republic. The authors also acknowledge the assistance provided by the Research Infrastructure NanoEnvicZ,

supported by the Ministry of Education, Youth and Sports of the Czech Republic under Project No. LM2015073 and Project No. 8E15B009. We thank Jana Stráská, Ondřej Tomanec, and Claudia Aparicio (all from the Regional Centre of Advanced Technologies and Materials, Faculty of Science, Palacky University in Olomouc, Czech Republic) for TEM, SEM, and XRD measurements, respectively.

Appendix A. Supplementary data

Supplementary data related to this article can be found at <https://doi.org/10.1016/j.electacta.2017.11.106>.

References

- [1] A. Fujishima, K. Honda, Electrochemical photolysis of water at a semiconductor electrode, *Nature* 238 (1972) 37–38.
- [2] A. Wolcott, W.A. Smith, T.R. Kuykendall, Y. Zhao, J.Z. Zhang, Photoelectrochemical water splitting using dense and aligned TiO₂ nanorod arrays, *Small* 5 (2009) 104–111.
- [3] I.S. Cho, Z. Chen, A.J. Forman, D.R. Kim, P.M. Rao, T.F. Jaramillo, X. Zheng, Branched TiO₂ nanorods for photoelectrochemical hydrogen production, *Nano Lett.* 11 (2011) 4978–4984.
- [4] S. Srivastava, J.P. Thomas, M.A. Rahman, M. Abd-Ellah, M. Mohapatra, D. Pradhan, N.F. Heinig, K.T. Leung, Size-selected TiO₂ nanocluster catalysts for efficient photoelectrochemical water splitting, *ACS Nano* 8 (2014) 11891–11898.
- [5] L. Liu, X. Chen, Titanium dioxide nanomaterials: self-structural modifications, *Chem. Rev.* 114 (2014) 9890–9918.
- [6] L.D. Li, J.Q. Yan, T. Wang, Z.-J. Zhao, J. Zhang, J.L. Gong, N.J. Guan, Sub-10 nm rutile titanium dioxide nanoparticles for efficient visible-light-driven photocatalytic hydrogen production, *Nat. Commun.* 6 (2015) 5881.
- [7] M. Xu, P.M. Da, H.Y. Wu, D.Y. Zhao, G.F. Zheng, Controlled Sn-Doping in TiO₂ nanowire photoanodes with enhanced photoelectrochemical conversion, *Nano Lett.* 12 (2012) 1503–1508.
- [8] W.Q. Fang, Z.Y. Huo, P.R. Liu, X.L. Wang, M. Zhang, Y. Jia, H.M. Zhang, H.J. Zhao, H.G. Yang, X.D. Yao, Fluorine-doped porous single-crystal rutile TiO₂ nanorods for enhancing photoelectrochemical water splitting, *Chem. Eur. J.* 20 (2014) 11439–11444.
- [9] H. Zhu, J. Tao, X. Dong, Preparation and photoelectrochemical activity of Cr-Doped TiO₂ nanorods with nanocavities, *J. Phys. Chem. C* 114 (2010) 2873–2879.
- [10] C.Z. Wang, Z. Chen, H.B. Jin, C.B. Cao, J.B. Li, Z.T. Mi, Enhancing visible-light photoelectrochemical water splitting through transition-metal doped TiO₂ nanorod arrays, *J. Mater. Chem. A* 2 (2014) 17820–17827.
- [11] I.S. Cho, C.H. Lee, Y.Z. Feng, M. Logar, P.M. Rao, L.L. Cai, D.R. Kim, R. Sinclair, X.L. Zheng, Co-doping titanium dioxide nanowires with tungsten and carbon for enhanced photoelectrochemical performance, *Nat. Commun.* 4 (2013) 1723.
- [12] W.T. Sun, Y. Yu, H.Y. Pan, X.F. Gao, Q. Chen, L.M. Peng, CdS quantum dots sensitized TiO₂ nanotube-array photoelectrodes, *J. Am. Chem. Soc.* 130 (2008) 1124–1125.
- [13] J.C. Bian, C. Huang, L.Y. Wang, T.F. Hung, W.A. Daoud, R.Q. Zhang, Carbon dot loading and TiO₂ nanorod length dependence of photoelectrochemical

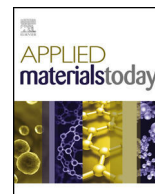
- properties in carbon dot/TiO₂ nanorod array nanocomposites, *ASC Appl. Mater. Interfaces* 6 (2014) 4883–4890.
- [14] H.B. Yang, J.W. Miao, S.F. Hung, F.W. Huo, H.M. Chen, B. Liu, Stable quantum dot photoelectrolysis cell for unassisted visible light solar water splitting, *ACS Nano* 8 (2014) 10403–10413.
- [15] F.S. Li, K. Fan, B. Xu, E. Gabrielsson, Q. Daniel, L. Li, L.C. Sun, Organic dye-sensitized tandem photoelectrochemical cell for light driven total water splitting, *J. Am. Chem. Soc.* 137 (2015) 9153–9159.
- [16] J. Luo, Y. Ma, H.Y. Wang, J.Y. Chen, Preparation of polypyrrole sensitized TiO₂ nanotube arrays hybrids for efficient photoelectrochemical water splitting, *Electrochim. Acta* 167 (2015) 119–125.
- [17] L.Y. Wang, W.A. Daoud, BiOI/TiO₂-nanorod array heterojunction solar cell: growth, charge transport kinetics and photoelectrochemical properties, *Appl. Surf. Sci.* 324 (2015) 532–537.
- [18] Q. Liu, H. Lu, Z.W. Shi, F.L. Wu, J. Guo, K.M. Deng, L. Li, 2D ZnIn₂S₄ Nanosheet/1D TiO₂ nanorod heterostructure arrays for improved photoelectrochemical water splitting, *ACS Appl. Mater. Interfaces* 6 (2014) 17200–17207.
- [19] I. Thomann, B.A. Pinaud, Z.B. Chen, B.M. Clemens, T.F. Jaramillo, M.L. Brongersma, Plasmon enhanced solar-to-fuel energy conversion, *Nano Lett.* 11 (2011) 3440–3446.
- [20] P.A. DeSario, J.J. Pietron, D.E. DeVantier, T.H. Brintlinger, R.M. Stroud, D.R. Rolison, Plasmonic enhancement of visible-light water splitting with Au–TiO₂ composite aerogels, *Nanoscale* 5 (2013) 8073–8083.
- [21] X. Zhang, Y. Liu, S.T. Lee, S.H. Yang, Z.H. Kang, Coupling surface plasmon resonance of gold nanoparticles with slow-photon-effect of TiO₂ photonic crystals for synergistically enhanced photoelectrochemical water splitting, *Energy Environ. Sci.* 7 (2014) 1409–1419.
- [22] J. Zhang, X. Jin, P.I. Morales-Guzman, X. Yu, H. Liu, H. Zhang, L. Razzari, J.P. Claverie, Engineering the absorption and field enhancement properties of Au–TiO₂ nanohybrids via whispering gallery mode resonances for photocatalytic water splitting, *ACS Nano* 10 (2016) 4496–4503.
- [23] S.C. Warren, E. Thimsen, Plasmonic solar water splitting, *Energy Environ. Sci.* 5 (2012) 5133–5146.
- [24] S.K. Cushing, J.T. Li, F.K. Meng, T.R. Senty, S. Suri, M.J. Zhi, M. Li, A.D. Bristow, N.Q. Wu, Photocatalytic activity enhanced by plasmonic resonant energy transfer from metal to semiconductor, *J. Am. Chem. Soc.* 134 (2012) 15033–15041.
- [25] X. Liang, T.T. You, D.P. Liu, X.F. Lang, E.Z. Tan, J.H. Shi, P.G. Yin, L. Guo, Direct observation of enhanced plasmon-driven catalytic reaction activity of Au nanoparticles supported on reduced graphene oxides by SERS, *Phys. Chem. Chem. Phys.* 17 (2015) 10176–10181.
- [26] K. Qian, B.C. Sweeny, A.C. Johnston-Peck, W.X. Niu, J.O. Graham, J.S. DuChene, J.J. Qiu, Y.C. Wang, M.H. Engelhard, D. Su, E.A. Stach, W.D. Wei, Surface plasmon-driven water reduction: gold nanoparticle size matters, *J. Am. Chem. Soc.* 136 (2014) 9842–9845.
- [27] L.Q. Liu, S.X. Ouyang, J.H. Ye, Gold-nanorod-photosensitized titanium dioxide with wide-range visible-light harvesting based on localized surface plasmon resonance, *Angew. Chem. Int. Ed.* 52 (2013) 6689–6693.
- [28] E. Wientjes, J. Renger, A.G. Curto, R. Cogdell, N.F. van Hulst, Strong antenna-enhanced Fluorescence of A Single light-harvesting complex shows photon antibunching, *Nat. Commun.* 5 (2014) 4236.
- [29] Z.W. Liu, W.B. Hou, P. Pavaskar, M. Aykol, S.B. Cronin, Plasmon resonant enhancement of photocatalytic water splitting under visible illumination, *Nano Lett.* 11 (2011) 1111–1116.
- [30] Y.C. Pu, G.M. Wang, K.D. Chang, Y.C. Ling, Y.K. Lin, B.C. Fitzmorris, C.M. Liu, X.H. Lu, Y.X. Tong, J.Z. Zhang, Y.J. Hsu, Y. Li, Au nanostructure-decorated TiO₂ nanowires exhibiting photoactivity across entire UV-visible region for photoelectrochemical water splitting, *Nano Lett.* 13 (2013) 3817–3823.
- [31] M. Wu, W.J. Chen, Y.H. Shen, F.Z. Huang, C.H. Li, S.K. Li, Situ growth of matchlike ZnO/Au plasmonic heterostructure for enhanced photoelectrochemical water splitting, *ACS Appl. Mater. Interfaces* 6 (2014) 15052–15060.
- [32] S. Naya, T. Niwa, T. Kume, H. Tada, Visible-light-induced electron transport from small to large nanoparticles in bimodal gold nanoparticle-loaded titanium(IV) oxide, *Angew. Chem. Int. Ed.* 53 (2014) 7305–7309.
- [33] J. Wang, S.L. Pan, M.Y. Chen, D.A. Dixon, Gold nanorod-enhanced light absorption and photoelectrochemical performance of α -Fe₂O₃ thin-film electrode for solar water splitting, *J. Phys. Chem. C* 117 (2013) 22060–22068.
- [34] B. Liu, E.S. Aydil, Growth of oriented single-crystalline rutile TiO₂ nanorods on transparent conducting substrates for dye-sensitized solar cells, *J. Am. Chem. Soc.* 131 (2009) 3985–3990.
- [35] H.K. Yuan, C.G. Khoury, H. Hwang, C.M. Wilson, G.A. Grant, T. Vo-Dinh, Gold nanostars: surfactant-free synthesis, 3D modelling, and two-photon photoluminescence imaging, *Nanotechnology* 23 (2012) 075102.
- [36] J.T. Li, S.K. Cushing, P. Zheng, T. Senty, F.K. Meng, A.D. Bristow, A. Manivannan, N.Q. Wu, Solar hydrogen generation by a CdS-Au-TiO₂ sandwich nanorod array enhanced with Au nanoparticle as electron relay and plasmonic photosensitizer, *J. Am. Chem. Soc.* 136 (2014) 8438–8449.
- [37] J.S. DuChene, B.C. Sweeny, A.C. Johnston-Peck, D. Su, E.A. Stach, W.D. Wei, Prolonged hot electron dynamics in plasmonic-metal/semiconductor heterostructures with implications for solar photocatalysis, *Angew. Chem. Int. Ed.* 53 (2014) 7887–7891.
- [38] F. Hao, C.L. Nehl, J.H. Hafner, P. Nordlander, Plasmon resonances of a gold nanostar, *Nano Lett.* 7 (2007) 729–732.
- [39] J. Bisquert, A. Zaban, M. Greenshtein, I. Mora-Sero, Determination of rate constants for charge transfer and the distribution of semiconductor and electrolyte electronic energy levels in dye-sensitized solar cells by open-circuit photovoltage decay method, *J. Am. Chem. Soc.* 126 (2004) 13550–13559.
- [40] A. Zaban, M. Greenshtein, J. Bisquert, Determination of the electron lifetime in nanocrystalline dye solar cells by open-circuit voltage decay measurements, *ChemPhysChem* 4 (2003) 859–864.
- [41] V. Subramanian, E.E. Wolf, P.V. Kamat, Catalysis with TiO₂/gold nanocomposites. Effect of metal particle size on the Fermi level equilibration, *J. Am. Chem. Soc.* 126 (2004) 4943–4950.
- [42] T. Lopes, L. Andrade, F. Le Formal, M. Gratzel, K. Sivula, A. Mendes, Hematite photoelectrodes for water splitting: evaluation of the role of film thickness by impedance spectroscopy, *Phys. Chem. Chem. Phys.* 16 (2014) 16515–16523.
- [43] T. Lopes, L. Andrade, H.A. Ribeiro, A. Mendes, Characterization of photoelectrochemical cells for water splitting by electrochemical impedance spectroscopy, *Int. J. Hydrog. Energy* 35 (2010) 11601–11608.
- [44] S. Linic, P. Christopher, D.B. Ingram, Plasmonic-metal nanostructures for efficient conversion of solar to chemical energy, *Nat. Mater.* 10 (2011) 911–921.
- [45] D. Melnikau, D. Savateeva, A. Susha, A. Rogach, Y. Rakovich, Strong plasmon-exciton Coupling in A Hybrid system of gold nanostars and J-aggregates, *Nanoscale Res. Lett.* 8 (2013) 134.

Appendix [A8]

Very thin thermally stable TiO₂ blocking layers with enhanced electron transfer for solar cells

S. Kment*, H. Krysova, Z. Hubicka, H. Kmentova, L. Kavan*,
R. Zboril*

Applied Materials Today 9, 122-129, 2017



Very thin thermally stable TiO₂ blocking layers with enhanced electron transfer for solar cells

Stepan Kment^{a,*}, Hana Krysova^b, Zdenek Hubicka^c, Hana Kmentova^a, Ladislav Kavan^{b,*}, Radek Zboril^{a,*}

^a Regional Centre of Advanced Technologies and Materials, Faculty of Science, Palacky University, Slechtitelu 27, 783 71 Olomouc, Czech Republic

^b J. Heyrovsky Institute of Physical Chemistry ASCR, v.v.i., Dolejskova 2155/3, 182 23 Prague 8, Czech Republic

^c Institute of Physics ASCR, v.v.i., Na Slovance 2, 182 21 Prague 8, Czech Republic

ARTICLE INFO

Article history:

Received 9 April 2017

Received in revised form 29 May 2017

Accepted 29 May 2017

Keywords:

TiO₂ blocking layer

Solar cell

Cyclic voltammetry

Impedance spectroscopy

Photochemistry

ABSTRACT

Very thin TiO₂ blocking layers (BLs) are important components for achieving high solar power conversion efficiencies (PCEs) in the dye-sensitized solar cells, and particularly perovskite solar cells (PSCs). When reasonably thin, TiO₂ BLs prevent recombination of photogenerated charges at the conductive fluorine-doped tin oxide (FTO) glass substrate used in these devices. However, all previous attempts to generate efficient TiO₂ BLs have been hampered by an insufficient charge transfer rate at quasi-amorphous TiO₂ and very low thermal stability, leading to the loss of blocking properties after thermal calcination. In this work, we report the deposition of homogenous very thin (~30 nm) TiO₂ BLs by combining advanced high impulse power magnetron sputtering (HiPIMS) and additional bipolar medium-frequency (MF) magnetron co-sputtering. The as-deposited TiO₂ films were shown to provide excellent blocking properties which were preserved even after thermal treatment at 450 °C. Moreover, TiO₂ BLs thermally treated at 450 °C show a well-developed rutile structure and 70 times higher photocurrents compared to the as-deposited layers. This work opens possibilities for the utilization of very thin TiO₂ layers in solar cell technologies providing a double mode of action: blocking functionality and efficient electron transport.

© 2017 Elsevier Ltd. All rights reserved.

1. Introduction

Since dye-sensitized solar cells (DSCs) based on the photo-sensitization of TiO₂ nanoparticles were first designed by Grätzel and O'Regan in 1991 [1], the concept has become one of the most promising alternatives to silicon-based photovoltaic cells. The simplest type of DSCs are constructed from a TiO₂ photoanode, adsorbed dye molecules and a redox mediator in an electrolyte. In contrast, in solid-state dye-sensitized solar cells (SSDSCs), which represent the next generation of DSCs, charge transport is realized by a solid hole-conductive material [2]. This concept has been further modified by using an organo-lead halide perovskite as the light absorber in so-called perovskite solar cells (PSCs) representing a “younger sister” of DSCs [3]. PSC-based devices have yielded breakthrough results, with solar power conversion efficiencies (PCEs) of 15.7% [4], 16.2% [5], and 21.1% [6] achieved only within the last three years. It is expected that the efficiency will be further

improved by e.g. applying various interlayers based on graphene and/or other 2D materials [7,8].

One of the key limitations of DSCs, SSDSCs and PSCs is back recombination of the photogenerated charges owing to the different types of materials (e.g., perovskite layer, nanoparticulate photoanode, hole transport layer, etc.) and interfaces that the charges have to pass through before their extraction to the electrodes. The recombination of photoinjected electrons with oxidized mediator (e.g., triiodide in the electrolyte) or the hole-transporter is one of most detrimental processes that occurs at both the TiO₂ surface and uncovered surface of the conductive charge collector layer (typically a transparent film of fluorine-doped tin oxide, FTO) [2,9]. The extent of recombination over the FTO substrate is relatively low in liquid-type DSCs but leads to serious PCE losses in SSDSCs and PSCs [10]. To prevent the photogenerated charge carriers from contacting the conductive FTO substrate directly, and thereby shunting the device, an individual compact (nonporous) blocking layer (BL) can be deposited between the FTO substrate and the light-absorbing layer [11].

Ideally, the BL should be pinhole-free whilst completely covering the relatively rough FTO surface. Furthermore, it should be thick enough to prevent charge tunneling from the FTO into the

* Corresponding authors.

E-mail addresses: stepan.kment@upol.cz (S. Kment), kavan@jh-inst.cas.cz (L. Kavan), radek.zboril@upol.cz (R. Zboril).

electrolyte but, at the same time, reasonably thin to maintain a sufficient charge transfer rate from the mesoporous TiO₂ into the FTO [12]. However, synthesis of perfectly compact films of very low thickness (below 50 nm) to preserve their blocking functionality even after thermal treatment at elevated temperature (~500 °C) remains an unsolved and highly challenging task [13,14].

Very thin coatings of TiO₂ are the most frequently used blocking layers (BLs) [9,14–16], although other oxides, including zinc oxide [4], aluminum oxide [17], cesium carbonate [18], and very recently also tin oxide [19], have also been studied as viable options and other materials based on TiO₂-based BLs have been fabricated using a broad range of methods. The approach based on a spray pyrolysis described by Kavan and Grätzel [20] in 1995 has been routinely applied in most of the reported SSDSCs and PSCs. Spray pyrolysis and the sol-gel method [15] represent top-down strategies that are usually hampered by difficulties in controlling homogeneous formation of the blocking film. In these approaches, a sufficient and homogeneous coverage of the FTO substrate is usually accomplished by increasing the film thickness, which simultaneously increases the undesired internal resistance of the device. In contrast, bottom-up approaches, involving atomic layer deposition (ALD) [21], DC magnetron sputtering [22,23] or electrochemical deposition [11], have been shown to improve the homogeneity of very thin BL coverage of the FTO support. Kavan, Grätzel et al. comprehensively tested all the abovementioned techniques and concluded that, independently of the method used, all the TiO₂ films lost their blocking ability when thermally treated at a temperature of 500 °C owing to the formation of cracks and/or pinholes [9]. This is a significant limitation because SSDSC and PSC photoanodes often consist of a mesoporous TiO₂ layer whose preparation commonly requires a thermal sintering step.

In this work, we successfully addressed the thermal instability issue of TiO₂ BLs by applying a very high-energy plasma-assisted deposition method based on a combination of reactive high impulse power magnetron sputtering (HiPIMS) and reactive medium frequency (MF) pulsed magnetron sputtering techniques. HiPIMS is a novel state-of-the-art technique that utilizes working conditions capable of producing crystalline films during the deposition cycle while keeping the temperature of the substrate very low (~150 °C) [24]. Further, it has been shown that the properties of the films, e.g., crystallinity, texture, grain size, density, porosity, etc., can be readily controlled by adjusting the energy of ions from the HiPIMS discharge [25]. It is also known that HiPIMS can ionize a high fraction of sputtered particles and a high magnitude of ion flux toward the substrate is generated during the “on” time of the HiPIMS pulse [26–29]. By combination of HiPIMS and MF sputtering discharges, very thin, dense rutile TiO₂ buffer layers were grown on a FTO surface at a low temperature (below 150 °C). Most importantly, both the as-deposited films and those thermally treated at 450 °C exhibited excellent blocking properties toward the FTO surface. Moreover, the annealed films substantially outperformed the function of all BLs developed to date. Further, electrochemical data showed that these films provide a highly rectifying interface for charge-transfer reactions of model redox probes and contribute to a high performance of developed photoanodes.

2. Material and methods

2.1. Preparation of the TiO₂ very thin blocking layers

The experimental apparatus for the TiO₂ reactive high impulse power magnetron sputtering (HiPIMS) combined with mid-frequency (MF) magnetron sputtering deposition can be seen in Fig. S1. A circular unbalanced magnetron system with Ti target with diameter 50 mm was placed in the continuously pumped vacuum

reactor. The floating unheated substrate was placed 70 mm from the target surface. A working gas mixture of Ar + O₂ was used for the reactive sputtering process. The mass flow of Ar was Q_{Ar} = 20 sccm and the mass flow of oxygen was Q_{O₂} = 10 sccm. The total gas pressure was held on the value 0.8 Pa during the deposition process. The HiPIMS power supply together with MF bipolar source were connected to the magnetron cathode. The frequency of MF source was 300 kHz. The “ON” time of HiPIMS pulse was T_{ON} = 100 μs and the pulsing period was T_{per} = 10 ms. The average discharge current was held on the constant value of I_{AV} = 800 mA. The TiO₂ films were deposited on fluorine doped tin oxide (FTO) coated glass (TCO22-7, Solaronix, Switzerland) with the constant thickness around 30 nm. Two specific cases of TiO₂ deposition conditions are presented in this paper. These are the bare HiPIMS deposition without additional MF plasma excitation (T_{HiPIMS}) and the HiPIMS deposition with bipolar additional MF plasma excitation (T_{MF}). The films were investigated in the form of as-deposited samples and also after their annealing at 450 °C for 1 h. These films were labeled in the text in accordance to the as-deposited samples as T_{HiPIMS(c)} and T_{MF(c)}, respectively.

Fig. S2 shows typical current and voltage waveforms in HiPIMS as well as HiPIMS + medium frequency (MF) reactive sputtering of TiO₂ thin films. Fig. S2a shows bare HiPIMS waveforms without an additional MF discharge between HiPIMS pulses. The pulse discharge current is in this case I_p = 80 A and it corresponds for our titanium target with diameter 50 mm to the pulse discharge current density of j_p = 4.2 A cm⁻². In Fig. S2a, the short delay between the onset of voltage pulse and the onset of the discharge current can be seen. It is a typical phenomenon for molecular gasses where it is more complicated to start the discharge without any preionization. This delay is not observed in Fig. S2b denoting the MF plasma excitation between HiPIMS pulses. This feature results from the MF plasma excitation causing the preionization before the start of high power pulse. The magnitude of positive voltage maximum is U_{pos} = 400 V in case of the bipolar MF plasma excitation (Fig. S2b). Generally, it can be stated that the average heating flux to the substrate in the bare HiPIMS is quite low but the flux of ionized sputtered particles during the HiPIMS pulse when the films grows is high [30]. When the bipolar MF plasma during the “OFF” time of HiPIMS pulses is added the substrate will be bombarded by argon ions during this “OFF” time and this bombardment will increase average heating flux to the substrate but the flux of ionized sputtered particles during the “ON” time of HiPIMS pulse will be similar like in the case of bare HiPIMS [31–33].

2.2. Characterization of the films

Crystalline structure of the films was analyzed by Raman spectroscopy. The spectra were measured at room temperature with an unpolarized beam in back-scattering mode using an RM 1000 Renishaw Raman microscope. The spectra were excited with the 514.5 nm line of an Ar⁺ laser, and the Raman response was recorded in the spectral range of 100–1000 cm⁻¹ with a resolution of ~1 cm⁻¹. The area of the focused laser on the sample was ~4 μm². Surface images were captured by scanning electron microscope (SEM) Hitachi SU6600 with accelerating voltage 10 kV. The elemental analysis was performed using energy dispersive spectrometry (EDS) that was acquired in SEM by Thermo Noran System 7 with Si(Li) Detector. Surface topography images were also captured by atomic force microscope (AFM) INTEGRA Aura.

2.3. Electrochemical and photoelectrochemical properties of the films

Photoelectrochemical and electrochemical experiments were carried out in a one-compartment cell using Autolab Pgstat 101

controlled by the NOVA software with three electrodes in the system. The TiO₂ thin film on FTO was the working electrode, the reference electrode was Ag/AgCl (sat. KCl) and a platinum rod was the counter electrode. 0.1 M solution of Na₂SO₄ (pH 10) was used as the electrolyte for photoelectrochemical experiments. The electrolyte pH was carefully controlled and adjusted by adding H₂SO₄ or NaOH. The TiO₂ films were illuminated from the front side (from film/electrolyte interface) and the TiO₂ film area (1 cm²) was defined by a teflon tape. As the source of radiation the Hg lamp (Oriel) was used. Optical filter ensured range of wavelength 320–380 nm. The light intensity was 6.5 mW cm⁻². Furthermore, the films were tested under the illumination of solar light simulator AM 1.5 G with the intensity of 100 mW cm⁻². Chopped-light polarization curves were measured with 10 s dark/light interval and scan rate 5 mV s⁻¹.

Cyclic voltammetry (CV) measurements in aqueous electrolyte containing [Fe(CN)₆]³⁻/[Fe(CN)₆]⁴⁻ redox probe were performed for evaluation of blocking effect of the deposited layers. The scan rate was 100 mV s⁻¹ and the electrolyte solution was 0.5 mM K₄[Fe(CN)₆] + 0.5 mM K₃[Fe(CN)₆] in aqueous 0.5 M KCl, pH 2.5.

Impedance spectra were measured at potentials from 1.3 V to -0.3 V vs Ag/AgCl in acidic medium (pH 2.5). The electrolyte pH was carefully controlled and adjusted by adding HCl. The electrolyte solution was purged with Ar and the measurements were carried out under argon atmosphere in the hermetically closed electrochemical cell. Impedance spectra were evaluated using Zview (Scribner) software.

The measured potentials vs. Ag/AgCl were converted to the reversible hydrogen electrode (RHE) scale following the Nernst equation:

$$E_{\text{RHE}} = E_{\text{Ag/AgCl}} + 0.059 \text{ pH} + E_{\text{Ag/AgCl}}^{\circ} \quad (1)$$

where E_{RHE} is the converted potential vs. RHE, $E_{\text{Ag/AgCl}}^{\circ} = 0.207 \text{ V}$ at 25 °C, and $E_{\text{Ag/AgCl}}$ is the experimentally measured potential against the Ag/AgCl (sat KCl) reference.

3. Results and discussion

In this work, we firstly combined the HiPIMS mode with medium frequency (MF) pulsed magnetron sputtering. Coupling of HiPIMS magnetron sputtering with MF pulsed excitation can increase the heating flux toward the substrate whilst simultaneously maintaining a high ion flux on the substrate. This substrate treatment reduces the internal stress of the deposited films, which is an essential property governing the compactness after thermal annealing.

All described films had a comparable thickness of around 30 nm (see below) and were strongly adherent to the FTO substrate and highly transparent. Raman spectra of the as-deposited films and films after annealing at 450 °C in air for 1 h are presented in Fig. 1. The as-deposited layers (T_{HiPIMS} and T_{MF}) exhibited polycrystalline structures with varying content of anatase and rutile phases. The T_{MF} sample showed a much higher crystallinity (mixture of anatase and rutile phases) compared to the T_{HiPIMS} sample, which was almost amorphous with only traces of rutile structure. The crystalline structure achieved in the T_{MF} sample was attributed to the high ion flux (energetic bombardment) and increased heating flux toward the substrate surface. To examine the structural changes upon thermal treatment, the films were annealed at 450 °C in air for 1 h. It is widely reported in the literature that recrystallization due to post deposition thermal sintering strongly depends on the microstructure and crystallinity of the as-deposited sample [34,35]. As expected, the thermodynamically more stable rutile structure was identified as the single phase in the $T_{\text{MF(c)}}$ sample due to the polymorphous transformation of anatase. The sample $T_{\text{HiPIMS(c)}}$ did not undergo any structural changes due to the thermal annealing, as

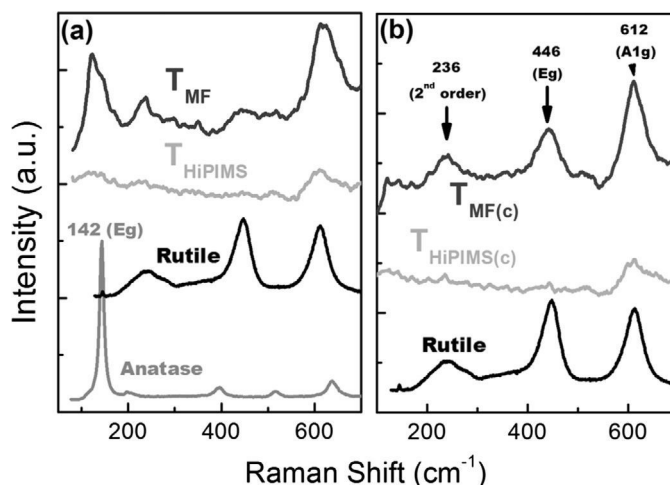


Fig. 1. Raman spectroscopy results. Raman spectra of very thin TiO₂ blocking films: (a) as-deposited TiO₂ films; (b) TiO₂ films annealed at 450 °C in air for 1 h. Reference spectra of anatase and rutile crystalline phases are also shown. The contributions of Raman peaks originating from the FTO substrate have been extracted for better clarity. Spectra are offset for clarity in the intensity scale.

reflected by almost identical Raman spectra (compare T_{HiPIMS} and $T_{\text{HiPIMS(c)}}$ in Fig. 1a and b) of the as-deposited and annealed samples. This was likely because the still low temperature (450 °C) prevented any significant crystallization and there was a limited amount of rutile nuclei in the as-deposited amorphous layer. The strong variation in the Raman band intensities between the thermally treated and as-deposited layers can be attributed to the different texture of the films induced by calcination, as discussed in our previous work [25].

The AFM profile scan in Fig. 2a indicates that the thickness of the TiO₂ BL was 30 nm. For this measurement, the TiO₂ film was deposited under identical plasma conditions as the other samples but on a highly flat fused silica substrate to avoid experimental error due to the very rough FTO surface. Fig. 2b–d presents surface SEM images of a blank FTO substrate and FTO covered by TiO₂ blocking overlayers after thermal annealing. A rough surface due to the FTO grains containing highly asymmetrical shapes with diameters in the range of several tens of nanometers was a common feature of this type of substrate (Fig. 2b). After coating of the TiO₂ blocking films, the FTO pattern remained unchanged with clearly recognizable FTO grains. These images also verified the extremely low thickness (~30 nm) of the films and their compactness over the support. Importantly, the films prepared without MF discharge ($T_{\text{HiPIMS(c)}}$) suffered from cracks and pinholes after the thermal annealing, as shown by the insets in Fig. 2c and Fig. S3, which was presumably caused by high internal stress. No observable defects were identified for the HiPIMS + MF deposited films (T_{MF}), indicating homogeneous coverage of the FTO support. With regard to the elemental composition, no differences were observed among the films. Besides the main elements, including titanium, oxygen and tin (originating from the FTO substrate), residual nitrogen due to plasma substrate treatment/activation was detected in the energy dispersive X-ray spectroscopy (EDS) spectra, as shown in Fig. S4.

The surface topography was also monitored by AFM. Corresponding 2D and 3D surface topography images are shown in Figs. S5 and S6. The images were analyzed to assess surface roughness (RMS). Owing to the very low thickness of the TiO₂ films homogeneously covering the relatively rough surface of FTO (RMS = 150 nm), only a slight decrease in the RMS values (50–100 nm) was identified upon thermal annealing (see description in Fig. S6), in good agreement with the SEM results.

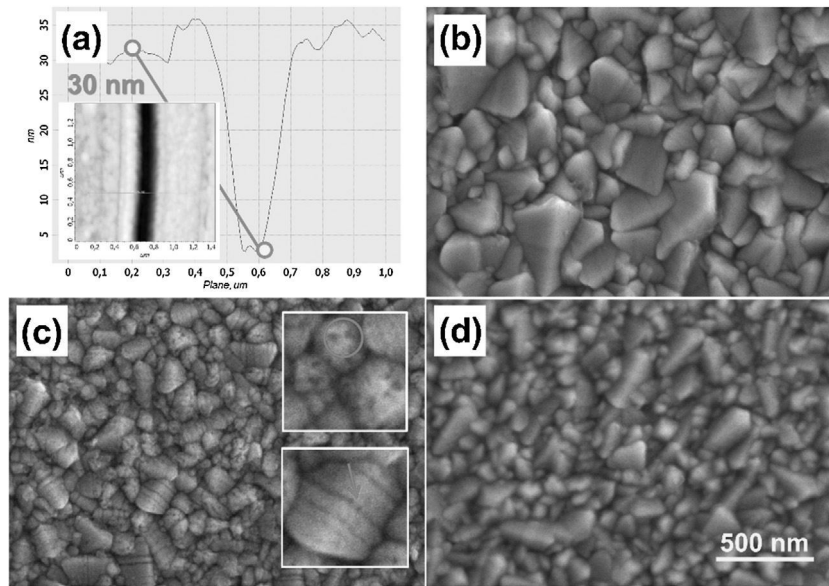


Fig. 2. AFM and SEM observations. (a) Thickness of TiO₂ BL measured from AFM cross-section depth profile scan. Top-view SEM images of calcinated TiO₂ blocking layers: (b) blank FTO, (c) $T_{\text{HiPIMS(c)}}$ layer, and (d) $T_{\text{MF(c)}}$. The insets in (c) show magnified regions containing homogeneity defects, such as pinholes (upper image) and cracks (lower image), of the $T_{\text{HiPIMS(c)}}$ BL. The scale bar of 500 nm applies to all the SEM images.

Electrochemical and photoelectrochemical experiments were carried out to test the functional properties of the TiO₂ BLs. Cyclic voltammetry (CV) was considered a suitable method for evaluating the blocking effect of the studied TiO₂ films. CV measurements were carried out in aqueous electrolyte solution containing [Fe(CN)₆]³⁻/[Fe(CN)₆]⁴⁻ redox couple as a model pH independent redox probe with a simple one-electron transfer reaction [9,15]. The redox potential of [Fe(CN)₆]^{3-/4-} (0.595 V vs. RHE) is sufficiently positive of the flatband potential of TiO₂ (both anatase and rutile) at all pH values in aqueous electrolyte solutions [36]. The flatband potential, φ_{FB} , of a rutile single-crystal electrode can be calculated from the Nernstian pH-dependence (Eq. (1)):

$$\begin{aligned} \varphi_{\text{FB}} &= -0.16 - 0.059 \text{ pH (rutile, V vs. Ag/AgCl)} \\ &= -0.047 - 0.059 \text{ pH V vs. RHE} \end{aligned} \quad (2)$$

Thus, TiO₂ behaves as an electrochemically rectifying material against the [Fe(CN)₆]³⁻/[Fe(CN)₆]⁴⁻ redox couple. In other words, a good quality TiO₂ BL fully covering the FTO substrate will prevent the flow of any anodic currents corresponding to the oxidation of ferrocyanide. The onset of cathodic current due to ferricyanide reduction occurs at more negative potentials than the TiO₂ flatband potential. Under such conditions, the TiO₂ electrode is in the accumulation regime and shows metallic-like behavior. Therefore, defects in the BL, such as cracks and/or pinholes, can be directly and sensitively identified by monitoring the anodic current, which is related to ferrocyanide oxidation taking place solely at the uncovered (naked) parts of the FTO layer. Fig. 3 compares cyclic voltammograms of the reference blank FTO substrate and TiO₂ BLs fabricated by the HiPIMS method (T_{HiPIMS}) and HiPIMS with additional MF sputtering discharges (T_{MF}). Fig. 3a shows the blocking ability of the as-deposited TiO₂ layers. The films fabricated by the HiPIMS method (T_{HiPIMS}) and with additional bipolar MF signal (T_{MF}) both showed excellent blocking properties, i.e. there were no indications of anodic currents in the voltammograms. It should be mentioned that high quality BLs at low temperatures have been reported by other authors. However, preserving the blocking properties after thermal treatment still remains the key challenge.

To evaluate the thermal stability with respect to blocking performance, the FTO/TiO₂ electrodes were thermally treated at 450 °C in air for 1 h. These tests were conducted because fabrication of typical photoanodes for DSCs or electron collecting layers in PSCs usually requires thermal sintering of a mesoporous TiO₂ layer as one of the constituents forming the electrodes. The $T_{\text{MF(c)}}$ sample maintained its properties after the thermal procedure, i.e., the blocking capability was fully preserved (Fig. 3b). In contrast, the as-deposited TiO₂ layer prepared by HiPIMS (T_{HiPIMS}) completely lost its blocking function after thermal annealing ($T_{\text{HiPIMS(c)}}$). The peak current densities of the $T_{\text{HiPIMS(c)}}$ sample were lower than those of bare FTO and showed considerably larger peak-to-peak separation, indicating larger charge transfer resistance due to the surface covering [9,37]. This can be explained by the different structure of the two types of films tested. The microstructure of HiPIMS films produced under a high energy flux toward the substrate have been shown to feature a high density of nanoscale grains, which are associated with a relatively high internal stress generated due to densification of the grain boundaries of the film [38,39]. The as-deposited HiPIMS films (T_{HiPIMS}) exhibited considerably lower crystallinity than the T_{MF} films. Thus, rather than improving the crystallization (see Raman spectra in Fig. 1), thermal annealing, of the T_{HiPIMS} sample caused relaxation of the interstitial stress, most likely accompanied by the creation of defects in the form of pinholes and cracks over the film, thereby disrupting its blocking properties (Fig. 2c). From our tests (not shown here) the blocking ability started to decrease at the temperature of annealing of ~250 °C. In contrast, the T_{MF} films were prepared by using a very high energy ion flux (HiPIMS) in combination with considerably higher heating flux (MF) on the substrate, minimizing the internal stress in the film and increasing the overall extent of crystallization. Therefore, the HiPIMS mode coupled with the bipolar MF sputtering signal was identified as the optimal plasma deposition conditions for preserving the blocking functionality of the TiO₂ layer after thermal treatment. The efficiently balanced energetic ion and heating fluxes yielded high quality crystalline films with sufficient density to provide excellent blocking properties in both the as-deposited (T_{MF}) and thermally annealed ($T_{\text{MF(c)}}$) films.

To probe the ability of the films to withdraw photogenerated electrons toward the FTO substrate, and thus to work as

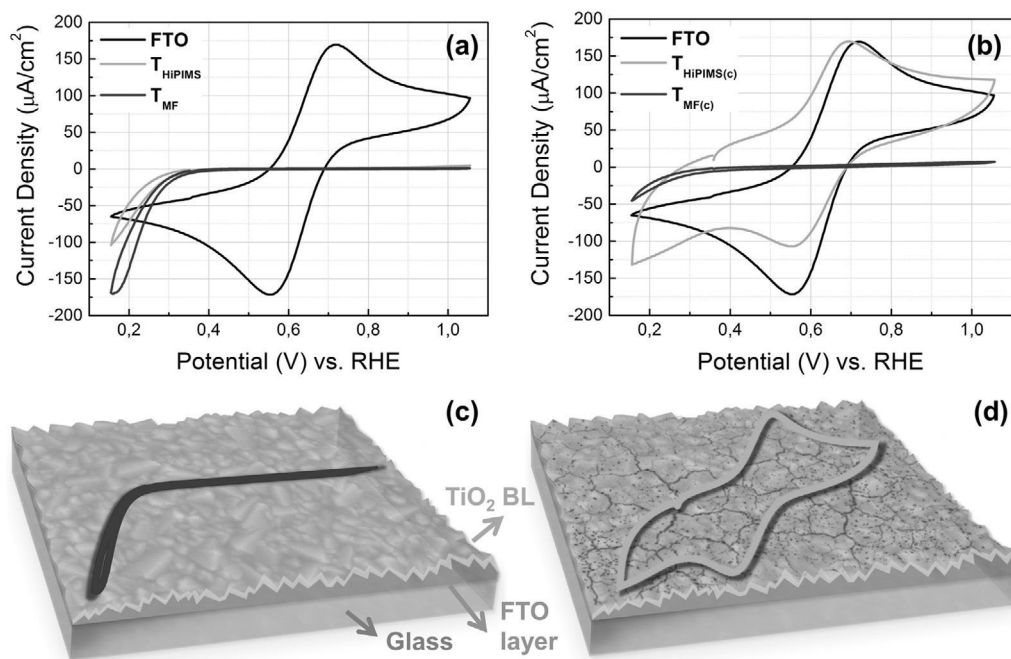


Fig. 3. Cyclic voltammograms analyses. Cyclic voltammograms of bare FTO and TiO₂ electrodes prepared by HiPIMS and HiPIMS with additional MF signal on FTO. (a) As-deposited films without heat treatment and (b) films calcined at 450 °C for 1 h in air. Schematic of a high-quality fully blocking film (c) and a damaged counterpart lacking blocking ability (d).

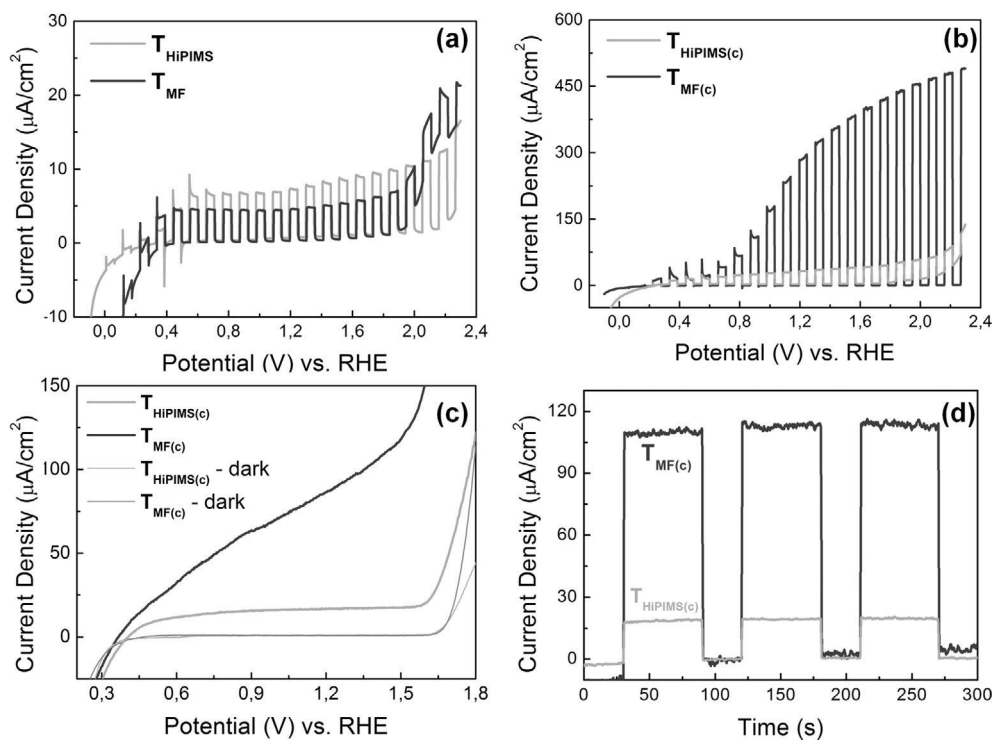


Fig. 4. Linear sweep voltammograms and chopped light chronoamperometry measurements. Linear sweep voltammograms of (a) as-deposited films and (b) films after thermal annealing at 450 °C for 1 h. The experiments were carried out under chopped light UV light irradiation (c) linear sweep voltammograms and (d) chopped light chronoamperometry scans recorded at 1.3 V vs. RHE. The experiments were carried out with annealed TiO₂ BLs under solar simulator AM 1.5 light illumination.

an electron transport layer (ETL), measurements of current density versus applied potential were performed. Fig. 4 displays J - V polarization curves under chopped light conditions. The as-deposited TiO₂ films (Fig. 4a) showed comparable photoactivity with plateau-like dependency of the J - V curves. The maximum current density reached for HiPIMS deposition alone (T_{HiPIMS}) was

very low ($8.5 \mu\text{A cm}^{-2}$) but even lower for the HiPIMS mode with additional MF applied voltage (T_{MF} , $5.5 \mu\text{A cm}^{-2}$). Both these values were recorded at 1.55 vs. RHE reference electrode. One reason for such low photocurrents might be that the interface required for efficient charge transfer between the TiO₂ layers and the FTO charge collector was not properly developed. This would be espe-

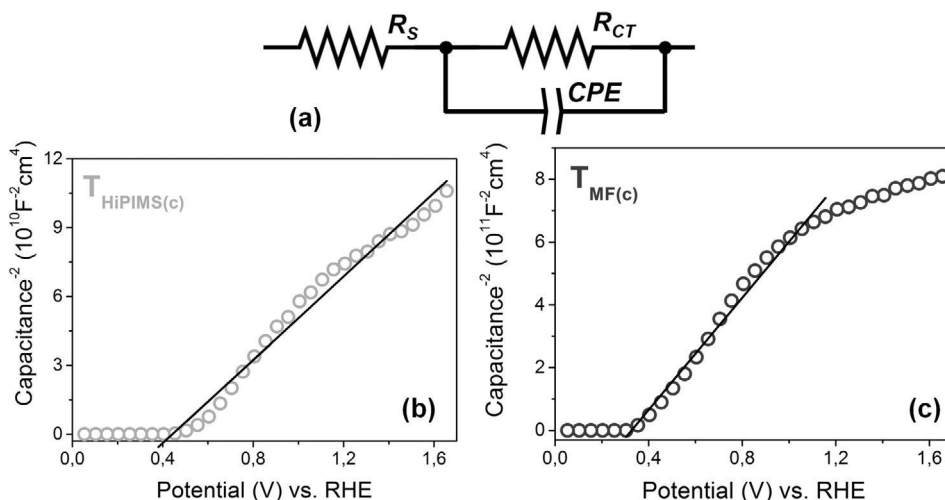


Fig. 5. Circuit representation and Mott-Schottky plots. (a) Equivalent circuit used for fitting the electrochemical impedance spectra. Mott-Schottky plots of FTO electrode covered with TiO_2 film fabricated under (b) HIPIMS alone ($T_{\text{HIPIMS}(c)}$) and (c) HiPIMS + MF additional plasma discharge ($T_{\text{MF}(c)}$). The TiO_2 photoanodes were annealed at 450°C for 1 h in air.

cially pertinent for the sample T_{HIPIMS} because it exhibited the lowest thermal as well as energetic ion flux on the substrate during plasma deposition, which also resulted in the lowest crystallinity of the films, as verified by Raman spectroscopy. The low extent of crystallinity most likely also contributed to the poor photoactivity. In the case of the T_{MF} film, the presence of an anatase admixture may be another factor contributing to such low photoefficiency. This contaminant may induce electronic states within the TiO_2 band gap that act as recombination centers for the photoelectrochemical (PEC) process.

This hypothesis was supported by the following PEC analysis of TiO_2 layers thermally treated at 450°C for 1 h. After thermal annealing, the anatase Raman scattering peak vanished entirely from the spectrum of $T_{\text{MF}(c)}$ film and simultaneously the PEC activity rose dramatically (see Figs. 2b and 4b, respectively). A photocurrent of $388 \mu\text{A cm}^{-2}$ at 1.55 V vs. RHE was recorded, suggesting a 70-fold enhancement for the $T_{\text{MF}(c)}$ film. A maximum photocurrent of $490 \mu\text{A cm}^{-2}$ was recorded at 2.3 V vs. RHE. Conversely, only a slight improvement of the PEC performance was observed for the $T_{\text{HIPIMS}(c)}$ sample, reaching a photocurrent of $42 \mu\text{A cm}^{-2}$ at 1.55 V vs. RHE, which was only four times higher than that of its as-deposited counterpart (T_{HIPIMS}). This supports our previous conclusion that thermal annealing of the (T_{HIPIMS}) films contributed to better charge transfer dynamics but did not improve the crystallinity, which was very poor and the main restriction on PEC performance. The annealed films were further tested by linear sweep voltammetry and chronoamperometry under standard solar simulating conditions of AM 1.5 (intensity 100 mW cm^{-2}) light irradiation. A current density of $110 \mu\text{A cm}^{-2}$ at 1.3 V vs. RHE was obtained for the $T_{\text{MF}(c)}$ films (Fig. 4c and d). It is worth noting that this value was very similar to the PEC activity of recently reported very thin TiO_2 films (comparable thickness $\sim 20 \text{ nm}$) deposited by an ALD technique [40,41]. Further, in line with the previous PEC experiments, under standard solar simulating conditions, the $T_{\text{MF}(c)}$ films outperformed the $T_{\text{HIPIMS}(c)}$ BLs by a factor of five. The chronoamperometry scans recorder at constant applied potential of 1.3 V vs. RHE also show a very fast response on the light/dark periods as well as sufficient stability of the produced films (Fig. 4d).

Electrochemical impedance spectroscopy (EIS) was applied to further evaluate the properties of the TiO_2 BLs. The tests were performed with acidic (pH 2.5) aqueous electrolyte solution free from any other redox couples. The recorded EIS spectra were best-fitted to the equivalent circuit shown in Fig. 5a, where R_S characterizes the ohmic resistance of the electrode, electrical contacts and elec-

trolyte solution, R_{CT} denotes the charge transfer resistance and CPE represents a constant phase element modeling the space charge capacitance. More detailed description is given elsewhere [9,15].

Proton insertion into TiO_2 is usually assumed to be a faradaic reaction with rate proportional to the reciprocal value of charge transfer resistance (Eq. (2)):



In the absence of an external potential, the interface TiO_2 /aqueous electrolyte solution is usually characterized by upwards band bending. This is caused by adjustment of the Fermi level of TiO_2 with the corresponding energy level in solution. Electrons are depleted from the space charge region and the interfacial capacitance is given by the Mott-Schottky equation (Eq. (3)):

$$\frac{1}{C_{SC}^2} = \left(\frac{2}{e\epsilon_0\epsilon_r N_D} \right) \left(\varphi - \varphi_{FB} - \frac{kT}{e} \right) + \frac{1}{C_H^2} \quad (4)$$

where ϵ_r is the dielectric constant of the semiconductor (in the case of rutile, $\epsilon_r = 160$) [42], ϵ_0 is the permittivity of free space, C_{SC} is the capacitance of the space-charge (depletion) region normalized to the electrode area, N_D is the number of donors per unit volume, φ is the applied potential, φ_{FB} is the flatband potential, k is Boltzmann's constant, T is the temperature, and e is the electronic charge [43]. C_H is the Helmholtz capacitance of the electrochemical double layer and is usually much larger than C_{SC} for low donor concentrations. Thus, the last part of the equation can be neglected [44,45].

Measurements were recorded by scanning from positive to negative potentials over the range 1.3 V to -0.3 V vs. Ag/AgCl (1.655–0.55 V vs. RHE). Fig 5b and c shows Mott-Schottky plots for the calcined BLs ($T_{\text{HIPIMS}(c)}$) and $T_{\text{MF}(c)}$). Mott-Schottky plots corresponding to the as-deposited (without thermal treatment) films are presented in Fig. S7. It can be seen from these plots that all three systems showed a linear zone with a positive slope, which can be attributed to n-type semiconductor behavior. From extrapolation of the linear region and the slope of the plots, the flatband potential (φ_{FB}) and apparent majority carrier density (N_D), respectively, were obtained. The resulting values are summarized in Table 1. The main finding was that the as-deposited films contained a significantly larger number of surface defects, such as oxygen vacancies and crystallinity imperfections, in line with the aforementioned results (Raman spectroscopy, crystallinity and linear voltammetry, PEC performance). In particular, Mott-Schottky curves for the as-deposited TiO_2 films exhibited nonlinear behavior (Fig. S7) at

Table 1
Flatband potentials φ_{FB} and number of donors N_D for the tested layers.

Electrode	φ_{FB} (V) vs. RHE	N_D (cm ⁻³)
T_{HiPIMS}	0.64	8.81×10^{18}
$T_{\text{HiPIMS(c)}}$	0.41	9.77×10^{18}
T_{MF}	0.35	3.56×10^{19}
$T_{\text{MF(c)}}$	0.31	9.17×10^{17}

the highest voltages applied. Such non-ideal characteristics have been directly linked to the presence of surface states in the work by Schreiber et al. [46]. The films deposited without additional MF signal (T_{HiPIMS} and $T_{\text{HiPIMS(c)}}$) showed a noteworthy shift of the flatband potential toward the cathodic region. This phenomenon has been linked to specific ion adsorption due to the surface states presented [47]. The role of surface states on the flatband potential was also studied by Ge et al., who observed a similar shift [48]. These states can be related to the low crystallinity of the T_{HiPIMS} and $T_{\text{HiPIMS(c)}}$ films and may be responsible for the generally low PEC activity of the as-deposited films owing to a high extent of charge recombination. Lastly, the carrier density (N_D) was considerably lower for the $T_{\text{MF(c)}}$ films than the as-deposited T_{MF} counterpart owing to the reduced number of oxygen vacancies over the samples as a result of the thermal treatment in air. In other words, the density of recombination centers (e.g., oxygen vacancies) was effectively suppressed. In contrast, the number of donors was slightly increased for TiO_2 deposited under HiPIMS conditions alone (compare N_D values for T_{HiPIMS} and $T_{\text{HiPIMS(c)}}$ in Table 1). This corresponds well to the results obtained from the linear and cyclic voltammetry measurements. As shown in Figs. 3 and 4 for the $T_{\text{MF(c)}}$ films, thermal annealing caused a considerable increase in the photocurrent densities as well as improved their blocking ability. In contrast, the photocurrents remained almost unchanged and the blocking function was entirely lost in the T_{HiPIMS} and $T_{\text{HiPIMS(c)}}$ films, respectively.

4. Conclusions

Highly efficient and thermally stable TiO_2 BLs were prepared by combining high impulse power magnetron sputtering (HiPIMS) and bipolar medium frequency (MF) magnetron co-sputtering. The MF discharge was generated during the “OFF” periods of the main HiPIMS deposition discharge. Owing to the very high ion flux (i.e., ion bombardment) commonly associated with HiPIMS discharge and additional high thermal flux generated by MF co-sputtering toward the FTO substrate, growth of very thin TiO_2 films (~30 nm) was achieved. TiO_2 films deposited by the combined HiPIMS/MF approach showed reasonable crystallinity and excellent blocking ability in the as-deposited state. Most importantly, the blocking functionality of the films was fully preserved even after thermal treatment at 450 °C, whereas the blocking function was completely lost in films prepared by HiPIMS alone. Moreover, the photocurrent density of newly developed TiO_2 BLs was estimated to be about 70 times higher than that of as-deposited films. Finally, the PEC behavior was shown to be consistent with EIS measurements, which revealed the presence of surface states (e.g., oxygen vacancies, crystalline defects) that most probably act as recombination centers. These states were passivated by thermal calcination in the case of films prepared by HiPIMS + MF. Overall, our results suggest that very thin TiO_2 films prepared by HiPIMS + MF may not only function as BLs but also as highly efficient electron transfer layers. Titania films with such a double mode of action may offer a promising option for improving the performance of current dye-sensitized and perovskite-based solar cells.

Acknowledgements

The authors acknowledge the support from the Ministry of Education, Youth and Sports of the Czech Republic (LO1305) and the assistance provided by the Research Infrastructure NanoEnviCz, supported by the Ministry of Education, Youth and Sports of the Czech Republic under Project No. LM2015073. The authors gratefully acknowledge the support by the Operational Program Research, Development and Education – European Regional Development Fund, project no. CZ.02.1.01/0.0/0.0/15_003/0000416 of the Ministry of Education, Youth and Sports of the Czech Republic. This work was supported by the Grant Agency of the Czech Republic (contract No. 13-07724S and No. 15-19705S).

Appendix A. Supplementary data

Supplementary data associated with this article can be found, in the online version, at doi:10.1016/j.apmt.2017.05.008.

References

- [1] B. O'Regan, M. Grätzel, A low-cost, high-efficiency solar cell based on dye-sensitized colloidal TiO_2 films, *Nature* 353 (1991) 737–740.
- [2] U. Bach, D. Lupo, P. Comte, J.E. Moser, F. Weissörtel, J. Salbeck, H. Spreitzer, M. Grätzel, Solid-state dye-sensitized mesoporous TiO_2 solar cell with high photon-to-electron conversion efficiencies, *Nature* 395 (1998) 583–585.
- [3] L. Kavan, Electrochemistry and dye-sensitized solar cells, *Curr. Opin. Electrochem.* (2017), <http://dx.doi.org/10.1016/j.coelec.2017.03.008> (in press).
- [4] D.Y. Liu, T.L. Kelly, Perovskite solar cells with a planar heterojunction structure prepared using room-temperature solution processing techniques, *Nat. Photon.* 8 (2014) 133–138.
- [5] N.J. Jeon, J.H. Noh, Y.C. Kim, W.S. Yang, S. Ryu, S. Il Seol, Solvent engineering for high-performance inorganic-organic hybrid perovskite solar cells, *Nat. Mater.* 13 (2014) 897–903.
- [6] M. Saliba, T. Matsui, J.-Y. Seo, K. Domanski, J.-P. Correa-Baena, M.K. Nazeeruddin, S.M. Zakeeruddin, W. Tress, A. Abate, A. Hagfeldt, M. Grätzel, Cesium-containing triple cation perovskite solar cells: improved stability, reproducibility and high efficiency, *Energy Environ. Sci.* 9 (2016) 1989–1997.
- [7] Z. Liu, S.P. Lau, F. Yan, Functionalized graphene and other two-dimensional materials for photovoltaic devices: device design and processing, *Chem. Soc. Rev.* 44 (2015) 5638–5679.
- [8] J. Zhou, Novel hetero-bilayered materials for photovoltaics, *Appl. Mater. Today* 2 (2016) 24–31.
- [9] L. Kavan, N. Tétreault, T. Moehl, M. Grätzel, Electrochemical characterization of TiO_2 blocking layers for dye-sensitized solar cells, *J. Phys. Chem. C* 118 (2014) 16408–16418.
- [10] Y.Z. Wu, X.D. Yang, H. Chen, K. Zhang, C.J. Qin, J. Liu, W.Q. Peng, A. Islam, E.B. Bi, F. Ye, M.S. Yin, P. Zhang, L.Y. Han, Highly compact TiO_2 layer for efficient hole-blocking in perovskite solar cells, *Appl. Phys. Express* 7 (2014) 052301.
- [11] P.J. Cameron, L.M. Peter, S. Hore, How important is the back reaction of electrons via the substrate in dye-sensitized nanocrystalline solar cells? *J. Phys. Chem. B* 109 (2005) 930–936.
- [12] J.-H. Yum, P. Chen, M. Grätzel, M.K. Nazeeruddin, Recent developments in solid-state dye-sensitized solar cells, *ChemSusChem* 1 (2008) 699–707.
- [13] T. Moehl, J.H. Im, Y.H. Lee, K. Domanski, F. Giordano, S.M. Zakeeruddin, M.I. Dar, L.-P. Heiniger, M.K. Nazeeruddin, N.-G. Park, M. Grätzel, Strong photocurrent amplification in perovskite solar cells with a porous TiO_2 blocking layer under reverse bias, *J. Phys. Chem. Lett.* 5 (2014) 3931–3936.
- [14] T.-S. Su, T.-Y. Hsieh, C.-Y. Hong, T.-C. Wei, Electrodeposited ultrathin TiO_2 blocking layers for efficient perovskite solar cells, *Sci. Rep.* 5 (2015) 16098.
- [15] L. Kavan, M. Zúkalova, O. Vik, D. Havlicek, Sol-gel titanium dioxide blocking layers for dye-sensitized solar cells: electrochemical characterization, *ChemPhysChem* 15 (2014) 1056–1061.
- [16] Y.G. Tu, J.H. Wu, M. Zheng, J.H. Huo, P. Zhou, Z. Lan, J.M. Lin, M.L. Huang, TiO_2 quantum dots as superb compact block layers for high-performance $\text{CH}_3\text{NH}_3\text{PbI}_3$ perovskite solar cells with an efficiency of 16.97%, *Nanoscale* 7 (2015) 20539–20546.
- [17] H.J. Jo, J.E. Nam, D.-H. Kim, J.-K. Kang, Improved performance of dye-sensitized solar cells with novel conjugated organic dye using aluminum oxide-coated nanoporous titanium oxide films, *J. Power Sources* 249 (2014) 385–391.
- [18] Q. Hu, J. Wu, C. Jiang, T.H. Liu, X.L. Que, R. Zhu, Q.H. Gong, Engineering of electron-selective contact for perovskite solar cells with efficiency exceeding 15%, *ACS Nano* 8 (2014) 10161–10167.
- [19] L. Kavan, L. Steier, M. Grätzel, Ultrathin buffer layers of SnO_2 by atomic layer deposition: perfect blocking function and thermal stability, *J. Phys. Chem. C* 121 (2017) 342–350.
- [20] L. Kavan, M. Grätzel, Highly efficient semiconducting TiO_2 photoelectrodes prepared by aerosol pyrolysis, *Electrochim. Acta* 40 (1995) 643–652.

- [21] A.K. Chandiran, A. Yella, M.T. Mayer, P. Gao, M.K. Nazeeruddin, M. Grätzel, Sub-nanometer conformal TiO₂ blocking layer for high efficiency solid-state perovskite absorber solar cells, *Adv. Mater.* 26 (2014) 4309–4312.
- [22] J. Cui, F.P. Meng, H. Zhang, K. Cao, H.L. Yuan, Y.B. Cheng, F. Huang, M.K. Wang, CH₃NH₃PbI₃-based planar solar cells with magnetron-sputtered nickel oxide, *ACS Appl. Mater. Interfaces* 6 (2014) 22862–22870.
- [23] D. Yang, R.X. Yang, J. Zhang, Z. Yang, S.Z. Liu, C. Li, High efficiency flexible perovskite solar cells using superior low temperature TiO₂, *Energy Environ. Sci.* 8 (2015) 3208–3214.
- [24] S. Kment, Z. Hubicka, J. Krysa, J. Olejnicek, M. Cada, I. Gregora, M. Zlamal, M. Brunclikova, Z. Remes, N. Liu, L. Wang, R. Kirchgorg, C.Y. Lee, P. Schmuki, High-power pulsed plasma deposition of hematite photoanode for PEC water splitting, *Catal. Today* 230 (2014) 8–14.
- [25] S. Kment, P. Schmuki, Z. Hubicka, L. Machala, R. Kirchgorg, N. Liu, L. Wang, K. Lee, J. Olejnicek, M. Cada, I. Gregora, R. Zboril, Photoanodes with fully controllable texture: the enhanced water splitting efficiency of thin hematite films exhibiting solely (110) crystal orientation, *ACS Nano* 9 (2015) 7113–7123.
- [26] U. Helmersson, M. Lattemann, J. Bohlmark, A.P. Ehiasarian, J.T. Gudmundsson, Ionized physical vapor deposition (IPVD): a review of technology and applications, *Thin Solid Films* 513 (2006) 1–24.
- [27] V. Kouznetsov, K. Macák, J.M. Schneider, U. Helmersson, I. Petrov, A novel pulsed magnetron sputter technique utilizing very high target power densities, *Surf. Coat. Technol.* 122 (1999) 290–293.
- [28] A. Anders, J. Andersson, A. Ehiasarian, High power impulse magnetron sputtering: current–voltage–time characteristics indicate the onset of sustained self-sputtering, *J. Appl. Phys.* 102 (2007) 113303.
- [29] M. Čada, P. Adámek, V. Straňák, Š. Kment, J. Olejníček, Z. Hubička, R. Hippler, Angle-resolved investigation of ion dynamics in high power impulse magnetron sputtering deposition system, *Thin Solid Films* 549 (2013) 177–183.
- [30] G. West, P. Kelly, P. Barker, A. Mishra, J. Bradley, Measurements of deposition rate and substrate heating in a HiPIMS discharge, *Plasma Process. Polym.* 6 (2009) S543–S547.
- [31] J.W. Bradley, H. Bäcker, Y. Aranda-Gonzalvo, P.J. Kelly, R.D. Arnell, The distribution of ion energies at the substrate in an asymmetric bi-polar pulsed DC magnetron discharge, *Plasma Sources Sci. Technol.* 11 (2002) 165–174.
- [32] C. Muratore, J.J. Moore, J.A. Rees, Electrostatic quadrupole plasma mass spectrometer and Langmuir probe measurements of mid-frequency pulsed DC magnetron discharges, *Surf. Coat. Technol.* 163–164 (2003) 12–18.
- [33] J.W. Bradley, T. Welzel, Physics and phenomena in pulsed magnetrons: an overview, *J. Phys. D: Appl. Phys.* 42 (2009) 093001.
- [34] A. Amin, D. Köhl, M. Wuttig, The role of energetic ion bombardment during growth of TiO₂ thin films by reactive sputtering, *J. Phys. D: Appl. Phys.* 43 (2010) 405303.
- [35] D.A.H. Hanaor, C.C. Sorrell, Review of the anatase to rutile phase transformation, *J. Mater. Sci.* 46 (2011) 855–874.
- [36] L. Kavan, M. Grätzel, S.E. Gilbert, C. Klemenz, H.J. Scheel, Electrochemical and photoelectrochemical investigation of single-crystal anatase, *J. Am. Chem. Soc.* 118 (1996) 6716–6723.
- [37] R.S. Nicholson, Theory and application of cyclic voltammetry for measurement of electrode reaction kinetics, *Anal. Chem.* 37 (1965) 1351–1355.
- [38] D. Magnfält, G. Abadias, K. Sarakinos, Atom insertion into grain boundaries and stress generation in physically vapor deposited films, *Appl. Phys. Lett.* 103 (2013) 051910.
- [39] A. Saedi, M.J. Rost, Thermodynamics of deposition flux-dependent intrinsic film stress, *Nat. Commun.* 7 (2016) 10733.
- [40] I.A. Cordova, Q. Peng, I.L. Ferrall, A.J. Rieth, P.G. Hoertz, J.T. Glass, Enhanced photoelectrochemical water oxidation via atomic layer deposition of TiO₂ on fluorine-doped tin oxide nanoparticle films, *Nanoscale* 7 (2015) 8584–8592.
- [41] Q. Peng, B. Kalanyan, P.G. Hoertz, A. Miller, D.H. Kim, K. Hanson, L. Alibabaei, J. Liu, T.J. Meyer, G.N. Parsons, J.T. Glass, Solution-processed, antimony-doped tin oxide colloid films enable high-performance TiO₂ photoanodes for water splitting, *Nano Lett.* 13 (2013) 1481–1488.
- [42] U. Diebold, The surface science of titanium dioxide, *Surf. Sci. Rep.* 48 (2003) 53–229.
- [43] L. Kavan, Electrochemistry of titanium dioxide: some aspects and highlights, *Chem. Rec.* 12 (2012) 131–142.
- [44] B. Seger, S.D. Tilley, T. Pedersen, P.C.K. Vesborg, O. Hansen, M. Grätzel, I. Chorkendorff, Silicon protected with atomic layer deposited TiO₂: conducting versus tunnelling through TiO₂, *J. Mater. Chem. A* 1 (2013) 15089–15094.
- [45] R. De Gryse, W.P. Gomes, F. Cardon, J. Vennik, Interpretation of Mott–Schottky plots determined at semiconductor/electrolyte systems, *J. Electrochem. Soc.* 122 (1975) 711–712.
- [46] R. Schrebler, L.A. Ballesteros, H. Gómez, P. Grez, R. Córdova, E. Muñoz, R. Schrebler, J.R. Ramos-Barrado, E.A. Dalchiele, Electrochemically grown self-organized hematite nanotube arrays for photoelectrochemical water splitting, *J. Electrochem. Soc.* 161 (2014) H903–H908.
- [47] A.J. Bard, F.-R.F. Fan, A.S. Gioda, G. Nagasubramanian, H.S. White, On the role of surface states in semiconductor electrode photoelectrochemical cells, *Faraday Discuss. Chem. Soc.* 70 (1980) 19–31.
- [48] H. Ge, H. Tian, Y.G. Zhou, S.Y. Wu, D.L. Liu, X.Z. Fu, X.-M. Song, X.C. Shi, X.X. Wang, N. Li, Influence of surface states on the evaluation of the flat band potential of TiO₂, *ACS Appl. Mater. Interfaces* 6 (2014) 2401–2406.

Appendix [A9]

High-power pulsed plasma deposition of hematite photoanode for PEC water splitting

S. Kment*, Z. Hubicka, J. Krysa, J. Olejnicek, M. Cada, M. Zlamal,
M. Brunclikova, Z. Remes, N. Liu, L. Wang, R. Kirchgeorg,
Ch. Y. Lee, P. Schmuki

Catalysis Today 230, 8-14, 2014



High-power pulsed plasma deposition of hematite photoanode for PEC water splitting



S. Kment^{a,*}, Z. Hubicka^b, J. Krysa^c, J. Olejniczek^b, M. Cada^b, I. Gregora^b, M. Zlamal^c, M. Brunclikova^b, Z. Remes^b, N. Liu^d, L. Wang^d, R. Kirchgeorg^d, Ch.Y. Lee^d, P. Schmuki^d

^a Palacky University, RCPTM, Joint Laboratory of Optics, 17. listopadu 12, 771 46 Olomouc, Czech Republic

^b Institute of Physics, Academy of Sciences of the Czech Republic, Na Slovance 2, 14800 Prague, Czech Republic

^c Department of Inorganic Technology, Institute of Chemical Technology Prague, Technicka 5, 16628 Prague, Czech Republic

^d Department of Materials Science and Engineering, University of Erlangen-Nuremberg, Martensstrasse 7, D-91058 Erlangen, Germany

ARTICLE INFO

Article history:

Received 7 July 2013

Received in revised form

24 September 2013

Accepted 17 November 2013

Available online 17 December 2013

Keywords:

Hematite

Thin films

Photoelectrochemical water splitting

HiPIMS

Hollow cathode plasma jet

Electrical properties

ABSTRACT

The fabrication of crystalline α -Fe₂O₃ hematite thin films by means of novel high power impulse magnetron sputtering (HiPIMS) and high power hollow cathode plasma jets system is reported. The coatings are based on low temperature pulsed-plasma reactive sputtering. These methods were compared with a more common method of medium frequency (MF) pulsed reactive DC magnetron sputtering. Although both high power methods yielded crystalline structure of the films already during the depositions, the films had to be thermally treated at elevated temperature in order to improve their physical (crystallinity) and electronic properties. The deposition methods used and the effect of the post deposition thermal annealing were judged on the basis of physical properties such as crystalline structure, optical absorption, surface topography, electronic properties, and electrical behavior. The functional properties were investigated under simulated photoelectrochemical water splitting conditions. Despite the revealed hematite phase of the as-deposited films, these were almost photoelectrochemically inactive. The annealing improved crystal structure of the deposited films and increased their dark conductivity. Furthermore the annealing initiated the diffusion of tin atoms from FTO (fluorine doped tin oxide) substrate into the film increasing its extrinsic conductivity. These improvements lead to higher photoefficiency.

© 2013 Elsevier B.V. All rights reserved.

1. Introduction

Hydrogen is highly attractive environmentally friendly fuel that might significantly help supply rapidly increasing global demand for energy. One of the most promising approaches how to sustainably produce hydrogen is photoelectrochemical water splitting. Hematite iron oxide (α -Fe₂O₃) has been identified as a suitable photoactive material to be applied as a photoanode in a photoelectrochemical cell (PEC). The advantages of hematite lay in its chemical stability in aqueous environment, nontoxicity, abundance, and low cost. Moreover, hematite possesses a band gap between 2.0 eV and 2.2 eV, which allows absorbing a substantial fraction of solar spectrum. With this band gap and assuming the standard solar illumination conditions (AM 1.5 G, 100 mW cm⁻²) theoretical maximal solar-to-hydrogen (STH) conversion efficiency can be calculated at 15% [1]. However, among the most discussed limitations of hematite preventing to reach such a high efficiency

are listed the low absorptivity (especially for longer wavelengths) and very short diffusion length of photogenerated holes. Therefore, the aim of this work was to investigate these drawbacks in the hematite films fabricated by unique and sophisticated plasma-assisted methods. The dependence of physical properties of the deposited films on thickness (100–25 nm) was also studied. It was already demonstrated that hematite films in this thickness range can be described as physically thin but capable of obtaining relatively high photoefficiency [2,3].

The majority of hematite coatings have been fabricated by chemical methods such as colloidal doctor blading [4], anodic electrodeposition [5,6], and chemical vapor deposition (CVD) [7], with a common target to achieve a very high surface area via the nanostructuring (nanoporous, nanowires, nanorods, cauliflower-like nanostructures, etc.) of the films. However, very often these structures suffer from poor adhesion to the substrate. Only few works have proposed using DC magnetron sputtering for hematite deposition (e.g. [8]) although it is a commonly used technology for production of a wide range of semiconductor functional thin films. What is more, the approach of RF sputtering of a Fe₂O₃ target in Ar/O₂ atmosphere has been mostly used [9]. This work reports

* Corresponding author. Tel.: +420 585634365; fax: +420 585634958.
E-mail address: kment@jointlab.upol.cz (S. Kment).

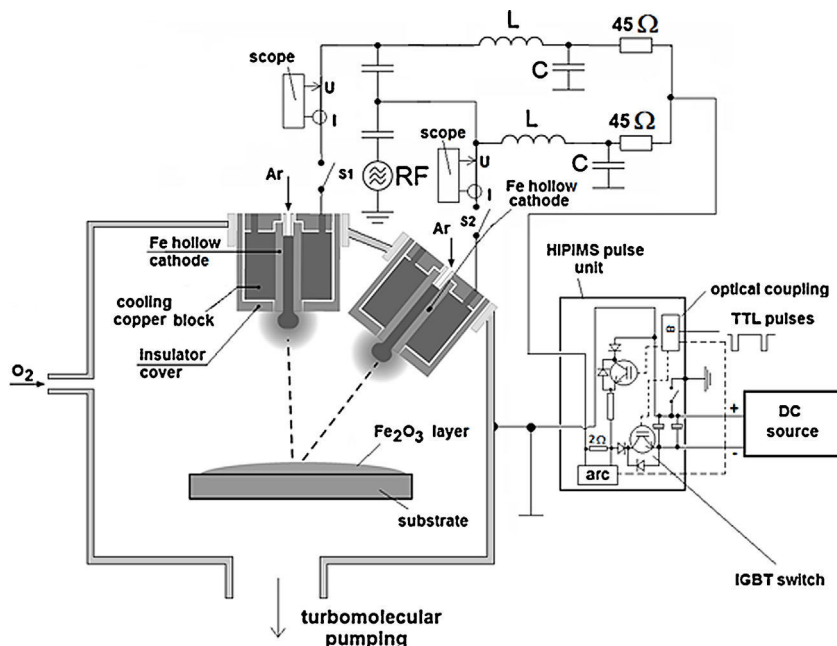


Fig. 1. Pulsed hollow cathode plasma jet sputtering system for the deposition of hematite thin films.

on application of state-of-the-art low temperature plasma assisted methods including high power impulse magnetron sputtering (HiPIMS) and DC pulsed dual hollow cathode plasma jets system for the deposition of highly adherent hematite thin films.

The HiPIMS discharges are operated in pulse modulated regime with a low repetition frequency (typically about 100 Hz) and a short duty cycle ($\sim 1\%$) with applying high peak powers ($\sim \text{kW}/\text{cm}^2$) during the active part of the modulation cycle [10]. A distinguishing feature of HiPIMS is its high degree of ionization of the sputtered metal and a high rate of molecular gas dissociation due to very high plasma density near the target (order of 10^{13} ions cm^{-3}). Furthermore, the energy of impinging metal ions can be tuned e.g. by external substrate bias to improve thin film adhesion, homogeneity, density, crystallinity and/or texture. HiPIMS was also applied for reactive sputtering processes [11,12].

The plasma jet sputtering system consists of insulated water-cooled cylindrical nozzles made from the material to be sputtered (in our case iron), which simultaneously work as the hollow cathodes. As a consequence of so-called hollow cathode effect highly dense sputtering plasma is generated inside the nozzle when DC and/or RF voltages are being applied [13]. The hollow cathode discharges (HC) are also pulse modulated with various repetition frequencies, which are, however, generally higher than in HiPIMS (in the order of kHz) and thus with corresponding duty cycles of tens of percent. The in-house developed hollow cathode system used for this study is in more details described elsewhere [14,15].

Both these methods have been recently the subject of an initial study focused on measuring the ratio of ionized to neutral fluxes of depositing particles (parameter r) on the substrate during the deposition of Fe_2O_3 hematite films [16]. The first study of physical properties of hematite Fe_2O_3 thin films (crystalline structure, surface morphology) deposited by HiPIMS magnetron and pulsed hollow cathode was already done in this work. It was shown that both methods provided a high degree of ionization of the sputtered particles ($r=0.44$ and $r=0.18$, for HiPIMS and HC, respectively) for the highest pulse powers applied (HiPIMS – 3.5×10^4 W and HC – 5×10^3 W). In this continuing work the main attention was paid to the investigation of the properties of the fabricated hematite films in terms of the crystallinity, optical properties, surface morphology, electrical properties and particularly water splitting photoactivity.

In order to demonstrate the advantages of the introduced high power plasmatic methods a more common medium frequency (MF, 50 kHz) DC pulsed reactive sputtering was also applied for the hematite thin films deposition. This method in the previous study [16] showed very small ionization of the sputtered particles.

2. Experimental

The films depositions were carried out in an ultra-high vacuum (UHV) reactor continuously pumped down by a turbo-molecular pump providing the base pressure of 10^{-5} Pa. The hematite films were deposited onto carefully cleaned fused-silica (SiO_2) and fluorine-doped tin oxide (FTO, TCO-7, Solaronix) glass substrates at room temperature. The HiPIMS deposition employed a metallic target of pure iron (99.995%, Plasmaterials) with outer diameter 50 mm and an Ar–O₂ atmosphere as working gases mixture. Since the iron target exhibits a ferromagnetic behavior the thickness of the target was reduced to 1.8 mm in order to be magnetically saturated and the magnetic field lines could be present with sufficient intensity at the surface of the magnetron target. The gases were fed to the reactor with the flow rates of 30 sccm (standard cubic centimeters per minute) and 12 sccm corresponding to argon and oxygen, respectively. The operating pressure of 1 Pa was set. The pulsing frequency of DC HiPIMS discharge was in the range 70–1000 Hz with the “ON” time of 100 μs and the maximal current density achieved in a pulse was $5 \approx \text{A cm}^{-2}$ at 70 Hz.

Analogously, the dual hollow cathodes made from pure iron (99.995%, Plasmaterials) were sputtered by the plasma discharge generated inside the nozzles. The hollow cathode plasmatic arrangement is seen in Fig. 1. Argon was delivered to the system through the nozzles with the flow rate of 80 sccm in each of them. Whereas oxygen as the reactive gas was fed to the reactor by a lateral enter with the flow rate of 40 sccm. The deposition pressure was also 1 Pa. The plasma discharge was pulse modulated with the frequencies in the range 1–2.5 kHz and the “ON” time of 100 μs . The maximum attained pulsed current density in such hollow cathode discharge was approximately $\approx 3 \text{ A cm}^{-2}$.

Additionally the iron oxide thin films were also deposited by DC pulsed magnetron sputtering with a medium repetition pulsing frequency of 50 kHz with “ON” time of 15 μs . In terms of the

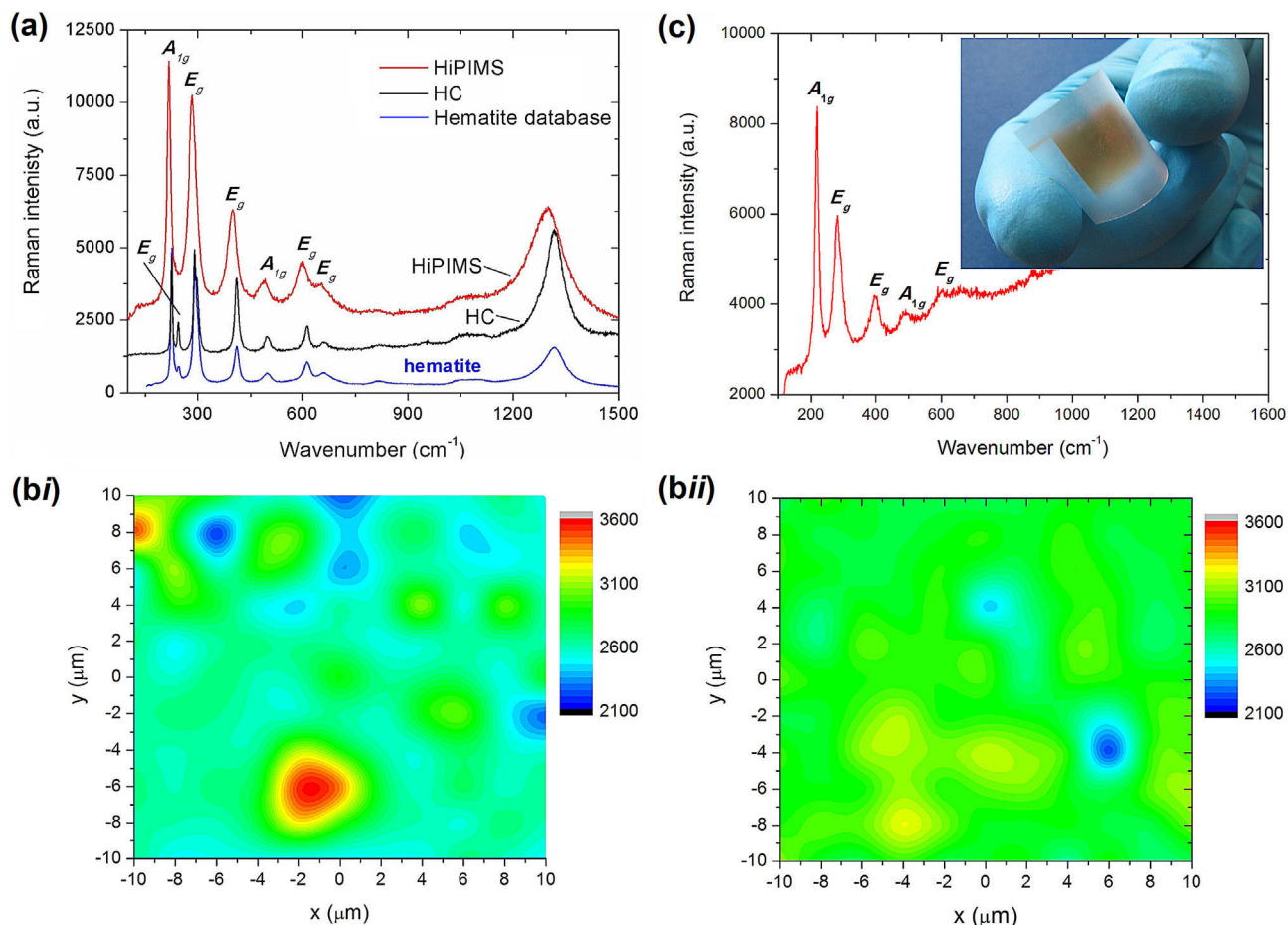


Fig. 2. (a) Raman spectra of the as-deposited films. (bi) Raman intensity map of the 225 cm^{-1} hematite Raman peak – HiPIMS. (bii) The intensity map – HC. (c) The Raman spectrum and a photograph of the HiPIMS hematite film deposited onto a polymer substrate.

degree of the ionized particles and the energy, with which they are impinging the substrate, this method is close to standard DC magnetron sputtering. However, since also in this case the reactive sputtering of the iron target was used, the MF pulsing mode had to be used in order to discharge oxidized target surface and suppress the generation of undesirable arc events on the target surface, and to stabilize the reactive sputtering process.

The crystalline structure of the layers was determined using XRD by an X'Pert MRD powder diffractometer (parallel beam geometry

realized with Goebel mirror in the primary beam and parallel plate collimator and graphite monochromator in the secondary beam) and Raman spectroscopy by Renishaw Raman Microscope RM 1000 (unpolarized beam in back scattering mode of a 514.5 nm Ar^+ laser). Under these conditions also Raman mapping was done by scanning the surface area of $10\text{ }\mu\text{m} \times 10\text{ }\mu\text{m}$. The surface images were captured by SEM (Hitachi S-520). The 3D topography scans were performed by AFM (Theicroscopes) and further analyzed to assess the surface RMS roughness. The optical properties were

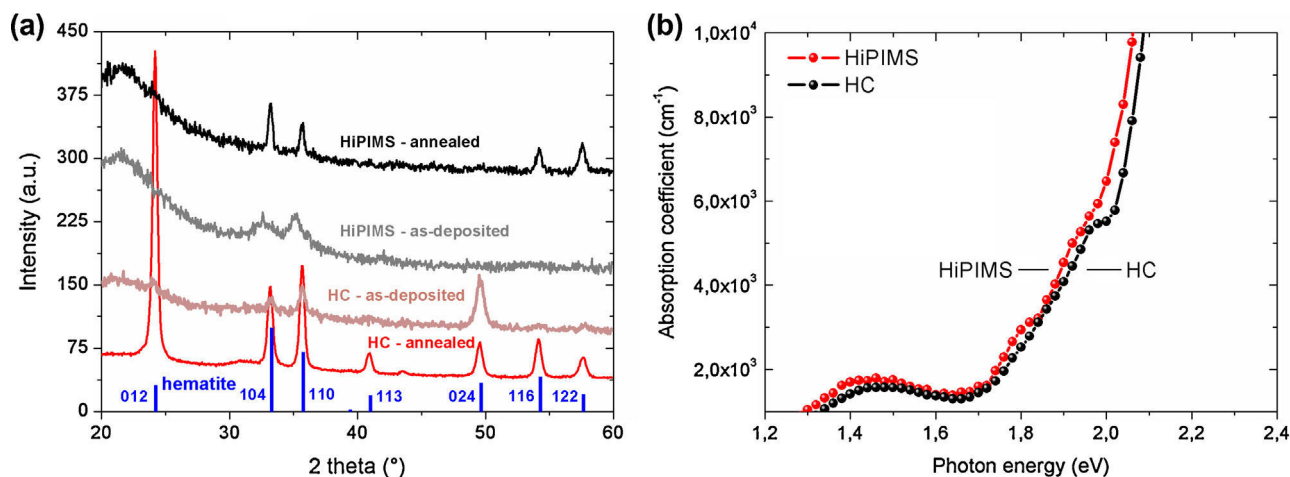


Fig. 3. (a) The XRD spectra of the films deposited on the fused silica substrates. (b) Optical properties of the hematite films.

measured by Photothermal Deflection Spectroscopy (PDS) based on the deviation of the laser beam collinear with the sample surface [17]. The X-ray photoelectron (XPS) spectra were recorded by the ESCA Probe P photoelectron spectrometer (Omicron Nanotechnology Ltd., Germany) using monochromatic AlK α X-ray source under the CAE (Constant Analyzer Energy) mode with the constant pass energy of 50 eV.

The photoelectrochemical measurements were performed using a standard three-electrode configuration, in which hematite films deposited onto the FTO substrates served as the working electrode, the Ag/AgCl (3 M KCl) introduced the reference electrode, and platinum plate was employed as the counter electrode. As the electrolyte 1 M NaOH was used. The system utilized simulated AM 1.5 (100 mW cm $^{-2}$) illumination. The measured potentials vs Ag/AgCl were converted to the reversible hydrogen electrode (RHE) scale according to the Nernst equation:

$$E_{\text{RHE}} = E_{\text{Ag/AgCl}} + 0.059 \text{ pH} + E_{\text{Ag/AgCl}}^{\circ}$$

where E_{RHE} is the converted potential vs. RHE, $E_{\text{Ag/AgCl}}^{\circ} = 0.205 \text{ V}$ at 25 °C, and $E_{\text{Ag/AgCl}}$ is the experimentally measured potential against Ag/AgCl reference.

3. Results and discussion

Both applied methods provided highly adhered transparent layers with typical brown-red color (see Graphical abstract). The thickness of the films for the physical characterization was 100 nm.

The crystalline structure of as-deposited samples was assessed by Raman spectroscopy (Fig. 2). The Raman spectra in Fig. 2a denote that the hematite crystalline phase was achieved already during the depositions. The database hematite spectrum is presented for the reference and it unambiguously matches the measured HiPIMS and HC Raman spectra [18]. The Raman mapping of the most intense hematite Raman peak at 225 cm $^{-1}$ was also performed with the aim to evaluate the extent of the crystallization over a larger area of the samples (Fig. 2bi and ii). It was revealed that only slightly better crystallinity was obtained via the hollow cathode plasma jet (see Fig. 2bii). Corresponding 2D Raman map embodied superior homogeneity over the scanning area of the samples and also higher intensity.

Hematite films were also deposited onto a polycarbonate substrate having the melting temperature below 150 °C by HiPIMS. Fig. 2c illustrates that even such thermally sensitive substrate was not damaged by the deposition itself, and moreover, the hematite crystalline film was still accomplished. The experiment was done in order to demonstrate the very low temperature of the substrate during the deposition process as well as to verify the capability of the method to provide crystalline films onto a thermally sensitive but flexible and predominantly low-weight polymer substrate useful for further applications. However, in this case the second plasmatic source to provide doping of the films will have to be added, since the thermally driven doping is obviously not possible (see next paragraphs).

The films were further annealed at 650 °C for 30 min and characterized using XRD with the aim to explore the effect of the thermal treatment. In Fig. 3a the XRD spectra of the as-deposited and annealed films are seen along with the characteristic database diffractogram of hematite (hexagonal α -Fe $_2$ O $_3$ – JCPDS 33-0664). Almost all database peaks are distinguishable in the XRD spectrum of the HC annealed film. The film was slightly textured showing the preferential orientation of the plane (0 1 2). This preferred plane orientation, however, was not recognized for as-deposited HC samples. Instead the (0 2 4) plane was dominant. The preferential orientation of the HC films may result from the glancing angle sputtering [19] caused by one of the nozzles, which was not positioned

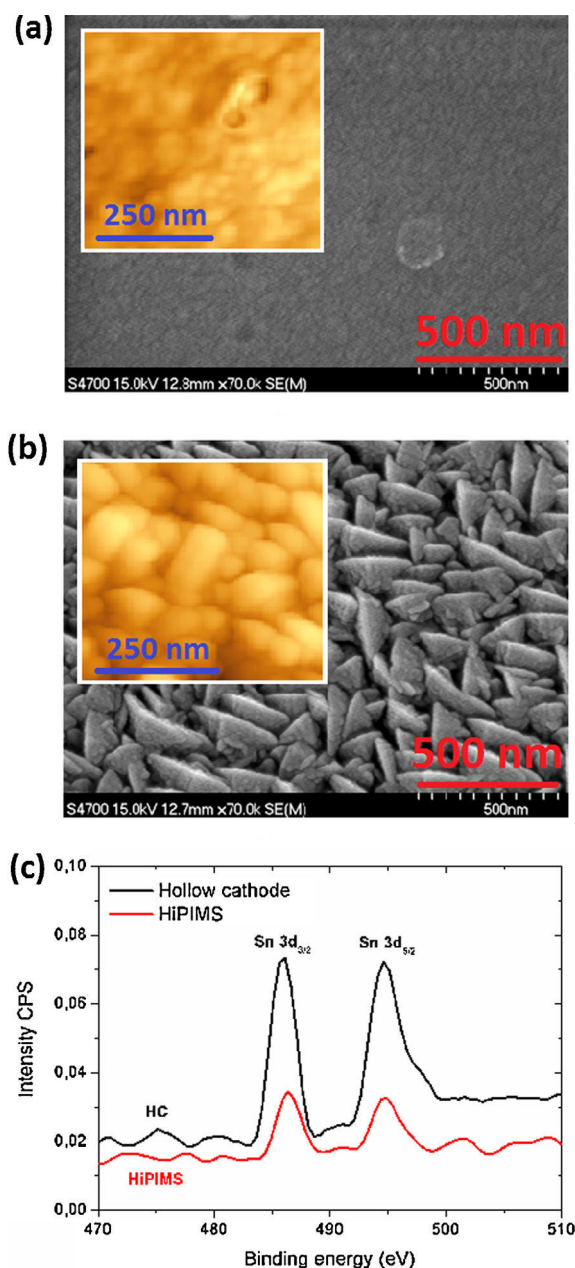


Fig. 4. The surface properties of the films. (a) HC and (b) HiPIMS films. (c) The Sn 3d XPS spectra of the films annealed at 650 °C for 30 min.

perpendicularly to the substrate (see Fig. 1). The angle between the nozzles was 45°. The HiPIMS film exhibited the polycrystalline nature more than a texture regardless of some missing peaks, which were probably due to the low XRD intensity.

The absorption spectra are shown in Fig. 3b. These data also served to examine the optical band gap. The indirect band gap energy width of almost identical values (HiPIMS – 1.99 eV and HC – 2.02 eV), which are from the region of the theoretical values, were estimated based on a Tauc plot [4].

With help of SEM and AFM the surface morphology of the films were visualized (Fig. 4a and b). From the captured images it is clearly seen that the HiPIMS films consist of very small densely packed particles. Nevertheless, such organizations are a common feature of HiPIMS produced thin films in general. Contrary the HC films embodied much bigger grains arranging a nanograin or nanopyramids patterns. The different grain size was reflected in the

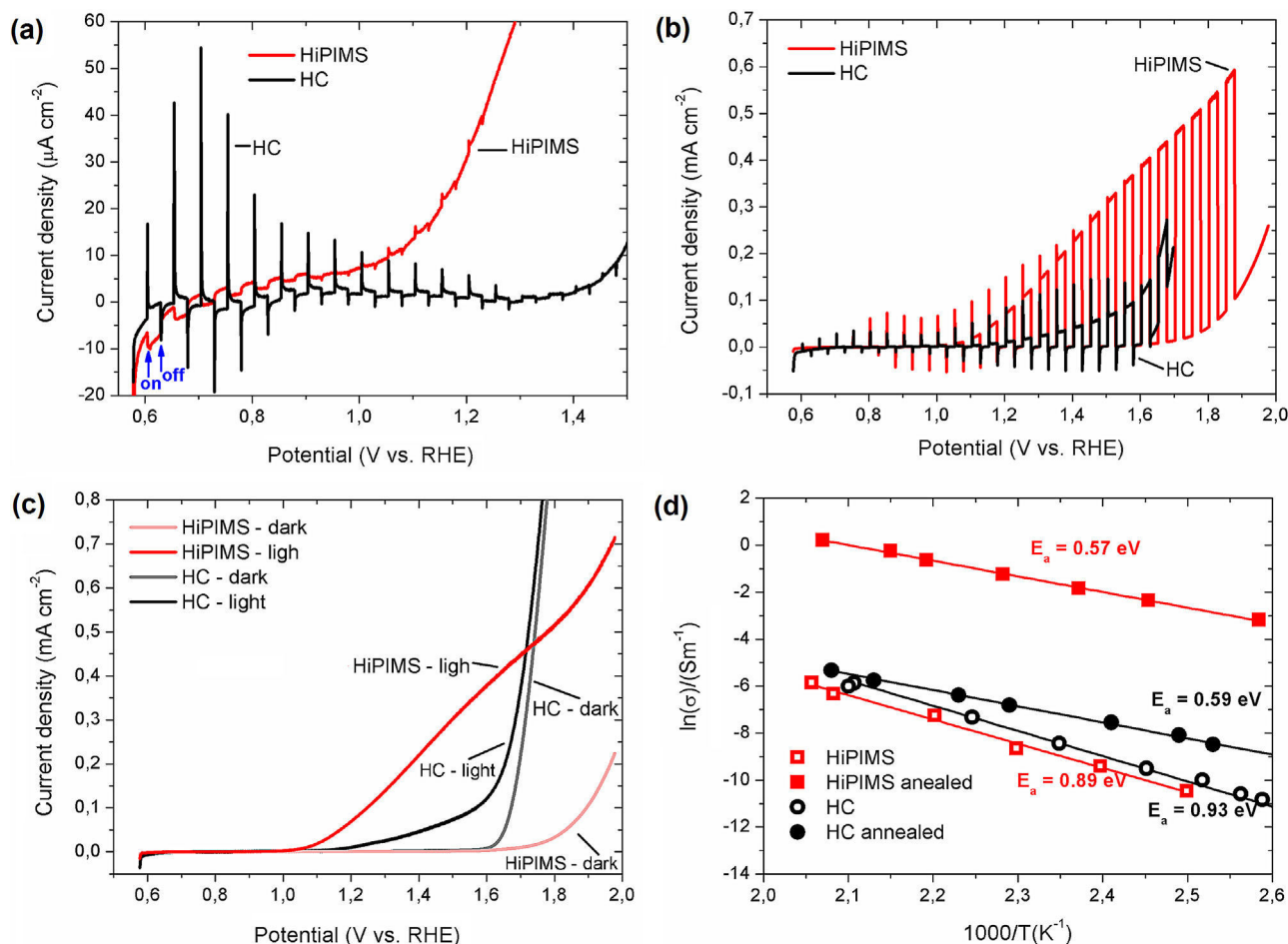


Fig. 5. Photoelectrochemical characteristics of hematite films recorder at conditions: 1M NaOH solution (pH 13.2), 5 mV s^{-1} scan rate, AM 1.5 100 mW cm^{-2} simulated sunlight. (a) Chopped light illumination I - V photocurrent curves of as-deposited films; (b) chopped light illumination I - V photocurrent curves of the annealed films at 650°C for 30 min; (c) continuous light illumination I - V photocurrent curves of annealed hematite films at 650°C for 30 min; (d) electrical properties of the films.

measured surface RMS roughness, which was 19.5 nm and 1.8 nm for the HC and HiPIMS films, respectively.

To verify the successful tin doping of hematite via the thermal diffusion from the FTO substrate XPS sputtering depth profile was done of the samples annealed at 650°C . Fig. 4c represents XPS Sn 3d peaks at the surface of the films after a short surface sputtering to eliminate the contaminants such as e.g. carbon.

Fig. 5a–c shows photoelectrochemical performance of hematite films under the conditions simulating the PEC water splitting. As stated in the introduction the hematite films struggle with short diffusion length of the holes. Hence in order to moderate this drawback and to maximize the absorption the very thin films were fabricated for PEC water splitting [1,20,21]. Although both types of as-deposited films were crystalline, they behaved almost inactive in the PEC system. It is also generally known that hematite suffers from a small electrical conductivity, which is most commonly addressed by adding impurities to hematite increasing scattering of carriers. Some impurities behave like donors and generate N type conductivity [1,4,8,9,20,22]. The high density of defects and imperfections in crystalline structure, and thus a high extend of backward electron-hole pairs recombination of as-deposited hematite films, is probably the main reason for the poor photoactivity. The phenomenon is seen as the high and sharp photocurrent spikes under chopped light I - V characteristic (Fig. 5a, HC films). The positive photocurrent spikes represent the accumulation of holes at the hematite–electrolyte [23].

Thus, in the next step the films were annealed in air at 650°C for 30 min. It is already known that such high temperature is needed

for the diffusion of tin from the FTO substrate into hematite to occur [24]. The diffused tin ions provide for the extrinsic doping of hematite improving its electronic properties [4,25]. The presence of the tin in the films was proved by XPS (see Fig. 4c). Fig. 5b represents the chopped light PEC photoresponses of the annealed films whereas the Fig. 5c denotes the photocurrent curves in dark as well as under continuous illumination. A considerable increase of the photoactivity is evident in both cases of the methods used, but the HiPIMS led to significantly enhanced photocurrents (HiPIMS – 0.09 mA cm^{-2} and HC – 0.015 mA cm^{-2} , at 1.23 V vs. RHE). One of the possible explanations is apparently related to a very high energy of ions and sputtered particles (can be higher than 20 eV [26]) bombarding the substrate during the deposition by means of HiPIMS. As a consequence the interface and electrical conductivity between the FTO and hematite film is significantly enhanced. The ion flux energy toward the substrate is considerable lower and substantial shorter in time when HC is used. A common feature of HiPIMS systems is a relatively slow deposition rate caused by positively ionized sputtered metal particles traveling backwards to the cathode. To the contrary, the very high flow rate of the working gas (up to supersonic) through the nozzles, results in much higher deposition rate in case of the HC based deposition. Therefore, in order to obtain 25 nm hematite films the depositions lasted 25 min and below 1 min for HiPIMS and HC, respectively [16]. Second reason for the boosted photoactivity of HiPIMS is apparently attributed to the much smaller grains, which are beneficial for the process in terms of reduced electron-hole recombination due to optimal matching of nanoparticle size with the hole diffusion length [1,18,27].

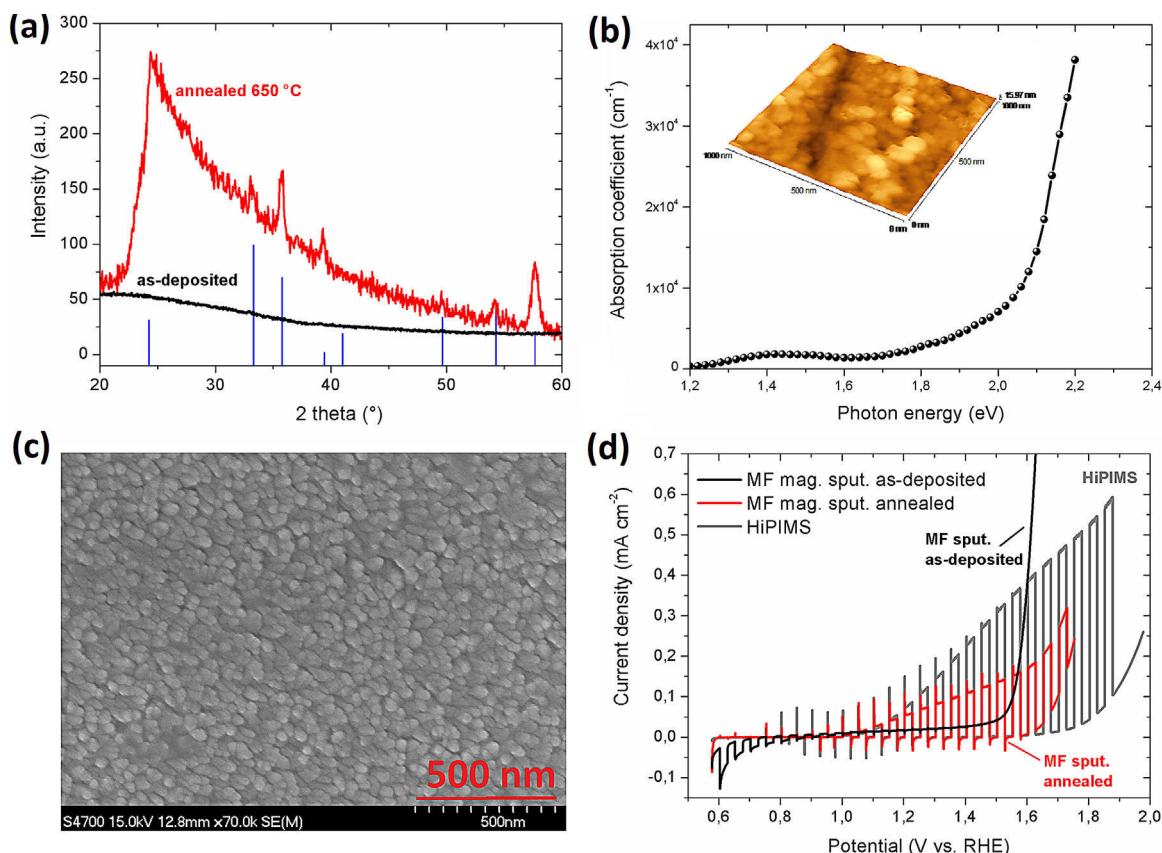


Fig. 6. The characterization of MF pulsed DC magnetron sputtering hematite thin film. (a) XRD spectra, (b) optical properties and the AFM image as the inserts and (c) SEM surface image; (d) photoelectrochemical behavior of the films investigated under the same conditions as described in Fig. 5.

Furthermore, as stated in the introduction the HiPIMS produces a great portion of the sputtered particles to be ionized. This might particularly be beneficial for effective ionic plasma doping [28] under significantly lower temperature of the substrate comparing to the thermal diffusion. In this way also the concentration of dopants would be more effectively controlled. Moreover a deposition of photoactive materials onto polymeric substrates (see Fig. 2c) would be generally possible. In case of the HC system the current configuration of two plasmatic jets enables of using one nozzle to be made from the main material (iron) and second one made from the desired dopant (tin) to also accomplish the plasmatic doping.

Temperature dependence of electrical conductivity (σ) was measured by van der Pauw method and the results are presented in Fig. 5d. The activation energies E_a were calculated from the gradient of the linear fit of Arrhenius plot and for all samples were in the range 0.57 eV (annealed HiPIMS) to 0.93 eV (unannealed HC) with experimental error less than 0.02 eV. These energies are close to previously reported values of hematite thin films prepared by high temperature processes [29,30] but approximately twice higher in comparison with values reported by Miller et al. [31] who studied low-temperature sputtering of iron oxide thin films. Obtained results can be summarized in following conclusions: (i) Conductivity of annealed samples is higher in comparison with samples without thermal treatment, which is mainly due to improving of crystalline structure and increased mobility due to lower concentration of defects. (ii) Activation energy is significantly lower for annealed samples.

Since the described high power plasma deposition methods are still at the beginning of their research in relation to the fabrication of photoactive hematite thin films, these layers were also deposited by more widespread technology of medium frequency (MF) pulsed DC magnetron sputtering for the comparison. One of the main and

crucial differences is that the as-deposited films in this case did not reveal any crystallinity as it is seen from the XRD spectrum in Fig. 6a. When the films were thermally annealed at 650 °C for 30 min the polycrystalline nature of hematite was also achieved. By means of Tauc analysis of absorption spectra (Fig. 6b), the band gap was assessed to be 2.04 eV, which is very close to the HiPIMS and HC methods and also within the tabulated region. Surface properties were again analyzed by AFM (Fig. 6b insert) and SEM (Fig. 6c). From the obtained surface pictures it is evident that the MF films form bigger grains, which are still smaller than in the HC films. This also resulted in the surface roughness RMS of 3.8 nm. However, what is the most important is the assessment of the solar driven photoelectrochemical activity. As it was expected due to the amorphous structure, the as-deposited MF films were PEC inactive as it is shown in Fig. 6d. To keep the same experimental steps the films were further thermally treated at 650 °C for 30 min and then chopped light I - V dependence was recorded. As same as in the previous cases the annealing caused an obvious photoactivity of the films with the current density of 0.06 A cm^{-2} at 1.23 V against RHE. The photoactivity is smaller than in case of the HiPIMS films (see Fig. 6d), but on the other hand higher than for HC films. The worst functionality of the HC films is apparently the consequence of the biggest grains. The HiPIMS hematite films also showed better PEC functionality than the films prepared by magnetron sputtering used as the literature references [8,9].

4. Conclusion

This contribution aimed at introducing two very promising new methods for hematite iron oxide fabrication. Hematite thin films were deposited by means of low temperature HiPIMS and HC plasmatic systems as well as more established method of medium

frequency DC reactive magnetron sputtering. Both high power methods were capable of producing crystalline films during the coating cycle under the low temperature of substrates. Contrary the MF technique provided only amorphous iron oxide thin films. Despite the used deposition technique all the as-deposited films were almost PEC inactive. Since the as-deposited HiPIMS and HC films were crystalline the main reason for the poor photoresponse was apparently a high rate of electron-hole pairs' recombination. The photoactivity was remarkably enhanced by annealing the films at 650 °C, which provided for the films doping by tin increasing their conductivity. The highest overall photoactivity was identified for the HiPIMS generated films.

Acknowledgements

This work was supported by the Grant Agency of the Czech Republic (project 13-29241P) and (project P108/12/2104); by the Operational Program Research and Development for Innovations – European Social Fund (project CZ.1.05/2.1.00/03.0058), Operational Program Education for Competitiveness – European Social Fund (project CZ.1.07/2.3.00/20.0017), and the project LH 12043 of the Ministry of Education, Youth and Sports of the Czech Republic.

References

- [1] K. Sivula, F. Le Formal, M. Grätzel, *ChemSusChem* 4 (2011) 432–449.
- [2] F. Le Formal, M. Grätzel, K. Sivula, *Adv. Funct. Mater.* 20 (2010) 1099–1107.
- [3] T. Hisatomi, H. Dotan, M. Stefik, K. Sivula, A. Rothchild, M. Grätzel, N. Mathews, *Adv. Mater.* 24 (2012) 2699–2702.
- [4] K. Sivula, R. Zboril, F. Le Formal, R. Robert, A. Weidenkaff, J. Tucek, J. Frydrych, M. Grätzel, *J. Am. Chem. Soc.* 132 (2010) 7436–7444.
- [5] L. Wang, C.H.-Y. Lee, P. Schmuki, *Electrochem. Commun.* 30 (2013) 21–25.
- [6] S. Grigorescu, C.H.-Y. Lee, K. Lee, S. Albu, I. Paramasivam, I. Demetrescu, P. Schmuki, *Electrochem. Commun.* 23 (2012) 59–62.
- [7] S. Tilley, M. Cornuz, K. Sivula, M. Grätzel, *Angew. Chem. Int. Ed.* 49 (2010) 6405–6408.
- [8] J.A. Glasscock, P.R.F. Barnes, I.C. Plumb, N. Savvides, *J. Phys. Chem. C* 111 (2007) 16477–16488.
- [9] H. Tang, M.A. Matin, H. Wang, T. Deutsch, M. Al-Jassin, *J. Appl. Phys.* 110 (2011) 123511–123517.
- [10] D. Lundin, K. Sarakinos, *J. Mater. Res.* 27 (2012) 780–792.
- [11] M. Aiempnanakit, A. Aijaz, D. Lundin, U. Helmersson, T. Kubart, *J. Appl. Phys.* 113 (2013) 133302–133308.
- [12] T. Kubart, M. Aiempnanakit, J. Andersson, T. Nyberg, S. Berg, U. Helmersson, *Surf. Coat. Technol.* 205 (2011) S303–S306.
- [13] V. Kolobov, L.D. Tsendin, *Plasma Sources Sci. Technol.* 4 (1995) 551–556.
- [14] S. Kment, Z. Hubicka, P. Kluson, J. Krysa, L. Jastrabik, *Catal. Today* 161 (2011) 8–14.
- [15] S. Kment, P. Kluson, Z. Hubicka, J. Krysa, M. Cada, *Electrochim. Acta* 54 (2009) 3352–3359.
- [16] Z. Hubicka, S. Kment, J. Olejnicek, M. Cada, T. Kubart, M. Brunclikova, P. Ksirova, P. Adamek, Z. Remes, *Thin Solid Films* (2013), <http://dx.doi.org/10.1016/j.tsf.2013.09.031> (in press).
- [17] S. Kment, P. Kluson, Z. Hubicka, J. Krysa, M. Cada, I. Gregora, A. Deyneka, H. Zabova, L. Jastrabik, *Electrochim. Acta* 55 (2010) 1548–1556.
- [18] C. Barrato, P.P. Lottici, D. Bersani, G. Antonioli, *J. Sol-Gel Sci. Technol.* 13 (1998) 667–671.
- [19] Y.E. Lee, S.G. Kim, Y.J. Kim, H.J. Kim, *J. Vac. Sci. Technol. A* 15 (1997) 1194–1199.
- [20] T.W. Hamann, *Dalton Trans.* 41 (2012) 7830–7834.
- [21] K. Itah, J.O.M. Bockris, *J. Electrochem. Soc.* 131 (1984) 1266–1271.
- [22] J. Liu, Ch. Liang, H. Zhang, Z. Tian, S. Zhang, *J. Phys. Chem. C* 116 (2012) 4986–4992.
- [23] L. Xi, S.Y. Chiam, W.F. Mak, P.D. Tran, J. Barber, S.C.J. Loo, L.H. Wong, *Chem. Sci.* 4 (2013) 164–169.
- [24] L. Wang, Ch.-Y. Lee, P. Schmuki, *Electrochim. Acta* 91 (2013) 307–313.
- [25] J. Frydrych, L. Machala, J. Tucek, K. Siskova, J. Filip, J. Pechousek, K. Safarova, M. Vondracek, J.H. Seo, O. Scheeweiss, M. Grätzel, K. Sivula, R. Zboril, *J. Mater. Chem.* 22 (2012) 23232–23239.
- [26] J. Bohlmark, M. Lattermann, J.T. Gudmundsson, A.P. Ehasarian, Y. ArandaGonzalvo, N. Brenning, U. Helmersson, *Thin Solid Films* 515 (2006) 1522–1526.
- [27] D.K. Borra, A. Braun, E.C. Constable, *Energy Environ. Sci.* 6 (2013) 407–425.
- [28] A. Anders, *Surf. Coat. Technol.* 204 (2010) 2864–2868.
- [29] R.F.G. Gardner, F. Sweett, D.W. Tanner, *J. Phys. Chem. Solids* 24 (1963) 1183–1196.
- [30] J.A. Glasscock, P.R.F. Barnes, I.C. Plumb, A. Bendavid, P.J. Martin, *Thin Solid Films* 516 (2008) 1716–1724.
- [31] E.L. Miller, D. Paluselli, B. Marsen, R.E. Rocheleau, *Thin Solid Films* 466 (2004) 307–313.

Appendix [A10]

On the improvement of PEC activity of hematite thin films deposited by high-power pulsed magnetron sputtering method

S. Kment*, Z. Hubicka, J. Krysa, D. Sekora, M. Zlamal, J. Olejnicek, M. Cada, P. Ksirova, Z. Remes, P. Schmuki, E. Schubert, R. Zboril

Applied Catalysis B Environmental 265, 344-350, 2015



On the improvement of PEC activity of hematite thin films deposited by high-power pulsed magnetron sputtering method



S. Kment^{a,*}, Z. Hubicka^b, J. Krysa^c, D. Sekora^d, M. Zlamal^c, J. Olejnicek^b, M. Cada^b, P. Ksirova^b, Z. Remes^b, P. Schmuki^e, E. Schubert^d, R. Zboril^a

^a Palacky University, RCPTM, Joint Laboratory of Optics, 17. listopadu 12, 771 46 Olomouc, Czech Republic

^b Institute of Physics, Academy of Sciences of the Czech Republic, Na Slovance 2, 14800 Prague, Czech Republic

^c Department of Inorganic Technology, Institute of Chemical Technology Prague, Technická 5, 16628 Prague, Czech Republic

^d Department of Electrical Engineering, University of Nebraska - Lincoln, Lincoln Nebraska 68588, USA

^e Department of Materials Science and Engineering, University of Erlangen-Nuremberg, Martensstrasse 7, D-91058 Erlangen, Germany

ARTICLE INFO

Article history:

Received 13 July 2014

Received in revised form 3 October 2014

Accepted 6 October 2014

Available online 14 October 2014

Keywords:

Hematite

Very thin films

Photoelectrochemical water splitting

HiPIMS

ALD

Alumina passivation layer.

ABSTRACT

The work deals with fabrication of iron oxide (α -Fe₂O₃) hematite films by a novel high-power impulse magnetron sputtering method (HiPIMS). Hematite is regarded as a highly promising material for sustainable production of hydrogen via photoelectrochemical (PEC) water splitting. Some of the crucial issues of hematite are a large overpotential needed to develop the water oxidation photocurrent onset, high extent of surface defects acting as traps, and a short diffusion length (2–4 nm) of photogenerated holes. We report on minimizing these limits by deposition of highly photoactive nanocrystalline very thin (~30 nm) absorbing hematite films by HiPIMS and their passivation by ultra-thin (~2 nm) atomic layer deposited (ALD) isocrystalline alumina oxide (α -Al₂O₃) films. A new approach of one-step annealing of this bilayer system is introduced. The films were judged on the basis of physical properties such as crystalline structure, optical absorption, surface topography, and electronic properties. The functional properties were investigated under simulated photoelectrochemical (PEC) water-splitting conditions. The shift by 1 V vs. RHE and the maximal photocurrent value of 0.48 mA cm⁻² at 1.23 V vs. RHE were achieved.

© 2014 Elsevier B.V. All rights reserved.

1. Introduction

Iron oxide (α -Fe₂O₃) in hematite crystalline structure has recently attracted much attention as possibly convenient material to be used for hydrogen production via photoelectrochemical (PEC) water splitting. It is due to its favorable properties such as a band gap between 2.0 and 2.2 eV, which allows absorbing a substantial fraction of solar spectrum, chemical stability in aqueous environment, nontoxicity, abundance, and low cost. For such band gap and assuming the standard solar illumination conditions (AM 1.5 G, 100 mW cm⁻²) theoretical maximal solar-to-hydrogen (STH) conversion efficiency has been calculated at 15% [1].

On the other hand, hematite also possesses certain handicaps hindering to reach such high efficiency. Among the most cited limitations are [1–3]: (i) the nonideal position of hematite's conduction band, which is too low for spontaneous water reduction; (ii) the low absorptivity (especially for longer wavelengths) near its band-edge

due to an indirect nature of the band gap; (iii) poor majority carriers concentration leading a low electrical conductivity and (iv) the penetration depth of photons in hematite is $\alpha^{-1} = 118$ nm at $\lambda = 550$, however, due to extremely high bulk recombination rate (time constants in the range of 10 ps), the majority of the photogenerated holes undergo bulk recombination before reaching the semiconductor liquid junction (SCLJ), which causes very short diffusion length of the holes (L_D 2–4 nm) [4].

For each of these drawbacks, several more or less effective solutions have been proposed. The first limitation mentioned can be addressed by applying photovoltaic cell (e.g. dye-sensitized solar cell—DSSC) and/or a p-type semiconductor acting as the photocathode to provide the additional energy needed. In order to optimize solar photon harvesting, the cell can be placed on the top of hematite electrode or vice versa to work in a tandem ensuring that photons not absorbed by the first cell are transmitted to and subsequently absorbed by the second [5,6]. Doping with elements such as Sn, Ti, Si, Pt, etc. [7–10] can significantly increase the electronic conductivity by increasing the number of majority carriers' concentration. The negative effect of the short diffusion length of photogenerated holes can be suppressed by using very

* Corresponding author. Tel.: +420585634365; fax: +420585634958.
E-mail addresses: stepan.kment@upol.cz, kment@fzu.cz (S. Kment).

thin films of hematite or their careful nanostructuring in various dimensions and architectures (wormlike structure [11], nanorods [12], nanowires [13], etc.).

A large overpotential with respect to the flat band potential, V_{fb} , necessary to promote water oxidation is another key issue. For hematite Fe_2O_3 , the flat band potential has been found to be around 0.5 V [1,14] versus the reversible hydrogen electrode (RHE). In the ideal case, the photocurrent is observed at all potentials more anodic than V_{fb} . The hematite, however, does not usually generate water oxidation photocurrent until the potential of 0.8–1.0 V vs. RHE [15]. Of course a certain external bias is consumed to suppress the energy deficit due to the aforementioned unsuitable energy level of the valance band. The remaining overpotential (0.5–0.6 V) has been attributed to two main reasons. The first one is the slow oxygen evolution reaction kinetics (OER), which has been addressed by anchoring various OER catalyst nanoparticles (IrO_2 , Co–Pi, etc.) onto the hematite surface [15,16]. The second one suggests the presence of electronic surface states originated from oxygen vacancies and crystalline defects, which serve as traps for photogenerated holes. As a consequence, the so-called Fermi-level pinning has been observed. The corundum isocrystalline oxide structures (Al_2O_3 , Ga_2O_3 , or In_2O_3) have been applied to effectively passivate these surface states and thus reduce the overpotential [17–19].

In this contribution, the attention was paid to the photoelectrochemical (PEC) processes with respect to the photogenerated holes. We clearly demonstrate the synergic effect of very thin nanocrystalline hematite films overlaid by passivating atomic layer deposition (ALD) Al_2O_3 ultra-thin (2 nm) coatings. This approach suppresses the negative impact of the short diffusion length of the holes, decrease the required overpotential for the photocurrent onset, and increase the overall current density value due to eliminating the charge backward recombination.

The hematite films were prepared by a novel low-temperature plasma deposition technique known as high-power impulse magnetron sputtering (HiPIMS). Generally, HiPIMS discharges work under pulse-modulated regime with a low repetition frequencies (typically about 100 Hz) and very short duty cycles (~1%), during which very high peak power powers are applied (~kW/cm²) to the cathode (metal deposition target). A distinguishing feature of HiPIMS is its high degree of ionization of the sputtered metal and a high rate of molecular gas dissociation owing to very high plasma density near the target (order of 10^{13} ions cm⁻³) [20,21]. This method is thus particularly convenient to implement the highly active hematite films in more complex and sophisticated 1D nanostructures (i.e. nanotubes) and the so-called host scaffold–guest absorber structures recently applied for PEC water splitting reactions. Such organizations provide a significant enhancement of the absorbed photon to current efficiency (APCE) due to a high surface area [22,23] simultaneously suppressing recombination of the holes in bulk.

Very thin hematite films demonstrating enhanced carrier collection and the APCE have been previously fabricated by spray pyrolysis [24] and ALD method [25]. Hisatomi et al. [24] demonstrated the maximum photocurrent density of 0.7 mA cm⁻² at around 1.6 V vs. RHE and around 0.25 mA cm⁻² at 1.23 V vs. RHE obtained by the system consisting of hematite (20 nm) electrode modified by an Nb_2O_5 underlayer (2.0 nm) and deposited at 520 °C. To the best of our knowledge, the combination of very thin hematite electrode and passivating overlayer has not been introduced yet.

2. Experimental

The preparation of hematite films was carried out in an ultra-high vacuum (UHV) chamber continuously pumped down by a

combination of rotary and turbo-molecular pumps providing the base pressure of 10^{-5} Pa. The depositions were performed as the low-temperature HiPIMS reactive sputtering of pure iron target (99.995%, 50 mm outer diameter, Plasmaterials). Owing to a ferromagnetic behavior of the iron target, its thickness had to be reduced to 18 mm in order to ensure magnetic field of a sufficient intensity present at the surface of the magnetron target. The Ar–O₂ working gas mixture with the flow rates of 30 and 12 sccm (standard cubic centimeters per minute), respectively, was used. The operating pressure was 1 Pa. The average discharge current was always held constant on the value $I_{AV} = 600$ mA for the described experiments with HiPIMS magnetron. The pulsing frequency of HiPIMS discharge was varied in the range $f_p = 70$ –1000 Hz and the “ON” time when the discharge was active was held on constant value $T_{ON} = 100$ μs and the maximal current density achieved in a pulse was 5 A cm⁻² at 70 Hz. The distance between the magnetron target and the substrate was $l_s = 60$ mm. All these deposition conditions were kept constant during each deposition. The same technique has been used for photoactive hematite coating recently [26]. In that previous work, the ratio of ionized to neutral fluxes of depositing particles (parameter r) on the surface of substrate during hematite deposition was investigated. It was shown that the HiPIMS provides a high degree of ionization of sputtered particles ($r = 0.44$) for the highest pulse power applied (3.5×10^4 W). As the substrates carefully cleaned (combination of acetone, ethanol, and deionized water ultrasonic baths) transparent conductive fluorine-doped tin oxide (FTO, TCO-7, Solaronix) coated glass slides were applied. The HiPIMS deposition was carried at room temperature. However, a slight increase in the temperature of the substrate (~100 °C) can be expected owing to the sputtering process itself. The film thickness was measured by a set of techniques including optical ellipsometry, XPS, and SEM.

The depositions of Al_2O_3 overlayers were performed by means of Cambridge Nanotech–Fiji commercial ALD system. As the precursors, trimethylaluminum and water were used. The temperature raised up to 150 °C due to the ALD itself. Coatings consisted of 4 (~4 Å), 6 (~6 Å), 10 (~10 Å), and 20 (~20 Å) ALD cycles were compared. The ALD process was in-situ monitored by optical ellipsometry.

The crystalline phase of the Fe_2O_3 films was determined by Raman spectroscopy using Renishaw Raman Microscope RM 1000 (unpolarized beam in back scattering mode of a 514.5 nm Ar⁺ laser). Optical properties were investigated by means of photothermal deflection spectroscopy (PDS) based on the deviation of the laser beam collinearly propagated with the sample surface [27]. The surface topography images were obtained with help of SEM (Hitachi S-520) and AFM (Thericroscopes). The 3D AFM scans served to estimate the surface RMS roughness.

The photoelectrochemical measurements were carried with help of a standard three-electrode arrangement, which has been previously applied for testing other photoresponding coatings [28,29]. In this configuration, the hematite-coated FTO substrate served as the working electrode, the Ag/AgCl (3 M KCl) introduced the reference electrode, and platinum plate was employed as the counter electrode. As the electrolyte, 1 M NaOH solution (pH 13.6) was used.

The measured potentials vs Ag/AgCl were converted to the reversible hydrogen electrode (RHE) scale according to the Nernst equation:

$$E_{RHE} = E_{Ag/AgCl} + 0.059pH + E_{Ag/AgCl}^{\circ}$$

where E_{RHE} is the converted potential vs. RHE, $E_{Ag/AgCl}^{\circ} = 0.207$ V at 25 °C, and $E_{Ag/AgCl}$ is the experimentally measured potential against Ag/AgCl reference. The Mott–Schottky characteristics were

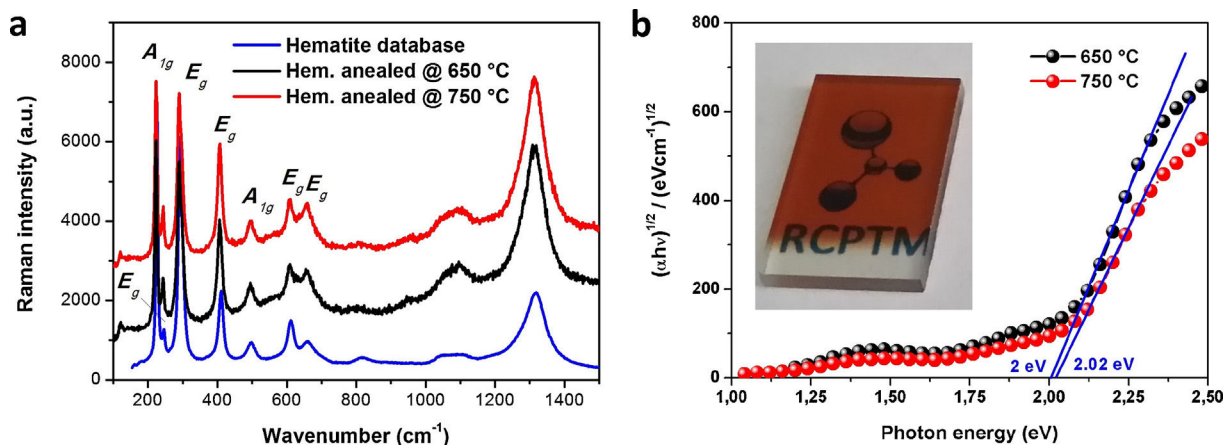


Fig. 1. HiPIMS-deposited Fe_2O_3 thin films annealed at 650 and 750 °C for 40 min: (a) Raman spectra and (b) the band gap energy width estimation based on Tauc analysis. Inset: the photograph of HiPIMS as-deposited film deposited onto FTO transparent substrate.

recorded using Zahner IM6 (Zahner Elektrik, Kronach, Germany). The measurements were performed under dark conditions at frequency of 500 Hz in 1 M NaOH electrolyte, with an amplitude of ± 10 mV.

The time stability of the hematite photoanodes as well as the concentration of produced hydrogen were tested by the following set-up. A two-chamber glass cell with 1 M NaOH water solution working as the electrolyte was used. Anode and cathode chambers were separated by the glass frit to prevent mixing of the electrolyte. Potential of +1.5 V vs. RHE was applied to the sample (working electrode). Platinum sheet was applied as the counter-electrode. Each chamber was bubbled by argon gas (1 ml/min) separately. The illuminated area of the photoanode was 2 cm². The chambers were open to air by glass capillary to avoid mixing with air. Output gas from cathode chamber (platinum counter electrode) was analyzed by a gas chromatograph (Master, Dani) equipped with a plot column (Rt[®]-Msieve 5A, Restek) and a mTCD detector (Vici).

3. Results and discussion

3.1. Physical properties

The HiPIMS method was capable of reproducibly producing highly adherent iron oxide thin films. In our previous work, we have shown that the hematite crystalline structure can be obtained already during the deposition process although the temperature of the substrate does not exceed 150 °C [30]. This ability is a significant feature of the HiPIMS method. Regardless of this phenomenon, the films have to be annealed at elevated temperature in order to provoke interdiffusion of Sn from the FTO substrate into the hematite leading to Sn-doping. Besides increasing the donor density and thus the conductivity, the annealing also enhances the crystallinity itself and orderliness, which reduces the amount of the surface states and consequently the electron–hole pairs recombination [30]. In this study, two sets of bare hematite standards were prepared. Keeping the identical deposition conditions, the

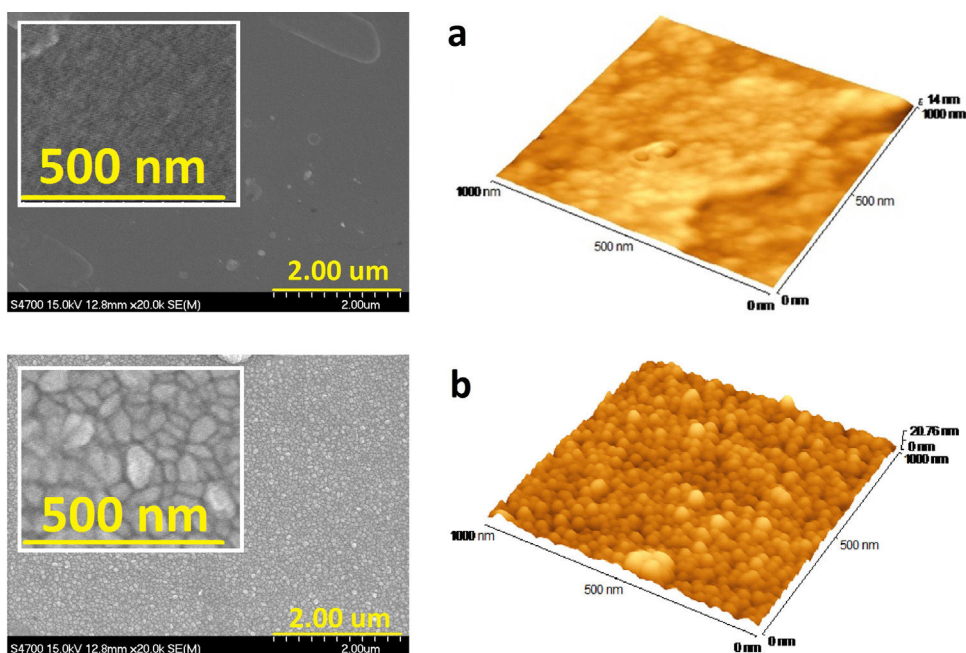


Fig. 2. Surface SEM (left column) and AFM (right column) images of hematite films: (a) films annealed at 650 °C and (b) films annealed at 750 °C, both for 40 min.

as-deposited hematite films were in the first case annealed at 650 °C and in the second at 750 °C always for 40 min. Fig. 1a shows the Raman spectra of the films prepared in this way. It is not observed a big difference between films calcinated at various temperatures. Both types exhibited only hematite Fe_2O_3 crystalline structure. The spectra show typical Raman bands of hematite, which are: A_{1g} (222 and 496 cm^{-1}), E_g (242, 291, 408, and 610 cm^{-1}), and the 2-magnon scattering band at 1313 cm^{-1} . Fig. 1b depicts the optical band gap estimation based on the Tauc analysis of the absorption coefficient. Similarly, the temperature of the annealing did not cause a significant distinction of the optical characteristics since both types of films revealed the band gap energy around 2 eV, which is in the region of the tabulated values.

On the other hand, a certain difference was observed by examining surface morphology as it is seen from SEM and AFM images shown in Fig. 2. While the annealing at 650 °C led to very smooth surface of densely packed hematite nanoparticles, the increase of the temperature up to 750 °C initiated forming of slightly bigger grains obviously providing a higher surface area. This phenomenon was reflected also in the surface RMS roughness, which was assessed from AFM scans as 2 and 3.5 nm for 650 and 750 °C annealed films, respectively.

3.2. Photoelectrochemical water-splitting activity

Simulated PEC water-splitting activity was explored via the measurement of water oxidation photocurrent density as a function of applied potential under standard AM 1.5 (intensity 100 mW cm^{-2}) illumination. The polarization curves are presented in Fig. 3. Our preceding studies have demonstrated relatively high value of photocurrent density (0.45 mA cm^{-2} at 1.7 V vs. RHE) for very thin planar hematite films deposited by HiPIMS and annealed at 650 °C for 40 min [30]. Identically fabricated films representing the same physical properties as foreshown were used as the reference for this continuous work. These films, however, also undergo the typical weaknesses such as too anodic photocurrent onset potential at 1.09 V vs. RHE and thus relatively low water oxidation photocurrent density at 1.23 V (the thermodynamic potential for water splitting) vs. RHE of 0.08 mA cm^{-2} (see Fig. 3). In the next step, therefore, the as-deposited HiPIMS Fe_2O_3 films were coated with Al_2O_3 overlayers using the ALD technique. The number of 10 ALD coating cycles was kept the same for this type of experiment, which corresponded to the 1 nm thick Al_2O_3 film (calibrated by optical ellipsometry). Such prepared bilayer systems were then annealed

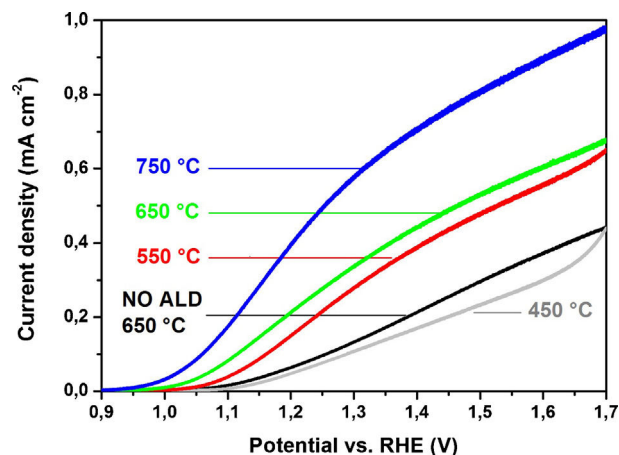


Fig. 3. Photoelectrochemical water-splitting activity of bare and ALD Al_2O_3 overlaid hematite films thermally treated at different temperatures. The bare (without ALD Al_2O_3 coating) hematite film annealed at 650 °C was used as the reference. The HiPIMS Fe_2O_3 /ALD Al_2O_3 films were then annealed at 450, 550, 650, and 750 °C always for 40 min. The PEC characteristics were recorded under solar light AM 1.5 simulated conditions with the intensity of 100 mW cm^{-2} , using 1 M NaOH solution as the electrolyte, and with the scan rate 5 mV s^{-1} .

at different temperatures (450, 550, 650, and 750 °C). This introduces other strategy than commonly used two-phase annealing, in which the as-prepared iron oxide films are calcinated first followed by the ALD coating and their subsequent thermal treatment. As it is evident from Fig. 3 when the bilayer system was annealed at 450 °C, the photocurrent values did not even reach the maxima of the bare hematite photoelectrode. This temperature level is probably still too low to improve the hematite crystallinity and more importantly owing to poor charge transfer among hematite particles themselves as well as between the FTO charge collecting substrate and the hematite film [31]. The polarization curve also showed more cathodic water oxidation dark current onset, which has been previously attributed to the photoelectrode imperfection such as inhomogeneity, low crystallinity, surface defect states, etc. After annealing at 550 °C, the photocurrent raised considerably but the applied overpotential remained almost unchanged. It emerges from this that the extent of surface photogenerated holes traps is effectively reduced. The increased photocurrent is hereupon a consequence of minimizing backward recombination of the charges. While the photogenerated holes still undergo, the slow OER kinetics reflected in the unshifted photocurrent onset.

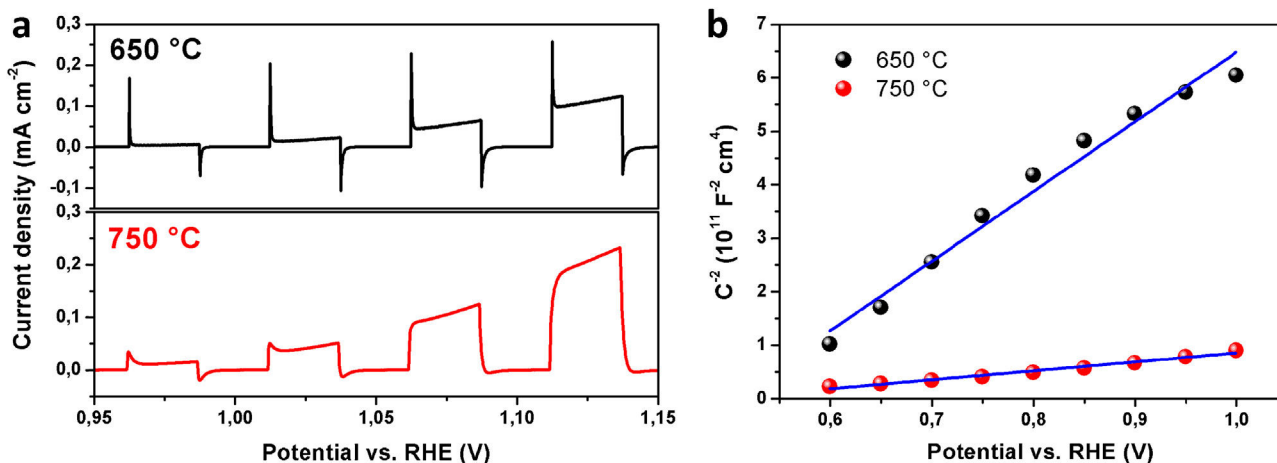


Fig. 4. Electrochemical characteristics of bare hematite films without ALD alumina passivation layer: (a) transient photocurrents measured under chopped light illumination (solar light AM 1.5, intensity 100 mW cm^{-2}) with periods of 5 s light/5 s dark; (b) Mott-Schottky plots of the films measured in dark, in 1 M NaOH electrolyte at frequency 500 Hz.

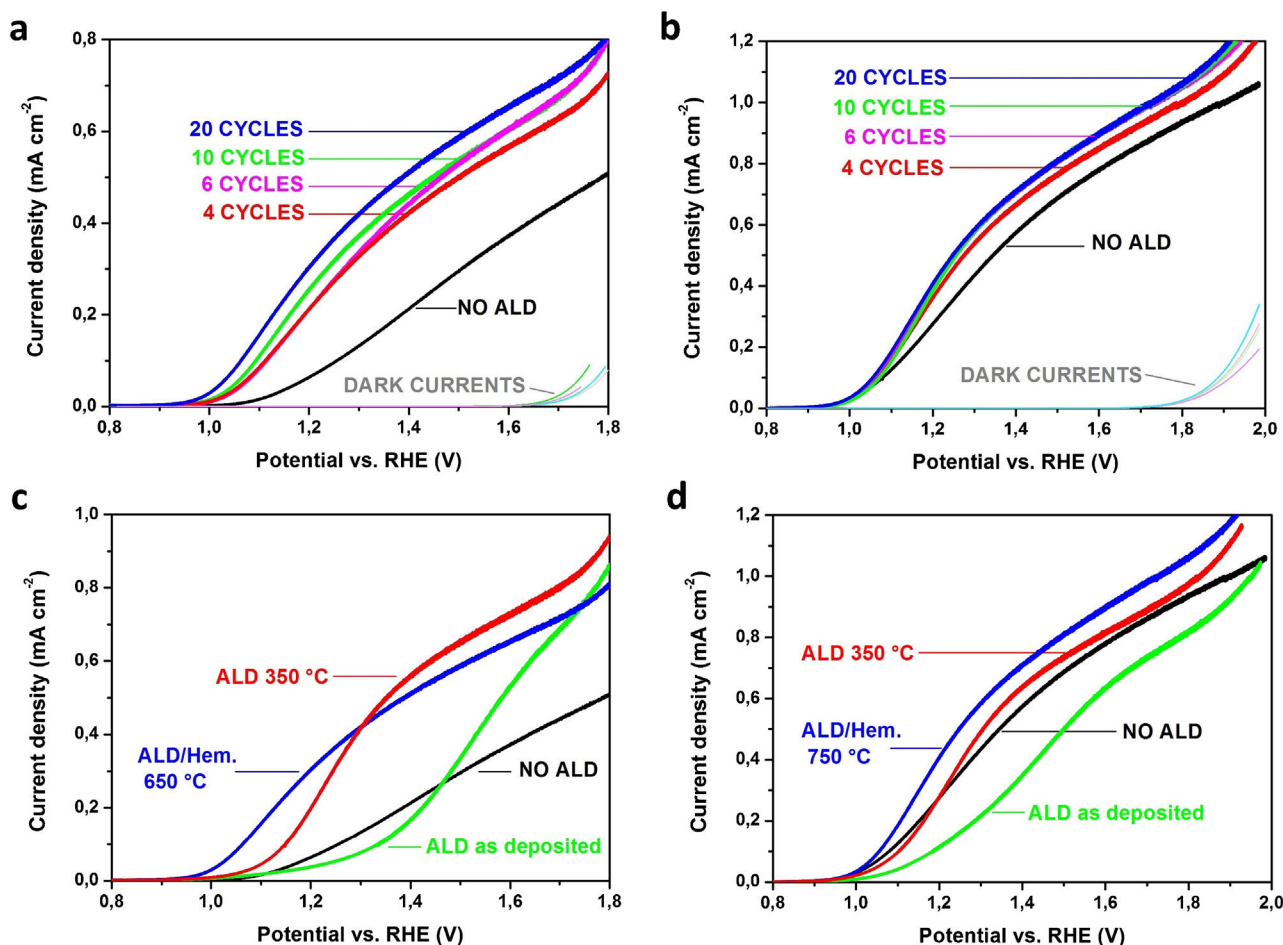


Fig. 5. PEC activity of the hematite films—the effect of ALD passivation Al_2O_3 overlayers: (1) the as-deposited hematite films annealed together with the as-deposited Al_2O_3 overlayers—the effect of number of ALD coating cycles: (a) annealed at $650^\circ\text{C}/40$ min; (b) annealed at $750^\circ\text{C}/40$ min. (2) The annealing of as-deposited hematite prior to the ALD coatings—(c) as-deposited hematite annealed at $650^\circ\text{C}/40$ min; (d) as-deposited hematite annealed at $750^\circ\text{C}/40$ min. Photocurrent then measured with as-deposited ALD 2 nm alumina overlayers (green curve) and 2 nm ALD alumina overlayers annealed at 350°C for 20 min (red curve). The blue curves represent the hematite/2 nm ALD alumina overlayers annealed at 650 and 750°C for 40 min, respectively (reference). The PEC characteristics were recorded under solar light AM 1.5 simulated conditions with the intensity of 100 mW cm^{-2} , using 1 M NaOH solution as the electrolyte, and with the scan rate 5 mV s^{-1} . The dark current curves represent the polarization curves recorded without illumination.

Further increase in the annealing temperature to 650 and 750°C led to the targeted polarization curves characteristics. Not only the overall photocurrent maxima were increased, but simultaneously their onset potential were also radically shifted cathodically. Several favorable effects apparently contributed to this phenomenon. Firstly, the crystallinity of hematite is enhanced, meaning that more organized nanocrystals providing boosted charge transfer among the grain boundaries are developed. This assumption is supported by the SEM and AFM investigations and it is also in good agreement with other previously reported studies [4,31,32]. Secondly, less undesirable surface states are generated and these are further sufficiently passivate in a high extent by the ALD coatings. Consequently, the OER kinetics is improved and recombination of electron–hole pairs is eliminated. This is evident from the measurements of dynamic polarization curves of bare hematite films (without the alumina overlayers). The photocurrents displayed in Fig. 4 were recorded on the hematite films annealed at 650 and 750°C for 40 min under the chopped light illumination. The effect of surface recombination is seen as the transient current response (the spikes) when the light is turned on and off. It has been proposed previously that the anodic current spikes are the consequence of the accumulated holes at the electrode/electrolyte interface. These holes are not injected to the electrolyte due to the slow water oxidation kinetics. On the contrary, they have ability to oxidize the

trap states in the bulk as well as on the surface. Conversely, the cathodic transient spikes are generated upon the light-off, denoting the back recombination of the accumulated holes at the SCLJ by the electrons diffusing from the external circuit [18,33]. Since the extent of generation of the current spikes is much lower for the films annealed at 750°C (Fig. 4a, the upper graph) also a lower concentration of the surface states can apparently be expected in case of these films. It significantly contributes to the enhanced overall PEC efficiency (see Fig. 3). Thirdly, one have to also take into consideration the doping of hematite by tin due to the thermally driven diffusion from FTO substrate, which increase the conductivity of hematite electrode. The presence of Sn in the films was verified by providing the XPS measurements data in our previous paper [30]. Additionally, the role of the Sn-doping was investigated by Mott–Schottky analysis as presented in Fig. 4b. From the plot of experimental capacitance data, C^{-2} as a function of applied potential V , the carrier density and flat band potentials can be assessed according to the Mott–Schottky equation [34] using the slope and intercept, respectively. Whereas the flat band potential of 0.5 V vs. RHE was the same for both types of the films, the donor densities of the hematite were calculated to be 1.35×10^{18} for 650°C and $1.05 \times 10^{19}\text{ cm}^{-3}$ for 750°C annealed hematite films. These data confirmed the increase in electron donors at higher temperature treatment owing to enhanced Sn-doping [35].

In the following experiments, the role of number of ALD cycles was scrutinized. Fig. 5a and b denotes the polarization curves recorded for 4, 6, 10 and 20 ALD coatings onto as-deposited iron oxide films, which correspond closest to 0.4, 0.6, 1 and 2 nm thin alumina overlayers, respectively. These systems were again annealed at 650 and 750 °C for 40 min. The graphs also include dark polarization curves obtained without the films exposure by the light. In the case of layers (meaning the $\text{Al}_2\text{O}_3/\text{Fe}_2\text{O}_3$ assemblies) annealed at 650 °C, merely a slender shift of the photocurrent potential onset is seen with respect to the number of ALD alumina-coating cycles. The most apparently is shifted the system with 20 ALD cycles by 50–0.9 V vs. RHE comparing to rest of ALD-treated hematite films. It means that the maximum shift of the photocurrent onset potential achieved was by 100 mV from 1 to 0.9 V vs. RHE for the 650 °C annealed assembly of ALD $\text{Al}_2\text{O}_3/\text{HiPIMS Fe}_2\text{O}_3$. A substantially positive effect of the ALD passivation layers on the overall PEC activity characterized by the photocurrents is evident (see Fig. 5a). More than double increase of the photocurrent density was identified. Interesting features revealed the measurements of the bilayer system annealed at 750 °C. From Fig. 5b, it can be concluded that the ALD coatings did not influence the position of the photocurrent onset potential. The passivation of surface traps resulted only in slightly higher obtained photocurrents. However, if we compare the bare hematite coatings without the ALD treatment, the photocurrent onset is already for 750 °C annealed film shifted cathodically. Moreover, much higher photocurrent was achieved. One of the sources of the surface traps is the crystallinity imperfection. It seems that the calcination at the temperature level of 750 °C had a certain self-limiting effect towards the surface defects similarly to the work by Morrish et al. [36]. This finding corresponds well with afore-described photocurrent transient behavior, which revealed the less concentration of surface states for the hematite films thermally treated at 750 °C. The very high photocurrent achieved (0.48 mA cm^{-2} , at 1.23 V vs. RHE, 20 ALD alumina cycles) pushes these types of films among the champions of ultra-thin hematite photoelectrodes.

A different approach was next used. First, the reference hematite films were prepared by the annealing of as-deposited HiPIMS films at 650 and 750 °C analogously to previous experiments for 40 min. These films were overlaid by the alumina 20 cycles ALD coatings, which showed the best performance in the precious tests, and these were annealed once more at 350 °C for 20 min or left as-prepared. The photocurrent characteristics of these films are available in Fig. 5c and d, including the bare hematite films and the most active photoanodes previously identified for both temperatures used. It is clearly evident that the as-deposited alumina ALD coatings affected both reference hematite coatings strongly negatively. The reason is that the amorphous alumina films apparently suffer from a high degree of disorder inhibiting the hole injection from Fe_2O_3 into the electrolyte [18]. From the graphs, it can also be concluded that the simultaneous annealing of hematite and the ALD alumina passivation layers is more beneficial as always higher photocurrent at 1.23 V vs. RHE was reached. The presence of the alumina overlayer helps releasing the stress in the hematite films during the calcination and thus also much more minimizes the amount of defects than if the thermal treatments are separated [37].

The photocatalytic H_2 evolution was measured under simulated solar irradiation in 1 M NaOH electrolyte. Fig. 6 shows the time course for hydrogen evolution over hematite photoanodes with and without ALD passivation coatings. The results very well correspond to the preceding findings and discussions. We observed a similar stabilization stage as referred by Carraro et al. During this beginning period, an equilibrium of the evolving hydrogen in the PEC cell is established. Next, the PEC cell worked in a steady-state regime producing almost constant concentration of hydrogen over a long testing time. The highest concentration of evolved hydrogen was

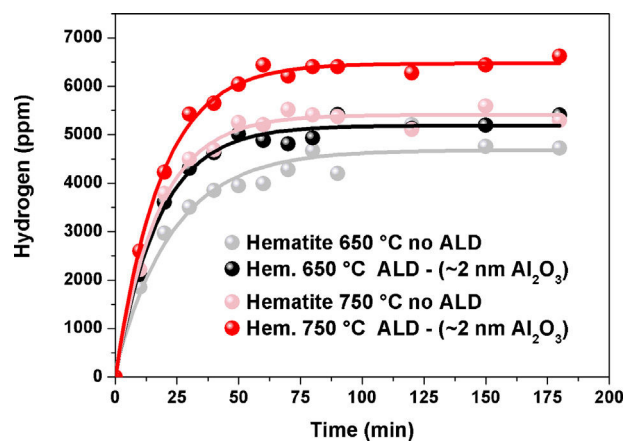


Fig. 6. Time course of hydrogen evolution using the bare hematite films annealed at 650 and 750 °C for 40 min and the hematite films coated by 20 ALD cycles (2 nm) of Al_2O_3 followed by the annealing at 650 and 750 °C as the photoanodes. The systems were illuminated by simulated solar light AM 1.5 with intensity 100 mW cm^{-2} , the applied potential to the photoanodes was 1.5 V vs. RHE, and the electrolyte was 1 M NaOH (pH ~ 13.6). The illuminated area of the photoanode was 2 cm^2 .

achieved of the hematite photoanode annealed at 750 °C together with 2 nm (20 ALD cycles) Al_2O_3 overlayers. To the contrary, the lowest concentration of produced hydrogen was measured for bare hematite photoelectrode annealed at 650 °C. Moreover, this measurement proved the long-term stability of both untreated and treated hematite photoanodes. It is obvious that alumina was not dissolved in the electrolyte despite problematic thermodynamic stability at such high pH (~ 13.6 for 1 M NaOH). The scans lasted 3 h during which the hydrogen evolution remained highly stable.

4. Conclusion

The HiPIMS method was successfully applied for reactive deposition of photoactive very thin ($\sim 30 \text{ nm}$) hematite films. The as-deposited hematite films were annealed at 650 and 750 °C always for 40 min. The Raman spectra revealed only the hematite crystalline structure for both types. The band gap was estimated to be around 2 eV in both cases. Hematite films annealed at 750 °C showed more developed crystal grains and higher surface roughness. In order to increase the overall photoefficiency by suppressing the negative effect of surface states serving as the traps for photo-generated holes as well as by shifting the oxidation photocurrent onset potential more cathodically the hematite films were overlaid by ultra-thin (0.4–2 nm) Al_2O_3 films using the ALD method. Several annealing steps were applied on these bilayer systems. We have demonstrated for the first time that the one annealing step of the as-deposited $\text{Fe}_2\text{O}_3/\text{as-deposited Al}_2\text{O}_3$ is more effective due to relaxation of the hematite film stress reducing the generation of the surface defects. The maximal shift of the photocurrent onset potential by 0.1 V vs. RHE was achieved for system of HiPIMS hematite/ALD (2 nm) alumina passivation layer annealed simultaneously at 650 °C for 40 min. On the other hand, the highest photocurrent value reached at 1.23 V vs. RHE was 0.48 mA cm^{-2} of the identical system but annealed together at 750 °C for 40 min.

Acknowledgements

This work was supported by the Grant Agency of the Czech Republic (project 13-29241P and project P108/12/2104), by the Operational Program Research and Development for Innovations - European Social Fund (project CZ.1.05/2.1.00/03.0058), Operational Program Education for Competitiveness - European Social Fund (project CZ.1.07/2.3.00/20.0017), and the project LD 12043 of the

Ministry of Education, Youth and Sports of the Czech Republic, and by National Science Foundation (USA) projects RII (EPS-1004094) and MRSEC (DMR-0820521).

References

- [1] K. Sivula, F. Le Formal, M. Gratzel, *ChemSusChem* 4 (2011) 432–449.
- [2] M.G. Walter, E.L. Warren, J.R. McKone, S.W. Boettcher, Q. Mi, E.A. Santori, N.S. Lewis, *Chem. Rev.* 110 (2010) 6446–6473.
- [3] D.K. Bora, A. Braun, E.C. Constable, *Energy Environ. Sci.* 6 (2013) 407–425.
- [4] K. Sivula, R. Zboril, F. Le Formal, R. Robert, A. Weidenkaff, J. Tucek, J. Frydrych, M. Grätzel, *J. Am. Chem. Soc.* 132 (2010) 7436–7444.
- [5] M.T. Mayer, Ch. Du, D. Wang, *J. Am. Chem. Soc.* 134 (2012) 12406–12409.
- [6] J. Brilliet, J.H. Yum, M. Cornuz, T. Hisatomi, R. Solariska, J. Augustynski, M. Gratzel, K. Sivula, *Nat. Photon.* 6 (2012) 823–827.
- [7] J. Frydrych, L. Machala, K. Tucek, K. Siskova, J. Filip, J. Pechousek, K. Safarova, M. Vondracek, J.H. Seo, O. Schneeweiss, M. Gratzel, K. Sivula, R. Zboril, *J. Mater. Chem.* 22 (2012), 23232–23239.
- [8] I. Cesar, K. Sivula, A. Kay, R. Zboril, M. Gratzel, *J. Phys. Chem. C* 113 (2009) 772–782.
- [9] Y.S. Hu, A. Kleiman-Schwarsstein, A.J. Forman, D. Hazen, J.N. Park, E.W. McFarland, *Chem. Mater.* 20 (2008) 3803–3805.
- [10] J. Liu, C.H. Liang, H.M. Zhang, Z.F. Tian, S.Y. Zhang, *J. Phys. Chem. C* 116 (2012) 4986–4992.
- [11] J.Y. Kim, G. Magesh, D.H. Youn, J.W. Jang, J. Kubota, K. Domen, J.S. Lee, *Sci. Rep.-UK* 3 (2013) 2681, a. n.
- [12] A. Mao, K. Shin, J.K. Kim, D.H. Wang, G.Y. Han, J.H. Park, *ACS Appl. Mater. Int.* 3 (2011) 1852–1858.
- [13] L. Li, Y. Yum, F. Meng, Y. Tan, R.J. Hamers, J. Song, *Nano Lett.* 12 (2012) 724–731.
- [14] K. Sivula, *J. Phys. Chem. Lett.* 4 (2013) 1624–1633.
- [15] S. Tilley, M. Cornuz, F. Le Formal, J.H. Yum, M. Gratzel, *Angew. Chem. Int. Ed.* 49 (2010) 6405–6408.
- [16] B. Klahr, S. Gimenez, F. Fabregat-Santiago, J. Bisquert, T.W. Haman, *J. Am. Chem. Soc.* 134 (2012) 16693–16700.
- [17] T. Hisatomi, F. Le Formal, M. Cornuz, J. Brilliet, N. Tetreault, K. Sivula, M. Gratzel, *Energy Environ. Sci.* 4 (2011) 2512–2515.
- [18] F. Le Formal, N. Tetreault, M. Cornuz, T. Moehl, M. Gratzel, K. Sivula, *Chem. Sci.* 2 (2011) 737–743.
- [19] M. Barroso, C.A. Mesa, S.R. Pendlebury, A.J. Cowan, T. Hisatomi, K. Sivula, M. Gratzel, D.R. Klug, J.R. Durrant, *Natl. Acad. Sci. USA* 109 (2012) 15640–15645.
- [20] D. Lundin, K. Sarakinos, *J. Mater. Res.* 27 (2012) 780–792.
- [21] M. Cada, P. Adamek, V. Stranak, S. Kment, J. Olejnicek, Z. Hubicka, R. Hippler, *Thin Solid Films* 549 (2013) 177–183.
- [22] L. Wang, A. Palacios-Padros, R. Kirchgeorg, A. Tighineanu, P. Schmuki, *ChemSusChem* 7 (2014) 421–424.
- [23] K. Sivula, F. Le Formal, M. Gratzel, *Chem. Mater.* 21 (2009) 2867.
- [24] T. Hisatomi, H. Dotan, M. Stefik, K. Sivula, A. Rotchild, M. Gratzel, N. Mathews, *Adv. Mater.* 24 (2012) 2699–2702.
- [25] B.M. Klahr, T.W. Hamann, *J. Phys. Chem. C* 115 (2011) 8393–8399.
- [26] Z. Hubicka, S. Kment, J. Olejnicek, M. Cada, T. Kubart, M. Brunclikova, P. Ksirova, P. Adamek, Z. Remes, *Thin Solid Films* 549 (2013) 184–191.
- [27] S. Kment, P. Kluson, Z. Hubicka, J. Krysa, M. Cada, I. Gregora, A. Deyneka, H. Zabova, L. Jastrabik, *Electrochim. Acta* 55 (2010) 1548–1556.
- [28] S. Kment, P. Kluson, Z. Hubicka, J. Krysa, M. Cada, *Electrochim. Acta* 54 (2009) 3352–3359.
- [29] M. Morozova, P. Kluson, J. Krysa, M. Zlamal, O. Solcova, S. Kment, T. Steck, *J. Sol-gel Sci. Tech.* 52 (2009) 398–407.
- [30] S. Kment, Z. Hubicka, J. Krysa, J. Olejnicek, M. Cada, I. Gregora, M. Zlamal, M. Brunclikova, Z. Remes, N. Liu, L. Wang, R. Kirchgeorg, C.Y. Lee, P. Schmuki, *Catal. Today* 230 (2014) 8–14.
- [31] X. Zong, S. Thaweesak, H. Xu, Z. Xing, J. Zou, G. Lu, L. Wang, *Phys. Chem. Chem. Phys.* 15 (2013) 12314–12321.
- [32] D.K. Bora, A. Braun, S. Erat, O. Safonova, T. Graule, E.C. Constable, *Curr. Appl. Phys.* 12 (2012) 817–825.
- [33] H. Dotan, K. Sivula, M. Grätzel, A. Rotshild, S.C. Warren, *Energy Environ. Sci.* 4 (2011) 958–964.
- [34] D.Ch. Bohn, A.K. Agrawal, E.C. Walter, M.D. Vaudin, A.A. Herzing, P.M. Haney, A.A. Talin, V.A. Szalai, *J. Phys. Chem. C* 116 (2012) 15290–15296.
- [35] Y. Ling, G. Wang, D.A. Wheeler, J.Z. Zhang, Y. Li, *Nano Lett.* 11 (2011) 2119–2125.
- [36] R. Morrish, M. Rahman, J.M. Don MacElroy, *ChemSusChem* 4 (2011) 274–479.
- [37] D. Gan, P.S. Ho, Y. Pang, R. Huang, J. Leu, J. Maiz, T. Scherban, *J. Mater. Res.* 21 (2006) 1512–1518.

Appendix [A11]

Photoanodes with fully controllable texture: the enhanced water splitting efficiency of thin hematite films exhibiting solely (110) crystal orientation

S. Kment*, P. Schmuki, Z. Hubicka, L. Machala, R. Kirchgeorg, N. Liu, L. Wang, K. Lee, J. Olejnicek, M. Cada, I. Gregora, R. Zboril*

ACS Nano 9, 7113-7123, 2015

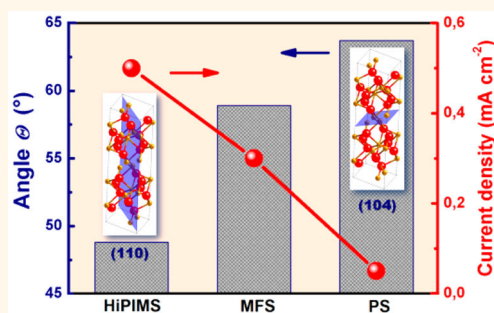
Photoanodes with Fully Controllable Texture: The Enhanced Water Splitting Efficiency of Thin Hematite Films Exhibiting Solely (110) Crystal Orientation

Stepan Kment,^{*,†} Patrik Schmuki,^{*,‡} Zdenek Hubicka,[§] Libor Machala,[†] Robin Kirchgeorg,[‡] Ning Liu,[‡] Lei Wang,[‡] Kiyong Lee,[‡] Jiri Olejnicek,[§] Martin Cada,[§] Ivan Gregora,[§] and Radek Zboril^{*,†}

[†]Regional Centre of Advanced Technologies and Materials, Joint Laboratory of Optics and Departments of Experimental Physics and Physical Chemistry, Faculty of Science, Palacky University, 17 listopadu 1192/12, 771 46 Olomouc, Czech Republic, [‡]Department of Materials Science and Engineering, University of Erlangen-Nuremberg, Martensstrasse 7, D-91058 Erlangen, Germany, and [§]Institute of Physics, Academy of Sciences of the Czech Republic, Na Slovance 2, 14800 Prague, Czech Republic

ABSTRACT Hematite, $\alpha\text{-Fe}_2\text{O}_3$, is considered as one of the most promising materials for sustainable hydrogen production *via* photoelectrochemical water splitting with a theoretical solar-to-hydrogen efficiency of 17%. However, the poor electrical conductivity of hematite is a substantial limitation reducing its efficiency in real experimental conditions. Despite of computing models suggesting that the electrical conductivity is extremely anisotropic, revealing up to 4 orders of magnitude higher electron transport with conduction along the (110) hematite crystal plane, synthetic approaches allowing the sole growth in that direction have not been reported yet. Here, we present a strategy for controlling the crystal orientation of very thin hematite films

by adjusting energy of ion flux during advanced pulsed reactive magnetron sputtering technique. The texture and effect of the deposition mode on the film properties were monitored by XRD, conversion electron Mössbauer spectroscopy, XPS, SEM, AFM, PEC water splitting, IPCE, transient photocurrent measurements, and Mott–Schottky analysis. The precise control of the synthetic conditions allowed to fabricate hematite photoanodes exhibiting fully textured structures along (110) and (104) crystal planes with huge differences in photocurrents of 0.65 and 0.02 mA cm^{-2} (both at 1.55 V *versus* RHE), respectively. The photocurrent registered for fully textured (110) film is among record values reported for thin planar films. Moreover, the developed fine-tuning of crystal orientation having a huge impact on the photoefficiency would induce further improvement of thin hematite films mainly if cation doping will be combined with the controllable texture.



KEYWORDS: Hematite · iron oxide · texture · PEC water splitting · pulsed magnetron sputtering · conversion electron Mössbauer spectroscopy

Future needs for electric power generation driven by sustainable energy sources require a focused shift from fossil fuels to a combination of wind, water, solar and other renewable sources.¹ Hydrogen production from photoelectrochemical (PEC) water splitting driven by solar power is one such clean technology that can be used for environmentally friendly fuel production.² In a standard PEC cell, at least one of the electrodes comprises a photoactive material to simultaneously allow solar light harvesting and oxidation (taking place on a

so-called photoanode) or reduction (on the photocathode) half reactions.³ Iron oxide ($\alpha\text{-Fe}_2\text{O}_3$) with hematite crystalline structure possesses many advantageous properties for use as a photoanode material.⁴ The material's substantial light absorption, offering potential conversion of up to 17% of the sun's energy into hydrogen (band gap energy between 2.0 and 2.2 eV),⁵ non-toxicity, high stability in aqueous environments, ample abundance and low cost are generally superior compared to other photoanodes. On the other hand, factors

* Address correspondence to stepan.kment@upol.cz (S. Kment), schmuki@ww.uni-erlangen.de (P. Schmuki), radek.zboril@upol.cz (R. Zboril).

Received for review March 22, 2015 and accepted June 17, 2015.

Published online June 17, 2015
10.1021/acsnano.5b01740

© 2015 American Chemical Society

limiting high performance include its nonideal conduction band edge energy with respect to reductive hydrogen evolution, poor absorptivity, short charge diffusion length and large overpotential required to promote water oxidation. Several approaches have been used to address such nonideal optical and electronic behavior, *e.g.*, nanostructuring photoanodes,⁶ application of a tandem cell approach,⁷ and deposition of ultrathin isocrystalline films to passivate surface traps.^{8,9}

Efficient transport of majority charge carriers through hematite is another key factor affecting the overall PEC performance of hematite. Substitutional doping increases the donor density, and thus carrier conductivity,¹⁰ which is otherwise very poor. The earliest studies on the electrical properties of hematite were conducted by Morin.^{11,12} Unusually, low values of basic electronic characteristics, including the mobility of charge carriers ($\sim 10^{-2}$ cm²/V s), electrical conductivity ($\sim 10^{-14}$ Ω⁻¹ cm⁻¹), conduction electron concentrations ($\sim 10^{18}$ cm⁻³ at 1000 K) and activation-energy type electron mobility ($\sim 10^{-2}$ cm² V⁻¹ s⁻¹) were reported in these works. The electrical conductivity was shown to be related to Fe²⁺/Fe³⁺ valence alternation on spatially localized iron (3d) orbitals, leading to electron transfer from one iron atom to another.¹³ Later, computed modeling approaches reliably matched empirical data with a small polaron model that considered both the effect of the relatively large size of the Fe²⁺ ion and associated lattice distortion (polaron).^{13–15} On the basis of this concept, the conductivity of electrons or holes is ascribed to hopping of polarons from site to site, which is conditional to a certain activation energy.^{15,16} The temperature dependent activation energy, E_g , affects both the carrier generation and hopping mobility. The mobility of carriers has been shown to increase with increasing temperature, and therefore has been attributed to a phonon-assisted transport mechanism.¹⁷ Pure hematite is ostensibly antiferromagnetic at room temperature (or weakly ferromagnetic owing to slight spin canting). The iron cations are in a high-spin d⁵ configuration, in which the spins are coupled ferromagnetically along (001) basal planes and antiferromagnetically along the [001] direction, both assembled in so-called iron bilayers. Detailed investigations of hematite conductivity have revealed that, although the shortest Fe–Fe distance is along the [001] direction, the electrical conductivity is highly anisotropic, exhibiting up to 4 orders of magnitude higher electron transport with conduction along the iron bilayer (001) basal plane.¹⁸ Interestingly, the perpendicular direction (parallel to [001]) was identified as the least facile transport pathway. This discrepancy was ascribed to the magnetic structure of hematite and explained on the basis of the Hund's rule. Specifically, electron transport (n-type conductivity) is allowed throughout

the environment of parallel spins of the iron bilayers (along the same (001) plane), but it is forbidden to hop across the oxygen planes to an iron layer with opposite spins (moving along [001] direction). The only possible movement along the [001] direction is that of holes, defined as Fe³⁺ → Fe⁴⁺ electron transfer (p-type conductivity), which is slower than the movement of electrons in hematite.¹⁷ Therefore, it is evident that methods to generate a specific and controllable texture may significantly improve the overall PEC activity of hematite photoanodes, as previously suggested by Grätzel *et al.*¹⁹ However, this challenging aim has not yet been accomplished.

In the present work, we attempted to tune the crystal orientation and texture of hematite photoanodes by carefully controlling the energy of particles bombarding the substrate during a plasma assisted deposition procedure, *i.e.*, a magnetron sputtering process. Although the effect of deposition plasma parameters on the crystal structure of functional coatings has partially been discussed in several works,^{20–22} none of them dealt with textured hematite photoanodes for PEC hydrogen production. The texture effect is generally associated with the surface chemistry, which influences the relative growth rates of the preferred crystal phases. The surface chemistry in sputtering based deposition processes is determined by the energy and nature (ionized or neutral metal species and ion-to-neutral flux ratio) of the impinging species.²³

RESULTS AND DISCUSSION

The highly oriented hematite films examined in this study were fabricated by DC pulse reactive magnetron sputtering of a pure iron target working as a cathode in an Ar/O₂ gas mixture. Detailed description of the plasma deposition system and characterization techniques used is provided in Methods and Supporting Information Figure S1. Three different pulsing regimes of deposition magnetron discharge were used: (i) high impulse power magnetron sputtering mode (HiPIMS, 0.1 kHz), (ii) pulsing sputtering mode (PS, 1 kHz), and (iii) medium frequency sputtering mode (MFS, 50 kHz). As a result of different pulsing frequencies, f_p , and duty factors of a pulsing cycle, d_{ur} , used, various cathode pulse current densities were reached. During each deposition, the average current, I_{AV} , and, consequently, average current density, j_{AV} , were kept constant at 600 mA and 32 mA/cm², respectively. The deposition plasma properties of each coating mode applied are summarized in Table 1. Except the X-ray powder diffraction (XRD) investigation, for which the hematite films were deposited onto amorphous fused silica and commercial Pt/TiO₂/SiO₂/Si substrates, for all the remaining experiments presented, the hematite films were fabricated onto tin doped fluorine oxide substrates (FTO). After plasma coatings, all the

as-deposited films were thermally treated at the same temperature of 650 °C for 30 min in air to improve the crystallinity and charge transfer between hematite and charge collecting back contact (FTO) of the photoanode.

XRD patterns of films are presented in Figure 1 and Supporting Information Figure S2. It can be seen that the main variation was in the two most intense diffraction peaks corresponding to (110) and (104) reflections (in hexagonal coordinates) due to hematite, α -Fe₂O₃ (Figure 1). Only in the case of the MFS films, both these diffraction peaks occurred, suggesting the common polycrystalline hematite form. The main reflection observed in the spectrum for the PS film was from the (104) plane, whereas the desired preferential phase orientation along the (110) plane was unambiguously identified in the XRD pattern of the HiPIMS film. The (110) reflection peak broadening suggested that the HiPIMS films were composed of nanocrystalline grains when compared to the remaining types of tested photoanodes (MFS, PS).

Generally, the short duty cycles and low repetition frequency of the HiPIMS discharge (see Table 1) resulted in a high power density (~ 2 kW/cm²) and high plasma density ($\sim 10^{18}$ – 10^{19} m⁻³) in the pulse; however, the values averaged over the whole period were much smaller (comparable or even lower than in the DC mode).²⁴ Owing to the high power of the HiPIMS

pulse, a large fraction of the sputtered metal (here Fe) particles were ionized in the target region. Thus, the high energy ion flux, bombarding the substrate, was considerably enhanced, potentially hugely affecting the film crystallinity, texture, grain size, microstructure, density, adhesion, *etc.*, by influencing surface diffusion.²⁵ Surface diffusion is one of the most crucial parameters affecting the crystal growth. Energetic bombardment in the HiPIMS mode removes adsorbed impurities and facilitates surface diffusion and migration, allowing adatoms to be accommodated in certain preferential plane orientation,^{26,27} in this study, orientation along the (110) plane. In comparison with the HiPIMS approach, the energy of particles impinging the substrate is negligible in the case of the MFS mode.²⁸ Thus, this mode resulted in formation of polycrystalline grains without any preferential plane orientations, which was consistent with XRD data of natural isotropic hematite powder (JCPDS 33-0664). On the other hand, the reflection peak at $2\theta = 33.3^\circ$, presented in the PS photoanode XRD spectrum, was attributed to (104) reflection. As reported in Table 1, the pulse discharge current during the PS deposition was 10-fold smaller than that for the HiPIMS mode. Thus, the energy of particles bombarding the substrate surface was lower in the former case but still much higher than expected in the MFS method. As a result, hematite adatoms tended to assemble in a different way, ultimately leading to the (104) texture. It is worth noting that, to the best of our knowledge, the majority of textured hematite films described in the literature were not obtained intentionally but most likely produced as a side effect of addition of metal dopants,^{29–31} variation of the temperature,³² and formation of 1D α -Fe₂O₃ nano-architectures.³³ The only direct approach leading to highly oriented hematite films along the (110) direction was proposed by Seki *et al.*³⁴ They used α -Al₂O₃(110) oriented substrates to epitaxially grow Rh doped hematite films by pulsed laser deposition method. However, the almost suppression of (104)

TABLE 1. Properties of Plasma Discharges during Deposition of the Hematite Photoanodes

sample acronym ^a	pulse discharge cathode current density	discharge pulsing frequency	duty factor of pulsing cycle	discharge current in pulse
	j [A/cm ²]	f_p [kHz]	d_p [%]	[A]
HiPIMS	3.2	0.1	1%	60
PS	0.32	1	10%	6
MFS	0.046	50	70%	0.9

^a HiPIMS, high impulse power magnetron sputtering; PS, pulse sputtering; MFS, medium frequency sputtering.

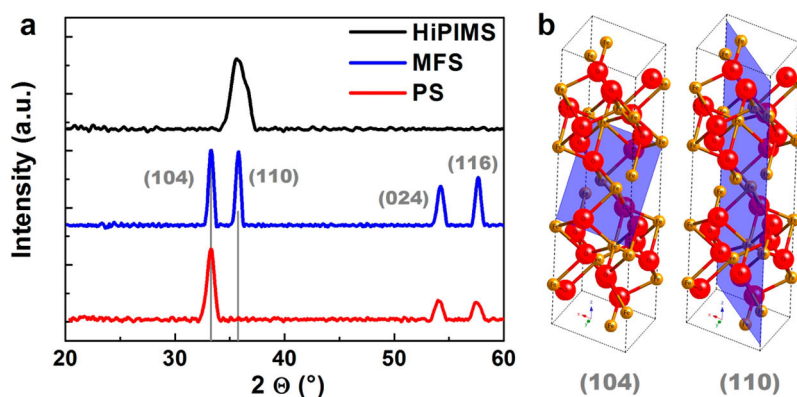


Figure 1. (a) X-ray diffraction patterns of hematite films deposited on the amorphous fused silica substrates; (b) models of the hematite crystal lattice with (104) and (110) preferentially oriented planes displayed.

alignment in favor of the (110) orientation and its impact on the hematite PEC activity has not previously been reported.

The hematite crystal structure of the films deposited on the FTO substrates was further verified using Raman spectroscopy. In Supporting Information Figure S3, all seven predicted Raman active phonon modes ($2A_{1g} + 5E_g$) of the hematite structure without any admixtures are clearly observed. The lowest A_{1g} mode at $\sim 223\text{ cm}^{-1}$ exhibited largest intensity for HiPIMS samples, whereas the intensities of other modes are more comparable. This phenomenon can also be attributed to the (110) texture of the HiPIMS films. The obtained Raman data were analyzed similarly to the work by Munisso *et al.*³⁵ Preliminary simulations of the Raman response of A_{1g} and E_g modes in a crystal of D_{3d} symmetry in backscattering configuration seem to indicate that, for a broad choice of model parameters, the ratio between the averaged response of A_{1g} and E_g modes tends to be larger in case of prevailing (110) orientation of the surface than for other situations where the scattering vector is not perpendicular to the c -axis. This is particularly the case of the HiPIMS hematite films. More details about the model applied are given in Supporting Information.

Further evidence for strong preferential orientation of the crystallites was provided by ^{57}Fe conversion electron Mössbauer spectroscopy (CEMS).^{36,37} CEMS spectra of the HiPIMS, MFS and PS samples are presented in Figure 2, which shows that all the spectra could be fitted with one magnetically split (sextet) component with hyperfine parameters typical for well crystalline hematite (Supporting Information Table S1). Considering the detection limit of Mössbauer spectroscopy ($\sim 3\%$ of relative spectrum area), hematite was the only iron containing phase in all three analyzed samples. Preferential orientation of the magnetic moments (*i.e.*, texture effect) could be identified and quantified by evaluation of the relative intensities of the spectral lines. Generally, the intensities of spectral lines in a sextet are in the ratio of $3:x:1:1:x:3$, where x varies from 0 to 4. The texture effect can be quantified through angle θ , which is defined as the average angle between the magnetic moments and direction of the γ -ray beam originating from the Mössbauer source. The angle θ can be determined directly by using the equation $x = [4(1 - \cos^2 \theta)/(1 + \cos^2 \theta)]$. In the absence of the texture effect ($x = 2$), the value of θ is $\sim 55^\circ$. Smaller values of θ imply that magnetic moments are preferentially oriented along the γ -ray beam, which is perpendicular to the layer surface. In contrast, θ values larger than 55° indicate preferential orientation of the magnetic moments along the layer surface. The determined values of x and θ including errors are presented in Supporting Information Table S1. Clearly, the hematite film

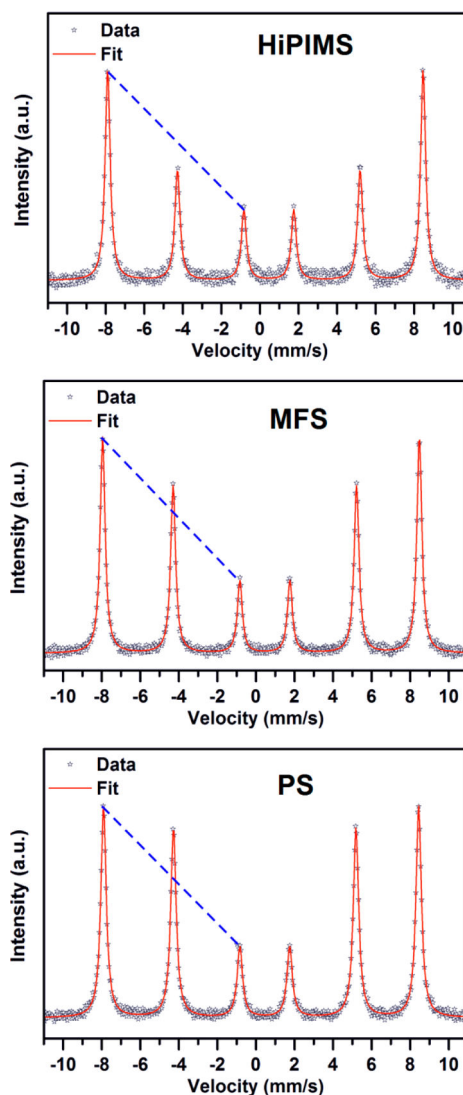


Figure 2. CEMS spectra of the hematite photoanode samples. The texture effect determined from the differences in relative intensity of the second spectral line.

prepared by the HiPIMS method exhibited preferential crystal orientation perpendicular to the substrate surface, as indicated by the θ value of $48.8 \pm 1.4^\circ$, whereas the film prepared by the PS approach showed preferential growth along the surface, as reflected by the θ value of $63.7 \pm 0.6^\circ$.

The surface morphology of the films was analyzed by atomic force microscopy (AFM) and the results are presented in Figure 3a and Supporting Information Figure S3. These figures also show scanning electron microscopy (SEM) cross-section images, which confirmed that all the films had a comparable thickness of 45 nm. This thickness was identified as optimal for the PEC water splitting activity in our previous study.³⁸ When the thickness was minimized, the negative effect of the short diffusion length of photogenerated holes was effectively suppressed.^{38,39} The AFM surface image shown in Figure 3a suggests that the hematite crystallites in the HiPIMS film were predominantly aligned

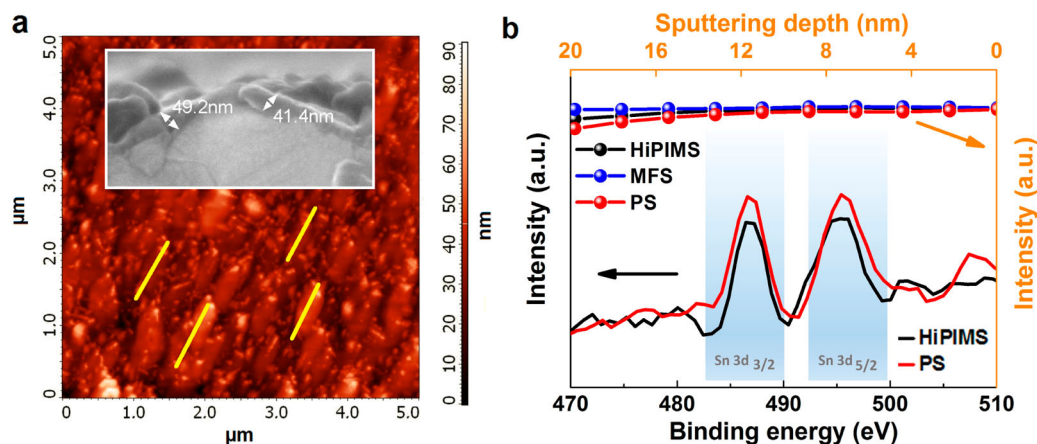


Figure 3. (a) AFM surface morphology image of HiPIMS fabricated photoanode. The yellow lines indicate the preferential orientation of crystallites. The inset shows the SEM cross-section image describing the thickness of the film to be around 45 nm; (b) the high resolution Sn 3d XPS spectra (bottom x and left y axis) with Sn depth profiling (up x and right y axis).

vertical to the substrate, which is another indication of their preferential orientation. In contrast, only randomly oriented grains in the MFS film were observed by AFM (Supporting Information Figure S5a). Although a slightly patterned surface can be distinguished in the AFM image of the PS film (Supporting Information Figure S5b), the preferential orientation detected by XRD was not as well reflected or recognizable as in the case of the HiPIMS film. The reason can be probably found in the preferential (104) orientation of the hematite grains, which is parallel toward the substrate.

To determine whether the observed properties and functionality were influenced by different concentrations of tin dopant serving as the carriers' donor, the elemental composition of the photoanodes was investigated by X-ray photoelectron spectroscopy (XPS). The high resolution XPS Sn 3d peaks intensities are presented in Figure 3b for the HiPIMS and PS films, since these two photoanodes exhibited the biggest difference in water splitting activity (see discussion below), along with XPS Sn 3d depth profile curves for all three types of films. Two main peaks at 487.9 eV (Sn 3d_{3/2}) and 496.3 eV (Sn 3d_{5/2}) showing almost identical overall intensity were apparent in the spectra of the HiPIMS and PS films. In case of the MFS electrode, the Sn 3d peaks are seen in the full XPS survey and as a high resolution depth profile peaks (Sn 3d_{3/2} and Sn 3d_{5/2}) evolution in Supporting Information Figure S6. The concentration XPS Sn 3d depth profiles for all three photoanodes (Figure 3b) were almost totally overlapped, suggesting their equivalent elemental composition. Moreover, almost equal full survey representative XPS spectra as same as the XPS O, Fe and Sn elemental depth profiles are seen in Supporting Information Figures S6a and S7, respectively. All these XPS analyses thus confirmed that the relatively low temperature of thermal annealing (650 °C), which is the main driving force for the Sn doping coming from

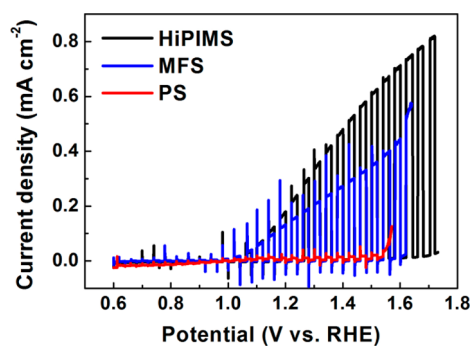


Figure 4. Simulated PEC water splitting activity of hematite photoanodes deposited under different energy of substrate ion bombardment. The PEC characteristics were recorded under solar light AM 1.5 simulated conditions with an intensity of 100 mW cm⁻², using 1 M KOH solution as the electrolyte, and with a scan rate of 1 mV s⁻¹.

the FTO substrate, did not caused any significant difference of the films composition among all three tested photoanodes.

Large differences in the PEC simulated water splitting performance were observed between the tested films (Figure 4). In these experiments, *J*–*V* polarization curves were measured under standard AM 1.5 G (intensity 100 mW cm⁻²) chopped light illumination. The highest photocurrent values (0.28 mA cm⁻² at 1.23 V and 0.65 mA cm⁻² at 1.55 V *versus* RHE) were obtained with the HiPIMS fabricated hematite photoanodes. These values are among the highest PEC water splitting performances reported recently on bare (without any modifications) planar thin film hematite electrodes. A brief comparison is given in Table 2.^{40–44} Since all experimental conditions were kept identical and the examined photoanodes differed principally in the preferential alignment of the crystallites, the excellent photoactivity of the HiPIMS photoanode was most likely due to the favorable conductivity of the majority carriers (electrons) along the [110] axis (*c*-axis) perpendicularly connected to the FTO substrate.

TABLE 2. Recently Reported PEC Water Splitting Current Density Values on Bare (without any Modifications) Hematite Planar Thin Film Photoanodes under 1.5 AM (100 mW cm^{-2}) Illumination in 1 M NaOH Electrolyte

reference	J at 1.23 V vs RHE [mA cm^{-2}]	J at 1.4 V vs RHE [mA cm^{-2}]
This work	0.28	0.5
40	0.11	0.2
41	0.18	0.6
42	0.05	0.1
43	0.18	0.4
44	0.10	0.3

We argue that a smaller size of the grains could only partially contribute to the enhanced photoactivity, as deduced from the XRD peak broadening seen in Figure 1. On the other hand, any noticeable difference of the XRD peak width corresponding to the PS and MFS electrodes was not revealed, while the difference in their PEC activity was significant. The second highly textured hematite photoanode deposited using the PS mode exhibited an almost negligible plateau photocurrent of 0.02 mA cm^{-2} at 1.23 V *versus* RHE, which remained almost constant until the water oxidation dark current onset. This drastic decrease can be explained by the synergetic effect of low electron and hole mobilities within the (104) plane oriented parallel to the *c*-axis and its nonideal oxygen dominated surface termination, which is believed to cause much higher surface recombination due to the high density of surface states acting as traps.⁴⁵ This issue was irrelevant for the (110) preferential orientation because its surface termination was dominated by Fe(III) ions. Moreover, this hypothesis was proved experimentally by measuring transient photocurrents, as discussed below. The most cathodically shifted dark current onset (Figure 4) corresponding to the PS photoanode can also be attributed to the surface or defect states. According to the work by Peter *et al.*,⁴⁶ these states can initiate water oxidation without illumination throughout the electron transfer that involves tunneling across the space-charge region. In between the two extremes (HiPIMS and PS films), the photoactivity of the untextured MFS films showed a photocurrent maxima of 0.14 mA cm^{-2} at 1.23 V and 0.38 mA cm^{-2} at 1.55 V *versus* RHE. This result is consistent with the XRD patterns, which showed that both discussed planes were present almost equally. Hence, the negative and positive roles of the preferential planes as well as surface terminations probably compensated each other, resulting in the average PEC performance.

Figure 5 shows a graph of the photocurrent maxima recorded at 1.55 V *versus* RHE plotted against the angle θ (from CEMS). The results clearly support the previous findings regarding the principal effect of crystal orientation on the PEC performance. Among

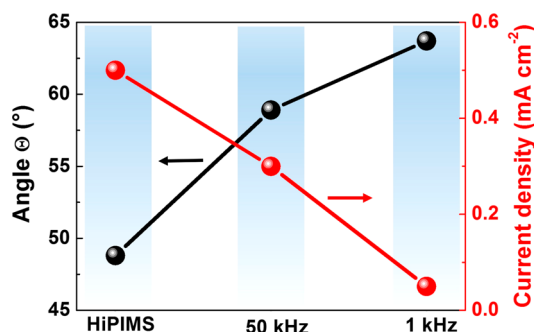


Figure 5. Correlation between the texture effect expressed as the angle θ and the PEC activity of the films expressed as the photocurrent value read at 1.5 V *versus* RHE.

the prepared films, only the MFS method led to an untextured polycrystalline film composition, as confirmed by XRD, AFM, and CEMS techniques. The angle θ was determined to be $58.9 \pm 0.4^\circ$ for the MFS sample, which supports the aforementioned result. The lowest angle θ of $48.8 \pm 1.4^\circ$, which can be attributed to the (110) preferential orientation, was obtained with the HiPIMS film. In contrast, the PS film showed the largest angle θ of $63.7 \pm 0.6^\circ$, corresponding to the (104) preferential plane orientation. All the photoanodes showed highly consistent results from the methods employed for characterization, including XRD, Raman spectroscopy, CEMS, AFM, and PEC activity.

As stated above, the various preferential orientations of hematite crystallites also determine the organization of terminating atoms (Fe, O) at the surface. Figure 6a compares transient photocurrents under chopped monochromatic light (360 nm) illumination measured at an applied potential of 1.5 V *versus* RHE. The photocurrent transients exhibited negative and positive spike characteristics, suggesting strong surface recombination. On the basis of the previously proposed explanation, the anodic current spikes (positive current response) were attributed to accumulated holes at the photoelectrode/electrolyte interface, which were not injected into the electrolyte due to slow water oxidation kinetics. Instead, they are trapped by surface states. Conversely, the cathodic transient spikes (negative current response) were generated when the light was off, indicating back recombination of the accumulated (trapped) holes at the interface by electrons diffusing from the external circuit.⁴⁷ Oxygen vacancies have been proposed to act as electron traps and recombination centers.⁴⁸ If this is the case, the probability of defect states is expected to be much higher for a surface with a greater proportion of terminal oxygen ions. In agreement with theory,⁴⁰ the highest ratio between the steady state photocurrent and the transient photocurrent spike maximum demonstrating the lowest surface recombination was observed for the HiPIMS photoanode. For this photoanode, the extent of backward electron/hole

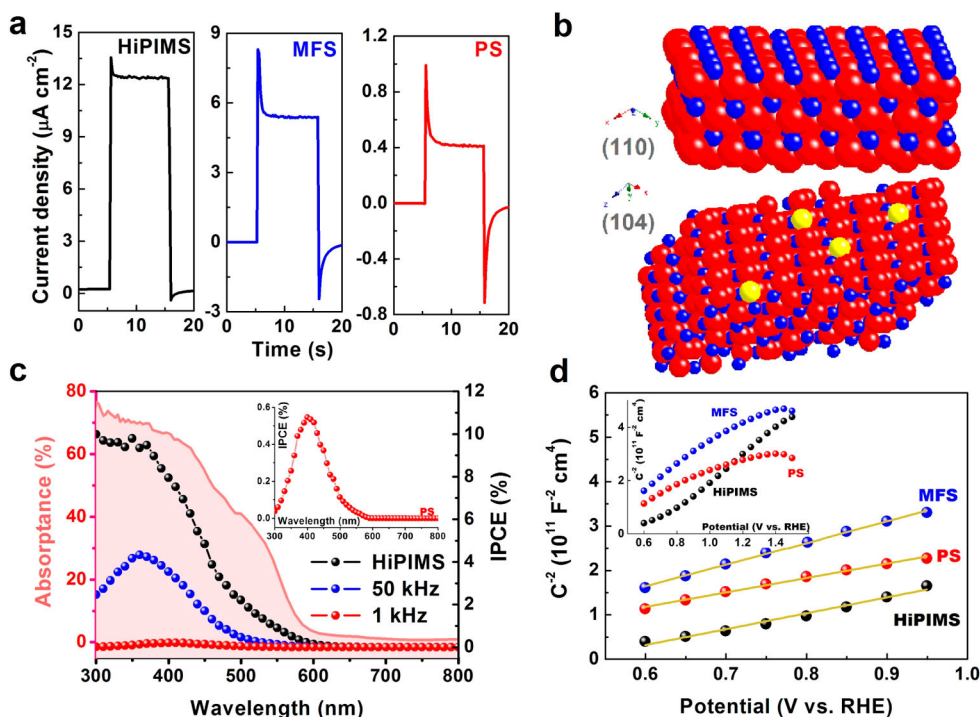


Figure 6. (a) Transient photocurrents initiated by the monochromatic (360 nm) light illumination and measured under an applied potential bias of 1.5 V; (b) models of hematite crystal lattices of (110) and (104) surface terminating planes; the blue, red, and yellow balls represent iron and oxygen atoms, and oxygen vacancies acting as the surface traps, respectively; (c) IPCE characteristics; (d) Mott–Schottky plots. All electrochemical experiments were done in 1 M KOH electrolyte.

recombination was reduced owing to the Fe(III) surface termination of the (110) plane and its substantially higher conductivity (Figure 6b). In contrast, this ratio was lowest for the (104) plane orientation displaying oxygen termination and the lowest conductivity among the examined films (Figure 6b). The assumption of the surface recombination due to oxygen vacancies was furthermore supported by measuring polarization curves in the electrolyte containing 0.5 M H₂O₂ introducing an easily oxidized hole scavenger that readily capture the photogenerated holes at the electrode/electrolyte interface. In this way the surface recombination is efficiently minimized. Current density plots as a function of applied potential are presented in Supporting Information Figure S8. Under dark conditions, the water oxidation dark current onsets showed the same trend (Supporting Information Figure S8a) as in the situation without presence of H₂O₂ in the electrolyte as it is seen in the Figure 4. When the electrodes absorbed light (Supporting Information Figure S8b), the photocurrent onsets were cathodically shifted in case of all three electrodes examined, which is, on the other hand, a common feature of the photoanodes, when a hole scavenger is applied.^{47,48} Then, the photocurrents propagated over the entire potential range until the water oxidation dark current onset. A noteworthy increase of the photocurrent was observed for the PS films when compared to the photocurrent maxima reached in the bare NaOH electrolyte (see Figure 4). It indicated that the

injection barrier (the recombination centers) for the holes was overcome. To the contrary, a much lower concentration of defect states was expected for the HiPIMS electrode having the iron dominated surface termination. As a consequence, indeed, the photocurrent maxima remained nominally the same apart from the aforementioned shift of the photocurrent onset.

Next, the incident photon to current efficiency (IPCE) was measured over the spectral range of 300–600 nm. The obtained IPCE data are plotted in Figure 6c together with the UV–vis absorption spectrum of the HiPIMS photoanode measured by photothermal deflection spectroscopy (PDS).⁴⁹ The basic optical properties of the HiPIMS and PS types of photoanodes were similar, as shown in Supporting Information Figure S9. The UV–vis absorption spectra in Figure 6c (filled area beneath the red absorption curve) qualitatively follow the detected IPCE behavior between 380 and 800 nm. As expected, the main trends of the IPCE curves were consistent with the AM 1.5 generated PEC polarization curves (see Figure 4). The highest IPCE value of 11% at around 350 nm was achieved with the HiPIMS photoanode. Considerably worse IPCE values of 4% and only 0.9% were obtained with the MFS and PS photoanodes, respectively. Hisatomi *et al.*⁵⁰ have attributed a similar decrease in IPCE to deteriorating charge transport. Thus, this may explain the results for our fabricated hematite coatings.

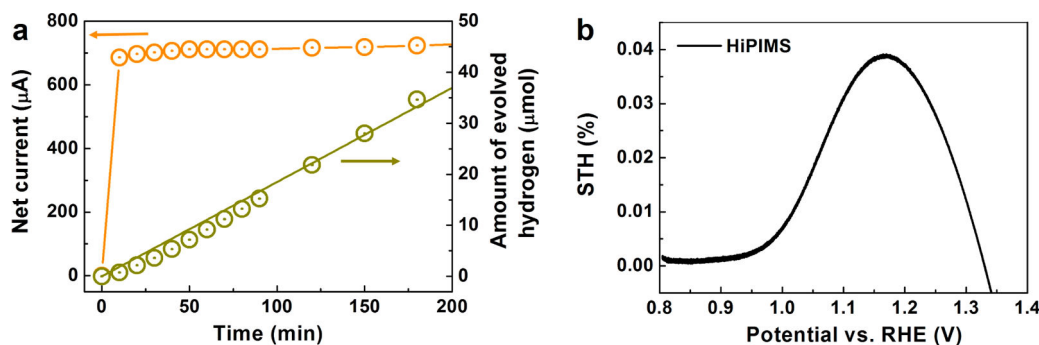


Figure 7. (a) Water splitting efficiency of the HiPIMS fabricated photoanode expressed as the amount of evolved hydrogen (green circles) and the long-term stability (orange circles). The measurements were performed by illuminating 2 cm^2 of the photoanode's area using AM 1.5 G light source of 100 mW/cm^2 intensity and with constant applied potential to the hematite photoanode of 1.5 V versus RHE. (b) Solar-to-hydrogen efficiency calculated according to eq 2.

To further elucidate the electronic properties of the photoanodes in contact with an electrolyte, electrochemical impedance measurements were performed. These nonilluminated measurements are typically presented as Mott–Schottky plots, which can be used to estimate the flat band potential (V_{fb}) and apparent density of donors (N_{D}) of PEC photoelectrodes according to the Mott–Schottky equation.⁵¹ The linear parts of the obtained Mott–Schottky plots are shown in Figure 6d. From the slopes of the linear extrapolations, the apparent donor densities were calculated as 4.92×10^{18} , 3.62×10^{18} , and $5.42 \times 10^{18}\text{ cm}^{-3}$, for the HiPIMS, MFS, and PC films, respectively. These values are clearly very similar, despite the different plasma deposition modes used. This is an important result, which verifies that the superior photoefficiency is not caused or improved by a high density of majority carriers, and it furthermore supports the conclusions derived from the XPS examination. Moreover, over an extended applied potential region ($0.4\text{--}1.6\text{ V}$), the Mott–Schottky curves exhibited nonlinear behavior, as shown in the inset in Figure 6d. These nonideal characteristics have been directly linked to the presence of surface states in the work by Schreiber *et al.*⁵² This further indicates that the surface states are due to the oxygen-rich surfaces, since the nonlinear trends of the Mott–Schottky curves were particularly pronounced for the MFS and PC hematite films (inset in Figure 6d).

The hydrogen evolution due to the solar-driven water splitting with the HiPIMS photoanode applied in the PEC system was measured by gas chromatography over a period of 200 min. The amount of photo-generated hydrogen gas as a function of operating time is presented in Figure 7a. The graph also contains the photocurrent values reached during the measurement under the applied voltage of 1.5 V versus RHE, which was kept constant. The graph denotes sufficiently long time stability of the HiPIMS electrode. The same electrodes have been repeatedly used during one year without any significant changes of their photoactivity. The Faradaic efficiency was estimated to

be above 95%, which indicates that most of photo-generated charges were consumed by the PEC water splitting reactions. Figure 7b shows the solar-to-hydrogen efficiency (STH) as a function of applied potential until the 1.23 V versus RHE. The main issue causing the low observed STH is viewed in the high photocurrent onset potential, which can, on the other hand, still be shifted cathodically by several approaches.^{9,53} In this way, the overall photoefficiency would be remarkably enhanced.

CONCLUSION

In summary, we have developed a powerful method for reproducibly generating hematite crystalline films highly oriented along the (110) plane. The hematite films were synthesized by a reactive magnetron sputtering technique utilizing deposition modes differing in the energy of ion flux. It was demonstrated that by careful selection of the deposition plasma parameters, the energy of heavy ions impinging on the surface of the substrate can be tuned to control the texture of the growing films. The highest energy bombarding particles were achieved with the HiPIMS technique, which generated hematite films with the desired crystalline alignment along the (110) direction. In contrast, the PS and MFS modes gave significantly lower energy and negligible bombardment, respectively. While the MFS mode showed no texture effect at all, the PS mode led to partial preferential orientation of the (104) plane. In agreement with the (110) texture conductivity prediction, the HiPIMS fabricated photoanodes demonstrated the highest PEC water splitting activity. In contrast, the hematite films showing preferential orientation along the (104) crystalline plane exhibited 10 times lower photocurrent maxima. The present results would induce further works enabling the controllable texture of hematite films and resulting in enhanced PEC performances. In this respect, HiPIMS technique is very promising approach, mainly if other parameters (*e.g.*, cation doping) will be involved and combined with the texture related phenomena. Described plasma deposition system is suitable for a combination of these highly active

textured hematite films with various so-called host-scaffold nanoarchitectures, which would induce further

improvement of the overall photoefficiency by a substantial increase in the light harvesting.

METHODS

Fe₂O₃ thin films were deposited by DC pulse reactive magnetron sputtering of the cathode made of a pure iron target (99.95%) in a gas mixture of Ar + O₂. A circular balanced magnetron with a target diameter of 50 mm was used. The magnetron was placed in a high vacuum reactor chamber continuously pumped by turbomolecular and roughing pump. A substrate was placed in a distance of 50 mm from the surface of the iron target. For all the conditions presented in this work, the total gas pressure and partial pressures of argon and oxygen were held constant by controlling of their particular mass flow rate into the reactor chamber. The flow of argon was $Q_{Ar} = 26$ sccm and oxygen $Q_{O_2} = 20$ sccm. The total pressure in the reactor was $p = 1.2$ Pa. Three different pulsing regimes of magnetron discharge operation were tested in this deposition experiment. For all experiments, the total average discharge current I_{AV} , and consequently the average current density j_{AV} , was held constant. The average current and current density were held on the value $I_{AV} = 600$ mA and $j_{AV} = 32$ mA/cm², respectively. The cathode pulse current density was the main parameter varied in this experiment. The change of pulse discharge current density, j_D , was provided by the change of pulsing frequency, f_p , together with the change of duty factor, d_w , of pulsing cycle. The films were deposited all with the same thickness of $t_h = 45$ nm in order to rule out influence of different thickness on structure, texture and other properties of hematite films. The films were deposited on glass substrate with SnO:F transparent conductive electrode (FTO, TCO-7, Solaronix), fused silica substrate, and multilayered substrate consisting of Pt/TiO₂/SiO₂/Si (Advanced Ceramic Coating Technology) with the hematite coating on the Pt side.

The crystalline phase of the Fe₂O₃ films was determined by X-ray powder diffraction (XRD) employing an X'Pert MRD powder diffractometer (parallel beam geometry realized with the Goebel mirror in the primary beam and parallel plate collimator and graphite monochromator in the secondary beam) and using Raman spectroscopy with a Renishaw Raman Microscope RM 1000 (unpolarized beam in back scattering mode of a 514.5 nm Ar⁺ laser). Optical properties were investigated by means of photothermal deflection spectroscopy (PDS) based on the deviation of the laser beam collinearly propagated with the sample surface. The surface topography images were recorded by an Ntegra Aura. The cross-section images were obtained with help of a field emission scanning electron microscope (Hitachi FE-SEM S4800, Japan). Chemical characterization was carried out by X-ray photoelectron spectroscopy (PHI 5600, spectrometer) using Al K α monochromatized radiation.

The samples of hematite thin films were characterized by ⁵⁷Fe conversion electron Mössbauer spectroscopy (CEMS) employing a CEMS2010 spectrometer. The CEMS spectrometer is equipped with a proportional continuous gas flow counter filled with a Penning mixture consisting of 90% He and 10% CH₄. A 50 mCi ⁵⁷Co(Rh) Mössbauer γ -ray source (14.41 keV) was used inside the spectrometer. Unfolded spectra were registered at room temperature to 1024 channels for 3–5 days and then fitted by the MossWinn 4.0 software package. The CEMS method enables to selectively characterize iron containing phases (including amorphous or nanocrystalline) within the depth of layers up to 300 nm. Moreover, a texture effect (*i.e.*, a preferential orientation of magnetic moments) can be observed and quantified through the relative intensity of the second spectral line of a sextet component.

The photoelectrochemical experiments were carried out under simulated AM 1.5 (100 mW cm⁻²) illumination provided by a solar simulator (300 W Xe with optical filter, Solarlight; room temperature) in 1 M KOH solution. A three-electrode configuration was used in the measurements, with the iron oxide electrode as the working electrode (photoanode), an Ag/AgCl (3 M KCl) as the reference electrode, and a platinum foil as the

counter electrode. Photocurrent *versus* voltage ($I-V$) characteristics were recorded by scanning the potential from OCP to 0.4 V (*versus* Ag/AgCl) with a scan rate of 1 mV s⁻¹ using a Jaisle IMP 88 PC potentiostat.

Photocurrent spectra were acquired at an applied potential of 0.5 V (*versus* Ag/AgCl) in 1 M KOH recorded with 10 nm steps in the range of 300–700 nm using an Oriel 6365 150 W Xe-lamp equipped with a Oriel Cornerstone 7400 1/8 m monochromator. Incident photocurrent conversion efficiencies (IPCE) were calculated by $IPCE = (1240i_{ph})/(\lambda I_{light})$, where i_{ph} is the photocurrent density (mA cm⁻²), λ is the incident light wavelength (nm), and I_{light} (mW cm⁻²) is the intensity of light source at each wavelength. The Mott–Schottky curves were acquired with a Zahner IM6 potentiostat (Zahner Elektrik, Kronach, Germany). Measurements were obtained under dark conditions at a frequency of 500 Hz in 1 M KOH solution. A three-electrode configuration was used in the measurements, where the α -Fe₂O₃ electrode served as the working electrode (photoanode), a saturated Ag/AgCl as the reference electrode and a platinum foil as the counter electrode.

The measured potentials *versus* Ag/AgCl were converted to the reversible hydrogen electrode (RHE) scale following the Nernst equation:

$$E_{RHE} = E_{Ag/AgCl} + 0.059 \text{ pH} + E^{\circ}_{Ag/AgCl} \quad (1)$$

where E_{RHE} is the converted potential *versus* RHE, $E^{\circ}_{Ag/AgCl} = 0.1976$ at 25 °C, and $E_{Ag/AgCl}$ is the experimentally measured potential against the Ag/AgCl reference.

The time stability of the hematite photoanodes and the concentration of produced hydrogen were tested by the following setup. Two chamber glass cell with 1 M NaOH water solution working as the electrolyte was used. Anode and cathode chambers were separated by the glass frit to prevent mixing of the electrolyte. Potential of +1.5 V *versus* RHE was applied to the sample (working electrode). Platinum sheet was used as the counter electrode. Each chamber was bubbled by argon gas (1 mL/min) separately. The illuminated area of the photoanode was 2 cm². The chambers were open to air by glass capillary to avoid mixing with air. Output gas from cathode chamber (platinum counter electrode) was analyzed by gas chromatograph (Master, Dani) equipped with plot column (Rt-Msieve 5A, Restek) and mTCD detector (Vici).

The solar-to-hydrogen efficiency η_{STH} was calculated according to the eq 2:

$$\eta_{STH(\%)} = J_p[(1.23 - V_{app})/I_0] \quad (2)$$

where J_p is the photocurrent density (in mA/cm²), I_0 is the intensity of incident light (in mW/cm²), and V_{app} is the applied potential to the photoanode in (V *versus* RHE).

Conflict of Interest: The authors declare no competing financial interest.

Supporting Information Available: Schematic arrangement of HIPIMS deposition system, extended X-ray diffraction spectra, Raman spectra, model polarized Raman spectra, additional AFM and SEM images, XPS full survey spectra, current density *versus* applied potential curves, optical properties, values of Mössbauer hyperfine parameters, and recently reported PEC water splitting current density values. The Supporting Information is available free of charge on the ACS Publications website at DOI: 10.1021/acsnano.5b01740.

Acknowledgment. The authors acknowledge support from the Ministry of Education, Youth and Sports of the Czech Republic (LO1305), the Grant Agency of the Czech Republic (project 13-29241P) and from the Ministry of Education, Youth and Sports of the Czech Republic (project LH12043).

REFERENCES AND NOTES

- Chu, S.; Majumdar, A. Opportunities and Challenges for a Sustainable Energy Future. *Nature* **2012**, *488*, 294–303.
- Walter, M. G.; Warren, E. L.; McKone, J. R.; Boettcher, S. W.; Mi, Q.; Santori, E. A.; Lewis, N. S. Solar Water Splitting Cells. *Chem. Rev.* **2010**, *110*, 6446–6473.
- Gratzel, M. Photoelectrochemical Cells. *Nature* **2001**, *404*, 338–344.
- Sivula, K.; Le Formal, F.; Grätzel, M. Solar Water Splitting: Progress Using Hematite (α -Fe₂O₃) Photoelectrodes. *ChemSusChem* **2011**, *4*, 432–449.
- Murphy, A. B.; Barnes, P. R. F.; Randeniya, L. K.; Plumb, I. C.; Grey, I. E.; Horne, M. D.; Glasscock, J. A. Efficiency of Solar Water Splitting Using Semiconductor Electrodes. *Int. J. Hydrogen Energy* **2006**, *31*, 1999–2017.
- Kim, J. Y.; Magesh, G.; Youn, D. H.; Jang, J.-W.; Kubota, J.; Domen, K.; Lee, J. S. Single-Crystalline, Wormlike Hematite Photoanodes for Efficient Solar Water Splitting. *Sci. Rep.* **2013**, *3*, 2681.
- Brillet, J.; Yum, J. H.; Cornuz, M.; Hisatomi, T.; Solarska, R.; Augustynski, J.; Grätzel, M.; Sivula, K. Highly Efficient Water Splitting by a Dual-Absorber Tandem cell. *Nat. Photonics* **2012**, *6*, 823–827.
- Liu, R.; Zheng, Z.; Spurgeon, J.; Yang, X. Enhanced Photoelectrochemical Water-Splitting Performance of Semiconductors by Surface Passivation layers. *Energy Environ. Sci.* **2014**, *7*, 2504–2517.
- Kment, S.; Hubicka, Z.; Krysa, J.; Sekora, D.; Zlamal, M.; Olejnicek, J.; Cada, M.; Ksirova, P.; Remes, Z.; Schmuki, P.; et al. On the Improvement of PEC Activity of Hematite Thin Films Deposited by High-Power Pulsed Magnetron Sputtering Method. *Appl. Catal., B* **2015**, *165*, 344–350.
- Ling, Y.; Wang, G.; Wheeler, D. A.; Zhang, J. Z.; Li, Y. Sn-Doped Hematite Nanostructures for Photoelectrochemical Water Splitting. *Nano Lett.* **2011**, *11*, 2119–2125.
- Morin, F. J. Electrical Properties of α -Fe₂O₃ and α -Fe₂O₃ Containing Titanium. *Phys. Rev.* **1951**, *83*, 1005–1010.
- Morin, F. J. Electrical Properties of α -Fe₂O₃. *Phys. Rev.* **1954**, *93*, 1195–1199.
- Rosso, K. M.; Smith, D. M. A.; Dupuis, M. An *ab Initio* Model of Electron Transport in Hematite (α -Fe₂O₃) Basal Planes. *J. Chem. Phys.* **2003**, *118*, 6455–6466.
- Iordanova, N.; Dupuis, M.; Rosso, K. M. Charge Transport in Metal Oxides: A Theoretical Study of Hematite α -Fe₂O₃. *J. Chem. Phys.* **2005**, *122*, 144305.
- Liao, P.; Toroker, M. C.; Carter, E. A. Electron Transport in Pure and Doped Hematite. *Nano Lett.* **2011**, *11*, 1775–1781.
- Bosman, A. J.; Vandaal, H. J. Small Polaron versus Band Conduction in Some Transition Metal Oxides. *Adv. Phys.* **1970**, *19*, 1–117.
- Goodenough, J. B. Metallic Oxides. *Prog. Solid State Chem.* **1971**, *5*, 145–399.
- Nakau, T. Electrical Conductivity of α -Fe₂O₃. *J. Phys. Soc. Jpn.* **1960**, *15*, 727.
- Cornuz, M.; Grätzel, M.; Sivula, K. Preferential Orientation in Hematite Films for Solar Hydrogen Production via Water Splitting. *Chem. Vap. Depos.* **2010**, *16*, 291–295.
- Helmersson, U.; Lattemann, M.; Bolmark, J.; Ehasarian, A. P.; Gudmundsson, J. T. Ionized Physical Vapor Deposition (IPVD): A Review of Technology and Applications. *Thin Solid Films* **2006**, *513*, 1–24.
- Fujimura, N.; Nishihara, T.; Goto, S.; Xu, J. F.; Ito, T. Control of Preferred Orientation for ZnO_x Films—Control of Self-Texture. *J. Cryst. Growth* **1993**, *130*, 269–279.
- Wan, D. Y.; Huang, F. Q.; Wang, Y. M.; Mou, X. L.; Xu, F. F. Highly Surface-Textured ZnO:Al Films Fabricated by Controlling the Nucleation and Growth Separately for Solar Cell Applications. *ACS Appl. Mater. Interfaces* **2010**, *2*, 2147–2152.
- Ehasarian, A. P.; Vetuska, A.; Gonzalvo, Y. A.; Safran, G.; Szekely, L.; Barna, P. B. Influence of High Power Impulse Magnetron Sputtering Plasma Ionization on the Microstructure of TiN Thin Films. *J. Appl. Phys.* **2011**, *109*, 104314.
- Sarakinos, K.; Alami, J.; Konstantinidis, S. High Power Pulsed Magnetron Sputtering: A Review on Scientific and Engineering State of the Art. *Surf. Coat. Technol.* **2010**, *204*, 1661–1684.
- Samuelsson, M.; Lundin, D.; Jensen, J.; Raadu, M. A.; Gudmundsson, J. T.; Helmersson, U. On the Film Density Using High Power Impulse Magnetron Sputtering. *Surf. Coat. Technol.* **2010**, *205*, 591–596.
- Patsalas, P.; Gravalidis, S.; Logothetidis, S. Surface Kinetics and Subplantation Phenomena Affecting the Texture, Morphology, Stress, and Growth Evolution of Titanium Nitride Films. *J. Appl. Phys.* **2004**, *96*, 6234–6246.
- Agura, H.; Suzuki, A.; Matsushita, T.; Aoki, T.; Okuda, M. Low Resistivity Transparent Conducting Al-Doped ZnO Films Prepared by Pulsed Laser Deposition. *Thin Solid Films* **2003**, *445*, 263–267.
- Bohlmarm, J.; Lattemann, M.; Gudmundsson, J. T.; Ehasarian, A. P.; Gonzalvo, Y. A.; Brenning, N.; Helmersson, U. The Ion Energy Distributions and Ion Flux Composition from a High Power Impulse Magnetron Sputtering Discharge. *Thin Solid Films* **2006**, *515*, 1522–1526.
- Kay, A.; Cesar, I.; Grätzel, M. New Benchmark for Water Photooxidation by Nanostructured α -Fe₂O₃ films. *J. Am. Chem. Soc.* **2006**, *128*, 15719–15721.
- Zhang, X.; Li, H.; Wang, S.; Fan, F. F.; Bard, J. A. Improvement of Hematite as Photocatalyst by Doping with Tantalum. *J. Phys. Chem. C* **2014**, *118*, 16842–16850.
- Liu, J.; Cai, Y. Y.; Tian, Z. F.; Ruan, G. S.; Ye, Y. X.; Liang, C. H.; Shao, G. S. Highly Oriented Ge-Doped Hematite Nano-sheet Arrays for Photoelectrochemical Water Oxidation. *Nano Energy* **2014**, *9*, 282–290.
- Bora, D. K.; Braun, A.; Erat, S.; Safonova, O.; Graule, T.; Constable, E. C. Evolution of Structural Properties of Iron Oxide Nano Particles during Temperature Treatment from 250 °C–900 °C: X-ray Diffraction and Fe K-Shell Pre-Edge X-ray Absorption Study. *Curr. Appl. Phys.* **2012**, *12*, 817–825.
- Wang, L.; Lee, C.-Y.; Schmuki, P. Solar Water Splitting: Preserving the Beneficial Small Feature Size in Porous α -Fe₂O₃ Photoelectrodes during Annealing. *J. Mater. Chem. A* **2013**, *1*, 212–215.
- Seki, M.; Yamahara, H.; Tabata, H. Enhanced Photocurrent in Rh-Substituted α -Fe₂O₃ Thin Films Grown by Pulsed Laser Deposition. *Appl. Phys. Express* **2012**, *5*, 115801.
- Munisso, M. C.; Zhu, W.; Pezzotti, G. Raman Tensor Analysis of Sapphire Single Crystal and Its Application to Define Crystallographic Orientation in Polycrystalline Alumina. *Phys. Status Solidi B* **2009**, *246*, 1893–1900.
- Cesar, I.; Sivula, K.; Kay, A.; Zboril, R.; Grätzel, M. Influence of Feature Size, Film Thickness, and Silicon Doping on the Performance of Nanostructured Hematite Photoanodes for Solar Water Splitting. *J. Phys. Chem. C* **2009**, *113*, 772–782.
- Frydrych, J.; Machala, L.; Tucek, J.; Siskova, K.; Filip, J.; Pechousek, J.; Safarova, K.; Vondracek, M.; Seo, J. H.; Schneeweiss, O.; et al. Facile Fabrication of Tin-Doped Hematite Photoelectrodes—Effect of Doping on Magnetic Properties and Performance for Light-Induced Water Splitting. *J. Mater. Chem.* **2012**, *22*, 23232–23239.
- Kment, S.; Hubicka, Z.; Krysa, J.; Olejnicek, J.; Cada, M.; Gregora, I.; Zlamal, M.; Brunclikova, M.; Remes, Z.; Liu, N.; et al. High-Power Pulsed Plasma Deposition of Hematite Photoanode for PEC Water Splitting. *Catal. Today* **2014**, *230*, 8–14.
- Le Formal, F.; Gratzel, M.; Sivula, K. Controlling Photoactivity in Ultrathin Hematite Films for Solar Water-Splitting. *Adv. Funct. Mater.* **2010**, *20*, 1099–1107.
- Zhang, Y.; Jiang, S.; Song, W.; Zhou, P.; Ji, H.; Ma, W.; Hao, W.; Chen, Ch.; Zhao, J. Nonmetal P-doped Hematite Photoanode with Enhanced Electron Mobility and High Water Oxidation Activity. *Energy Environ. Sci.* **2015**, *8*, 1231–1236.
- Steier, L.; Herraiz-Cardona, I.; Gimenez, S.; Fabregat-Santiago, F.; Bisquert, J.; Tilley, S. D.; Gratzel, M. Understanding the Role of Underlayers and Overlayers in Thin Film Hematite Photoanodes. *Adv. Funct. Mater.* **2014**, *24*, 7681–7688.

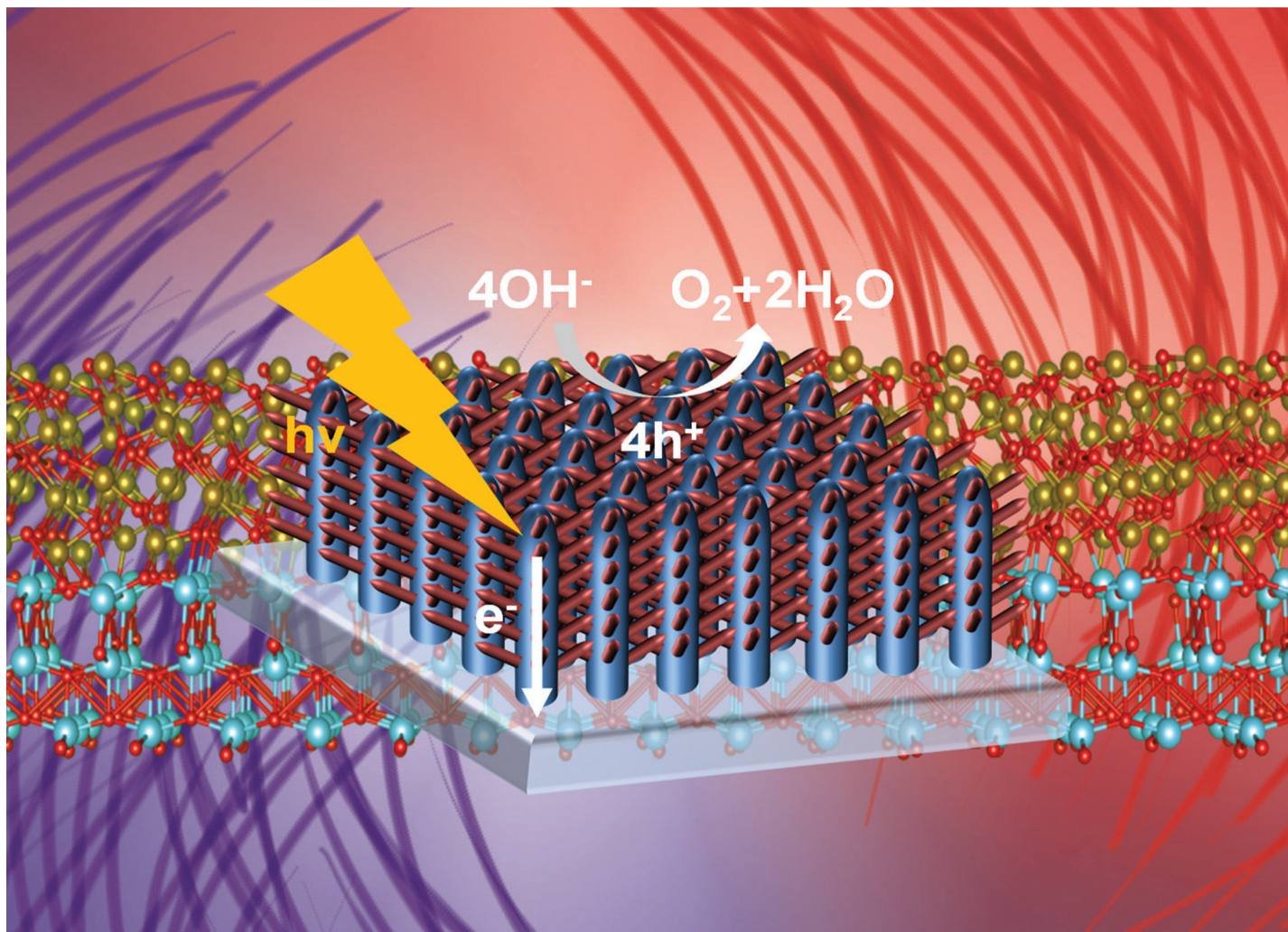
42. Kim, D. W.; Riha, S. C.; DeMarco, E. J.; Martinson, A. B. F.; Farha, O. K.; Hupp, J. T. Green Lighting Photo Electrochemical Oxidation of Water by Iron Oxide. *ACS Nano* **2014**, *8*, 12199–12207.
43. Young, K. M. H.; Hamann, T. W. Enhanced Photocatalytic Water Oxidation Efficiency with Ni(OH)₂ Catalysts Deposited on α -Fe₂O₃ via ALD. *Chem. Commun.* **2014**, *50*, 8727.
44. Zandi, O.; Beardslee, J. A.; Hamann, T. Substrate Dependent Water Splitting with Ultrathin α -Fe₂O₃ Electrodes. *J. Phys. Chem. C* **2014**, *118*, 16494–16503.
45. Kilner, J.; Skinner, S.; Irvine, S.; Edwards, P. *Functional Materials for Sustainable Energy Applications*; Woodhead Publishing Ltd.: New York, NY, 2012.
46. Peter, L. M.; Wijayantha, K. G. U. Photoelectrochemical Water Splitting at Semiconductor Electrodes: Fundamental Problems and New Perspectives. *ChemPhysChem* **2014**, *15*, 1983–1995.
47. Dotan, H.; Sivula, K.; Gratzel, M.; Rothschild, A.; Warren, S. C. Probing the Photoelectrochemical Properties of Hematite (α -Fe₂O₃) Electrodes Using Hydrogen Peroxide as a Hole Scavenger. *Energy Environ. Sci.* **2011**, *4*, 958–964.
48. Sivula, K. Metal Oxide Photoelectrodes for Solar Fuel Production, Surface Traps, and Catalysis. *J. Phys. Chem. Lett.* **2013**, *4*, 1624–1633.
49. Kment, S.; Kluson, P.; Hubicka, Z.; Krysa, J.; Cada, M.; Gregora, I.; Deyneka, A.; Zaboava, H.; Jastrabik, L. Double Hollow Cathode Plasma Jet-Low Temperature Method for the TiO_{2-x}N_x Photoresponding Films. *Electrochim. Acta* **2010**, *55*, 1548–1556.
50. Hisatomi, T.; Dotan, H.; Stefik, M.; Sivula, K.; Rothschild, A.; Gratzel, M.; Mathews, N. Enhancement in the Performance of Ultrathin Hematite Photoanode for Water Splitting by an Oxide Underlayer. *Adv. Mater.* **2012**, *24*, 2699–2702.
51. Klahr, B. M.; Martinson, A. B. F.; Hamann, T. W. Photoelectrochemical Investigation of Ultrathin Film Iron Oxide Solar Cells Prepared by Atomic Layer Deposition. *Langmuir* **2011**, *27*, 461–468.
52. Schrebler, R.; Ballesteros, L. A.; Gomez, H.; Grez, P.; Cordova, R.; Munoz, E.; Schrebler, R.; Ramos-Barrado, J. R.; Dalchiele, A. Electrochemically Grown Self-Organized Hematite Nanotube Arrays for Photoelectrochemical Water Splitting. *J. Electrochem. Soc.* **2014**, *161*, H903–H908.
53. Zandi, O.; Hamann, T. W. Enhanced Water Splitting Efficiency Through Selective Surface State Removal. *J. Phys. Chem. Lett.* **2014**, *5*, 1522–1526.

Appendix [A12]

α -Fe₂O₃/TiO₂ 3D hierarchical nanostructures for enhanced photoelectrochemical water splitting

H. Han, F. Riboni, F. Karlicky, **S. Kment**, A. Goswami, P. Sudharag, J. Yoo, L. Wang, O. Tomanec, M. Petr, O. Haderka, Ch. Terashima, A. Fujishima, P. Schmuki, R. Zboril

Nanoscale 9, 134-142, 2017

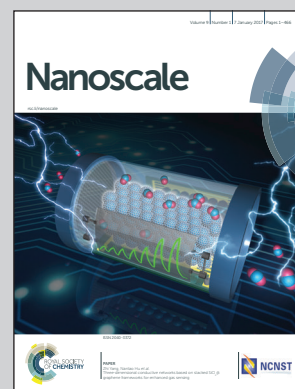


Showcasing research from the Regional Center of Advanced Technologies and Materials, Palacky University, Czech Republic, Institute for Surface Science and Corrosion, Friedrich-Alexander University, Germany, and Photocatalysis International Research Center, Tokyo University of Science, Japan.

α -Fe₂O₃/TiO₂ 3D hierarchical nanostructures for enhanced photoelectrochemical water splitting

We have explored the effect of hierarchical heterostructure α -Fe₂O₃/TiO₂ nanotube morphology on photoelectrochemical water splitting by synthesizing varying morphologies of electrodes. Our electrode design strategy with systematic analysis offers significant insight into the controlling factors and can potentially be applied to other electrodes for PEC water splitting.

As featured in:



See Patrik Schmuki, Radek Zboril et al., *Nanoscale*, 2017, 9, 134.



rsc.li/nanoscale

Registered charity number: 207890



Cite this: *Nanoscale*, 2017, 9, 134

α -Fe₂O₃/TiO₂ 3D hierarchical nanostructures for enhanced photoelectrochemical water splitting†

Hyungkyu Han,^a Francesca Riboni,^b Frantisek Karlicky,^{a,c} Stepan Kment,^a Anandarup Goswami,^a Pitchaimuthu Sudhagar,^d Jeongeun Yoo,^b Lei Wang,^b Ondrej Tomanec,^a Martin Petr,^a Ondrej Haderka,^a Chiaki Terashima,^d Akira Fujishima,^d Patrik Schmuki*^{b,e} and Radek Zboril*^a

We report the fabrication of 3D hierarchical hetero-nanostructures composed of thin α -Fe₂O₃ nanoflakes branched on TiO₂ nanotubes. The novel α -Fe₂O₃/TiO₂ hierarchical nanostructures, synthesized on FTO through a multi-step hydrothermal process, exhibit enhanced performances in photo-electrochemical water splitting and in the photocatalytic degradation of an organic dye, with respect to pure TiO₂ nanotubes. An enhanced separation of photogenerated charge carriers is here proposed as the main factor for the observed photo-activities: electrons photogenerated in TiO₂ are efficiently collected at FTO, while holes are transferred to the α -Fe₂O₃ nanobranches that serve as charge mediators to the electrolyte. The morphology of α -Fe₂O₃ that varies from ultrathin nanoflakes to nanorod/nanofiber structures depending on the Fe precursor concentration was shown to have a significant impact on the photo-induced activity of the α -Fe₂O₃/TiO₂ composites. In particular, it is shown that for an optimized photo-electrochemical structure, a combination of critical factors should be achieved such as (i) TiO₂ light absorption and photo-activation vs. α -Fe₂O₃-induced shadowing effect and (ii) the availability of free TiO₂ surface vs. α -Fe₂O₃-coated surface. Finally, theoretical analysis, based on DFT calculations, confirmed the optical properties experimentally determined for the α -Fe₂O₃/TiO₂ hierarchical nanostructures. We anticipate that this new multi-step hydrothermal process can be a blueprint for the design and development of other hierarchical heterogeneous metal oxide electrodes suitable for photo-electrochemical applications.

Received 31st August 2016,
Accepted 1st November 2016

DOI: 10.1039/c6nr06908h

www.rsc.org/nanoscale

Introduction

Titanium dioxide (TiO₂) represents the most widely investigated semiconductor photocatalyst for *e.g.*, photo-oxidation reactions, photo-electrochemical (PEC) water splitting, and anodes in solar cells.^{1–3} The intrinsic key advantages of TiO₂ are well established (*i.e.*, it is cheap, abundant, environmentally friendly, and corrosion-resistant); however, (i) its

relatively large optical band-gap (3.0–3.2 eV) that hampers the use of sunlight to promote photoreactions, (ii) the high rate of recombination of photogenerated electron/hole (e⁻/h⁺) pairs and (iii) the low rate of charge transfer to reactants still represent serious challenges to be overcome. In particular, the generation of long-living and spatially separated charge carriers appears of primary importance. For this, one-dimensional arrangements of TiO₂ (*e.g.*, in the form of nanotubes, nanorods and nanofibers grown on a conductive substrate) are beneficial, since the orthogonal carrier separation in these structures is facilitated by the preferential percolation of e⁻ to the back contact and the parallel accumulation of h⁺ at the semiconductor/electrolyte interface.^{3,4} Also, combining TiO₂ with another semiconductor with a suitable band gap and band offsets has been often proposed as a valuable approach to achieve larger e⁻/h⁺ separation.⁵ In a composite photocatalytic system, the intimate contact between two or more semiconductors promotes the mobility of charge carriers between the different components, enhancing their separation and, hence, the photoactivity of the composite system compared to that of the single counterparts. Owing to the availability of a large number of semiconducting materials, an ade-

^aRegional Centre of Advanced Technologies and Materials, Department of Physical Chemistry, Faculty of Science, Palacky University, Slechtitelu 11, 783 71 Olomouc, Czech Republic. E-mail: radek.zboril@upol.cz

^bDepartment of Materials Science and Engineering, University of Erlangen-Nuremberg, Martensstrasse 7, D-91058 Erlangen, Germany

^cDepartment of Physics, Faculty of Science, University of Ostrava, 30. dubna 22, 701 03 Ostrava, Czech Republic

^dPhotocatalysis International Research Center, Research Institute for Science and Technology, Tokyo University of Science, 2641 Yamazaki, Noda, Chiba 278-8510, Japan

^eDepartment of Chemistry, Faculty of Science, King Abdulaziz University, P.O. Box 80203, Jeddah 21569, Saudi Arabia. E-mail: schmuki@www.uni-erlangen.de

† Electronic supplementary information (ESI) available. See DOI: 10.1039/c6nr06908h

quate selection in terms of band alignment (specific for different reactions) is clearly required. For instance, coupling TiO₂ and α -Fe₂O₃ nanostructures is, in principle, a promising approach for increasing the efficiency of titania for PEC applications, as long as TiO₂ is the light absorbing material and the major contributor to the photogeneration of charge carriers. With this arrangement, from the mechanistic point of view, electrons photopromoted in TiO₂ are transferred to the back contact (also, taking advantage of the long electron diffusion length typical of TiO₂ nanotubes, *i.e.*, ~ 20 μm),⁶ while holes can be trapped in the valence band of α -Fe₂O₃, which that lies at a more negative potential than that of TiO₂, and easily conveyed to the electrolyte. This spatial separation reduces e^-/h^+ recombination probability and leads to an enhanced performance of the α -Fe₂O₃/TiO₂ composite materials. Clearly, an essential prerequisite, often overlooked in the literature,⁷ is that the hematite layer does not shade the TiO₂ nanostructures and allows its photoactivation. Indeed, if e^- are photo-generated in α -Fe₂O₃, they cannot be transferred to TiO₂ due to an unfavorable conduction band alignment of the two oxides. Hence, in this regard, also a fine tuning of the composite nanoarchitecture has to be achieved to avoid the undesired detrimental effect of classic α -Fe₂O₃/TiO₂ heterostructures.⁷

We report the fabrication of α -Fe₂O₃/TiO₂ 3D hierarchical nanostructures, with a specific composition and tailored architecture that meet all the aforementioned requirements. Aligned TiO₂ nanotubes of a pure anatase composition (highly desired for PEC applications) were grown on FTO glass *via* a sacrificial template-based hydrothermal approach; their surface was modified with α -Fe₂O₃ nanostructures, whose morphologies varied from thin nanoflakes to nanorods, to surface agglomerates, depending on the amount of Fe precursor. This approach was shown to have a significant impact on the photo-induced activity of the α -Fe₂O₃/TiO₂ composites. In particular, under specific preparation conditions, α -Fe₂O₃ nanobranches were grown perpendicular to the TiO₂ NTs, leaving the TiO₂ surface partially exposed to both the electrolyte and light; this configuration provided a twofold increase in the PEC and photocatalytic (PC) activities of bare TiO₂ nanotubes, since it enabled an optimized light absorption and photoactivation of TiO₂, coupled with an efficient collection of photo-generated charges (*i.e.*, e^- to FTO and h^+ to α -Fe₂O₃). We

believe that the experimental control over the morphology and related light-promoted activity of α -Fe₂O₃/TiO₂ hierarchical materials can be extended to other semiconductor oxide combinations and be adopted as a defined strategy to improve their performance in photo-electrochemical reactions.

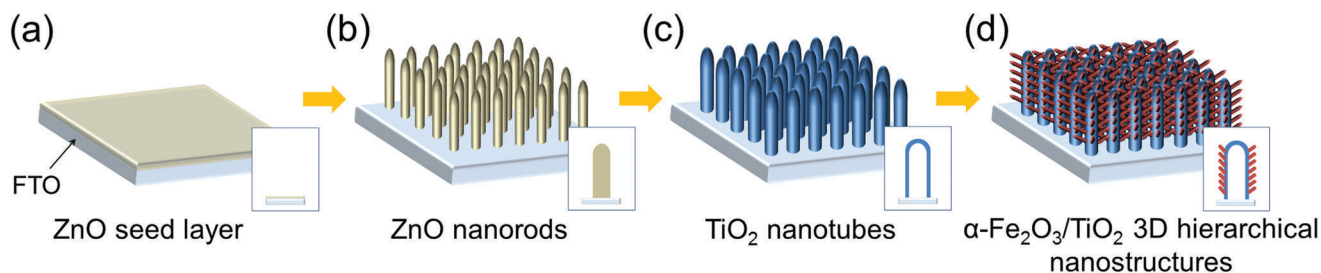
Experimental

Fabrication of TiO₂ nanotube arrays on FTO glass

The procedure for the fabrication of α -Fe₂O₃/TiO₂ 3D hierarchical nanostructures is reported in Scheme 1. First, a thin ZnO seed layer was deposited on FTO glass by spin coating a 20 mM zinc acetate dihydrate [Zn(O₂CCH₃)₂·2H₂O] aqueous solution at 4000 rpm for 35 s. ZnO nanorods (NRs), which served as a sacrificial template for the growth of TiO₂ nanotubes (see below), were grown hydrothermally from the seed layer at 85 °C for 10 h starting from an aqueous solution of 25 mM zinc nitrate hexahydrate [Zn(NO₃)₂·6H₂O] and 25 mM hexamethylenetetramine (C₆H₁₂N₄). The as-synthesized ZnO NRs on FTO were immersed for 30 min in an aqueous solution containing 75 mM ammonium hexafluorotitanate [(NH₄)₂TiF₆] and 0.2 M boric acid (H₃BO₃). (NH₄)₂TiF₆ hydrolyzes to TiO_x on the individual ZnO nanorods, and the ZnO template is simultaneously dissolved in the acidic environment (where acids are produced by (NH₄)₂TiF₆ hydrolysis and H₃BO₃). To achieve a complete removal of residual ZnO inside the TiO₂ tubes, the NT arrays were immersed in a 0.5 M boric acid solution for 1 h. Finally, the samples were rinsed with DI water and annealed in Ar at 500 °C for 30 min.^{8,9}

Preparation of Fe₂O₃/TiO₂ hierarchical nanotube arrays on FTO glass

TiO₂ nanotubes on FTO glass were immersed for 2 days at room temperature in an aqueous solution of iron(III) nitrate nonahydrate [Fe(NO₃)₃·9H₂O], containing different amounts of Fe precursor (0.01–0.05 M). The samples, immersed in the iron(III) solution, were then transferred to an oven and kept at 90 °C for 2 h. Finally, they were rinsed with DI water and annealed in air at 450 °C for 2 h to convert amorphous FeOOH into crystalline α -Fe₂O₃.



Scheme 1 Schematic representation of the α -Fe₂O₃/TiO₂ 3D hierarchical nanostructure formation process: (a) first a ZnO seed layer is deposited on FTO and (b) ZnO nanorods are grown; (c) afterwards, TiO₂ nanotubes are grown *via* a hydrothermal process and the ZnO sacrificial template is simultaneously dissolved; (d) finally, α -Fe₂O₃ nanobranches are formed on the surface of the TiO₂ NTs.

Following the same procedure, pure α -Fe₂O₃ layers were also grown directly on FTO glass from 0.01–0.05 M precursor solutions.

Characterization

For the morphological characterization of the α -Fe₂O₃/TiO₂ hierarchical composites, a field-emission scanning electron microscope (FE-SEM, Hitachi S4800, Japan), a field-emission transmission electron microscope (FE-TEM, JEOL 2010F) and a high-resolution transmission electron microscope (HRTEM, FEI TITAN G2 60-300) were employed. The crystallographic properties of the materials were analyzed by X-ray diffraction (XRD) performed with an X'pert Philips MPD (equipped with a Panalytical X'celerator detector), using iron-filtered Co-K α radiation ($\lambda = 1.78901$ Å, 40 kV, 30 mA). XRD data were then converted to Cu-K α radiation, according to the relationships in $(\theta_{\text{Cu}}) = (\lambda_{\text{Cu}}/\lambda_{\text{Co}}) \times \sin(\theta_{\text{Co}})$, where λ_{Cu} is 1.54056 Å. X-ray photoelectron spectroscopy (XPS, PHI 5600, US) was used to characterize the chemical composition of the materials.

Photo-electrochemical characterization and photocatalytic activity

The photo-electrochemical experiments were carried out in a three-electrode configuration, under simulated AM 1.5G (100 mW cm⁻²) illumination provided by a solar simulator (150 W Xe with optical filter). TiO₂ and α -Fe₂O₃/TiO₂ NT electrodes served as photoanodes, an Ag/AgCl (3 M KCl) as the reference electrode, and a platinum foil as the counter electrode. 1 M NaOH aqueous solution was used as the electrolyte, and the solution was bubbled with N₂ for 30 min prior to measurements. Photocurrent *versus* voltage (*I*-*V*) characteristics were recorded by scanning the potential from -0.8 to 1.3 V (*vs.* Ag/AgCl (3 M KCl)) with a scan rate of 10 mV s⁻¹ using a Series 300 Potentiostat/Galvanostat/ZRA potentiostat. Photocurrent transients for the TiO₂ and Fe₂O₃/TiO₂ NT electrodes were measured at +0.26 V (*vs.* Ag/AgCl (3 M KCl)) in 1 M NaOH.

Electrochemical impedance was measured in a Princeton Applied Research potentiostat (PARSTAT 2273). The frequency was varied in the 1 MHz–1 mHz range, with a potential amplitude of 10 mV. The measurements were carried out in a three-electrode configuration, with Pt serving as the counter electrode and Ag/AgCl as the reference electrode, at +0.26 V (*vs.* Ag/AgCl (3 M KCl)) and under simulated AM 1.5G (100 mW cm⁻²) illumination provided by a solar simulator (150 W Xe with an optical filter). 1 M NaOH was used as the electrolyte.

The photocatalytic degradation of Rhodamine B (RhB) was carried out in a 5 mL quartz cuvette filled with a 1 mM dye solution. A 300 W Xe lamp, equipped with an AM 1.5G filter, was used as an irradiation source and the degradation of RhB was monitored with a Lambda XLS – Perkin Elmer spectrophotometer measuring the decrease in the intensity of the dye main absorption band ($\lambda = 554$ nm) from samples withdrawn from the photoreactor every 30 min. Overall, each photodegradation experiment lasted for 2 h.

Theoretical analysis

We performed electronic structure calculations using a density functional theory (DFT) corrected by an additional Hubbard-like term (DFT+U). For modeling bulk anatase TiO₂ and bulk α -Fe₂O₃ hematite, the experimental lattice constants $a_1 = 3.785$ Å and $c_1 = 9.514$ Å (tetragonal unit cell)¹⁰ and $a_2 = 5.0355$ Å and $c_2 = 13.7471$ Å (rhombohedral unit cell)¹¹ were used, respectively. We used the Perdew–Burke–Ernzerhof (PBE)¹² generalized gradient approximation (GGA) to DFT and we selected the effective on-site Coulomb interaction parameters $U = 7.5$ eV for Ti atoms and $U = 4.3$ eV for Fe atoms. This choice provides good agreement with the band gaps of bulk TiO₂ and bulk α -Fe₂O₃ (Fig. S1†). We also created the corresponding layers. The predicted dominant growth face of the α -Fe₂O₃ surface is the (0001) surface. Therefore, following ref. 13, we used a single-iron terminated (0001) layer. For simplicity, we used an oxygen terminated (001) TiO₂ anatase layer, following ref. 14. Because of the lattice mismatch between α -Fe₂O₃ (0001) and TiO₂ (001) surfaces, it was necessary to introduce a larger computational supercell for simulating the α -Fe₂O₃ (0001)/TiO₂ (001) interface. Within all those computed by using the Cell Match utility,¹⁵ the 15.14 Å \times 38.04 Å supercell with 142 atoms (36 Fe, 86 O, 20 Ti) was selected – the thickness of the layer was in some cases reduced to 81 atoms (18 Fe, 51 O, 12 Ti).

All the DFT+U calculations were performed using the VASP code¹⁶ with the PAW formalism.¹⁷ For the initial bulk calculations, the first Brillouin zones were sampled by 10 \times 10 \times 4 *k*-points. For surface calculations, 10 \times 10 \times 2 and 7 \times 7 \times 1 *k*-points were used for TiO₂ (001) and α -Fe₂O₃ (0001), respectively, and the atomic positions were relaxed until the change in forces was less than 10⁻² eV Å⁻¹. Finally, for the large supercell of TiO₂/Fe₂O₃ interfaces, 2 \times 1 \times 2 *k*-points were used and atomic positions were relaxed until the change in energy was less than 10⁻³ eV. A cut-off energy of 300 eV was applied together with normal accuracy of VASP. The optical absorption spectrum corresponded to the imaginary part of the dielectric function $\epsilon(\omega)$. A Gaussian broadening of 50 meV and 128 sampling points were used for the dielectric function.

Results and discussion

Materials characterization

Scheme 1 represents the procedure for growing α -Fe₂O₃-branched TiO₂ nanotubes (Fe₂O₃/TiO₂ NTs) on FTO glass. In detail, upon the deposition of a ZnO seed layer (a), ZnO NRs are hydrothermally grown on the seeded substrate (b) and subsequently converted to TiO₂ NTs *via* a liquid-phase deposition, with the simultaneous dissolution of the ZnO backbone, *i.e.*, the sacrificial template (c). Due to the lattice mismatch between FTO and ZnO, the seeding procedure is crucial as it overcomes the high-energy nucleation step typical of hydrothermal methods based on a crystal nucleation-growth sequence.¹⁸ According to previous studies, the selective etching of the ZnO NR template may be ascribed to fluoroboric

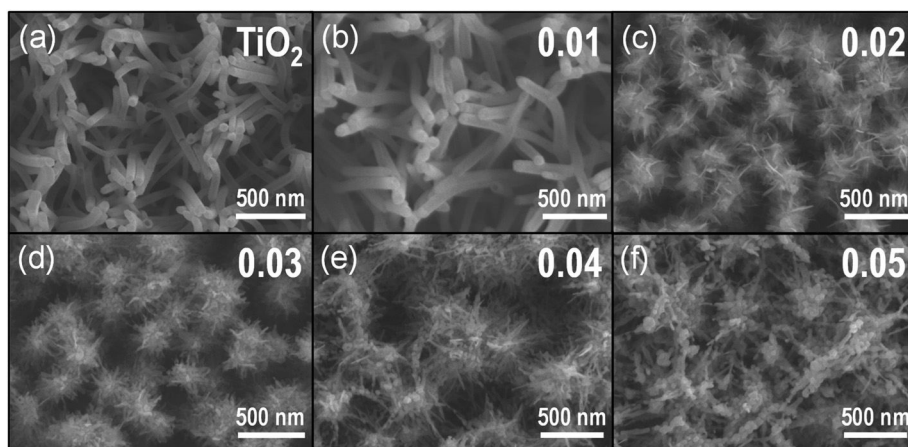


Fig. 1 Top view SEM images of (a) TiO_2 NTs and (b–f) $\alpha\text{-Fe}_2\text{O}_3/\text{TiO}_2$ NT composites prepared from $\text{Fe}(\text{III})$ solutions with different hematite precursor concentrations (*i.e.*, 0.01–0.05 M).

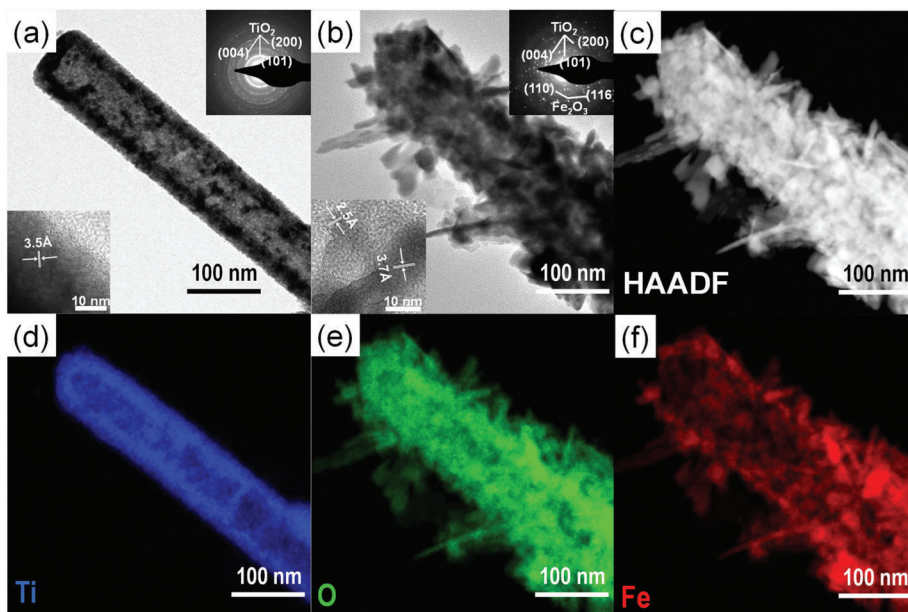


Fig. 2 (a) TEM image of TiO_2 NTs; insets: HRTEM image (lower corner) and the corresponding SAED pattern (upper corner). (b) TEM image of 0.02 $\text{Fe}_2\text{O}_3/\text{TiO}_2$ NTs; insets: HRTEM image (lower corner) and the corresponding SAED pattern (upper corner). (c) HAADF image of 0.02 $\text{Fe}_2\text{O}_3/\text{TiO}_2$ NTs. (d–f) Ti, O and Fe elemental mapping of the 0.02 $\text{Fe}_2\text{O}_3/\text{TiO}_2$ NT sample.

acid (HBF_4) formed in solution from the Ti-precursor hydrolysis in combination with H_3BO_3 .⁸ SEM images (Fig. 1a, S2 and S3(a)†) show that vertically aligned TiO_2 nanotubes ($\sim 1.5 \mu\text{m}$ in thickness and with a $\sim 80 \text{ nm}$ diameter) are formed well anchored on the FTO substrate. TEM and selected-area electron diffraction (Fig. 2(a)) confirm that, upon annealing, amorphous TiO_2 is converted into crystalline anatase. The NTs exhibit $\sim 20 \text{ nm}$ thick walls and a lattice fringe $d = 3.5 \text{ \AA}$ (inset of Fig. 2(a)) that is assigned to the interplanar distance of the (101) plane of anatase. This is also consistent with the XRD results showing a full anatase phase composition for pure TiO_2 NTs (Fig. 3(a)). Finally, evidence for the formation of pure

TiO_2 NTs on FTO glass is also provided by energy-dispersive X-ray (EDX) analysis (Fig. S4†), where only the peaks corresponding to Ti, O and Sn (from the FTO support) can be observed.

Immersion of TiO_2 NTs in the $\text{Fe}(\text{NO}_3)_3$ solution at $90 \text{ }^\circ\text{C}$ results in the seeding and growth of FeOOH -branches on TiO_2 NTs, that is, under optimized conditions the surface of TiO_2 nanotubes is active for FeOOH nucleation (Scheme 1(d)). Different concentrations of Fe-precursor were investigated (0.01–0.05 M) that correspondingly led to different nanoarchitectures (*i.e.*, from a homogeneous thin layer to dense and packed nanobranches/agglomerates); annealing at $450 \text{ }^\circ\text{C}$ in

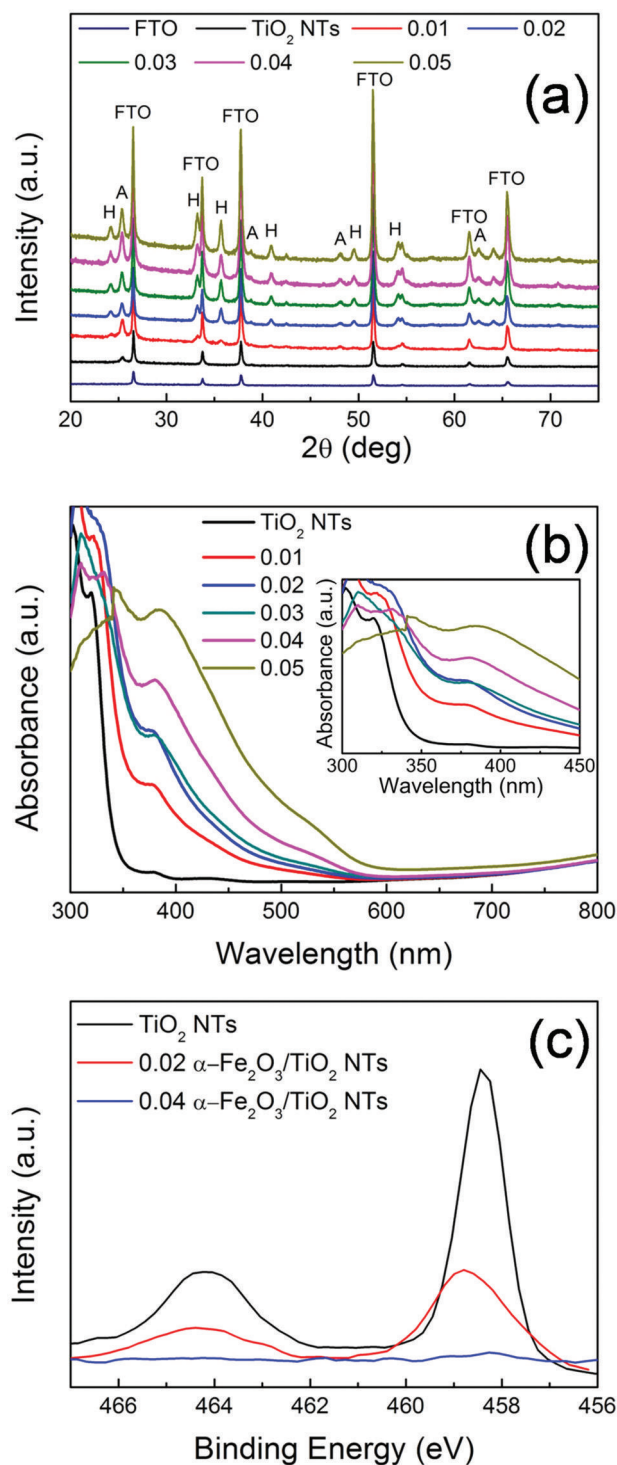


Fig. 3 (a) XRD of TiO_2 NTs and $\alpha\text{-Fe}_2\text{O}_3/\text{TiO}_2$ NT composites; A = anatase reflections, H = hematite reflections. (b) UV-vis absorption spectra of TiO_2 NTs and $\alpha\text{-Fe}_2\text{O}_3/\text{TiO}_2$ NT composites; the inset shows the absorption characteristics of the samples in the 300–450 nm wavelength region. (c) XPS spectra of TiO_2 NTs, 0.02 and 0.04 $\text{Fe}_2\text{O}_3/\text{TiO}_2$ NT composites. In (a, b) 0.01–0.05 labels indicate the different concentrations of the starting $\text{Fe}(\text{III})$ precursor solutions.

Table 1 Diameter and length of $\alpha\text{-Fe}_2\text{O}_3$ nanobranches grown on TiO_2 NTs from $\text{Fe}(\text{III})$ solutions with different hematite precursor concentrations (*i.e.*, 0.01–0.05 M)

$[\text{Fe}(\text{NO}_3)_3]$ (M)	d (nm)	Length (nm)
0.01	n/a	~10 (shell)
0.02	8–10	30–140
0.03	20–30	60–140
0.04	40–50	80–250
0.05	30–50	80–280

air for 2 h converted the initially amorphous FeOOH into crystalline $\alpha\text{-Fe}_2\text{O}_3$. Table 1 summarizes the diameter and length of the $\alpha\text{-Fe}_2\text{O}_3$ nanostructures, as a function of the $\text{Fe}(\text{NO}_3)_3$ solution concentration. Except for the 0.01 $\text{Fe}_2\text{O}_3/\text{TiO}_2$ sample that exhibits a limited thickening of the TiO_2 tube walls consistent with the formation of a conformal hematite shell layer (Fig. 1(b)), in all the other cases, a 3D-hierarchical $\alpha\text{-Fe}_2\text{O}_3/\text{TiO}_2$ composite is formed (Fig. 1, S2, S3† and Scheme 1(d)). In detail, for the 0.02 $\text{Fe}_2\text{O}_3/\text{TiO}_2$ sample, short $\alpha\text{-Fe}_2\text{O}_3$ nanobranches ($d \sim 10$ nm, $l \sim 30\text{--}140$ nm) grow on the TiO_2 NT surface; a further increase in the precursor concentration results instead in longer and more densely packed nanobranches. The observed trend suggests that the thin FeOOH conformal layer that forms on TiO_2 tubes at very low precursor concentrations acts as a seed layer for the growth of hierarchical nanostructures promoted by a larger amount of Fe^{3+} ions in solution.

However, in contrast to the formation of energy-minimized structures (*i.e.*, the nanobranches) for 0.02–0.04 M $\text{Fe}(\text{NO}_3)_3$ solutions, when the iron precursor concentration exceeds the optimum (*i.e.*, for $[\text{Fe}(\text{NO}_3)_3] > 0.04$ M), the Fe^{3+} species adsorbed on the surface of TiO_2 NTs tend to aggregate and promote the formation of iron oxide-based clusters (see for instance the ~ 300 nm long aggregates for the 0.05 M $\text{Fe}(\text{NO}_3)_3$ solution in Fig. 1(f), S2 and S3(f)†).

The formation of surface aggregates is certainly to be avoided in heterocomposite materials for light-induced applications where the core structure (in this case, the TiO_2 nanotubes) is the major photoactive semiconductor (see below). HRTEM, exemplarily shown for the 0.02 $\text{Fe}_2\text{O}_3/\text{TiO}_2$ sample (Fig. 2(b)), confirms (i) the formation of a 3D- $\text{Fe}_2\text{O}_3/\text{TiO}_2$ nanobranch architecture and (ii) the conversion of amorphous FeOOH into crystalline $\alpha\text{-Fe}_2\text{O}_3$ hematite, upon adequate annealing. In line with this, the distance between adjacent lattice fringes ($d = 2.5$ Å and $d = 3.7$ Å) in the $\alpha\text{-Fe}_2\text{O}_3$ nanobranches can be assigned to the interplanar distance of the (110) and (012) planes of hematite, respectively (inset of Fig. 2(b)).^{19–21}

HAADF image and EDX elemental mapping (Fig. 2(c–f)) clearly show a TiO_2 nanotube-backbone with $\alpha\text{-Fe}_2\text{O}_3$ dendritic nanostructures and also confirm the formation of a heterocomposite material where Ti, O and Fe co-exist. In this regard, experimental evidence is also provided by means of Auger Electron Spectroscopy (AES) horizontal mapping across the

α -Fe₂O₃/TiO₂ layers, performed for the different Fe-precursor solutions. As shown by the concentration scans of Ti, O and Fe superimposed on the original SEM image of the 0.02 Fe₂O₃/TiO₂ sample (Fig. S5†), iron concentration peaks in the outer-shell and extends up to \sim 60 nm from the TiO₂ NT walls; correspondingly, titanium concentration is higher in the core, while oxygen is homogeneously distributed within the inner and outer layers, in line with the formation of two distinct oxides that is, Fe₂O₃ and TiO₂. These observations on the morphology and chemical composition of 0.02 Fe₂O₃/TiO₂ also hold for the other Fe-precursor concentrations; see, for instance, HAADF images and AES horizontal mapping of 0.01 and 0.03 Fe₂O₃/TiO₂ in Fig. S6 and S7,† respectively. In particular, the horizontal mapping of 0.01 Fe₂O₃/TiO₂ shows a lower amount of α -Fe₂O₃ and, most importantly, a \sim 10 nm thick hematite layer that covers the TiO₂ inner backbone (Fig. S6(g)†).

XRD patterns of the different heterocomposites are reported in Fig. 3. Aside from the reflections assigned to FTO (*i.e.*, SnO₂ cassiterite – see also Fig. S8†), all the other peaks belong to TiO₂ (A) and α -Fe₂O₃ (H). Typically, TiO₂ nanostructures grown *via* the hydrothermal method on FTO are mainly composed of rutile phase²² due to a favorable matching between rutile and cassiterite crystal lattices.²³ Here, contrary to this expectation and in line with TEM (Fig. 2a), pure anatase TiO₂ nanotubes were obtained (main reflections at $2\theta \sim 25.4^\circ$), most likely due to the presence of the ZnO sacrificial template that is dissolved during the tubes formation and that seemingly prevents TiO₂ preferential seeding in the form of rutile.⁹

Besides the low-intensity peaks (*e.g.*, $2\theta \sim 25^\circ$) corresponding to the (012) plane, the most intense diffraction peaks of α -Fe₂O₃ (*i.e.*, $2\theta \sim 34^\circ$ and 36°) correspond to the (104) and (110) planes, respectively. This, combined with TEM analysis (Fig. 2b), confirms the polycrystalline nature of the film.^{24,25} It is noteworthy that the (110) orientation of hematite, with its surface termination dominated by Fe(III) ions features a high conductivity.^{24–26} In addition, the prevalence of the (110) reflection indicates a strong preferential orientation growth of hematite with the [110] axis vertical to the substrate.

Both aspects are beneficial for facilitating charge transfer from the substrate (TiO₂) to the electrolyte, through α -Fe₂O₃, in view of photo-electrochemical applications (see discussion below).²⁷

The optical properties of the investigated samples were determined by UV-vis spectroscopy (Fig. 3(b)). All the samples show (or partially maintain) the typical absorption edge at *ca.* 380–400 nm owing to TiO₂ optical band-gap excitation (\sim 3.2 eV). In addition, the α -Fe₂O₃/TiO₂ heterocomposites also exhibit absorption features that extend to the visible region. In particular, the light absorption onset around 600 nm corresponds to the \sim 2.1 eV optical band-gap of hematite.^{24,28} This reflects the bi-composite nature of the 0.01–0.05 Fe₂O₃/TiO₂ samples that exhibit the distinct optical properties of both oxide counterparts and indicates a *tandem* contribution of the two components to the photo-electrochemical activity of the investigated materials.

The effect of the bi-composite nature on the optical properties of α -Fe₂O₃/TiO₂ is also confirmed by theoretical calculations performed on a TiO₂ layer and an α -Fe₂O₃/TiO₂ heterocomposite layer, modeled as in Fig. 4a and S9.† DFT calculations revealed an absorption edge for pure anatase (001) TiO₂ in the 380–400 nm range (black curve in Fig. 4b), while the presence of α -Fe₂O₃ on TiO₂ significantly extends the simulated optical absorption to the visible range (red curve in Fig. 4b). This trend is qualitatively in line with the experimental absorption spectra reported in Fig. 3b.

Moreover, a more careful analysis of the experimental UV-vis absorption characteristics (inset of Fig. 3b) points out that the structure decorated with the largest amount of α -Fe₂O₃ (*i.e.*, 0.05 M Fe(NO₃)₃) shows the lowest absorbance in the 300–350 nm range, where typically TiO₂ absorbs photons. This is attributed to a “shading effect”, *i.e.*, the increase in the density and thickness of hematite-based nanobranches optically shades the underneath structure, so that TiO₂ is actually exposed to a lower specific photon flux and light absorption consequently drops. The shading effect on TiO₂, that may also physically prevent the percolation of the electro-

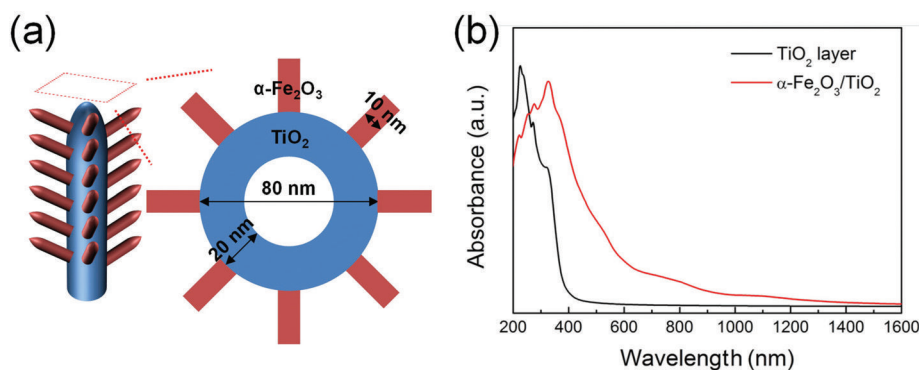


Fig. 4 (a) Schematic representation of α -Fe₂O₃ nanobranches on TiO₂ nanotubes. (b) Optical absorption spectra of pure TiO₂ and α -Fe₂O₃/TiO₂ composite, determined through a DFT+U method.

lyte to the tube surface with a detrimental consequence on the PEC activity, is also confirmed by XPS (Fig. 3(c)): for pure TiO₂ and α -Fe₂O₃/TiO₂ heterocomposites with a small amount of hematite (e.g., 0.02 Fe₂O₃/TiO₂), the typical Ti 2p_{3/2} and 2p_{1/2} peaks were observed at ca. 458 eV and 464 eV, respectively; however, for larger nominal amounts of α -Fe₂O₃, the intensity of Ti 2p features drastically drops (it nearly vanishes for 0.04 Fe₂O₃/TiO₂). This further supports the observation that, with increasing iron precursor concentration, longer and denser hematite nanobranches grow on the supporting TiO₂ tubes, eventually leading to clusters formation that act as a barrier for both light penetration and electrolyte percolation.

Therefore, for an optimized photo-electrochemical structure, a combination of critical factors should be achieved such as (i) TiO₂ light absorption and photoactivation vs. α -Fe₂O₃-

induced shadowing effect and (ii) the availability of free TiO₂ surface vs. α -Fe₂O₃-coated surface.

Photo-electrochemical and photocatalytic activities

Fig. 5(a) provides the current–potential curves of the electrodes under AM 1.5G illumination in 1 M NaOH electrolyte. All the electrodes exhibit a photocurrent onset at ca. -0.8 V vs. Ag/AgCl that is typical of TiO₂. This demonstrates that, in α -Fe₂O₃/TiO₂ composites, TiO₂ absorbs UV photons and generates charge carriers. Due to the natural upwards band bending (enhanced by the applied bias) in TiO₂ tube walls, electrons photopromoted in the conduction band are collected in the center of material and, through a preferential orthogonal pathway, are transported along the tubes to the back-contact (FTO). By contrast, positive holes migrate from the valence band of TiO₂ to that of α -Fe₂O₃ that mediates their transfer to the environment, i.e., the electro-

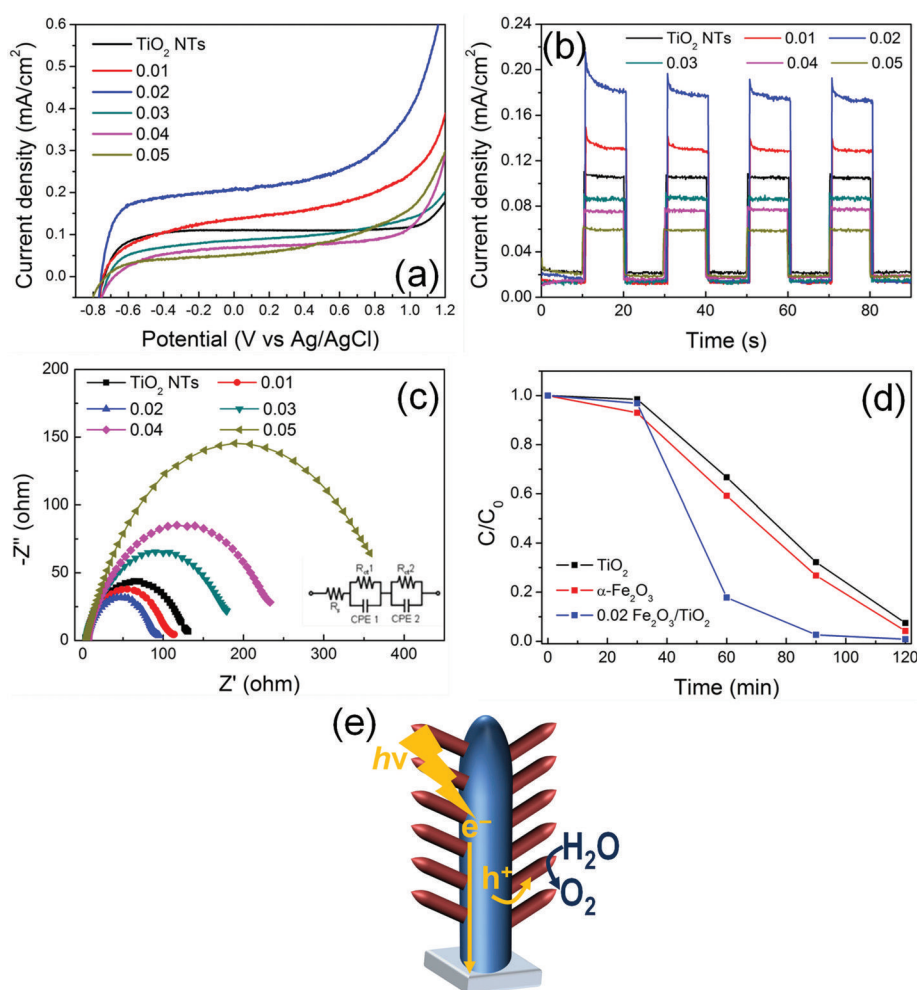


Fig. 5 (a) Current–potential characteristics of TiO₂ and α -Fe₂O₃/TiO₂ NT layers on FTO, measured in 1 M NaOH at 10 mV s⁻¹ scan rate, under AM 1.5G illumination. (b) Photo-transient characteristics of TiO₂ and α -Fe₂O₃/TiO₂ NT layers on FTO, measured in 1 M NaOH at +0.26 V vs. Ag/AgCl and under AM 1.5G chopped light illumination. (c) Nyquist plots of electrochemical impedance measurements of TiO₂ and α -Fe₂O₃/TiO₂ NT layers; inset: equivalent circuit for the nanotube structures. (d) Photocatalytic degradation of RhB ($C_0 = 1$ mM) performed under AM 1.5G illumination. (e) Sketch of the proposed charge photogeneration and transfer mechanism in the optimized 0.02 α -Fe₂O₃/TiO₂ NT layer.

lyte, and decreases the probability of charge recombination.^{29,30} A sketch of the proposed mechanism is reported in Fig. 5(e). An increase in photocurrent density is indeed observed for the composite materials, with respect to plain TiO₂ NTs.

The beneficial effect of combining the two oxides is observed with the composite heterostructures decorated with a relatively low amount of hematite (*i.e.*, with a ~10–30 nm thick Fe₂O₃ layer). In particular, the 0.02 Fe₂O₃/TiO₂ sample provides an optimized arrangement that leads to the highest photocurrent; moreover, Fig. S10† shows that the photo-electrode features an adequate stability, for continuous illumination under AM 1.5G simulated sunlight at 0.8 V *vs.* Ag/AgCl for extended times.

The same relative trend is also observed in transient photo-response measurements (Fig. 5(b)). All the transients have a similar shape and exhibit an initial decay of photocurrent, particularly evident for the Fe₂O₃-modified TiO₂ electrodes. This indicates that beneficial charge carrier separation is enabled in the system, with hematite that works as a hole-transfer mediator (from TiO₂) to the electrolyte. Nevertheless, also a minor contribution of α -Fe₂O₃ as an active photocatalyst should be considered.

In addition, *I*-*V* and photo-transient characteristics of pure α -Fe₂O₃ layers (Fig. S11†) confirmed that hematite suffers from a low PEC ability compared to both pure TiO₂ and Fe₂O₃/TiO₂ arrays. The photocurrent enhancement (*i.e.*, *ca.* 4 \times) can be attributed to the Fe₂O₃/TiO₂ heterojunction, which reduces electron-hole recombination by enhancing photogenerated charge carrier separation.

Typically, the formation of titania/hematite core/shell heterocomposites is reported to limit the performance of TiO₂ in photo-electrochemical applications. This stems from the fact that, in most common configurations, a hematite layer is grown/deposited over TiO₂ and usually shades the core, hence preventing TiO₂ surface reactive sites from absorbing light.⁷ Instead, the observed enhanced PEC performance of the heterocomposite materials is here attributed to the dendritic nanostructure which simultaneously exposes the TiO₂ nanotubes to the AM 1.5G-filtered irradiation, enabling the photo-generation of charges also in the supporting tubes, and efficiently separates e⁻ and h⁺ while minimizing the distance that photogenerated holes have to diffuse through to reach the electrolyte.²⁴ Moreover, the α -Fe₂O₃ 1D nanobranches grow directly connected to the TiO₂ NTs (that is, no polymers or binders were used in the reported procedure). This configuration not only provides a preferential direction for hole diffusion from TiO₂ with no extra-layers to be tunneled, but is also compatible with the short diffusion length of holes that typically affects both TiO₂ (*i.e.*, *ca.* 10 nm) and α -Fe₂O₃ (*i.e.*, 2–4 nm).³¹ Finally, the directional electron flow along the axial direction of the 1D TiO₂ NTs is further beneficial in view of reducing the probability of electron-hole recombination since it promotes the collection of negative charges at FTO.

The Electrochemical Impedance Spectroscopy (EIS) results show that the charge transfer resistance (R_{ct}) in the low-frequency zone correlates with the photocurrent responses (Fig. 5c). Indeed, the 0.02 α -Fe₂O₃/TiO₂ sample exhibits the

lowest R_{ct} value not only compared to pure TiO₂ nanotubes and pure α -Fe₂O₃ thin layers (Fig. S12†), but also compared to all the other investigated α -Fe₂O₃/TiO₂ hierarchical heterostructures, thus confirming that thin α -Fe₂O₃ nanoflakes branched on TiO₂ nanotubes and the formation of a Fe₂O₃/TiO₂ heterojunction facilitate charge transfer and, hence, are beneficial in terms of the PEC performance.³²

The proposed mechanism is also supported by the results of Rhodamine B (RhB) photodegradation (Fig. 5(d)). The experiment was performed with a pure TiO₂ NT sample, a pure α -Fe₂O₃ layer and a 0.02 Fe₂O₃/TiO₂ sample. RhB is typically decomposed by the \cdot OH radicals generated in solution through the reaction of photogenerated charges with water.³³ In line with an enhanced e⁻/h⁺ separation and, hence, a more favorable holes injection into the solution, ~90% of the initial RhB was degraded within the first 60 min of irradiation with 0.02 Fe₂O₃/TiO₂, in contrast with ~30–40% RhB photo-degraded with the pure single oxides.

Conclusion

α -Fe₂O₃/TiO₂ 3D-hierarchical nanostructured materials that consist of vertically aligned TiO₂ nanotubes modified with different amounts of α -Fe₂O₃ nanoflakes were successfully fabricated on FTO glass *via* a multi-step hydrothermal approach. In contrast with previous studies that reported on the detrimental effect of α -Fe₂O₃ on the TiO₂ PEC activity, the here proposed α -Fe₂O₃/TiO₂ dendritic nanostructures provide an ideal architecture for (i) the optimized light absorption and activation of TiO₂ and (ii) a straightforward transfer of photogenerated charges, enabled by the direct connection of TiO₂ NTs with both the e⁻ collector (*i.e.*, FTO) and the h⁺ collector (*i.e.*, α -Fe₂O₃). The morphology of the α -Fe₂O₃ nanostructures that varies from ultra thin nanoflakes (for dilute Fe precursor solution) to nanorod/nanofiber structures (for higher Fe precursor concentration) was shown to have a significant impact on the photo-induced activity of the α -Fe₂O₃/TiO₂ composites. In particular, a two-times higher photocurrent density and faster photocatalytic degradation of RhB in aqueous solution were measured with the 0.02 α -Fe₂O₃/TiO₂ hierarchical nanocomposite. For larger hematite precursor concentrations, the decrease in the α -Fe₂O₃/TiO₂ PEC activity was attributed either to (i) the formation of hematite clusters – in this case, the short diffusion length of holes in α -Fe₂O₃ could no longer be overcome and charge carriers are more likely prone to recombine in TiO₂, or (ii) an α -Fe₂O₃ dense layer that blocks the active surface sites of TiO₂ and reduces the amount of photons available to promote e⁻/h⁺.

Follow-up studies may be beneficial in view of improving the light-promoted activity of the reported α -Fe₂O₃/TiO₂ hierarchical materials; however, this new multi-step hydrothermal process holds large potential as it can be finely tuned and adjusted also for the design and development of other hierarchical heterogeneous metal oxide electrodes with suitable photo-electrochemical characteristics.

Acknowledgements

The authors gratefully acknowledge the support by Project No. LO1305 and Project No. 8E15B009 of the Ministry of Education, Youth and Sports of the Czech Republic, Project No. 15-19705S of the Grant Agency of the Czech Republic, and the Research Infrastructure NanoEnviCz, supported by the Ministry of Education, Youth and Sports of the Czech Republic under Project No. LM2015073. The DFG, and the DFG cluster of excellence "Engineering of Advanced Materials", as well as DFG "funCOS" are also gratefully acknowledged for financial support.

References

- 1 A. L. Linsebigler, G. Lu and J. T. Yates Jr., *Chem. Rev.*, 1995, **95**(3), 735.
- 2 A. Fujishima, X. Zhang and D. a. Tryk, *Surf. Sci. Rep.*, 2008, **63**, 515.
- 3 K. Lee, A. Mazare and P. Schmuki, *Chem. Rev.*, 2014, **114**, 9385.
- 4 P. Roy, S. Berger and P. Schmuki, *Angew. Chem., Int. Ed.*, 2011, **50**, 2904.
- 5 M. Dahl, Y. Liu and Y. Yin, *Chem. Rev.*, 2014, **114**, 9853.
- 6 R. P. Lynch, A. Ghicov and P. Schmuki, *J. Electrochem. Soc.*, 2010, **157**(3), G76.
- 7 T. H. Jeon, W. Choi and H. Park, *J. Phys. Chem. C*, 2011, **115**(14), 7134.
- 8 C. Xu, P. H. Shin, L. Cao, J. Wu and D. Gao, *Chem. Mater.*, 2010, **22**(1), 143.
- 9 H. Han, T. Song, E. K. Lee, A. Devadoss, Y. Jeon, J. Ha, Y. C. Chung, Y. M. Choi, Y. G. Jung and U. Paik, *ACS Nano*, 2012, **6**(9), 8308.
- 10 J.-Y. Liao, B.-X. Lei, H.-Y. Chen, D.-B. Kuang and C.-Y. Su, *Energy Environ. Sci.*, 2012, **5**(2), 5750.
- 11 E. N. Maslen, V. a. Streltsov, N. R. Streltsova and N. Ishizawa, *Acta Crystallogr., Sect. B: Struct. Sci.*, 1994, **50**(4), 435.
- 12 J. P. Perdew, K. Burke and M. Ernzerhof, *Phys. Rev. Lett.*, 1996, **77**(18), 3865.
- 13 P. Liao and E. a. Carter, *Phys. Chem. Chem. Phys.*, 2011, **13**, 15189.
- 14 H. Han, T. Song, J.-Y. Bae, L. F. Nazar, H. Kim and U. Paik, *Energy Environ. Sci.*, 2011, **4**(11), 4532.
- 15 P. Lazic, *Comput. Phys. Commun.*, 2015, **197**, 324.
- 16 G. Kresse and J. Furthmüller, *Phys. Rev. B: Condens. Matter*, 1996, **54**(16), 11169.
- 17 G. Kresse and D. Joubert, *Phys. Rev. B: Condens. Matter*, 1999, **59**(3), 1758.
- 18 E. J. W. Crossland, N. Noel, V. Sivaram, T. Leijtens, J. a. Alexander-Webber and H. J. Snaith, *Nature*, 2013, **495**(7440), 215.
- 19 D. E. Janney, J. M. Cowley and P. R. Buseck, *Clays Clay Miner.*, 2000, **48**(1), 111.
- 20 S. Li, G. Qin, X. Meng, Y. Ren and L. Zuo, *J. Mater. Sci.*, 2013, **48**(17), 5744.
- 21 Y. Li, X. Wei, B. Zhu, H. Wang, Y. Tang, T. C. Sum and X. Chen, *Nanoscale*, 2016, **8**, 11284.
- 22 J. Xi, O. Wiranwetchayan, Q. Zhang, Z. Liang, Y. Sun and G. Cao, *J. Mater. Sci.: Mater. Electron.*, 2012, **23**(9), 1657.
- 23 W. H. Baur, *Acta Crystallogr.*, 1956, **9**(6), 515.
- 24 A. Kay, I. Cesar and M. Grätzel, *J. Am. Chem. Soc.*, 2006, **128**(49), 15714.
- 25 S. Kment, P. Schmuki, Z. Hubicka, L. Machala, R. Kirchgeorg, N. Liu, L. Wang, K. Lee, J. Olejnicek, M. Cada, I. Gregora and R. Zboril, *ACS Nano*, 2015, **9**(7), 7113.
- 26 X. Zhang, P. Klaver, R. van Santen, M. C. M. van de Sanden and A. Bieberle-Hütter, *J. Phys. Chem. C*, 2016, **120**(32), 18201.
- 27 Y. Fu, J. Chen and H. Zhang, *Chem. Phys. Lett.*, 2001, **350**(5–6), 491.
- 28 A. Duret and M. Grätzel, *J. Phys. Chem. B*, 2005, **109**(36), 17184.
- 29 S. J. a. Moniz, S. a. Shevlin, X. An, Z. X. Guo and J. Tang, *Chem. – Eur. J.*, 2014, **20**(47), 15571.
- 30 Z. Li, S. Feng, S. Liu, X. Li, L. Wang and W. Lu, *Nanoscale*, 2015, **7**(45), 19178.
- 31 L. Wang, C. Y. Lee and P. Schmuki, *Electrochem. Commun.*, 2014, **44**, 49.
- 32 L. Wang, N. T. Nguyen and P. Schmuki, *ChemSusChem*, 2016, **1**.
- 33 L. You-ji and C. Wei, *Catal. Sci. Technol.*, 2011, **1**(5), 802.